ADVANCED BIOMATERIALS AND SYSTEMS RELEASING BIOACTIVE AGENTS FOR PRECISE TISSUE REGENERATION

EDITED BY: Rui Guo, Zhengwei Mao and Gang Wu
PUBLISHED IN: Frontiers in Bioengineering and Biotechnology and
Frontiers in Materials

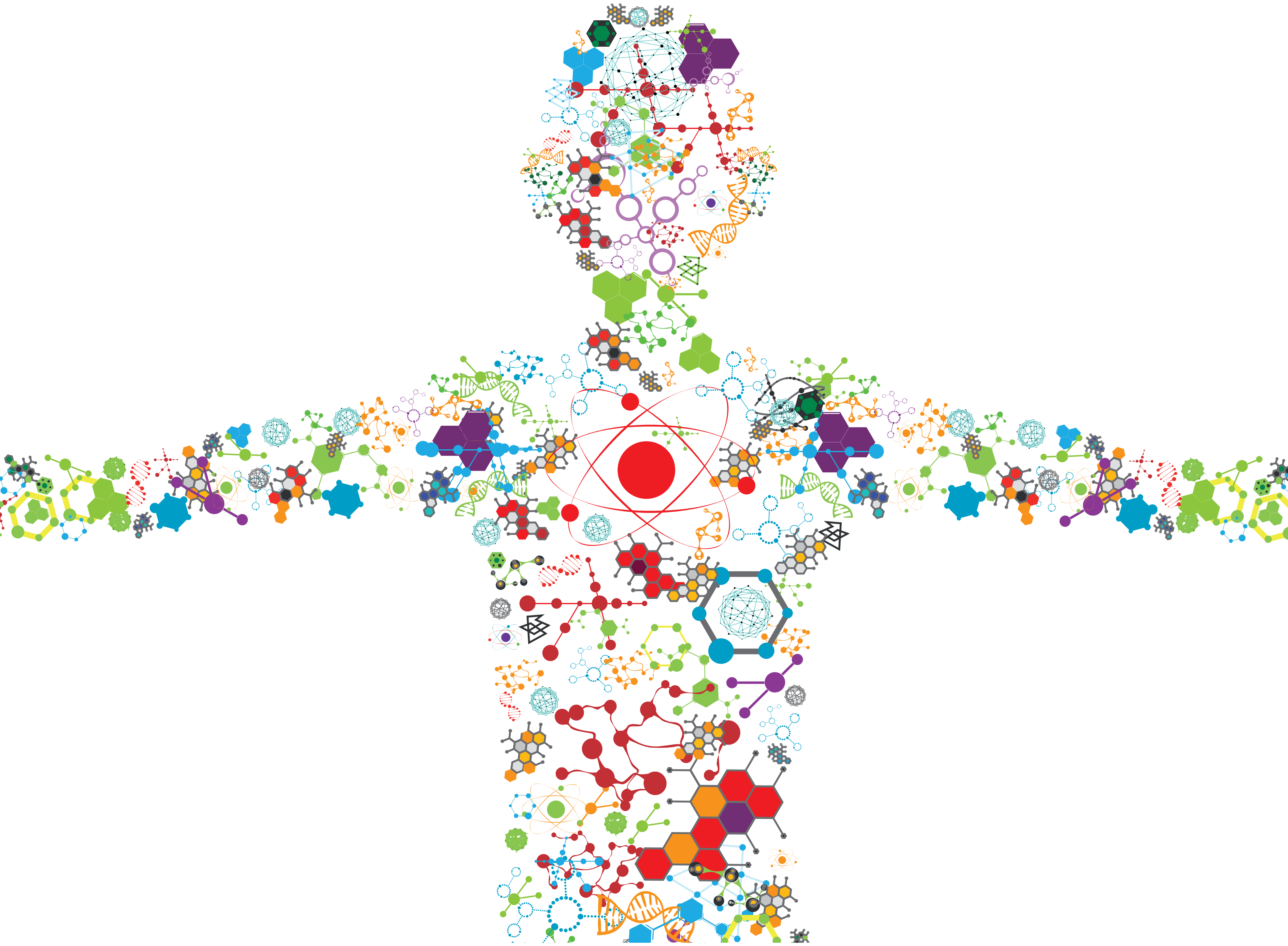

frontiers Research Topics

ISSN 1664-8714
ISBN 978-2-88971-536-7
DOI 10.3389/978-2-88971-536-7

About Frontiers

Frontiers is more than just an open-access publisher of scholarly articles: it is a pioneering approach to the world of academia, radically improving the way scholarly research is managed. The grand vision of Frontiers is a world where all people have an equal opportunity to seek, share and generate knowledge. Frontiers provides immediate and permanent online open access to all its publications, but this alone is not enough to realize our grand goals.

Frontiers Journal Series

The Frontiers Journal Series is a multi-tier and interdisciplinary set of open-access, online journals, promising a paradigm shift from the current review, selection and dissemination processes in academic publishing. All Frontiers journals are driven by researchers for researchers; therefore, they constitute a service to the scholarly community. At the same time, the Frontiers Journal Series operates on a revolutionary invention, the tiered publishing system, initially addressing specific communities of scholars, and gradually climbing up to broader public understanding, thus serving the interests of the lay society, too.

Dedication to Quality

Each Frontiers article is a landmark of the highest quality, thanks to genuinely collaborative interactions between authors and review editors, who include some of the world's best academicians. Research must be certified by peers before entering a stream of knowledge that may eventually reach the public - and shape society; therefore, Frontiers only applies the most rigorous and unbiased reviews.
Frontiers revolutionizes research publishing by freely delivering the most outstanding research, evaluated with no bias from both the academic and social point of view. By applying the most advanced information technologies, Frontiers is catapulting scholarly publishing into a new generation.

What are Frontiers Research Topics?

Frontiers Research Topics are very popular trademarks of the Frontiers Journals Series: they are collections of at least ten articles, all centered on a particular subject. With their unique mix of varied contributions from Original Research to Review Articles, Frontiers Research Topics unify the most influential researchers, the latest key findings and historical advances in a hot research area! Find out more on how to host your own Frontiers Research Topic or contribute to one as an author by contacting the Frontiers Editorial Office: frontiersin.org/about/contact

ADVANCED BIOMATERIALS AND SYSTEMS RELEASING BIOACTIVE AGENTS FOR PRECISE TISSUE REGENERATION

Topic Editors:
Rui Guo, Jinan University, China
Zhengwei Mao, Zhejiang University, China
Gang Wu, VU University Amsterdam, Netherlands

Citation: Guo, R., Mao, Z., Wu, G., eds. (2021). Advanced Biomaterials and Systems Releasing Bioactive Agents for Precise Tissue Regeneration.
Lausanne: Frontiers Media SA. doi: 10.3389/978-2-88971-536-7

Table of Contents

frontiers
in Bioengineering and Biotechnology

EDITORIAL
published: 08 September 2021
doi: 10.3389/fbioe.2021.763685

Editorial: Advanced Biomaterials and Systems Releasing Bioactive Agents for Precise Tissue Regeneration

Rui Guo[1] *and Gang Wu*[2,3]*

[1]Key Laboratory of Biomaterials of Guangdong Higher Education Institutes, Guangdong Provincial Engineering and Technological Research Centre for Drug Carrier Development, Department of Biomedical Engineering, Jinan University, Guangzhou, China, [2]Department of Oral and Maxillofacial Surgery/Pathology, Amsterdam UMC and Academic Center for Dentistry Amsterdam (ACTA), Vrije Universiteit Amsterdam (VU), Amsterdam Movement Science (AMS), Amsterdam, Netherlands, [3]Department of Oral Cell Biology, Academic Centre for Dentistry Amsterdam (ACTA), University of Amsterdam and Vrije Universiteit Amsterdam, Amsterdam, Netherlands

Keywords: biomaterials, tissue engineering, bioactive agent, bone regeneration, modification

Editorial on the Research Topic

Advanced Biomaterials and Systems Releasing Bioactive Agents for Precise Tissue Regeneration

To provide a scientific forum for the researchers in this field, we started this research topic—*Advanced Biomaterials and Systems Releasing Bioactive Agents for Precise Tissue Regeneration* in February 2020. Until now, there are two mini reviews, four reviews and 11 original research articles are published with about 100 authors involved. We hereby sincerely thank all the efforts and contributions of these excellent researchers to this successful research topic.

Bone regeneration is still one of the hottest topic in the field of tissue engineering with nine articles (one mini review, one review and seven original researches) published in this direction. These authors reported the functionalization of biomaterials with various types of bioactive agents, such as icaritin (naturally derived small molecule) and Ginsenoside Rg1, BMP-2 (recombinant proteineous growth factor), histatin-1 (naturally derived peptide), four chemical elements, such as silicon and copper, to significantly improve the bio-functions of biomaterials, such as osteoconductivity, osteoinductivity, and anti-bacterial properties. The biomaterials involve metallic implants and ceramic bone-defect-filling materials without or with the incorporation of organic phase to improve their properties, such as osteoconductivity and slow release of bioactive agents. In addition to the studies reporting the development of novel regenerative materials, Liu et al., also reported the incorporation of ultrasmall superparamagnetic iron oxide nanoparticles in bone grafts, which could facilitate the non-invasively monitor the biodegradation and remodeling of bone grafts after implantation. Furthermore, Li et al. also reported a simplified and effective method to create an experimental murine periodontitis model, which could be used to study the pathological mechanisms of periodontitis and developing potential periodontal tissue regeneration strategies. Apart from the original research articles, two reviews were also also published, which focused on smart hydrogel-based bioink/scaffolds for bone tissue regeneration and bioactive modification strategy to promote osseointegration in osteoporotic microenvironment, respectively.

Apart from bone tissue engineering, the authors also made excellent reports and reviews to summarize recent advances, provide monitoring method and novel reconstructive materials

Edited and reviewed by:
Hasan Uludag,
University of Alberta, Canada

Correspondence:
Gang Wu
g.wu@acta.nl

Specialty section:
This article was submitted to Biomaterials,
a section of the journal
Frontiers in Bioengineering and Biotechnology

Received: *24 August 2021*
Accepted: *26 August 2021*
Published: *08 September 2021*

Citation:
Guo R and Wu G (2021) Editorial: Advanced Biomaterials and Systems Releasing Bioactive Agents for Precise Tissue Regeneration .
Front. Bioeng. Biotechnol. 9:763685.
doi: 10.3389/fbioe.2021.763685

and alternative treatment options for diverse diseases, such as macular degeneration, gastric cancer, bile duct restoration, urethra, periphery nerve injury, and coronary artery disease. In addition to the above disease-targeting publications, there is still one review focusing on the synthesis, modification, characterization and medical applications of AuNPs.

In summary, this research topic covers many recent significant advances in bioactive agents-functionalized biomaterials with diversely targeting diseases, which make a good contribution to the progress of advanced biomaterials for precise tissue regeneration.

AUTHOR CONTRIBUTIONS

All authors listed have made a substantial, direct and intellectual contribution to the work, and approved it for publication.

FUNDING

GW acknowledges financial support from the grants from Key Research and Development Plan of Zhejiang Province (No. 2021C04013).

Conflict of Interest: The authors declare that the research was conducted in the absence of any commercial or financial relationships that could be construed as a potential conflict of interest.

frontiers
in Bioengineering and Biotechnology

ORIGINAL RESEARCH
published: 19 May 2020
doi: 10.3389/fbioe.2020.00462

Development of 3D-Printed Sulfated Chitosan Modified Bioresorbable Stents for Coronary Artery Disease

*Tianyang Qiu[1], Wei Jiang[2], Pei Yan[1], Li Jiao[1] and Xibin Wang[1]**

[1] Key Laboratory of Fundamental Science for Advanced Machining, Beijing Institute of Technology, Beijing, China, [2] School of Mechanical Engineering, Beijing Institute of Technology, Beijing, China

Bioresorbable polymeric stents have attracted great interest for coronary artery disease because they can provide mechanical support first and then disappear within a desired time period. The conventional manufacturing process is laser cutting, and generally they are fabricated from tubular prototypes produced by injection molding or melt extrusion. The aim of this study is to fabricate and characterize a novel bioresorbable polymeric stent for treatment of coronary artery disease. Polycaprolactone (PCL) is investigated as suitable material for biomedical stents. A rotary 3D printing method is developed to fabricate the polymeric stents. Surface modification of polymeric stent is performed by immobilization of 2-N, 6-O-sulfated chitosan (26SCS). Physical and chemical characterization results showed that the surface microstructure of 3D-pinted PCL stents can be influenced by 26SCS modification, but no significant difference was observed for their mechanical behavior. Biocompatibility assessment results indicated that PCL and S-PCL stents possess good compatibility with blood and cells, and 26SCS modification can enhance cell proliferation. These results suggest that 3D printed PCL stent can be a potential candidate for coronary artery disease by modification of sulfated chitosan (CS).

Keywords: bioresorbable stent, 3D printing, sulfated chitosan, mechanical property, biocompatibility

OPEN ACCESS

Edited by:
Rui Guo,
Jinan University, China

Reviewed by:
Yong He,
Zhejiang University, China
Haonan Li,
University of Nottingham Ningbo
China, China

Correspondence:
Xibin Wang
cutting0@bit.edu.cn

Specialty section:
This article was submitted to
Biomaterials,
a section of the journal
Frontiers in Bioengineering and
Biotechnology

Received: *29 February 2020*
Accepted: *21 April 2020*
Published: *19 May 2020*

Citation:
Qiu T, Jiang W, Yan P, Jiao L and Wang X (2020) Development of 3D-Printed Sulfated Chitosan Modified Bioresorbable Stents for Coronary Artery Disease. Front. Bioeng. Biotechnol. 8:462. doi: 10.3389/fbioe.2020.00462

INTRODUCTION

Coronary artery disease is a leading killer of human life in the world, and percutaneous coronary intervention (PCI) with stent implantation has become a standard treating method to restore the blood flow. Bioresorbable stents (BRSs) have attracted great attention as potential candidate in treatment of coronary artery disease, because they are made of bioresorbable materials that can dissolve or be absorbed in the human body, which can provide the mechanical support and then disappear without the occurrence of long-term complications (Waksman, 2006). However, there are still some challenges in BRSs technology, such as manufacturing technique and long-term biocompatibility.

Polycaprolactone (PCL) has become potential material candidate for medical application due to its good ductility, processing property, biodegradability, and biocompatibility. Generally, PCL has a long degradation time (2–3 years) due to the low crystallinity degree (Lakshmi and Cato, 2007). PCL has been widely applied in form of microspheres, nanospheres, and implants. The porous PCL-based scaffolds were widely investigated for bone tissue engineering, and *in vitro* safety and efficacy results showed that they had excellent mechanical properties, biocompatibility, and bioactivity (Mondrinos et al., 2006; Puppi et al., 2012; Khoshroo et al., 2016). Vurugonda et al. (2017) developed copolymer of poly-lactic acid (PLLA) and PCL stents for cardiovascular application. Results highlighted that the mechanical strength, degradation behavior, and drug release behavior of stents were significantly improved, while their samples were fabricated in tabular design which is not suitable for stent application. The braided PCL stents showed superior compression properties and recovery ability by incorporating PPDO monofilaments and annealing, but their degradation rates were attenuated under dynamic loading (Zhao et al., 2018, 2019). Kim et al. (2019) investigated drug-eluting PCL mesh network tubular stent for salivary gland disease. Results showed that their mechanical properties were improved by incorporating antibiotic particles, and a sustained drug release was observed. However, the elongation ratios of drug-eluting stents were dramatically decreased which may limit their expansion behavior.

Extensive research has been carried out to manufacture metallic stents by continuous or pulsed laser cutting, including 316LVM steel, magnesium alloy, and CoCr alloy (Raval et al., 2004; Demir et al., 2012; Demir and Previtali, 2017). Results showed that excellent geometries of stents were obtained, while the desired surface quality required selective process gas, acid pickling, and electrochemical polishing. Flege et al. (2012) first developed polymeric stents by selective laser melting technique. Results suggested that the as manufactured polymeric stents are biocompatible at interaction with human coronary artery smooth muscle cells. Guerra and Ciurana (2017) and Guerra A. J. et al. (2017b) introduced the application of fiber laser cutting on PCL stent manufacture, and addressed that the *in vitro* degradation of stent can be accelerated by increasing input energy density. Although laser cutting is capable to fabricate metallic or polymeric stents, there is still a challenge for manufacturing composite material stents. Moreover, laser cutting is a thermal process, which may cause thermal problems including heat affected zones, micro cracks, and dross deposition.

Recently, the 3D printing technique has been considered as an alternation in stent industry, due to its advantages in design personalization. Park et al. (2015) fabricated a helical drug-coated PCL stent by using 3D rapid prototyping, and good results were obtained from degradation test and animal experiments. 3D printing technique was also used to fabricate PCL-GR, PCL/PLA composite stents (Guerra A. et al., 2017a; Misra et al., 2017). Physical and chemical results showed that 3D printing process had strong effects on the dimensional precision but little influence on the material structure of stents (Guerra and Ciurana, 2018). Biological and mechanical analysis results showed good agreement with rigorous requirements of BRSs (Guerra et al., 2018a). These results also suggested that 3D printing process was highly suitable for manufacturing composite stents. To the best knowledge of author, the application of 3D printing process in stent manufacture is still in the early stage, and further research needs to be developed in terms of machining quality and biocompatibility assessment for BRSs.

Stents come in contact with blood, and incompatibility can cause short-term and long-term complications, such as vessel damage, restenosis, thrombosis, and inflammation (Hu et al., 2015). To overcome these problems, stent modified with chitosan (CS) may be a potential method to improve the bioactivity of cardiovascular remodeling and neointimal formation. CS is a common heparin-like polysaccharide, which has attracted enormous interest for several features, including hydrophilicity, biocompatibility, biodegradability, and bioactivity (Kumar, 2000). 2-*N*, 6-*O*-sulfated CS (26SCS) modified PLGA scaffolds have been widely investigated to improve the bioactivity of vascular endothelial growth factor (VEGF), heparin-binding epidermal growth factor (HB-EGF), bone morphology protein-2 (BMP-2) in angiogenesis, wound healing, and bone regeneration, and the desired results were obtained from morphological observation, releasing profiles, and bioactivity assessment (Kong et al., 2014; Yu et al., 2015, 2018; Peng et al., 2017). 26SCS modified PCL scaffolds were also studied as bone BMP-2 delivery vehicle to accelerate osteoinduction, and results highlighted that 26SCS modified PCL scaffold may enhance the cellular response, release behavior, and osteoinductive activity (Cao et al., 2017). 26SCS and PCL nanofibers were used to fabricate bioactive nanocomposite scaffolds, which can enhance osteoblast-like cells viability and attachment (Ghaee et al., 2017). Overall, blends of 26SCS and other polymers have shown potential improvement in mechanical properties, cell adhesion, and cell proliferation. Therefore, 26SCS modification shows great potential to enhance biocompatibility of cardiovascular stents. However, there has been little research focusing on the fabrication and characterization of 26SCS modified PCL stents.

In this study, 3D printing technique is used to produce PCL stent, and sulfated CS is used to modify the surface of PCL stent. Physical and chemical feature of sulfated CS is characterized by ^{13}C NMR test, elemental analysis, Fourier transform infrared spectroscopy (FTIR), and differential scanning calorimetry (DSC). The 3D-printed PCL and S-PCL stents are analyzed by scanning electron microscopy (SEM), mechanical test, degradation test, and biocompatibility assessment to investigate their morphology, mechanical property, blood, and cell compatibility. Moreover, the effects of sulfated CS on stent performance are presented by comparison between PCL and S-PCL stents.

MATERIALS AND METHODS

Materials

Commercially available PCL was purchased from Maya Reagent Co., Ltd. (Zhejiang, China). It is a biodegradable polymer with a glass transition temperature of −60°C and a melting temperature of 60°C. CS (95% deacetylated, Mw $10 \sim 20 \times 10^4$ Da) was purchased from Shanghai Macklin Biochemical Co., Ltd. (Shanghai, China). Chlorosulfonic acid ($HClSO_3$), N, N-dimethylformamide (DMF), and ethylenediamine (ED) were provided by Shanghai Aladdin Bio-Chem Technology Co., Ltd. (Shanghai, China). Sodium hydroxide (NaOH) and ethanol were provided by Guangzhou Chemical Reagent Factory (Guangzhou, China). Mouse fibroblasts (L929) were obtained from Guangzhou

Military Hospital. All cell-culture related reagents were obtained from Gibco (Grand Island, NY, United States).

Synthesis of Sulfated Chitosan

2-N, 6-O-sulfated chitosan was synthesized according to previous method (Zhou et al., 2009; Cao et al., 2014). In brief, sulfating reagent was prepared by adding 5 mL $HClSO_3$ dropwise to 20 mL DMF cooled at 0°C, and the mixture was stirred for stabilization. CS suspension was prepared by mixture with DMF and kept overnight. Sulfating reagent was added in the CS suspension for reaction, kept at 70°C for 4 h. At the end of reaction, the obtained mixture was cooled to room temperature, neutralized with NaOH, and precipitated with ethanol. The 26SCS powder was obtained after the precipitate was dissolved in deionized water, dialyzed, and lyophilized for 2 days.

Fabrication of PCL Stents

3D printing method was used to produce a tabular stent with a diameter of 3 mm and a length of 10 mm. As shown in **Figure 1**, the 3D printing machine is based on the electrospinning. The machine provides a maximum X axis translation of 50 mm, a needle temperature of 200°C, a pressure of 600 kPa, and a repositioning precision of 20 μm. The 3D printing process requires the conversion of PCL particles to filaments. The particles are melted in heating chamber, and then transferred to the extruder needle at pressure of 7 kPa. The produced filaments are deposited onto a controlled metallic rotatory mandrel under voltage of 4 kV.

Screening experiments were performed to optimize the processing parameters for 3D printing of PCL stents. 3D printing trajectory (as shown in **Figure 1A**) was applied to manufacture the stent uniformly. As a result, the stents were printed at 90°C needle temperature, 1000 mm/min translational velocity, and 1000 r/min rotational velocity (**Table 1**).

Sulfated Chitosan Immobilization on PCL Stents

According to the previously described method of Croll et al. (2004), 26SCS immobilization was carried out after the aminolysis of PCL stent (**Figure 2**). Specifically, PCL stents were soaked in ED with a concentration of 0.2 mol/L for 2 h at room temperature. Stents were washed by ice water for the desired time period, and then immersed in 26SCS solution with a concentration of 10 mg/mL for 4 h. Afterward, the aminated stents were washed repeatedly to remove the redundant 26SCS and dried in a vacuum oven for 24 h at 37 °C. Then the modified stents were stored in a desiccator for further use, and named as S-PCL stents. The unmodified stents were used as negative control, and named as PCL stents.

Characterization of 2-N, 6-O-Sulfated Chitosan

^{13}C NMR spectra were measured by instrument (AV III 500 MHz, Bruker, Germany), in deuterated acid solvent with a concentration of 5%. Elemental analysis (Vario EL Cube, Elementar, Germany) was performed to evaluate the mass proportion changes of carbon (C), nitrogen (N), hydrogen (H), and sulfur (S) in 26SCS. FTIR spectroscopy (Tensor 27, Bruker, Germany) was used to determine the structural changes of CS during the synthesis process. DSC (STA 449 F3, NETZSCH, Germany) was carried out to record the mass change of CS and 26SCS with the increase of temperature.

Characterization of PCL and S-PCL Stents

Morphological Observation of Stents

The 3D-printed PCL and S-PCL stents were morphologically characterized by SEM (S3400, Hitachi, Japan). The stents were sputter coated with gold and mounted on the instrument plate by conductive coating, and then the surface morphology was captured and analyzed with different magnifications at an accelerating voltage of 5 kV.

Mechanical Characterization of Stents

The mechanical properties were evaluated by lateral crush resistance tests on both PCL and S-PCL stents at room temperature. Five parallel tests were conducted for each group of stents on mechanical test instrument (ElectroForce 3220, Bose, United States). The stent was placed between two plates of testing machine, and compressed by controlling the constant displacement of the upper plate at a rate of 1 mm/min to a displacement of 2 mm. The load–displacement curve was measured directly from the instrument, and then the crush resistance stiffness was extracted.

In vitro Degradation Assessment

The dried S-PCL stents were incubated with phosphate buffered saline (PBS, ST476, Beyotime, China) at 37°C, after the initial weight was recorded. The volume ratio of PBS and sample is required to be at least 30:1, to make sure that samples are totally immersed in PBS solution. Lysozyme was added to accelerate the degradation of S-PCL stents. At predefined time intervals (t = 10, 20, 30, 40, 50, 60 days), samples were weighed to record their final weights. The degradation rate is calculated by the following equation:

$$Degradation\ (\%) = \frac{m_i - m_f}{m_i} \times 100\% \tag{1}$$

Where the m_{i} and m_{f} represent the initial weight and final weight, respectively.

Blood Compatibility Assessment

The extract tests were used to evaluate the biocompatibility of PCL and S-PCL stents, according to ISO 10993-12 (2012). The PCL and S-PCL stents were immersed in serum-free Dulbecco's modified Eagle's Medium (DMEM) and placed in a container at 37°C for 24 h to obtain the extracts of stents. Different concentrations of extracts were obtained by diluting the mother liquor with DMEM, and then stored at 4°C for further use.

In vitro Hemolysis Assay

In this study, fresh whole blood of male Sprague–Dawley rats was used to assess the blood compatibility of PCL and S-PCL stents. In

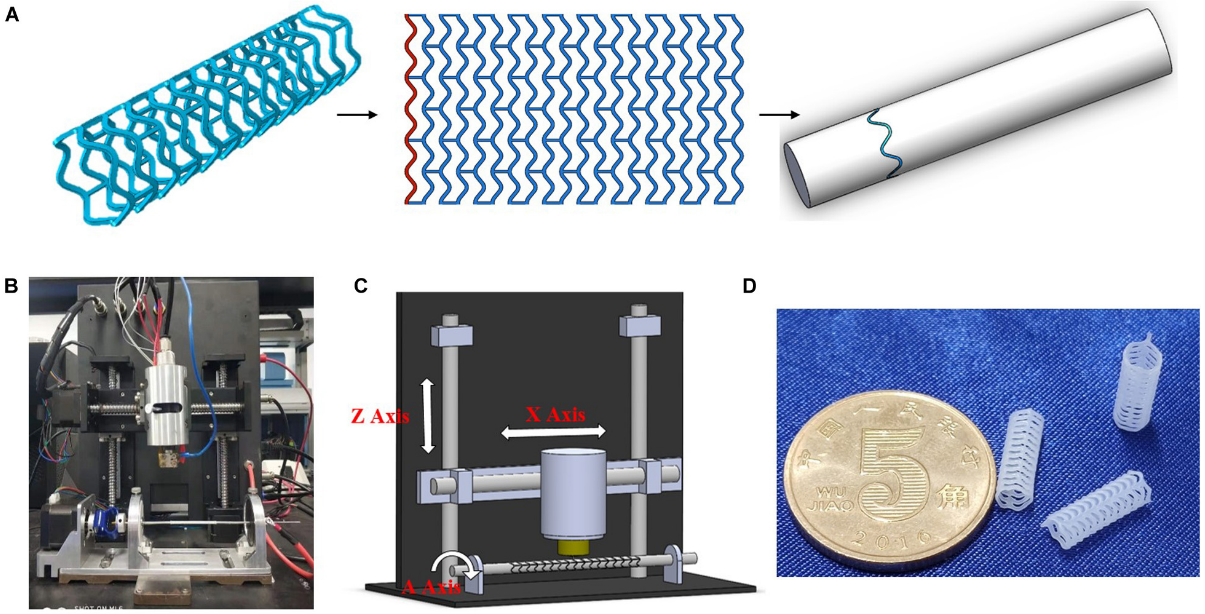

FIGURE 1 | 3D-printing trajectory strategy **(A)**, 3D printer machine **(B)**, machine methodology **(C)**, and 3D-printed PCL stents **(D)**.

TABLE 1 | Optimized processing parameters for 3D printing of PCL stents.

Stent	Z(mm)	V_T (mm/min)	V_R (r/min)	Mandrel diameter	Mandrel material
PCL	1.5	1000	1000	2.5	Brass

Z: distance between needle and mandrel, V_T: needle translational velocity, V_R: mandrel rotational velocity.

this assay, 4 mL extracts of PCL and S-PCL stents were incubated with 200 μL suspension of 16% red blood cells (RBCs) suspension in centrifuge tubes, respectively. While the deionized water and PBS were used as positive and negative controls, respectively. Three parallel tests were carried out for each group. Then the test samples were centrifuged under 1000 *g* for 5 min to collect the supernatant at predefined time points of 1, 3, 5, 8, 18, and 24 h. The optical density (OD) of RBCs was measured at 540 nm by microplate reader (MULTISKAN MK3, ThermoFisher).

Morphology of RBCs

The whole blood was centrifuged under 1000 *g* for 5 min, and then the RBCs were collected. The extracts of PCL and S-PCL stent (1 mL) were mixed and incubated with RBCs (50 μL) for 1 h at 37°C, centrifuge the mixture, and remove the supernatant to obtain RBCs. After washing RBCs with PBS, 4% paraformaldehyde was added to fix cells for 1 h. Subsequently, the fixed RBCs were dehydrated using ethanol of 70, 85, 95, and 100% in turn. Finally, the SEM was conducted to observe the morphology of RBCs.

Blood Coagulation Assay

The whole blood was centrifuged under 1000 *g* for 5 min, and the upper serum was collected for testing. The extracts of PCL and S-PCL stent (30 μL) were mixed and incubated with serum (270 μL) for 10 min at 37°C. The activated partial thromboplastin time (APTT) and prothrombin time (PT) were measured by automatic hematology analyzer (BC-5000, Mindray, Shenzhen). It should be noted that PBS was used as negative control in this assay.

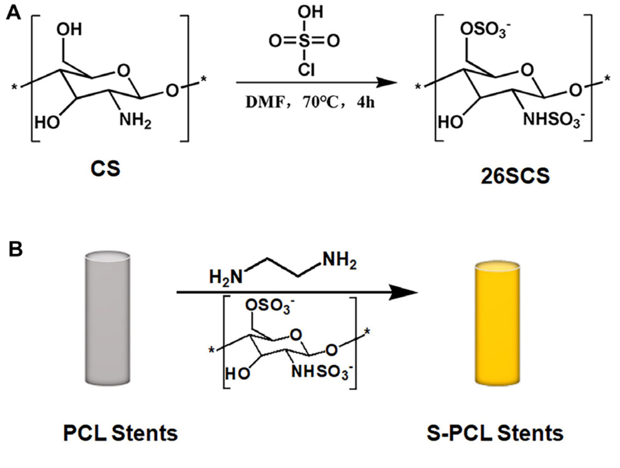

FIGURE 2 | Schematic reaction of 2-N, 6-O-sulfated chitosan **(A)** and aminolysis reaction of sulfated chitosan with PCL stents **(B)**. * means the repetition of molecular structure.

In vitro Biocompatibility Assessment

Cell Viability

Mouse fibroblasts (L929 cells) were cultured in 96-well plate in DMEM at a density of 5×10^3 cells/well, and allowed to

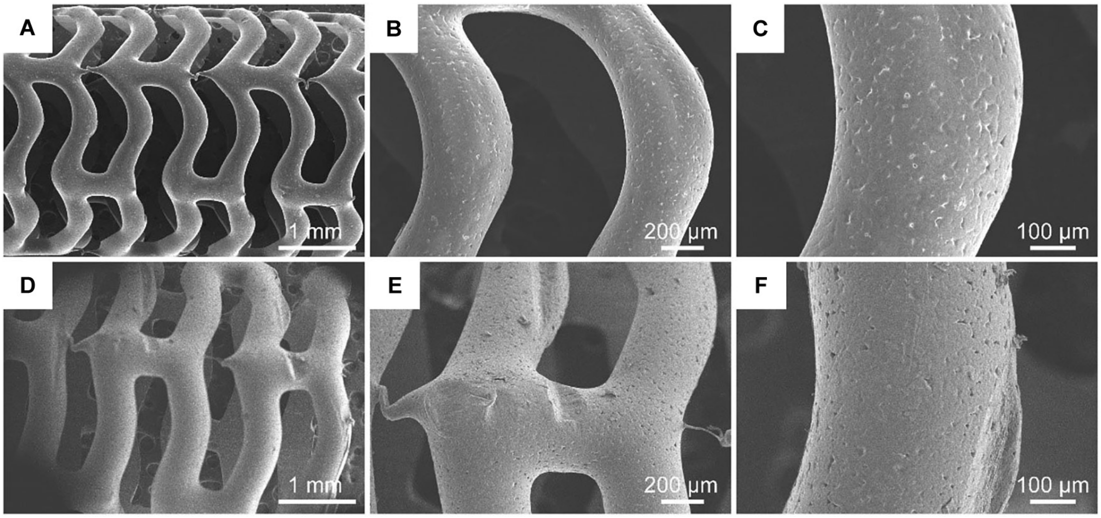

FIGURE 3 | SEM images of PCL stent **(A–C)** and S-PCL stent **(D–F)** with different magnifications.

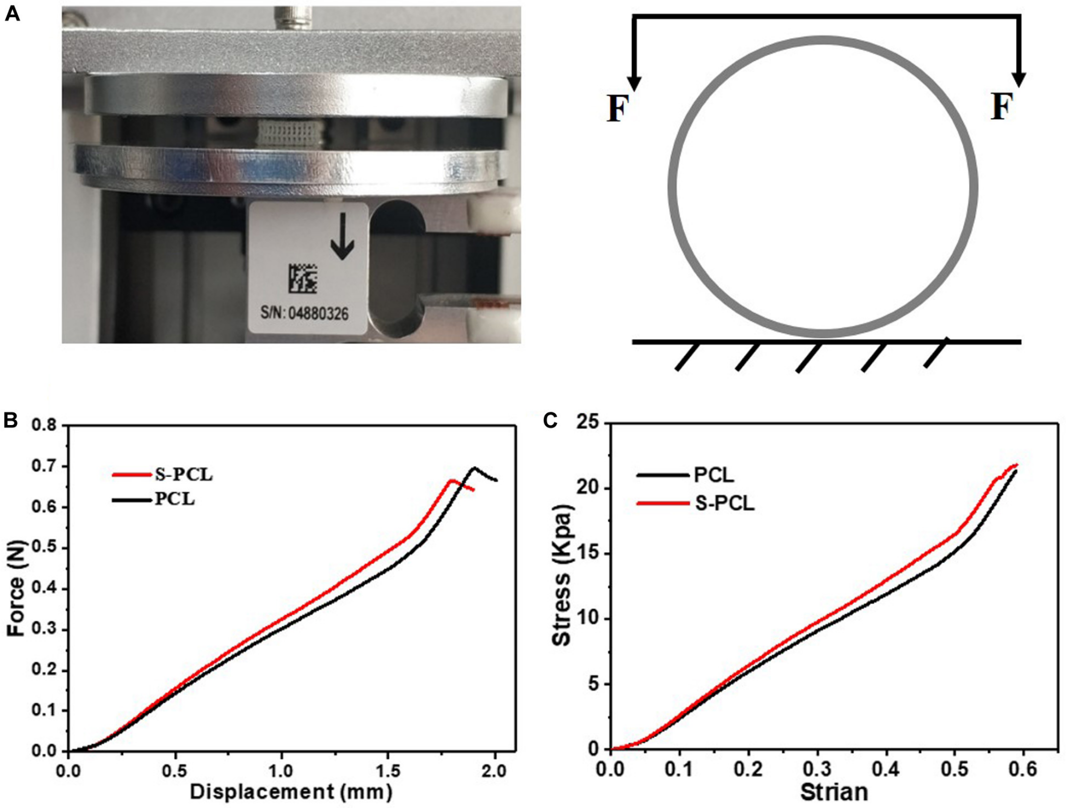

FIGURE 4 | Lateral crush resistance test **(A)**, force–displacement curve **(B)**, and stress–strain curve **(C)**.

attach overnight at 37°C in a humidified environment of 5% CO_2, and the medium of DMEM was supported with 10% fetal bovine serum and 1% penicillin/streptomycin. Subsequently, DMEM was removed and replaced with series of extract solution. Negative control was designed by cell culture with DMEM and PBS. Pure DMEM and PBS were used as positive control and negative controls, respectively. After 24 h of culturing cells, L929 was washed using PBS, and fresh DMEM (containing 10% CCK-8) was added into each well. After 1 h incubation, OD of each cell was measured at 450 nm using a microplate reader.

Live/Dead Staining

The 3D-printed PCL and S-PCL stents were immersed in 75% ethanol, sterile PBS, and DMEM medium in turn for 1 h to sterilize, respectively. L929 cells at a concentration of 2 × 10^5/mL were seeded on the surface of sterilized stents and cultured at 37°C in a humidified environment of 5% CO_2 for 7 days. The Calcein-AM and propidium iodide (PI) were added for staining, and the L929 cells Live/Dead staining images were obtained by inverted fluorescence microscope (TE2000-S, Nikon, Japan).

Cytoskeletal Immunofluorescence Staining

Phosphate buffered saline solution was used to wash the L929 cell-loaded stents for three times, and paraformaldehyde with a concentration of 4% was added to fix for 0.5 h. The stents were washed with PBS for another three times, and then treated with 0.5% Triton-X-100, phalloidin, and DAPI for 10, 30, 10 min, respectively. Finally, anti-fluorescence quencher was added and stored in dark at 4°C. The immunofluorescence staining images were captured by laser confocal microscope (FV3000, Olympus, Japan).

Cell Proliferation

The L929 cells with a concentration of 2 × 10^4/mL were seeded on the surface of sterilized stents and incubated at 37°C in a humidified environment of 5% CO_2. The CCK-8 reagent was added to each stent, and the OD of stent at 1, 3, and 7 days was measured at 450 nm using a microplate reader.

RESULTS AND DISCUSSION

Characterization of Sulfated Chitosan

Supplementary Figure S1 is the result of the ^{13}C NMR spectra of 26SCS. The magnitudes of chemical shift in 26SCS are in good agreement with the data in the previous report (Vikhoreva et al., 2005). There are two peaks at 69 and 60 ppm which represents C6 and C2 of 26SCS, respectively. The stable signal at C2 confirms the low sulfation of aminogroups in synthesized sulfated CS. This suggests that the sulfonation reaction occurs at the location of C6 and C2 of 26SCS.

The mass proportion is 33.19, 5.49, 2.63, and 5.52% for carbon (C), nitrogen (N), hydrogen (H), and sulfur (S), respectively, as shown in **Supplementary Table S1**. The appearance of sulfur (S) confirms the successful synthesis of 26SCS by using $HClSO_3$. The calculated degree of sulfonation is 44%.

The FTIR spectra of CS and 26SCS powders are shown in **Supplementary Figure S2**. There are two significant absorption peaks at 1220 and 800 cm^{-1} for 26SCS compared with CS. The absorption peak at 1220 cm^{-1} can be attributed to stretching vibrations of O = S = O groups, and the peak at 800 cm^{-1} are related to stretching vibrations of C-O-S groups (Ghaee et al., 2016). The occurrence of new peaks indicated that synthesis of sulfated CS was successful.

Supplementary Figure S3 shows the mass change of CS and 26SCS with the increase of temperature. There are two stages during the mass loss process of CS and 26SCS. During the first stage, mass loss is mainly caused by water loss, where CS and26 SCS possesses 4 and 9% drop for mass, respectively. Afterward, their mass loss has a dramatic drop to 50%, which results in degradation. It can be found that 26SCS has a faster degradation rate than that of CS, which might be caused by the degradation of sulfonic acid groups.

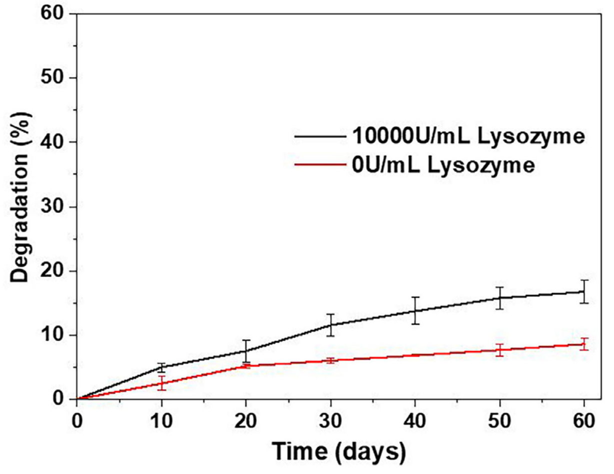

FIGURE 5 | Degradation behavior of S-PCL stents.

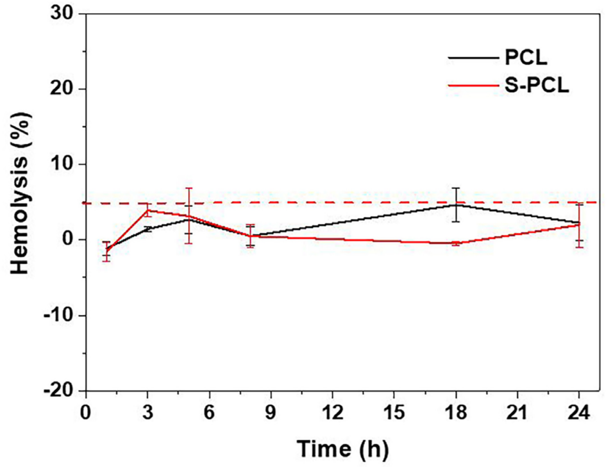

FIGURE 6 | Hemolytic percentage of RBCs incubated with PCL and S-PCL stent extracts at different time points.

Characterization of Stents

Morphology Observation of Stents

Figure 3 shows the surface morphology of PCL and S-PCL stents with different magnifications. The 3D-printed PCL and S-PCL stents behaved in tabular shapes with uniform diameters. Under large magnification, the surface of PCL stent was smooth, but the S-PCL stent had a rough and porous surface. This result indicates that the stent surface quality is affected by modification of 26SCS.

The surface quality of stent over the manufacturing process makes effect on their blood compatibility, anti-thrombosis,

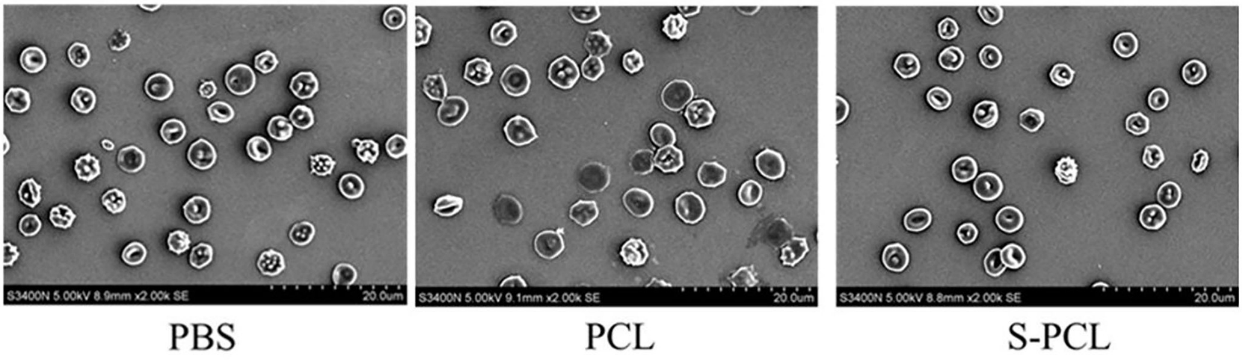

FIGURE 7 | Morphology of RBCs in extracts of PCL and S-PCL stent and PBS solution.

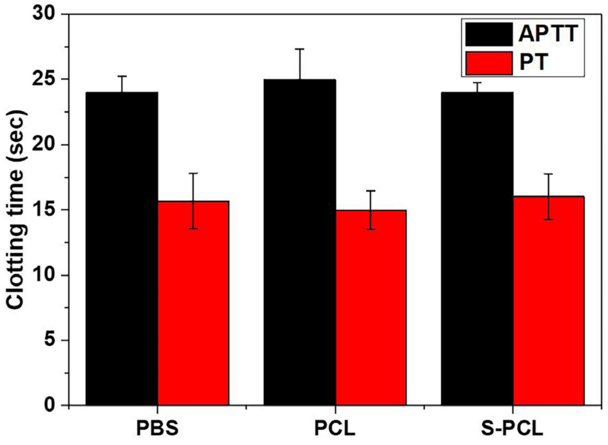

FIGURE 8 | Effect of PCL and S-PCL stent on APTT and PT compared to PBS control.

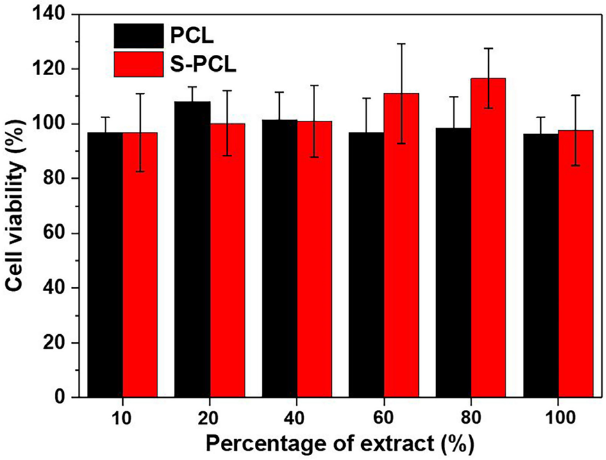

FIGURE 9 | Cell viability with different percentages of PCL and S-PCL stent extracts.

and vessel healing after deployment in human body. Guerra et al. (2018b) reported that ultraviolet sterilization method can increase surface roughness of 3D-printed PCL stent, and further influence its mechanical properties and degradation behavior. It was also reported that rough surface of stents can highly improve endothelial cell attachment and growth, and smooth surface contributes to endothelia cell migration (Lutter et al., 2014). These results highlight the importance of surface morphology characterization for medical devices. It should be noted that the 26SCS modification can produce a relative rough surface, and this may improve the biological performance of PCL stents.

Mechanical Properties of Stents

Figure 4A shows the testing machine and schematic diagram for lateral crush resistance test, and **Figures 4B,C** show the force–displacement behavior and stress–strain behavior for PCL and S-PCL stents, respectively. There was no significant difference on the force–displacement or stress–strain behavior between PCL and S-PCL stents, which suggested that 26SCS modification made no effect on the mechanical properties of PCL stents.

Bioresorbable stents undergo large deformation and high stresses while being implanted in diseased vessels under cyclic pulsatile loadings, and therefore the assessment of mechanical properties is crucial in stenting technology. In this study, lateral crush resistance tests were performed to simulate the *in vivo* loadings experienced by stents. The obtained mechanical results were similar with those reported for poly (L-lactic-acid) stents by Wang et al. (2018). It is a fact that bioresorbable polymer has low mechanical strength compared to metal. However, the mechanical properties of these polymers are more dependent on their microscopic characteristics, such as degree of crystallinity, molecular weight, and chemical structure, which make it easy for material processing and improvements. Therefore, bioresorbable polymers such as PCL and PLLA have been considered as potential material candidates for stents.

In vitro Degradation Study

The mechanical properties of BRSs are highly affected by the degradation process. **Figure 5** shows the *in vitro* degradation behavior of S-PCL stents with and without lysozyme. The

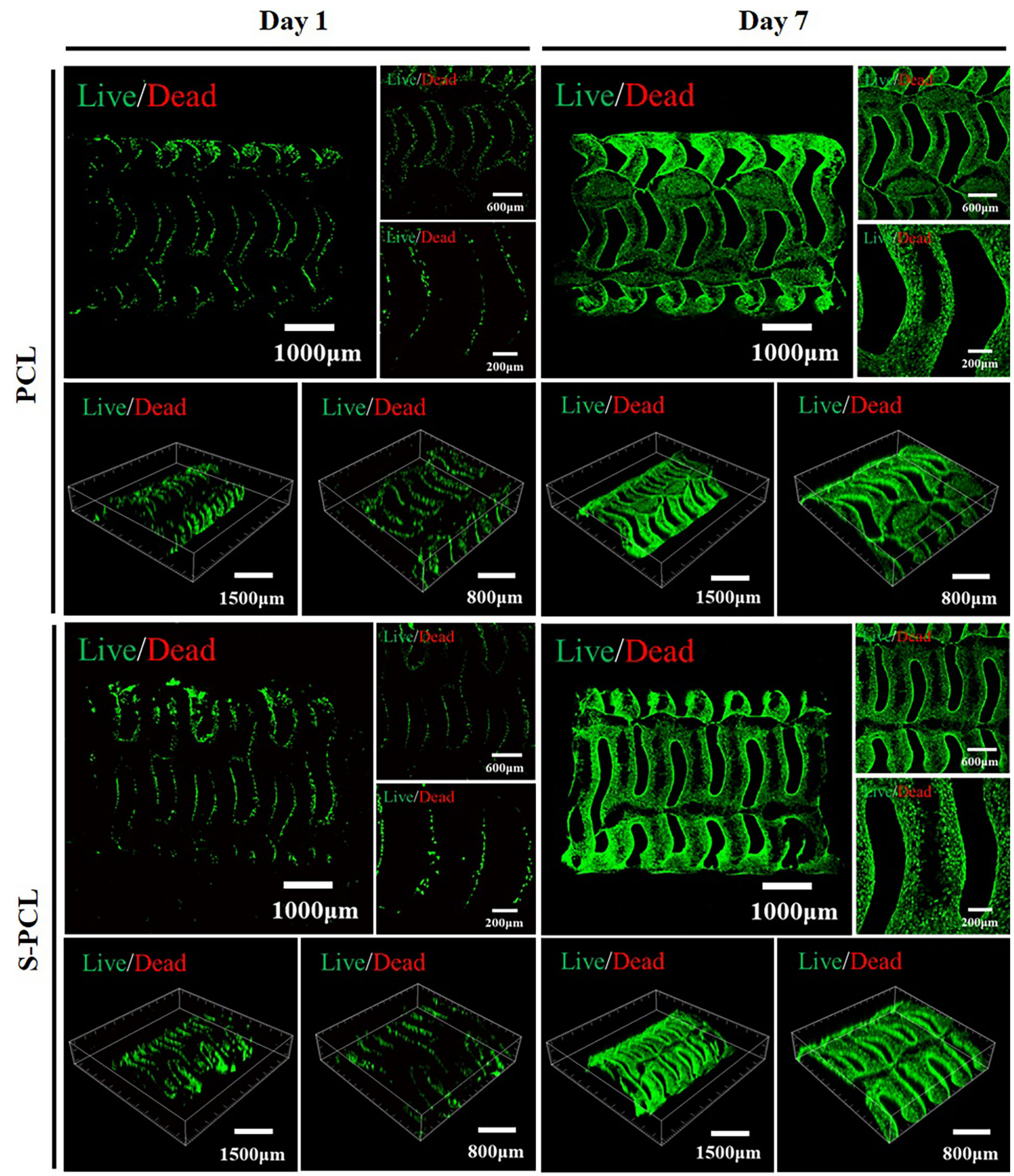

FIGURE 10 | Live/Dead staining images of L929 cells seeded on the PCL and S-PCL stents after 1 and 7 days.

S-PCL stent showed gradual mass decrease with the increase of degradation time. The weight loss of S-PCL is 16 and 7% with and without lysozyme at 60 days, respectively. It is obvious that lysozyme can accelerate the degradation of S-PCL stent at body temperature.

It is well known that degradation of polymer occurs by the way of hydrolysis and enzymatic degradation. Generally, PCL mainly undergoes hydrolytic degradation by the breakup of ester groups, and then experience intracellular degradation when it is highly crystalline with low molecular weight

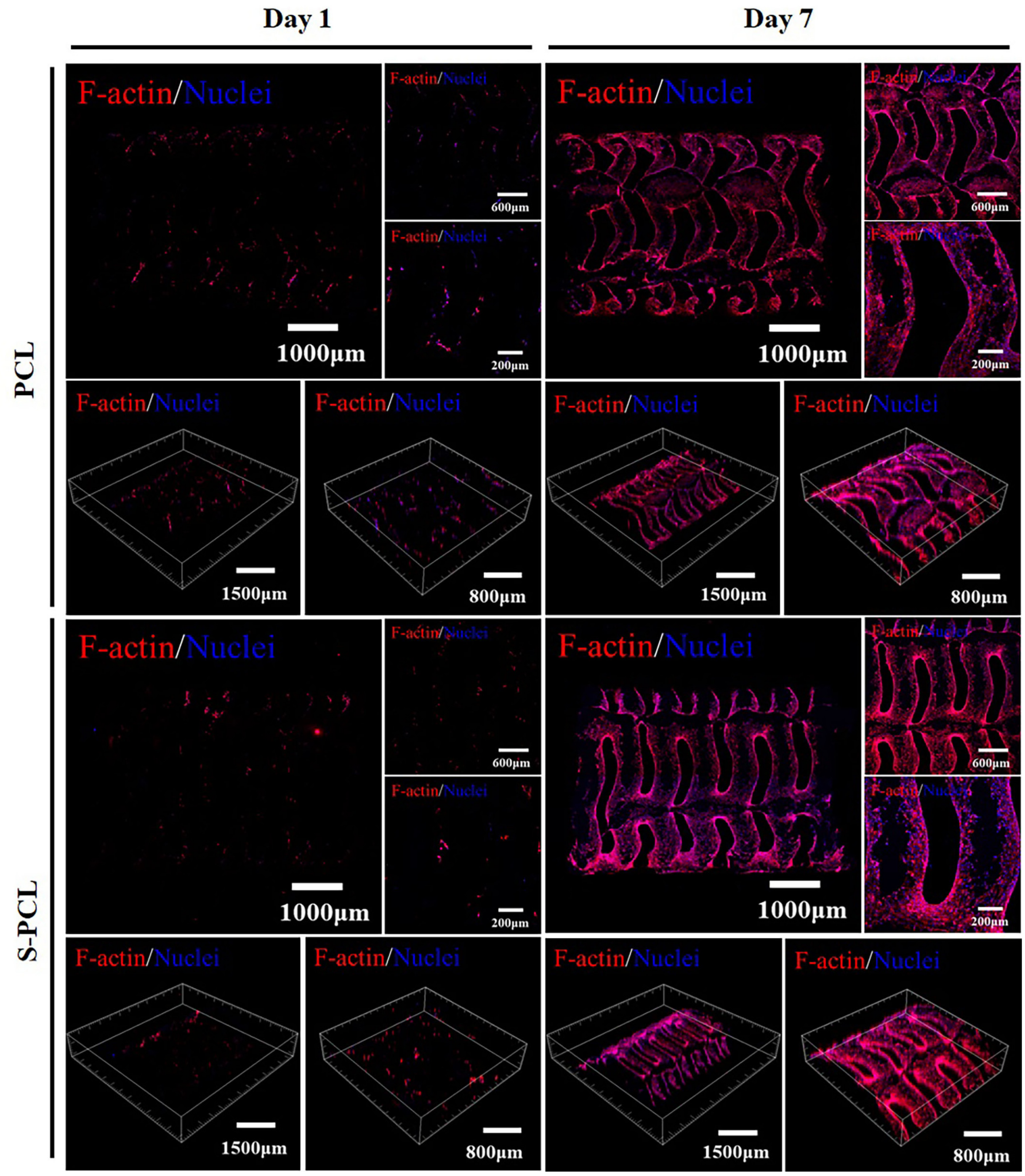

FIGURE 11 | Cytoskeleton fluorescence staining images of L929 cells seeded on PCL and S-PCL stents after 1 and 7 days.

(Woodruff and Hutmacher, 2010). It is reported that the degradation rate of PCL is extremely low, and the total *in vivo* degradation takes at least 2 years (Sun et al., 2006; Zong et al., 2015). The addition of lysozyme sped up degradation rate by two times, as show in our degradation result. It can be concluded that enzymatic degradation is faster than hydrolytic degradation for PCL. Therefore, it might be useful to modify the degradation rate of polymer by adding suitable aseptic and non-toxic enzyme, such as lysozyme.

Blood Compatibility Assessment

In vitro Hemolysis Analysis

The polymeric stents are deployed in human blood vessels for the treatment of coronary artery disease, and therefore the

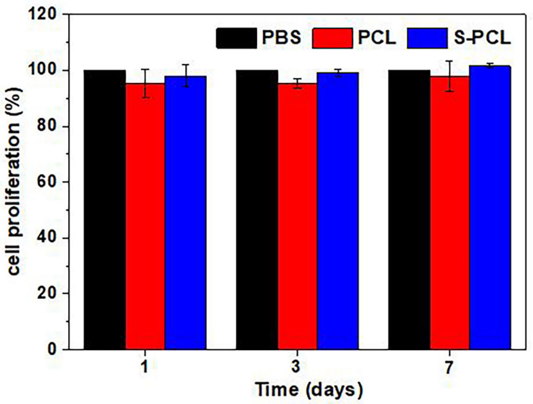

FIGURE 12 | Cell proliferation on PCL and S-PCL stents compared to PBS control.

blood compatibility assessment is essential. RBCs, as one of key components in whole blood, usually have a volume fraction of 40–50%, and its principal function is to deliver oxygen to the tissues by blood flow through circulatory system. Hemolysis test can produce deep understanding of complicated interactions between foreign material and RBCs membrane, and thus often used to assess the hemocompatibility of biomedical polymers. In this study, the *in vitro* hemolysis assay was conducted to investigate the influence of PCL and S-PCL stent extracts on the hemolytic behavior of RBCs. Generally, material is considered as non-hemolytic with hemolysis below 2%, and hemolytic but acceptable whereas the hemolysis between 2 and 5% (Vurugonda et al., 2017). The result showed that all test samples produced hemolysis below 5%, which indicated that both PCL and S-PCL stents possess good hemocompatibility, as shown in **Figure 6**.

Morphology of RBCs

Scanning electron microscopy was used to investigate the influence of PCL and S-PCL stent on the morphology of RBCs, and PBS was used as control. Normally, RBCs behave in circular shape with concaves, which makes easy to identify the morphological change by interaction with foreign materials. As shown in **Figure 7**, there is no aggregation of RBCs, and the morphology is as normal as that of PBS control. The result reveals that the PCL and S-PCL stents have little impact on the morphology of RBCs.

Liu et al. (2012) reported that interactions between foreign materials and RBCs are caused by hydrophobic function with the lipid bilayer and electrostatic function with surface charges. With the increase of hydrophobicity, biomaterials may partition into the RBCs membrane and destroy the lipid bilayer, which lead to hemolysis of RBCs. In this study, PCL is considered as hydrophobic polymer, but there is no morphological change observed while interacting with RBCs. As reported, the effect of hydrophobized polymer on RBC morphology is dependent on the concentration of polymers (Liu et al., 2010). Therefore, a relatively low concentration of PCL and S-PCL stent extracts may hardly result in the morphological change of RBCs.

APTT/PT

The APTT and PT are generally used to evaluate the blood coagulation function. The results showed that there are no significant differences on APTT and PT magnitudes between PCL and S-PCL stents with PBS control (**Figure 8**), which suggested that PCL and S-PCL stents have good blood compatibility.

Generally, bioresorbable polymers are considered as non-toxic and less likely to cause severe inflammatory response. However, the cytotoxic effect of biodegradable polymer on cells was proved to be dependent on their components, molecular weight, and manufacturing technique. Wang et al. (2014) reported that PLLA/PCL microparticles with low molecular weight induced cytotoxicity and prevented endothelial cell function, while Kang et al. (2008) found that high molecular weight PLLA and PLGA particles were non-toxic to cancer cells. Stents, made by blending PLLA and PCL, were proved to minimize the local acidification and the chronic inflammatory response (Liao et al., 2008). Nanofibrous PLACL/collagen stents possess admirable cardiac cell attachment and growth, compared to direct synthetic PLACL blends (Mukherjee et al., 2011). Therefore, biocompatibility tests were carried out to investigate the biocompatibility of 3D-printed PCL and S-PCL stents, in terms of cell viability assay, hemolysis assay, and blood coagulation assay. All these results showed that both PCL and S-PCL stents are non-toxic and blood compatible, which suggest that 3D-printed stents can be potential biomedical devices in coronary vessels.

In vitro Biocompatibility Assessment

In vitro Cytotoxicity Analysis

The *in vitro* cytotoxicity is an important biological parameter in the evaluation of biocompatibility of medical devices. Standard CCK-8 assay was carried out to evaluate the L919 cell viability in incubation with the extracts of PCL and S-PCL stents, as shown in **Figure 9**. The cytotoxic assay indicated that all 3D-printed PCL and S-PCL stents were non-toxic to L929 cells. There was no significant difference of the cell viability between PCL and S-PCL stents, which suggested that both PCL and S-PCL stents were compatible with cell culture. It should be noted that the cell viability of S-PCL stents was higher than that of PCL stents at 60%, 80% concentration of extract, with an approximately 20% increase, which indicated that cell proliferation was enhanced. This positive effect may be caused by 26SCS modification, and thus 26SCS might contribute to enhancement of cell proliferation.

In vitro Live/Dead Staining

Figure 10 shows the Live/Dead staining images of PCL and S-PCL stents after cell culture of 1 and 7 days. The live cells were stained to green and the dead cells were stained to red by Calcein-AM and PI, respectively. It is clear that L929 cells show increasing survival rates on both PCL and S-PCL stents when the cell culture time increases from 1 to 7 days. Moreover, the cells-loaded S-PCL stents obtained a higher survival rate than PCL stents at 7 days. This indicates that both 3D-printed PCL and S-PCL stents have excellent cells compatibility, and S-PCL stents show potential enhancement of cell adhesion and growth.

Cytoskeletal Immunofluorescence Staining

Figure 11 shows the cell adhesion and coverage on the PCL and S-PCL stents after cell culture of 1 and 7 days. The red fluorescent labeled F-actin grows in more and more uniform distribution with the increase of cell culture time, which suggests that the cells behave in extended state and firmly attach to the surface of PCL and S-PCL stents. The coverage of L929 cells on S-PCL stents is also slightly higher than that of PCL stents at 7 days. This suggests that the surface of 3D-printed PCL and S-PCL stents is favorable for cell proliferation.

In vitro Cell Proliferation

The standard CCK-8 assay was also used to evaluate the cell proliferation on PCL and S-PCL stents, and results are shown in **Figure 12** at 1, 3, and 7 days. It was found that the cells seeded on both PCL and S-PCL stents produced high proliferation rate over the culture period. There was no significant difference between two types of stents, compared to the control group. This suggested that both PCL and 26SCS were favorable for the cell attachment and growth.

CONCLUSION

In this study, a novel PCL stent was fabricated by 3D printing technique. 26SCS was successfully synthesized and used to modify the surface of PCL stent. Physical characterization results showed that PCL stent obtained good surface which is suitable for endothelial cell attachment and growth, by surface modification of 26SCS.The mechanical property is comparable to that of the existing bioresorbable polymeric stents. The degradation rate of PCL stent was improved by function of lysozyme. *In vitro* data demonstrated that PCL stents possessed non-cytotoxicity, admirable blood compatibility, and excellent cell compatibility, and 26SCS modification could enhance their cell viability and cell proliferation. Altogether, this current study produces that PCL and S-PCL stents can be potential medical devices for coronary artery disease.

DATA AVAILABILITY STATEMENT

The raw data supporting the conclusions of this article will be made available by the authors, without undue reservation, to any qualified researcher. Requests to access the datasets should be directed to qiutianyangustu@126.com.

AUTHOR CONTRIBUTIONS

TQ designed and carried out the experiments and wrote the manuscript. WJ collected the data and drew the figures. PY and LJ developed analysis tools. XW analyzed the experimental results.

FUNDING

This work was supported by the National Natural Science Foundation of China (NSFC) (51905037) and supported by Beijing Institute of Technology Education Foundation (No. 447). The fund from Beijing Institute of Technology Education Foundation supported the materials purchase and experiments, and the fund from NSFC will be used to pay for open access publication fees.

SUPPLEMENTARY MATERIAL

The Supplementary Material for this article can be found online at: https://www.frontiersin.org/articles/10.3389/fbioe.2020.00462/full#supplementary-material

REFERENCES

Cao, L., Wang, J., Hou, J., Xing, W., and Liu, C. (2014). Vascularization and bone regeneration in a critical sized defect using 2-n,6-o-sulfated chitosan nanoparticles incorporating bmp-2. *Biomaterials* 35, 684–698. doi: 10.1016/j.biomaterials.2013.10.005

Cao, L. Y., Yu, Y. M., Wang, J., Werkmeister, J. A., McLean, K. M., and Liu, C. S. (2017). 2-N, 6-O-sulfated chitosan-assisted BMP-2 immobilization of PCL scaffolds for enhanced osteoinduction. *Mater. Sci. Eng. C* 74, 298–306. doi: 10.1016/j.msec.2016.12.004

Croll, T., O'Connor, A. J., Stevens, G. W., and Cooper-White, J. J. (2004). Controllable surface modification of poly (lactic-co-glycolic acid) (PLGA) by hydrolysis or aminolysis I: physical, chemical, and theoretical aspects. *Biomacromolecules* 5, 463–473. doi: 10.1021/bm0343040

Demir, A. G., and Previtali, B. (2017). Additive manufacturing of cardiovascular cocr stents by selective laser melting. *Mater. Des.* 119, 338–350. doi: 10.1016/j.matdes.2017.01.091

Demir, A. G., Previtali, B., Colombo, D., Ge, Q., and Biffi, C. A. (2012). Fiber laser micromachining of magnesium alloy tubes for biocompatible and biodegradable cardiovascular stents. Fiber lasers ix: technology, systems, and applications. *Int. Soc. Opt. Photon.* 8237:823730. doi: 10.1117/12.910131

Flege, C., Vogt, F., Simon, H., Jauer, L., Borinski, M., Schulte, V. A., et al. (2012). Development and characterization of a coronary polylactic acid stent prototype generated by selective laser melting. *J. Mater. Sci. Mater. Med.* 24, 241–255. doi: 10.1007/s10856-012-4779-z

Ghaee, A., Nourmohammadi, J., and Danesh, P. (2016). Novel chitosan-sulfonated chitosan-polycaprolactone-calcium phosphate nanocomposite scaffold. *Carbohydr. Polym.* 157, 695–703. doi: 10.1016/j.carbpol.2016.10.023

Ghaee, A., Nourmohammadi, J., and Danesh, P. (2017). Novel chitosan-sulfonated chitosan-polycaprolactone-calcium phosphate nanocomposite scaffold. *Carbohydr. Polym.* 157, 695–703. doi: 10.1016/j.carbpol.2016.10.023

Guerra, A., Roca, A., and de Ciurana, J. (2017a). A novel 3D additive manufacturing machine to biodegradable stents. *Proc. Manuf.* 13, 718–723. doi: 10.1016/j.promfg.2017.09.118

Guerra, A. J., Cano, P., Rabionet, M., Puig, T., and Ciurana, J. (2018a). 3D-printed PCL/PLA composite stents: towards a new solution to cardiovascular problems. *Materials* 11:1679. doi: 10.3390/ma11091679

Guerra, A. J., Cano, P., Rabionet, M., Puig, T., and Ciurana, J. (2018b). Effects of different sterilization processes on the properties of a novel 3D-printed polycaprolactone stent. *Polym. Adv. Technol.* 29, 2327–2335. doi: 10.1002/pat.4344

Guerra, A. J., and Ciurana, J. (2017). Effect of fibre laser process on in-vitro degradation rate of a polycaprolactone stent a novel degradation study method. *Polym. Degrad. Stabil.* 142, 42–49. doi: 10.1016/j.polymdegradstab.2017.05.028

Guerra, A. J., and Ciurana, J. (2018). 3D-printed bioabsordable polycaprolactone stent: the effect of process parameters on its physical features. *Mater. Des.* 137, 430–437. doi: 10.1016/j.matdes.2017.10.045

Guerra, A. J., Farjas, J., and Ciurana, J. (2017b). Fibre laser cutting of polycaprolactone sheet for stents manufacturing: a feasibility study. *Opt. Laser Technol.* 95, 113–123. doi: 10.1016/j.optlastec.2017.03.048

Hu, T., Yang, J., Cui, K., Rao, Q., Yin, T., Tan, L., et al. (2015). Controlled slow-release drug-eluting stents for the prevention of coronary restenosis: recent progress and future prospects. *ACS Appl. Mater. Interfaces* 7, 11695–11712. doi: 10.1021/acsami.5b01993

ISO 10993-12 (2012). *Biological Evaluation of Medical Devices*. Geneva: ISO.

Kang, Y., Wu, J., Yin, G., Huang, Z., Yao, Y., and Liao, X. (2008). Preparation, characterization and in vitro cytotoxicity of indomethacin-loaded plla/plga microparticles using supercritical co2 technique. *Eur. J. Pharm. Biopharm.* 70, 85–97. doi: 10.1016/j.ejpb.2008.03.011

Khoshroo, K., Kashi, T. S. J., Moztarzadeh, F., Tahriri, M., Jazayeri, H., and Taybi, L. (2016). Development of 3D PCL microsphere/TiO 2 nanotube composite scaffolds for bone tissue engineering. *Mater. Sci. Eng. C* 70(Pt 1), 586–598. doi: 10.1016/j.msec.2016.08.081

Kim, T. H., Lee, J.-H., Ahn, C. B., Hong, J. H., Son, K. H., and Lee, J. W. (2019). Development of a 3D-printed drug-eluting stent for treating obstructive salivary gland disease. *ACS Biomater. Sci. Eng.* 5, 3572–3581. doi: 10.1021/acsbiomaterials.9b00636

Kong, X., Wang, J., Cao, L., Yu, Y., and Liu, C. (2014). Enhanced osteogenesis of bone morphology protein-2 in2-N,6-O-sulfated chitosan immobilized PLGA scaffolds. *Coll. Surf. B Biointerfaces* 122, 359–367. doi: 10.1016/j.colsurfb.2014.07.012

Kumar, M. N. V. R. (2000). A review of chitin and chitosan applications. *React. Funct. Polym.* 46, 1–27. doi: 10.1016/S1381-5148(00)00038-9

Lakshmi, S. N., and Cato, T. L. (2007). Biodegradable polymers as biomaterials. *Prog. Polym. Sci.* 32, 762–798. doi: 10.1016/j.progpolymsci.2007.05.017

Liao, S., Chan, C. K., and Ramakrishna, S. (2008). Stem cells and biomimetic materials strategies for tissue engineering. *Mater. Sci. Eng. C* 28, 1189–1202. doi: 10.1016/j.msec.2008.08.015

Liu, Z., Janzen, J., and Brooks, D. E. (2010). Adsorption of amphiphilic hyperbranched polyglycerol derivatives onto human red blood cells. *Biomaterials* 31, 3364–3373. doi: 10.1016/j.biomaterials.2010.01.021

Liu, Z., Jiao, Y., Wang, T., Zhang, Y., and Xue, W. (2012). Interactions between solubilized polymer molecules and blood components. *J. Control. Release* 160, 14–24. doi: 10.1016/j.jconrel.2012.02.005

Lutter, C., Nothhaft, M., Rzany, A., Garlichs, C. D., and Cicha, I. (2014). Effect of specific surface microstructures on substrate endothelialisation and thrombogenicity: importance for stent design. *Clin. Hemorheol. Microcirc.* 59, 219–233. doi: 10.3233/ch-141839

Misra, S. K., Ostadhossein, F., Babu, R., Kus, J., Tankasala, D., Sutrisno, A., et al. (2017). 3D-printed multidrug-eluting stent from graphene-nanoplatelet-doped biodegradable polymer composite. *Adv. Healthc. Mater.* 6:1700008. doi: 10.1002/adhm.201700008

Mondrinos, M. J., Dembzynski, R., Lu, L., Byrapogu, V. K., Wootton, D. M., Lelkes, P. I., et al. (2006). Porogen-based solid freeform fabrication of polycaprolactone–calcium phosphate scaffolds for tissue engineering. *Biomaterials* 27, 4399–4408. doi: 10.1016/j.biomaterials.2006.03.049

Mukherjee, S., Venugopal, J. R., Ravichandran, R., Ramakrishna, S., and Raghunath, M. (2011). Evaluation of the biocompatibility of placl/collagen nanostructured matrices with cardiomyocytes as a model for the regeneration of infarcted myocardium. *Adv. Funct. Mater.* 21, 2291–2300. doi: 10.1002/adfm.201002434

Park, S. A., Lee, S. J., Lim, K. S., Bae, I. H., Lee, J. H., Kim, W. D., et al. (2015). In vivo evaluation and characterization of a bio-absorbable drug-coated stent fabricated using a 3D-printing system. *Mater. Lett.* 141, 355–358. doi: 10.1016/j.matlet.2014.11.119

Peng, X., Yu, Y., Wang, Z., Zhang, X., Wang, J., and Liu, C. (2017). Potentiation effect of HB-EGF on facilitating wound healing via 2-N,6-O-sulfated chitosan nanoparticles modified PLGA scaffold. *R. Soc. Chem.* 7, 43161–43171. doi: 10.1039/c7ra07719j

Puppi, D., Mota, C., Gazzarri, M., Dinuccio, D., Antonio, G., Mairam, M., et al. (2012). Additive manufacturing of wet-spun polymeric scaffolds for bone tissue engineering. *Biomed. Microdev.* 14, 1115–1127. doi: 10.1007/s10544-012-9677-0

Raval, A., Choubey, A., Engineer, C., and Kothwala, D. (2004). Development and assessment of 316LVM cardiovascular stents. *Mater. Sci. Eng. A* 386, 331–343. doi: 10.1016/j.msea.2004.07.051

Sun, H., Mei, L., Song, C., Cui, X., and Wang, P. (2006). The in vivo degradation, absorption and excretion of pcl-based implant. *Biomaterials* 27, 1735–1740. doi: 10.1016/j.biomaterials.2005.09.019

Vikhoreva, G., Bannikova, G., Stolbushkina, P., Panov, A., Drozd, N., and Makarov, V. (2005). Preparation and anticoagulant activity of a low-molecular-weight sulfated chitosan. *Carbohydr. Polym.* 62, 327–332. doi: 10.1016/j.carbpol.2005.05.022

Vurugonda, U., Rednam, P. J., and Sinha, M. (2017). Development of biodegradable scaffold using polylactic acid and polycaprolactone for cardiovascular application. *Int. J. Polym. Mater. Polym. Biomater.* 67, 78–85. doi: 10.1080/00914037.2017.1297945

Waksman, R. (2006). Update on bioabsorbable stents: from bench to clinical. *J. Interv. Cardiol.* 19, 414–421. doi: 10.1111/j.1540-8183.2006.00187.x

Wang, P. J., Nezami, F. R., Gorji, M. B., Berti, F., Petrini, L., Wierzbicki, T., et al. (2018). Effect of working environment and procedural strategies on mechanical performance of bioresorbable vascular scaffolds. *Acta Biomater.* 82, 34–43. doi: 10.1016/j.actbio.2018.10.020

Wang, Y., Van den Akker, N. M. S., Molin, D. G. M., Gagliardi, M., Cees, V. D. M., Lutz, M., et al. (2014). A nontoxic additive to introduce x-ray contrast into poly(lactic acid). implications for transient medical implants such as bioresorbable coronary vascular scaffolds. *Adv. Healthc. Mater.* 3, 290–299. doi: 10.1002/adhm.201300215

Woodruff, M. A., and Hutmacher, D. W. (2010). The return of a forgotten polymer—polycaprolactone in the 21st century. *Prog. Polym. Sci.* 35, 1217–1256. doi: 10.1016/j.progpolymsci.2010.04.002

Yu, Y. M., Chen, J., Chen, R., Cao, L. Y., Tang, W., Lin, D., et al. (2015). Enhancement of VEGF-mediated angiogenesis by 2-N,6-O-sulfated chitosan-coated hierarchical PLGA scaffolds. *ACS Appl. Mater. Interfaces* 7, 9982–9990. doi: 10.1021/acsami.5b02324

Yu, Y. M., Chen, R., Sun, Y., Pan, Y. Z., Tang, W., Zhang, S., et al. (2018). Manipulation of VEGF-induced angiogenesis by 2-N, 6-O- sulfated chitosan. *Acta Biomater.* 71, 510–521. doi: 10.1016/j.actbio.2018.02.031

Zhao, F., Wang, F., King, M. W., and Wang, L. (2019). Effect of dynamic and static loading during in vitro degradation of a braided composite bioresorbable cardiovascular stent. *Mater. Lett.* 250, 12–15. doi: 10.1016/j.matlet.2019.04.097

Zhao, F., Xue, W., Wang, F., Liu, L., Shi, H., and Wang, L. (2018). Composite self-expanding bioresorbable prototype stents with reinforced compression performance for congenital heart disease application: computational and experimental investigation. *J. Mech. Behav. Biomed. Mater.* 84, 126–134. doi: 10.1016/j.jmbbm.2018.05.009

Zhou, H., Qian, J., Wang, J., Yao, W., Liu, C., Chen, J., et al. (2009). Enhanced bioactivity of bone morphogenetic protein-2 with low dose of 2-n, 6-o-sulfated chitosan in vitro and in vivo. *Biomaterials* 30, 1715–1724. doi: 10.1016/j.biomaterials.2008.12.016

Zong, C., Wang, M., Yang, F., Chen, G., Chen, J., and Tang, Z. (2015). A novel therapy strategy for bile duct repair using tissue engineering technique: pcl/plga bilayered scaffold with hmscs. *J. Tissue Eng. Regen. Med.* 11, 966–976. doi: 10.1002/term.1996

Conflict of Interest: The authors declare that the research was conducted in the absence of any commercial or financial relationships that could be construed as a potential conflict of interest.

frontiers
in Bioengineering and Biotechnology

ORIGINAL RESEARCH
published: 25 May 2020
doi: 10.3389/fbioe.2020.00444

A Simplified and Effective Method for Generation of Experimental Murine Periodontitis Model

Danfeng Li[1,2†], Yi Feng[1,2†], Hang Tang[1,2], Lijia Huang[2], Zhongchun Tong[2], Cheng Hu[1,2], Xiaodan Chen[2] and Jiali Tan[1,2*]

[1] Department of Orthodontics, Hospital of Stomatology, Guanghua School of Stomatology, Sun Yat-sen University, Guangzhou, China, [2] Guangdong Provincial Key Laboratory of Stomatology, Sun Yat-sen University, Guangzhou, China

Periodontitis, a common disease that can lead to bone destruction, periodontal attachment loss, and tooth loss, is the major cause for oral tissue engineering. Experimental periodontitis is a suitable disease-model for studying bone regeneration and the potential therapeutic role of biomaterials on periodontal tissue engineering, as this *in vivo* model could be employed to mimic the natural host response under bacteria-caused oral pathological environments. Although large animals with ligature-induced periodontitis have mostly been used for experiments, a mouse model is a better choice for several reasons. Inserting ligature threads through the interproximal space between the teeth is the key step in establishing a periodontitis model, and it is easy to achieve in large animals, but difficult in mice due to the limited operating space. In this work, we provide a new and proven approach for periodontitis induction in mice using C+ nickel-titanium root canal files and stainless-steel ligature wires. The validity of this method was assessed by evaluating alveolar bone loss via micro-CT and detecting periodontal inflammation by histological staining and qPCR after the treatments. Progressive alveolar bone loss was observed from day 3 after the ligature-placement. Infiltration and accumulation of F4/80+ macrophage was also detected. In accordance with the histological results, there was upregulation of the expression levels of the inflammatory genes *Il1β*, *Tnf-α*, and *Il6* in gingival tissues isolated from the ligation sites. Our results suggest that this novel method could resolve the difficulty of ligature-placement in mice and consequently contribute to further use of mouse models for studying the pathological mechanisms of periodontitis and developing potential periodontal tissue regeneration strategies. C+ files, which are made of nickel-titanium, are tough, elastic, and sufficiently thin to pass through the interproximal space between the teeth after pre-bending to form an appropriate angle, thus providing an access for ligature wire insertion. As a common tool in the dental clinic, it is familiar to researchers of oral biology, and can provide the feasibility for wide application of our method.

Keywords: periodontitis, bone loss, animal model, periodontal tissue defects, tissue engineering model

Edited by:
Gang Wu,
VU University
Amsterdam, Netherlands

Reviewed by:
Shengbin Huang,
Wenzhou Medical University, China
Binbin Li,
Peking University, China

***Correspondence:**
Jiali Tan
tanjiali@mail.sysu.edu.cn

[†] These authors have contributed equally to this work

Specialty section:
This article was submitted to Biomaterials,
a section of the journal
Frontiers in Bioengineering and Biotechnology

Received: *27 February 2020*
Accepted: *17 April 2020*
Published: *25 May 2020*

Citation:
Li D, Feng Y, Tang H, Huang L, Tong Z, Hu C, Chen X and Tan J (2020) A Simplified and Effective Method for Generation of Experimental Murine Periodontitis Model.
Front. Bioeng. Biotechnol. 8:444.
doi: 10.3389/fbioe.2020.00444

INTRODUCTION

Periodontitis is a chronic inflammatory disease caused by bacterial pathogens and is characterized by inflammatory infiltration and progressive alveolar bone loss (Hajishengallis et al., 2012), and it is highly prevalent all over the world (Lamont et al., 2018). In addition to being the major cause of bone destruction, periodontal attachment loss, and tooth loss in adults, periodontitis is associated with an increased risk of developing fatal systemic disorders such as atherosclerosis (Hajishengallis, 2015), hypertension (Schiffrin and Engert, 2019), rheumatoid arthritis (Potempa et al., 2017), and diabetes (Blasco-Baque et al., 2017; Xiao et al., 2017).

Previous studies on periodontitis therapy examined the clearance of pathogenic bacteria and usage of biomaterials for repairing periodontal defects (Ouchi and Nakagawa, 2020). Thus, there is a strong need to determine the most optimal preventive therapies for periodontitis and perform research on regenerative treatments using appropriate animal models (Liu et al., 2018; Kourtzelis et al., 2019). For example, Datey et al. used a rat periodontitis model and tested the effect of shockwave treatment in combination with antimicrobials on periodontitis (Datey et al., 2019). Apart from the significance of studying periodontitis itself, it is also a suitable model for studying bone regeneration and investigating the potential therapeutic functions (such as anti-inflammation, anti-osteoclast, and osteogenesis) of biomaterials on periodontal tissue engineering, as it is easily obtained and accessible for observation (Eskan et al., 2012; Manilay and Zouali, 2014; Tsukasaki et al., 2018).

Previous studies showed that the animal models of periodontal bone defects, formed by flap surgery and removing alveolar bone tissue with a dental bur, are one of the most widely used bone defect models in the study of periodontal bone reconstruction and regeneration (Nasajpour et al., 2018; Hasani-Sadrabadi et al., 2019). We have been engaged in the research on intervention strategies of periodontal tissue repair under periodontitis. We established a supramolecular hydrogel SDF-1/BMP2/NapFFY, which could effectively repair alveolar bone defects in rats. The above results were published in Tan et al. (2019). We anticipate that the biomaterials developed could replace bone transplantation in a clinical setting for repair of periodontal bone defects under periodontitis. Periodontitis is one of the most common diseases that can lead to alveolar bone defects in oral clinics, which is caused by periodontitis pathogens. Different from the bone defects caused by mechanical factors, periodontitis creates a more complex periodontal ecological environment. Therefore, compared with the animal models of alveolar bone defects constructed by mechanical methods, the animal models of alveolar bone defects under experimental periodontitis are more appropriate to be used to simulate the periodontal micro-environment of periodontitis.

The ligature model is one of the most commonly used models to induce periodontitis because the ligature around the molar accelerates the formation of bacterial-plaque and leads to progressive periodontal attachment loss (Marchesan et al., 2018). In the past decade, dog, rabbit, and rat animal models have been used to study the pathogenesis and mechanisms of periodontitis because oral surgery and ligation are easily accomplished (Bhattarai et al., 2016; Courbon et al., 2019). There is experimental demand for gene-editing strains and experiments with high-quality immunochemical detection reagents, and therefore, mouse models have been increasingly applied to study periodontitis (Offenbacher et al., 2018). Additionally, small animals cost less than larger animals, and it is convenient to maintain mice in specific pathogen-free (SPF) environments. It is the technical problem in inserting the ligature into the interproximal spaces between the molars of the mice that makes use of the mouse model unpopular, because the oral cavity and teeth of the mice are too narrow, and it is difficult for operators to clearly see and place ligatures. Researchers have attempted to implement various methods for ligature-induced periodontitis in mice (Marchesan et al., 2018). Even so, more simple and economical methods are expected to solve the operative difficulties in periodontitis induction.

Here, we carried out an effective method for experimental periodontitis induction using pre-bent C+ Ni-Ti canal files to form an angle that is adapted to the small size of the oral cavity and placing a 0.2-mm orthodontic ligature between the maxillary molars. In this work, we introduce the procedures for ligature placement in detail and present the data that verify the effectiveness of experimental periodontitis induction. This model is suitable for periodontitis induction and is expected to aid in the study of pathological mechanisms and potential therapeutic treatments in periodontitis. In addition to the mechanism of periodontitis, this model can be used for study on the properties of biomaterials and periodontal tissue engineering research.

MATERIALS AND METHODS

Animals

Wild-type female C57BL/6 mice (6–8 weeks old, 18–22 g in weight) were purchased from the animal center of Sun Yat-sen University (Guangzhou, China). All animal-related treatments described in these experiments were approved by the Institutional Animal Care and Use Committee (IACUC) of Sun Yat-sen University. Mice were randomly divided into each group (sham or ligature insertion) and maintained in an SPF environment with a temperature of 22 ± 2°C, 55% humidity, light/dark cycle of 12/12 h, and standard food and water (provided by the animal center) *ad libitum*. Mice were euthanized at 0, 1, 3, 6, and 10 days after surgery followed by micro-computed tomography (CT), histological staining, and quantitative PCR (qPCR) studies. The subject was excluded if the inserted ligatures fell out 3 days after ligature-placement. The investigators were blinded to the group while the data measurements and outcome evaluations were being performed.

Establishment of Experimental Periodontitis in a Murine Model

The previous method of ligature placement around the maxillary second molar is difficult to achieve in mice due to the limited operating space (Marchesan et al., 2018). We explored a simplified method to establish experimental periodontitis model by C+ Ni-Ti root canal files and 0.2-mm orthodontic ligature wires. Mice were anesthetized with an intraperitoneal injection of 1% pentobarbitone (dissolved in PBS, 100 μl/20 g) before the surgery to induce periodontitis. Experimental periodontitis was induced by C+ files (8#, 10#, or 15#, DENTSPLY Maillefer, Switzerland) and insertion of ligature wire (Orthodontic Stainless Ligature Wire, 0.2 mm in diameter) between the left maxillary molars, as described in detail in **Table 1**. The sham control mice received the same surgery but without wire-placement. The mice were monitored and kept warm until they recovered from the anesthesia. Every 3 days, the mice were anesthetized, and the presence of the ligature wire was evaluated. Animals in which the ligature wire was absent were excluded from the study. After the periodontitis induction, the mice were euthanized by an overdose of anesthesia.

Micro-CT Analysis

Maxillary samples were collected at 0, 1, 3, 6, and 10 days (Jiao et al., 2013) after surgery and scanned with a Scanco μCT50 scanner (Scanco Medical AG, Brutishly, Switzerland) with a resolution of 20 μm at 70 kVp and 200 μA. The 3D images from the buccal and palatal sides were constructed using Materialize Mimics v17.0 software. As for bone loss evaluation, the distance between the cemento-enamel junction (CEJ) and alveolar bone crest (ABC) was measured by the abovementioned software. Twelve sites from each maxillary molar were chosen for measurement, and averaged distances were calculated. Each measurement was repeated three times.

Histological Analysis

The maxillae were dissected at 0, 3, 6, and 10 days after experimental periodontitis treatment and were subsequently fixed with 4% paraformaldehyde. For tissue immunofluorescent staining, the maxillae were then decalcified with 0.5 M ethylenediaminetetraacetic acid (EDTA) for 48 h and embedded at −80°C with compound (OCT, Sakura Finetek, Torrance, CA, USA). Frozen sections were sliced at −25°C and stored at −20°C. After antigen repairing and blocking for 1 h at room temperature in 3% bovine serum albumin (BSA), the slices were incubated overnight using the primary antibody of rat-anti-mouse anti-F4/80 (Abcam Cat# ab16911, RRID:AB_443548). Then, goat-anti-rat Alexa Fluor® 488 secondary antibodies (Abcam Cat#ab150157, RRID:AB_2722511) were used at 1/200 dilution to further stain the slices on the following day. The slices were counterstained with Hoechst 33342 Staining Dye Solution (ab228551) for 10 min at 25°C. Laser-scanning confocal microscopy was employed to detect the fluorescent distribution.

RNA Extraction and qPCR Analysis

At 0, 3, 6, and 10 days after the wire insertion, total RNA was isolated and purified from the gingival tissues surrounding three maxillary molars via a series of centrifugation and extraction treatments using TRIzol reagent, chloroform, isopropanol, and 75% diethyl pyrocarbonate (DEPC)-ethanol. First-strand cDNA was synthesized with 1 μg of total RNA and an oligo (dT) primer using a commercial kit (All-in-One cDNA Synthesis SuperMix, Cat: B24403, Bimake) according to the manufacturer's instructions. The expression levels of inflammatory genes including *Il1b*, *Tnf-α*, and *Il6* were detected by qPCR using the Roche Real-Time PCR System with SYBR Green (FastStart Essential DNA Green Master, Cat: 35732800, Roche, USA). The detection was independently replicated twice. The expression levels were normalized by β-actin mRNA level.

Statistical Analyses

Differences between multiple groups were evaluated using one-way-ANOVA analysis (Tukey's multiple comparisons test). Differences at $P < 0.05$ were considered significant. Statistical analyses were performed using the GraphPad Prism software version 7.0 (GraphPad Software, La Jolla, CA, USA).

RESULTS

Morphometric Evaluation of Alveolar Bone Loss After Experimental Periodontitis Induction

For experimental periodontitis induction, the tip of a C+ nickel-titanium root canal file was pre-bent and slowly filed into the interproximal space between the maxillary molars (**Figure 1A**). The orthodontic ligatures (0.20 mm in width, 3–5 mm in length) were inserted (**Figure 1B**), as shown in the detailed procedure illustrated in **Figure 1C**. Furthermore, we present a simple method for fixing the mice to the operating table and exposing the oral cavity using orthodontic ligature wire. More importantly, the average operative time for the model by five independent operators is shown in **Supplementary Figure 1**. After practicing three times with mice exhibiting different health conditions, the operators were able to successfully place ligature wires on one side of the maxillary molars in less than 10 min, which saved a lot of time. This method is simple and easy to conduct.

To analyze alveolar bone loss, the distances between the cemento-enamel junction (CEJ) and alveolar bone crest (ABC) were measured at four sites for each maxillary molar (both palatal and buccal, distal and mesial) in three-dimensionally constructed images. The mean distances for 12 sites from each sample were calculated and are presented in millimeters (**Figures 2A,B**). Both the buccal side and the palatal side were used for evaluation of ligature-induced bone loss in order to reliably assess the damage to the alveolar bone. Morphological alterations in buccal and palatal alveolar bone caused by the progression of wire-induced periodontitis are visually presented in 3D-constructed images, showing prominent bone loss at the mesial and distal sites of the second molar 3 days after periodontitis induction (**Figure 2C**). As shown, the specimens from the experimental periodontitis groups displayed abrupt aggravation of bone loss from day 3 to day 6 and relatively smooth progression from day 6 to day 10 by assessing the CEJ-ABC distances of 12 sites in the palatal and buccal surfaces.

Notably, the CEJ-ABC distance values in the 1d-group were similar to those of the control group that received no ligatures, indicating that the observed progressive alveolar bone loss could hardly be caused by operative damage caused by placement of the orthodontic wire itself (**Figure 2D**). Furthermore, the average CEJ-ABC distance in the control group was 0.24 ± 0.01 mm,

TABLE 1 | Detailed procedure of the modified method to induce experimental periodontitis.

Step	Treatments (using the left side of the maxillary molars as an example)	
1	Exposure of the operating view in the oral cavity	• Hold the curved tweezers with the left hand and point its curved tip upward to prop open the mandible of the mouse and prevent the tongue from falling down to obstruct the view • Tie an orthodontic ligature (6–8 cm in length) around the maxillary incisor and tape it to the operating table
2	Pretreatment with C+ files	• Pre-bend 5 mm of the tip of the 8#, 10#, or 15# C+ nickel-titanium root canal files • Hold the C+ file with the right hand and carefully use it as a probe to determine the interproximal region between the 1st and 2nd molar and the 2nd and 3rd molar • Slowly file into the adjacent space and gently pull back ∼2 mm to form a path between the interproximal space. Then separate the filled gingival tissues, for the purpose of the following orthodontic ligature placement ✧ The reason for the above operation: 1. Because of the flexibility of the orthodontic ligature, it is easily bent and deformed. Thus, it is difficult to insert into the interproximal space because of the blockage of gingival tissues. 2. Being a type of dental root canal file with both stiffness and elasticity, C+ nickel-titanium files are clinically used to locate the narrow orifice of calcified root canals. Because they are sufficiently thin and can pass through the interproximal space, and operators can determine correct placement by touch and feeling feedback, C+ root canal files enable access so that the orthodontic ligature can be successfully placed
3	Insertion of the orthodontic ligature wires	• Prepare the orthodontic ligature wires (0.20 mm in width, 3–5 mm in length). ✧ If the wire is too long, it could easily pierce the oral mucosa and enter the buccinator, which will adversely affect the ability of mice to eat and could inhibit adequate food intake. Furthermore, a wire that is too long will be easily licked and removed by the tongue, causing it to fall off from the interproximal space. Conversely, if the ligature is too short, it is difficult to clamp and bend it into an appropriate angle for further insertion • Slightly bend the orthodontic ligature wire into a "(" shape, in order to form a proper angle for subsequent insertion • Hold the needle holder with the right hand, and clamp the ligature with the tip of the needle holder • Gently probe the adjacent region prepared by the root canal files above with the orthodontic ligature to determine the correct location, and then gently insert the orthodontic ligature into the interproximal space
4	Completion	• Slightly move the ligature with tweezers to repeatedly check whether the ligature has been properly placed

which is larger than the thickness of the orthodontic ligature wire (0.2 mm), indicating that the alveolar bone loss might not be caused by the trauma of wire-insertion. In sum, these data demonstrate that this new method of orthodontic wire placement can simulate progressive bone loss and is appropriate for establishing experimental periodontitis.

Inflammatory Infiltration in Gingival Tissue After Ligature Insertion

A predominance of macrophage infiltration has been observed in the lower region of chronic periodontitis lesions (Kourtzelis et al., 2019; Zhuang et al., 2019). Among the immune cells, macrophages are intensively studied because they might respond to microbial pathogens and further activate the adaptive immune response.

Slices of sagittal molar regions were prepared, and the areas between the first and the second molar were observed by confocal microscopy to detect infiltrated immune cells (**Figure 3A**). As the data show, there were increasing numbers of F4/80+ macrophages in the periodontal tissue between the first molar and the second molar 6 days after periodontitis induction (**Figure 3B**). These results indicate that immune cell infiltration occur and also illustrate the potential role of macrophages in the development of periodontitis.

Differential Expression of Inflammatory Genes Throughout the Duration of Periodontitis

The gingival tissues in the molar region were collected after periodontitis treatments (**Figure 4A**). The mRNA levels of the inflammatory genes *Tnfα*, *Il1β*, and *Il6* were detected on different days after ligature-insertion [baseline (0), 3, 6, and 10 d]. As expected, all three inflammatory genes were upregulated after wire insertion as compared to the control group. The expression level of *Il1β* significantly increased 3 days after the periodontitis operation, which reflects the two well-known cytokines that are characteristic of inflammation in periodontitis and are universally used as detection markers in the acute phase of chronic inflammation.

In accordance with the histological data, the expression of the inflammatory genes *Il6* and *Tnfα* markedly increased 10 days after ligature insertion compared with baseline (**Figure 4B**). Apart from being a protective response to the accumulated microbial pathogens, this increase could trigger the downstream molecular signals that are recognized to accelerate inflammatory disease progression. The primers that were used in the qPCR experiments are listed in **Figure 4C**. Overall, the results suggest that this model could be appropriate for host response research during periodontitis duration. These results indicated that a simplified orthodontic ligature-induced periodontitis model in

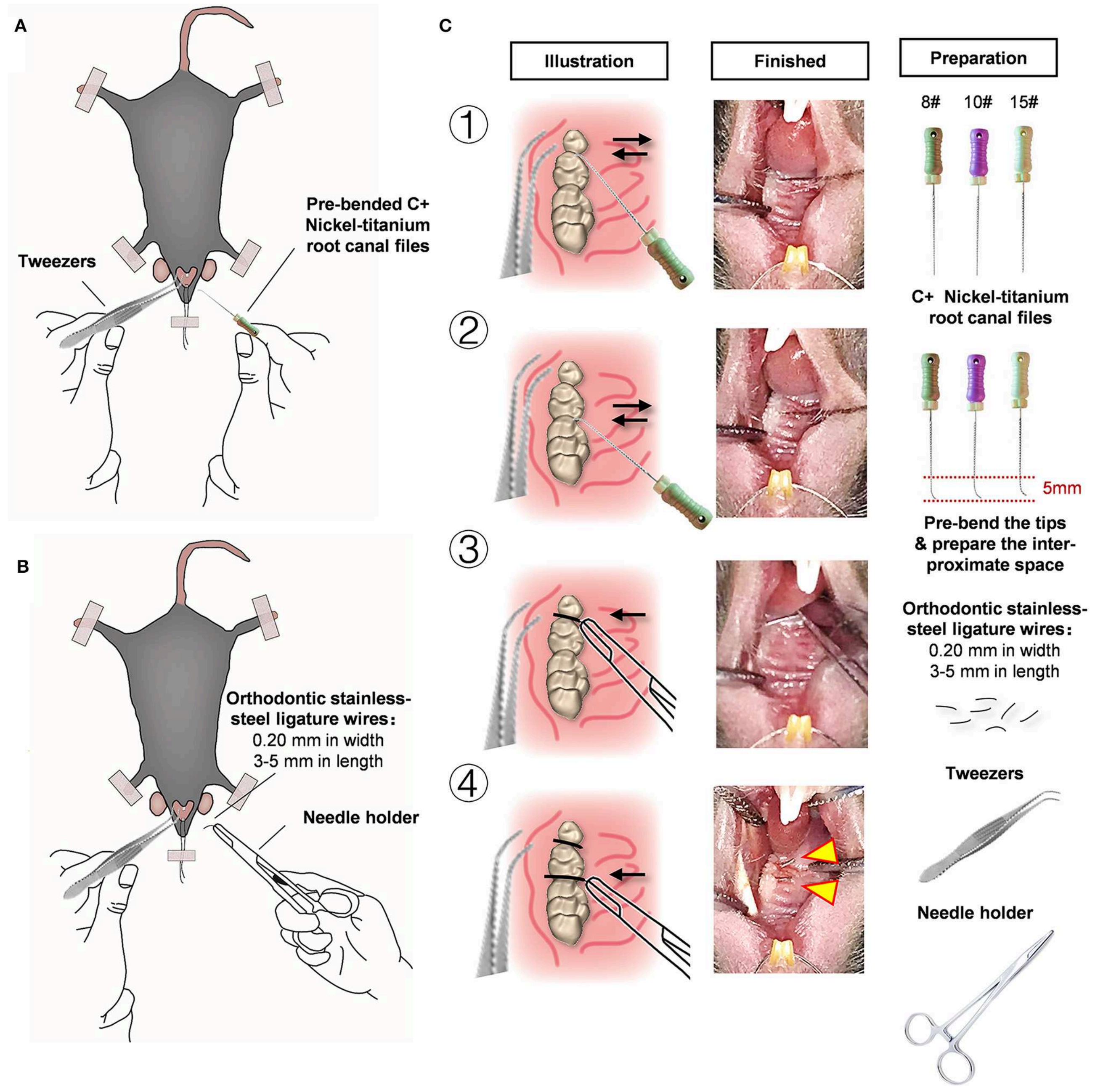

FIGURE 1 | An effective and simple experimental mice model for periodontitis research. **(A)** Pre-bend the 5 mm tip area of the C+ nickel-titanium root canal file, then slowly file into the adjacent space. **(B)** Orthodontic ligature wires (cut by 0.2 mm in width, 3–5 mm in length) were inserted through interdentium between the first molar and second molar, and the second molar and third molar using a needle holder. **(C)** Detailed procedures and preparation of the modified wire-placement treatment.

mice was successfully established to mimic the inflammation that occurs in the periodontium.

DISCUSSION

Periodontitis is a highly prevalent disease that leads to periodontal attachment loss, bone destruction, tooth loss, and systemic diseases. Experimental periodontitis is a suitable model for exploring anti-inflammatory, osteogenic, and anti-osteoclast characteristics of biomaterials in bone regeneration, as it is easy to create and is accessible for observation. The application of animal models has been limited by several factors, such as small oral cavity size, operative difficulty, and expense (Suzuki et al., 2006). Mice are the most ideal animal models for pathological and therapeutic research of periodontitis, because the mouse-derived antigen of the experimental specimen

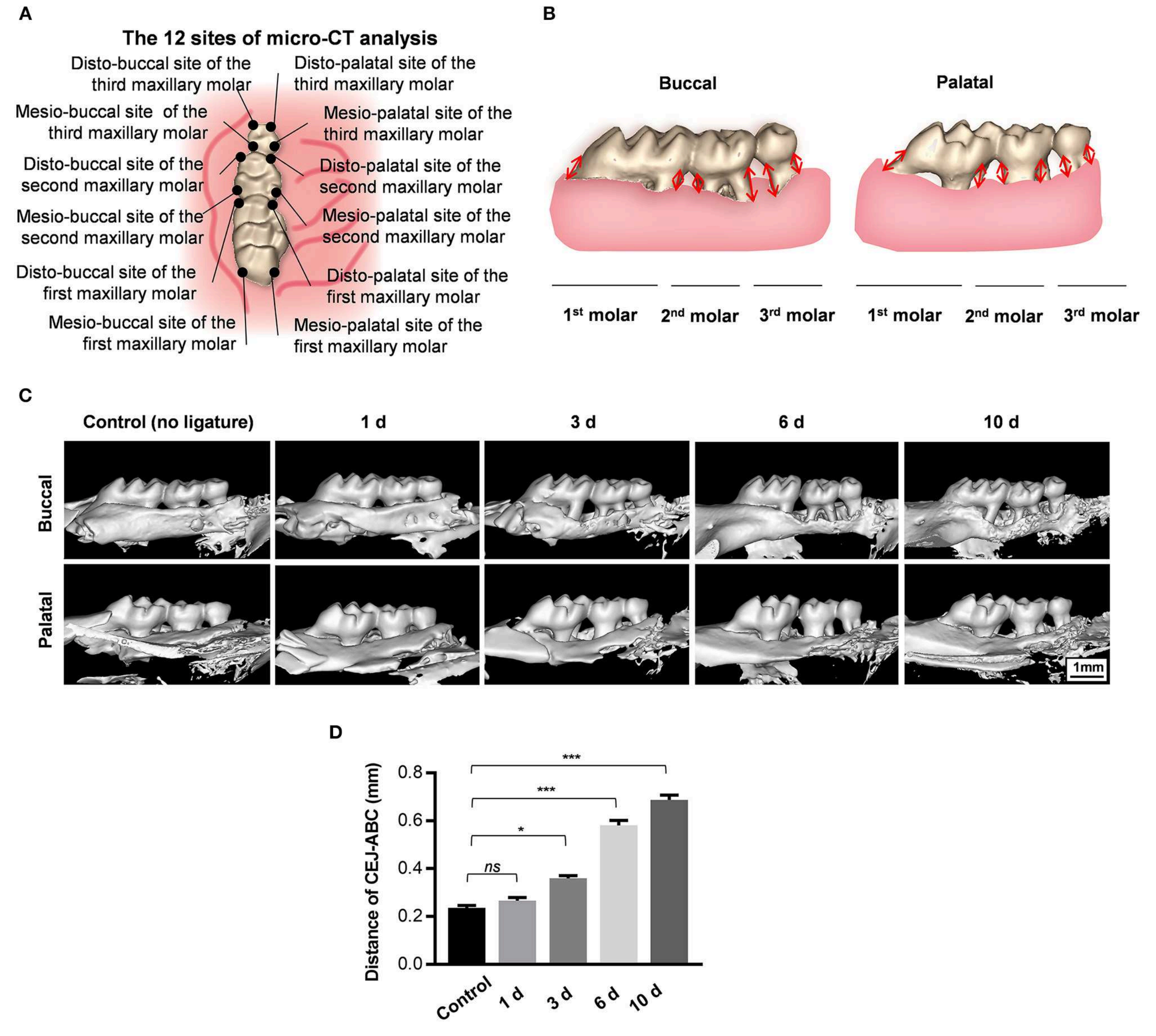

FIGURE 2 | Orthodontic ligature wire insertion induces progressive alveolar bone loss. **(A)** Anatomical direction of maxillary molars. **(B)** Schematics of strategy for bone loss measurement by assessing the distances from the cementoenamel junctions to the alveolar bone crest (CEJ-ABC) on buccal and palatal side. **(C)** Representative sagittal 3D images viewed from the buccal side and palatal side of the maxillary molars 0, 1, 3, 6, and 10 d after ligature-insertion. **(D)** Statistical analysis of the linear distance of CEJ-ABC 0, 1, 3, 6, and 10 d after experimental periodontitis operation. Data are shown as mean ± SD. ($^{*}P < 0.05$, $^{***}P < 0.001$, ns, not significant, $n = 3$, One-way ANOVA, Tukey's multiple comparisons test).

can be detected sensitively with high-quality immunochemical detection reagents. Furthermore, the cost of experiments with small animals is lower than that of large animals. In addition, compared with large animals, it is more convenient to keep mice in SPF environments for long-period researches.

According to the traditional method, inserting the ligature threads through the interproximal space between the 2nd and 3rd molars and the interproximal space between the 1st and 2nd molars is the key step to establishing the periodontitis model, and it is easy to achieve in large animals, but difficult in mice due to the limited operating space. As murine molars have a size range of 0.4–1.2 mm^2, the traditional ligature placement around the maxillary second molar requires proficient technical skill (Marchesan et al., 2018). Furthermore, it is difficult to insert 0.2-mm stainless steel orthodontic ligature wire into the interproximal space because of the blockage of gingival tissues, which creates a barrier. Although 0.2-mm stainless steel orthodontic ligature wire is sufficiently durable to pass through the interproximal space and could promote bacterial accumulation (Alves de Souza et al., 2008),

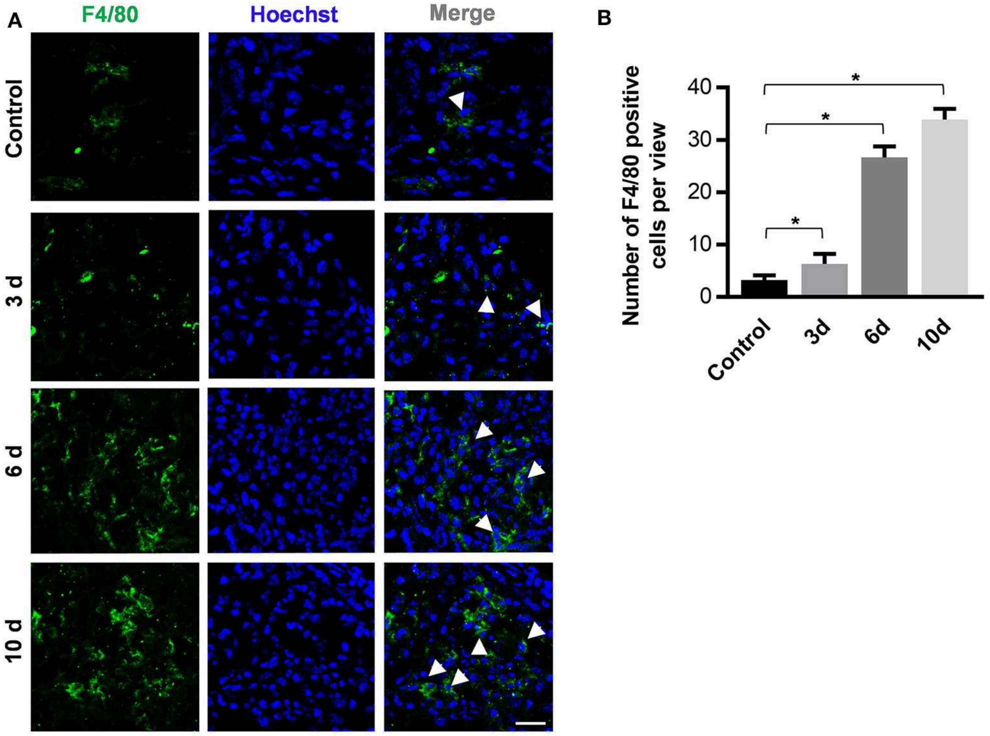

FIGURE 3 | The periodontitis induction method of orthodontic wire insertion aggravates macrophage infiltration in periodontal tissues. **(A)** Sliced sections of periodontal tissues which were collected at 0, 3, 6, and 10 days after wire-placement. The interproximal space between the first molar and the second molar is observed. Representative confocal images of stained periodontal tissues. Arrowheads mark F4/80+ cells. (scale bar, 25 μm). **(B)**The number of F4/80 positive cells in the view of **(A)** between the first and the second molars were calculated at all time points. Data are shown as mean ± SD. *$P < 0.05$. ($n = 3$, One-way ANOVA, Tukey's multiple comparisons test).

orthodontic wires are easily bent and deformed. In this work, we provide a unique perspective on a new method using orthodontic ligature wires and C+ Nickel titanium root canal files.

C+ nickel-titanium root canal files are stiff and durable, yet elastic. They have been used by dental operators to probe the narrow orifice of calcified root canals and determine their location via tactile feedback, which will indicate the sites of the tiny interproximal space between molars. An appropriate angle can be formed in pre-bent C+ nickel titanium root canal files, which are sufficiently thin and can pass through the interproximal space to assist with identifying the blockage of gingival tissues, thus providing an access point for the insertion of orthodontic ligature wires. To the best of our knowledge, we are the first to report a method for initiating experimental periodontitis using C+ nickel-titanium root canal files and orthodontic ligature wires.

Accordingly, micro-CT, histological staining, and inflammatory gene detection by qPCR were used to confirm the effect of experimental periodontitis induction. As the results show, the new approach simulates progressive bone loss and accelerates inflammatory infiltration. Hajishengallis et al. reported that the placement of ligature threads in mice caused alveolar bone loss by the natural accumulation of bacteria but not by mechanical trauma (Abe and Hajishengallis, 2013). Studies also reported that endogenous microorganisms could lead to periodontitis in ligation-treated mice (Abe and Hajishengallis, 2013; Jiao et al., 2013). Similar to the ligature threads that are used in the ligature model, orthodontic ligature wires, which are applied in dental treatments, provide an ideal habitat for the oral bacteria that cause periodontal diseases (Chun et al., 2007). As reported, orthodontic wire-induced oral plaque is the major cause for periodontal inflammation in orthodontic treatments (Liu et al., 2011).

Our data also verified that insertion of 0.20-mm orthodontic ligatures would not harm the alveolar bone or gingival tissue because no bone loss was observed in micro-CT analysis 1 day after wire placement. The results revealed that sustaining the successful periodontitis phenotype was dependent on accumulation of an endogenous oral microbiota rather than as a result of operative trauma to the periodontium. Like previously reported ligature models (Liu et al., 2018; Kourtzelis et al., 2019), our orthodontic-wire-induced gingival inflammation and alveolar bone loss but did not result in robust inflammation or bone damage. We took the study by Jiao et al. (2013) for reference, which applied the mice model by 10-day ligature placement. And the studies have induced alveolar bone loss and inflammatory infiltration, which represent the successful

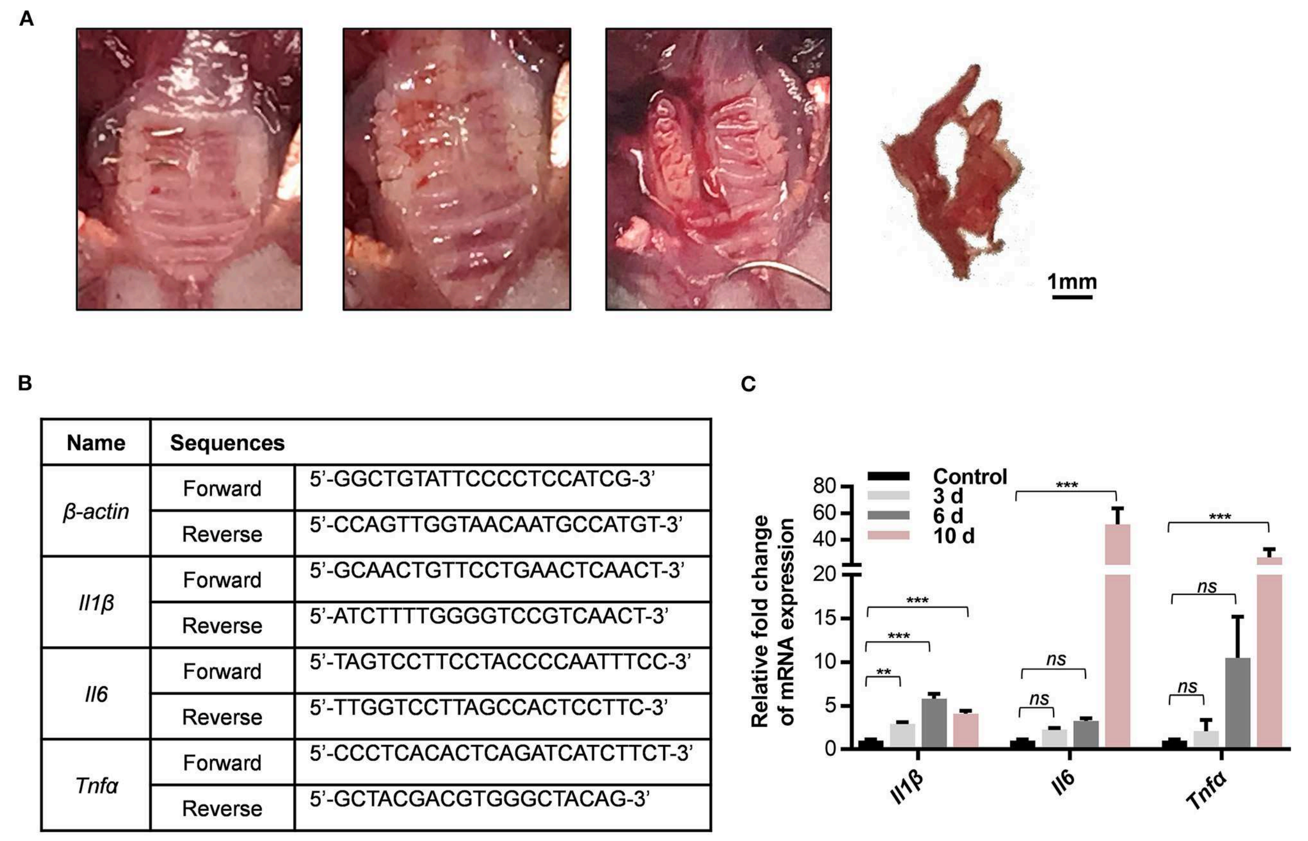

Name	Sequences	
β-actin	Forward	5'-GGCTGTATTCCCCTCCATCG-3'
	Reverse	5'-CCAGTTGGTAACAATGCCATGT-3'
Il1β	Forward	5'-GCAACTGTTCCTGAACTCAACT-3'
	Reverse	5'-ATCTTTTGGGGTCCGTCAACT-3'
Il6	Forward	5'-TAGTCCTTCCTACCCCAATTTCC-3'
	Reverse	5'-TTGGTCCTTAGCCACTCCTTC-3'
Tnfα	Forward	5'-CCCTCACACTCAGATCATCTTCT-3'
	Reverse	5'-GCTACGACGTGGGCTACAG-3'

FIGURE 4 | The new method for periodontitis induction increases expression of inflammatory gene in periodontal tissues. **(A)** Collection of gingival tissues around the ligature side of maxillary molars. **(B)** Sequences of gene-specific primers used in qPCR analysis. **(C)** The mRNA levels of *Il1β*, *Il6,* and *Tnfα* in whole gingival tissues including on 0, 3, 6, and 10 days after ligature-placed sites were determined by qPCR experiments. Results are shown as fold increase relative to the control tissues without experimental periodontitis treatment in mean ± SD. ($^{**}P < 0.01$, $^{***}P < 0.001$, ns, not significant, $n = 3$, One-way ANOVA, Tukey's multiple comparisons test).

establishment of periodontitis. We decided to execute the mice 10 days after periodontitis induction so as to prove that our method could promote alveolar bone loss as effectively as the traditional one. Thus, this method can be used to mimic alveolar bone loss and gingival inflammation in periodontitis with minimal assistance and is appropriate for establishing experimental periodontitis.

The most noteworthy advantage of our method is that the tools of our presented method are economic and feasible. Focusing on the same problem, Marchesan et al. recently developed an approach to place ligature threads between molars, using an appliance they designed by 3D-printing technique (Marchesan et al., 2018). In this work, we provide a new and proven method using orthodontic ligature wires and C+ Nickel titanium root canal files. These two tools are common in dental clinics but not usual in other institutes. The other researchers may probably not be as familiar with these tools as the dental researchers. However, since using the C+ Ni-Ti root canal files and orthodontic ligature wires is economic and feasible, more researchers could learn this simple method and apply it to their future research after reading this work. More importantly, our facile method can be conducted by a single operator without assistance and in less than 10 min after practicing, thus saving much time. Our modified wire-induced periodontitis model can be used in conjunction with periodontal pathogens to mimic the host response and develop anti-bacterial therapy. The short operative time of our method is advantageous for the survival of exogenous anaerobic periodontal pathogens.

We think this technique can be further used in rats, rabbits, dogs, goats, or larger animals by using thicker ligature wires and larger sizes of C+ Ni-Ti root canal files. The creative technique can greatly improve research efficiency, success rate, and technical limitations. In addition to pathological mechanism research, experimental periodontitis is a suitable disease model for studying bone regeneration and elucidating the potential therapeutic role of biomaterials on periodontal tissue engineering. Once serious alveolar bone loss has occurred, it is difficult to achieve restoration and regeneration. Tao et al. developed an injectable woven bone-like hydrogel to help alveolar ridge bone remodeling after tooth extraction, so as to preserve enough bone for the insertion of dental implants (Yang et al., 2020). In oral clinic, it is common that periodontitis leads to alveolar bone loss, tooth loosening, and falling off, which require dental implant treatment. Establishing the animal model mimicking the bone microenvironment is becoming increasingly necessary to explore bone substitute biomaterials. This *in vivo* periodontitis model could be used preclinically to investigate potential tissue engineering treatments under bacteria-caused pathological oral environments. Using this model to test the antibacterial, anti-inflammatory, and osteogenic properties of biomaterials under the condition of periodontitis will help to verify the therapeutic effect of biomaterials on alveolar bone defects caused by periodontitis, so as to provide evidence for their future clinical applications. What is more, our study inspired an enlightening thought that we can create novel and efficient methods for establishing traditional animal models through multidisciplinary collaboration. Cross-subject research is a new trend in the future. This technique is a new combination of clinical endodontics and basic periodontological research.

In conclusion, we explored a novel approach to generating a mouse model of periodontitis induction. The results showed that progressive alveolar bone loss and periodontal inflammation were observed after placement of orthodontic ligature wires. Therefore, our model could be suitable for studying the pathogenesis of periodontitis, the mechanism of periodontal defects, and regenerative treatments.

DATA AVAILABILITY STATEMENT

The datasets generated for this study are available on request to the corresponding author.

ETHICS STATEMENT

The animal study was reviewed and approved by Institutional Animal Care and Use Committee (IACUC), Sun Yat-sen University (Approval No. SYSU-IACUC-2020-000146).

AUTHOR CONTRIBUTIONS

DL performed the research, analyzed data, and wrote the paper. YF participated in the research and wrote the paper. ZT, LH, and CH assisted in the animal experiments, sample preparation, and consultation of periodontitis bacteria. HT and XC involved in the routine management, procurement of laboratory and the study. JT conceived of and organized the research. DL and YF contributed equally in this work. All authors contributed to manuscript revision, read and approved the submitted version.

FUNDING

The study was supported by the National Natural Science Foundation of China (81873710), Guangdong Financial Fund for High-Caliber Hospital Construction (174-2018-XMZC-0001-03-0125/C-05), Guangzhou Foundation for Science and Technology Planning Project, China (201704030083), the Fundamental Research Funds for the Central Universities(19ykzd15), Sun Yat-sen University Technological Achievement Transformation Project (87000-18843231). The funding bodies contributed to the conception, design and progress of the study. Additionally, the corresponding author is the principal investigator for the funding bodies above.

ACKNOWLEDGMENTS

We are grateful for Prof. Bin Cheng and Prof. Yan Wang for their instruction and contribution in our research.

SUPPLEMENTARY MATERIAL

The Supplementary Material for this article can be found online at: https://www.frontiersin.org/articles/10.3389/fbioe.2020.00444/full#supplementary-material

REFERENCES

Abe, T., and Hajishengallis, G. (2013). Optimization of the ligature-induced periodontitis model in mice. *J. Immunol. Methods* 394, 49–54. doi: 10.1016/j.jim.2013.05.002

Alves de Souza, R., Borges de Araujo Magnani, M. B., Nouer, D. F., Oliveira da Silva, C., Klein, M. I., Sallum, E. A., et al. (2008). Periodontal and microbiologic evaluation of 2 methods of archwire ligation: ligature wires and elastomeric rings. *Am. J. Orthod. Dentofacial Orthop.* 134, 506–512. doi: 10.1016/j.ajodo.2006.09.067

Bhattarai, G., Poudel, S. B., Kook, S. H., and Lee, J. C. (2016). Resveratrol prevents alveolar bone loss in an experimental rat model of periodontitis. *Acta Biomater.* 29, 398–408. doi: 10.1016/j.actbio.2015.10.031

Blasco-Baque, V., Garidou, L., Pomie, C., Escoula, Q., Loubieres, P., Le Gall-David, S., et al. (2017). Periodontitis induced by *Porphyromonas gingivalis* drives periodontal microbiota dysbiosis and insulin resistance via an impaired adaptive immune response. *Gut* 66, 872–885. doi: 10.1136/gutjnl-2015-309897

Chun, M-J., Shim, E., Kho, E-H., Park, K-J., Jung, J., Kim, J-M., et al. (2007). Surface modification of orthodontic wires with photocatalytic titanium oxide for its antiadherent and antibacterial properties. *Angle Orthod.* 77, 483–488. doi: 10.2319/0003-3219(2007)077[0483:Smooww]2.0.Co;2

Courbon, G., Rinaudo-Gaujous, M., Blasco-Baque, V., Auger, I., Caire, R., Mijola, L., et al. (2019). *Porphyromonas gingivalis* experimentally induces periodontis and an anti-CCP2-associated arthritis in the rat. *Ann. Rheum. Dis.* 78, 594–599. doi: 10.1136/annrheumdis-2018-213697

Datey, A., Thaha, C. S. A., Patil, S. R., Gopalan, J., and Chakravortty, D. (2019). Shockwave therapy efficiently cures multispecies chronic periodontitis in a humanized rat model. *Front. Bioeng. Biotechnol.* 7:382. doi: 10.3389/fbioe.2019.00382

Eskan, M. A., Jotwani, R., Abe, T., Chmelar, J., Lim, J. H., Liang, S., et al. (2012). The leukocyte integrin antagonist Del-1 inhibits IL-17-mediated inflammatory bone loss. *Nat. Immunol.* 13, 465–473. doi: 10.1038/ni.2260

Hajishengallis, G. (2015). Periodontitis: from microbial immune subversion to systemic inflammation. *Nat. Rev. Immunol.* 15, 30–44. doi: 10.1038/nri3785

Hajishengallis, G., Darveau, R. P., and Curtis, M. A. (2012). The keystone-pathogen hypothesis. *Nat. Rev. Microbiol.* 10, 717–725. doi: 10.1038/nrmicro2873

Hasani-Sadrabadi, M. M., Sarrion, P., Nakatsuka, N., Young, T. D., Taghdiri, N., Ansari, S., et al. (2019). Hierarchically patterned polydopamine-containing membranes for periodontal tissue engineering. *ACS Nano* 13, 3830–3838. doi: 10.1021/acsnano.8b09623

Jiao, Y., Darzi, Y., Tawaratsumida, K., Marchesan, J. T., Hasegawa, M., Moon, H., et al. (2013). Induction of bone loss by pathobiont-mediated Nod1 signaling in the oral cavity. *Cell Host Microbe* 13, 595–601. doi: 10.1016/j.chom.2013.04.005

Kourtzelis, I., Li, X., Mitroulis, I., Grosser, D., Kajikawa, T., Wang, B., et al. (2019). DEL-1 promotes macrophage efferocytosis and clearance of inflammation. *Nat. Immunol.* 20, 40–49. doi: 10.1038/s41590-018-0249-1

Lamont, R. J., Koo, H., and Hajishengallis, G. (2018). The oral microbiota: dynamic communities and host interactions. *Nat. Rev. Microbiol.* 16, 745–759. doi: 10.1038/s41579-018-0089-x

Liu, H., Sun, J., Dong, Y., Lu, H., Zhou, H., Hansen, B. F., et al. (2011). Periodontal health and relative quantity of subgingival *Porphyromonas gingivalis* during orthodontic treatment. *Angle Orthod.* 81, 609–615. doi: 10.2319/082310-352.1

Liu, Z., Chen, X., Zhang, Z., Zhang, X., Saunders, L., Zhou, Y., et al. (2018). Nanofibrous spongy microspheres to distinctly release miRNA and growth factors to enrich regulatory T cells and rescue periodontal bone loss. *ACS Nano* 12, 9785–9799. doi: 10.1021/acsnano.7b08976

Manilay, J. O., and Zouali, M. (2014). Tight relationships between B lymphocytes and the skeletal system. *Trends Mol. Med.* 20, 405–412. doi: 10.1016/j.molmed.2014.03.003

Marchesan, J., Girnary, M. S., Jing, L., Miao, M. Z., Zhang, S., Sun, L., et al. (2018). An experimental murine model to study periodontitis. *Nat. Protoc.* 13, 2247–2267. doi: 10.1038/s41596-018-0035-4

Nasajpour, A., Ansari, S., Rinoldi, C., Rad, A. S., Aghaloo, T., Shin, S. R., et al. (2018). A multifunctional polymeric periodontal membrane with osteogenic and antibacterial characteristics. *Adv. Funct. Mater.* 28:1703437. doi: 10.1002/adfm.201703437

Offenbacher, S., Jiao, Y., Kim, S. J., Marchesan, J., Moss, K. L., Jing, L., et al. (2018). GWAS for Interleukin-1beta levels in gingival crevicular fluid identifies IL37 variants in periodontal inflammation. *Nat. Commun.* 9:3686. doi: 10.1038/s41467-018-05940-9

Ouchi, T., and Nakagawa, T. (2020). Mesenchymal stem cell-based tissue regeneration therapies for periodontitis. *Regen. Ther*. 14, 72–78. doi: 10.1016/j.reth.2019.12.011

Potempa, J., Mydel, P., and Koziel, J. (2017). The case for periodontitis in the pathogenesis of rheumatoid arthritis. *Nat. Rev. Rheumatol.* 13, 606–620. doi: 10.1038/nrrheum.2017.132

Schiffrin, E. L., and Engert, J. C. (2019). Periodontitis and hypertension: causally linked by immune mechanisms. *Eur. Heart J.* 40, 3471–3473. doi: 10.1093/eurheartj/ehz729

Suzuki, S., Mitani, A., Koyasu, K., Oda, S., Yoshinari, N., Fukuda, M., et al. (2006). A model of spontaneous periodontitis in the miniature goat. *J Periodontol.* 77, 847–855. doi: 10.1902/jop.2006.050203

Tan, J., Zhang, M., Hai, Z., Wu, C., Lin, J., Kuang, W., et al. (2019). Sustained release of two bioactive factors from supramolecular hydrogel promotes periodontal bone regeneration. *ACS Nano* 13, 5616–5622. doi: 10.1021/acsnano.9b00788

Tsukasaki, M., Komatsu, N., Nagashima, K., Nitta, T., Pluemsakunthai, W., Shukunami, C., et al. (2018). Host defense against oral microbiota by bone-damaging T cells. *Nat. Commun.* 9:701. doi: 10.1038/s41467-018-03147-6

Xiao, E., Mattos, M., Vieira, G. H. A., Chen, S., Correa, J. D., Wu, Y., et al. (2017). Diabetes enhances IL-17 expression and alters the oral microbiome to increase its pathogenicity. *Cell Host Microbe* 22, 120–128.e124. doi: 10.1016/j.chom.2017.06.014

Yang, T., Xie, P., Wu, Z., Liao, Y., Chen, W., Hao, Z., et al. (2020). The injectable woven bone-like hydrogel to perform alveolar ridge preservation with adapted remodeling performance after tooth extraction. *Front. Bioeng. Biotechnol.* 8:119. doi: 10.3389/fbioe.2020.00119

Zhuang, Z., Yoshizawa-Smith, S., Glowacki, A., Maltos, K., Pacheco, C., Shehabeldin, M., et al. (2019). Induction of M2 macrophages prevents bone loss in murine periodontitis models. *J. Dent. Res.*. 98, 200–208. doi: 10.1177/0022034518805984

Conflict of Interest: The authors declare that the research was conducted in the absence of any commercial or financial relationships that could be construed as a potential conflict of interest.

frontiers
in Bioengineering and Biotechnology

ORIGINAL RESEARCH
published: 29 May 2020
doi: 10.3389/fbioe.2020.00517

BMP2-Functionalized Biomimetic Calcium Phosphate Graft Promotes Alveolar Defect Healing During Orthodontic Tooth Movement in Beagle Dogs

Shijie Jiang [1,2†], ***Tie Liu*** [2,3†], ***Gang Wu*** [4], ***Wen Li*** [1,2], ***Xiaoxia Feng*** [1,2], ***Janak L. Pathak*** [5*] **and** ***Jiejun Shi*** [1,2*]

[1] Department of Orthodontics, The Affiliated Stomatology Hospital, Zhejiang University School of Medicine, Hangzhou, China, [2] Key Laboratory of Oral Biomedical Research of Zhejiang Province, Zhejiang University School of Stomatology, Hangzhou, China, [3] Department of Oral Implantology, The Affiliated Stomatology Hospital, Zhejiang University School of Medicine, Hangzhou, China, [4] Department of Oral Implantology and Prosthetic Dentistry, Academic Centre of Dentistry Amsterdam (ACTA), Vrije Universiteit Amsterdam and University of Amsterdam, Amsterdam, Netherlands, [5] Key Laboratory of Oral Medicine, Guangzhou Institute of Oral Disease, Affiliated Stomatology Hospital of Guangzhou Medical University, Guangzhou, China

Background: Grafting of biomaterial in alveolar defect facilitates bone healing and orthodontic treatment. BMP2-functionalized biomimetic calcium phosphate (BioCaP) graft had shown excellent bone defect healing potential in many preclinical studies. In this study, we aimed to investigate the influence of BioCaP graft on surgical alveolar bone defect healing during orthodontic tooth movement (OTM) in beagle dogs.

Methods: Nine Beagle dogs were randomly assigned to three groups: control, deproteinized bovine bone (DBB), and BioCaP. The maxillary second premolars were protracted into the defects of the extracted maxillary first premolar for 8 weeks. The rate of OTM, alveolar remodeling and bone defect healing were evaluated by histology, histomorphometry, and cone beam computed tomography (CBCT) imaging. Periodontal probing depth was analyzed. Gingival cervicular fluid was collected at week 4 and 8, and the IL-1β level was measured by ELISA.

Results: The histological sections of the bone defect showed more newly formed bone in the BioCaP group. The percentage of new bone formation in the BioCaP group was 1.61-, and 1.25-fold higher compared to the control and DBB group, respectively. After 8 weeks of OTM, the resorption rate of BioCaP was 1.42-fold higher compared to DBB. The root resorption index in the DBB group was 1.87-, and 1.39-fold higher compared to the control and BioCaP group, respectively. CBCT images showed 1.92-, and 1.36-fold higher bone mineral density in the BioCaP group compared to the control and DBB group, respectively. There was no significant difference in OTM among the three groups. The distance between the enamel cementum and the crest of the alveolar ridge in the control group was 1.45-, and 1.69-fold higher compared to DBB and BioCaP group, respectively. Periodontal probing depth at week 8 was reduced in the BioCaP group compared to the control. IL-1β concentration in the gingival cervicular fluid was significantly lower in the BioCaP group compared to the control group at week 4 and 8.

Edited by:
Nihal Engin Vrana,
Sparta Medical, France

Reviewed by:
Sergey V. Dorozhkin,
Independent Researcher, Moscow,
Russia
Yoshinori Shirakata,
Kagoshima University, Japan

***Correspondence:**
Janak L. Pathak
j.pathak@gzhmu.edu.cn
Jiejun Shi
sjiejun@zju.edu.cn

† These authors have contributed equally to this work and share first authorship

Specialty section:
This article was submitted to Biomaterials, a section of the journal Frontiers in Bioengineering and Biotechnology

Received: *02 March 2020*
Accepted: *01 May 2020*
Published: *29 May 2020*

Citation:
Jiang S, Liu T, Wu G, Li W, Feng X, Pathak JL and Shi J (2020) BMP2-Functionalized Biomimetic Calcium Phosphate Graft Promotes Alveolar Defect Healing During Orthodontic Tooth Movement in Beagle Dogs. Front. Bioeng. Biotechnol. 8:517. doi: 10.3389/fbioe.2020.00517

Conclusion: BioCaP graft robustly promoted bone regeneration and alveolar bone defect healing without affecting OTM. BioCaP graft caused less alveolar bone recession and root resorption of traction tooth with favorable periodontal attachment level indicating that BioCaP as a bioactive and functional bone filling material for alveolar bone defects during orthodontic treatment.

Keywords: biomimetic calcium phosphate granules, deproteinized bovine bone (DBB) graft, orthodontic tooth movement, alveolar defects, bone regeneration

INTRODUCTION

Alveolar bone defects are frequently encountered during orthodontic treatment. The alveolar defects during orthodontic treatment are mainly caused by the removal of neighboring teeth, surgical-orthodontic treatment, and severe periodontitis. Grafting of biomaterials in alveolar defects before orthodontic tooth movement (OTM) had shown successful bone regeneration during orthodontic treatment (Hossain et al., 1996). Previous studies had confirmed that the bone-filling materials facilitate teeth movement and stimulate alveolar bone deposition under orthodontic force (Hossain et al., 1996; Yilmaz et al., 2000; Oltramari et al., 2007; Klein et al., 2019; Nagy et al., 2019). Therefore, the cost-effective alveolar bone defect-filling materials are in high demand in orthodontic clinics.

Alveolar bone surgery can speed up orthodontic tooth movement (Hibino and Wong, 2009; Kim et al., 2015b). Usually, the orthodontic force is applied for at least 3 months after alveolar bone healing (Mayer et al., 1994; Nakamoto et al., 2002). Teeth traction force can be applied immediately to accelerate OTM after the graft material is placed into the surgical defect (Ahn et al., 2014). The early stage of OTM after material grafted in alveolar surgical defect promotes bone regeneration (Ahn et al., 2014). Bone graft materials and techniques accelerate tooth movement into the alveolar defect with healthy bone regeneration (Reichert et al., 2010; Ahn et al., 2014; Tsai et al., 2017). In the case of bone grafting during orthodontic treatment, bone regeneration, graft stability, and any side effects around orthodontic teeth or the periodontium should be meticulously evaluated (Hossain et al., 1989, 1996; Sheats et al., 1991; Araujo et al., 2001; Kawamoto et al., 2002). The satisfactory outcome of early OTM following regenerative surgery suggests that the biomechanical stimulation may not jeopardize the regenerative effect (Tsai et al., 2017). Therefore, the ideal bone grafting materials for orthodontic treatment should have the potential to protect the orthodontic teeth and enhance alveolar bone regeneration.

BMP2 is a potent osteogenic growth factor that also promotes alveolar bone regeneration (King et al., 1997). Literature had reported various BMP2-loaded biomaterials for alveolar bone regeneration (Selvig et al., 2002; Rao et al., 2013; Oortgiesen et al., 2014). However, the clinical use of BMP2-loaded biomaterials for alveolar bone regeneration is still controversial mainly due to the adverse effects of burst released high dose BMP2 (James et al., 2016). We have developed BMP2-functionalized biomimetic calcium phosphate (BioCaP) granules with excellent biocompatibility, osteoconductivity, and osteoinductivity (Liu et al., 2014, 2017; Wang et al., 2019). Biomimetic coating of BMP2 and calcium phosphate onto the surface of the material is an attractive approach for controlled release of BMP2 (Wernike et al., 2010; Wang et al., 2017). BioCaP has shown sustained release of BMP2 both *in vitro* and in bone defect site (Zheng et al., 2014; Liu et al., 2017, 2018). Moreover, BioCaP promoted critical size bone defect healing in both small animal and large animal models (rats, rabbit, dog, and sheep) in different anatomical sites (cranial defects and femoral defects) (Liu et al., 2010, 2014, 2017, 2018; Wang et al., 2017, 2019). One cubic centimeter (1 mL) of BioCaP granules loads 140 μg of BMP2 and robustly promotes critical size bone defect healing (Liu et al., 2017, 2018; Wang et al., 2017). A dose of 1.5 mg/ml of rhBMP2 was identified as the most effective concentration for *de novo* Bone (Boyne et al., 1997, 2005). BioCaP bone graft reduces the dose of BMP2 required for *in vivo* bone regeneration by 10-fold (Boyne et al., 1997, 2005; Liu et al., 2017, 2018; Wang et al., 2017). That could minimize the adverse effects of high dose BMP2 during clinical uses as well as reduced the economic burden of expensive rhBMP2. Therefore, the BioCaP granules could be a promising bone graft for alveolar bone defect healing during orthodontic treatment. However, the potential of BioCaP to heal alveolar bone defect during orthodontic treatment and its effect on OTM has not been investigated yet.

The aim of this study was to analyze the efficacy of BioCaP-graft on surgical alveolar bone defect healing during orthodontics tooth movement (OTM) in a large animal model. We analyzed surgical alveolar bone defect healing in the canine orthodontic treatment model. And DBB bone graft was used as a standard control. We studied the possible effect of BioCaP bone graft on OTM. BioCaP granules robustly enhanced alveolar bone regeneration and preserved the root resorption of OTM teeth compared to DBB. Moreover, the BioCaP bone graft in alveolar defect adjacent to OTM teeth did not obstruct the OTM, reduced inflammation, and preserved periodontal tissue. Our findings indicate BioCaP as a promising osteoinductive biomaterial to improve alveolar bone regeneration during orthodontic treatment.

MATERIALS AND METHODS

Fabrication of BioCaP

BioCaP was fabricated by refining a well-established biomimetic mineralization technique described in our previous studies (Wu et al., 2011; Liu et al., 2013, 2014, 2017). Briefly, a CaP solution (200 mM HCl, 20 mM $CaCl_2 \cdot 2H_2O$, 680 mM NaCl, and 10 mM

Na_2HPO_4) was buffered by TRIS (250 mM) to a pH of 7.4. In order to sterilize the CaP solution, it was filtered with a vacuum filter (0.22 μm pore) before buffering. All the following procedures were performed under aseptic conditions. After buffering, the solution was incubated in a shaking water bath (50 agitations/min) at 37°C for 24 h. The solution was removed, and the precipitated material was gently washed by Milli-Q water, filtered, and compressed to a block using a vacuum exhaust filtering (0.22 μm pore, Corning, NY, USA). After drying at room temperature for 2 h, the compacted block was ground and filtered in metallic filter mesh to obtain different sizes (250–1,000 μm) of granules.

Biomimetic Coating and BMP2 Incorporation

The superficial coating of calcium and phosphate was deposited on BioCaP according to the procedure described before (Liu et al., 2005; Wu et al., 2010). Briefly, the coating solution, 40 mM HCl, 4 mM $CaCl_2 \cdot 2H_2O$, 136 mM NaCl, 2 mM Na_2HPO_4, and 50 mM TRIS (pH 7.4) in total volume of 20 ml was prepared. BioCaP was incubated in the coating solution in a shaking water bath (50 agitations/min) at 37°C for 24 h. The protein BMP-2 (INFUSE® Bone Graft, Medtronic, USA) was added in the supersaturated solution (coating solution) of calcium phosphate at a final concentration of 1 μg/ml, and was subsequently co-precipitated into the biomimetic calcium phosphate coating of the BioCaP granules. The samples were then freeze-dried and characterized as described previously (Zheng et al., 2014; Liu et al., 2017). The entire procedure was conducted under sterile conditions. BioCaP granules with a diameter of 250−1,000 μm were selected in this experiment, which is the size of DBB granules used in this study.

Experimental Groups and Animal Model

All *in vivo* experiments of this study were carried out in accordance with the principles of the Basel Declaration and recommendations of Zhejiang University Laboratory Animal Center. The protocol was approved by the Ethics committee of the Zhejiang University Laboratory Animal Center (ethic approval number: ZJU20190057, approval date: 2019.05.20). Nine male Beagle dogs (1 year old, 11–13 Kg body weight) were housed in separate cages in the SPF level large animal room of Zhejiang University Laboratory Animal Center. Total 18 examples of maxillary second premolars were randomly allocated to three equal groups to receive the following treatments: Control group (no treatment-negative control), BioCaP group (experiment group), and DBB group (positive control group).

After intraperitoneal anesthesia with 3% pentobarbital sodium (1 ml/kg body weight), dental models of all groups were taken from alginate impression materials (Harbin Dental Equipment Factory, China) and sent to the processing plant (Technical Center of Dental Hospital Affiliated to Medical College of Zhejiang University to produce orthodontic traction devices. Before surgery, the alveolar region of each dog was scanned for CBCT images using NEWTOM 3G QR-DVT9000 CBCT machine (QR r.s.l, Verona, Italy).

Under anesthesia, each dog was fixed on the experimental table in the supine position and injected with the acute infiltration anesthesia Primacaine (SATELEC, France) into the gingival of first and second premolar on both sides of the maxillary. After skin disinfection (0.5% iodophor solution) to the operation sites, the gingival of bilateral maxillary first premolars were cut, and the gingival flaps were pushed to the buccal side. After extraction of the first premolars, a 4.5 mm diameter, and 6 mm deep bone defect was prepared by using a slow-speed dental motor (Korea, MARATHON-3) crack drill at the extraction wound. This defect did not contact with the root of maxillary second premolar. About 110 mm^3 volume of BioCaP and DBB granules were implanted in the Bio-CaP and DBB group, respectively. The control group defect was left empty. The implant was covered with Bio-Guide (Geistlieh AG, Switzerland) and sutured the gingival flap at the bone defect. Penicillin (500 U/day) was injected intramuscularly up to 3 days after surgery.

Orthodontic Traction

CBCT image was taken after 1 week of surgery. Orthodontics appliance was bonded on the maxillary arch, and the distance from the fourth premolar cervix to the second premolar cervix of each side was measured by vernier caliper. The orthodontic appliance consisted of a 0.019 × 0.025 inch stainless steel square wire as sectional archwire with tip back for bodily movement of the second premolar, attached with standard tubes (0.022 × 0.028 inch) on the maxillary canine and second premolar. The maxillary second premolar was pulled by a 0.012 inch nickel-titanium closed coiled spring (GRIKIN Advanced Material Co., Ltd., China) to the alveolar bone defect (mesial direction) using the canine teeth as an anchorage. The nickel-titanium closed coiled spring was pulled to until the Orthodontic dynamometer force value is 150 g, and was fixed on the orthodontic appliance by a 0.010 inch ligation wire. After traction, soft food was served. The orthodontic appliances were checked every 3 days to make sure they were not debonding. The distance from the cervix of maxillary 4th premolar to the cervix of maxillary 2nd premolar of each dog was measured every 2 weeks. The traction force was added to maintain the pulling force generated by the coil spring. The change of the distance from the maxillary fourth premolar cervix to maxillary second premolar cervix was considered as the OTM (Kim et al., 2015a). Periodontal probing depth analysis of orthodontic tooth indicates the status of periodontal tissue (Hung and Douglass, 2002). Periodontal probing depth of the maxillary second premolar was measured at the mesial side (mesial-buccal side, mid-buccal side, distal-buccal side, mesial-palatal side, mid-palatal side, and distal-palatal side) in every 2 weeks.

Level of IL-1β in Gingival Crevicular Fluid

Gingival crevicular fluid (GCF) is a biological exudate from periodontal tissue and its concentration of pro-inflammatory cytokines, including interleukin-1β (IL-1β) indicates alveolar bone resorption, and inflammation (de Aguiar and Perinetti, 2017). After 4 and 8 weeks of OTM, GCF was collected from the mesial gingival crevice of the second premolar using a no. 30 sterile paper point (Javed et al., 2014). The volume of GCF and the concentration of IL-1β were analyzed. Briefly, the sterile paper point was inserted in the mid-buccal gingival crevice of the orthodontic tooth and held in place for 60 seconds. The GCF volume density was considered as 1, and the volume of GCF was showed by the difference in weight. After sample collection, paper points were transferred to sterile microcentrifuge tubes and stored in −80°C refrigerator. The adsorbed volume of GCF in each paper point was weighed using an analytic digital balance before and after collection immediately. Each paper point was eluted by 80 μl phosphate buffer (0.01 mol/l pH 7.4) for 1 h and the buffer solution was centrifuged at 3,000 rpm for 20 min in at 4°C. IL-1β concentration in the eluted solution was analyzed by enzyme-linked immunosorbent assay (ELISA, Shanghai Haling Biological Technology Co., Ltd.).

Alveolar Tissue Collection and Histology

After 8 weeks of traction, CBCT was taken again, and all Beagle dogs were sacrificed with an overdose of sodium pentobarbital. The maxillary bone with maxillary teeth was collected and fixed in the 10% formalin solution for 48 h. The hard tissue section and staining were processed at the Department of Oral Pathology of Beijing PLA General Hospital. Briefly, after 70, 80, 90, 95, and 100% alcohol dehydration (24 h for each liquid), the mixture of 3:1, 1:1, 1:3 alcohol and Technovit 7200 (volume ratio) was pre-impregnated (24 h for each liquid), and finally soaked in pure Technovit 7200 solution for 3 days, and then polymerized and embedded in embedding machine (Germany EXAKT-520). Tissue grinding slices were made by using a hard tissue-slicing machine (German EXAKT-300CP) to cut 200 microns thick slices. The slices were polished by grinding machine (German EXAKT-400CS). The final thickness of the grinding disc was determined by the thickness measurement induction device and micrometer. Each section was stained by MC NEAL's staining method (Liu et al., 2017). Each hard tissue slice contains the mesial root of the second premolar, and the section passed through the median section of the alveolar bone defect.

Data Collection

Analysis of Newly Formed Bone

The alveolar bone defect area occupied by mineralized bone (lamellar and immature type), granules of bone filling material, and other tissues were determined by the use of a point-counting procedure and a lattice with 100 points (Zhang et al., 2011). The percentage of new bone as new bone formation ratio was calculated by dividing the area of bone tissue by the total area of the defect at each slice.

Residual Ratio of Bone Filling Material

The percentage of bone filling material was calculated by dividing the area of residual bone filling material by the total area of defect at each slice after traction of 2 months. We prepared the same size bone defect on a plastic model and filled the blood-soaked bone filling material to imitate the operation. Sections were made in the median section to estimate the percentage of bone defect area of these two kinds of filling materials (BioCaP or DBB) in the original condition. The residual rate of bone filling material was obtained by dividing the percentage of material in the section after traction by the percentage of original material (Liu et al., 2017).

Tooth Resorption Index Analysis

Image-Pro Plus 6.0 software was used to measure the area of resorption lacunae and the total root area on the mesial surface of the mesial root of the maxillary second premolar (orthodontic traction tooth) in each slice, and the root resorption index was calculated by using the following formula (Goldie and King, 1984).

$$\textit{Root resorption index} = \frac{\textit{Resorption area}}{\textit{Total root area}}$$

Radiographic Gray Value of Bone Mineral Density

CBCT images were taken under anesthesia before surgery, 1 week after surgery, and 8 weeks after OTM. All CBCT images were imported to Mimics 15.0 software (Materialise Company, Belgium) and 3-dimension remodels built. We found the area of alveolar bone defect in the CBCT images 1 week after surgery and measured the volume data of the defect and filling materials. Through this localization, we also found the location of the alveolar bone defect in CBCT reconstruction images after 2 months of traction. We measured the Gray value, which serves as an indicator for bone density of the alveolar bone defects in all groups. By calculating the average radiographic gray value of bone defect area in 6 sections from buccal to palatal side, the parameters of bone mineral density were developed.

The Retraction Distance of Alveolar Ridge

The maxillary second premolars (orthodontic teeth) were found in the CBCT images before surgery, and the distances from the enamel-cementum boundary to the alveolar crest of the mesial side of the mesial root were measured in 3 sections from buccal to palatal side. The original height of alveolar crest was obtained by calculating the average of the above three values. And the height of alveolar crest after traction was calculated in the same way in the CBCT images 2 months after traction. The retraction distance of alveolar ridge was obtained by subtracting the height of alveolar ridge after traction from the original height of the alveolar ridge.

Statistical Analysis

Data were submitted to SPSS ver. 19.0 (IBM Corporation, NY, U.S.A.) for analysis. All data are presented as mean values with the standard deviation (mean ± SD). A comparison of data within groups was performed using analysis of variance (ANOVA) followed by a post-Dunnett T3 test when ANOVA suggested a significant difference between groups. The significance level was set at $p < 0.05$.

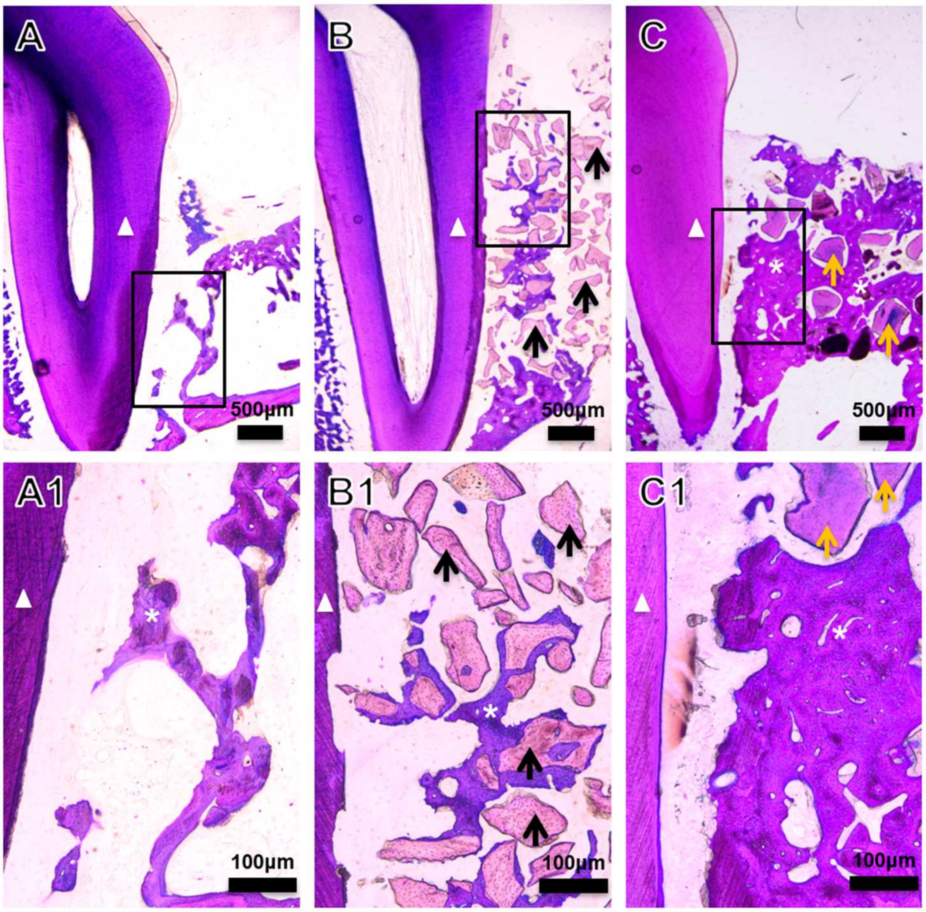

FIGURE 1 | Representative histological images of the bone defect slices from **(A)** Control, **(B)** DBB, and **(C)** BioCaP group at week 8. **(A1–C1)** are high-resolution images of **(A–C)**, respectively. White triangle, dental root; asterisk, newly formed bone; black arrow, DBB; yellow arrow, BioCaP.

RESULTS

BioCaP Graft Enhanced Bone Regeneration and Alveolar Bone Defect Healing During OTM

The amount of encapsulated BMP2 in BioCaP granules and their release profile are well-documented in our previous studies (Liu et al., 2014, 2017, 2018; Zheng et al., 2014; Wang et al., 2019). Similarly, the extensive physicochemical characterization of BioCaP is available in our published papers (Liu et al., 2014, 2017; Wang et al., 2019). Histological images showed very less amount of newly formed bone in the control group (**Figures 1A,A1**). Bone regeneration was slightly improved in the DBB group (**Figures 1B,B1**). We observed robust bone regeneration in the BioCaP group compared to the control group and DBB group (**Figure 1**). High-resolution images illustrated newly formed bone nearby or around the BioCaP granules. Dental root erosion was observed in the DBB group (**Figure 1**). The area of newly formed bone tissue was evidently less in DBB-group compared to the BioCaP group. Multinucleated osteoclast-like cells were observed only in the DBB group, which explains the dental root erosion in the DBB group (**Figures 2A,A1**). The absence of multinucleated osteoclast-like cells in the BioCaP group indicates the less immunogenicity and higher biocompatibility of BioCaP granules. A densely stained newly formed bone was observed in the BioCaP group (**Figures 2B,B1**). Similarly, blood vessels like structures were observed only in BioCaP group (**Figures 2B,B1**). In the control group, most of the bone defect area was filled with fibrous connective tissue (data not shown).

Quantitative analysis data showed 1.30-fold higher newly formed bone percentage in the DBB group compared to the control group (**Figure 3A**). In the BioCaP group, newly formed bone percentage was increased by 1.61-, and 1.25-fold compared to the control group and DBB group, respectively. Remaining graft material at week 8 was 1.45-fold higher in the DBB group compared to the BioCaP group (**Figure 3B**). Resorption rate of graft material was 1.42-fold higher in the BioCaP group compared to the DBB group (**Figure 3C**).

BioCaP Graft Enhanced Bone Mineral Density in the Alveolar Defects

CBCT images were taken at baseline, 1 week after grafting, and 8 weeks after OTM (**Supplementary Figure 1**). We measured the Gray value, which serves as an indicator for the bone density of

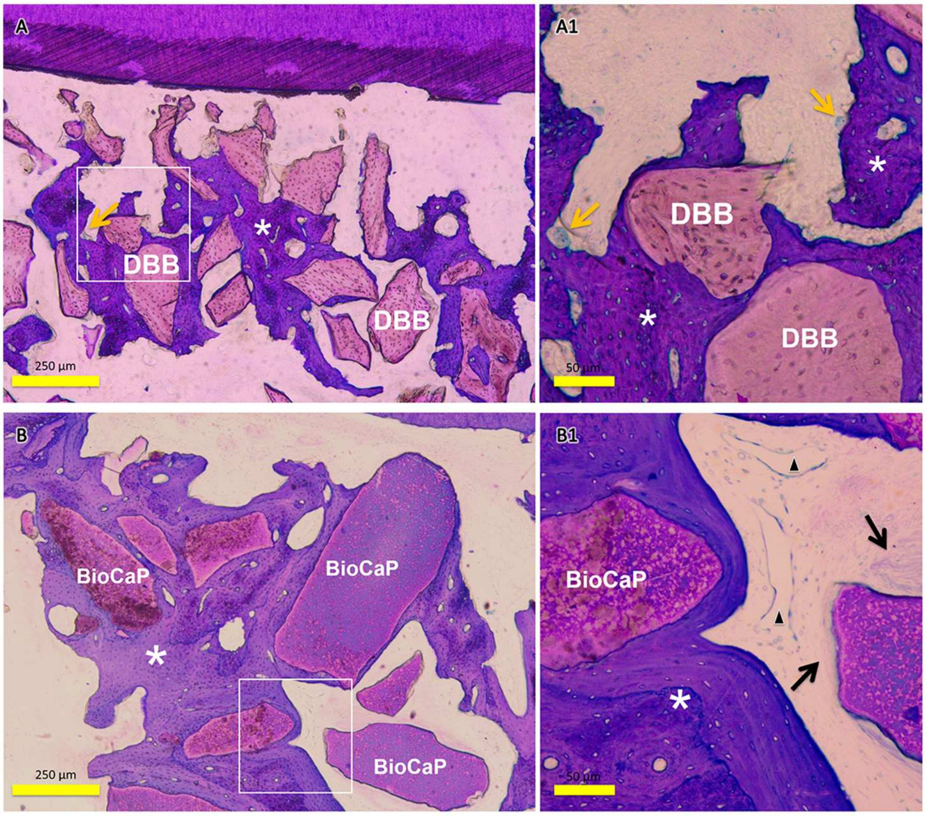

FIGURE 2 | Representative histological images of the bone defect slice in DBB group and Bio-CaP group. **(A)** Bone remodeling process in DBB group at week 8. **(A1)** High-resolution image of **(A)**. **(B)** Bone remodeling process in BioCaP group at week 8. **(B1)** High-resolution image of **(B)**. Yellow arrows, multinucleated cells; asterisk, newly formed bone; black arrow, fibrous tissue; black triangle, blood vessel like structure.

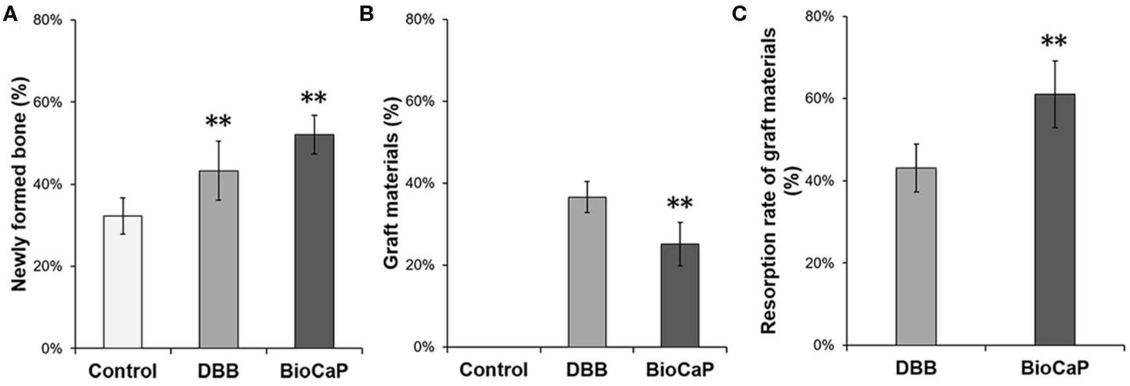

FIGURE 3 | BioCaP grafting enhanced bone formation and degradation of graft material. **(A)** Percentage of newly formed bone at week 8. **(B)** Percentage of remaining graft materials at week 8. **(C)** The resorption rate of graft materials at week 8. Data are presented as mean ± SD, from six independent experiments. Significant effect of the treatment, $^{**}p < 0.01$.

the alveolar bone defects in all groups. The bone density in the BioCaP group was 1.92-, and 1.36-fold higher compared to the control and DBB group, respectively. Both histological and CBCT images showed distinct bony alveolar ridge in the BioCaP group compared to the DBB group (**Figures 1**, **4**). In contrast, almost empty alveolar defects in the control group and mostly DBB filled alveolar defect were observed in the DBB group (**Figures 1**, **4**).

BioCaP Graft Alleviated Root Resorption and Alveolar Retraction

The root resorption index in the DBB group was 1.87-fold higher compared to the control group (**Figure 5A**). Although the higher trend of the root resorption index was observed in the DBB group compared to the BioCaP group, the effect was not statistically significant. The distance between the enamel

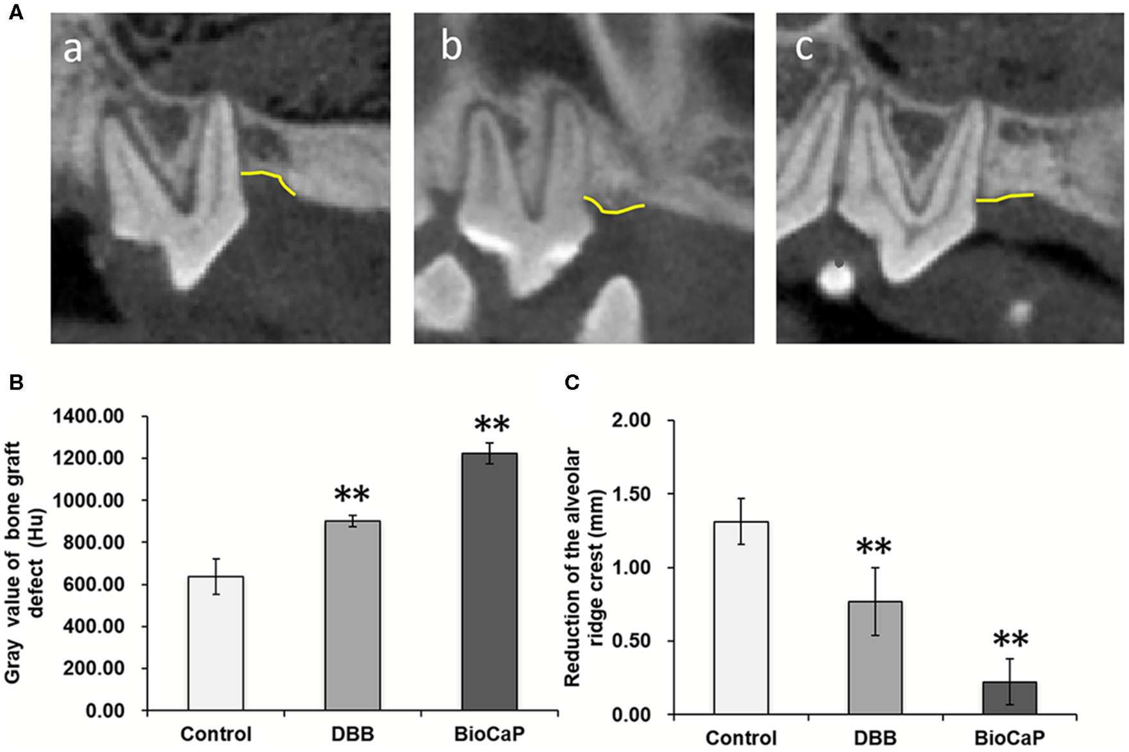

FIGURE 4 | (A) Representative CBCT images at week 8, (a) Control, (b) DBB, and (c) Bio-CaP group. **(B)** Gray value of bone graft defect (Hu). **(C)** Reduction of the alveolar ridge crest (mm). Data are presented as mean ± SD, from six independent experiments. Significant effect of the treatment, ** $p < 0.01$. Yellow line, alveolar bone ridge.

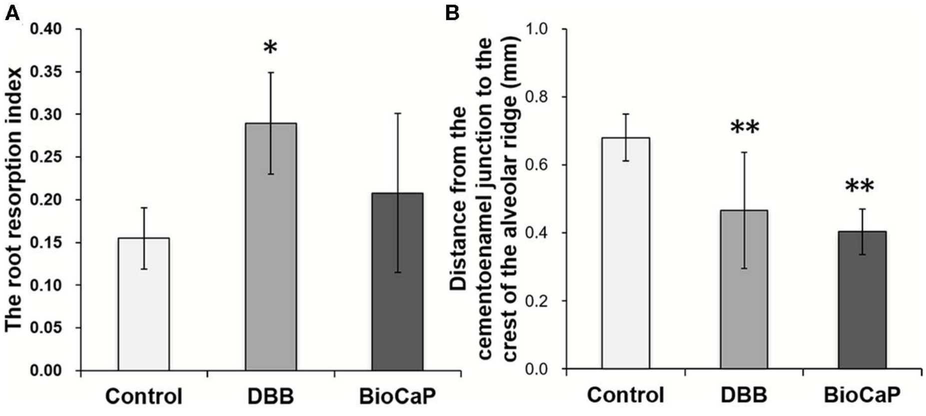

FIGURE 5 | Bio-CaP didn't affect the dental root resorption and maintained the distance from the enamel cementum to the crest of the alveolar ridge. **(A)** The root resorption index at week 8. **(B)** The distance from the enamel cementum to the crest of the alveolar ridge at week 8. Data are presented as mean ± SD, from six independent experiments. Significant effect of the treatment, *$p < 0.05$, and **$p < 0.01$.

cementum and the crest of the alveolar ridge in the control group was 1.45-, and 1.69-fold higher compared to DBB and BioCaP group, respectively (**Figure 5B**). There was no significant difference in distance from the enamel cementum to the crest of the alveolar ridge between the DBB and the BioCaP group (**Figure 5B**). BioCaP did not affect root resorption and resulted in the minimum distance between the enamel cementum and the crest of the alveolar ridge compared to the control and DBB group.

BioCaP Graft Favored Maintaining the Periodontal Attachment

Periodontal probing depth of orthodontic teeth was measured every 2 weeks during orthodontic traction. The periodontal probing depth tends to increase in the control group compared to the DBB group, but the difference was not statistically significant. The PDD was lowest in the BioCaP group compared to the control group and DBB group. However, the periodontal probing depth in the control group was significantly greater than the BioCaP group only at week 8. There was no significant difference in periodontal probing depth between DBB and BioCaP group at all the tested time points (**Table 1**).

The Differences in OTM Value Were Not Significant Among the Tested Groups

OTM was measured every 2 weeks for all groups during Orthodontic traction. All sites of alveolar bone defect and extraction healed smoothly after the surgical procedure. There was no incidence of infection, suppuration, or death. After the activation of the orthodontic device, the orthodontic teeth (bilateral maxillary second premolars) started to move in the mesial direction. CBCT images before and after orthodontic exertion revealed that the mesial root of all maxillary second premolars was located within the area of alveolar bone defects (**Figure 4A**). The total OTM was 2.90 ± 0.84 mm in BioCaP group, 3.59 ± 1.25 mm in the DBB group, and 3.42 ± 1.55 mm in the control group (**Table 2**). There was no significant difference in the distance traveled during OTM among the three groups (**Figures 6A,B**).

BioCaP Graft Alleviated IL-1β Concentration in GCF

DBB or BioCaP graft did not affect GCF volume in the OTM site at week 4 and 8 (**Figure 7A**). However, the concentration of IL-1β in GCF was the lowest in the BioCaP group compared to the control and DBB group (**Figure 7B**). DBB group failed to reduce the IL-1β concentration in GCF compared to the control group. Our results indicate the anti-inflammatory or less immunogenic property of the BioCaP scaffolds.

DISCUSSION

The impact of various xenograft or biomaterial grafts in the orthodontic treatment had been reported (Hossain et al., 1989, 1996; Araujo et al., 2001, 2009; Reichert et al., 2010). Xenograft or biomaterial grafts facilitates orthodontic treatment but has inferior bone regenerative potential compared to auto-bone graft. This might be mainly due to the lack of osteoinductive potential of the bone grafts. DBB materials, such as Bio-Oss^R, are acellular products from bovine bone, which has been widely used to augment alveolar ridge. However, the osteoinductivity and biodegradability of DBB are unsatisfactory (Araujo et al., 2001; Ahn et al., 2014). In this study, we aimed at evaluating whether the biomimetic and osteoinductive BioCaP could be better graft material for alveolar bone defect in sequent OTM compared to the commonly used DBB xenograft. BioCaP graft robustly enhanced bone regeneration and graft biodegradation compared to DBB. Moreover, the BioCaP graft did not influence the OTM rate and was less immunogenic compared to DBB, but preserved the orthodontic tooth root erosion, reduced inflammation, and maintained the periodontal attachment as illustrated in **Figure 8**. The results of our study indicate BioCaP as a promising graft material for alveolar or periodontal bone regeneration during orthodontic treatment.

TABLE 1 | Periodontal probing depth (mm) of orthodontic teeth.

Group	Control	DBB	BioCaP
0 week	1.67 ± 0.52	1.58 ± 0.39	1.58 ± 0.38
2 weeks	2.25 ± 0.52	1.92 ± 0.20	1.50 ± 0.55
4 weeks	2.08 ± 0.66	1.75 ± 0.76	1.42 ± 0.49
6 weeks	1.92 ± 0.58	1.42 ± 0.38	1.33 ± 0.61
8 weeks	2.17 ± 0.75*	1.67 ± 0.41	1.25 ± 0.42

*Data are presented as mean ± SD from six independent experiments (n = 6). Significant difference compared to BioCaP group, *p < 0.05.*

TABLE 2 | OTM at 2 weeks interval.

Group	1–2 weeks	3–4 weeks	5–6 weeks	7–8 weeks	Total
Control	0.93 ± 0.33	0.83 ± 0.41	1.09 ± 0.58	0.58 ± 0.26	3.42 ± 1.55
DBB	0.75 ± 0.29	0.98 ± 0.30	0.80 ± 0.37	1.06 ± 0.59	3.59 ± 1.25
BioCaP	0.65 ± 0.19	0.80 ± 0.29	0.53 ± 0.26	0.92 ± 0.23	2.90 ± 0.84

Data are presented as mean ± SD from six independent experiments (n = 6).

Fabrication technique of BMP2-functionalized BioCaP granules, physicochemical properties, *in vitro* and *in vivo* BMP2 release profile, biocompatibility, osteoconductivity, osteoinductivity, and bone defect healing potential of BioCaP had been extensively investigated in our previous studies (Hunziker et al., 2012; Liu et al., 2014, 2017, 2018; Zheng et al., 2014; Wang et al., 2017, 2019). DBB xenograft lacks osteoinductivity but has been commonly used as alveolar defect filling material during OTM treatment. In this study, BioCaP robustly enhanced alveolar bone defect healing during OTM. Histological images and CBCT images clearly indicate the higher amount of newly formed bone and distinct alveolar ridge in the BioCaP group compared to the DBB group. Alveolar bone defect healing process and duration in the dog are similar to that in humans (Giannobile et al., 1994). Therefore, we used orthodontic traction in the surgical alveolar bone defect in Beagle dogs. Immediate orthodontic traction after alveolar bone grafting accelerates OTM and bone mineralization in the tension side (Ahn et al., 2014). Furthermore, Seifi and Ghoraishian (2012) concluded that tooth movement could start immediately before healing of the grafting site. In this study, we started orthodontic traction 1 week after BioCaP or DBB grafting, which coincides with the early stage of woven bone formation (Ahn et al., 2014). Orthodontic treatment facilitates the healing of not only woven bone but also alveolar bone (Araujo et al., 2001; Reichert et al., 2010). In this study, only BioCaP grafting showed effective bone regeneration and alveolar bone defect healing in comparison to empty defect or DBB grafting (**Figures 1–4**). Our result indicates

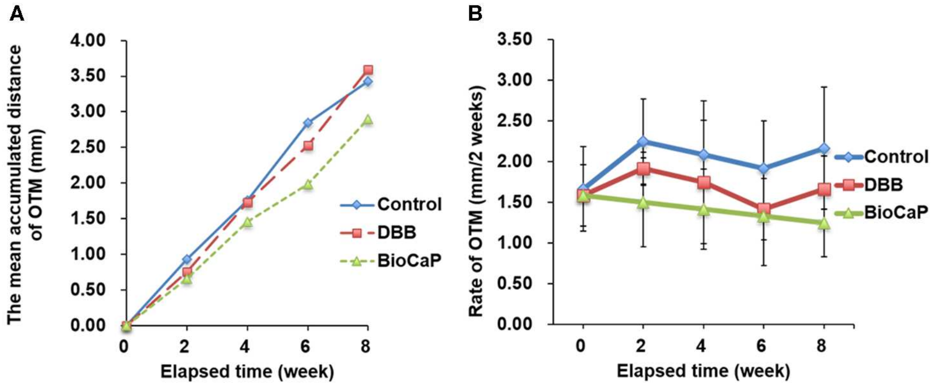

FIGURE 6 | The distances of OTM were less in Bio-CaP group compared to other groups. **(A)** The mean accumulated distance of OTM at 8 weeks, **(B)** Rate of OTM at 2 weeks interval. Data are from six independent experiments.

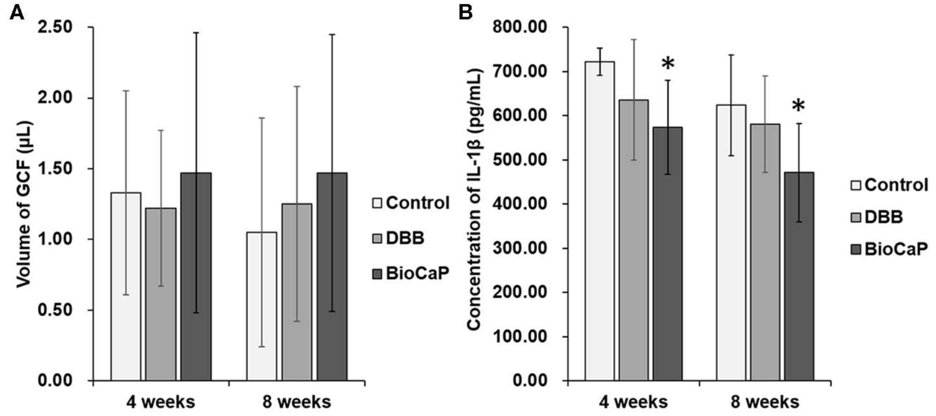

FIGURE 7 | In BioCaP group the volume of GCF was not affected but and IL-1β concentration was reduced. **(A)** Volume of GCF and **(B)** Concentration of IL-1β in GCF at week 4 and 8 of OTM. Data are presented as mean ± SD, from six independent experiments. Significant effect of the treatment, $^{*}p < 0.05$.

the BioCaP as a cost-effective graft material to fill alveolar bone defects during orthodontic treatment.

OTM is affected by the cellular and mineral components of the periodontium, which are influenced by the grafting material and OTM timing. Higher OTM is observed during the immediate application of orthodontic force after implantation of graft compared to the application of orthodontic force after 2 or 12 weeks after grafting (Ahn et al., 2014). Orthodontic traction started 2 weeks after the implantation of bone graft in alveolar bone defect has no detrimental effects on orthodontic movement (Cardaropoli et al., 2006). Early traction force allows orthodontic teeth movement into the bone graft area. In this study, similar OTM distance and rate of OTM were observed in control, DBB, and BioCaP group, indicating that both DBB and BioCaP did not obstruct the OTM during 8 weeks. But Machibya et al. (2018) reported higher OTM in the DBB group compared to CaP or no graft group. This discrepancy might be caused by the different starting times of orthodontic traction, i.e., at least 1 month after grafting and OTM timing of 6 weeks (Machibya et al., 2018). Our results indicate that early orthodontic traction (1 week after grafting) in BioCaP grafted defect enhanced alveolar bone defect healing without hampering OTM.

Biomaterial immunogenicity directly affects bone regeneration via inducing foreign body reaction-mediated inflammation in the defect site (Velard et al., 2013; Klopfleisch and Jung, 2017). The proinflammatory environment in the defect will recruit more immune cells such as monocytes and macrophages inducing the formation of multinucleated giant cells and osteoclasts (Velard et al., 2013). Multinucleated cells not only resorb the native bone or tooth cementum but also inhibit bone regeneration via further upregulation of pro-inflammatory cytokines. In this study, multinucleated osteoclast-like cells were observed only in the DBB group but not in the control and BioCaP group. Dental root resorption is another important issue during biomaterial grafting and/or orthodontic treatment. BMP2-loaded graft had shown orthodontic tooth root resorption in the dose (BMP2) dependent manner (Kawamoto et al., 2002, 2003). Dose of 40 μg BMP2/100 μl graft resorbs the dentine, and 10 μg BMP2/100 μl graft only resorbs the cementum of orthodontic tooth root (Kawamoto et al., 2002, 2003), which

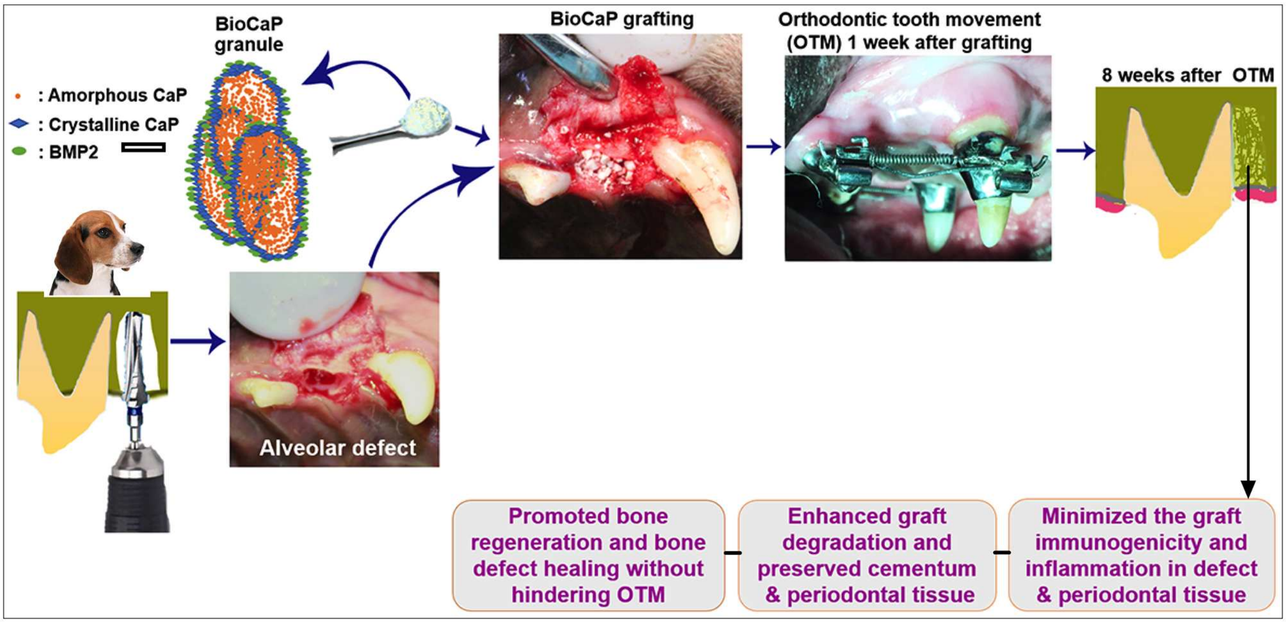

FIGURE 8 | Scheme illustrating the procedure and main findings of this study.

might be the effect of burst release of BMP2 from the graft materials. In this study, the root surface was not in direct contact with the graft material during grafting, but it might come in contact with graft material during OTM. We found that 14 µg BMP2 in 100 µl of BioCaP did not resorb the cementum of orthodontic tooth root. This might be the effect of sustained controlled release of a low dose of BMP2 from BioCaP around the tooth root. Another possible reason for cementum erosion of orthodontic tooth root in the DBB group could be the higher activity of the DBB immunogenicity-induced multinucleated osteoclast-like cells. Similarly, our previous study reported the higher numbers of multinucleated osteoclast-like cells in DBB-grafted femoral defect compared to in BioCaP grafted defect (Wu et al., 2011; Liu et al., 2017). Our study revealed that the BioCaP graft protects the erosion of orthodontic tooth root.

Angiogenesis facilitates bone and periodontal tissue regeneration via osteogenesis-angiogenesis coupling (Huang et al., 2015; Hu and Olsen, 2016). In this study, histological images showed higher numbers of blood vessel-like structures in the BioCaP group. Similarly, bone regeneration and alveolar defect healing were enhanced in the BioCaP group. This indicates the possibility of the BioCaP-mediated osteogenesis-angiogenesis coupling. Degradation of graft materials in a certain duration is essential for proper bone healing. In our previous study, BioCaP showed excellent degradation properties during bone defect healing (Liu et al., 2017). In this study, both the graft degradation rate and bone regeneration were higher in the BioCaP group. Spontaneous dissolution in body fluid and higher cellular activity-based resorption controls the degradation of BioCaP graft (Hunziker et al., 2012; Zheng et al., 2014). The higher resorption of graft material enhances, and the higher amount of newly formed bone inhibits OTM. In this study, the OTM rate was slightly less but statistically not significant in the BioCaP group compared to other groups. This result might be the combined effect of higher bone formation and higher graft degradation in the BioCaP group.

The higher periodontal probing depth indicates a higher degree of periodontal damage (Preshaw, 2015). In this study, only the BioCaP but not DBB graft was able to reduce periodontal probing depth compared to the control group. This indicates the ability of BioCaP to protect the periodontal damage during OTM. The higher level of proinflammatory cytokines in alveolar defect inhibits bone defect healing. Similarly, the higher level of proinflammatory cytokines in GCF causes inflammation and destroys the periodontal tissue. IL-1β is a key proinflammatory cytokine that causes periodontal damage (Cheng et al., 2020). In this study, only the BioCaP but not the DBB graft significantly reduced the level of IL-1β in GCF compared to the control at week 4 and 8. The less immunogenicity of BioCaP graft may reduce the recruitment of immune cells not only in the alveolar defect but also around the periodontal tissue of orthodontic tooth alleviating the concentration of inflammatory cytokines in GCF.

In this study, we analyzed the efficacy of biomimetic and osteoinductive BioCaP graft on alveolar bone defect healing during orthodontic traction. We used the standard protocol to fabricate the BioCaP and adopted the established dog model for alveolar bone defect and orthodontic traction. This experiment model highly resembles the human alveolar bone defect healing during orthodontic treatment. The autologous bone graft is the gold standard for alveolar bone defect healing. A limitation of this study is that we did not compare the effect of BioCaP with the autologous bone graft. Hybrid polymer based biomaterials such as a combination of biodegradable polymer, osteoconductive CaP/HAP, and osteoinductive bioglass/magnesium could be effective for alveolar bone regeneration during OTM (Lei et al., 2019). Moreover, periodontal tissue and periodontal ligaments should be monitored during orthodontic treatment and/or alveolar bone defect healing. Another limitation of this study is that we evaluated bone formation and OTM only up to 8 weeks. To address these issues, future studies that compare the effect of BioCaP with auto bone graft on alveolar bone defect healing during orthodontic traction in 12 and 16 weeks are recommended.

CONCLUSION

In conclusion, the results of this study showed that the biocompatible, osteoconductive, osteoinductive BioCaP graft is more effective on alveolar bone defect healing and protection of orthodontic tooth root during orthodontic treatment compared to commonly used DBB. Biomimetic BioCaP granules carrying a low dose of BMP2 and giving slow and sustained release of BMP2 show less immunogenicity, high biodegradability, and proangiogenic potential. BioCaP graft reduces the inflammation in GCF and periodontal probing depth in the orthodontic tooth. Our results suggest BioCaP as a cost-effective graft material for filling the bone defect during orthodontic treatment.

DATA AVAILABILITY STATEMENT

The datasets generated for this study are available on request to the corresponding author.

ETHICS STATEMENT

The animal study was reviewed and approved by the Ethics committee of the Zhejiang University Laboratory Animal Center.

AUTHOR CONTRIBUTIONS

JS, GW, JP, and SJ: study concept and design. SJ and TL: data acquisition and analysis. SJ and WL: performed experiments. SJ and XF: animal experiments. SJ, JS, and TL: manuscript preparation. JP and WL: manuscript review. GW: preparation of BioCaP granules. All authors: read and approved the submitted version.

FUNDING

This study was supported by Science Technology Department of Zhejiang Province of China (2013C33154), Zhejiang Provincial Natural Science Foundation of China (LQ15H140001), National Natural Science Foundation of China (81500891), and High-Level University Construction Talents of Guangzhou Medical University of China (B185006003014 and B195002003017).

ACKNOWLEDGMENTS

We thank Bing Xia, Weihua Zhang, and Mingdi Xiang from the Department of Radiology, The Affiliated Stomatology Hospital, Zhejiang University School of Medicine, for assistance in cone-beam computed tomography. We thank Dongsheng Wang from the Department of Oral Pathology, Beijing PLA General Hospital, for hard tissue sectioning.

SUPPLEMENTARY MATERIAL

The Supplementary Material for this article can be found online at: https://www.frontiersin.org/articles/10.3389/fbioe.2020.00517/full#supplementary-material

Supplementary Figure 1 | Representative CBCT images taken at baseline, 1 week after grafting, and 8 weeks after OTM in control, DBB, and BioCaP group.

REFERENCES

Ahn, H. W., Ohe, J. Y., Lee, S. H., Park, Y. G., and Kim, S. J. (2014). Timing of force application affects the rate of tooth movement into surgical alveolar defects with grafts in beagles. *Am. J. Orthod. Dentofacial Orthop.* 145, 486–495. doi: 10.1016/j.ajodo.2013.12.021

Araujo, M., Linder, E., and Lindhe, J. (2009). Effect of a xenograft on early bone formation in extraction sockets: an experimental study in dog. *Clin. Oral Implants Res.* 20, 1–6. doi: 10.1111/j.1600-0501.2008.01606.x

Araujo, M. G., Carmagnola, D., Berglundh, T., Thilander, B., and Lindhe, J. (2001). Orthodontic movement in bone defects augmented with Bio-Oss (R) - an experimental study in dogs. *J. Clin. Periodont.* 28, 73–80. doi: 10.1034/j.1600-051x.2001.280111.x

Boyne, P. J., Lilly, L. C., Marx, R. E., Moy, P. K., Nevins, M., Spagnoli, D. B., et al. (2005). *De novo* bone induction by recombinant human bone morphogenetic protein-2 (rhBMP-2) in maxillary sinus floor augmentation. *J. Oral Maxillofac. Surg.* 63, 1693–1707. doi: 10.1016/j.joms.2005.08.018

Boyne, P. J., Marx, R. E., Nevins, M., Triplett, G., Lazaro, E., Lilly, L. C., et al. (1997). A feasibility study evaluating rhBMP-2/absorbable collagen sponge for maxillary sinus floor augmentation. *Int. J. Periodontics Restorative Dent.* 17, 11–25. doi: 10.1016/S0901-5027(97)80852-1

Cardaropoli, D., Re, S., Manuzzi, W., Gaveglio, L., and Cardaropoli, G. (2006). Bio-oss collagen and orthodontic movement for the treatment of infrabony defects in the esthetic zone. *Int. J. Period. Restor. Dent.* 26, 553–559. doi: 10.1097/01.mat.0000178249.99478.08

Cheng, R., Wu, Z., Li, M., Shao, M., and Hu, T. (2020). Interleukin-1β is a potential therapeutic target for periodontitis: a narrative review. *Int. J. Oral Sci.* 12:2. doi: 10.1038/s41368-019-0068-8

de Aguiar, M. C., and Perinetti, G. (2017). The gingival crevicular fluid as a source of biomarkers to enhance efficiency of orthodontic and functional treatment of growing patients. *Biomed. Res. Int.* 2017:3257235. doi: 10.1155/2017/3257235

Giannobile, W. V., Finkelman, R. D., and Lynch, S. E. (1994). Comparison of canine and non-human primate animal models for periodontal regenerative therapy: results following a single administration of PDGF/IGF-I. *J. Periodontol.* 65, 1158–1168. doi: 10.1902/jop.1994.65.12.1158

Goldie, R. S., and King, G. J. (1984). Root resorption and tooth movement in orthodontically treated, calcium-deficient, and lactating rats. *Am. J. Orthod. Dentofacial Orthop.* 85, 424–430. doi: 10.1016/0002-9416(84)90163-5

Hibino, K., and Wong, R. W. (2009). Orthodontic tooth movement enhancing bony apposition in alveolar bony defect: a case report. *Cases J.* 2, 116–116. doi: 10.1186/1757-1626-2-116

Hossain, M. Z., Kyomen, S., and Tanne, K. (1996). Biologic responses of autogenous bone and beta-tricalcium phosphate ceramics transplanted into bone defects to orthodontic forces. *Cleft Palate Craniofac. J.* 33, 277–283. doi: 10.1597/1545-1569_1996_033_0277_broaba_2.3.co_2

Hossain, M. Z., Yamada, T., and Yamauchi, K. (1989). Biodegradable ceramic as a bone graft substitute followed by orthodontic tooth movement. *Nihon Kyosei Shika Gakkai Zasshi* 48, 483–495.

Hu, K., and Olsen, B. R. (2016). Osteoblast-derived VEGF regulates osteoblast differentiation and bone formation during bone repair. *J. Clin. Invest.* 126, 509–526. doi: 10.1172/JCI82585

Huang, C., Ness, V. P., Yang, X., Chen, H., Luo, J., Brown, E. B., et al. (2015). Spatiotemporal analyses of osteogenesis and angiogenesis via intravital imaging in cranial bone defect repair. *J. Bone Miner. Res.* 30, 1217–1230. doi: 10.1002/jbmr.2460

Hung, H. C., and Douglass, C. W. (2002). Meta-analysis of the effect of scaling and root planing, surgical treatment and antibiotic therapies on periodontal probing depth and attachment loss. *J. Clin. Periodontol.* 29, 975–986. doi: 10.1034/j.1600-051X.2002.291102.x

Hunziker, E. B., Enggist, L., Kuffer, A., Buser, D., and Liu, Y. (2012). Osseointegration: the slow delivery of BMP-2 enhances osteoinductivity. *Bone* 51, 98–106. doi: 10.1016/j.bone.2012.04.004

James, A. W., LaChaud, G., Shen, J., Asatrian, G., Nguyen, V., Zhang, X., et al. (2016). A review of the clinical side effects of bone morphogenetic protein-2. *Tissue Eng. Part B Rev.* 22, 284–297. doi: 10.1089/ten.teb.2015.0357

Javed, F., Al-Daghri, N. M., Wang, H. L., Wang, C. Y., and Al-Hezaimi, K. (2014). Short-term effects of non-surgical periodontal treatment on the gingival crevicular fluid cytokine profiles in sites with induced periodontal defects: a study on dogs with and without streptozotocin-induced diabetes. *J. Periodontol.* 85, 1589–1595. doi: 10.1902/jop.2014.140150

Kawamoto, T., Motohashi, N., Kitamura, A., Baba, Y., Suzuki, S., and Kuroda, T. (2003). Experimental tooth movement into bone induced by recombinant human bone morphogenetic protein-2. *Cleft Palate Craniofac. J.* 40, 538–543. doi: 10.1597/1545-1569_2003_040_0538_etmibi_2.0.co_2

Kawamoto, T., Motohashi, N., Kitamura, A., Baba, Y., Takahashi, K., Suzuki, S., et al. (2002). A histological study on experimental tooth movement into bone induced by recombinant human bone morphogenetic protein-2 in beagle dogs. *Cleft Palate Craniofac. J.* 39, 439–448. doi: 10.1597/1545-1569_2002_039_0439_ahsoet_2.0.co_2

Kim, K. A., Choi, E. K., Ohe, J. Y., Ahn, H. W., and Kim, S. J. (2015a). Effect of low-level laser therapy on orthodontic tooth movement into bone-grafted alveolar defects. *Am. J. Orthod. Dentofacial Orthop.* 148, 608–617. doi: 10.1016/j.ajodo.2015.04.034

Kim, S. J., Kim, J. W., Choi, T. H., and Lee, K. J. (2015b). Restoration of a vertical alveolar bone defect by orthodontic relocation of a mesially impacted mandibular first molar. *Am. J. Orthod. Dentofacial Orthop.* 147, S122–S132. doi: 10.1016/j.ajodo.2014.04.026

King, G. N., King, N., Cruchley, A. T., Wozney, J. M., and Hughes, F. J. (1997). Recombinant human bone morphogenetic protein-2 promotes wound healing in rat periodontal fenestration defects. *J. Dent. Res.* 76, 1460–1470. doi: 10.1177/00220345970760080801

Klein, Y., Fleissig, O., Stabholz, A., Chaushu, S., and Polak, D. (2019). Bone regeneration with bovine bone impairs orthodontic tooth movement despite proper osseous wound healing in a novel mouse model. *J. Periodontol.* 90, 189–199. doi: 10.1002/JPER.17-0550

Klopfleisch, R., and Jung, F. (2017). The pathology of the foreign body reaction against biomaterials. *J. Biomed. Mater. Res. A* 105, 927–940. doi: 10.1002/jbm.a.35958

Lei, B., Guo, B., Rambhia, K. J., and Ma, P. X. (2019). Hybrid polymer biomaterials for bone tissue regeneration. *Front. Med.* 13, 189–201. doi: 10.1007/s11684-018-0664-6

Liu, T., Wu, G., Wismeijer, D., Gu, Z., and Liu, Y. (2013). Deproteinized bovine bone functionalized with the slow delivery of BMP-2 for the repair of critical-sized bone defects in sheep. *Bone* 56, 110–118. doi: 10.1016/j.bone.2013.05.017

Liu, T., Wu, G., Zheng, Y., Wismeijer, D., Everts, V., and Liu, Y. (2014). Cell-mediated BMP-2 release from a novel dual-drug delivery system promotes bone formation. *Clin. Oral Implants Res.* 25, 1412–1421. doi: 10.1111/clr.12283

Liu, T., Zheng, Y., Wu, G., Wismeijer, D., Pathak, J. L., and Liu, Y. (2017). BMP2-coprecipitated calcium phosphate granules enhance osteoinductivity of deproteinized bovine bone, and bone formation during critical-sized bone defect healing. *Sci. Rep.* 7:41800. doi: 10.1038/srep41800

Liu, Y., Groot, K., and Hunziker, E. (2005). BMP-2 liberated from biomimetic implant coatings induces and sustains direct ossification in an ectopic rat model. *Bone* 36, 745–757. doi: 10.1016/j.bone.2005.02.005

Liu, Y., Schouten, C., Boerman, O., Wu, G., Jansen, J. A., and Hunziker, E. B. (2018). The kinetics and mechanism of bone morphogenetic protein 2 release from calcium phosphate-based implant-coatings. *J. Biomed. Mater. Res. A* 106, 2363–2371. doi: 10.1002/jbm.a.36398

Liu, Y., Wu, G., and de Groot, K. (2010). Biomimetic coatings for bone tissue engineering of critical-sized defects. *J. R Soc. Interf.* 7(Suppl. 5), S631–S647. doi: 10.1098/rsif.2010.0115.focus

Machibya, F. M., Zhuang, Y., Guo, W., You, D., Lin, S., Wu, D., et al. (2018). Effects of bone regeneration materials and tooth movement timing on canine experimental orthodontic treatment. *Angle Orthod.* 88, 171–178. doi: 10.2319/062017-407

Mayer, T., Basdra, E. K., Komposch, G., and Staehle, H. J. (1994). Localized alveolar ridge augmentation before orthodontic treatment - a case-report. *Int. J. Oral Maxillofac. Surg.* 23, 226–228. doi: 10.1016/S0901-5027(05)80375-3

Nagy, P., Molnar, B., Nemes, B., Schupbach, P., and Windisch, P. (2019). Histologic evaluation of human intrabony periodontal defects treated with deproteinized bovine bone mineral in combination with orthodontic tooth movement: a case series. *Int. J. Periodontics Restorative Dent.* 40, 321–330. doi: 10.11607/prd.4346

Nakamoto, N., Nagasaka, H., Daimaruya, T., Takahashi, I., Sugawara, J., and Mitani, H. (2002). Experimental tooth movement through mature and immature bone regenerates after distraction osteogenesis in dogs. *Am. J. Orthod. Dentofacial Orthop.* 121, 385–395. doi: 10.1067/mod.2002.122368

Oltramari, P. V. P., de lima Navarro, R., Henriques, J. F. C., Taga, R., Cestari, T. M., Ceolin, J. F., et al. (2007). Orthodontic movement in bone defects filled with xenogenic graft: an experimental study in minipigs. *Am. J. Orthod. Dentofacial Orthop.*131, 302.e10-7. doi: 10.1016/j.ajodo.2006.07.020

Oortgiesen, D. A., Walboomers, X. F., Bronckers, A. L., Meijer, G. J., and Jansen, J. A. (2014). Periodontal regeneration using an injectable bone cement combined with BMP-2 or FGF-2. *J. Tissue Eng. Regen. Med.* 8, 202–209. doi: 10.1002/term.1514

Preshaw, P. M. (2015). Detection and diagnosis of periodontal conditions amenable to prevention. *BMC Oral Health* 15(Suppl. 1):S5. doi: 10.1186/1472-6831-15-S1-S5

Rao, S. M., Ugale, G. M., and Warad, S. B. (2013). Bone morphogenetic proteins: periodontal regeneration. *N Am. J. Med. Sci.* 5, 161–168. doi: 10.4103/1947-2714.109175

Reichert, C., Goetz, W., Smeets, R., Wenghoefer, M., and Jaeger, A. (2010). The impact of nonautogenous bone graft on orthodontic treatment. *Quintessence Int.* 41, 665–672. doi: 10.1016/j.tripleo.2010.03.041

Seifi, M., and Ghoraishian, S. A. (2012). Determination of orthodontic tooth movement and tissue reaction following demineralized freeze-dried bone allograft grafting intervention. *Dent. Res. J.* 9, 203–208. doi: 10.4103/1735-3327.95237

Selvig, K. A., Sorensen, R. G., Wozney, J. M., and Wikesjo, U. M. (2002). Bone repair following recombinant human bone morphogenetic protein-2 stimulated periodontal regeneration. *J. Periodontol.* 73, 1020–1029. doi: 10.1902/jop.2002.73.9.1020

Sheats, R. D., Strauss, R. A., and Rubenstein, L. K. (1991). Effect of a resorbable bone graft material on orthodontic tooth movement through surgical defects in the cat mandible. *J. Oral Maxillofac. Surg.* 49, 1299–1303. doi: 10.1016/0278-2391(91)90307-8

Tsai, H., Yao, C. J., and Wong, M. (2017). Early orthodontic tooth movement into regenerative bony defects: a case report. *Int. J. Periodontics Restor. Dent.* 37, 581–589. doi: 10.11607/prd.2868

Velard, F., Braux, J., Amedee, J., and Laquerriere, P. (2013). Inflammatory cell response to calcium phosphate biomaterial particles: an overview. *Acta Biomater.* 9, 4956–4963. doi: 10.1016/j.actbio.2012.09.035

Wang, D., Liu, Y., Liu, Y., Yan, L., Zaat, S. A. J., Wismeijer, D., et al. (2019). A dual functional bone-defect-filling material with sequential antibacterial and osteoinductive properties for infected bone defect repair. *J. Biomed. Mater. Res. A* 107, 2360–2370. doi: 10.1002/jbm.a.36744

Wang, D., Tabassum, A., Wu, G., Deng, L., Wismeijer, D., and Liu, Y. (2017). Bone regeneration in critical-sized bone defect enhanced by introducing osteoinductivity to biphasic calcium phosphate granules. *Clin. Oral Implants Res.* 28, 251–260. doi: 10.1111/clr.12791

Wernike, E., Hofstetter, W., Liu, Y., Wu, G., Sebald, H.-J., Wismeijer, D., et al. (2010). Long-term cell-mediated protein release from calcium phosphate ceramics. *J. Biomed. Mater. Res. A.* 92, 463–474. doi: 10.1002/jbm.a.32411

Wu, G., Hunziker, E. B., Zheng, Y., Wismeijer, D., and Liu, Y. (2011). Functionalization of deproteinized bovine bone with a coating-incorporated depot of BMP-2 renders the material efficiently osteoinductive and suppresses foreign-body reactivity. *Bone* 49, 1323–1330. doi: 10.1016/j.bone.2011.09.046

Wu, G., Liu, Y., Iizuka, T., and Hunziker, E. B. (2010). The effect of a slow mode of BMP-2 delivery on the inflammatory response provoked by bone-defect-filling polymeric scaffolds. *Biomaterials* 31, 7485–7493. doi: 10.1016/j.biomaterials.2010.06.037

Yilmaz, S., Kilic, A. R., Keles, A., and Efeoglu, E. (2000). Reconstruction of an alveolar cleft for orthodontic tooth movement. *Am. J. Orthod Dent. Orthop.* 117, 156–163. doi: 10.1016/S0889-5406(00)70226-5

Zhang, D., Chu, F., Yang, Y., Xia, L., Zeng, D., Uludag, H., et al. (2011). Orthodontic tooth movement in alveolar cleft repaired with a tissue engineering bone: an experimental study in dogs. *Tissue Eng. Part A* 17, 1313–1325. doi: 10.1089/ten.tea.2010.0490

Zheng, Y., Wu, G., Liu, T., Liu, Y., Wismeijer, D., and Liu, Y. (2014). A novel BMP2-coprecipitated, layer-by-layer assembled biomimetic calcium phosphate particle: a biodegradable and highly efficient osteoinducer. *Clin. Implant Dent. Relat. Res.* 16, 643–654. doi: 10.1111/cid.12050

Conflict of Interest: The authors declare that the research was conducted in the absence of any commercial or financial relationships that could be construed as a potential conflict of interest.

frontiers
in Bioengineering and Biotechnology

ORIGINAL RESEARCH
published: 30 June 2020
doi: 10.3389/fbioe.2020.00697

Ultrasmall Superparamagnetic Iron Oxide Labeled Silk Fibroin/Hydroxyapatite Multifunctional Scaffold Loaded With Bone Marrow-Derived Mesenchymal Stem Cells for Bone Regeneration

Qin Liu[1]†, Longbao Feng[2]†, Zelong Chen[1], Yong Lan[3], Yu Liu[3], Dan Li[3], Chenggong Yan[1] and Yikai Xu[1]**

[1] *Department of Medical Imaging Center, Nanfang Hospital, Southern Medical University, Guangzhou, China,* [2] *Key Laboratory of Biomaterials of Guangdong Higher Education Institutes, Guangdong Provincial Engineering and Technological Research Center for Drug Carrier Development, Department of Biomedical Engineering, Jinan University, Guangzhou, China,* [3] *Guangzhou Beogene Biotech Co., Ltd., Guangzhou, China*

Numerous tissue-engineered constructs have been investigated as bone scaffolds in regenerative medicine. However, it remains challenging to non-invasively monitor the biodegradation and remodeling of bone grafts after implantation. Herein, silk fibroin/hydroxyapatite scaffolds incorporated with ultrasmall superparamagnetic iron oxide (USPIO) nanoparticles were successfully synthesized, characterized, and implanted subcutaneously into the back of nude mice. The USPIO labeled scaffolds showed good three-dimensional porous structures and mechanical property, thermal stability for bone repair. After loaded with bone marrow-derived mesenchymal stem cells (BMSCs), the multifunctional scaffolds promoted cell adhesion and growth, and facilitated osteogenesis by showing increased levels of alkaline phosphatase activity and up-regulation of osteoblastic genes. Furthermore, *in vivo* quantitative magnetic resonance imaging (MRI) results provided valuable information on scaffolds degradation and bone formation simultaneously, which was further confirmed by computed tomography and histological examination. These findings demonstrated that the incorporation of USPIO into BMSCs-loaded multifunctional scaffold system could be feasible to noninvasively monitor bone regeneration by quantitative MRI. This tissue engineering strategy provides a promising tool for translational application of bone defect repair in clinical scenarios.

Keywords: tissue engineering, multifunctional scaffold, bone marrow-derived mesenchymal stem cells, bone regeneration, magnetic resonance imaging

Edited by:
Gang Wu,
VU University Amsterdam,
Netherlands

Reviewed by:
Lia Rimondini,
University of Eastern Piedmont, Italy
Rajendra Kumar Singh,
Institute of Tissue Regeneration Engineering (ITREN), South Korea
Sandra Hofmann,
Eindhoven University of Technology,
Netherlands
Bregje De Wildt,
Eindhoven University of Technology,
Netherlands, in collaboration with reviewer SH

****Correspondence:***
Chenggong Yan
ycgycg007@gmail.com
Yikai Xu
yikaixu917@gmail.com

† These authors have contributed equally to this work

Specialty section:
This article was submitted to Biomaterials,
a section of the journal Frontiers in Bioengineering and Biotechnology

Received: *23 March 2020*
Accepted: *03 June 2020*
Published: *30 June 2020*

Citation:
Liu Q, Feng L, Chen Z, Lan Y, Liu Y, Li D, Yan C and Xu Y (2020) Ultrasmall Superparamagnetic Iron Oxide Labeled Silk Fibroin/Hydroxyapatite Multifunctional Scaffold Loaded With Bone Marrow-Derived Mesenchymal Stem Cells for Bone Regeneration.
Front. Bioeng. Biotechnol. 8:697.
doi: 10.3389/fbioe.2020.00697

INTRODUCTION

Over the past decades, large progress has been made to develop new scaffolds and strategies in the field of bone tissue engineering. Many different bone implant materials have been designed and evaluated in recent years (Bose et al., 2012; Walmsley et al., 2015; Roman et al., 2017; Roseti et al., 2017). However, only very few of the works have been translated into clinical practice successfully on account of various limitations. One of the challenges to be addressed is the lack of effective methods to track the fate and function of these materials upon implantation (Tang et al., 2016; Sajesh et al., 2019). Tissue grafts nowadays is usually multifaceted and may include cells, biomolecules, and biomaterials. Hence, tissue regeneration has proven problematic partly because the healing and remodeling process remains poorly understood. Plenty of tissue engineering studies still utilize conventional tools, such as histological techniques. This requires tissue specimens by invasive methods, meaning that long-term follow-up assessment is extremely limited (Seung et al., 2015). Therefore, strategies for non-invasive imaging show great potential in the field of bone tissue engineering to facilitate longitudinal assessment of implants.

Non-invasive imaging modalities *in vivo* include optical imaging, micro-computed tomography, magnetic resonance imaging (MRI), and positron emission tomography (Appel et al., 2013; Nam et al., 2015; Eisenstein et al., 2016). In particular, MRI is highly suitable for monitoring tissue-engineered implants, owing to its safety without radiation exposure, excellent soft-tissue contrast, and high resolution without penetration depth restriction. However, the application of MRI in tissue engineering is often hampered by the inherent low contrast of the prepared biomaterials. Hence, some recent reports focused on the incorporation of contrast agents in the biomaterials, such as the ultrasmall superparamagnetic iron oxide (USPIO), to make tissue-engineered scaffolds traceable (Singh et al., 2014a; Sun et al., 2014; Mertens et al., 2015; Wang et al., 2017; Hu et al., 2018). Ultrasmall superparamagnetic iron oxide nano-particles can dramatically shorten the transverse relaxation time (T2) with high sensitivity, which opens up new perspectives for tissue engineering. It has been demonstrated that incorporation of USPIO into collagen-based scaffolds can successfully visualize their location and degradation by MRI (Mertens et al., 2014).

Biomaterials play a crucial role in bone tissue engineering by providing a three-dimensional (3D) scaffold to support cell proliferation and deposition of the extracellular matrix (Ho-Shui-Ling et al., 2018). Recently, silk fibroin (SF) received intensive attention as a biomaterial in fabrication of 3D porous scaffolds because of its unique mechanical properties and tunable biodegradation rate (Yang et al., 2007; Kasoju and Bora, 2012; Ma et al., 2018). However, pristine silk has high solubility and hence presents higher degradation rates compared to natural bone. In this sense, hydroxyapatite (HA), the most present mineral in bone, has been widely used to fabricate scaffolds for bone repair (Zhou and Lee, 2011). Recent studies showed that scaffolds composed of different combinations of SF and HA presented great potential for skeletal regeneration with excellent biological and mechanical properties (Ding et al., 2016; Behera et al., 2017; Farokhi et al., 2018). Furthermore, bone marrow-derived mesenchymal stem cells (BMSCs) embedded in the scaffolds have been widely applied as an advantageous therapeutic option for bone regeneration, and they hold potential to differentiate into osteoblasts both *in vitro* and *in vivo* (Bianco et al., 2001; Crane and Cao, 2014; Oryan et al., 2017).

In this study, we incorporated USPIO nanoparticles into SF/HA scaffolds to generate MRI contrast for visualization. After characterization analysis and biocompatibility evaluation, USPIO-labeled and unlabeled scaffolds were cultivated with BMSCs and implanted subcutaneously into the back of nude mice, to monitor scaffolds resorption and bone remodeling at predefined time points by longitudinal MRI (**Figure 1**). The extent of bone regeneration was further confirmed by CT examination and histological analysis.

MATERIALS AND METHODS

Materials

Bombyx mori silk cocoons in the experiment were kindly donated by Sijia Min from Zhejiang University. Ultrasmall superparamagnetic iron oxide was from Aladdin Reagents Co. Ltd (Shanghai, China), Fetal bovine serum (FBS), alpha modified eagle medium (α-MEM) from Gibco (Grand Island, NY, United States). The Cell Counting Kit-8 was from Dojindo (Kumamoto, Japan) and the LIVE/DEAD^{TM} Cell Imaging Kit was from Invitrogen (Carlsbad, CA, United States). The ALP kit was from Jiancheng Bioengineering Institute (Nanjing, China). TRIzol Reagent, PrimeScript^{TM} RT Master Mix, and SYBR$^{®}$ Premix Ex Taq^{TM} were from Takara Bio (Kyoto, Japan). All other chemicals were purchased from Sigma–Aldrich (St. Louis, MO, United States), and used without further purification. Preparations of 6% SF solution, HA and USPIO nanoparticles are supplied in **Supplementary Material**.

Synthesis of 3D Porous USPIO/SF/HA Scaffolds

Fifty mg of HA was dispersed by ultrasonication in 1ml deionized water containing different concentrations of USPIO (0.25, 0.5, 0.75, 1.0, and 1.5%, w/w). Then, 9 ml 6% SF solution was dropped in the mixture of HA and USPIO along with vigorous vortex mixing, and 120 μl of the mixture was pouring in a 96-well plate. Finally, 3D porous scaffolds can be obtained by a freeze-drying process. Scaffolds were sterilized with ^{60}Co irradiation before cell seeding.

Scaffold Characterization

X-ray diffraction (XRD) of HA and USPIO nano-particles was performed using a Rigaku-Rotaflex Diffractometer (RU-200BH) with a Co-ka radiation (k = 1.79 Å) at 30 kV and 44 mA. The infrared spectra of the scaffold were determined using an FT-IR spectrometer (Vertex 70, Bruker, Germany). Samples were ground and mixed with KBr at a ratio of 1:5. The data were then recorded at a wave length range of 400-4000 cm^{-1} with the accumulation of 20 scans with a resolution

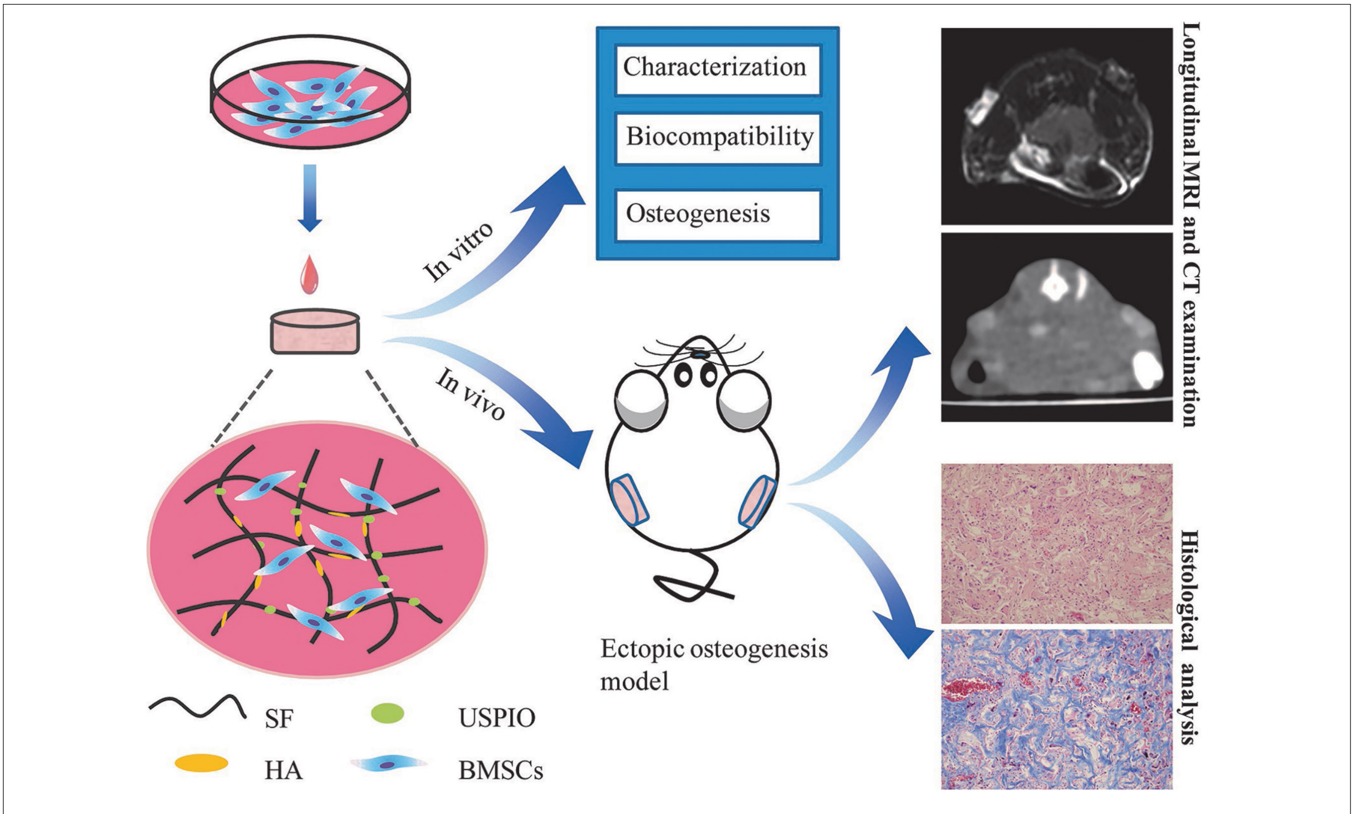

FIGURE 1 | Design of the USPIO-labeled SF/HA multifunctional scaffold system for *in vitro* and *in vivo* studies.

of 4 cm^{-1}. The thermal stability was obtained using a Thermo Gravimetric Analyzer (209F3Tarsus, Netzsch, Germany) under N2 atmosphere at a heating rate of 10 °C/min. Mechanical characterization of 3.5 mm height scaffolds was performed by the testing machine (MTS QT/1L, MTS Systems Corporation, United States) at a compression speed of 1 mm/min, and the compressive modulus were then calculated according to the stress-strain data. The microstructure and pore size of the scaffolds was then analyzed by a SEM microscope (XL-30; Philips, Best, Netherlands). For this purpose, scaffolds were fixed in 2.5% glutaraldehyde and coated with a fine layer of gold sputtering. The pore sizes were measured using commercially available software (Image J software, NIH Image, United States). The sample porosity was measured by ethanol displacement method.

MRI Evaluation *in vitro*

For MRI, the scaffolds were embedded in 1% (w/v) agarose phantoms, and measured with a clinical 3T whole-body MRI scanner (Philips Achieva, Best, Netherlands). T2 weighted imaging (T2WI), T2 mapping, and T2* mapping sequences were performed. T2WI were acquired using a multi-slice, multi-shot spin-echo sequence [time of repetition (TR) = 3328 ms, time of echo (TE) = 80 ms, field of view (FOV) = 80 mm × 40 mm, matrix size = 64 × 64, and slice thickness = 1 mm]. For transverse (T2) relaxometry, images were acquired at 6 echo times [TE range 8–48 ms] using spin-echo sequences [TR = 1500 ms, FOV = 40 mm × 40 mm, reconstruction matrix = 288, slice thickness = 1 mm]. For transverse (T2*) relaxometry, images at 6 echo times [TE range 5.4–35.1 ms] were acquired by using a multi-shot, multi-slice fast-field gradient-echo sequence [TR = 804 ms, FOV = 40 mm × 40 mm, reconstruction matrix = 112, slice thickness = 0.8 mm, and flip angle = 45°]. T2 and T2* relaxation times (R2 and R2*) were calculated using the Imalytics Preclinical Software (Philips Technology GmbH, Aachen, Germany).

Cytotoxicity Assay

Primary isolation of BMSCs and cell passage are supplied in **Supplementary Material**. For cytotoxicity assays, scaffolds were placed into 48-well plates and seeded with BMSCs at a density of 2.0 × 10^3 cells/well in advance. Control group without scaffolds was also seeded with the same number of cells. After 1, 3, 5, and 7 days, the culture media was removed and the cell counting kit-8 (CCK-8) solution was added according to the manufacturer's instructions. The optical density at 450 nm was measured after 2 h of incubation. All experiments were performed in triplicates.

BMSCs Seeded Onto Scaffolds

Scaffolds pre-treated with basal medium (α-MEM) for 24 h were divided into two groups (USPIO-labeled group and non-labeled group). In preparation, BMSCs at passage 3 were seeded onto scaffolds in 48-well culture plates with 50μl suspension of 2.5 × 10^5 cells/well. After cell attachment, 500 μl growth medium (α-MEM medium supplemented with 10%

(v/v) fetal bovine serum, 1% (v/v) penicillin and streptomycin) or osteogenic medium (with extra addition of 50 μM ascorbic acid 2-phosphate, 10 mM β-glycerol phosphate, and 100 nM dexamethasone) was added. The cell-seeded scaffolds were maintained under standard culture conditions (37°C, 5% CO_2), changing the culture medium every 3 days.

Cell Adhesion and Morphology Studies

The morphology of BMSCs on scaffolds was observed by SEM (Hitachi, S-3000N, Japan) after osteogenic induction for 7 and 14 days. The samples were washed with PBS and fixed in 2.5% glutaraldehyde, after which they were dehydrated in graded alcohol, dried in a critical point drier and sputter coated with gold before observation. A Live/Dead assay was performed to assess the growth of BMSCs on both groups. Scaffolds were incubated in calcein (staining for live cells presenting green fluorescence) and ethidium homodimer-1 (staining for dead cells presenting green fluorescence) working solution for 15 min in the dark, and observed by a confocal laser scanning microscope (Olympus FluoView FV10i, Tokyo, Japan). Histological examination was also performed to confirm the existence of BMSCs and USPIO in scaffolds after 7 and 14 days. The specimens were fixed in 4% paraformaldehyde and were dehydrated step-wise using ethanol, immersed in xylene, and embedded in paraffin. Sections of 5 μm were cut and stained by hematoxylin-eosin and Prussian blue, respectively.

In vitro Osteogenic Induction Evaluation

After 1, 7, 14, and 21 days of osteogenic induction, quantitative real-time PCR was performed using the LightCycler®480 Real Time PCR System (LightCycler®480, Roche, Switzerland). Gene expression of ALP, BMP-2, Collagen I, Runx, and GAPDH (as an endogenous control) were investigated using predesigned primers (supplied in **Supplementary Material**). Relative expression of the genes was determined using the $\Delta\Delta$Ct method. The alkaline phosphatase (ALP) activity in the medium was assayed using an ALP kit according to the instructions, measuring the absorbance at 405 nm.

Ectopic Osteogenesis Model

Immune-deficient nude CD-1 nu/nu male mice were purchased from Guangdong Provincial Medical Laboratory Animal Center (China). All animal handling and surgical procedures were performed in accordance with our Institutional Animal Care and Use Committee (Nanfang Hospital, Southern Medical University, China). Groups were showed as follows: non-labeled group, USPIO-labeled group, non-labeled group with BMSCs, USPIO-labeled group with BMSCs. The cell-laden scaffolds were cultured in osteogenic medium for 1 week before implantation. Animals were anesthetized by 0.1% (v/v) of pentobarbital sodium before surgery. Scaffolds were implanted into the bilateral back of the subcutaneous tissue of mice, respectively, and then sutured the skin.

MRI and CT Evaluation *in vivo*

At 2, 6, and 8 weeks after implantation, mice bearing scaffolds were anesthetized by 0.1% (v/v) of pentobarbital sodium. Then MRI and CT scanning were successively examined. All animals were subjected to T2WI, T2 and T2* mapping at 2, 6, and 8 weeks after implantation. All sequences were acquired as the *in vitro* MRI experiments described above. Regions of interest (ROI) were manually outlined from the subcutaneous implanted area in the maximal long-axis slice using the Imalytics Preclinical Software (Philips Technology GmbH, Aachen, Germany).The density evolution and new bone formation were assessed using a 256-section multi–detector row CT scanner (Brilliance iCT; Philips Healthcare, Cleveland, OH) with the following parameters: 0.5-s gantry rotation time, 120 kVp tube voltage, 30 mA tube current, 0.67 mm thickness, and 0.2 mm increment. The density of newly formed bone was measured by Philips Brilliance Workspace Versio 3.5 (Philips Medical Systems).

Histological Examination

After 2, 6, and 8 weeks followed by the MRI and CT examination, one mouse in each group was sacrificed at predefined time points, and the implants were harvested. The specimens were immediately fixed in 4% (wt/v) paraformaldehyde for 48 h, and decalcified in neutral 10% ethylene diamine tetraacetic acid (EDTA) solution for 2 months at room temperature. Then, half of the specimens were dehydrated step-wise using ethanol, immersed in xylene, and embedded in paraffin. Sections of 5 μm were cut and stained by hematoxylin-eosin and Masson trichrome for morphological analysis and bone extracellular matrix deposition. The remaining samples were used to quantify the residual iron oxide particles in scaffolds by inductively coupled plasma mass spectrometry (ICP-MS). After decomposed in digestion system with nitric acid and washed with deionized water, the total amount of iron was detected with high-resolution sector field ICP-MS (Optima 2000DV, Perkin Elmer, United States).

Statistical Analysis

All data were presented as the mean ± standard deviation of triplicate trials ($n = 3$). Statistical analysis was performed with the SPSS software (version 22.0, IBM, United States). The normality and homogeneity of variance of the data was confirmed by Kolmogorov-Smirnov test and Levene Statistic. Differences in cellular experiment were evaluated with one-way ANOVA (Bonferroni as post-hoc analyses). Repeated-measurement ANOVA was performed to evaluate differences among different time intervals for *in vivo* experiments. Significant differences are given as $^{*}P < 0.05$, $^{**}P < 0.01$, or $^{***}P < 0.001$.

RESULTS

Characterizations of SF/HA Composites

As showed in **Figure 2A**, the scaffold composite was cylinder-shaped with a diameter of 5 mm and height of 3 mm. The XRD of HA and USPIO nano-particles was showed in **Figure 2B**. The peaks of (2 2 0), (3 1 1), (4 0 0), (4 2 2), and (5 1 1) at 30.1°, 35.4°, 43.1°, 53.6°, and 56.9°confirmed the cubic crystallinity of iron oxide in the form of magnetite (Fe_3O_4, **Figure 2B**). The 2 angles at 26.7°, 31.7°, 46.9°, 49.5° and 53.3° were indexed to be (0 0 2), (2 1 1), (2 2 2), (2 1 3), and (0 0 4) reflections of HA, respectively. The FTIR spectra of scaffolds were separately obtained (**Figure 2C**). The FTIR spectrum of SF showed amide I, II, and III peaks at 1658, 1527, and 1242 cm^{-1}, respectively. The HA spectrum showed the characteristic absorption bands in the region of 1100 cm^{-1}, which corresponded to the O–H stretch, and at 603 cm^{-1}, which corresponded to the PO_4^{-3} stretch. The characteristic absorbance peak at 627 cm^{-1} confirmed the Fe–O stretch within USPIO. All the characteristic absorption peaks mentioned above could be found in the composite scaffolds. The mass drop in weight (%) was obtained by thermogravimetry (**Figure 2D**). The scaffolds with different concentrations of USPIO exhibited better thermal stability than SF alone and simple SF/HA scaffolds. These scaffolds showed almost the same weight loss in the transition temperature of 200–400°C, which indicated that the USPIO probably has positive effects on SF/HA in thermostability. The mechanical properties of the scaffolds are shown in the stress-strain curve (**Figure 2E**). The compressive modulus of each scaffold was defined by the slope of the initial linear section of the stress-strain curve. The hybrid scaffolds possessed higher compressive modulus (from 0.64 ± 0.08MPa to 1.18 ± 0.13MPa) than pure SF scaffolds (0.61 ± 0.15MPa), and the compressive modulus of the scaffolds containing 0.75% USPIO were the best (1.18 ± 0.13MPa), following by the concentration of 0.25%(1.16 ± 0.10MPa). These results indicated that the incorporation of HA and USPIO nano-particles strengthened the mechanical property and thermal stability of scaffold to a certain extent, which are suitable for further studies. The microstructure of cross sectioned scaffolds was observed by SEM, as presented in **Figure 3A**. The scaffolds exhibited a porous structure, and the pores were uniform and well interconnected with an average size of 118.4 ± 2.8 μm, presenting a total porosity of 91.5 ± 3.0% (supplied in **Supplementary Material**). Similar structure was found in the morphology of the USPIO labeled scaffolds, which might be attributed to the low amounts of USPIO incorporated.

MRI *in vitro*

T2 weighted images of SF and SF/HA scaffolds labeled by different concentrations of USPIO and the corresponding R2 and R2* values are shown in **Figure 3B**. The T2WI images revealed that the MRI signal intensity of labeled scaffolds decreased with the increasing concentration of negative contrast agent USPIO. Quantitative R2 and R2* relaxometry values correlated well with the amount of USPIO incorporated (**Figures 3C,D**). Strong negative contrast on T2WI images could be observed even with USPIO concentrations lower than 0.5% (w/w). However, incorporation of USPIO concentrations of higher

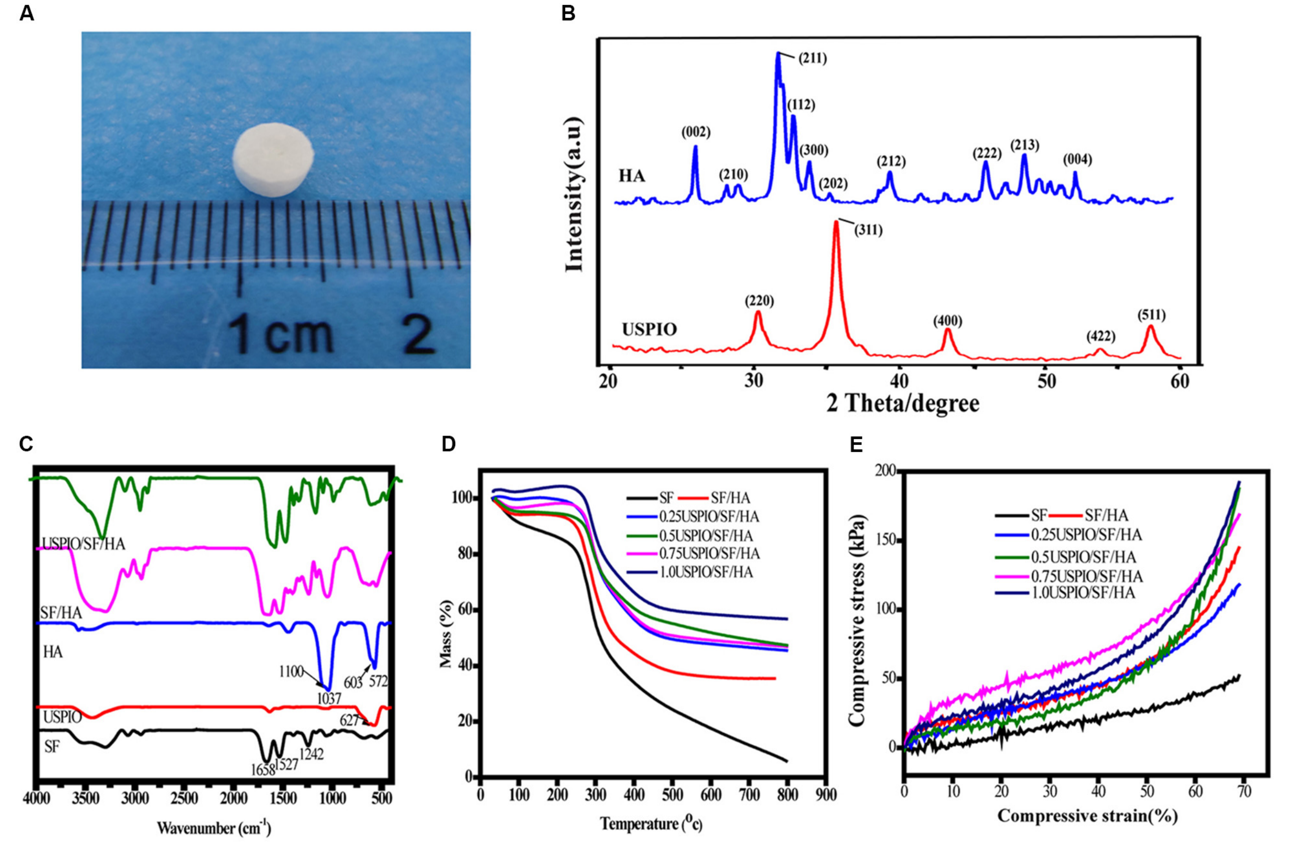

FIGURE 2 | Characterization of scaffolds with different amounts of USPIO incorporated (0–1, w/w%). Gross observation of scaffold **(A)**, X-ray diffraction of HA and USPIO nanoparticles **(B)**, Fourier transform infrared spectroscopy **(C)**, Thermogravimetric analysis **(D)**, and Stress–Strain curve **(E)**.

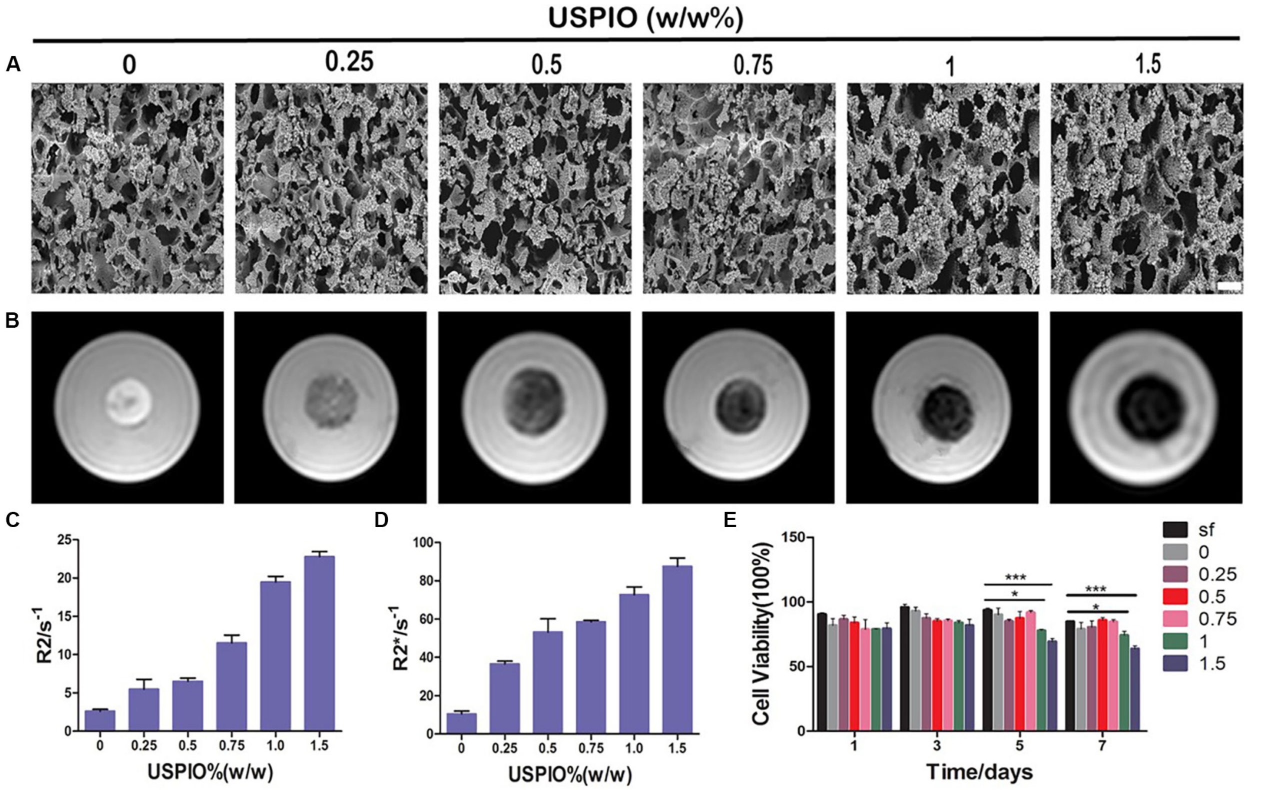

FIGURE 3 | SEM, MRI analysis and cytotoxicity of scaffolds with increasing incorporated amounts of USPIO. **(A)** SEM images show structural properties of scaffolds with incorporation of USPIO nanoparticles. Scale bar indicates 50 μm. **(B)** T2 weighted images demonstrate that the MR signal intensity of USPIO-labeled scaffolds decreased according to USPIO amounts. **(C,D)** Quantitative R2- and R2*-relaxometry analysis. **(E)** CCK-8 results show high cell viability of BMSCs ($n = 3$, *$P < 0.05$, **$P < 0.01$, or ***$P < 0.001$).

than 1% (w/w) produced apparent MRI image deformation, which made it difficult to measure the boundary and the size of the scaffolds accurately. Therefore, incorporation of USPIO concentration of 0.5–1% (w/w), which produced ideal and uniform contrast enhancement, was considered suitable for visualization of the scaffolds.

Cytotoxicity Assay

The cell viabilities were assessed by the CCK-8 assay (**Figure 3E**). The final calculation of the percentage of cell viability was as follows: percentage of cell viability = $(A_{treatment} - A_{blank})/(A_{control} - A_{blank}) \times 100\%$ (where, A = absorbance). There, treatment groups were the cells treated with scaffolds, control groups were with cells contained, and blank groups were only with growth medium contained. Throughout 7 days of culture, no apparent reduction in cell growth rate was found in all scaffolds. However, the viabilities of SF/HA scaffolds with high concentration of USPIO ($\geq$1%, w/w) were slightly lower than those in the non-labeled scaffolds over time ($P < 0.05$), which revealed that the excessive amount of iron particles might affect the growth rate of cells. Therefore, comprehensive considering of the CCK-8 assay, MRI contrast and mechanical property, the SF/HA scaffolds labeled with 0.75% (w/w) USPIO were chosen for the subsequent *in vitro* and *in vivo* experiments.

Cell Adhesion and Morphology Seeded on Scaffolds

After 7 and 14 days of culture, the morphology of cells on scaffolds (non-labeled group and 0.75% USPIO-labeled group) was observed by the SEM (**Figure 4A**). Bone marrow-derived mesenchymal stem cells extended, interconnected on the scaffolds surface in 7 days. After 14 days of culture, multilayer cells overlaid almost the entire surface of the scaffold. The Live/Dead cell analysis (**Figure 4B**) observed by confocal fluorescence images showed that the vast majority of the cells throughout the scaffolds were stained green (live) with few cells stained red (dead) on the scaffolds. H&E staining also proved the adhesion and growth of BMSCs on the scaffolds by showing an increasing number of cells (**Figure 4C**). These findings indicated that porous structures of SF/HA scaffold could promote cell attachment and growth. Furthermore, uniform distribution of blue spots stained for iron particles could be observed in USPIO labeled scaffolds by Prussian blue staining (**Figure 4D**).

Evaluation of Osteogenic Differentiation

As shown in **Figure 5A**, the ALP activity, an early marker for osteogenic differentiation, increased significantly in USPIO-labeled and unlabeled scaffolds over time, and reached a peak

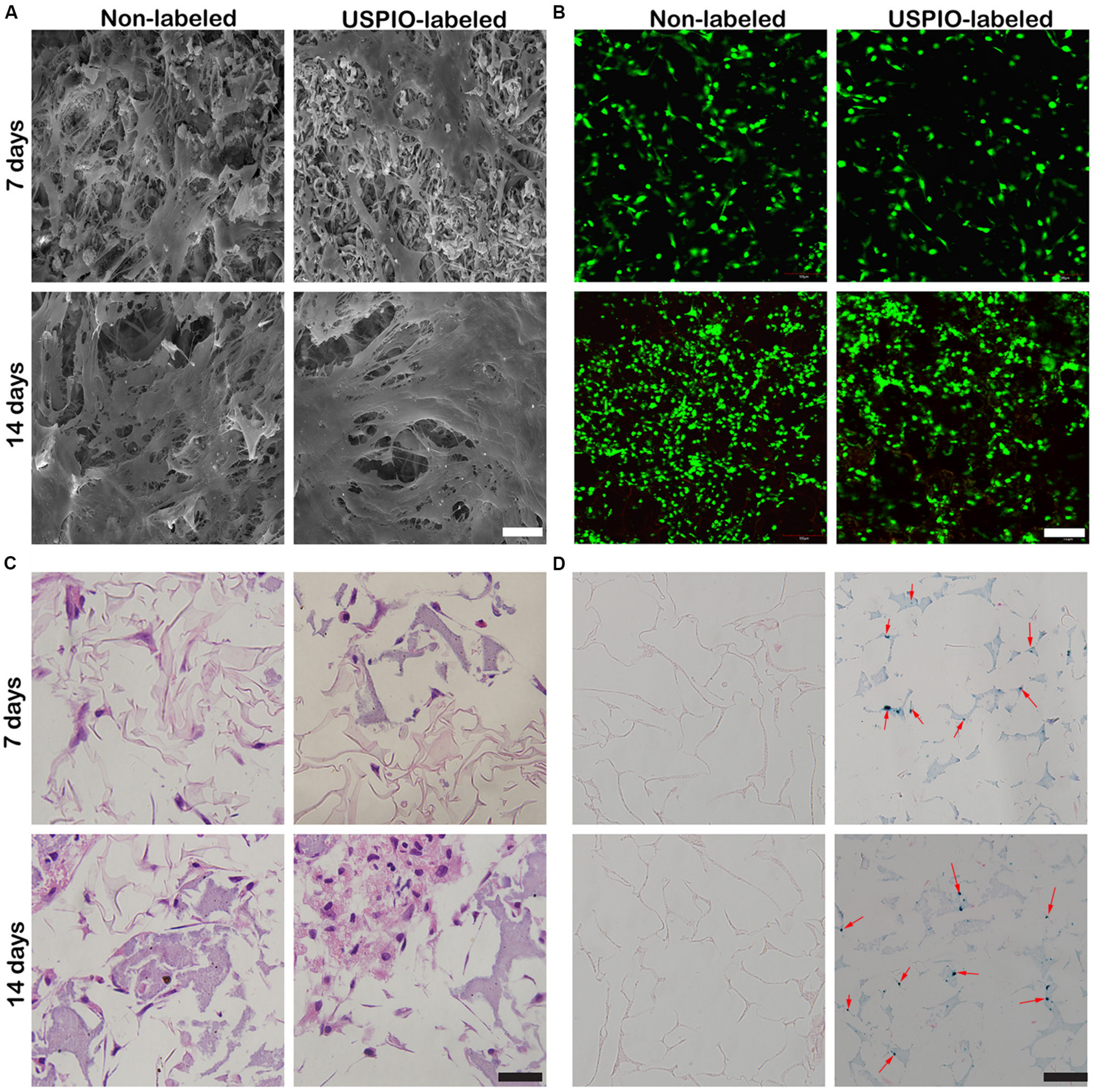

FIGURE 4 | Cell adhesion and growth cultured with USPIO-labeled and unlabeled scaffolds at 7 and 14 days. **(A,B)** SEM and Live/Dead staining show BMSCs adhered to scaffolds. Scale bar indicates 40 μm for SEM and 100 μm for Live/Dead staining. **(C,D)** H&E and Prussian staining of scaffold composites. Scale bar indicates 50 μm.

on day 21 for both groups. Likewise, osteogenic gene expression of BMSCs cultured on both scaffolds was evaluated by qRT-PCR at 1, 7, 14, and 21 days. As illustrated in **Figure 5B**, the related genes expression of ALP, BMP-2, and Runx demonstrated a significant upregulation on both groups, and reached peak at 21 days. The differences of the ALP, BMP-2, and Runx gene expression between 21 days and other time points were significant (all $P < 0.001$). The expression of Coll I showed a similar tendency, but it reached its peak at 14 days and decreased thereafter. The expression of osteogenic markers demonstrated the osteoconductivity for bone formation of SF/HA scaffolds.

MRI and CT Evaluations *in vivo*

The T2WI images of nude mice bearing subcutaneous implants (**Figures 6A,B**) showed diverse performance in different groups. The signal intensity on T2WI in the USPIO-labeled groups with or without BMSCs decreased from 2 to 6 weeks after implantation, and then increased gradually with the corresponding decrease of the R2 and R2* values (**Figure 6C**).

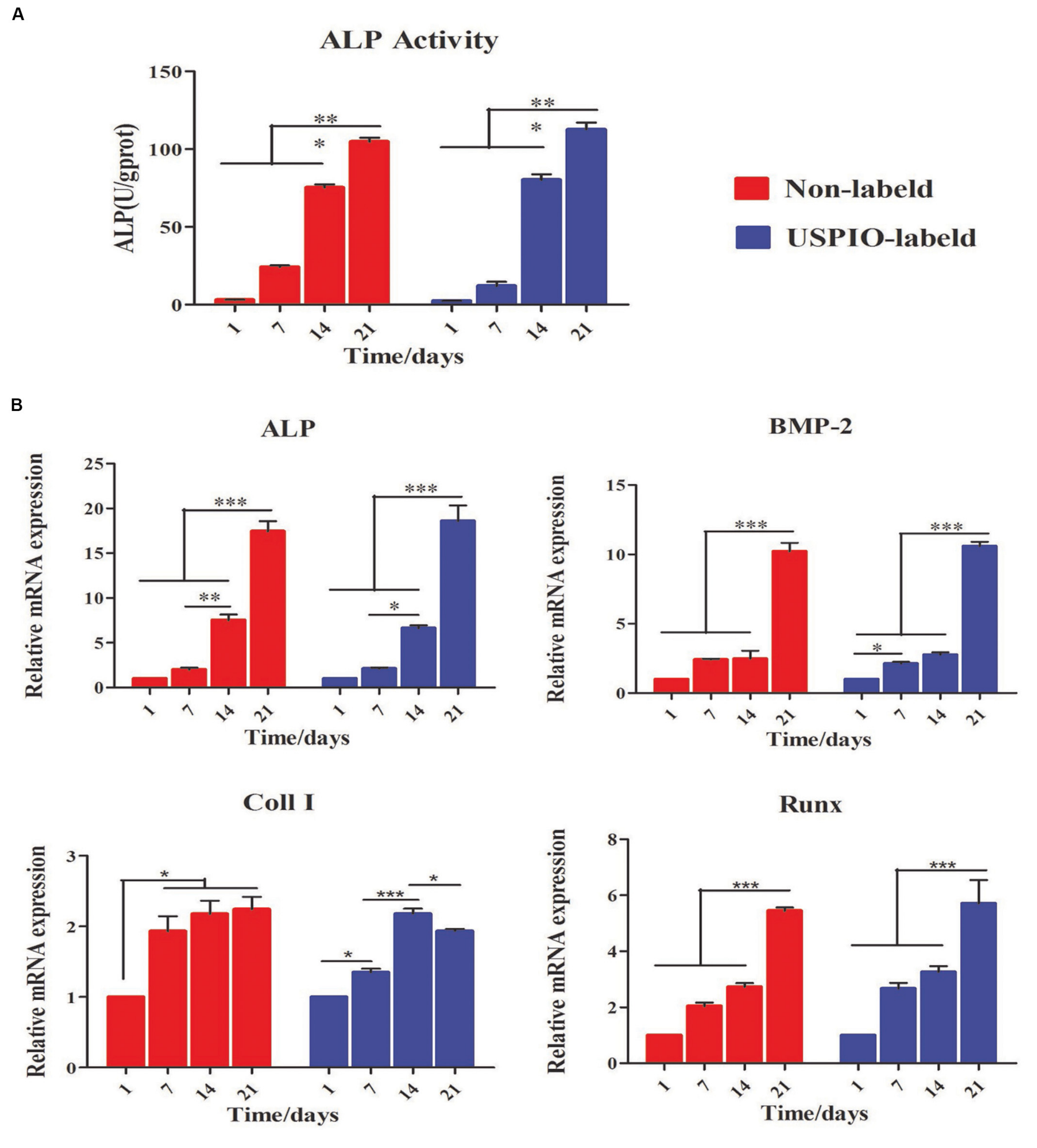

FIGURE 5 | Evaluation of osteogenic differentiation for BMSCs/scaffold composites. **(A)** ALP activity increases for both groups at 1, 7, 14 and 21 days. **(B)** Expression of osteogenic genes (Alp, Bmp-2, Coll I, and Runx) for BMSCs loaded on scaffolds is up-regulated over time ($^*P < 0.05$, $^{**}P < 0.01$, or $^{***}P < 0.001$).

For the USPIO labeled groups, the R2 and R2* values at 8 weeks were significantly lower than those at 2 weeks (both $P < 0.01$). In contrast, signals in the regular implants group showed a tendency to decrease with time, along with the increasing R2 values ($P < 0.05$) and relatively stable R2* values.

CT imaging was also performed simultaneously to demonstrate the internal changes of implants (**Figure 7A**). In the BMSCs loaded group, spots of high density on CT were seen at 8 weeks, and the corresponding mean CT value reached 93.9 ± 3.2HU (**Figure 7B**), which was significantly higher than that at 2 weeks (32.6 ± 1.6HU, $P < 0.001$) and

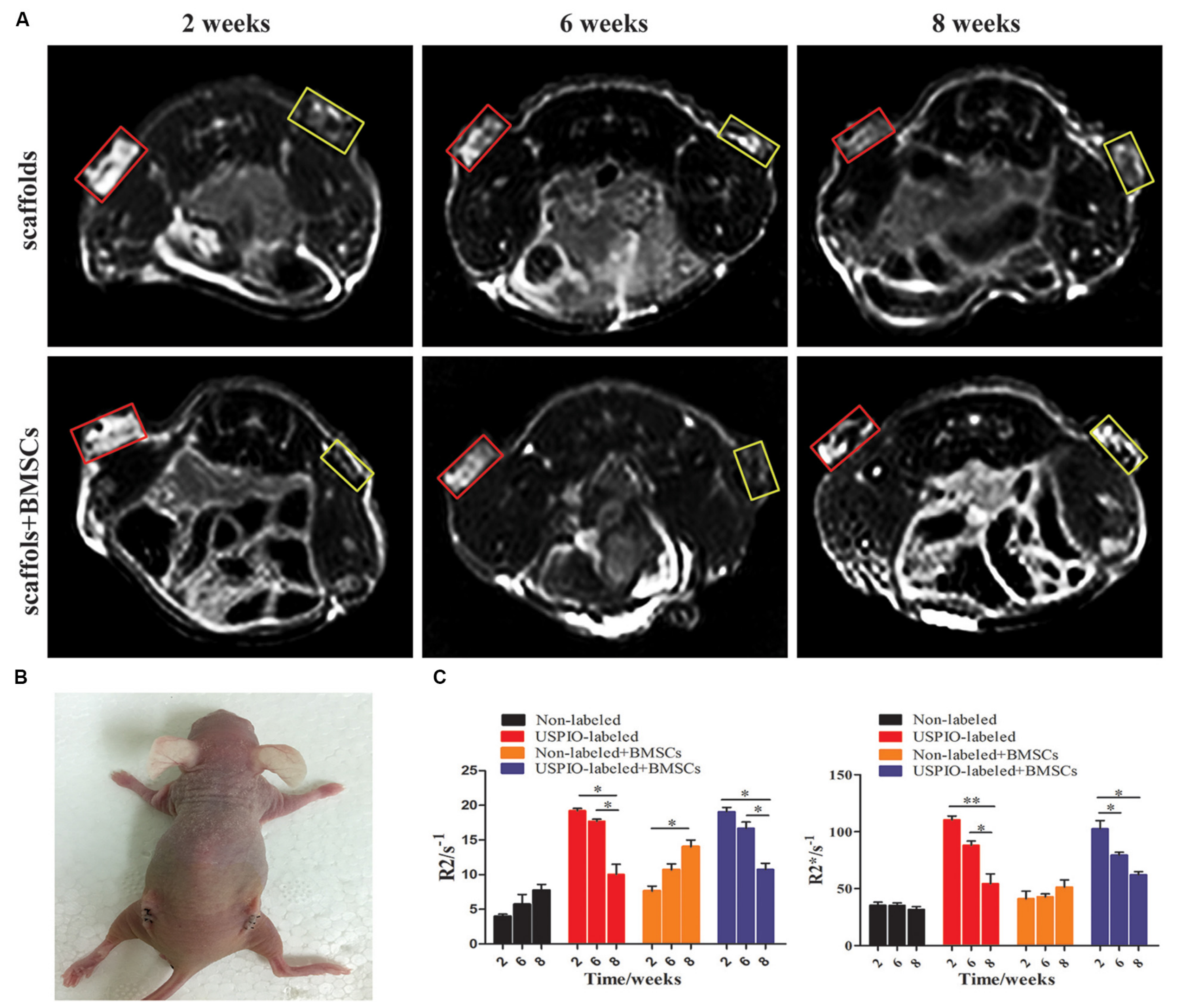

FIGURE 6 | Ectopic osteogenesis model and MR analysis for *in vivo* studies. **(A)** MRI of scaffolds implanted nude mice at 2, 6, 8 weeks (yellow box: USPIO-labeled scaffolds, red box: non-labeled scaffolds). **(B)** Scaffolds implanted on the back of the nude mice bilaterally. **(C)** Quantitative R2- and R2*-relaxometry analysis (*$P < 0.05$, **$P < 0.01$, or ***$P < 0.001$).

6 weeks (66.2 ± 5.5 HU, $P < 0.001$). Furthermore, the CT density in the USPIO-labeled groups was comparable to the unlabeled groups at each time point. But higher CT density was observed in the BMSCs loaded group compared with acellular scaffolds ($P < 0.05$), which confirmed the newly formed bone matrix components.

Histological Examination

H&E and Masson trichrome staining demonstrated that a growing amount of osteoid deposition and neovascularization in scaffolds loaded with BMSCs over 8 weeks. Remnants of the scaffolds were also observed, which was incorporated well within the matrix and decreased over time. In contrast, the acellular scaffolds showed poor osteoid tissue formation (**Figures 8A,B**). The quantitative results of ICP-MS (**Figure 9**) proved the degradation of the iron particles over time, which correlated well with the changes of MRI signal *in vivo*.

DISCUSSION

Bone tissue engineering, which entraps functional cells in 3D implantable scaffolds at the site of injury, has shown promise for the regeneration of bone defects. Recent advances in regenerative medicine have led to new strategies for bone tissue reconstruction (Kim et al., 2014; Melke et al., 2016; Raeisdasteh et al., 2017). Regenerative scaffold-based strategies are proposed to provide structural, biological and biomechanical supports that are imperative for bone regeneration. Sophisticated cell-based techniques are feasible for bone repair, but such approaches are difficult for the proper visualization of the fate of cells and

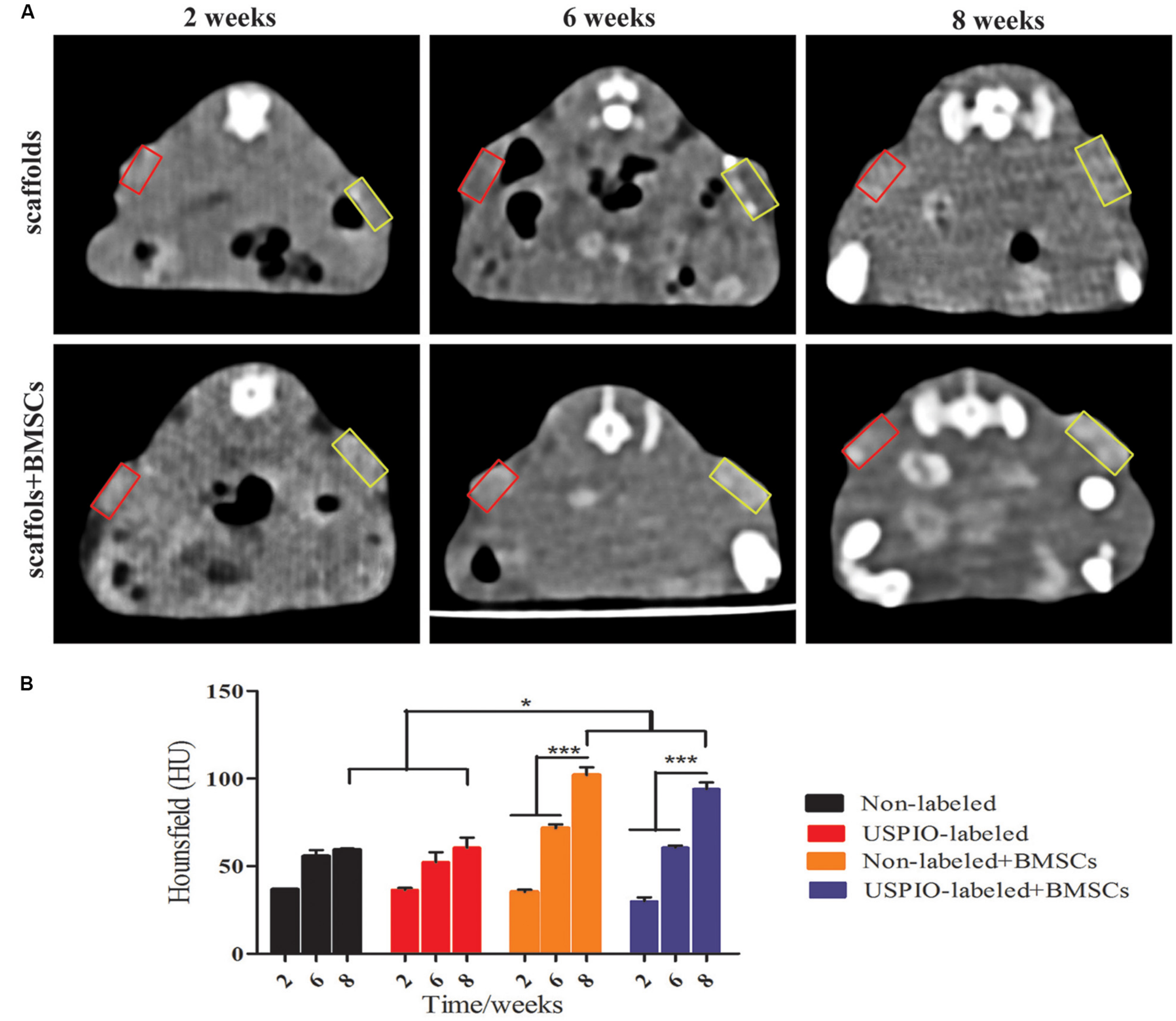

FIGURE 7 | CT analysis for *in vivo* studies. **(A)** CT images of mice show increased density over 2, 6, 8 weeks (yellow box: USPIO-labeled scaffolds, red box: non-labeled scaffolds). **(B)** CT values confirm subcutaneous bone formation of scaffolds ($^*P < 0.05$, $^{**}P < 0.01$, or $^{***}P < 0.001$).

materials after implantation. Our results demonstrated that a 3D SF/HA blended and USPIO labeled scaffold could longitudinally monitor bone tissue engineering by quantitative MRI.

As reported before, the incorporation of nanoparticles could enhance the mechanical property of biomaterials (Dashnyam et al., 2014; Ganesh et al., 2014; Singh et al., 2014b). In this study, we found that SF/HA scaffold is mechanically stronger compared with native silk fibron, which could be attributed to the increased stiffness and compressive strength of native bone by the nano-HA particles (Kasoju and Bora, 2012). Also, the incorporation of USPIO into scaffolds showed better thermal stability than pure SF and SF/HA scaffolds. These results suggest that the scaffolds developed in this study exhibited favorable mechanical property and thermal stability, which are well suited for bone tissue engineering application. Then scaffold composites were confirmed to enhance osteogenic differentiation by facilitating the expression of ALP and osteogenic gene in 21 days *in vitro*. It has been reported that magnetic nanoparticles showed an enhanced osteogenesis to prompt stem cell proliferation and osteogenic differentiation *in vitro* and *in vivo* (Yun et al., 2016; Hu et al., 2018). However, no significant difference was found in osteogenic induction effect between USPIO labeled and unlabeled groups in this study. This may be due to that the low concentration of incorporated USPIO made weak magnetic impact for BMSCs to differentiate.

Thus far, extensive studies have developed scaffolds labeled with various imaging agents in tissue engineering. In this regard, each imaging modality has unique advantages along with intrinsic limitations. For example, Zhang et al. (2016) demonstrated the use of fluorescent labeling coupled to

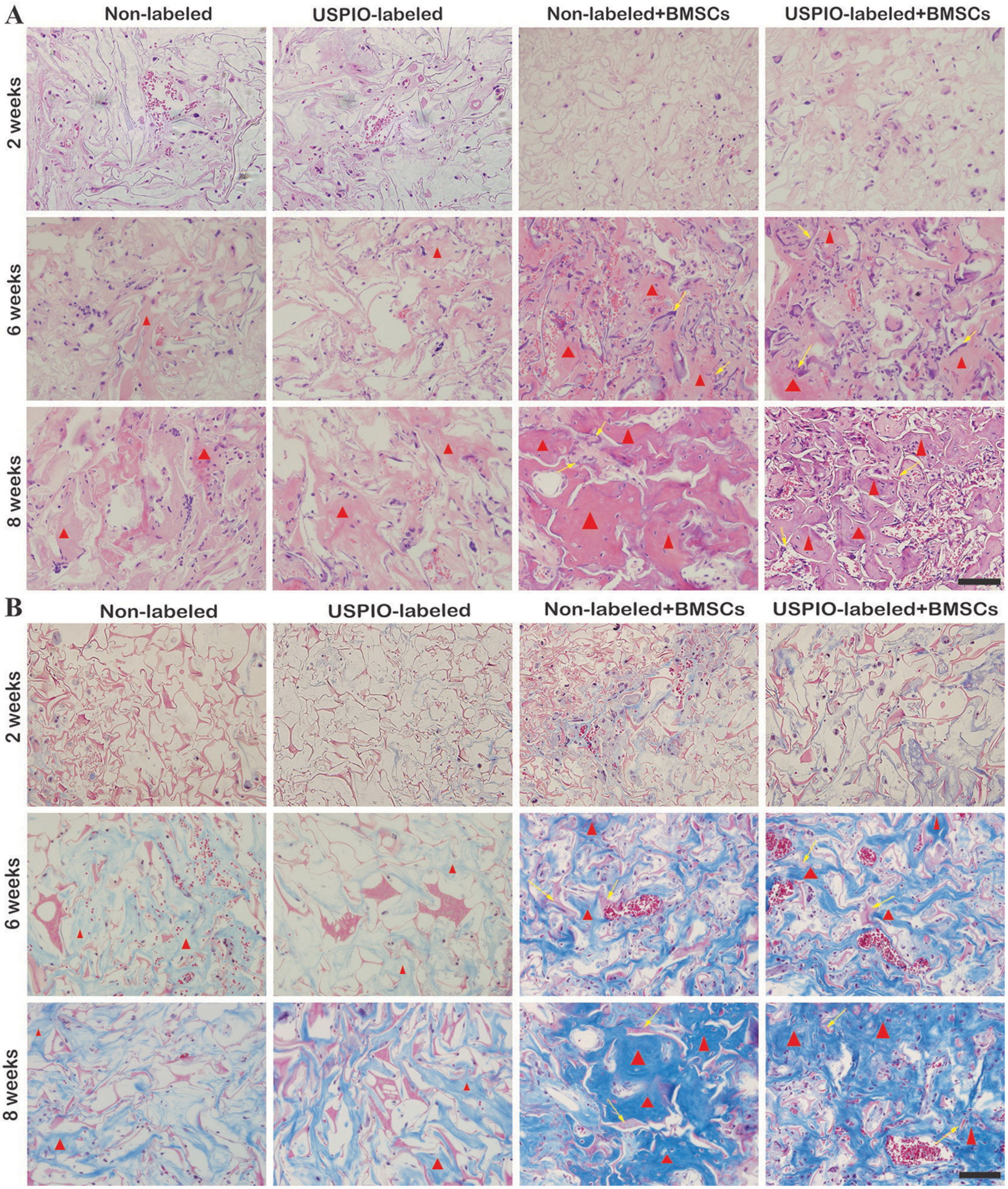

FIGURE 8 | H&E staining **(A)** and Masson trichrome staining **(B)** show osteoid deposition (red triangle) and typical residual scaffold incorporated well within the matrix (yellow arrows) in BMSCs-load scaffolds.

optical imaging for tissue engineering to monitor hyaluronan hydrogels, which was limited by poor light penetration depth of fluorescein. Haralampieva et al. reported scaffolds labeled with radioactive agents used in positron emission tomography imaging toward potential noninvasive tracking of bioengineered muscle tissues (Haralampieva et al., 2016), but

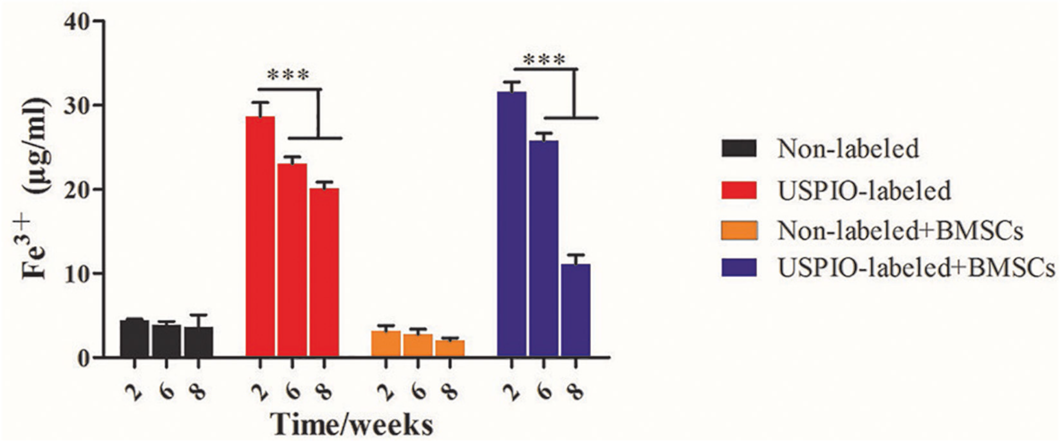

FIGURE 9 | Concentrations of Fe^{3+} by ICP-MS in scaffolds decrease after implantation *in vivo* over time.

it is somewhat limited by poor spatial resolution and radiation risk. Wang et al. utilized CT to noninvasively dynamic monitor biodegradable polymers regarding the microstructure of tissue engineering constructs labeled with gold nanoclusters (Wang et al., 2020). Recent image-guided tissue engineered approaches highlight the superiority of MRI for providing functional information about the biological response of implanted material (Hartman et al., 2002; Szulc and Cheng, 2019). Nevertheless, only few MRI studies have focused on *in vivo* imaging of musculoskeletal tissue implants longitudinally. More recently, we developed a novel multifunctional USPIO labeled cellulose nanocrystal/SF hydrogels that allowed the non-invasive monitoring of hydrogel degradation and cartilage regeneration after *in vivo* implantation in a rabbit model (Chen et al., 2018).

Previous studies have elucidated the relationships between MRI quantitative parameters and regenerative medicine (Cheng et al., 2010; Hu et al., 2018). T2 and T2* mapping, with the calculated R2 and R2* values, could track the absorption and function of the scaffolds. R2* values have been reported to reflect the concentration of USPIO loaded in the scaffolds, thus the increase of R2* is indicative of the degradation of the USPIO-labeled implants (Chen et al., 2018). However, scaffold degradation and bone regeneration occurred simultaneously within the scaffolds, which may complicate the MRI signals. In this study, the R2 values tended to decrease over time for USPIO-labeled scaffolds. These results hence indicate that the decreased relaxation rate caused by the released iron might outweigh the factor as shown in the non-labeled scaffolds. On the contrary, the R2 values of the unlabeled group with BMSCs increased gradually over time. This can be attributed to the ossification promotion contributed by the BMSCs embedded within the scaffolds. Additionally, density values of CT scanning revealed the evolution of bone generation progress in grafts. Though no remarkable enhancement in density was found on CT values at week 2 and 6 ($P > 0.05$), the increase tendency in MRI R2 signals of BMSCs loaded group was observed. Thus, in our study, the combination of MRI and CT examination provided enough information on both scaffolds degradation and ossification in ectopic bone formation, and this system seemed to be feasible in the follow-up of bone repair. In Prussian blue staining, we found that USPIO particles distributed uniformly in scaffold structures, and the same reduction trends were observed in histological examination and ICP-MS. So we speculate that the iron release progress may reflect the degradation of scaffolds. Although MRI and CT can visualize the multifunctional scaffold and provide valuable feedback on the reconstruction and healing process in depth, one inherent limitation of this method is that an ectopic osteogenesis model was chosen to avoid the bleeding of bone defect in situ influenced on MRI signals. Another main limitation is the lack of measurement of calcification after implantation by quantitative MRI. Future studies are required to employ advanced imaging methods, such as quantitative susceptibility mapping (QSM) and spectral CT, to provide separate quantification of compositions in this multifunctional scaffold system, and to improve comprehensive evaluation of tissue engineering strategies for bone regeneration.

CONCLUSION

In conclusion, we developed a USPIO labeled BMSCs-loaded multifunctional scaffold system, which can be feasible for longitudinally monitoring the resorption and function of bone regeneration scaffolds by quantitative MRI and CT. These findings provide new understanding on the non-invasive follow-up of the scaffold system and the potential transitional application of bone tissue engineering strategy for its clinic practice.

DATA AVAILABILITY STATEMENT

The datasets generated for this study are available on request to the corresponding authors.

ETHICS STATEMENT

The animal study was reviewed and approved by Nanfang Hospital, Southern Medical University, Guangzhou, China.

AUTHOR CONTRIBUTIONS

QL designed the study and performed the experiments, analyzed the data, and drafted the manuscript. LF performed the experiments and analyzed the data. ZC involved in the design of study, performed animal experiments, and wrote and reviewed the manuscript. YoL developed scaffold and characterized the properties. YuL and DL contributed to the sample analysis and data interpretation. CY and YX designed the study, discussed the data, wrote and revised the manuscript. All authors contributed to the article and approved the submitted version.

FUNDING

This work was supported by the National Natural Science Foundation of China (Grant Numbers: 81871334 and 81801764); the Natural Science Foundation of Guangdong Province (Grant Numbers: 2017A050506011, 2018030310343, and 2020B1515020008); Medical Scientific Research Foundation of Guangdong Province (Grant Number: A2018014); and the Pearl River S&T Nova Program of Guangzhou (Grant Numbers: 201710010155 and 201806010072).

SUPPLEMENTARY MATERIAL

The Supplementary Material for this article can be found online at: https://www.frontiersin.org/articles/10.3389/fbioe.2020.00697/full#supplementary-material

REFERENCES

Appel, A. A., Anastasio, M. A., Larson, J. C., and Brey, E. M. (2013). Imaging challenges in biomaterials and tissue engineering. *Biomaterials* 34, 6615–6630. doi: 10.1016/j.biomaterials.2013.05.033

Behera, S., Naskar, D., Sapru, S., Bhattacharjee, P., Dey, T., Ghosh, A. K., et al. (2017). Hydroxyapatite reinforced inherent RGD containing silk fibroin composite scaffolds: promising platform for bone tissue engineering. *Nanomedicine* 13, 1745–1759. doi: 10.1016/j.nano.2017.02.016

Bianco, P., Riminucci, M., Gronthos, S., and Robey, P. G. (2001). Bone marrow stromal stem cells: nature, biology, and potential applications. *Stem Cells* 19, 180–192. doi: 10.1007/978-1-61779-815-3_14

Bose, S., Roy, M., and Bandyopadhyay, A. (2012). Recent advances in bone tissue engineering scaffolds. *Trends Biotechnol.* 30, 546–554. doi: 10.1016/j.tibtech.2012.07.005

Chen, Z., Yan, C., Yan, S., Liu, Q., Hou, M., Xu, Y., et al. (2018). Non-invasive monitoring of in vivo hydrogel degradation and cartilage regeneration by multiparametric MR imaging. *Theranostics* 8, 1146–1158. doi: 10.7150/thno.22514

Cheng, H. L., Loai, Y., Beaumont, M., and Farhat, W. A. (2010). The acellular matrix (ACM) for bladder tissue engineering: a quantitative magnetic resonance imaging study. *Magn. Reson. Med.* 64, 341–348. doi: 10.1002/mrm.22404

Crane, J. L., and Cao, X. (2014). Bone marrow mesenchymal stem cells and TGF-beta signaling in bone remodeling. *J. Clin. Invest.* 124, 466–472. doi: 10.1172/JCI70050

Dashnyam, K., Perez, R. A., Singh, K., Lee, E. J., and Kim, H. W. (2014). Hybrid magnetic scaffolds of gelatin–siloxane incorporated with magnetite nanoparticles effective for bone tissue engineering. *RSC Adv.* 4, 40841–40851. doi: 10.1039/C4RA06621A

Ding, Z., Fan, Z., Huang, X., Lu, Q., Xu, W., and Kaplan, D. L. (2016). Silk-Hydroxyapatite nanoscale scaffolds with programmable growth factor delivery for bone repair. *ACS Appl. Mater. Interfaces* 8, 24463–24470. doi: 10.1021/acsami.6b08180

Eisenstein, N. M., Cox, S. C., Williams, R. L., Stapley, S. A., and Grover, L. M. (2016). Bedside, benchtop, and bioengineering: physicochemical imaging techniques in biomineralization. *Adv. Healthc. Mater.* 5, 507–528. doi: 10.1002/adhm.201500617

Farokhi, M., Mottaghitalab, F., Samani, S., Shokrgozar, M. A., Kundu, S. C., Reis, R. L., et al. (2018). Silk fibroin/hydroxyapatite composites for bone tissue engineering. *Biotechnol. Adv.* 36, 68–91. doi: 10.1016/j.biotechadv.2017.10.001

Ganesh, N., Ashokan, A., Rajeshkannan, R., Chennazhi, K., Koyakutty, M., and Nair, S. (2014). Magnetic resonance functional nano-hydroxyapatite incorporated poly(caprolactone) composite scaffolds for in situ monitoring of bone tissue regeneration by MRI. *Tissue Eng. Part A.* 20, 2783–2794. doi: 10.1089/ten.TEA.2014.0161

Haralampieva, D., Betzel, T., Dinulovic, I., Salemi, S., Stoelting, M., Krämer, S. D., et al. (2016). Noninvasive PET imaging and tracking of engineered human muscle precursor cells for skeletal muscle tissue engineering. *J. Nuclear Med.* 57, 1467–1473. doi: 10.2967/jnumed.115.170548

Hartman, E. H., Pikkemaat, J. A., Vehof, J. W., Heerschap, A., Jansen, J. A., and Spauwen, P. H. M. (2002). In vivo magnetic resonance imaging explorative study of ectopic bone formation in the rat. *Tissue Eng.* 8, 1029–1036. doi: 10.1089/107632702320934128

Ho-Shui-Ling, A., Bolander, J., Rustom, L. E., Johnson, A. W., Luyten, F. P., and Picart, C. (2018). Bone regeneration strategies: engineered scaffolds, bioactive molecules and stem cells current stage and future perspectives. *Biomaterials* 180, 143–162. doi: 10.1016/j.biomaterials.2018.07.017

Hu, S., Zhou, Y., Zhao, Y., Xu, Y., Zhang, F., Gu, N., et al. (2018). Enhanced bone regeneration and visual monitoring via superparamagnetic iron oxide nanoparticle scaffold in rats. *J. Tissue Eng. Regen. Med.* 12, e2085–e2098. doi: 10.1002/term.2641

Kasoju, N., and Bora, U. (2012). Silk fibroin in tissue engineering. *Adv. Healthc. Mater.* 1, 393–412. doi: 10.1002/adhm.201200097

Kim, J. J., Singh, R. K., Seo, S. J., Kim, T. H., Kim, J. H., Lee, E. J., et al. (2014). Magnetic scaffolds of polycaprolactone with functionalized magnetite nanoparticles: physicochemical, mechanical, and biological properties effective for bone regeneration. *RSC Adv.* 4, 17325–17336. doi: 10.1039/C4RA00040D

Ma, D., Wang, Y., and Dai, W. (2018). Silk fibroin-based biomaterials for musculoskeletal tissue engineering. *Mater. Sci. Eng. C Mater. Biol. Appl.* 89, 456–469. doi: 10.1016/j.msec.2018.04.062

Melke, J., Midha, S., Ghosh, S., Ito, K., and Hofmann, S. (2016). Silk fibroin as biomaterial for bone tissue engineering. *Acta Biomater.* 31, 1–16. doi: 10.1016/j.actbio.2015.09.005

Mertens, M. E., Hermann, A., Bühren, A., Olde-Damink, L., Möckel, D., Gremse, F., et al. (2014). Iron oxide-labeled collagen scaffolds for non-invasive MR imaging in tissue engineering. *Adv. Funct. Mater.* 24, 754–762. doi: 10.1002/adfm.201301275

Mertens, M. E., Koch, S., Schuster, P., Wehner, J., Wu, Z., Gremse, F., et al. (2015). USPIO-labeled textile materials for non-invasive MR imaging of tissue-engineered vascular grafts. *Biomaterials* 39, 155–163. doi: 10.1016/j.biomaterials.2014.10.076

Nam, S. Y., Ricles, L. M., Suggs, L. J., and Emelianov, S. Y. (2015). Imaging strategies for tissue engineering applications. *Tissue Eng. Part B* 21, 88–102. doi: 10.1089/ten.TEB.2014.0180

Oryan, A., Kamali, A., Moshiri, A., and Eslaminejad, M. B. (2017). Role of mesenchymal stem cells in bone regenerative medicine: what is the evidence? *Cells Tissues Organs* 204, 59–83. doi: 10.1159/000469704

Raeisdasteh, H. V., Davaran, S., Ramazani, A., and Salehi, R. (2017). Design and fabrication of porous biodegradable scaffolds: a strategy for tissue engineering. *J. Biomater. Sci. Polym. Ed.* 28, 1797–1825. doi: 10.1080/09205063.2017.1354674

Roman, A. P., Singh, R. K., Kim, T. H., and Kim, H. W. (2017). Silica-based multifunctional nanodelivery systems toward regenerative medicine. *Mater. Horizons* 4, 772–799. doi: 10.1039/C7MH00017K

Roseti, L., Parisi, V., Petretta, M., Cavallo, C., Desando, G., Bartolotti, I., et al. (2017). Scaffolds for bone tissue engineering: state of the art and new perspectives. *Mater. Sci. Eng. C* 78, 1246–1262. doi: 10.1016/j.msec.2017.05.017

Sajesh, K. M., Ashokan, A., Gowd, G. S., Sivanarayanan, T. B., Unni, A. K. K., Nair, S. V., et al. (2019). Magnetic 3D scaffold: a theranostic tool for tissue regeneration and non-invasive imaging in vivo. *Nanomedicine* 18, 179–188. doi: 10.1016/j.nano.2019.02.022

Seung, Y. N., Laura, M. R., Laura, J. S., and Emelianov, S. Y. (2015). Imaging strategies for tissue engineering applications. *Tissue Eng. Part B Rev.* 21, 88–102. doi: 10.1089/ten.teb.2014.0180

Singh, R. K., Patel, K. D., Kim, J. J., Kim, T. H., Kim, J. H., Shin, U. S., et al. (2014a). Multifunctional hybrid nanocarrier: magnetic CNTs ensheathed with mesoporous silica for drug delivery and imaging system. *ACS Appl. Mater. Interfaces* 6, 2201–2208. doi: 10.1021/am4056936

Singh, R. K., Patel, K. D., Lee, J. H., Lee, E. J., Kim, J. H., Kim, T. H., et al. (2014b). Potential of magnetic nanofiber scaffolds with mechanical and biological properties applicable for bone regeneration. *PLoS One* 9:e91584. doi: 10.1371/journal.pone.0091584

Sun, Y., Geutjes, P., Oosterwijk, E., and Heerschap, A. (2014). In vivo magnetic resonance imaging of Type I collagen scaffold in rat: improving visualization of bladder and subcutaneous implants. *Tissue Eng. Part C Methods* 20, 964–971. doi: 10.1089/ten.TEC.2014.0046

Szulc, D. A., and Cheng, H. M. (2019). One-step labeling of collagen hydrogels with polydopamine and manganese porphyrin for non-invasive scaffold tracking on magnetic resonance imaging. *Macromol. Biosci.* 19:e1800330. doi: 10.1002/mabi.201800330

Tang, D., Tare, R. S., Yang, L. Y., Williams, D. F., Ou, K. L., and Oreffo, R. O. (2016). Biofabrication of bone tissue: approaches, challenges and translation for bone regeneration. *Biomaterials* 83, 363–382. doi: 10.1016/j.biomaterials.2016.01.024

Walmsley, G. G., McArdle, A., Tevlin, R., Momeni, A., Atashroo, D., Hu, M. S., et al. (2015). Nanotechnology in bone tissue engineering. *Nanomedicine* 11, 1253–1263.

Wang, W., Tao, H., Zhao, Y., Sun, X., Tang, J., Selomulya, C., et al. (2017). Implantable and biodegradable macroporous iron oxide frameworks for efficient regeneration and repair of infracted heart. *Theranostics* 7, 1966–1975. doi: 10.7150/thno.16866

Wang, X., Ai, A., Yu, Z., Deng, M., Liu, W., Zhou, G., et al. (2020). Dual-modal non-invasive imaging in vitro and in vivo monitoring degradation of PLGA scaffold based gold nanoclusters. *Mater. Sci. Eng. C Mater. Biol. Appl.* 107:110307. doi: 10.1016/j.msec.2019.110307

Yang, Y., Ding, F., Wu, J., Hu, W., Liu, W., Liu, J., et al. (2007). Development and evaluation of silk fibroin-based nerve grafts used for peripheral nerve regeneration. *Biomaterials* 28, 5526–5535. doi: 10.1016/j.biomaterials.2007.09.001

Yun, H. M., Kang, S. K., Singh, R. K., Lee, J. H., Lee, H. H., Park, K. R., et al. (2016). Magnetic nanofiber scaffold-induced stimulation of odontogenesis and pro-angiogenesis of human dental pulp cells through Wnt/MAPK/NF-κB pathways. *Dental Mater.* 32, 1301–1311. doi: 10.1016/j.dental.2016.06.016

Zhang, Y., Rossi, F., Papa, S., Violatto, M. B., Bigini, P., Sorbona, M., et al. (2016). Non-invasive in vitro and in vivo monitoring of degradation of fluorescently labeled hyaluronan hydrogels for tissue engineering applications. *Acta Biomater.* 30, 188–198. doi: 10.1016/j.actbio.2015.11.053

Zhou, H., and Lee, J. (2011). Nanoscale hydroxyapatite particles for bone tissue engineering. *Acta Biomater.* 7, 2769–2781. doi: 10.1016/j.actbio.2011.03.019

Conflict of Interest: YoL, YuL, and DL were employed by the company Beogene Biotech.

The remaining authors declare that the research was conducted in the absence of any commercial or financial relationships that could be construed as a potential conflict of interest.

frontiers
in Bioengineering and Biotechnology

ORIGINAL RESEARCH
published: 10 July 2020
doi: 10.3389/fbioe.2020.00774

Effective Reconstruction of Functional Urethra Promoted With ICG-001 Delivery Using Core-Shell Collagen/Poly(Llactide-co-caprolactone) [P(LLA-CL)] Nanoyarn-Based Scaffold: A Study in Dog Model

Kaile Zhang[1]†, Xiaolan Fang[2]†‡, Jingjing Zhu[3], Ranxing Yang[1], Ying Wang[1], Weixin Zhao[4], Xiumei Mo[3]* and Qiang Fu[1]*

[1] Department of Urology, Affiliated Sixth People's Hospital, Shanghai Jiao Tong University, Shanghai, China, [2] Diagnostic Laboratory, Greenwood Genetic Center, Greenwood, SC, United States, [3] Biomaterials and Tissue Engineering Laboratory, College of Chemistry, Chemical Engineering and Biotechnology, Donghua University, Shanghai, China, [4] Wake Forest Institute for Regenerative Medicine, Winston-Salem, NC, United States

Edited by:
Gang Wu,
VU University Amsterdam,
Netherlands

Reviewed by:
Elif Vardar,
Centre Hospitalier Universitaire Vaudois (CHUV), Switzerland
Ahmed El-Fiqi,
Dankook University, South Korea

****Correspondence:***
Xiumei Mo
xmm@dhu.edu.cn
Qiang Fu
jamesqfu@aliyun.com

†These authors have contributed equally to this work

‡Present address:
Xiaolan Fang,
Diagnostic Laboratory, Greenwood Genetic Center, Greenwood, SC, United States

Specialty section:
This article was submitted to Biomaterials,
a section of the journal Frontiers in Bioengineering and Biotechnology

Received: *09 March 2020*
Accepted: *18 June 2020*
Published: *10 July 2020*

Citation:
Zhang K, Fang X, Zhu J, Yang R, Wang Y, Zhao W, Mo X and Fu Q (2020) Effective Reconstruction of Functional Urethra Promoted With ICG-001 Delivery Using Core-Shell Collagen/Poly(Llactide-co-caprolactone) [P(LLA-CL)] Nanoyarn-Based Scaffold: A Study in Dog Model. Front. Bioeng. Biotechnol. 8:774. doi: 10.3389/fbioe.2020.00774

Hypospadias and urethral stricture are common urological diseases which seriously affect voiding function and life quality of the patients, yet current clinical treatments often result in unsatisfactory clinical outcome with frequent complications. *In vitro* experiments confirmed that ICG-001 (a well-established Wnt signaling inhibitor) could effectively suppress fibroblast proliferation and fibrotic protein expression. In this study, we applied a novel drug-delivering nanoyarn scaffold in urethroplasty in dog model, which continuously delivers ICG-001 during tissue reconstruction, and could effectively promote urethral recovery and resume fully functional urethra within 12 weeks. Such attempts are essential to the development of regenerative medicine for urological disorders and for broader clinical applications in human patients.

Keywords: urethral stricture, nanoyarn, Wnt signaling, urethral reconstruction, urethroplasty

INTRODUCTION

Hypospadias and urethral stricture are common urological diseases which seriously affect voiding function and life quality of the patients. Current clinical treatment for such urethral defects are mainly based on transplantation of autologous tissues (e.g., penile flap or buccal mucosal graft), which is frequently accompanied with severe side effects (such as local injuries) and is often limited by the extremely low tissue amount from penile and oral mucosa. In addition, the efficiency of urethral repair might be compromised by insufficient wound healing or stricture formation in the lumen. There is an urgent need for novel biomaterials and clinical methods to facilitate the reconstruction of functional urethra from such urethral defects, and simultaneously promote wound healing and prevent fibrosis/scar formation for a satisfactory tissue recovery.

The rapid development of biomaterials brought in many trials of tissue-engineered urethra in preclinical and clinical studies, yet the successful rate varies, and the efficacy is often disappointing, especially in the scaffold without pre-loaded cells (Raya-Rivera et al., 2011; Li et al., 2013; Xie et al., 2013, 2014; Ramsay et al., 2016; Atala et al., 2017; Kajbafzadeh et al., 2017; Zhou et al., 2017). One possibility is that the small pore size of the experimental biomaterial might hinder the infiltration of local cells from the native tissue into scaffold. Another possibility is that the fibrosis related signaling [e.g., TGF-beta, connective tissue growth factor (CTGF/CCN2), platelet-derived growth factor (PDGF), interleukin 4 (IL-4), etc.] pathways are activated during the urethral reconstruction process, which promotes fibrosis and recurrence of urethral stricture (Sangkum et al., 2015). Effective inhibition of such signaling pathways are critical for post-injury tissue regeneration, particularly in tissue-engineered urethra models which human cells are pre-planted to bridge the novel urethra to the native urethra edges (Raya-Rivera et al., 2011; Guo et al., 2016). Although it has been reported that some stem cells might possess the property of inhibiting inflammation and fibrosis, previously applications of engineered human cells confronted a number of drawbacks and limitations in urethral reconstruction and stricture occurrence (Versteegden et al., 2017). Therefore, it has been a challenge to use the combination of biomaterial and preloaded human cells in the treatment of urethral defects *in vivo*, and it remains even more difficult to get translated from bench side to bedside.

In this study, we utilized a novel bioengineering method and produced a functional electrospun collagen/poly(L-lactide-co-caprolactone) [P(LLA-CL)] nanoyarn scaffold (**Figure 1B**) to improve urethroplasty efficiency. Nanoyarn has been verified to increase pore size comparing to traditional conjugated nanofibrous scaffold *in vitro* (Guo et al., 2016) and is expected to serve as a promising biomaterial for tissue reconstruction. A co-axial electrospinning system and a dynamic liquid system were integrated to deliver the Wnt pathway inhibitor ICG-001 and the drug release efficacy was evaluated *in vitro* (Guo et al., 2016). ICG-001 specifically binds to CREB-binding protein (CBP) and has been used widely as an antagonizer of Wnt/β-catenin-mediated transcription. We applied optimized concentration of ICG-001 in dog model and evaluated the urethroplasty outcome based on urethroscopy, urethrography, sono-urethrography and histology analysis (**Figure 1A**).

MATERIALS AND METHODS

Biomaterial for Nanoyarn Production

Poly(L-lactide-co-caprolactone) [P(LLA-CL)] (LA:CL = 50:50, *MW* = 300,000) was purchased from Daigang bioengineering Co., Ltd. (Jinan, China). Type I collagen was purchased from Ming-Rang BioTech Co., Ltd. (Sichuan, China). 2, 2, 2-trifluoroethanol was purchased from Fine Chemicals (Shanghai, China). ICG-001 was purchased from Selleck Chemicals (Shanghai, China).

Core-Shell ICG-001-Delivering Nanoyarn Fabrication

The fabrication of nanoyarn was reported previously using a co-axial electrospinning device (Donghua University, Shanghai) (Zhang et al., 2016; **Figure 1B**). Briefly, a hole (8 mm in diameter) was created in a basin, which allows the flow of water to form a water vortex. A pump was employed to recycle water back to maintain the water level after the water was drained through the hole into a tank below the basin. Electrospun nanofibers were generated and deposited on the water surface; then, the nanofibers were twisted into a bundle of nanoyarn in the water vortex and collected by a rotating mandrel (60 r/min) to form a nanoyarn scaffold. Nanofibrous scaffold fabricated with conjugated electrospinning technique was set as control group to compare the morphology and mechanical property with nanoyarn. For the construction of Collagen/P(LLA-CL) scaffolds, the solution of the core layer was 1 g collagen/P(LLA-CL) dissolved in 2, 2, 2-trifluoroethanol. Then it was mixed with 0.1, 0.5, 1, 2, and 4 mg ICG-001, respectively, in 60 μL DMSO solution and injected at a rate of 0.2 ml/h. The solution of the shell layer was 1g Collagen/P(LLA-CL) dissolved in 2, 2, 2-trifluoroethanol and fed at 0.8 ml/h. During the process of scaffold fabrication, room temperature was maintained at 22–25°C, and the relative humidity at 40–50%. A dynamic liquid system was used to collect the nanofibers to fabricate the ICG-001 delivering nanoyarn. The distance between the sprayer tip and the receiving water level was set to 15 cm and the positive voltage was 18 kV.

Scanning Electron Microscopy

Scanning electron microscope (SEM, Hitachi TM-100, Tokyo, Japan) was used to observe morphology of the scaffolds. Specimens were punched into 1.2 cm-diameter disks and cryopreserved at −80° for 2 h, then freeze-dried overnight and preserved in a vacuum container. Fibroblasts were seeded on the nanoyarn and conjugated nanofibrous scaffold specimens in the 24 wells culture dish for 3 days. The specimens with or without cells were imaged under SEM on first day and third day. The angle distribution was measured from 100 yarns in the SEM images.

Mechanical Property Test

Universal materials tester (H5K-S, Hounsfield, United Kingdom) was used to evaluate the tensile strength of the drug delivering nanoyarn. The conjugated electrospun nanofibrous scaffold and bladder acellular matrix graft (BAMG) were used as the control material. All the scaffold samples were prepared as longitudinal strips (20 mm in length and 10 mm in width). Each sample of scaffolds was fixed onto the clamps and pulled at 5 mm/min crosshead speed until rupture. The stress and strain data in the process were recorded.

Fourier-Transform Infrared Spectroscopy

The chemical components of ICG-001 delivering nanoyarn and its control scaffolds were, respectively, characterized by Fourier transform infrared spectrum (FTIR, Thermo Electro AVATAR 380, United States).

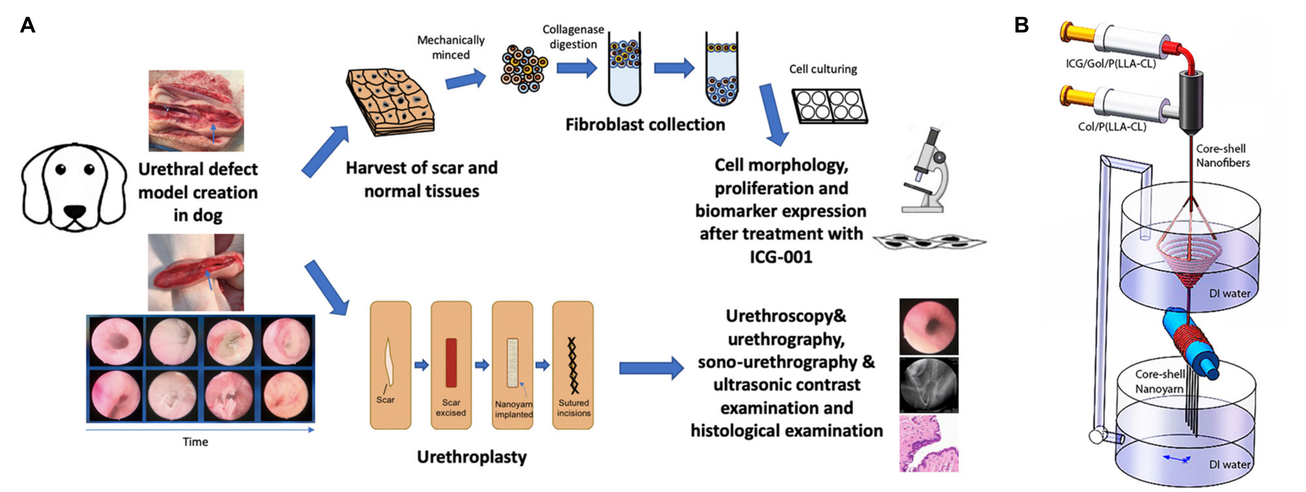

FIGURE 1 | Overview of key components in current study. **(A)** The flowchart of study design. **(B)** Fabrication process of ICG-001 delivered nanoyarn. The core-shell electrospinning system (top) contains two syringes containing ICG-001/Col/P(LLA-Cl) and Col/P(LLA-Cl), respectively. The dynamic liquid system (bottom) is integrated with core-shell electro-spinning system.

Fibroblasts Isolation

The animal protocol (SYXK 2011-0128) was approved by the Animal Ethics Committee of Shanghai Sixth People's Hospital, Shanghai, China. The project identification code is 14JC1492100, which was approved on September 1, 2014 by Science and Technology Commission of Shanghai, China. All the animal experiments were performed in accordance with the guidelines for animal care equivalent to the NIH Guide for Care and Use of Laboratory Animals. All the beagle dogs were with average body weight (BW) ∼20kg and were provided by Shanghai Academy of Agricultural Sciences.

Skin biopsies and fibroblasts harvest were performed to evaluate the biocompatibility and fibrosis inhibiting effect of ICG-001 delivering nanoyarn. Three beagle dogs were used. Each dog was pretreated with 15 mg/kg Ketamine, 2–3 mg/kg xylazine and 0.75 mg/kg acepromazine intramuscularly. Then they were anesthetized and maintained with 2% isoflurane. A small laparotomy excision was made above the pubic symphysis. A biopsy of skin specimen with 2 cm × 2 cm was excised from the skin of abdomen wall, then the defect was closed with 3-0 polyglactin sutures in two layers. The specimen was processed in a sterile condition. It was washed with PBS with 100 IU/mL penicillin and 100 μg/mL streptomycin. The fibroblasts were isolated, sorted and stored as previously reported (Guo et al., 2016), and were used in *in vitro* experiments in this study. The animals were euthanized after tissue collection.

Preparation of Fibroblasts Treated With ICG-001 Releasing Solution

To prepare the ICG-001 releasing solution, the ICG-001 delivering core-shell nanoyarn with different amount of ICG-001 was sterilized with ultraviolet for 2 h. To collect the ICG-001 medium, 2 mL of complete culture medium was used to immerse 120 mg ICG-001 delivering nanoyarn to get ICG-001 solution for 24 h. Six ICG-001 released media were prepared with nanoyarn with different concentrations of ICG-001 [0.1, 0.5, 1, 2, 4 mg and negative control (complete culture medium without ICG-001)].

To prepare the fibroblast treated with ICG-001 releasing solution, ten thousand fibroblasts were transferred to each well of 4-well chamber slides and cultured overnight. Five groups were set in the study by adding different IGC-001 solutions from the previous step. The fibroblasts were cultured for 3 days before they were used in further experiments.

Cell Morphology and Proliferation Assays

After culturing with ICG-001 containing culture medium for two days, the cells' morphology was observed under microscope, and cell proliferation was evaluated by the 3-(4,5-dimethylthiazol-2-yl)-2,5-diphenyltetrazolium bromide (MTT, Product #5655, SigmaAldrich, St. Louis, United States) assay at day 2 and 6 after seeding according to the protocol. After incubation at 37°C for three hours, the medium was transferred into 96-well plate. The data were read by enzyme-labeled instrument (Multiskan MK3, Thermo Fisher Scientific, Waltham, United States) at 492 nm to measure the absorbance of the solution.

Western Blot

Western blotting analysis was conducted to analyze the relative expression level of collagen type 1 and 3 in fibroblasts treated with culture medium released from the ICG-001 delivering nanoyarn as previously reported (Guo et al., 2016). The results were normalized using the expression of β-actin (Anti-beta Actin antibody, Cat# ab8226, Abcam, Cambridge, MA, United States). Mouse-anti-Collagen I and anti-Collagen III were purchased from Sigma-Aldrich, St. Louis, MO, United States (Cat# C2456 and Cat# C7805). Samples were incubated with primary antibodies at 4°C overnight and subsequently with HRP-conjugated goat anti-mouse secondary antibody (Cat# ab97023, Abcam, Cambridge, MA, United States) for one hour at room temperature. Anti-GAPDH antibody (Cat# ab9484, Abcam, Cambridge, MA, United States) was used as a protein loading control. The results were quantified using Quantity One software (version 4.5.2) and expression was normalized by comparing to GAPDH. The expression levels were compared using one-way ANOVA by Prism8 (GraphPad).

Urethroplasty and Postoperative Examinations in Beagle Dog

For urethral defects and follow-up urethroplasty, ten beagle dogs were used. The animals were randomly divided into 3 groups. Dogs in group 1 ($n = 2$) were treated with conjugated nanofibrous scaffold. Group 2 ($n = 4$) were treated with nanoyarn without ICG-001. Group 3 ($n = 4$) were treated with ICG-001 delivering nanoyarn. After general anesthesia (as described in Fibroblasts Isolation section), Foley F8 silicone catheters (Suzhou, Jiangsu, China) were inserted into the urethras (**Figures 2A,B**). Briefly, the skin approximately 3 cm from the external urethral orifice was sectioned, and the urethra was dissected from the corpus cavernosum. Ventral urethral defects (mean length of 2.0 cm and width of 0.8 cm) were created in the urethra of penile part of dogs. The scaffolds (length of 2 cm and width of 1 cm) were sutured to the defect with 6–0 absorbable polyglactin sutures (**Figures 2C–H**). The 8F silicone catheter was left in the urethra and fixed with 4–0 suture at the dog's gland, and with 6–0 absorbable sutures for 14 days postoperatively. The animals were observed twice daily before catheters were removed. In case the catheter was removed by the animal, another new catheter would be reinserted after anesthesia. The urethroscopy was used to observe the recovery process of the urethra. Photos of the urethral lumen were captured at 6 and 12 weeks post-surgery. Retrograde urethrograms were performed for the animals in 3 groups to assess urethral caliber under anesthesia at 6 and 12 weeks post-surgery. The contrast solution was injected into the urethra lumen to observe any leakage and stricture. Also, the dogs were undertaken the urethra contrast-enhance ultrasound test to check the condition of scar in the urethra at 6 and 12 weeks post-surgery. The bubble contrast solution was used to enhance the resolution. The animals were euthanized after urethroscopy and retrograde urethrograms at 12-week period. Urethral tissues were harvested for the following staining experiments.

Histology and Immunohistochemistry

The urethra specimens were rinsed with PBS and fixed in 4% paraformaldehyde for 15 min at room temperature followed by dehydration and paraffin embedding. Hematoxylin-eosin (H&E) and Masson staining were performed according to the protocol to evaluate vascularization and collagen distribution. For immunohistochemistry, the slides were processed and cryosectioned at 12-μm thickness using a cryostat (Leica CM1950). Immunohistochemical staining were performed using monoclonal antibodies against the SMCs (α-actin; Santa Cruz, Dallas, TX, United States), AE1/AE3 and CD31 (Cat#41-9003-82, and Cat#CF504773, Thermo Fisher Scientific, Waltham, United States). Then, the specimens on slides were treated with Biotin-Streptavidin (ABC) and DAB in Biotin-Streptavidin (ABC) IHC detection kits (Cat# ab64264, Abcam, Cambridge, MA, United States). The tissue sections were counter-stained with hematoxylin for the nuclei.

RESULTS

Morphology of Drug-Delivering Nanoyarn With Pre-loaded Fibroblasts

The thickness was measured for fibrous nano scaffolds (0.75 ± 0.16 mm, mean ± std), conjugated nano scaffolds (0.90 ± 0.21 mm), nanoyarn (0.93 ± 0.19 mm) and ICG-001 delivering nanoyarn (0.92 ± 0.14 mm), as well as the diameter (conjugated nano scaffolds (1.51 ± 0.351 μm), nanoyarn (2.447 ± 0.408 μm) and ICG-001 delivering nanoyarn (2.547 ± 0.508 μm), as previously reported (Guo et al., 2016). The thickness of core layer was 53 ± 15 nm, and the shell layer was 226 ± 27 nm. The water contact angle was measured as previously reported (fibrous nano scaffolds, 120.97 ± 6.13°; ICG-001 delivering nanoyarn, 87.9 ± 5.78°) (Guo et al., 2016).To confirm the physical properties of nano biomaterials for fibroblast growth, we observed the morphology of nanoyarn and the conjugated nanofibrous scaffold under SEM. For both of them, the direction of fibers was aligned. The angle distribution of the nanoyarn was 8.3 ± 4.5 degrees (mean ± std). Compared with conjugated nanofibrous scaffold (**Figures 3A,B**), the nanofibers in nanoyarn (**Figures 3E,F**) were twisted into thick yarns with more fibers, indicating a higher flexibility for the engineered tissue. This was confirmed in the following animal experiments, as nanoyarn was very convenient to handle and easy to suture during the surgery, and closely mimicking the native tissue to resume urethral function/plasticity. The pore size exhibited in nanoyarn was larger than conjugated nanofibrous scaffold (**Figure 3**), which would allow efficient cell infiltration from neighboring tissues. Compared with cells on conjugated nanofibrous scaffold (**Figures 3C,D**), in the cells-laden nanoyarn the cells grew along the yarns with abundant extracellular matrix (ECM) (**Figures 3G,H**). The quantitative data of the pore size, porosity and cell infiltration of nanoyarn, conjugated nano scaffold and nanofibrous scaffold was reported previously (Guo et al., 2016).

To optimize the mechanical characteristics of the nano biomaterials for *in vivo* experiments, we modified the setting of the parameters in previous experiments (Zhang et al., 2016), and evaluated the updated mechanical properties of various nano scaffolds (**Figure 4A** and **Table 1**). Comparing to non-woven nanofibrous scaffolds (BAMG) and conjugated nano scaffolds, nanoyarn showed lower maximum tensile strength and Young's modulus, higher elongation at break and higher elasticity in vertical and parallel directions (**Figure 4A** and **Table 1**), indicating better plasticity and strength. The properties of the present nanoyarn is more suitable for suture and manipulation in the dog model operation. In addition, we previously

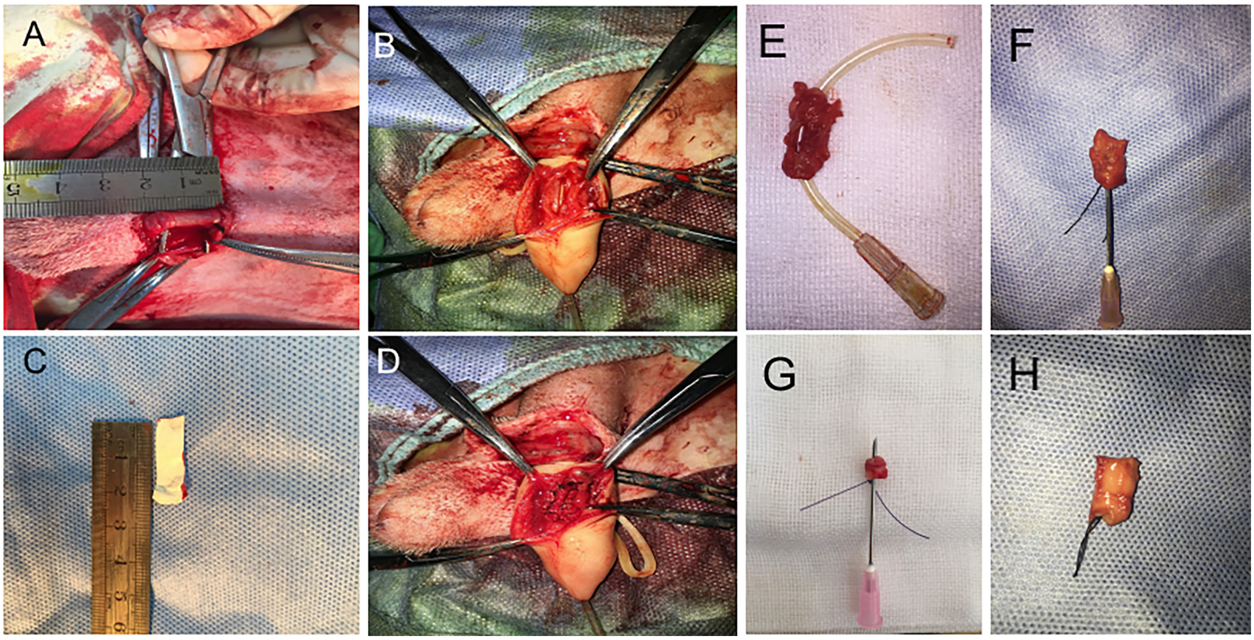

FIGURE 2 | The surgery process of urethral defect model creation and urethroplasty with biomaterial. **(A)** Dog urethra (diameter = 2 cm) was exposed and measured. **(B)** F8 catheter was inserted from the penile tip and kept in urethra, and the urethral wall was opened to 2 cm in length with a pair of scissors. **(C)** 2 cm × 0.5 cm ICG-001 delivering nanoyarn was prepared. **(D)** The ICG-001 delivered nanoyarn was implanted into the urethral defect area. **(E)** The fistula (in the gray dotted rectangle) formed in the middle of the repaired segment with conjugated scaffold. **(F)** Stricture formed in the urethra repaired by nanoyarn (the needle cannot pass through). **(G)** Unobstructed urethra was repaired with ICG-001 delivered nanoyarn (the needle could pass through). **(H)** A healthy urethra without repair was shown as a control.

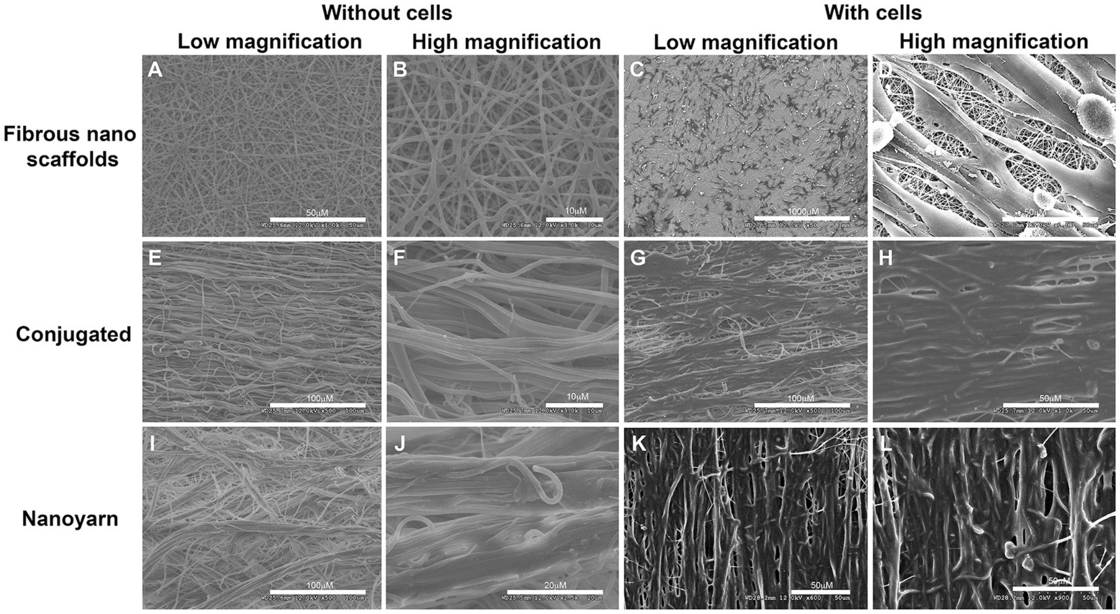

FIGURE 3 | Physical characteristics of different nano scaffolds under SEM. Fibrous nano scaffolds **(A–D)**, conjugated nanofibrous scaffold **(E–H)** and nanoyarn **(I–L)** were observed at different magnifications with or without preloaded fibroblasts. Scale bars are indicated in each figure.

evaluated the release efficacy and time range of ICG-001 from three different nano scaffolds *in vitro* (**Supplementary Figure 1**; Guo et al., 2016). The ICG-001 delivering nanoyarn showed similar polymer constitution comparing to control nanoyarn [collagen conjugated (Col/PLCL) or non-conjugated (PLCL)] (**Figure 4B**), suggestion that the load of ICG-001 in

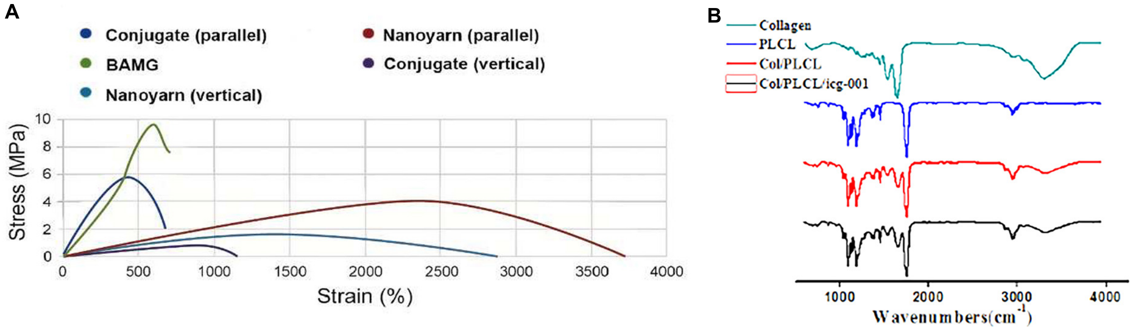

FIGURE 4 | Mechanical properties of different nano scaffolds. **(A)** The tensile strength of nanoyarn, conjugated scaffold and BAMG. **(B)** FTIR for different polymers in PLCL, control nanoyarn and drug (ICG-001) delivering nanoyarn.

TABLE 1 | The stress, strain and Young's modulus of various biomaterials (BAMG, conjugated scaffolds and nanoyarn).

	Stress (MPa)	Strain (%)	Young's modulus (Mpa)
BAMG	9.52 ± 1.32	627 ± 35	1.52 ± 0.13
Conjugate (parallel)	5.85 ± 0.37	415 ± 54	1.43 ± 0.21
Conjugate (vertical)	0.46 ± 0.13	836 ± 68	0.53 ± 0.09
Nanoyarn (parallel)	4.13 ± 0.29	2385 ± 216	0.16 ± 0.03
Nanoyarn (vertical)	1.87 ± 0.13	1423 ± 153	0.13 ± 0.02

the whole nanoyarn doesn't affect its physical composition, which is expected.

Released Medium From Nanoyarn Pretreated With 4 mg/ml ICG-001 Could Effectively Inhibit Fibroblast Proliferation and Suppress Protein Expression of Fibrosis Associated Proteins *in vitro*

To determine the optimal dosage of ICG-001 for effective inhibition of fibroblast proliferation and suppressed expression of fibrotic factors (e.g., Collagen I, Collagen III, etc.), we performed biocompatibility and anti-fibrosis assays. The released media from nanoyarn with 2 or 4 mg ICG-001 resulted in an obvious inhibition of cell growth in fibroblasts by morphological observation (**Figures 5A–F**). The cells maintained normal proliferation in less than 1 mg/ml released medium (**Figures 5A–D**). The cell proliferation inhibition effect was validated by MTS assay, which confirmed a significant decrease of proliferation with the 4 mg-ICG-001 medium at day 6 (**Figure 5G**). Significant decrease of Collagen I and III expression was also confirmed with the 4mg-ICG-001 medium (**Figures 5H,I**).

ICG-001 Delivering Nanoyarn Could Effectively Promote Urethral Reconstruction and Resume Fully Functional Urethra *in vivo*

After urethral defects were introduced into the dog models, urethroplasty was performed by implanting various biomaterials into the urethral defects with running suture (**Figure 2**). The nanoyarn with or without ICG-001 was very convenient to handle and suture, while the conjugated scaffold is pretty fragile. The recovery condition of urethral lumen was checked at 6 and 12 weeks post-surgery. Generally, the 4–0 absorbable Vicryl was still visible in the lumen after 6 weeks but disappeared at 12 weeks (**Figures 6A–F**). In the urethras repaired with conjugated nano scaffold, obvious fistula at the segment of urethroplasty was revealed (**Figures 6A,G**). A soft needle could be seen in the inner lumen of urethra when it was inserted from the outside of the fistula at the penile (**Figure 6A**). After 12 weeks, the fistulas remained in the urethras (**Figure 6D**) and was also detectable in the urethrography examination (**Figure 6J**). In the urethras repaired with nanoyarn, majority of urethras were kept unobstructed (**Figures 6B,H**), although urethral strictures were observed at 12 weeks post-surgery (**Figure 6K**), as the lumen became very narrow, and the urothelium looked pale, indicating fibrosis associated scar formation (**Figure 6E**). In the urethras repaired by ICG-001 delivering nanoyarn, unobstructed urethras were revealed at 6 and 12 weeks post-surgery, with no sign of urethral stricture or scar formation (**Figures 6C,F,I,L**).

To further validate those findings, we performed sonourethrography to test the efficacy of the biomaterials for urethroplasty and evaluate the tissue and scar formation in the lumen. 6 and 12 weeks post-surgery, ultrasonic contrast agent was injected into the orifice of the urethra repaired with the conjugated scaffold, but the lumen could not be filled due to the existence of fistula (**Figures 7A,D,G,J**). In urethra repaired with nanoyarn, the lumen was unobstructed with fluent flow of ultrasonic contrast agent at 6 weeks post-surgery (**Figures 7B,E**), yet hypertrophy was observed in the lumen which obstructed the flow of contrast agent at 12 weeks post-surgery (**Figures 7H,K**), likely causing urethral stricture. In the urethras repaired by ICG-001 delivering nanoyarn, the lumen kept unobstructed and wide at 6 weeks (**Figures 7C,F**) and 12 weeks post-surgery (**Figures 7I,L**). The overall successful rate of urethroplasty was summarized in **Table 2**.

To further evaluate the tissue reconstruction at cellular level, we performed immunohistological analysis. The urethras repaired by conjugate nano scaffolds were destroyed by serious fistula and inflammation associated with infection

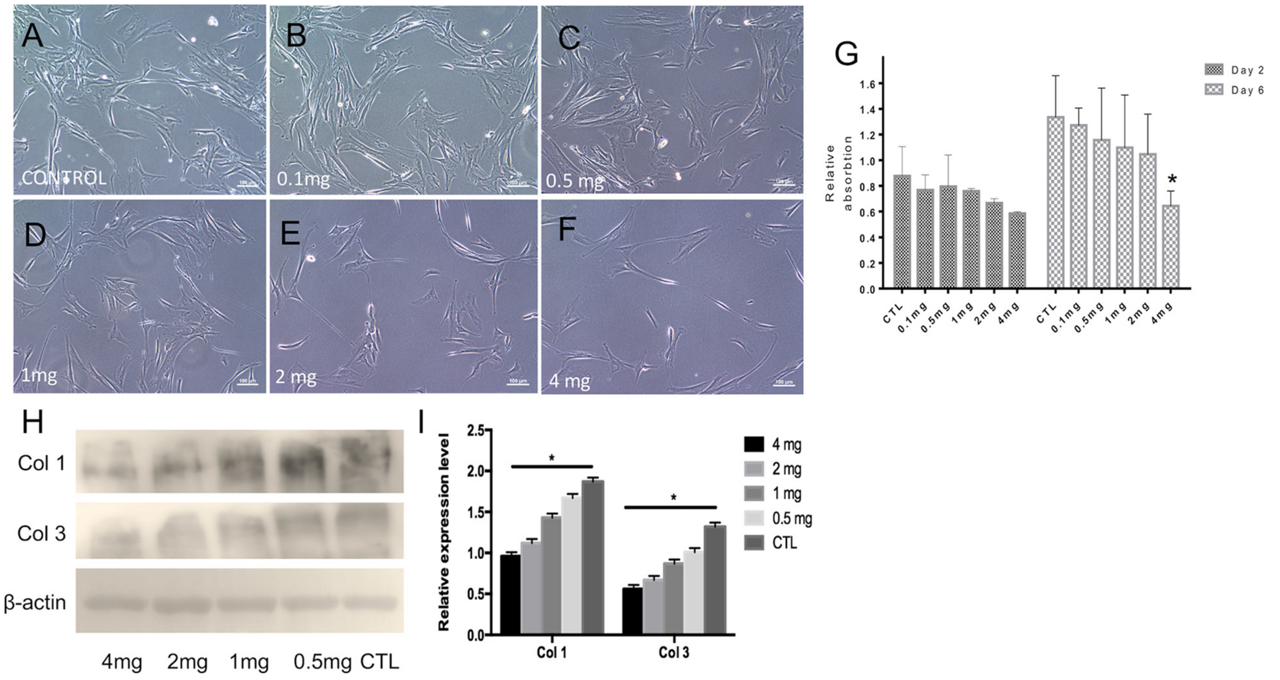

FIGURE 5 | Cell morphology, proliferation and collagen expression based on treatment with ICG-001 at various concentrations. **(A–F)** Fibroblasts incubated with released media from cells treated with different concentrations (0.1, 0.5, 1, 2, and 4 mg) of ICG-001 were observed under light microscope. Control (CTL) is not treated with ICG-001. **(G)** Cell proliferation was evaluated by MTT assay. **(H,I)** Western blotting and relative expression quantification of fibrosis related proteins [Collagen type I (Col 1), Collagen type III (Col 3)] were evaluated. *indicates significant difference ($p < 0.05$, comparing to control).

(**Figures 8A,E,I,M,Q**). In the urethras repaired by nanoyarn, the lumen surface formed discontinued epithelial layer (**Figures 8B,F**). The tissue showed a large amount of collagen (**Figure 8J**) and the CD31 expression was low (**Figure 8R**). In contrast, in the urethras repaired by ICG-001 delivering nanoyarn, the epithelial cells developed regular and continuous epithelium (**Figures 8C,G**), which is fairly similar to healthy control (**Figures 8D,H**). The tissue in the submucosa developed less collagen in the Masson image (**Figure 8K**) and more vessels were formed (**Figure 8S**).

DISCUSSION

The muscular anatomy of lower urinary tract, including the surrounding organs, were compared between human and male dogs, and histological analysis confirmed the anatomical resemblance between the two, especially in musculus detrusor vesicae, membranous urethra, prostate, etc. (Stolzenburg et al., 2002). Both male human and canine lower urinary tracts share similar components (urethra, urinary bladder and prostate), although the canines don't have seminal vesicles or Cowper's glands. Anatomically, the course of the second dorsal longitudinal urethral muscle system is similar in humans and dogs (Stolzenburg et al., 2002). However, the extension of the ventral longitudinal musculature is restricted to the region caudal of the prostate and it is more strongly developed in dog (Stolzenburg et al., 2002). The similarities and differences are taken into careful consideration during the design of this study. In preparation of the *in vivo* experiments, we have observed the histology of human urethra, which is similar to the canine urethra. The urethral lumen was surrounded by epithelium ECM, vessels and some muscles in the outer layer (data not shown). The thickness is also similar, which is around 1 mm. The observation is consistent with the literature, and it supports that dog model is feasible to test the nano materials for urethral reconstruction and clinical application.

In contrast to traditional electrospinning with simple receiving platform, dynamic liquid system was used to fabricate electrospun scaffold with larger pore size. Core-shell coaxial electrospinning system is popular for producing drug delivered scaffold. In present study, we combined the dynamic liquid system and core-shell electrospinning system together, and discovered that it could be utilized to fabricate a novel electrospun nanoyarn delivering certain kinds of bioactive agents with more stable release. ICG-001 is a Wnt signaling pathway inhibitor, which was reported as an adequate choice for antifibrosis. Thus, to facilitate a biological repair of urethra with less fibrosis and better vascularization and epithelial recovery, ICG-001 was delivered by the nanoyarn. The cells could expand well on the nanoyarn with an aligned growth style, which is necessary to mimic the native collagen fiber of biology.

Compared with BAMG and conjugated scaffold, the nanoyarn is a more elastic material with high strain rate. ICG-001 was delivered by the nano fiber, and the conditioned medium released from ICG-001-nanoyarn showed the effect of inhibition

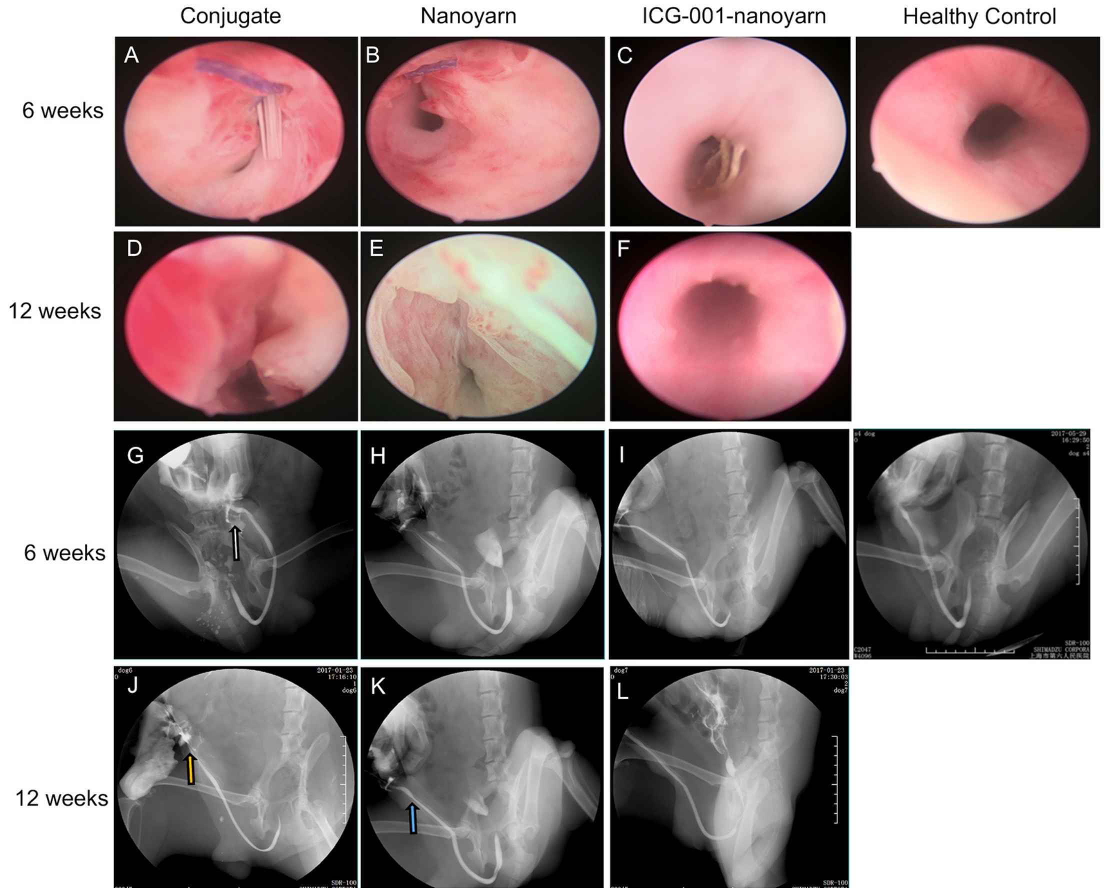

FIGURE 6 | Urethroscopy and urethrography examinations for urethras. Urethras repaired with conjugated nanofibrous scaffold **(A,D,G,J)**, nanoyarn **(B,E,H,K)** and ICG-001-delivering nanoyarn **(C,F,I,L)** at 6- and 12-week post-surgery. White and yellow arrow indicate the location of the fistulas. Blue arrow indicates the location of the urethral stricture.

of fibroblasts proliferation and suppression of fibrosis. After the urethral repair using various materials, urethroscopy, urethrographyh and ultrasound showed the best outcome derived from ICG-001 delivering nanoyarn with less leakage and urethral stricture rate. The histology demonstrated that the ICG-001 delivering nanoyarn is not only beneficial for the regeneration of epithelium and vessels, but also for the recovering of normal ECM of urethral by preventing abnormal deposition.

Ideal biomaterial should mimic natural ECM to allow cell adhesion, proliferation and differentiation in biological and architectural features, so as to facilitate tissue formation *in vivo* (Wu et al., 2014). Electrospinning is an efficient and frequently used technique to fabricate scaffolds for regenerative medicine (Barnes et al., 2007). However, due to its nature of layer-by-layer deposition of the nanofibers, traditional electrospun fibers have relatively small pore size which might inhibit cell filtration and hinder regenerative tissue formation (Sill and von Recum, 2008). Thus, how to generate nano scaffolds with 3D microstructures with ideal pore size remains a challenge and a unanswered question in tissue engineering field (Wu et al., 2014; Khorshidi et al., 2016). The previous attempts to solve this problem involved usage of salt leaching, ice crystal formation, sacrificial nanofibers and increasing the fiber diameter etc., which often affect the mechanical property and inhibit the cell growth of fibroblasts due to increased toxicity (Baker et al., 2009). In this study, we improved the traditional non-woven nano fibrous scaffolds and conjugated nano scaffolds, and utilized a novel electrospinning, dynamic liquid system to fabricate the nanoyarn, which has large pore size and 3D microstructures biomaterial through the natural water flow vortex without using any poisonous chemicals. In addition, collagens and P(LLA-CL) were combined to obtain good biocompatibility and mechanical strength. The mechanical property of nanoyarn allowed convenient usage in urethroplasty, and that could be adjusted by shifting the thickness and the density of deposited yarns to use in different types of soft tissues.

How to decrease the drug toxicity and increase drug delivery efficiency is another challenge. Compared with blending drug with the polymer materials directly, the core-shell co-axial electrospinning could decrease the burst release and protect the drug activity in the process of fabrication (Liao et al., 2009; Qian et al., 2014). *In vitro* experiments confirmed that nanoyarn could prevent the burst release in fibrous nano scaffolds, and improve

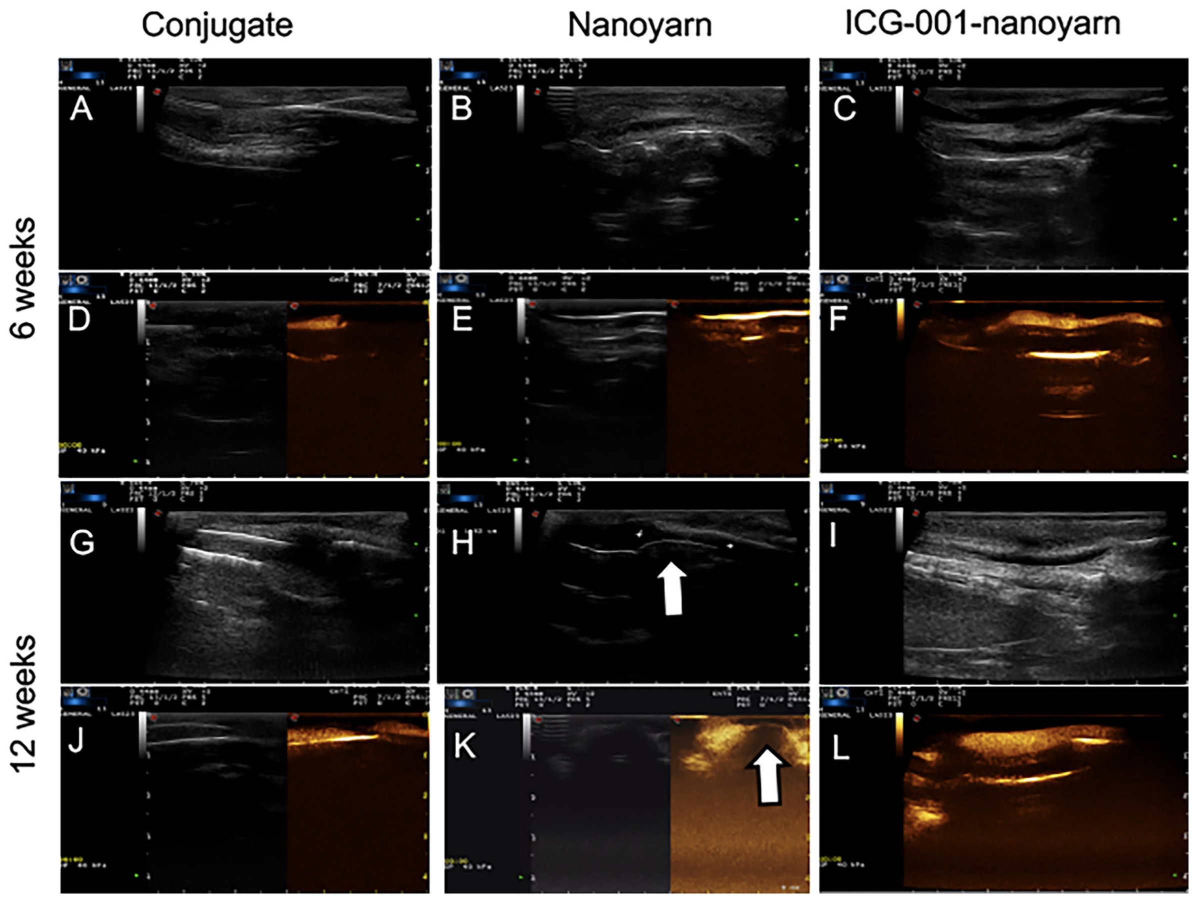

FIGURE 7 | Sonourethrography and ultrasonic contrast examinations for the urethras repaired with conjugated nanofibrous scaffold, nanoyarn and ICG-001-delivering nanoyarn. **(A–C,G–I)** Sonourethrography examination results. **(D–F,J–L)** Ultrasonic contrast examination results. The white arrows indicated the location of scar formation in the urethral lumen.

TABLE 2 | The successful rate of urethroplasty with various biomaterials.

	Conjugated scaffold (*n* = 4)			**Nanoyarn (*n* = 6)**			**ICG-nanoyarn (*n* = 6)**		
	Leakage	**Stricture**	**Success**	**Leakage**	**Stricture**	**Success**	**Leakage**	**Stricture**	**Success**
6 weeks	4	4	0	1	0	5	1	0	5
12 weeks	4	4	0	1	2	3	1	0	5
Success rate		0%			50%			83%	

the steady release of ICG-001 in conjugated nano scaffolds (Guo et al., 2016).

TEM of the nanoyarn with ICG-001 was performed, and the data were published in our previous *in vitro* study (Guo et al., 2016), while the present manuscript was more focused on the *in vivo* function of nanoyarn for the urethra reconstruction using dog model. The fibroblasts seeded on the ICG-001 delivering nanoyarn and conjugated nanofibrous scaffold could proliferate well (**Figure 3**; Guo et al., 2016). In the cell proliferation analysis, we found that the inhibition of fibroblast proliferation and block of collagen deposition showed a dose-dependent pattern. However, the concentration of ICG-001 is not the larger the better. The fibroblasts showed good tolerance to 2mg/ml (and less) ICG-001 in nanoyarn (**Figure 5**), which was used as the optimized dosage for *in vivo* experiment.

After the urethroplasty with three types of biomaterials (conjugated nano scaffold, control nanoyarn and drug-delivering nanoyarn) in dog models, we evaluated the successful rate based on urethral leakage and recurrent stricture. In the urethra repaired with conjugated scaffold, all the animals had leakage and stricture, probably due to the small pore size and low porosity, and unfavorable mechanical features (**Table 2** and **Figures 6A,D,G,J**, **7A,D,G,J**). The regenerated tissue was thin and fragile, and fistula and necrosis occurred. In the urethra repaired by the control nanoyarn, we observed a fair efficacy at six-week (**Table 2** and **Figures 6B,H**, **7B,E**). However, at

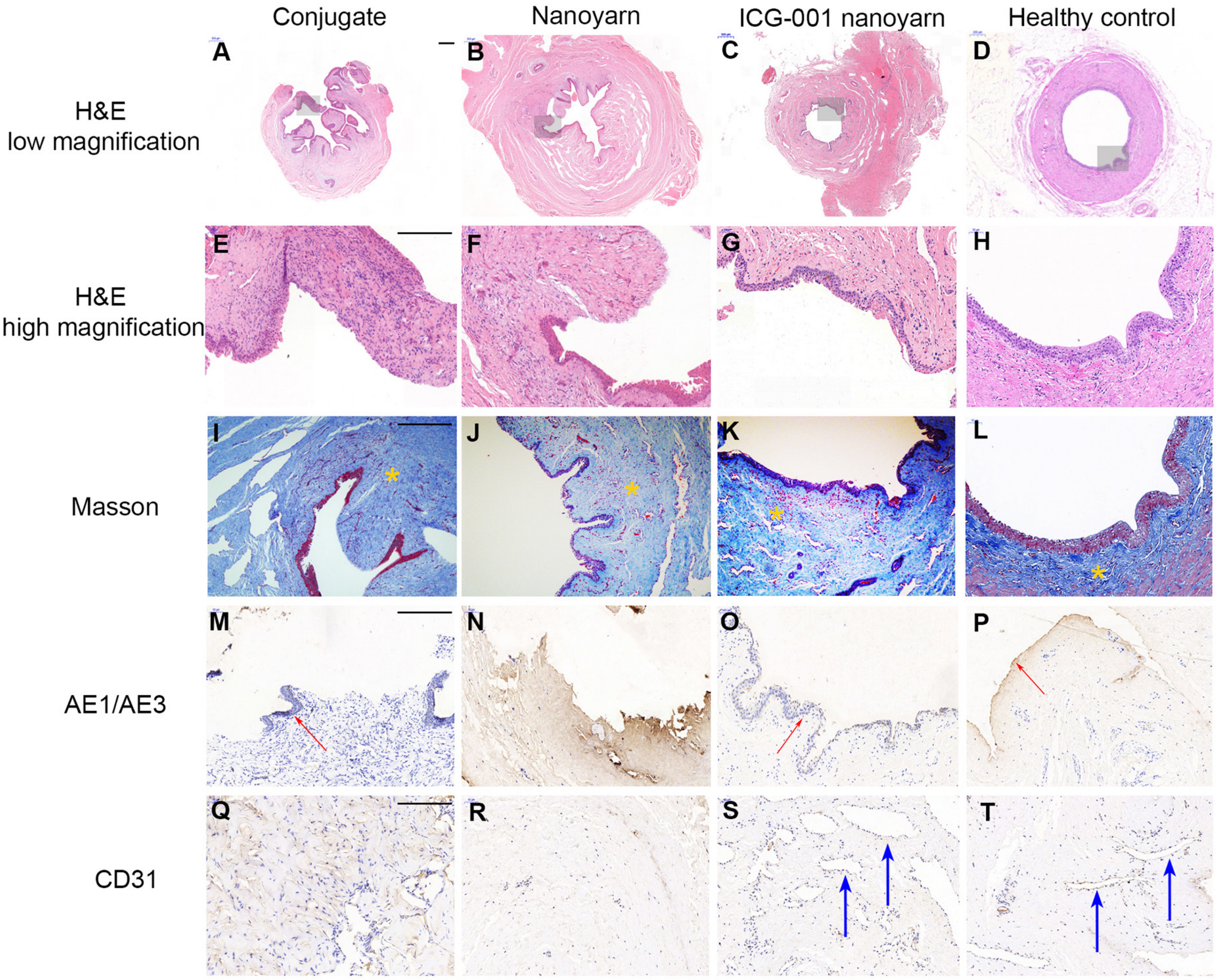

FIGURE 8 | Histological examination of urethras repaired with conjugated nanofibrous scaffold, nanoyarn and ICG-001-delivering nanoyarn. Urethras repaired by various nano scaffolds (12 weeks post urethroplasty) were analyzed based on H&E **(A–H)**, Mansson **(I–L)**, AE1/AE3 **(M–P)** and CD31 **(Q–T)** staining. Yellow asterisks indicate ECM in **(I–L)**. Note the deposited ECM in **(I,J)**, and the well-aligned ECM in **(K,L)**. Red arrows indicate the epithelium in **(M,O,P)**. Blue arrows indicate vessels in **(S,T)**. Scale bar is 200 μm.

12-week, the scar in the urethra became serious and led to urethral stricture in two dogs (**Figures 6E,K**, **7H,K**). In the urethra repaired by drug-delivering nanoyarn, we observed the highest overall success rate at 6 and 12 weeks post-surgery. With degradation of the biomaterials and efficient growth of local native cells, little biomaterial could be observed by urethroscopy at six weeks (**Figure 6C**). This is likely a result of gradual release of ICG-001 from nanoyarn, which suppressed the fibrosis of local cells near the urethral defect during the healing process. The recurrent stricture was completely suppressed in the urethra repaired by drug-delivering nanoyarn and was maintained at 12-week (**Figures 6F,L**, **7I,L**). Urethral leakage was controlled at very low rate for 12 weeks (**Table 2**). Overall, the drug-delivering nanoyarn showed the most effective clinical advantage in treating the urethral defects and could serve as a promising method to cure human patients who suffer from urethral complications.

For the histology of the urethra repaired with scaffolds (**Figure 8**), three kinds of scaffolds showed various outcomes. H&E stainning showed a gross condition of the repaired position. Majority of urethra repaired with conjugated scaffold possessed a fistula, and the local tissue is often with inflamation. The nanoyarn without ICG-001 results in a repair with fibrosis, and the epithelial layer could not get a complete regeneration. There was little or trace expression of AE1/AE3. The CD 31 stainning for vessels also showed a low expression in conjugated scaffold repaired urethra and nanoyarn without ICG-001. The CD 31 revealed large lumens of vessels in the urethra repaired with ICG-001 nanoyarn, indicating the tissue formation with more abundant blood supply. The masson stainning is responsible to show the alignment of ECM. In normal urethra and well repaired urethra, the ECM possesses a direction, but there is no direction in fibrosis or scar. The ICG-001 nanoyarn could facilitate a urethral regeneration without fibrosis.

CONCLUSION

In this study, we fabricated a dynamic liquid nanoyarn, which mimiced the native tissue matrix morphologically and structurally, and sufficiently allow cell proliferation and tissue regeneration. The urethroplasty in dog model using optimized ICG-001 delivering nanoyarn resulted in fully functional urethra after tissue reconstruction, confirming the efficacy of drug-delivering nanoyarn in treatments of urethral defect *in vivo*. It could potentially serve as an effective clinical application to cure urethral defects in human patients.

DATA AVAILABILITY STATEMENT

All datasets generated for this study are included in the article/**Supplementary Material.**

ETHICS STATEMENT

The animal study was reviewed and approved by the Animal Ethics Committee of Shanghai Sixth People's Hospital, Shanghai, China.

AUTHOR CONTRIBUTIONS

KZ and XF: experimental design. KZ, JZ, RY, and YW: experiments. KZ, XF, JZ, RY, YW, and WZ: data analysis. KZ, XF, JZ, XM, and QF: reagents/materials/analysis tools contribution. KZ, XF, XM, and QF: manuscript writing.

FUNDING

This work was supported by the National Natural Science Fund of China (Grant No. 81700590), Science and Technology Commission of Shanghai (Grant No. 17410742800), Shanghai Jiao Tong University Biomedical Engineering Cross Research Foundation (Grant No. YG2017QN15), and Shanghai "Rising Stars of Medical Talent" Youth Development Program.

ACKNOWLEDGMENTS

We appreciate the technical assistance from the Biomaterials and Tissue Engineering Laboratory, College of Chemistry & Chemical Engineering and Biotechnology at Donghua University for the fabrication of nano scaffolds. We also appreciate the technical assistance and advice from colleagues at Wake Forest Institute for Regenerative Medicine (WFIRM).

SUPPLEMENTARY MATERIAL

The Supplementary Material for this article can be found online at: https://www.frontiersin.org/articles/10.3389/fbioe.2020.00774/full#supplementary-material

FIGURE S1 | The cumulative release of the ICG-001 (concentration vs. time) delivered in different scaffolds in 8 weeks *in vitro*. Dynamic liquid electrospinning scaffold is the nanoyarn.

REFERENCES

Atala, A., Danilevskiy, M., Lyundup, A., Glybochko, P., Butnaru, D., Vinarov, A., et al. (2017). The potential role of tissue-engineered urethral substitution: clinical and preclinical studies. *J. Tissue Eng. Regener. Med.* 11, 3–19. doi: 10.1002/term.2112

Baker, B. M., Handorf, A. M., Ionescu, L. C., Li, W.-J., and Mauck, R. L. (2009). New directions in nanofibrous scaffolds for soft tissue engineering and regeneration. *Expert. Rev. Med. Dev.* 6, 515–532. doi: 10.1586/erd.09.39

Barnes, C. P., Sell, S. A., Boland, E. D., Simpson, D. G., and Bowlin, G. L. (2007). Nanofiber technology: designing the next generation of tissue engineering scaffolds. *Adv. Drug Deliv. Rev.* 59, 1413–1433. doi: 10.1016/j.addr.2007.04.022

Guo, X., Zhang, K., El-Aassar, M., Wang, N., El-Hamshary, H., El-Newehy, M., et al. (2016). The comparison of the Wnt signaling pathway inhibitor delivered electrospun nanoyarn fabricated with two methods for the application of urethroplasty. *Front. Mater. Sci.* 10:353. doi: 10.1007/s11706-016-0359-353

Kajbafzadeh, A.-M., Abbasioun, R., Sabetkish, S., Sabetkish, N., Rahmani, P., Tavakkolitabassi, K., et al. (2017). Future prospects for human tissue engineered urethra transplantation: decellularization and recellularization-based urethra regeneration. *Ann. Biomed. Eng.* 45, 1795–1806. doi: 10.1007/s10439-017-1857-x

Khorshidi, S., Solouk, A., Mirzadeh, H., Mazinani, S., Lagaron, J. M., Sharifi, S., et al. (2016). A review of key challenges of electrospun scaffolds for tissue-engineering applications. *J. Tissue Eng. Regener. Med.* 10, 715–738. doi: 10.1002/term.1978

Li, C., Xu, Y.-M., Liu, Z.-S., and Li, H.-B. (2013). Urethral reconstruction with tissue engineering and RNA interference techniques in rabbits. *Urology* 81, 1075–1080. doi: 10.1016/j.urology.2013.01.041

Liao, I.-C., Chen, S., Liu, J. B., and Leong, K. W. (2009). Sustained viral gene delivery through core-shell fibers. *J. Control Rel.* 139, 48–55. doi: 10.1016/j.jconrel.2009.06.007

Qian, W., Yu, D.-G., Li, Y., Liao, Y.-Z., Wang, X., and Wang, L. (2014). Dual drug release electrospun core-shell nanofibers with tunable dose in the second phase. *Int. J. Mol. Sci.* 15, 774–786. doi: 10.3390/ijms15010774

Ramsay, S., Ringuette-Goulet, C., Langlois, A., and Bolduc, S. (2016). Clinical challenges in tissue-engineered urethral reconstruction. *Transl. Androl. Urol.* 5, 267–270. doi: 10.21037/tau.2016.01.11

Raya-Rivera, A., Esquiliano, D. R., Yoo, J. J., Lopez-Bayghen, E., Soker, S., and Atala, A. (2011). Tissue-engineered autologous urethras for patients who need reconstruction: an observational study. *Lancet* 377, 1175–1182. doi: 10.1016/S0140-6736(10)62354-62359

Sangkum, P., Gokce, A., Tan, R. B. W., Bouljihad, M., Kim, H., Mandava, S. H., et al. (2015). Transforming growth factor-β1 induced urethral fibrosis in a rat model. *J. Urol.* 194, 820–827. doi: 10.1016/j.juro.2015.02.014

Sill, T. J., and von Recum, H. A. (2008). Electrospinning: applications in drug delivery and tissue engineering. *Biomaterials* 29, 1989–2006. doi: 10.1016/j.biomaterials.2008.01.011

Stolzenburg, J. U., Schwalenberg, T., and Do, M. (2002). Is the male dog comparable to human? A histological study of the muscle systems of the lower urinary tract. *Anat. Histol. Embryol.* 31, 198–205. doi: 10.1046/j.1439-0264.2002.00395.x

Versteegden, L. R. M., de Jonge, P. K. J. D., IntHout, J., van Kuppevelt, T. H., Oosterwijk, E., Feitz, W. F. J., et al. (2017). Tissue engineering of the urethra: a systematic review and meta-analysis of preclinical and clinical studies. *Eur. Urol.* 72, 594–606. doi: 10.1016/j.eururo.2017.03.026

Wu, J., Huang, C., Liu, W., Yin, A., Chen, W., He, C., et al. (2014). Cell infiltration and vascularization in porous nanoyarn scaffolds prepared by dynamic liquid electrospinning. *J. Biomed. Nanotechnol.* 10, 603–614. doi: 10.1166/jbn.2014.1733

Xie, M., Song, L., Wang, J., Fan, S., Zhang, Y., and Xu, Y. (2013). Evaluation of stretched electrospun silk fibroin matrices seeded with urothelial cells for urethra reconstruction. *J. Surg. Res.* 184, 774–781. doi: 10.1016/j.jss.2013.04.016

Xie, M., Xu, Y., Song, L., Wang, J., Lv, X., and Zhang, Y. (2014). Tissue-engineered buccal mucosa using silk fibroin matrices for urethral reconstruction in a canine model. *J. Surg. Res.* 188, 1–7. doi: 10.1016/j.jss.2013.11.1102

Zhang, K., Guo, X., Li, Y., Fu, Q., Mo, X., Nelson, K., et al. (2016). Electrospun nanoyarn seeded with myoblasts induced from placental stem cells for the application of stress urinary incontinence sling: an in vitro study. *Coll. Surf. B Biointerf.* 144, 21–32. doi: 10.1016/j.colsurfb.2016.03.083

Zhou, S., Yang, R., Zou, Q., Zhang, K., Yin, T., Zhao, W., et al. (2017). Fabrication of tissue-engineered bionic urethra using cell sheet technology and labeling by ultrasmall superparamagnetic iron oxide for full-thickness urethral reconstruction. *Theranostics* 7, 2509–2523. doi: 10.7150/thno.18833

Conflict of Interest: The authors declare that the research was conducted in the absence of any commercial or financial relationships that could be construed as a potential conflict of interest.

frontiers
in Bioengineering and Biotechnology

ORIGINAL RESEARCH
published: 30 July 2020
doi: 10.3389/fbioe.2020.00874

Brain Derived Neurotrophic Factor and Glial Cell Line-Derived Neurotrophic Factor-Transfected Bone Mesenchymal Stem Cells for the Repair of Periphery Nerve Injury

Qiang Zhang[1,2†], Ping Wu[1†], Feixiang Chen[1], Yanan Zhao[1], Yinping Li[1], Xiaohua He[1], Céline Huselstein[3], Qifa Ye[4,5], Zan Tong[1]* and Yun Chen[1,5]*

[1] Department of Biomedical Engineering and Hubei Province Key Laboratory of Allergy and Immune Related Diseases, School of Basic Medical Sciences, Wuhan University, Wuhan, China, [2] Hangzhou Singclean Medical Products Co., Ltd., Hangzhou, China, [3] CNRS UMR 7561 and FR CNRS-INSERM 32.09, Nancy University, Vandæuvre-lès-Nancy, France, [4] Zhongnan Hospital of Wuhan University, Institute of Hepatobiliary Diseases of Wuhan University, Transplant Center of Wuhan University, Wuhan, China, [5] Hubei Engineering Center of Natural Polymers-Based Medical Materials, Wuhan University, Wuhan, China

Edited by:
Rui Guo,
Jinan University, China

Reviewed by:
Guicai Li,
Nantong University, China
Zuyong Wang,
Hunan University, China

****Correspondence:***
Zan Tong
ztong@whu.edu.cn
Yun Chen
yunchen@whu.edu.cn

† These authors have contributed equally to this work

Specialty section:
This article was submitted to Biomaterials, a section of the journal Frontiers in Bioengineering and Biotechnology

Received: *18 May 2020*
Accepted: *08 July 2020*
Published: *30 July 2020*

Citation:
Zhang Q, Wu P, Chen F, Zhao Y, Li Y, He X, Huselstein C, Ye Q, Tong Z and Chen Y (2020) Brain Derived Neurotrophic Factor and Glial Cell Line-Derived Neurotrophic Factor-Transfected Bone Mesenchymal Stem Cells for the Repair of Periphery Nerve Injury. Front. Bioeng. Biotechnol. 8:874. doi: 10.3389/fbioe.2020.00874

Peripheral nerve injury is a common clinical neurological disease. In our previous study, highly oriented poly (L-lactic acid) (PLLA)/soy protein isolate (SPI) nanofiber nerve conduits were constructed and exhibited a certain repair capacity for peripheral nerve injury. In order to further improve their nerve repairing efficiency, the bone mesenchymal stem cells (BMSCs) overexpressing brain derived neurotrophic factor (BDNF) and glial cell line-derived neurotrophic factor (GDNF) were introduced into the conduits as seed cells and then were used to repair the 10-mm sciatic nerve defects in rats. The nerve repair efficiency of the functional nerve conduits was evaluated by gait experiment, electrophysiological test, and a series of assays such as hemotoxylin-eosin (HE) staining, immunofluorescence staining, toluidine blue (TB) staining, transmission electron microscopy (TEM) observation of regenerated nerve and Masson's trichrome staining of gastrocnemius muscle. The results showed that the conduits containing BMSCs overexpressing BDNF and GDNF double-factors group had better nerve repairing efficiency than blank BMSCs and single BDNF or GDNF factor groups, and superior to autografts group in some aspects. These data demonstrated that BDNF and GDNF produced by BMSCs could synergistically promote peripheral nerve repair. This study shed a new light on the conduits and stem cells-based peripheral nerve repair.

Keywords: poly (L-lactic acid), soy protein isolate, bone marrow mesenchymal stem cells, brain derived neurotrophic factor, glial cell line-derived neurotrophic factor

INTRODUCTION

Peripheral nerve injury (PNI) is a critical issue in the field of regenerative medicine (Wang et al., 2018; Li et al., 2020). Accelerating axonal regeneration and improving functional recovery after PNI is a clinical dilemma and a basic medical challenge (Li et al., 2019; Sayad-Fathi et al., 2019). In clinical practice, end-to-end suturing of proximal and distal stumps is the ideal method to repair short nerve defect (Guo et al., 2019; Wu et al., 2019). The gold standard of long nerve regeneration is autograft (Yi et al., 2018; Vijayavenkataraman, 2020). However, autograft requires sacrifice of a functional nerve, which may result in donor nerve sensory loss and neuropathic pain (Guo et al., 2018; Wu et al., 2020). Hence, the use of nerve guide conduits could avoid these problems (Chrzaszcz et al., 2018; Chen et al., 2019; Vijayavenkataraman et al., 2019). However, the reported nerve conduits could not fully meet the demands for quick and effective nerve repair (Carvalho et al., 2019; Riccio et al., 2019).

The classical strategy of tissue engineering is to construct composite nerve conduits with biodegradable polymer materials combined with seed cells or neurotrophic factors (Zhang et al., 2019). The addition of neurotrophic factors in nerve conduit could significantly improve the efficiency of nerve regeneration (Gao et al., 2016). Directly introducing exogenous neurotrophic factor into nerve guide conduit was reported (Labroo et al., 2018; Lin et al., 2019). However, these exogenous neurotrophic factors in the nerve conduits are easy to be lost or become inactive (Hobson et al., 2000; Moskow et al., 2019). What's worse, excessive exogenous neurotrophic factors may cause trapping of regenerating axons and formation of nerve coils (Eggers et al., 2013).

Therefore, seed cells producing neurotrophic factors were widely used to overcome these problems (Hsueh et al., 2014; Zhu et al., 2014; Hsu et al., 2017). Bone marrow mesenchymal stem cells (BMSCs) are most promising seed cells for nerve repair and regeneration (Gao et al., 2016; Xue et al., 2017). BMSCs had lots of advantages including wide range of sources, easy to isolate and culture, and immunological naivety (Cho et al., 2018; Cui et al., 2018). BMSCs could suppress neuronal cell death and promote nerve regeneration in conduit guided sciatic nerve repair in rats (Hsu et al., 2013). BMSCs producing BDNF were reported to promote motor functional recovery in spinal cord transfected rat (Xiong et al., 2016).

However, single neurotrophic factor is often not very effective (Li et al., 2006; Cangellaris and Gillette, 2018). Various endogenous neurotrophic factors for nerve regeneration were reported (Tajdaran et al., 2018; Liu et al., 2020). Among them, BDNF can promote the myelinization of neogenesis nerve (Lopes et al., 2017), GDNF can protect motor neurons from injury caused by nerve transection, and improve the re-innervation function of nerves (Eggers et al., 2008). Many studies have confirmed the role of BDNF and GDNF in PNI, but their synergy at a ratio of 1:1 has not been studied *in vivo* (Zurn et al., 1996; Fu et al., 2011; Hoyng et al., 2014; Wang et al., 2016; Hsu et al., 2019).

Our previous work has shown that PLLA/SPI composite nanofiber conduits (HO-PSNCs) can promote nerve regeneration. The nerve conduits were modified with biochemical cues by SPI blending and topographical cues by highly oriented electrospinning. The two strategies combined together could improve the hydrophilicity and biodegradability of the biomaterials, and promote neural cell growth, spreading, extension, and neurite outgrowth *in vitro*, and support the nerve regeneration *in vivo* (Zhang et al., 2020). In order to further elevate the efficiency of peripheral nerve repair, we constructed BDNF transfected BMSCs and GDNF transfected BMSCs, and then the BMSCs were introduced into HO-PSNCs conduits to bridge sciatic nerve defects in rats. Two factors system were compared to single factor system, which provide evidence for the synergistically application of endogenous neurotrophic factors in nerve regeneration.

EXPERIMENTAL SECTION

Materials

PLLA with a molecular weight of 150 kDa was supplied by Shenzhen Polymtek Biomaterial Co., Ltd (Shenzhen, China). Soy protein isolate (SPI) with weight-average molecular weight (M_w) of 2.05×10^5 was purchased from DuPont Protein Technology (Luohe, China). Other chemicals were of analytical grade agents.

Preparation of the HO-PSNCs Scaffolds

The HO-PSNCs nerve conduits (Highly oriented PLLA/SPI nanofibrous conduits) were prepared as previous work (Zhang et al., 2020). In brief, 10 g PLLA was added to 90 g hexafluoropropanol. Two gram SPI powder was added to 98 g hexafluoroisopropanol. PLLA solution and SPI solution were mixed at weight ratio of 80:20. The PLLA/SPI composite solution was added into a 5 mL syringe with a needle for electrospinning. The prepared nanofiber conduits were stored in a dryer.

BMSCs Culture and Identification

The BMSCs were isolated from the adult Sprague Dawley rats (120∼150 g). After the rats were euthanized, the rat femurs were dissected out and the marrow cavities were exposed. The marrow cavities were washed with α-modified Eagle's medium (α-MEM, Gibco) to collect the BMSCs. After the 1000 rpm centrifugal precipitation, the cells were re-suspended with complete α-MEM [containing 10% fetal bovine serum (FBS) and 1% penicillin-streptomycin (Gibco)]. Then the cells were cultured in a T75 flask at 37°C with 5% CO_2. After 72 h, the medium was replaced with fresh complete α-MEM. The cells were confirmed as BMSCs by the flow cytometry of evaluating the expression of CD11 and CD45, while the CD29 and CD90 were the negative control. Optical images and SEM images were also taken to exam the BMSCs.

Lentivirus Construction

The Trizol reagent (Invitrogen, United States) was used for RNA extraction. The reverse transcription was then performed with the cDNA Reverse Transcription Kit (Bio-Rad, United States). Lentiviral vectors pCDH-CMV-MCS-EF1-copGFP-T2A-Puro-BDNF and pCDH-CMV-MCS-EF1-copGFP-T2A-Puro-GDNF vectors were constructed using PCR. The primer sequences were as follows: BDNF, 5′-GCG GGA TCC GCC ACC ATG GTG ACC ATC CTT TTC CTT AC-3′ and 5′-GCG GCG GCC GCC TAT CTT CCC CTT TTA ATG G-3′; GDNF, 5′-GCG GGA TCC GCC ATT ATG GGA TGT CGT GGC TG-3′ and 5′-GCG GCG GCC GCT CAG ATA CAT CCA CAC CGT TTA GC-3′. The lentiviral packaging vectors (pLP1, pLP2, pLP) were co-transfected along with pCDH-CMV-MCS-EF1-copGFP-T2A-Puro, pCDH-CMV-MCS-EF1-copGFP-T2A-Puro-BDNF, or pCDH-CMV-MCS-EF1-copGFP-T2A-Puro-GDNF into 293T cells using Lipofectamine 2000 (Invitrogen, United States). After 48 h of transfection, the lentiviruses were collected after filtering the supernatant of cell culture medium.

Western Blot Analysis

Lentivirus overexpressing BDNF and GDNF were transfected into BMSCs for 48 h, and the overexpression of BDNF and GDNF in BMSCs were identified by western blot. The BMSCs (P3) were harvested and washed with cold PBS, then incubated with primary antibodies: anti-BDNF antibody (A16299, Abclonal, China, 1:1000), anti-GDNF antibody (A14639, Abclonal, China, 1:1000) and anti-β-actin antibody (GB1101, Servicebio, China, 1:2000). HRP signals were detected by Image Studio Digits Ver 4.0. Density values were normalized to β-actin and results are representative of three independent experiments.

Cell Seeding

The conduits were cut into 12 mm, washed with PBS twice, and soaked in 75% alcohol for 72 h and then repeatedly washed three times with PBS. The alcohol-sterile conduits were seeded with BMSCs overexpressing GFP (BMSC-Vector group), BMSCs overexpressing BDNF (BMSC-BDNF group), BMSCs overexpressing GDNF (BMSC-GDNF group), and BMSCs overexpressing BDNF and GDNF [BMSC-(BDNF + GDNF) group], respectively. Cell density was 5×10^4/conduit (according to our preliminary experiment), 37°C and 5% CO_2 under the condition of cultivation for 24 h. The BMSC-(BDNF + GDNF) group is 1:1 combination of BMSC-BDNF and BMSC-GDNF groups. To make the BMSCs distributed evenly, we firstly inoculated 2.5×10^4 cells in the inner wall of the conduits on the one side. We flipped the conduits for 180 degrees after the BMSCs were attached to the conduits for 12 h, then the other 2.5×10^4 BMSCs were inoculated in the inner wall of the conduits on the other side.

Animals Surgery

All the animals experiment procedures were approved by the Animal Care and Use Committees of Wuhan University and carried out in accordance with the "Guidelines and Regulations for the use and care of Animals of the Review Board of Hubei Medical Laboratory Animal Center". Adult SD rats (180∼200 g) were used to exam the nerve regeneration performance *in vivo*. The skins of anesthetized rats were cut to expose the right sciatic nerve. Blunt dissection is used to separate the muscles surrounding the nerve tissue. The sciatic nerve was then was severed into proximal and distal segments with 10 mm defects at the center of the right posterior limb. As shown in **Table 1**, 60 rats were divided into six groups randomly: defects connected with 10 mm autologous nerve grafts (Autograft group), 12 mm HO-PSNCs conduits (Control group), 12 mm HO-PSNCs + BMSCs overexpressing GFP conduits (BMSC-vector group), 12 mm HO-PSNCs + BMSCs overexpressing BDNF conduits (BMSC-BDNF group), 12 mm HO-PSNCs + BMSCs overexpressing GDNF conduits (BMSC-GDNF group), 12 mm HO-PSNCs + BMSCs overexpressing BDNF + BMSCs overexpressing GDNF conduits [BMSC-(BDNF + GDNF) group]. The 8-0 nylon was used to suture the proximal and the distal stumps nerve with depth of 1 mm into the conduits. 6-0 nylon was used to re-suture the muscle and skin layers.

TABLE 1 | Group codes in animal studies.

Group	12 mm HO-PSNCs	BMSCs overexpressing GFP	BMSCs overexpressing BDNF	BMSCs overexpressing GDNF
Autograft	×	×	×	×
Control	√	×	×	×
BMSC-vector	√	√	×	×
BMSC-BDNF	√	×	√	×
BMSC-GDNF	√	×	×	√
BMSC-(BDNF + GDNF)	√	×	√	√

The "√" indicates that the actional element was included, and the "×" indicates that the actional element is not included.

General Observation

Three months after surgery, SD rats were placed in a clean table and observed the movement behavior in the free environment. The whole movement process and foot condition of the rats were recorded with camera. After observation, SD rats were put into a beaker to observe the recovery of the legs and feet of the surgical side when the rats were standing.

Walking Track Analysis

In order to assess the behavior of the rats at 3 months after surgery, walking track analysis was performed. In briefly, the rats were walking along with a wooden walking alley. The white papers were put on the floor of the alley. The red paint was applied to the rat's plantar surface prior before walking on the floor of the alley. As the rats walking along the track, their left and right posterior limb footprints on the track were recorded. The following information was obtained from the footprints: distance from the heel to the top of the third toe (print length; PL); distance between the first and the fifth toe (toe spread; TS) and distance from the second to the fourth toe (intermediary toe spread; IT). These measures were also collected from the non-operated rat posterior limb (information for these posterior limbs are marked as NPL, NTS, and NIT) and the operated, experimental posterior limb (information for these posterior limbs are marked as EPL, ETS, and EIT). In the control groups, information of the right posterior limb was compared with those from the left ones. To calculate the sciatic function index (SFI), the information was fed into the following equation (1) from previous studies:

$$\begin{aligned} \mathrm{SFI} = -38.3 \times (\mathrm{EPL}-\mathrm{NPL})/\mathrm{NPL} + 109.5 \times (\mathrm{ETS}-\mathrm{NTS}) \\ /\mathrm{NTS} + 13.3 \times (\mathrm{EIT}-\mathrm{NIT})/\mathrm{NIT} - 8.8 \end{aligned} \tag{1}$$

Interpolating identical values of PL, TS, and IT from the right and the left hind feet results in a value close to zero in normal rats. A value of −100 implies total impairment.

Electrophysiology Evaluation

Three months after surgery, electrophysiology experiment was performed under anesthesia. The surgical sites were re-opened to expose the sciatic nerve. The electromyography was evaluated by an electrophysiology system (RM6240, China). The 10 mV electrical stimuli were applied to the nerve trunk at the proximal ends of the graft. Compound muscle action potentials (CMAPs) were recorded on the gastrocnemius muscle. The ratios of CMAPs in each group were used to assess the sciatic nerve functional recovery.

HE Staining and Immunofluorescence Staining

Three months after surgery, the regenerated nerves were harvested and then fixed in 4% paraformaldehyde solution for 48 h. The fixed nerve samples were dehydrated, paraffin-embedded and sectioned into 6-μm thick. A part of sections was stained with HE dying solution, and then observed under a light microscope (TE2000-U, Nikon, Japan). Another part of sections was used for immunofluorescence staining. In brief, the sections were incubated with mouse anti-NF200 antibody (diluted 1:200) and goat anti S100 antibody (diluted 1:50). After thorough washing with PBS, the sections were incubated with fluorescent secondary antibodies (Alexa Fluor-488 or -555 conjugated goat anti-mouse IgG diluted 1:200). Finally, sections were stained by DAPI and observed under a fluorescence microscope (TE2000-U, Nikon, Japan). To quantify the percentages of positive NF200 and S100 staining, fifteen fields of five images were randomly captured at 400 × magnification. The Image-Pro Plus software was used to calculate the percentages of positive NF200 and S100 staining.

Myelination Analysis

Three months after surgery, the regenerated nerves were collected and fixed in 2.5% glutaraldehyde solution at 4°C for 48 h. The regenerated nerves were then immobilized in 1% osmium acid, dehydrated, embedded and then sliced into 1 μm thick semi-thin sections. Through the toluidine blue staining, the sections were observed by optical microscope. Three sections per sample were randomly chosen and six images per section were randomly taken at 20 × magnification. Then 50 nm ultra-thin sections were stained with lead citrate and uranyl acetate. The ultrastructure of regenerated nerve fibers was observed by transmission electron microscope (TEM, HT7700, Hitachi, Japan). Five images were randomly captured at 400 × magnification and all axons from five images were analyzed. Toluidine blue stained images and TEM images were measured by Image-Pro Plus software to analyze the diameter and density of myelinated nerve fibers, the area of the myelinated axons and myelin sheath thickness.

Assessment of Gastrocnemius Muscles

Three months after surgery, normal and operative gastrocnemius muscles of the rats were harvested completely, washed with PBS, drained with filter paper, weighed and photographed. According to the equation (2), the muscle weight recovery rate of gastrocnemius was calculated as follows:

$$\mathrm{Wr}\,(\%) = [\mathrm{Ws}/\mathrm{Wn}] \times 100 \tag{2}$$

Wr: Muscle weight recovery rate; Ws: muscle weight of gastrocnemius on the operative side; Wn: muscle weight of normal lateral gastrocnemius muscle.

The gastrocnemius tissue was then fixed in 4% paraformaldehyde for more than 24 h. After dehydration, paraffin embedding and sectioning, 6 μm thick paraffin sections were prepared. Then Masson staining was carried out. Three different fields of vision were collected for each section. Image-pro plus software was used to calculate muscle fiber area (a) and collagen fiber area (b). Then, the percentage of collagen fiber area was calculated according to the equation (3):

$$\mathrm{c}\,(\%) = [\mathrm{b}/(\mathrm{a} + \mathrm{b})] \times 100 \tag{3}$$

a, cross-sectional area of muscle fibers; b, collagen fiber area; c, percentage of collagen fibers.

Statistical Analysis

All quantitative data was expressed as mean ± SEM. One-way analysis of variance (ANOVA) followed by *post hoc* test was used for statistics analysis. The difference ($P < 0.05$) was considered to be statistically significant.

RESULTS

Identification and Morphology of BMSCs

The light microscope and scanning electron microscope images of BMSCs are shown in **Supplementary Figures S1A,B**, respectively. The BMSCs were closely clustered, with long fusiform or flat cells and small cell bodies, but the protrusions were whirlpool or radial. The surface markers CD11b, CD45, CD29, and CD90 of BMSCs were identified by flow cytometry, and the results are shown in **Supplementary Figures S1C–F**. Normally, BMSCs expressed CD29 and CD90 on the cell surface, but not CD11b and CD45 (Zhang et al., 2012). According to **Supplementary Figures S1C–F**, strong positive CD29 and CD90 signals could be detected in BMSCs, while only weak positive CD11b and CD45 signals could be detected in BMSCs. According to the analysis, the positive expression of CD29 was more than 99%, the positive expression of CD90 was more than 95%, while the positive rate of CD11b and CD45 was less than 1%, indicating that the purity of BMSCs was more than 95%.

Construction of BDNF and GDNF Transfected BMSCs

The fluorescence images of BMSCs and BMSCs transfected with blank vectors, BDNF, GDNF are shown in **Figure 1A**. The BMSCs exhibited green fluorescence in the BMSC-vector, BMSC-BDNF and BMSC-GDNF groups, which could demonstrate the presence of the GFP protein in the three groups. The overexpressing BDNF and GDNF protein were detected by western blot. As shown in **Figures 1B,C**, higher protein expression levels of BDNF were detected in the BMSC-BDNF group, revealing that BMSCs transfected with BDNF overexpressing lentivirus could effectively express BDNF proteins. In the **Figures 1B,D**, the

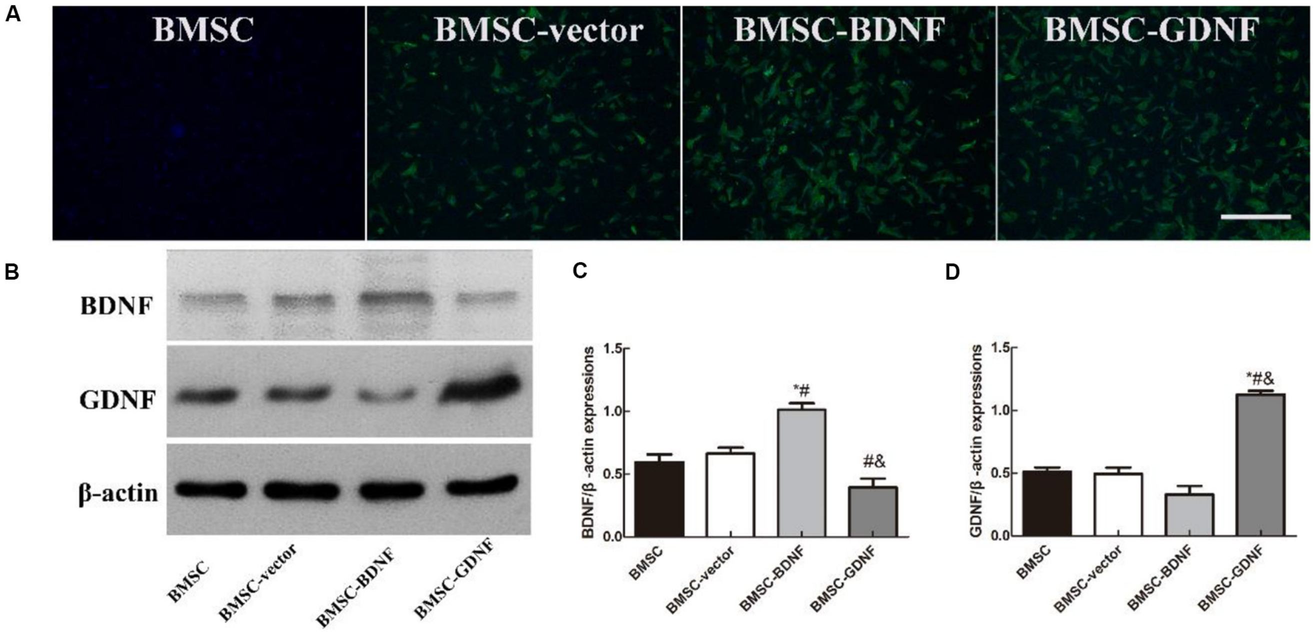

FIGURE 1 | Characterization of BMSC-BDNF and BMSC-GDNF. **(A)** Fluorescence images of BMSCs and BMSCs transfected with blank vectors, BDNF and GDNF. Scale bar = 20 μm. **(B)** The western blot analysis of BDNF and GDNF proteins. **(C)** The BDNF protein levels and **(D)** the GDNF protein levels in the BMSC, BMSC-vector, BMSC-BDNF and BMSC-GDNF groups. $^{*}P < 0.05$, compared with BMSC group; $^{\#}P < 0.05$, compared with BMSC-vector group; $^{\&}P < 0.05$, compared with BMSC-BDNF group.

GDNF protein in the BMSC-GDNF group was the highest among the four groups, revealing that BMSCs transfected with GDNF overexpressing lentivirus could effectively express GDNF proteins.

General Observation

Three months after surgery, the walking and standing behaviors of the rats were observed, and the images are shown in **Figure 2**. Compared with the normal posterior limbs of the rats, the surgical posterior limbs of the rats occasionally showed slight claudication during walking, indicating that the injured nerve recovered well (**Figure 2A**). Rats in all groups were able to stand in balance, indicating that the innervation function of the injured nerve on the legs and feet of rats recovered well (**Figure 2B**). Compared with the normal sides of the rat, the paws of the surgical side of the rats in each group were not fully expanded, indicating that the re-innervation ability of the regenerated nerve had not recovered to the normal levels. In Autograft and BMSC-(BDNF + GDNF) groups, the degrees of expansion of the paws on the surgical posterior limbs were greater than those in control, BMSC-vector, BMSC-BDNF and BMSC-GDNF groups, indicating that the abilities of the regenerated nerve in Autograft and BMSC-(BDNF + GDNF) groups to reinnervate the rat feet were stronger than those in control, BMSC-vector, BMSC-BDNF and BMSC-GDNF groups.

Neurologic Function Recovery

Motor functional recovery in all groups was determined at 3 months after surgery (**Figure 3**). The mean sciatic function index (SFI) values of Autograft, control, BMSC-vector, BMSC-BDNF, BMSC-GDNF and BMSC-(BDNF + GDNF) groups were −55.89, −57.59, −50.27, −52.15, −47.88, and −46.68, respectively. The rats in BMSC-(BDNF + GDNF) group had better functional recovery, showing a higher SFI value than that in Autograft, control, BMSC-vector and BMSC-BDNF groups, but not higher than that in BMSC-GDNF group. The mean SFI value of BMSC-GDNF group was higher than those of Autograft, control and BMSC-BDNF groups, while the mean SFI value of BMSC-GDNF group was similar with that of BMSC-vector group.

Neuroelectrophysiological Examination

Three months after surgery, the peak amplitude of CMAPs, conduction velocity and latency of CMAPs were recorded by the biological signal acquisition and analysis system (**Figure 4**). Representative CMAPs record of the surgical side of each group are shown in **Figure 4A**. CMAPs signals could be detected in all groups, but the waveforms of signal were different among groups, indicating that the conduction functions of the damaged nerves were restored with different levels. The mean peak amplitude of CMAPs in Autograft, control, BMSC-vector, BMSC-BDNF, BMSC-GDNF, and BMSC-(BDNF + GDNF) groups were 22.44, 10.86, 14.51, 15.86, 16.98, and 22.31 mV, respectively. The peak amplitude of CMAPs in control, BMSC-vector, BMSC-BDNF and BMSC-GDNF groups were significantly lower than that in Autograft and BMSC-(BDNF + GDNF) groups, while there was no significant difference between BMSC-(BDNF + GDNF) group and Autograft group (**Figure 4B**). The peak amplitude of CMAPs

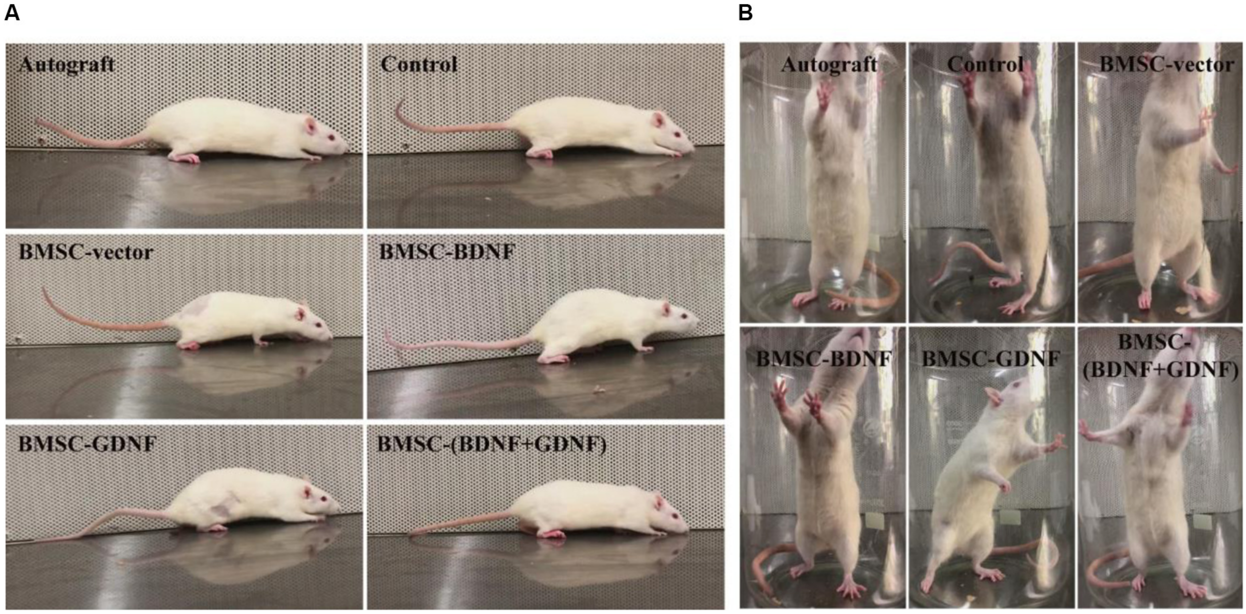

FIGURE 2 | General observation of the movement of rats at 3 months after surgery. Images of walking **(A)** and standing **(B)** of rats in each group.

in BMSC-BDNF and BMSC-GDNF groups were significantly higher than that in control and BMSC-vector groups, while the peak amplitude of CMAPs in BMSC-BDNF group was similar with that of BMSC-GDNF group. Compared with the peak amplitude of CMAPs in control, the peak amplitude of CMAPs in BMSC-vector was higher. These data indicated that the signal intensity of regenerative nerve in the BMSC-(BDNF + GDNF) group was closed to that of the Autograft group, while signal intensities in the BMSC-BDNF and BMSC-GDNF groups were higher than that of control and BMSC-vector groups.

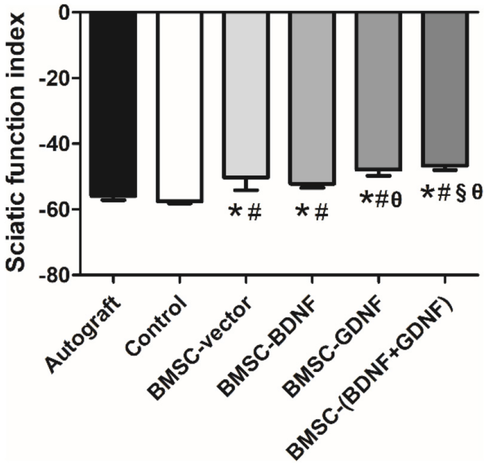

FIGURE 3 | Analysis of SFI values in each group. $^{*}P < 0.05$, compared with Autograft group; $^{\#}P < 0.05$, compared with control group; $^{\S}P < 0.05$, compared with BMSC-vector group; $^{\theta}P < 0.05$, compared with BMSC-BDNF group.

According to **Figures 4C,D**, the conduction velocity of CMAPs in BMSC-(BDNF+GDNF) and Autograft groups were significantly higher than that in the control, BMSC-vector, BMSC-BDNF and BMSC-GDNF groups. The latency of CMAPs in BMSC-(BDNF + GDNF) and Autograft groups was significantly lower than that in control, BMSC-vector, BMSC-BDNF and BMSC-GDNF groups. The conduction velocity of CMAPs in BMSC-BDNF and BMSC-GDNF groups were higher than that in control and BMSC-vector groups, while that in BMSC-vector group was higher than that in control group. The latency of CMAPs in BMSC-BDNF and BMSC-GDNF groups were lower than that in control and BMSC-vector groups, while in BMSC-vector group was lower than that in control group. These data indicated that the electrical signal transmission speed of the regenerative nerve in BMSC-(BDNF+GDNF) group was higher than that in the control, BMSC-vector, BMSC-BDNF and BMSC-GDNF groups, while closed to that in the Autograft group. In conclusion, nerves repaired with HO-PSNCs conduits loaded with BDNF and GDNF co-transfected BMSCs had better recovery of conduction function and could transmit electrical signals faster than BDNF or GDNF single-transfected BMSCs, and the ability was similar to that of the Autograft group.

HE Staining and Immunofluorescence Staining of Regenerated Nerves

Three months after surgery, the middle segments of the regenerated nerve were taken for HE staining, and the results are shown in **Figure 5A**. The regenerated nerve fibers in each group were arranged in order. These regenerated nerve fibers gathered into bundles, extending from the proximal end of the damaged nerve to the distal end. The regenerated nerve fibers in Autograft group were loose, while the regenerated nerve fibers in

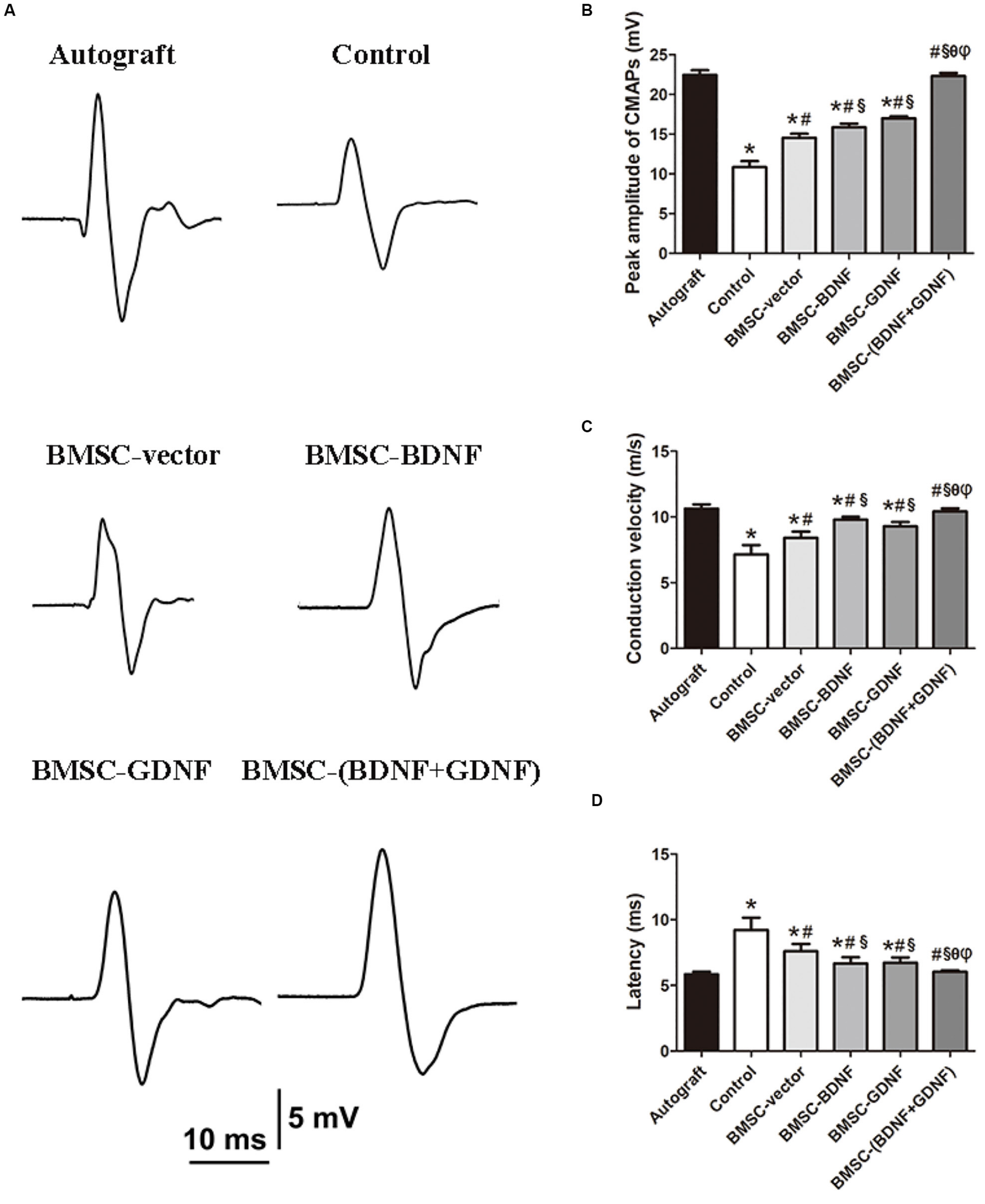

FIGURE 4 | The results of electrophysiological test. **(A)** Representative CMAPs recordings on the injured side for each group. The statistical results of peak amplitude of CMAPs **(B)**, conduction velocity **(C)**, and latency **(D)**. $^{*}P < 0.05$, compared with Autograft; $^{\#}P < 0.05$, compared with control group; $^{\$}P < 0.05$, compared with BMSC-vector group; $^{\theta}P < 0.05$, compared with BMSC-BDNF group; $^{\varphi}P < 0.05$, compared with BMSC-GDNF group.

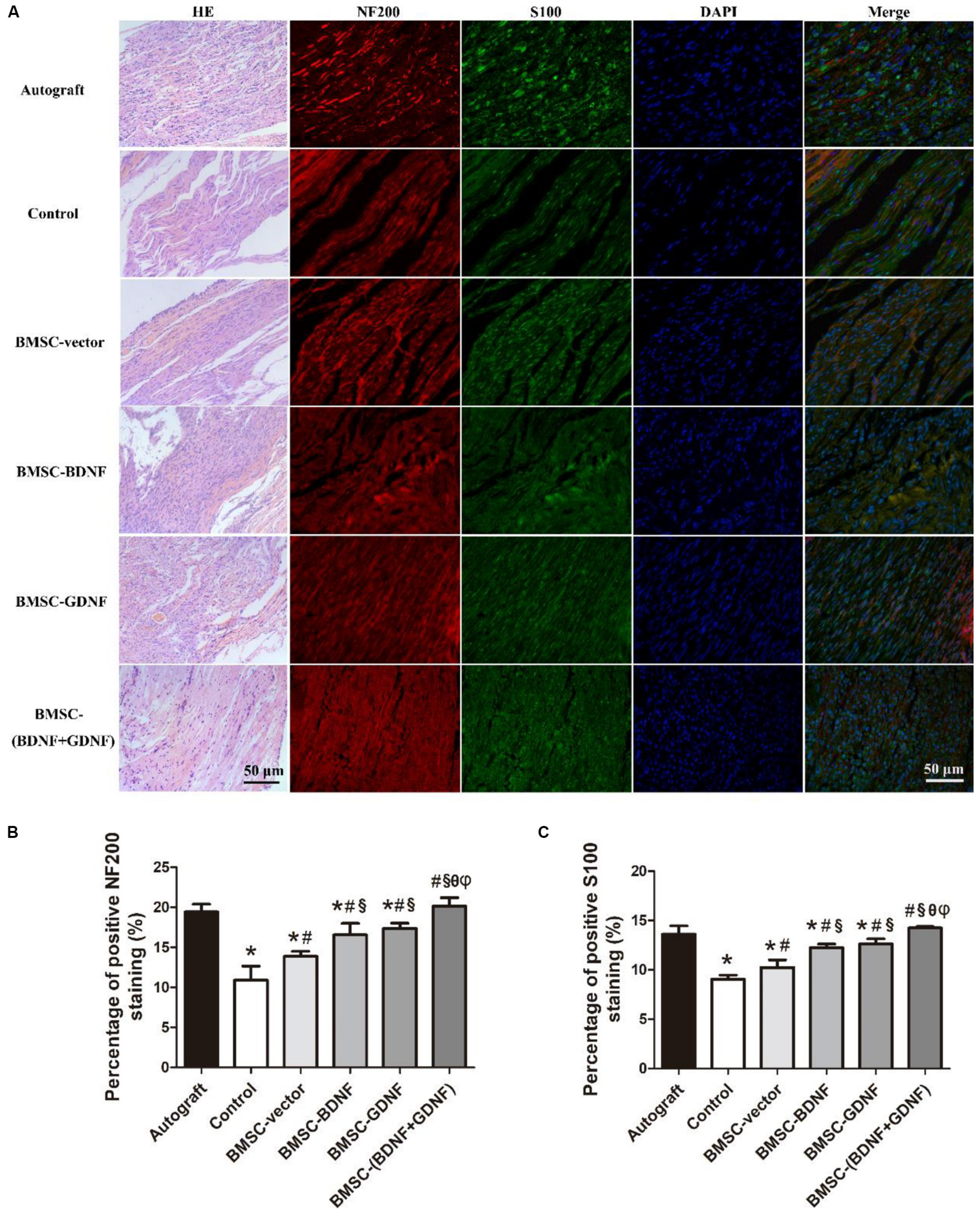

FIGURE 5 | HE-staining and immunofluorescence analysis of the regenerated nerves in each group at 3 months after surgery. **(A)** Images of HE-staining and immunofluorescence; **(B)** Percentage of positive NF200 staining and **(C)** percentage of positive S100 staining. $^{*}P < 0.05$, compared with Autograft; $^{\#}P < 0.05$, compared with control group; $^{\S}P < 0.05$, compared with BMSC-vector group; $^{\theta}P < 0.05$, compared with BMSC-BDNF group; $^{\varphi}P < 0.05$, compared with BMSC-GDNF group.

control, BMSC-vector, BMSC-BDNF, BMSC-GDNF, and BMSC-(BDNF + GDNF) groups were denser. The adhesion of the fiber bundles in control group was more dispersive than other conduit groups. In addition, the widths of the regenerated nerve tissues in the Autograft and BMSC-(BDNF+GDNF) groups were bigger than that of control, BMSC-vector, BMSC-BDNF and BMSC-GDNF groups.

The middle segments of the regenerated nerve were also taken for immunofluorescence staining of NF200 and S100, which NF200 is a specific marker of axon and S100 is the specific marker of Schwann cells, and the staining results are shown in **Figure 5A**. The Schwann cells and axons distribution of regenerated nerves were observed in all groups, indicating that the new regenerated tissue is indeed nerve tissue. The statistical results of positive cell percentages of NF200 and S100 are shown in **Figures 5B,C**. In **Figure 5B**, the positive cell percentage of NF200 in Autograft and BMSC-(BDNF + GDNF) groups were higher than that of control, BMSC-vector, BMSC-BDNF and BMSC-GDNF groups, while there was no difference between Autograft group and BMSC-(BDNF+GDNF) group. The positive cell percentage of NF200 in BMSC-BDNF and BMSC-GDNF groups were higher than that of control and BMSC-vector groups. Besides, the positive cell percentage of NF200 in BMSC-vector group was higher than that of control group. According to the **Figure 5C**, the positive cell percentage of S100 in Autograft and BMSC-(BDNF + GDNF) groups were higher than that of other groups, while the positive cell percentage of S100 in BMSC-BDNF and BMSC-GDNF groups were higher than that of control and BMSC-vector groups. In addition, the positive cell percentage of S100 in the BMSC-vector group was higher than that of control group.

In summary, these results showed that the nerve repair effect of BMSC-(BDNF + GDNF) group was highest among the conduit groups. The expression of NF200 and S100 of BMSC-vector group was higher than that of control group, while the expression of NF200 and S100 of BMSC-BDNF and BMSC-GDNF groups were higher than that of control and BMSC-vector groups.

Toluidine Blue Staining and Transmission Electron Microscopy of Regenerated Nerve

The cross sections of the middle segments of the regenerated nerve were further stained by toluidine blue (**Figure 6A**). The hollow myelinated nerve fibers could be clearly detected in each group, and these myelinated nerve fibers were evenly distributed in the regenerated nerve tissue. However, the density and size of myelinated nerve fibers were different in each group. The density of regenerated myelinated nerve fibers in Autograft, control, BMSC-vector, BMSC-BDNF, BMSC-GDNF, and BMSC-(BDNF + GDNF) groups were 16206.4, 10688.2, 13658.9, 14659.3, 14685.6, and 16940.5/mm^2, respectively (**Figure 6B**). According to the statistical analysis, the density of myelinated nerve fibers in control, BMSC-vector, BMSC-BDNF, and BMSC-GDNF groups were significantly lower than that in Autograft and BMSC-(BDNF + GDNF) groups, while that in BMSC-BDNF and BMSC-GDNF groups was significantly higher than that in control and BMSC-vector groups. In addition, the density of myelinated nerve fibers in BMSC-vector group was significantly higher than that in control group. These data indicated that the formation of myelinated nerve fibers in BMSC-(BDNF + GDNF) group was higher than BMSC-BDNF and BMSC-GDNF groups, while the formation of myelinated nerve fibers in BMSC-BDNF and BMSC-GDNF group were higher than control and BMSC-vector groups.

Transmission electron microscopy (TEM) images of the cross-section of the middle portion of the regenerated nerves were shown in **Figure 6A**. The histomorphometric parameters of the regenerated nerves including axon diameter, myelin sheath thickness and area of the myelinated axons were investigated (**Figures 6C–E**) and based on **Figure 6A**. As shown in **Figures 6A,C**, the mean axon diameters in Autograft, control, BMSC-vector, BMSC-BDNF, BMSC-GDNF, and BMSC-(BDNF + GDNF) groups were 6.38, 3.6, 4.2, 4.9, 5.07, and 6.4 μm, respectively. The axon diameters in Autograft and BMSC-(BDNF + GDNF) groups were significantly larger than those in control, BMSC-BMSC, BMSC-BDNF, and BMSC-GDNF groups, while there was no difference in axon diameters between Autograft group and BMSC-(BDNF + GDNF) group. The axonal diameters in BMSC-BDNF and BMSC-GDNF groups were larger than those in control and BMSC-vector groups, and there was no difference of axon diameters between BMSC-BDNF group and BMSC-GDNF group. In addition, the axonal diameters in BMSC-vector group were larger than that of control group. As shown in **Figures 6D,E**, tendencies of thickness of myelin sheaths and area of the myelinated axons were consistent with that of the axon diameter. These results demonstrated that the myelin regeneration ability in BMSC-(BDNF + GDNF) group were better than those in control, BMSC-vector, BMSC-BDNF and BMSC-GDNF groups, which was similar to those in Autograft group. Furthermore, the myelin regeneration ability in BMSC-BDNF and BMSC-GDNF groups were better than that of control and BMSC-vector, while the myelin regeneration and re-innervation ability in BMSC-vector group was better than that of control group.

Masson's Staining of the Gastrocnemius Muscle

The gastrocnemius muscles on the left and right sides of the rats were taken out and weighed 3 months after surgery. The gastrocnemius on the operative side in each group was smaller than that on the normal side (**Figure 7A**). As demonstrated in **Figure 7C**, the muscle weight recovery rates of Autograft, control, BMSC-vector, BMSC-BDNF and BMSC-GDNF groups were lower than that of BMSC-(BDNF + GDNF) group, while the muscle weight recovery rates of BMSC-BDNF and BMSC-GDNF groups were significantly higher than that of control and BMSC-vector groups. Moreover, the muscle weight recovery rate of BMSC-vector group was higher than that of control group. In the Masson's staining images of the gastrocnemius muscle, the muscle fibers were stained red and

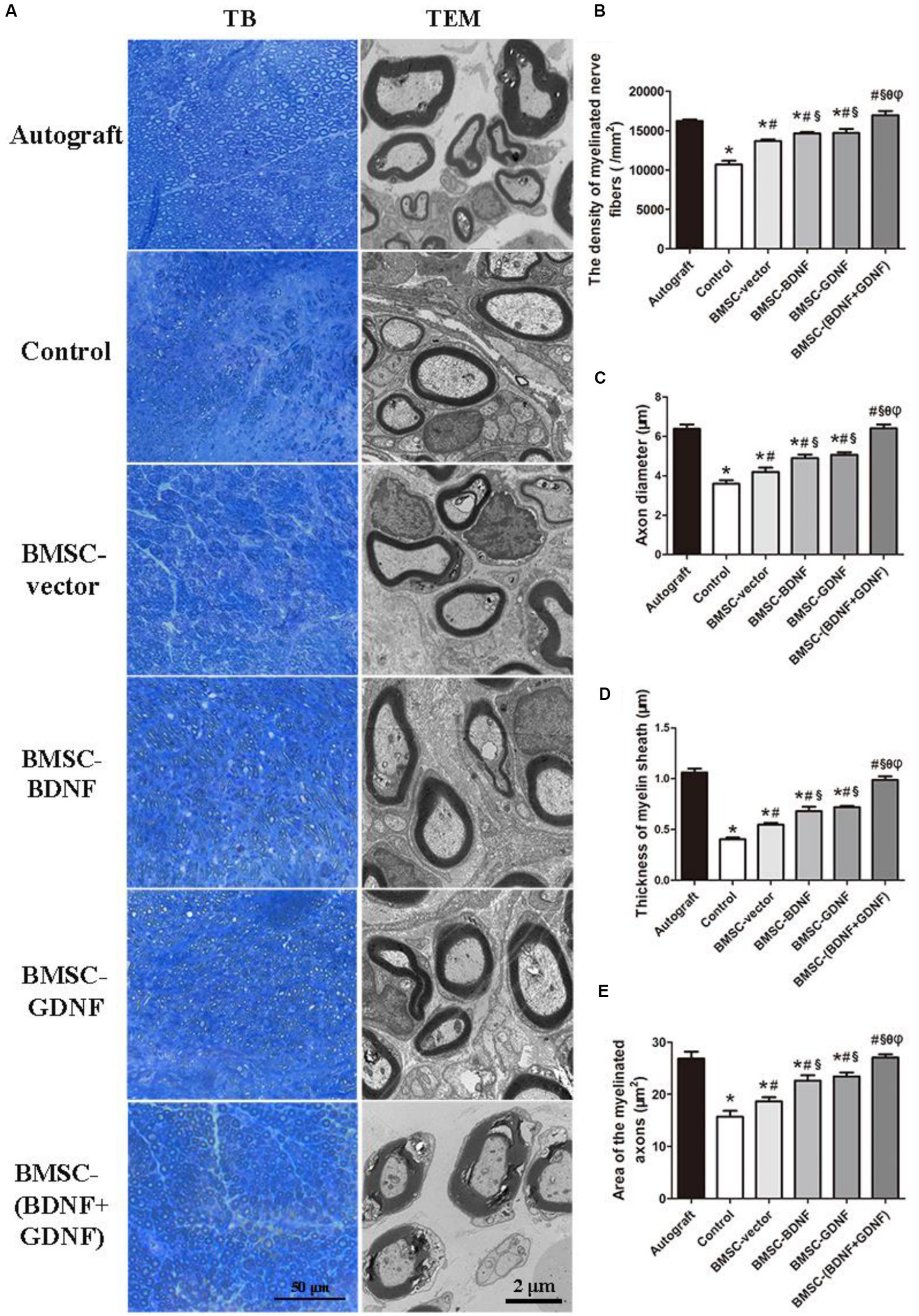

FIGURE 6 | Toluidine blue (TB) staining and transmission electron microscopy (TEM) analysis of regenerated nerves. **(A)** Images of toluidine blue staining and TEM cross sections of regenerated nerve; **(B)** The statistical density of myelinated nerve fibers in regenerated nerves in each group; **(C)** Axon diameter, **(D)** thickness of myelin sheath and **(E)** area of the myelinated axon of regenerated nerves. $^{*}P < 0.05$, compared with Autograft; $^{\#}P < 0.05$, compared with control group; $^{\S}P < 0.05$, compared with BMSC-vector group; $^{\theta}P < 0.05$, compared with BMSC-BDNF group; $^{\varphi}P < 0.05$, compared with BMSC-GDNF group.

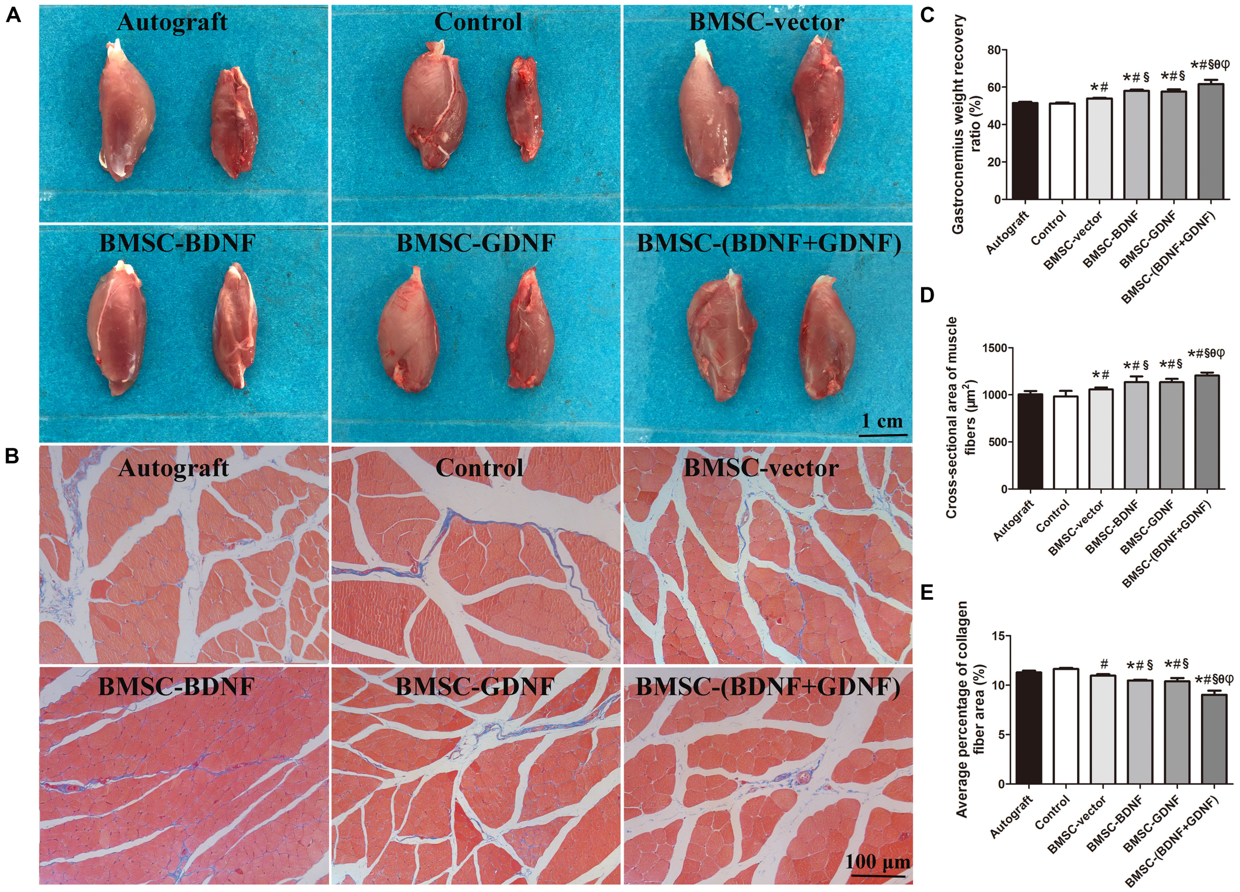

FIGURE 7 | Gastrocnemius muscle analysis. **(A)** Images of gastrocnemius muscle between normal and operative sides; **(B)** Masson's trichrome staining of cross sections of gastrocnemius muscle; **(C)** The gastrocnemius weight recovery ratio; **(D)** The cross sectional area of muscle fibers. **(E)** The average percentage of collagen fiber area. $^{*}P < 0.05$, compared with Autograft; $^{\#}P < 0.05$, compared with control group; $^{\$}P < 0.05$, compared with BMSC-vector group; $^{\theta}P < 0.05$, compared with BMSC-BDNF group; $^{\varphi}P < 0.05$, compared with BMSC-GDNF group.

the collagen fibers were stained blue (**Figure 7B**). Compared with BMSC-(BDNF + GDNF) group, the muscle fiber cross-sectional area of Autograft, control, BMSC-vector, BMSC-BDNF and BMSC-GDNF groups were significantly smaller, while the muscle fiber cross-sectional area of BMSC-BDNF and BMSC-GDNF groups were higher than that of Autograft, control and BMSC-vector groups (**Figure 7D**). Besides, the muscle fiber cross-sectional area of BMSC-vector group was higher than that of Autograft and control groups. As shown in **Figure 7E**, the collagen fiber area percentage of the BMSC-(BDNF + GDNF) group was significantly lower than that of Autograft, control, BMSC-vector, BMSC-BDNF and BMSC-GDNF groups, while the collagen fiber area percentage of BMSC-BDNF and BMSC-GDNF groups were significantly smaller than that of Autograft, control and BMSC-vector groups. Moreover, the collagen fiber area percentage of BMSC-vector group was smaller than that of Autograft and control groups. These results suggested that the re-innervation ability of the regenerated nerve in BMSC-BDNF and BMSC-GDNF groups were stronger than that of Autograft, control and BMSC-vector groups, while re-innervation ability of the regenerated nerve in BMSC-(BDNF + GDNF) group the was stronger than that of Autograft, control, BMSC-vector, BMSC-BDNF and BMSC-GDNF groups.

DISCUSSION

In this study, an efficient strategy for peripheral nerve repair is developed by combination of highly oriented nanofibrous nerve conduits (HO-PSNCs), seed cells (BMSCs), and neurotrophic factors (BDNF and GDNF). HO-PSNCs conduits could support peripheral nerve regeneration, but the repair effect was limited. The addition of seed cells (e.g., Schwann cells, Schwann cell-like cells and BMSCs) in nerve conduits were reported to promote nerve repair (Luo et al., 2015; Xue et al., 2017; Fu et al., 2019). Here, naïve BMSCs in HO-PSNCs conduits did improve the motor function, conduction function, nerve fiber morphology, protein expression, myelin regeneration and re-innervation ability of the regenerated nerve. However, other indexes of nerve regeneration had no significant change by naïve BMSCs. These data were consistent with the reports that BMSCs could promote conduit mediated nerve repair (Nijhuis et al., 2013; Gao et al., 2016).

Fu et al. (2011) reported that GDNF or BDNF transfected neural stem cells could promote the sciatic nerve regeneration, but he did not study the synergy effects in nerve regeneration. Although electrical stimulation can simultaneously promote the secretion of nutritional factors such as BDNF and GDNF during nerve regeneration, it has not been compared with single factor group (Willand et al., 2016). Wang et al. (2016) revealed that BDNF and GDNF fused to a laminin-binding domain in collagen tube had synergistical repair promoting effects of laryngeal nerve. Hoyng et al. (2014) identified the promoting effect of single factor BDNF, GDNF or NGF on the nerve regeneration, while the Hsu et al. constructed a CRISPR-based system for activating endogenous BDNF, GDNF, and NGF genes in adipose stem cell sheets to stimulate peripheral nerve regeneration (Hsu et al., 2019). In summary, no one has reported the synergistic effect of endogenous BDNF and GDNF (ratio = 1:1) on nerve regeneration.

Among the large number of neurotrophic factors, BDNF can promote the myelin formation of neogenesis nerves and GDNF can protect motor neurons from injury caused by nerve transection, which have been confirmed the role in the repair of PNI (Xiong et al., 2016; Lu et al., 2017). In our study, BMSCs overexpressing single factor exhibited many differences with naïve BMSCs group with improved conduction function, myelin regeneration and re-innervation ability of the regenerated nerve. All other indexes of nerve regeneration, such as SFI values and HE staining, had no significant change by introducing single neurotrophic factor to BMSC comparing to naïve BMSCs. These data were in constancy with the report that BMSC-BDNF need to combine with other factor to promote spinal cord recovery (Xiong et al., 2016). Altogether, naïve BMSCs, BMSCs overexpressing BDNF and BMSCs overexpressing GDNF as seed cells could efficiently improve peripheral nerve regeneration.

Interestingly, mixing BMSCs overexpressing BDNF and BMSCs overexpressing GDNF as seed cells in our study greatly elevated the repair of peripheral nerves. All BMSCs groups included the same cell number (5×10^4 cells). In this case, the expression levels of BDNF or GDNF in the double-factor group was half as much as that in the single-factor group. However, all the indexes of nerve regeneration were better than those of the single-factor groups. These data suggest that not the higher dose of single neurotrophic factors would make the better the effect of nerve regeneration, but BDNF and GDNF could synergistically promote nerve regeneration more effectively with different mechanisms of action. BDNF secreted by BMSCs can bind to p75NTR receptors of Schwann cells to promote myelinization (Xiao et al., 2009). GDNF has a strong role in promoting survival and growth of motor neurons, and the sciatic nerve contains motor and sensory axons emitted from spinal cord and DRG cells (Eric et al., 2002). The two factors functional in different aspects of nerve repair may collaborate in our study making high efficiency. Although the ratio of GDNF producing BMSC and BDNF producing BMSC need to be further optimized, our study provides an excellent system of mixing different seed cells with synergistic ability for nerve repair.

CONCLUSION

BMSCs overexpressing BDNF and BMSCs overexpressing GDNF were constructed and combined with the HO-PSNCs for peripheral nerve repair. Mixture of BMSCs overexpressing BDNF and BMSCs overexpressing GDNF as seed cells greatly improved the sciatic nerve repair comparing to the BMSCs-BDNF or BMSCs-GDNF single factor groups and similar to autograft group. Therefore, our study not only provided an optimal method of stem cell-based, multiple factors-mediated and conduit-guided for nerve repair, but also came up with a new strategy of seed cell mixture with synergistic ability for nerve repair.

DATA AVAILABILITY STATEMENT

The raw data supporting the conclusions of this article will be made available by the authors, without undue reservation.

ETHICS STATEMENT

The animal study was reviewed and approved by Animal Care and Use Committees of Wuhan University.

AUTHOR CONTRIBUTIONS

QZ, PW, and YC conceived the initial idea and designed the experiments. QZ, PW, FC, and YZ performed the experiments. QZ, PW, and ZT analyzed the data and wrote the manuscript. YL, XH, CH, QY, ZT, and YC revised the manuscript. YC and ZT worked on funding acquisition. All the authors have read and approved the final version of the manuscript.

FUNDING

This work was supported by the National Natural Science Foundation of China (Grant No. NSFC 81871493), the National Natural Science Foundation of Hubei Province of China (Grant No. 2017CFB240), and the Medical Science Advancement Program (Clinical Medicine) of Wuhan University (Grant Nos. TFLC2018002 and 2018003).

ACKNOWLEDGMENTS

We thank the technique support from the Experimental Teaching Center of Basic Medical Sciences, Wuhan University.

SUPPLEMENTARY MATERIAL

The Supplementary Material for this article can be found online at: https://www.frontiersin.org/articles/10.3389/fbioe.2020.00874/full#supplementary-material

REFERENCES

Cangellaris, O. V., and Gillette, M. U. (2018). Biomaterials for enhancing neuronal repair. *Front. Mater.* 5:21. doi: 10.3389/fmats.2018.00021

Carvalho, C. R., Oliveira, J. M., and Reis, R. L. (2019). Modern trends for peripheral nerve repair and regeneration: beyond the hollow nerve guidance conduit. *Front. Bioeng. Biotechnol.* 7:337. doi: 10.3389/fbioe.2019.00337

Chen, S., Zhao, Y., Yan, X., Zhang, L., Li, G., and Yang, Y. (2019). PAM/GO/gel/SA composite hydrogel conduit with bioactivity for repairing peripheral nerve injury. *J. Biomed. Mater. Res. A* 107, 1273–1283. doi: 10.1002/jbm.a.36637

Cho, H., Blatchley, M. R., Duh, E. J., and Gerecht, S. (2018). Acellular and cellular approaches to improve diabetic wound healing. *Adv. Drug Deliv. Rev.* 146, 267–288. doi: 10.1016/j.addr.2018.07.019

Chrzaszcz, P., Derbisz, K., Suszynski, K., Miodonski, J., Trybulski, R., Lewin-Kowalik, J., et al. (2018). Application of peripheral nerve conduits in clinical practice: a literature review. *Neurol. Neurochir. Polut.* 52, 427–435. doi: 10.1016/j.pjnns.2018.06.003

Cui, Y., Yao, Y., Zhao, Y., Xiao, Z., Cao, Z., Han, S., et al. (2018). Functional collagen conduits combined with human mesenchymal stem cells promote regeneration after sciatic nerve transection in dogs. *J. Tissue Eng. Regen. Med.* 12, 1285–1296. doi: 10.1002/term.2660

Eggers, R., de Winter, F., Hoyng, S. A., Roet, K. C., Ehlert, E. M., Malessy, M. J., et al. (2013). Lentiviral vector-mediated gradients of GDNF in the injured peripheral nerve: effects on nerve coil formation, Schwann cell maturation and myelination. *PLoS One* 8:e71076. doi: 10.1371/journal.pone.0071076

Eggers, R., Hendriks, W. T., Tannemaat, M. R., van Heerikhuize, J. J., Pool, C. W., Carlstedt, T. P., et al. (2008). Neuroregenerative effects of lentiviral vector-mediated GDNF expression in reimplanted ventral roots. *Mol. Cell. Neurosci.* 39, 105–117. doi: 10.1016/j.mcn.2008.05.018

Eric, G. F., Isabelle, D., Michael, P., Anne, D. Z., and Patrick, A. (2002). GDNF and NGF released by synthetic guidance channels support sciatic nerve regeneration across a long gap. *Eur. J. Neurosci.* 15, 589–601. doi: 10.1046/j.1460-9568.2002.01892.x

Fu, K. Y., Dai, L. G., Chiu, I. M., Chen, J. R., and Hsu, S. H. (2011). Sciatic nerve regeneration by microporous nerve conduits seeded with glial cell line-derived neurotrophic factor or brain-derived neurotrophic factor gene transfected neural stem cells. *Artif. Organs* 35, 363–372. doi: 10.1111/j.1525-1594.2010.01105.x

Fu, X., Wang, Y., Fu, W., Liu, D., Zhang, C., Wang, Q., et al. (2019). The combination of adipose-derived schwann-like cells and acellular nerve allografts promotes sciatic nerve regeneration and repair through the JAK2/STAT3 signaling pathway in rats. *Neuroscience* 422, 134–145. doi: 10.1016/j.neuroscience.2019.10.018

Gao, M., Lu, P., Lynam, D., Bednark, B., Campana, W. M., Sakamoto, J., et al. (2016). BDNF gene delivery within and beyond templated agarose multi-channel guidance scaffolds enhances peripheral nerve regeneration. *J. Neural Eng.* 13:066011. doi: 10.1088/1741-2560/13/6/066011

Guo, Q., Liu, C., Hai, B., Ma, T., Zhang, W., Tan, J., et al. (2018). Chitosan conduits filled with simvastatin/Pluronic F-127 hydrogel promote peripheral nerve regeneration in rats. *J. Biomed. Mater. Res. B Appl. Biomater.* 106, 787–799. doi: 10.1002/jbm.b.33890

Guo, Z., Liang, J., Poot, A. A., Grijpma, D. W., and Chen, H. (2019). Fabrication of poly (trimethylene carbonate)/reduced graphene oxide-graft-poly (trimethylene carbonate) composite scaffolds for nerve regeneration. *Biomed. Mater.* 14:024104. doi: 10.1088/1748-605X/ab0053

Hobson, M. I., Colin, G. J., and Terenghi, G. (2000). VEGF enhances intraneural angiogenesis and improves nerve regeneration after axotomy. *J. Anat.* 197, 591–605. doi: 10.1046/j.1469-7580.2000.19740591.x

Hoyng, S. A., De Winter, F., Gnavi, S., de Boer, R., Boon, L. I., Korvers, L. M., et al. (2014). A comparative morphological, electrophysiological and functional analysis of axon regeneration through peripheral nerve autografts genetically modified to overexpress BDNF, CNTF, GDNF, NGF, NT3 or VEGF. *Exp. Neurol.* 261, 578–593. doi: 10.1016/j.expneurol.2014.08.002

Hsu, M. N., Liao, H. T., Li, K. C., Chen, H. H., Yen, T. C., Makarevich, P., et al. (2017). Adipose-derived stem cell sheets functionalized by hybrid baculovirus for prolonged GDNF expression and improved nerve regeneration. *Biomaterials* 140, 189–200. doi: 10.1016/j.biomaterials.2017.05.004

Hsu, M. N., Liao, H. T., Truong, V. A., Huang, K. L., Yu, F. J., Chen, H. H., et al. (2019). CRISPR-based activation of endogenous neurotrophic genes in adipose stem cell sheets to stimulate peripheral nerve regeneration. *Theranostics* 9, 6099–6111. doi: 10.7150/thno.36790

Hsu, S. H., Kuo, W. C., Chen, Y. T., Yen, C. T., Chen, Y. F., Chen, K. S., et al. (2013). New nerve regeneration strategy combining laminin-coated chitosan conduits and stem cell therapy. *Acta Biomater.* 9, 6606–6615. doi: 10.1016/j.actbio.2013.01.025

Hsueh, Y. Y., Chang, Y. J., Huang, T. C., Fan, S. C., Wang, D. H., Chen, J. J., et al. (2014). Functional recoveries of sciatic nerve regeneration by combining chitosan-coated conduit and neurosphere cells induced from adipose-derived stem cells. *Biomaterials* 35, 2234–2244. doi: 10.1016/j.biomaterials.2013.11.081

Labroo, P., Hilgart, D., Davis, B., Lambert, C., Sant, H., Gale, B., et al. (2018). Drug-delivering nerve conduit improves regeneration in a critical sized gap. *Biotechnol. Bioeng.* 116, 143–154. doi: 10.1002/bit.26837

Li, G., Li, S., Zhang, L., Chen, S., Sun, Z., Li, S., et al. (2019). Construction of biofunctionalized anisotropic hydrogel micropatterns and their effect on schwann cell behavior in peripheral nerve regeneration. *ACS Appl. Mater. Interfaces* 11, 37397–37410. doi: 10.1021/acsami.9b08510

Li, G., Zhao, X., Zhang, L., Yang, J., Cui, W., Yang, Y., et al. (2020). Anisotropic ridge/groove microstructure for regulating morphology and biological function of Schwann cells. *Appl. Mater. Today* 18:100468. doi: 10.1016/j.apmt.2019.100468

Li, Q., Ping, P., Jiang, H., and Liu, K. (2006). Nerve conduit filled with GDNF gene-modified Schwann cells enhances regeneration of the peripheral nerve. *Microsurgery* 26, 116–121. doi: 10.1002/micr.20192

Lin, Y. F., Xie, Z., Zhou, J., Chen, H. H., Shao, W. W., and Lin, H. D. (2019). Effect of exogenous spastin combined with polyethylene glycol on sciatic nerve injury. *Neural Regen. Res.* 14, 1271–1279. doi: 10.4103/1673-5374.251336

Liu, H., Xu, X., Tu, Y., Chen, K., Song, L., Zhai, J., et al. (2020). Engineering microenvironment for endogenous neural regeneration after spinal cord injury by reassembling extracellular matrix. *ACS Appl. Mater. Interfaces* 12, 17207–17219. doi: 10.1021/acsami.9b19638

Lopes, C. D. F., Goncalves, N. P., Gomes, C. P., Saraiva, M. J., and Pego, A. P. (2017). BDNF gene delivery mediated by neuron-targeted nanoparticles is neuroprotective in peripheral nerve injury. *Biomaterials* 121, 83–96. doi: 10.1016/j.biomaterials.2016.12.025

Lu, Y., Gao, H., Zhang, M., Chen, B., and Yang, H. (2017). Glial cell line-derived neurotrophic factor-transfected placenta-derived versus bone marrow-derived mesenchymal cells for treating spinal cord injury. *Med. Sci. Monit.* 23, 1800–1811. doi: 10.12659/msm.902754

Luo, L., Gan, L., Liu, Y., Tian, W., Tong, Z., Wang, X., et al. (2015). Construction of nerve guide conduits from cellulose/soy protein composite membranes combined with Schwann cells and pyrroloquinoline quinone for the repair of peripheral nerve defect. *Biochem. Biophys. Res. Commun.* 457, 507–513. doi: 10.1016/j.bbrc.2014.12.121

Moskow, J., Ferrigno, B., Mistry, N., Jaiswal, D., Bulsara, K., Rudraiah, S., et al. (2019). Review: bioengineering approach for the repair and regeneration of peripheral nerve. *Bioact. Mater.* 4, 107–113. doi: 10.1016/j.bioactmat.2018.09.001

Nijhuis, T. H., Bodar, C. W., van Neck, J. W., Walbeehm, E. T., Siemionow, M., Madajka, M., et al. (2013). Natural conduits for bridging a 15-mm nerve defect: comparison of the vein supported by muscle and bone marrow stromal cells with a nerve autograft. *J. Plast. Reconstr. Aesthet. Surg.* 66, 251–259. doi: 10.1016/j.bjps.2012.09.011

Riccio, M., Marchesini, A., Pugliese, P., and De Francesco, F. (2019). Nerve repair and regeneration: biological tubulization limits and future perspectives. *J. Cell. Physiol.* 234, 3362–3375. doi: 10.1002/jcp.27299

Sayad-Fathi, S., Nasiri, E., and Zaminy, A. (2019). Advances in stem cell treatment for sciatic nerve injury. *Expert Opin. Biol. Ther.* 04, 1–11. doi: 10.1080/14712598.2019.1576630

Tajdaran, K., Chan, K., Gordon, T., and Borschel, G. H. (2018). Matrices, scaffolds, and carriers for protein and molecule delivery in peripheral nerve regeneration. *Exp. Neurol.* 319:112817. doi: 10.1016/j.expneurol.2018.08.014

Vijayavenkataraman, S. (2020). Nerve guide conduits for peripheral nerve injury repair: a review on design, materials and fabrication methods. *Acta Biomater.* 106, 54–69. doi: 10.1016/j.actbio.2020.02.003

Vijayavenkataraman, S., Kannan, S., Cao, T., Fuh, J. Y. H., Sriram, G., and Lu, W. F. (2019). 3D-printed PCL/PPy conductive scaffolds as three-dimensional porous nerve guide conduits (NGCs) for peripheral nerve injury repair. *Front. Bioeng. Biotechnol.* 7:266. doi: 10.3389/fbioe.2019.00266

Wang, B., Yuan, J., Chen, X., Xu, J., Li, Y., and Dong, P. (2016). Functional regeneration of the transected recurrent laryngeal nerve using a collagen scaffold loaded with laminin and laminin-binding BDNF and GDNF. *Sci. Rep.* 6:32292. doi: 10.1038/srep32292

Wang, J., Cheng, Y., Chen, L., Zhu, T., Ye, K., Jia, C., et al. (2018). In vitro and in vivo studies of electroactive reduced graphene oxide-modified nanofiber scaffolds for peripheral nerve regenerationu. *Acta Biomater.* 84, 98–113. doi: 10.1016/j.actbio.2018.11.032

Willand, M. P., Rosa, E., Michalski, B., Zhang, J. J., Gordon, T., Fahnestock, M., et al. (2016). Electrical muscle stimulation elevates intramuscular BDNF and GDNF mRNA following peripheral nerve injury and repair in rats. *Neuroscience* 334, 93–104. doi: 10.1016/j.neuroscience.2016.07.040

Wu, P., Xiao, A., Zhao, Y., Chen, F., Ke, M., Zhang, Q., et al. (2019). An implantable and versatile piezoresistive sensor for the monitoring of human–machine interface interactions and the dynamical process of nerve repair. *Nanoscale* 11, 21103–21108. doi: 10.1039/c9nr03925b

Wu, P., Zhao, Y., Chen, F., Xiao, A., Du, Q., Dong, Q., et al. (2020). Conductive hydroxyethyl cellulose/soy protein isolate/polyaniline conduits for enhancing peripheral nerve regeneration via electrical stimulation. *Front. Bioeng. Biotechnol.* 8:709. doi: 10.3389/fbioe.2020.00709

Xiao, J., Wong, A. W., Willingham, M. M., Kaasinen, S. K., Hendry, I. A., Howitt, J., et al. (2009). BDNF exerts contrasting effects on peripheral myelination of NGF-dependent and BDNF-dependent DRG neurons. *J. Neurosci.* 29, 4016–4022. doi: 10.1523/JNEUROSCI.3811-08.2009

Xiong, L. L., Li, Y., Shang, F. F., Chen, S. W., Chen, H., Ju, S. M., et al. (2016). Chondroitinase administration and pcDNA3.1-BDNF-BMSC transplantation promote motor functional recovery associated with NGF expression in spinal cord-transected rat. *Spinal Cord* 54, 1088–1095. doi: 10.1038/sc.2016.55

Xue, J., Yang, J., O'Connor, D. M., Zhu, C., Huo, D., Boulis, N. M., et al. (2017). Differentiation of bone marrow stem cells into schwann cells for the promotion of neurite outgrowth on electrospun fibers. *ACS Appl. Mater. Interfaces* 9, 12299–12310. doi: 10.1021/acsami.7b00882

Yi, S., Xu, L., and Gu, X. (2018). Scaffolds for peripheral nerve repair and reconstruction. *Exp. Neurol.* 319:112761. doi: 10.1016/j.expneurol.2018.05.016

Zhang, H., Fang, J., Su, H., Yang, M., Lai, W., Mai, Y., et al. (2012). Bone marrow mesenchymal stem cells attenuate lung inflammation of hyperoxic newborn rats. *Pediatr. Transplant.* 16, 589–598. doi: 10.1111/j.1399-3046.2012.01709.x

Zhang, L., Yang, W., Xie, H., Wang, H., Wang, J., Su, Q., et al. (2019). Sericin nerve guidance conduit delivering therapeutically repurposed clobetasol for functional and structural regeneration of transected peripheral nerves. *ACS Biomater. Sci. Eng.* 5, 1426–1439. doi: 10.1021/acsbiomaterials.8b01297

Zhang, Q., Tong, Z., Chen, F., Wang, X., Ren, M., Zhao, Y., et al. (2020). Aligned soy protein isolate-modified poly(L-lactic acid) nanofibrous conduits enhanced peripheral nerve regeneration. *J. Neural Eng.* 17:036003. doi: 10.1088/1741-2552/ab8d81

Zhu, S., Ge, J., Wang, Y., Qi, F., Ma, T., Wang, M., et al. (2014). A synthetic oxygen carrier-olfactory ensheathing cell composition system for the promotion of sciatic nerve regeneration. *Biomaterials* 35, 1450–1461. doi: 10.1016/j.biomaterials.2013.10.071

Zurn, A. D., Winkel, L., Menoud, A., Djabali, K., and Aebischer, P. (1996). Combined effects of GDNF, BDNF, and CNTF on motoneuron differentiation in vitro. *J. Neurosci. Res.* 44, 133–141. doi: 10.1002/(sici)1097-4547(19960415)44:2<133::aid-jnr5>3.0.co;2-e

Conflict of Interest: QZ was employed by the company Hangzhou Singclean Medical Products Co., Ltd.

The remaining authors declare that the research was conducted in the absence of any commercial or financial relationships that could be construed as a potential conflict of interest.

frontiers
in Bioengineering and Biotechnology

REVIEW
published: 13 August 2020
doi: 10.3389/fbioe.2020.00990

Multifunctional Gold Nanoparticles: A Novel Nanomaterial for Various Medical Applications and Biological Activities

Xiaopei Hu†, Yuting Zhang†, Tingting Ding, Jiang Liu* and Hang Zhao

State Key Laboratory of Oral Diseases, National Clinical Research Center for Oral Diseases, Chinese Academy of Medical Sciences Research Unit of Oral Carcinogenesis and Management, West China Hospital of Stomatology, Sichuan University, Chengdu, China

Nanotechnology has become a trending area in science and has made great advances with the development of functional, engineered nanoparticles. Various metal nanoparticles have been widely exploited for a wide range of medical applications. Among them, gold nanoparticles (AuNPs) are widely reported to guide an impressive resurgence and are highly remarkable. AuNPs, with their multiple, unique functional properties, and easy of synthesis, have attracted extensive attention. Their intrinsic features (optics, electronics, and physicochemical characteristics) can be altered by changing the characterization of the nanoparticles, such as shape, size and aspect ratio. They can be applied to a wide range of medical applications, including drug and gene delivery, photothermal therapy (PTT), photodynamic therapy (PDT) and radiation therapy (RT), diagnosis, X-ray imaging, computed tomography (CT) and other biological activities. However, to the best of our knowledge, there is no comprehensive review that summarized the applications of AuNPs in the medical field. Therefore, in this article we systematically review the methods of synthesis, the modification and characterization techniques of AuNPs, medical applications, and some biological activities of AuNPs, to provide a reference for future studies.

Keywords: AuNPs, synthesis, modification, characterization, medical applications, biological activities

Edited by:
Zhengwei Mao,
Zhejiang University, China

Reviewed by:
Rajendra Kumar Singh,
Institute of Tissue Regeneration Engineering (ITREN), South Korea
Michihiro Nakamura,
Yamaguchi University, Japan

Correspondence:
Jiang Liu
liujiang@scu.edu.cn

†These authors have contributed equally to this work

Specialty section:
This article was submitted to Biomaterials, a section of the journal Frontiers in Bioengineering and Biotechnology

Received: *28 April 2020*
Accepted: *29 July 2020*
Published: *13 August 2020*

Citation:
Hu X, Zhang Y, Ding T, Liu J and Zhao H (2020) Multifunctional Gold Nanoparticles: A Novel Nanomaterial for Various Medical Applications and Biological Activities. Front. Bioeng. Biotechnol. 8:990. doi: 10.3389/fbioe.2020.00990

INTRODUCTION

Nanomaterials are a novel type of material which has emerged in recent years. The term refers to a material in which at least one dimension, of three-dimensional space, is at the nanometer scale (0.1–100 nm), or is composed of the basic unit, which is approximately equivalent to the size of 10–100 atoms, is closely arranged together (Khan et al., 2017; Tayo, 2017). Nanoparticles are an example of nanomaterials, which now have the longest development time and are the most mature technology. Nanoparticles and nanotechnology are widely used and play an important role in a range of fields, such as medicine, biology, physics, chemistry and sensing, owing to their unique properties (Ramalingam, 2019). In comparison with other metal nanoparticles, noble metal (Cu, Hg, Ag, Pt, and Au) nanoparticles have increasingly attracted the attention of researchers (Ramalingam et al., 2014). Among these, gold nanoparticles (AuNPs) are known to be the most stable, and have now been prepared with various shapes and structures, including nanospheres, nanorods, nanocubes, nanobranches, nanobipyramids, nanoflowers, nanoshells, nanowires, and nanocages, by various synthetic techniques (**Figure 1**) (O'Neal et al., 2004; Chen et al., 2008; Li et al., 2015; Xiao et al., 2019). Moreover, they possess tunable and unique optical properties. Therefore, AuNPs have attracted extensive scientific and technological attention in recent decades. The optical properties of AuNPs are dependent on surface plasmon resonance (SPR), which is the fluctuation and interaction of electrons between negative and positive charges at the surface (Ramalingam, 2019). SPR can also be described in terms of surface plasmon polariton (SPP), which originates from propagating waves along a planar gold surface (Gurav et al., 2019). Due to their unique optical and electrical properties, and economic importance, AuNPs have abundant applications in various interdisciplinary branches of science, including medicine, material science, biology, chemistry and physics (Khan et al., 2019).

Especially, AuNPs are widely employed across the medical field owing to their excellent biocompatibility, which respectively results from their high chemical and physical stability, easy to functionalize with biologically active organic molecules or atoms (Pissuwan et al., 2019). AuNPs can directly conjugate and interact with diverse molecules containing proteins, drugs, antibodies, enzymes, nucleic acids (DNA or RNA), and fluorescent dyes on their surface, for diverse medical applications and biological activities (**Figure 2**) (Slocik et al., 2005; Ramalingam, 2019). Although AuNPs are so widespread and increasingly used in the medical field, there is no comprehensive review of their applications in medicine. Therefore, in this review, we have summarized the approaches that are available for synthesizing common AuNPs, as well as the techniques that are used to characterize them, based on their unique and diverse properties. We have also paid particular attention to the discussion of established medical applications of AuNPs.

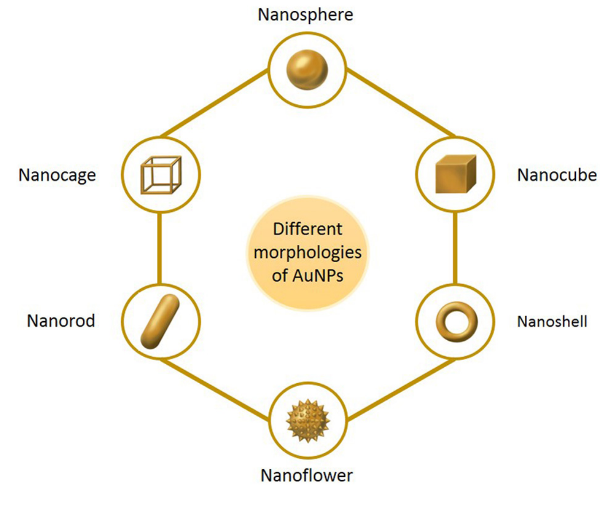

FIGURE 1 | The main morphologies of AuNPs.

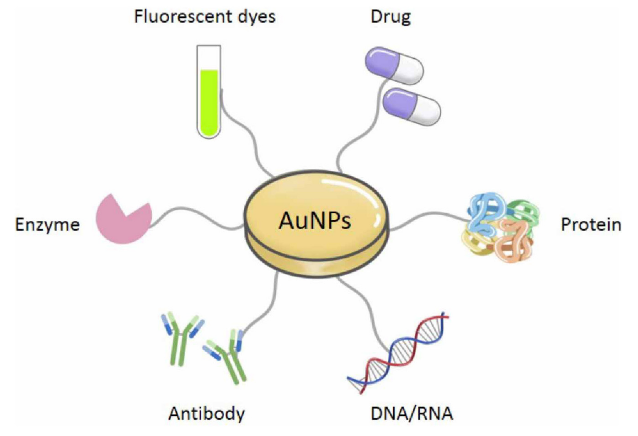

FIGURE 2 | Various connecting molecules of AuNPs.

SYNTHESIS AND MODIFICATION OF MULTIFUNCTIONAL AuNPs

Almost all the medical applications and biological activities of AuNPs was characterized based on the unique SPR, since the SPR can enhance the surface activity of AuNPs. Due to the excitation of SPR, the absorption spectrum connected with AuNPs shows a resonance band in the visible region, whose amplitude, spectral location and width can be modified by the diverse particle size and shape in the medium. Also, the SPR is strongly dependent on both size and shape (Ramalingam, 2019). Therefore, the preparation of size-controlled and shape-controlled AuNPs is essential for the medical applications and biological activities. The first report on AuNPs was published in 1857 by Faraday with light scattering potential of AuNPs confirmed by the change of red color and colloidal nature of nanomaterials (Faraday, 1857). Although AuNPs have a long history, the synthesis of small and stable structure of AuNPs is difficult, key challenge in nanotechnology. To our knowledge, there are two distinct approaches of synthesizing AuNPs, which are top–down and bottom–up respectively (**Figure 3**). The materials of AuNPs prepared by different methods are various, which are bulk material, small gold seeds or gold target, $HAuCl_4 \cdot 4H_2O$ and various biological extracts respectively. Furthermore, AuNPs can bind various active molecules, and have broad prospects in the application of diverse fields. Thus, the modification of AuNPs will also be introduced.

Top–Down Approach

Generally, the top–down approach is a subtractive process, starting with the slicing of bulk materials and ending with self-assembled nanoscale objects (Khanna et al., 2019). Micropatterning and photolithography are the most common approaches (Chen et al., 2009; Walters and Parkin, 2009). Yun et al. (2006) demonstrated micropatterning of a single layer of nanoparticles and micelles through conventional and soft lithographical methods. Although the approach is

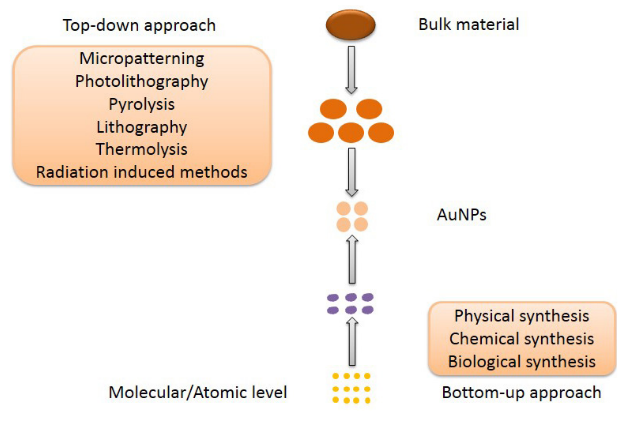

FIGURE 3 | The top–down and bottom–up approaches for AuNPs synthesis.

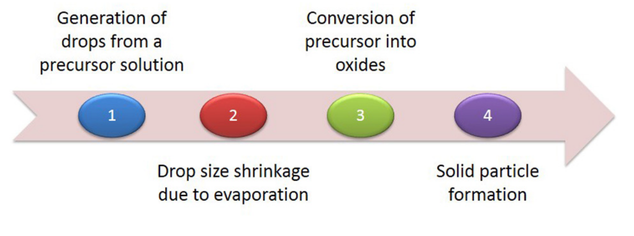

FIGURE 4 | The four major steps of pyrolysis.

fast, it has the limitation of synthesizing nanoparticles of uniform size. Thus, Chen et al. (2009) developed a novel patterning technique for AuNPs by removing salt-loaded micelles from substrate areas with a polymer stamp. They called the technique μ-contact (microcontact) deprinting, providing a fast and cheap way to produce nanoparticles on a wide range of substrates. In addition, there are several physical methods, such as pyrolysis, lithography, thermolysis and radiation induced methods in this category. Pyrolysis is another important technique frequently used, generally for the production of noble metal nanoparticles. As shown in **Figure 4**, pyrolysis has four major steps, from generation of drops from a precursor solution to solid particle formation (**Figure 4**) (Li et al., 2004). Pyrolysis has several disadvantages, such as the formation of porous films, low purity in some cases and limited products (Garza et al., 2010). In conclusion, the top–down approach has major limitations in the control of surface and structure of the AuNPs, which has a significant effect on their physical and chemical properties (Amblard et al., 2002; Sant et al., 2012). Size distribution is uncontrolled and enormous energy is required to maintain conditions of high-pressure and high-temperature during these synthetic procedures. Thus, it is very uneconomical and difficult to meet product requirements.

Bottom–Up Approach

As a popular nanomaterial, AuNPs are expected to present with applications in many areas. However, their yield is currently too low in existing methods of synthesis. Developing more convenient and adjustable methods to improve their preparation efficiency, in order to achieve production on a technical scale, has become the focus of research. The bottom–up approach has been an emerging strategy in recent years. There are three types of bottom–up synthesis approaches: (1) physical approaches, such as laser ablation, sputter deposition, ion implantation, γ-irradiation, optical lithography, microwave (MW) irradiation, ultrasound (US) irradiation, and ultraviolet (UV) irradiation (**Table 1**); (2) the chemical reduction of metal ions in solutions by introducing chemical agents and stabilizing agents, such as sodium hydroxide (NaOH), sodium borohydride ($NaBH_4$), cetyl-trimethylammonium bromide (CTAB), lithium aluminum hydride ($LiAlH_4$), sodium dodecyl sulfate (SDS), ethylene glycol (EG), and sodium citrate (**Figures 5**, **6**); (3) biological approaches, using intracellular or extracellular extracts of prokaryotic cells (bacteria and actinomycetes) or eukaryotic cells (algae, fungi, and yeast), and extracts from various plants (leaves, stem, flower, fruits, peel, bark, and root) (**Table 2**). These syntheses will be discussed in detail in the following parts.

Physical Approach

Most of the physical methods used to prepare nanoparticles involve controlling experimental parameters in the presence of a reducing agent, to modulate the structures and properties of AuNPs without contamination (**Table 1**). Laser ablation and ion implantation are the most common and important physical methods of synthesis. Laser ablation provides an approach which effectively alters the surface area, geometric shape, properties, fragmentation, and assembly of AuNPs in aqueous solution, a biocompatible medium (Correard et al., 2014; González-Rubio et al., 2016). For example, Vinod et al. (2017) synthesized pure AuNPs through laser ablation of a gold target in water, and these nanoparticles are inherently non-toxic. And these

TABLE 1 | Physical synthesis of AuNPs with different morphology and size.

Method	Morphology	Size (nm)	Author	References
γ-irradiation	Nanosphere	3–6	Le et al.	Le et al., 2019
Ion implantation	Crystalline	1.5–5	Morita et al.	Morita et al., 2017
Laser ablation	Nanosphere	10–15	Vinod et al.	Vinod et al., 2017
	Nanosphere	7	Hampp et al.	Riedel et al., 2020
Ultrasound irradiation	Polyhedral	15–40	Shaheen et al.	Bhosale et al., 2017
Microwave irradiation	Nanosphere	10–50	Luo et al.	Luo et al., 2018

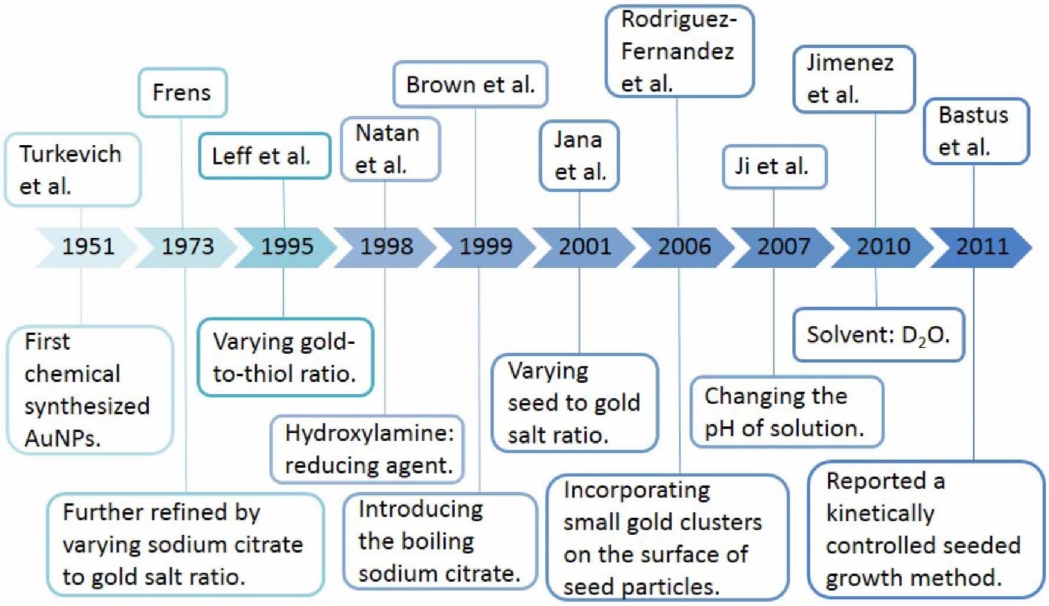

FIGURE 5 | The chemical synthesis of AuNPs using different reaction conditions.

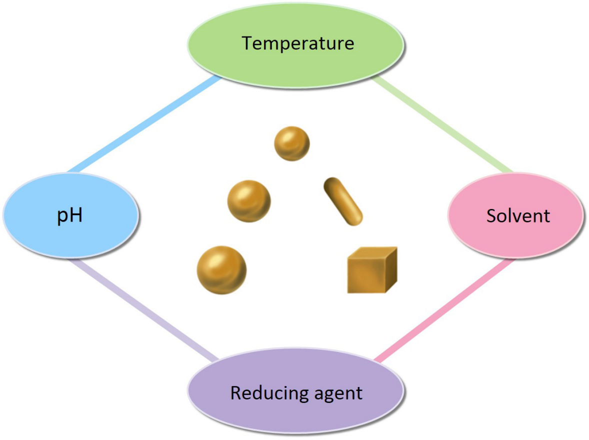

FIGURE 6 | The factors affecting the size and shape of AuNPs.

particles are photothermally active when excited with 532 nm laser irradiation. However, the yield of this method is low, and the method is inconvenient. Therefore, the development of convenient, high-efficiency methods is necessary, in order to scale up production. Recently, Riedel et al. (2020) synthesized spherical, silica-coated AuNPs, with an average diameter of 9 nm and a coating thickness of 2 nm, by improved pulsed laser ablation in liquid (PLAL), and this method offers great progress to the large-scale production of nanoparticles. Another promising method for synthesis of AuNPs is ion implantation, which has been extensively used to prepare AuNPs with precise physical, chemical, and biological properties. Nie et al. (2018) reported the synthesis of embedded AuNPs in Nd:YAG single crystals, using ion implantation, and subsequent thermal annealing. Both linear and non-linear absorption of the Nd:YAG crystals have been significantly enhanced.

Chemical Approach

The easiest and most commonly used approach to synthesis is the chemical reduction of metal ions in solutions (**Figure 5**). A typical synthesis of AuNPs is dependent on the reduction of Au(III) (from hydrogen tetrachloroaurate hydrate, $HAuCl_4$) to Au(0) atoms, formed as clusters and accumulated into large, polycrystalline particles via aggregation in the presence of reducing or stabilizing agent. Citrate-stabilized AuNPs were

TABLE 2 | Organisms mediated synthesis of AuNPs with different morphology and size.

Organism	Morphology	Size (nm)	Author	References
Garcinia mangostana	Nanosphere	20–40	Nishanthi et al.	Nishanthi et al., 2019
Couroupita guianensis	Nanocube	15–37	Singh et al.	Singh et al., 2016a
Acanthopanax sessiliflorus	Nanoflower	30–60	Ahn et al.	Ahn et al., 2017
Sporosarcina koreensis	Nanosphere	92	Singh et al.	Singh et al., 2016b
Sargassum swartzii	Nanosphere	35	Prema et al.	Prema et al., 2015

initially synthesized by Turkevich et al. (1951), which was also the first chemical synthesis of AuNPs. This synthesis was based on the single-phase aqueous reduction of $HAuCl_4$ by sodium citrate. This synthesis was further refined by Frens (1973) by varying the ratio of sodium citrate and gold salt in order to control the size of AuNPs, from 5 to 150 nm. However, the diameter (<30 nm) of AuNPs was too poor. Leff et al. (1995) synthesized surfactant-mediated AuNPs over a range of diameters from 1.5 to 20 nm, by varying the gold-to-thiol ratio (Leff et al., 1995). In 2007, adopting the classical reaction system, Ji et al. (2007) also synthesized AuNPs by changing the pH of solution, which can affect the composition of gold solute complexes, in order to alter the particle size. Then, Jimenez et al. (2010) synthesized small AuNPs with sodium citrate and heavy water (D_2O). This was a faster reduction method, and by increasingly replacing water with deuterium oxide, smaller diameters were obtained. Today, the aqueous method remains the most commonly used. However, the shape of AuNPs is irregular, and the size and size distribution obtained are quite poor. Thus, Natan and Brown (1998) reported the seeded growth of AuNPs (up to 100 nm in diameter) by using hydroxylamine as a mild reducing agent. And Brown et al. (1999) prepared AuNPs with highly uniform shape and size by introducing the boiling solution of sodium citrate. The mean diameters of the AuNPs produced were between 20 and 100 nm, and they exhibit improved monodispersity. A similar procedure, utilizing the reductant NH_2OH at room temperature, produces two populations of particles. The larger population is even more spherical than citrate-reduced particles of similar size, while the smaller population is very distinctly rod shaped. This work was improved by Jana et al. (2001) and Rodriguez-Fernandez et al. (2006). They synthesized monodispersed AuNPs with narrow size distributions, using ascorbic acid (AA) and CTAB, which are used as a reducing agent and cationic surfactant respectively. Jana et al. (2001) prepared the AuNPs with diameters of 5–40 nm by varying the ratio of seed to gold salt, whereas Rodriguez-Fernandez et al. (2006) prepared the AuNPs with diameters from 12 to 180 nm by incorporating small gold clusters on the surface of seed particles (Jana et al., 2001; Rodriguez-Fernandez et al., 2006). Although CTAB-based method can control the morphology of AuNPs, the thiolated cationic surfactant molecules that bind to the gold surface are difficult to remove and restrict further functionalization. The reason is that the strongly bound capping layer provided by the CTAB is difficult to exchange with the thiolated cationic surfactant molecules (Leonov et al., 2008). Thus, Bastus et al. (2011) reported a kinetically controlled seeded growth method for the synthesis of monodispersed citrate-stabilized AuNPs, with a uniform quasi-spherical shape of up to ∼200 nm, via the reduction of $HAuCl_4$ by sodium citrate. They also evaluated the effect of temperature and pH on their final shape. According to the mentioned above, it is known that the temperature, pH, the solvent, and the reducing/stabilizing agent of the reaction system play a crucial role in controlling the size and shape of AuNPs (**Figure 6**). This has also encouraged researchers to look for novel strategies to prepare AuNPs with controllable properties. Recent seed-mediated synthesis methods are considered very efficient, with respect to precise control of the size and shape of AuNPs.

Biological Approach

Although the synthesis of AuNPs by physical and chemical methods gives a high yield and is relatively cheap, there are a few disadvantages which have also been reported, such as the use of carcinogenic solvents, the contamination of precursors, and high toxicity (Ramalingam, 2019). To overcome these difficulties, researchers have investigated the biological production of AuNPs, and have explored the potential of micro-organisms, due to the quest for economically as well as environmentally benign methods (**Table 2**) (Jain N. et al., 2011; Ramalingam et al., 2019). Biological systems and agents are excellent examples of hierarchical organization of atoms or molecules and this has caused researchers to use a wide range of biological agents as potential cell factories for the production of nanomaterials (Gardea-Torresdey et al., 1999; Singaravelu et al., 2007; Kasthuri et al., 2008; Smitha et al., 2009). Using biological agents to reduce the metal ions requires benign conditions of external temperature and pressure, and little organic solvent (Khan et al., 2019). For example, Dubey et al. (2010) reported a rapid, green synthesis for AuNPs, using the lower amounts extract of *Rosa rugosa* leaf (Kumar et al., 2010). They also evaluated the effect of the quantity of leaf extract, the concentration of gold solution, the stability of AuNPs and different pH with zeta potentiometer. Although environmentally friendly and easy to regulate the shape and size of the nanoparticles, bacterial-mediated synthesis also has disadvantages, such as difficulty in handling and low yield (Azharuddin et al., 2019).

Modification

The size and morphology controlled AuNPs can be prepared based on different approaches above mentioned. AuNPs exhibit excellent physiochemical properties like unique SPR property, wide surface chemistry, high binding affinity, good biocompatibility, enhanced solubility, tunable functionalities for targeted delivery (Dreaden et al., 2012). Therefore, they have the ability to bind thiol and amine groups, which allows their modification for medical applications and biological activities (Shukla et al., 2005). On the one hand, AuNPs can directly attach ligands such as drug (**Table 3**), protein, DNA/RNA, enzyme, and so on (**Figure 2**). For instance, Podsiadlo et al. (2008) synthesized AuNPs bearing 6-Mercaptopurine (6-MP) and its riboside derivatives (6-Mercaptopurine-9-β-D-Ribofuranoside, 6-MPR). 6-MP and 6-MPR are loaded on the surfaces of AuNPs through sulfur-gold (Au–S) bonds known for their strength. They found substantial enhancement of the antiproliferative effect against K-562 leukemia cells compared to the free form of same drug. On the other hand, AuNPs are also used to conjugate with various drug with polymer functionalized for medical applications and biological activities. Recently, the design and preparation of polymer-functionalized AuNPs have attracted increasing interest. The AuNPs functionalized with polymer have more biocompatibility, stability, controlled release of drug, and enhanced therapeutic applications (Ramalingam, 2019). Some examples of polymer functionalized AuNPs for drug delivery are as shown in **Table 3**. For example, Venkatesan et al. (2013) developed AuNRs–doxorubicin

TABLE 3 | Functionalized AuNPs without/with polymer for drug delivery with different morphology and size.

Polymer	Drug	Morphology	Size (nm)	References
–	6-Mercaptopurine	Nanosphere	4–5	Podsiadlo et al., 2008
–	Dodecylcysteine	Nanosphere	3–6	Azzam and Morsy, 2008
–	Kahalalide F	Nanosphere	20, 40	Hosta et al., 2009
–	Phthalocyanine	Nanosphere	2–4	Wieder et al., 2006
–	Rose Bengal	Nanorod	–	Wang et al., 2014
PEG	Doxorubicin	Nanosphere	11	Asadishad et al., 2010
PSS	Doxorubicin	Nanorod	5	Venkatesan et al., 2013
Chitosan	5-fluorouracil	Nanosphere	20	Chandran and Sandhyarani, 2014
Glycyrrhizin	Lamivudine	Nanosphere	16	Borker et al., 2016
PCPP	Camptothecin	Nanosphere	25–30	Sivaraj et al., 2018

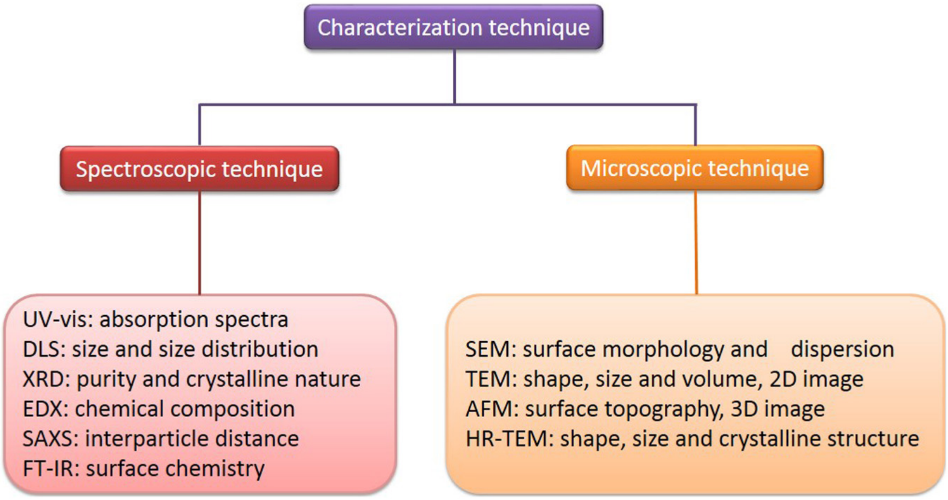

FIGURE 7 | Characterization of AuNPs.

conjugates (DOX@PSS-AuNRs) by an electrostatic interaction between the amine group ($-NH_2$) of DOX and the negatively charged PSS-AuNRs surface. DOX@PSS-AuNRs conjugates exhibited improved drug loading efficiency, higher biological stability and higher therapeutic efficiency than free DOX. Therefore, the unique physical and chemical properties of AuNPs functionalized with/without polymer can enhance the efficiency of drug deliver and therapeutic efficiency, and increase the multifunctional application.

CHARACTERIZATION OF MULTIFUNCTIONAL AuNPs

Various analytical techniques have been developed, in recent years, to characterize noble metal nanoparticles, according to their unique thermal, electrical, chemical, and optical properties, and to confirm their size (average particle diameter), shape, distribution, surface morphology, surface charge, and surface area (Roduner, 2006; Ray et al., 2015; Khanna et al., 2019). The characterization of AuNPs starts with a visual color change which can be observed with the naked eye, based on the principle of their unique and tunable SPR band (Ramalingam, 2019). The characterization of AuNPs has been shown schematically in **Figure 7**.

There are some indirect methods (spectroscopic technique) used to analyze the composition, structure, and crystal phase of AuNPs. Their striking optical properties are due to their SPR, which is monitored by UV-visible spectroscopy (UV-vis) (Sharma et al., 2016). The absorption spectra of AuNPs fall in the range of 500–550 nm (Poinern, 2014). It has been suggested a broadening of the SPR band width, which illustrates a redshift, can be used as an index of their state of aggregation, dispersity, size, and shape (Govindaraju et al., 2008; Shukla and Iravani, 2017). The size of AuNPs and their size distribution *in situ*, in the same range of hydrodynamic diameter, can be observed and measured by dynamic light scattering (DLS) (Wu et al., 2018). The purity and crystalline nature of AuNPs can be confirmed through X-ray diffraction (XRD), which gives a rough idea of the particle size, determined by the Debye-Scherer equation (Ullah et al., 2017). The chemical composition of AuNPs can be confirmed by energy-dispersive X-ray spectroscopy (EDX) (Shah et al., 2015). Small-angle X-ray scattering (SAXS) analysis can be used to provide a measure of the interparticle distance of AuNPs, of application to tumor imaging and tissue engineering (Allec et al., 2015). Fourier transform infrared spectroscopy (FT-IR) can investigate the surface chemistry to determine the functional atoms or groups bound to the surface of AuNPs (Dahoumane et al., 2016). The morphology of AuNPs can now be better characterized, due to recent developments in advanced microscopic techniques. These include scanning electron microscopy (SEM), transmission electron microscopy (TEM), high-resolution transmission electron microscopy (HR-TEM), and atomic force microscopy (AFM), which are commonly employed to determine and characterize their size, shape, and surface morphology (Azharuddin et al., 2019; Khanna et al., 2019). SEM provides nanoscale information about particles and determines their surface morphology and dispersion, while TEM is used to provide information about the number of material layers and broad evidence of uptake and localization, composition, polymer tethering, and physical properties (Marquis et al., 2009; Khanna et al., 2019). Also, TEM is commonly used as a quantitative method to measure size, volume, and shape, and it produces mainly two-dimensional (2D) image of three-dimensional (3D) nanoparticles (Quester et al., 2013). HR-TEM is used to determine the exact shape, size, and crystalline structure (Khanna et al., 2019). AFM, which is similar to the scanning probe microscopy, provides information about surface topography of AuNPs (Lu et al., 2004). AFM has the advantage of obtaining 3D images in a liquid environment (Lu et al., 2004; Khan et al., 2017). Some examples of the characterization of AuNPs, its morphology and size are as shown in **Table 4**.

MEDICAL APPLICATIONS OF MULTIFUNCTIONAL AuNPs

In the above parts, the synthesis, modification and characterization of AuNPs based on optical and physicochemical properties have been introduced. Although nearly all studies are in the experimental stages, it is clear that AuNPs have potential applications in different fields. Based on their characteristics, applications have been explored, particularly in medical field, including deliver carriers (drug, gene and protein deliver), therapeutics (PTT, PDT and RT), diagnostics, imaging, and other biological activities (**Figure 8** and **Table 5**). In the following sections, these applications will be discussed in detail.

Delivery Carriers

In recent years, the idea of using AuNPs as delivery carriers has attracted the wide attention of researchers. As shown in **Figure 9**, AuNPs can be used for the delivery of drug, gene, and protein.

Chemotherapy is the most common method of cancer therapy but its potential is limited in many cases. Traditional drug delivery (oral or intravenous administration) for chemotherapeutic drugs, results in the dissemination of the drug throughout the whole body, with only a fraction of the dose reaching the tumor site (Singh et al., 2018). Targeting of specific cells, organs, and tissues, in a controlled manner, has become a key issue and challenge. Drug delivery systems (DDSs) is a promising approach to general anticancer therapy, which may provide efficient targeted transport and overcome the limitation of biochemical barriers in the body, e.g., the brain blood barrier (Martinho et al., 2011). Moreover, DDSs can enable controlled function in delivering drugs for early detection of the diseases and damaged sites (Baek et al., 2016). There are many useful forms for drug delivery, including liposomes, liquid crystals, dendrimers, polymers, hydrogels, and nanoparticles (Yokoyama, 2014; Rigon et al., 2015). Among these, only a small number of polymers and liposomes have been clinically approved (Piktel et al., 2016). Thus, many researchers have started to focus on the popular AuNPs. AuNPs have been examined for potential anticancer drug delivery (Duncan et al., 2010). In addition, they also can be easily modified to transfer various drugs, which may be bound to AuNPs through physical encapsulation or by chemical (covalent or non-covalent) bonding. Conjugation of AuNPs with other drugs is also possible, but it should be remembered that functionalization can change the toxicity of AuNPs, and their ability to successfully load or attach the desired drugs. The use of modified AuNPs has reduced systemic drug toxicity and helped to decrease the possibility of the cancer developing drug resistance (Yokoyama, 2014). For example, Wójcik et al. (2015) using the MTT (3-(4,5-dimethylthiazol-2-yl)-2,5-diphenyltetrazolium bromide) assay, confirmed that glutathione-stabilized AuNPs (GSH-AuNPs) modified with non-covalent conjugation of the DOX were more active against feline fibrosarcoma cell lines than the activity exhibited by unmodified AuNPs.

Gene therapy is the use of exogenous DNA or RNA to treat or prevent diseases. Viral vectors are commonly used but cannot be functionalized and can activate host immune systems (Riley and Vermerris, 2017). Their 'design' is inflexible, they target specific sites in a biological system with high

TABLE 4 | Characterization of AuNPs and its morphology and size.

Author	Morphology	Size (nm)	Characterization	References
Falagan-Lotsch et al.	Nanorod	16–50	TEM, DLS, UV-vis	Falagan-Lotsch et al., 2016
Dam et al.	Nanostar	40	TEM, DLS	Dam et al., 2014
Balfourier et al.	Nanosphere	4–22	TEM, STEM, HR-TEM, EDX	Balfourier et al., 2019
Ni et al.	Nanosphere	5, 13, 45	DLS, UV-vis	Ni et al., 2019
Lin et al.	Nanosphere	∼10	TEM, SEM, DLS	Lin et al., 2019
Dash et al.	Nanosphere	15–23	HR-TEM, UV-vis, EDX, XRD, AFM, FT-IR	Dash et al., 2014
Lee et al.	Nanosphere Nanooctahedra Nanocube	75	TEM, SEM, UV-vis	Lee et al., 2019

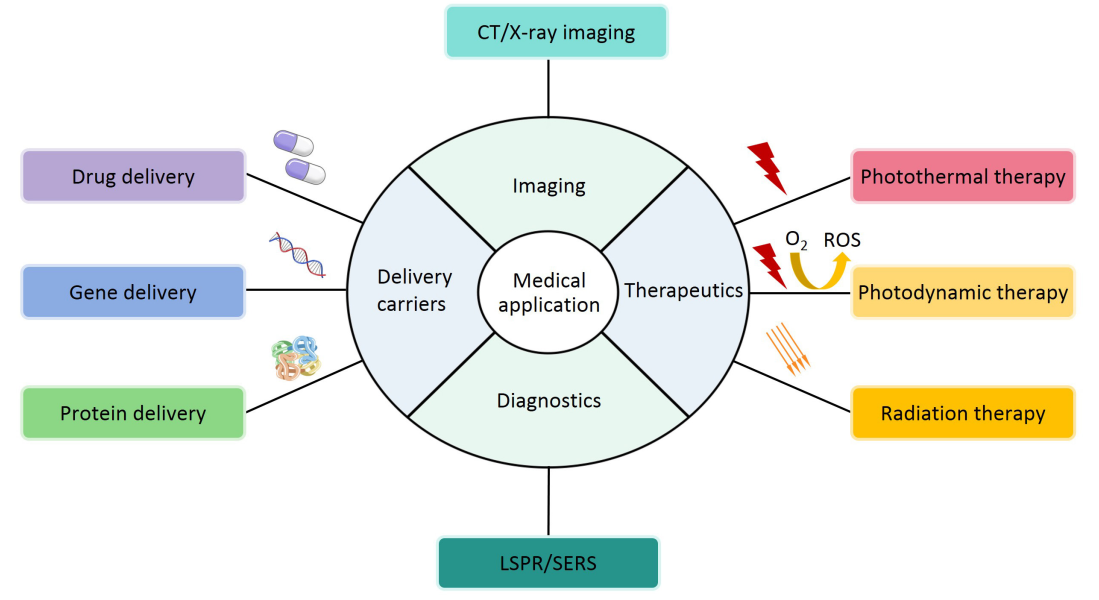

FIGURE 8 | A schematic representation of medical applications for AuNPs.

TABLE 5 | The application or activity of AuNPs with different morphology and size.

Author	Morphology	Size (nm)	Application/Activity	References
Tian et al.	Nanostar	40	PTT and CT	Tian et al., 2017
Rossi et al.	Nanosphere	5–10	Drug delivery and bioactivity	Rossi et al., 2016
Xu et al.	Nanocapsule	50	PTT, PDT and RT	Xu et al., 2019
Borkowska et al.	Nanocore	5.3 ± 0.7	Anticancer activity	Borkowska et al., 2020
Zheng et al.	Nanostar	7–10	PTT	Zheng et al., 2020
Liu et al.	Nanocapsule	30–40	Imaging	Liu et al., 2018
Venditti	Nanosphere	5	CT	Venditti, 2017
Yang et al.	Nanocube	50	PDT	Yang et al., 2018
Hu et al.	Nanosphere	100	PTT and RT	Hu et al., 2017
Yu et al.	Nanosphere	73.8	CT imaging and shRNA delivery	Yu et al., 2019
Zheng et al.	Nanosphere	2.04 ± 0.18	Drug delivery	Zheng et al., 2019
Shahbazi et al.	Nanosphere	19	Gene delivery	Shahbazi et al., 2019
Loynachan et al.	Nanocluster	2	Disease detection	Loynachan et al., 2019
Philip et al.	Nanosphere	37	SERS	Philip et al., 2018
Ramalingam et al.	Nanosphere	20–37	Anticancer and antimicrobial activity	Ramalingam et al., 2017
Filip et al.	Nanosphere	31	Anti-inflammation activity	Filip et al., 2019
Wang et al.	Nanobipyramid	–	Diagnosis	Wang et al., 2020
Ahmad et al.	Nanosphere	4–10	Antimicrobial activity	Ahmad et al., 2013
Tahir et al.	Nanosphere	2–10	Antioxidant activity	Tahir et al., 2015
Terentyuk et al.	Nanosphere	62	Antifungal activity	Terentyuk et al., 2014
El-Husseini et al.	Nanosphere	15	Diagnosis	El-Husseini et al., 2016

cytotoxicity and reduce the efficiency of gene therapy (Riley and Vermerris, 2017). The use of non-viral vectors system (such as metallic nanoparticles) can solve this problem. Recent studies have shown that AuNPs can protect nucleic acids through preventing their degradation by nucleases (Klebowski et al., 2018). The unique properties of AuNPs, conjugated to oligonucleotides, can make them potential gene carriers, via covalent and non-covalent bonding. Covalent AuNPs can activate immune-related genes in peripheral blood mononuclear cells, but not in an immortalized and lineage-restricted cell line (Ding et al., 2014). This shows promise application in its application for gene delivery systems. For example, Shahbazi et al. (2019) synthesized AuNPs core using the citrate reduction method, and developed a CRISPR nanoformulation, using colloidal AuNPs (AuNPs/CRISPR), with guide RNA and nuclease on the surface of AuNPs, with or without a single-strand DNA (ss DNA)

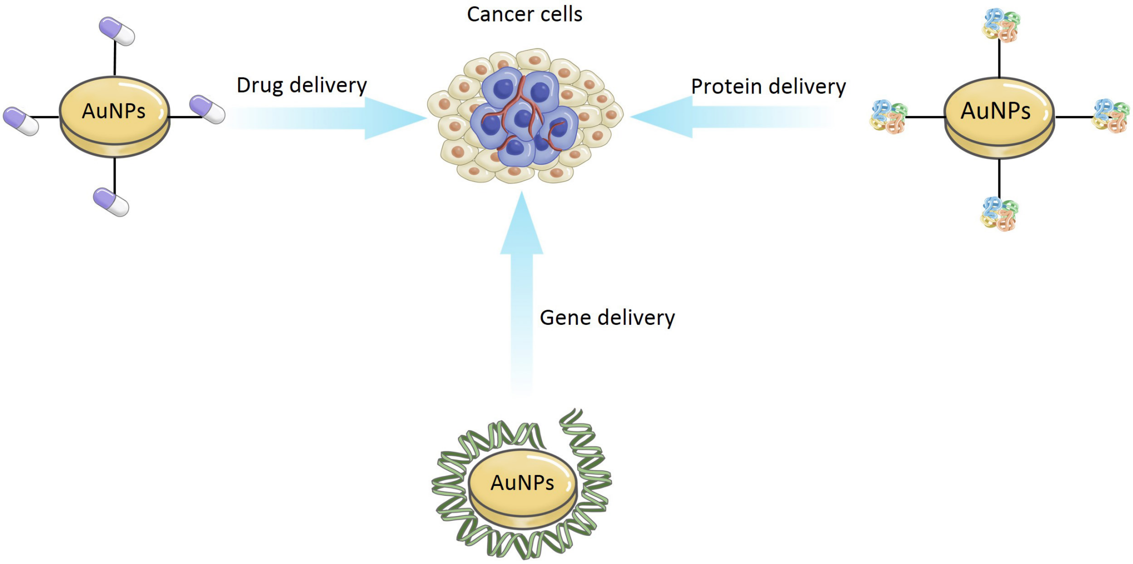

FIGURE 9 | The application of delivery carriers for AuNPs.

template to support homology-directed repair. The outcome was an efficient gene editing. They also demonstrated the non-toxicity delivery of entire CRISPR sequences into human blood stem and progenitor cells.

Recently, researchers have also found some evidence that AuNPs can be used as protein carriers. For instance, Joshi et al. (2006) obtained insulin directly bound to bare AuNPs (Au-insulin nanoparticles) via a covalent linkage, which have been confirmed more active than insulin bound via hydrogen bonds with amino acid-modified AuNPs (Au-Asp-insulin nanoparticles) in the transmucosal delivery of drugs for the treatment of diabetes. In this case, the efficiency of insulin delivery can be enhanced by coating the AuNPs with a non-toxic biopolymer, which can strongly adsorb insulin to its surface.

Therapeutics

In the following section, we will discuss photothermal therapy (PTT), photodynamic therapy (PDT), and radiation therapy (RT) applications of AuNPs, which continue to be under development (**Figure 10**).

PTT, also known as thermal ablation or optical hyperthermia, is a non-invasive and is widely applied for cancer therapy due to its benefits of real-time observation of tumor sites and photoinduced destruction of tumor cells or tissues (Singh et al., 2020). PTT uses materials with a high photothermal conversion efficiency, injected into the body, which gather near the tumor tissues by targeting recognition technology (Murphy et al., 2010; Mubarakali et al., 2011). Under the irradiation of external light sources, usually visible or near-infrared (NIR) light, photothermal materials (such as metal nanoparticles) can convert light energy into heat energy (photothermal conversion), result in the destruction of the tumor tissue, and kill the cancer cells (Murphy et al., 2010; Mubarakali et al., 2011). AuNPs as a photothermal material, with maximum absorption in the visible or NIR region, have a high photothermal conversion efficiency due to their SPR effect. In addition, the SPR peak of AuNPs can be adjusted to the NIR region by controlling their geometrical and physical parameters, such as size and shape, which contribute to the depth of effective penetration of PTT (Boyer et al., 2002; Orendorff et al., 2006; Bibikova et al., 2017). Therefore, many researchers have been focusing on the different size and shape of AuNPs for application in PTT (both *in vitro* and *in vivo*) due to their absorption peaks being in the visible or NIR region and their ability to load and deliver various anticancer drugs (Sharifi et al., 2019; Sztandera et al., 2019). AuNPs used in PTT are generally nanorods or nanoshells but, when introduced into a biological environment, the cellular uptake can be limited (Kim and Lee, 2018). Tian et al. (2017) synthesized gold nanostars (AuNSs) with pH (low) insertion peptides (pHLIPs) (AuNSs-pHLIP). They have low toxicity, are plasmon tunable in the NIR region, and exhibited excellent biocompatibility and effective PTT (Tian et al., 2017).

PDT is another form of light therapy, developed in recent decades, and used to destroy cancer cells and pathogenic bacteria (Abrahamse and Hamblin, 2016). PDT involves visible light, photosensitizer (PS), and molecular oxygen (O_2) from the tissues. PDT is completely dependent on the availability of O_2 in tissues. The process of PDT is that the PS absorbed by the tissue, is excited by laser light of a specific wavelength. Irradiating the tumor site can activate the PS that selectively accumulate in the tumor tissue, triggering a photochemical reaction to destroy the tumor. The excited PS will transfer energy to the surrounding O_2 to generate reactive oxygen species (ROS) and increase ROS level in the target sites. ROS can react with adjacent biological macromolecules to produce significant cytotoxicity, cell damage, even death or apoptosis (Imanparast et al., 2018; Falahati et al., 2019; Singh et al., 2020). As a PS, AuNPs can absorb the NIR light, accumulate in the tumor area, raise the temperature, and

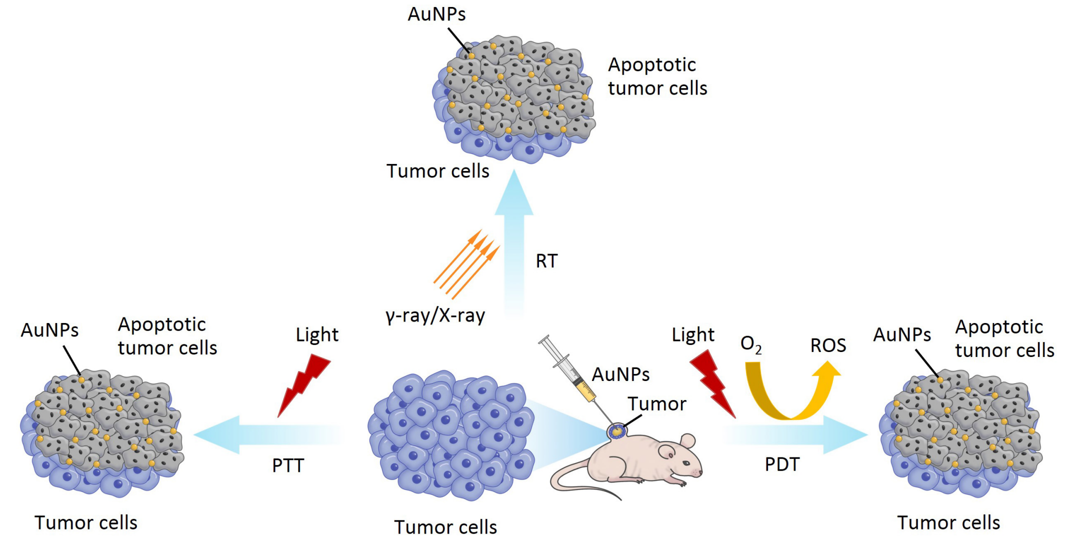

FIGURE 10 | The application of PTT, PDT and RT for AuNPs.

generate high levels of ROS, which can ultimately damage the tumor growth and promote cancer cell death (Jing et al., 2014). In addition, AuNPs have been considered for PS carriers due to their simple thiolation chemistry for the functionalization of desired molecules, enhancing its capability for loading PS drugs. For example, Yang et al. synthesized spherical AuNPs using UV-assisted reduction with sodium and chloroauric acid, and hollow gold nanorings with a sacrificial galvanic replacement method (Yang et al., 2018). They utilized AuNPs and gold nanorings as drug delivery carriers, with a PS enhancer, to compare and investigate the shape-dependent SPR response in PDT. They found that gold nanorings exhibited efficient PS activation and SPR in the NIR region. Therefore, these may be promising nanoparticles to address the current depth limitation of PDT, for deep tumor therapy.

Besides PTT and PDT, radiation therapy (RT) is one of the least invasive and commonly used methods in the treatment of various cancers (Sztandera et al., 2019). RT involves the delivery of high intensity ionizing radiations (such as γ-rays and X-rays) to tumor tissues, while simultaneously protecting the surrounding healthy cells, tissues, and organs, resulting in the death of tumor cells (Retif et al., 2015; Klebowski et al., 2018). γ-rays and X-rays are usually used to ionize cellular components (such as organelle) and water. Water is the main component of the cell, as well as the main target of the ionizing radiations, resulting in the lysis of the water molecules. This lysis is named radiolysis, which causes the formation of charged species and free radicals. The interaction of free radicals and membrane structure can also cause structural damage, leading to the apoptosis of cell (Kwatra et al., 2013). Recently, there have been many reports of radiosensitization using AuNPs in RT due to their high atomic number of gold (Jain S. et al., 2011; McMahon et al., 2011). The most probable mechanism of radiosensitization from AuNPs is that Auger electron production from the surface of the AuNPs can increase the production of ROS, reduce the total dose of radiation, and increase the dose administrated locally to the tumor sites, eventually resulting in cell death. Moreover, side effects can also be reduced (Jeynes et al., 2014; Retif et al., 2015).

Diagnostics

Diagnostics are very essential to medical science and clinical practice. Some diagnostic methods (such as immunoassay diagnosis) have been applied to clinical diagnosis but have limitations in precision molecular diagnostics because of their inaccuracy and low sensitivity (Ou et al., 2019). With the development of nanotechnology, the sensitivity, specificity, and multiplexing of diagnostic tests have been improved. AuNPs exhibit substantial and excellent optical properties, mainly including localized surface plasmon resonance (LSPR) and surface-enhanced Raman scattering (SERS), which play an important role in their application to diagnostics (Ou et al., 2019; Venditti, 2019). LSPR-based application of AuNPs is due to spectral modulation (**Figure 11**) (Ou et al., 2019). When

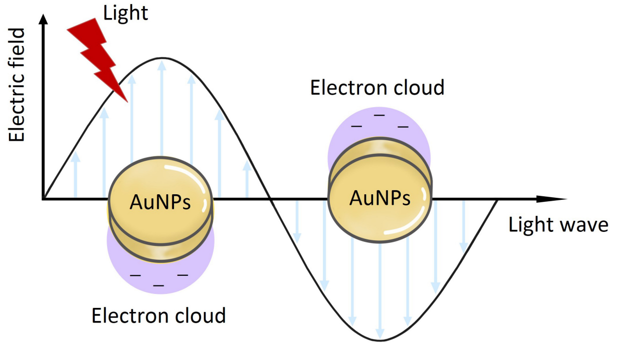

FIGURE 11 | The application of AuNPs on the LSPR.

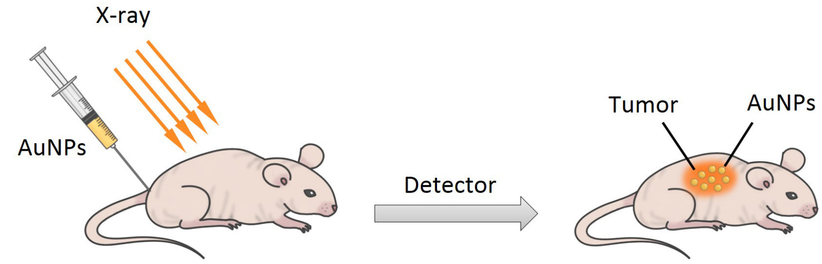

FIGURE 12 | A simple scheme for X-ray imaging.

the light is incident on the surface of AuNPs, if the incident photon frequency matches the overall vibration frequency of the electrons transmitted by the AuNPs, the AuNPs will strongly absorb the photon energy, and generate LSPR phenomenon, which is useful for diagnostics (Link and El-Sayed, 2003; Liu et al., 2011; Baek et al., 2016; Cordeiro et al., 2016). The LSPR peak of AuNPs is usually in the visible-NIR region, often at around 500 nm or from 800 and 1200 nm (Huang et al., 2009; Aldewachi et al., 2017). SERS is another very attractive spectroscopic technique in diagnostics, being non-invasive and having high sensitivity features (Boisselier and Astruc, 2009; Zhou et al., 2017). Fleischmann et al. (1974) reported the enhancement of a Raman scattering signal, which was the first observation of SERS. The enhancement of SERS can be explained by two mechanisms. One is the chemical enhancement due to charge transfer between gold atoms and molecules (Kawata et al., 2017). Another is the electromagnetic enhancement because of LSPR on the surface of metallic gold (Kawata et al., 2017). Spherical AuNPs are commonly used as the substrate for SERS, although non-spherical AuNPs have also been produced and explored for these applications (Tao et al., 2011; Yang et al., 2012). Nowadays, the phenomenon of LSPR and SERS in AuNPs has been widely used for the development of molecular diagnostics. For instance, El-Husseini et al. (2016) synthesized 15 nm unmodified citrate-coated AuNPs by the Frens method, for use in the diagnostic polymerase chain reaction (PCR) technique for detection of the equine herpes virus 1 (EHV-1). Their results showed that AuNPs-assisted PCR was more sensitive than the conventional PCR technique and, therefore, could be used as a more efficient molecular diagnostic tool for EHV-1.

Imaging

X-ray computed tomography (CT) is one of the most important and mature tissue imaging techniques widely used in various research and clinical environments with broad availability and fairly low cost (Kim et al., 2007). Specifically, CT is a non-invasive clinical diagnostic tool that can perform 3D visual reconstruction and tissue segmentation (Lusic and Grinstaff, 2013). The images of CT are composed of X-ray images, which are taken at different angles by rotating around an object to form a cross-sectional 3D image called a CT scan (Lusic and Grinstaff, 2013; Fuller and Köper, 2019). According to the content of the images, the contrast agent can attenuate the X-ray to improve the image quality to highlight the specific area, such as the structure of blood vessels or organs (Lusic and Grinstaff, 2013). The basis of CT imaging is the fact that healthy and diseased tissues or cells have different densities, which can generate in a contrast between normal and abnormal cells by using contrasting agents (such as iodinated molecules) (**Figure 12**) (Cormode et al., 2014). Iodinated molecules are usually used as a contrasting agent, due to their unique X-ray absorption coefficient (Klebowski et al., 2018). However, their usage has its own limitations, such as short imaging times, rapid renal clearance, reduced sensitivity and specificity, toxicity, and vascular permeation (Chien et al., 2012; Mackey et al., 2014). Therefore, it is very essential to explore and develop novel materials as contrasting agents for X-ray imaging. In recent years, AuNPs are attracting attention in imaging as an X-ray contrast agent because they can strongly absorb ionizing radiation to enhance the coefficient of X-ray absorption and convert the light energy to heat energy through the SPR effect (Rahman et al., 2014). Moreover, AuNPs have some advantages compared to iodinated molecules such as ease of synthetic manipulation, unique optical and electrical properties, non-toxicity, higher electron density, higher atomic number of gold, and higher X-ray absorption coefficient (Mackey et al., 2014; Singh et al., 2017). The key factors for potential application of AuNPs in enhanced X-ray CT imaging are their migration and accumulation at target sites and longer vascular retention time, and these allow non-invasive tracking and visualizing of the therapeutic cells (Yin et al., 2017; Meir and Popovtzer, 2018). For example, Liu et al. (2018) synthesized 30–40 nm sized gold nanocages (AuNCs) as part of an activatable probe, to investigate the potential of imaging. The AuNCs were PEGylated *via* conjugation with SH-PEG-NH_2. It is the first report to estimate protease activity *in vivo* using an imaging technique and activatable probe.

Others

Besides the various applications described above, some other applications involving antimicrobial (antibacterial and antifungal) activity, antioxidant activity, and anticancer activity need to be mentioned.

The increasing incidence of bacterial infection with drug resistance is a major issue for human health (Dutta et al., 2017). AuNPs are easily taken up by immune cells, due to their excellent cell affinity, which leads to precise delivery at the infected area, facilitating inhibition and damage to microbial pathogens

(Saha et al., 2007). AuNPs show excellent antibacterial activity against *E. coli* by absorbing light and converting it into heat (Singh et al., 2009). The growing drug resistance of fungal strains also demands the development of new drugs for better treatment of fungal diseases. Among the various nanoparticles, AuNPs are sensitive to candida cells, which can inhibit the growth and kill the fungal pathogen *C. albicans* (Wani and Ahmad, 2013; Yu et al., 2016). They increase the ROS and damage the cell membrane by their unique properties, which include converting light to heat when irradiated and strong anionic binding with fungal plasma membrane (Wani and Ahmad, 2013; Yu et al., 2016). Cancer is caused by many factors and is considered one of the main causes for death worldwide. In tumor cells, AuNPs have a tendency to enter subcellular organelles and increase the cellular uptake, which enhances anticancer activity (Kajani et al., 2016). AuNPs can increase the ROS level, to destroy cancer cells. However, the biocompatibility and selectivity of AuNPs, in targeting tumors, remains an important challenge. Therefore, new developing methods are required to overcome the question. Excessive ROS can lead to enzyme deactivation and nucleic acid damage, which can itself lead to diseases diabetes, aging, and cancer (Li et al., 2009). Ramalingam (2019) synthesized AuNPs using $NaBH_4$ and $HAuCl_4$ as a reducing agent and precursor, respectively. Furthermore, they investigated and confirmed the anticancer activity of their AuNPs in human lung cancer cells, and antimicrobial activity against human clinical pathogens, such as *P. aeruginosa*, *S. aureus*, *E. coli*, *V. cholera*, *Salmonella* sp., *K. pneumonia*. Their results suggested that AuNPs could potentially act as anticancer and antimicrobial agents. Moreover, AuNPs have also been confirmed as a potential antioxidant agent. They can inhibit the formation of ROS, thus increasing the antioxidant activity of defensive enzymes. The synergism and antagonism of AuNPs, in their antioxidant activity, require further investigation (Ramalingam, 2019). For instance, Tahir et al. (2015) produced AuNPs (2–10 nm) using the extract of *Nerium oleander* leaf, in a one-step, green synthetic method, and these AuNPs showed good antioxidant activity. Furthermore, the results showed that the extract of *Nerium oleander* leaf was very active for the reduction of AuNPs, and could be used as a reducing agent.

CONCLUSION

In summary, since Faraday first reported AuNPs in 1857 (Faraday, 1857), there have been many reports focusing on their synthesis, as well as comparisons with other metallic nanoparticles or noble metallic nanoparticles. In this review, we have described the synthesis and modification of AuNPs, the techniques of characterization, and their diverse medical applications and biological activities. Since the yield is low, using a top–down approach, a series of synthetic approaches to the production of AuNPs have been proposed. Additionally, the unique properties of AuNPs suggest its broad applications, including drug and gene delivery, PTT, photodynamic therapy (PDT), diagnosis, and imaging. Moreover, further applications, arising from their antimicrobial (antibacterial and antifungal), antioxidant, and anticancer activities, have also been discussed. As the properties of AuNPs become better understood, a considerable number of principal experiments and studies are needed to focus on function, along with the design of different therapies, generally involving PTT and PDT. Although the antimicrobial, anticancer, and antioxidant activities of AuNPs have been confirmed, they remain to be used in clinical treatment. As a drug and gene carrier, AuNPs may also have broad applications, in the future. Although AuNPs possess many useful properties, some studies have demonstrated their toxic effects, based on their physicochemical properties. Sabella et al. (2014) showed that the toxicity of AuNPs was related to their cellular internalization pathways. The safety of AuNPs remains a very urgent and controversial issue, as more important concerns are raised, and this needs to be properly addressed. In recent studies, researchers have reduced the toxicity of AuNPs by introducing functional groups to their surface, improved existing methods of synthesis, and have developed new and better methods. In conclusion, the unique properties of AuNPs should be identified, such as their optical properties with SPR bands, and as carriers with anticancer activity, to broaden their applications in various fields.

AUTHOR CONTRIBUTIONS

XH wrote the manuscript. YZ collected the literature and generated the figures and tables. TD edited and checked the manuscript format. JL and HZ reviewed the manuscript. All the authors contributed to the article and approved the submitted version.

FUNDING

This study was supported by the National Natural Science Foundations of China (Nos. 81922020 and 81970950), the Postdoctoral Research and Development Funding of Sichuan University (2020SCU12016), and the Research Funding for Talents Developing, West China Hospital of Stomatology Sichuan University (Nos. RCDWJS2020-4 and RCDWJS2020-14).

REFERENCES

Abrahamse, H., and Hamblin, M. R. (2016). New photosensitizers for photodynamic therapy. *Biochem. J.* 473, 347–364. doi: 10.1042/BJ20150942

Ahmad, T., Wani, I. A., Manzoor, N., Ahmed, J., and Asiri, A. M. (2013). Biosynthesis, structural characterization and antimicrobial activity of gold and silver nanoparticles. *Colloids Surf. B Biointerfaces* 107, 227–234. doi: 10.1016/j.colsurfb.2013.02.004

Ahn, S., Singh, P., Jang, M., Kim, Y. J., Castro-Aceituno, V., Simu, S. Y., et al. (2017). Gold nanoflowers synthesized using Acanthopanacis cortex extract inhibit inflammatory mediators in LPS-induced RAW264.7 *macrophages via NF-κB and AP*-1 pathways. *Colloids Surf. B Biointerfaces* 160, 423–428. doi: 10.1016/j.colsurfb.2017.09.053

Aldewachi, H., Chalati, T., Woodroofe, M. N., Bricklebank, N., Sharrack, B., and Gardiner, P. (2017). Gold nanoparticle-based colorimetric biosensors. *Nanoscale* 10, 18–33. doi: 10.1039/C7NR06367A

Allec, N., Choi, M., Yesupriya, N., Szychowski, B., White, M. R., Kann, M. G., et al. (2015). Small-angle X-ray scattering method to characterize molecular interactions: proof of concept. *Sci. Rep.* 5:12085. doi: 10.1038/srep12085

Amblard, J., Belloni, J., Remita, H., Khatouri, J., Cointet, C., and Mostafavi, M. (2002). Dose rate effects on radiolytic synthesis of gold-silver bimetallic clusters in solution. *J. Phys. Chem. B* 102, 4310–4321. doi: 10.1021/jp981467n

Asadishad, B., Vossoughi, M., and Alemzadeh, I. (2010). Folate-receptor-targeted delivery of doxorubicin using polyethylene glycol-functionalized gold nanoparticles. *Ind. Eng. Chem. Res.* 49, 1958–1963. doi: 10.1021/ie9011479

Azharuddin, M., Zhu, G. H., Das, D., Ozgur, E., Uzun, L., Turner, A. P. F., et al. (2019). A repertoire of biomedical applications of noble metal nanoparticles. *Chem. Commun.* 55, 6964–6996. doi: 10.1039/c9cc01741k

Azzam, E. M. S., and Morsy, S. M. I. (2008). Enhancement of the antitumour activity for the synthesised dodecylcysteine surfactant using gold nanoparticles. *J. Surfactants Deterg.* 11, 195–199. doi: 10.1007/s11743-008-1072-8

Baek, S. M., Singh, R. K., Kim, T. H., Seo, J. W., Shin, U. S., Chrzanowski, W., et al. (2016). Triple hit with drug carriers: pH- and temperature-responsive theranostics for multimodal chemo- and photothermal-therapy and diagnostic applications. *ACS Appl. Mater Interfaces* 8, 8967–8979. doi: 10.1021/acsami.6b00963

Balfourier, A., Luciani, N., Wang, G., Lelong, G., Ersen, O., Khelfa, A., et al. (2019). Unexpected intracellular biodegradation and recrystallization of gold nanoparticles. *Proc. Natl. Acad. Sci. U.S.A.* 117, 103–113. doi: 10.1073/pnas.1911734116

Bastus, N. G., Comenge, J., and Puntes, V. (2011). Gold nanoparticles of up to 200nm: size focusing versus Ostwald ripening. *Langmuir* 27, 11098–11105. doi: 10.1021/la201938u

Bhosale, M. A., Chenna, D. R., and Bhanage, B. M. (2017). Ultrasound assisted synthesis of gold nanoparticles as an efficient catalyst for reduction of various nitro compounds. *Chemistryselect* 2, 1225–1231. doi: 10.1002/slct.201601851

Bibikova, O., Singh, P., Popov, A., Akchurin, G., Skaptsov, A., Skovorodkin, I., et al. (2017). Shape-dependent interaction of gold nanoparticles with cultured cells at laser exposure. *Laser Phys. Lett.* 14:055901. doi: 10.1088/1612-202X/aa63ae

Boisselier, E., and Astruc, D. (2009). Gold nanoparticles in nanomedicine: preparations, imaging, diagnostics, therapies and toxicity. *Chem. Soc. Rev.* 38, 1759–1782. doi: 10.1039/B806051G

Borker, S., Patole, M., Moghe, A., and Pokharkar, V. (2016). Engineering of glycyrrhizin capped gold nanoparticles for liver targeting: in vitro evaluation and in vivo biodistribution study. *RSC Adv.* 6, 44944–44954. doi: 10.1039/C6RA05202A

Borkowska, M., Siek, M., Kolygina, D. V., Sobolev, Y. I., Lach, S., Kumar, S., et al. (2020). Targeted crystallization of mixed-charge nanoparticles in lysosomes induces selective death of cancer cells. *Nat. Nanotechnol.* 15, 331–341. doi: 10.1038/s41565-020-0643-3

Boyer, D., Tamarat, P., Maali, A., Lounis, B., and Orrit, M. (2002). Photothermal imaging of nanometer-sized metal particles among scatterers. *Science* 297, 1160–1163. doi: 10.1126/science.1073765

Brown, K. R., Walter, D. G., and Natan, M. J. (1999). Seeding of colloidal Au nanoparticle solutions. 2. improved control of particle size and shape. *Chem. Mater.* 12, 306–313. doi: 10.1021/cm980065p

Chandran, P. R., and Sandhyarani, N. (2014). An electric field responsive drug delivery system based on chitosan–gold nanocomposites for site specific and controlled delivery of 5-fluorouracil. *RSC Adv.* 4, 44922–44929. doi: 10.1039/C4RA07551J

Chen, H., Kou, X., Yang, Z., Ni, W., and Wang, J. (2008). Shape- and sizedependent refractive index sensitivity of gold nanoparticles. *Langmuir* 24, 5233–5237. doi: 10.1021/la800305j

Chen, J., Mela, P., Moller, P., and Lensen, M. C. (2009). Microcontact deprinting: a technique to pattern gold nanoparticles. *ACS Nano* 3, 1451–1456. doi: 10.1021/nn9002924

Chien, C. C., Chen, H. H., Lai, S. F., Hwu, Y., Petibois, C., Yang, C. S., et al. (2012). X-ray imaging of tumor growth in live mice by detecting gold-nanoparticle-loaded cells. *Sci. Rep.* 2:610. doi: 10.1038/srep00386

Cordeiro, M., Carlos, F. F., Pedrosa, P., Lopez, A., and Baptista, P. V. (2016). Gold nanoparticles for diagnostics: advances towards points of care. *Diagnostics* 6:43. doi: 10.3390/diagnostics6040043

Cormode, D. P., Naha, P. C., and Fayad, Z. A. (2014). Nanoparticle contrast agents for computed tomography: a focus on micelles. *Contrast Med. Mol. Imaging* 9, 37–52. doi: 10.1002/cmmi.1551

Correard, F., Maximova, K., Esteve, M. A., Villard, C., Roy, M., Al-Kattan, A., et al. (2014). Gold nanoparticles prepared by laser ablation in aqueous biocompatible solutions: assessment of safety and biological identity for nanomedicine applications. *Int. J. Nanomed.* 9, 5415–5430. doi: 10.2147/IJN.S65817

Dahoumane, S. A., Wujcik, E. K., and Jeffryes, C. (2016). Noble metal, oxide and chalcogenidebased nanomaterials from scalable phototrophic culture systems. *Enzyme Microb. Technol.* 95, 13–27. doi: 10.1016/j.enzmictec.2016.06.008

Dam, D. H., Culver, K. S., and Odom, T. W. (2014). Grafting aptamers onto gold nanostars increases *in vitro* efficacy in a wide range of cancer cell types. *Mol. Pharm.* 11, 580–587. doi: 10.1021/mp4005657

Dash, S. S., Majumdar, R., and Sikder, A. K. (2014). Saraca indicabark extract mediated green synthesis of polyshaped gold nanoparticles and its application in catalytic reduction. *Appl. Nanosci.* 4, 485–490. doi: 10.1007/s13204-013-0223-z

Ding, Y., Jiang, Z., Saha, K., Kim, C. S., Kim, S. T., Landis, R. F., et al. (2014). Gold nanoparticles for nucleic acid delivery. *Mol. Ther.* 22, 1075–1083. doi: 10.1038/mt.2014.30

Dreaden, E. C., Alkilany, A. M., Huang, X., Murphy, C. J., and El-Sayed, M. A. (2012). The golden age: gold nanoparticles for biomedicine. *Chem. Soc. Rev.* 41, 2740–2779. doi: 10.1039/C1CS15237H

Dubey, S. P., Lahtinen, M., and Sillanp, M. (2010). Green synthesis and characterizations of silver and gold nanoparticles using leaf extract of *Rosa rugosa*. *Colloids Surf. A Physicochem. Eng. Asp*. 364, 34–41. doi: 10.1016/j.colsurfa.2010.04.023

Duncan, B., Kim, C., and Rotello, V. M. (2010). Gold nanoparticle plateforms as drug and biomolecule delivery systems. *J. Control. Release* 148, 122–127. doi: 10.1016/j.jconrel.2010.06.004

Dutta, J., Naicker, T., Ebenhan, T., Kruger, H. G., Arvidsson, P. I., and Govender, T. (2017). Synthetic approaches to radiochemical probes for imaging of bacterial infections. *Eur. J. Med. Chem.* 133, 287–308. doi: 10.1016/j.ejmech.2017.03.060

El-Husseini, D. M., Helmy, N. M., and Tammam, R. H. (2016). The effect of gold nanoparticles on the diagnostic polymerase chain reaction technique for equine herpes virus 1 (EHV-1). *RSC Adv.* 6, 54898–54903. doi: 10.1039/C6RA08513J

Falagan-Lotsch, P., Grzincic, E. M., and Murphy, C. J. (2016). One low-dose exposure of gold nanoparticles induces long-term changes in human cells. *Proc. Natl. Acad. Sci. U.S.A.* 113, 13318–13323. doi: 10.1073/pnas.1616400113

Falahati, M., Attar, F., Sharifi, M., Saboury, A. A., Salihi, A., Aziz, F. M., et al. (2019). Gold nanomaterials as key suppliers in biological and chemical sensing, catalysis, and medicine. *Biochim. Biophys. Acta* 1864:129435. doi: 10.1016/j.bbagen.2019.129435

Faraday, M. (1857). Experimental relations of gold (and other metals) to light. *Philos. Trans. R. Soc.* 147, 145–181. doi: 10.1080/14786445708642410

Filip, G. A., Moldovan, B., Baldea, I., Olteanu, D., Suharoschi, R., Decea, N., et al. (2019). UV-light mediated green synthesis of silver and gold nanoparticles using Cornelian cherry fruit extract and their comparative effects in experimental inflammation. *J. Photochem. Photobiol. B Biol.* 191, 26–37. doi: 10.1016/j.jphotobiol.2018.12.006

Fleischmann, M., Hendra, P. J., and McQuillan, A. J. (1974). Raman spectra of pyridine adsorbed at a silver electrode. *Chem. Phys. Lett.* 26, 163–166. doi: 10.1016/0009-2614(74)85388-1

Frens, G. (1973). Controlled nucleation for the regulation of the particle size in monodisperse gold suspensions. *Nat. Phys. Sci.* 241, 20–22. doi: 10.1038/10.1038/physci241020a0

Fuller, M. A., and Köper, I. (2019). Biomedical applications of polyelectrolyte coated spherical gold nanoparticles. *Nano Converg.* 6:11. doi: 10.1186/s40580-019-0183-4

Gardea-Torresdey, J. L., Tiemann, K. J., Gamez, G., Dokken, K., Tehuacanero, S., and Jose-yacaman, M. (1999). Gold nanoparticles obtained by bio-precipitation from gold(III) solutions. *J. Nano Res.* 1, 397–404. doi: 10.1023/a:1010008915465

Garza, M., Hernández, T., Colás, R., and Gómez, I. (2010). Deposition of gold nanoparticles on glass substrate by ultrasonic spray pyrolysis. *Mater. Sci. Eng. B* 174, 9–12. doi: 10.1016/j.mseb.2010.03.068

González-Rubio, G., Guerrero-Martínez, A., and Liz-Marzán, L. M. (2016). Reshaping, fragmentation, and assembly of gold nanoparticles assisted by pulse lasers. *Acc. Chem. Res.* 49, 678–686. doi: 10.1021/acs.accounts.6b00041

Govindaraju, K., Basha, S. K., Kumar, V. G., and Singaravelu, G. (2008). Silver, gold and bimetallic nanoparticles production using single-cell protein (*Spirulina platensis*) Geitler. *J. Mater. Sci.* 43, 5115–5122. doi: 10.1007/s10853-008-2745-4

Gurav, D. D., Jia, Y. A., Ye, J., and Qian, K. (2019). Design of plasmonic nanomaterials for diagnostic spectrometry. *Nanoscale Adv.* 1, 459–469. doi: 10.1039/C8NA00319J

Hosta, L., Pla-Roca, M., Arbiol, J., Lopez-Iglesias, C., Samitier, J., Cruz, L. J., et al. (2009). Conjugation of Kahalalide F with gold nanoparticles to enhance in vitro antitumoral activity. *Bioconjug. Chem.* 20, 138–146. doi: 10.1021/bc800362j

Hu, R., Zheng, M., Wu, J., Li, C., Shen, D., Yang, D., et al. (2017). Core-shell magnetic gold nanoparticles for magnetic field-enhanced radio-photothermal therapy in cervical cancer. *Nanomaterials* 7:111. doi: 10.3390/nano7050111

Huang, C. C., Liao, H. Y., Shiang, Y. C., Lin, Z. H., Yang, Z. S., and Chang, H. T. (2009). Synthesis of wavelength-tunable luminescent gold and gold/silver nanodots. *J. Mater. Chem.* 19, 755–759. doi: 10.1039/B808594C

Imanparast, A., Bakhshizadeh, M., Salek, R., and Sazgarnia, A. (2018). Pegylated hollow goldmitoxantrone nanoparticles combining photodynamic therapy and chemotherapy of cancer cells. *Photodiagnosis Photodyn. Ther.* 23, 295–305. doi: 10.1016/j.pdpdt.2018.07.011

Jain, N., Bhargava, A., Majumdar, S., Tarafdar, J. C., and Panwar, J. (2011). Extracellular biosynthesis and characterization of silver nanoparticles using *Aspergillus flavus* NJP08: a mechanism perspective. *Nanoscale* 3, 635–641. doi: 10.1039/c0nr00656d

Jana, N. R., Gearheart, L., and Murphy, C. J. (2001). Seeding growth for size control of 5-40nm diameter gold nanoparticles. *Langmuir* 17, 6782–6786. doi: 10.1021/la0104323

Jain, S., Coulter, J. A., Hounsell, A. R., Butterworth, K. T., Mcmahon, S. J., Hyland, W. B., et al. (2011). Cell-specific radiosensitization by gold nanoparticles at megavoltage radiation energies. *Int. J. Radiat. Oncol. Biol. Phys. Int.* 79, 531–539. doi: 10.1016/j.ijrobp.2010.08.044

Jeynes, J. C. G., Merchant, M. J., Spindler, A., Wera, A. C., and Kirkby, K. J. (2014). Investigation of gold nanoparticle radiosensitization mechanisms using a free radical scavenger and protons of different energies. *Phys. Med. Biol.* 59, 6431–6443. doi: 10.1088/0031-9155/59/21/6431

Ji, X., Song, X., Li, J., Bai, Y., Yang, W., and Peng, X. (2007). Size Control of Gold Nanocrystals in citrate reduction: the third role of citrate. *J. Am. Chem. Soc.* 129, 13939–13948. doi: 10.1021/ja074447k

Jimenez, I. O., Romero, F. M., Bastus, N. G., and Puntes, V. (2010). Small gold nanoparticles synthesized with sodium citrate and heavy water: insights into the reaction mechanism. *J. Phys. Chem. C* 114, 1800–1804. doi: 10.1021/jp9091305

Jing, H., Zhang, Q., Large, N., Yu, C., Blom, D. A., Nordlander, P., et al. (2014). Tunable plasmonic nanoparticles with catalytically active high-index facets. *Nano Lett.* 14, 3674–3682. doi: 10.1021/nl5015734

Joshi, H. M., Bhumkar, D. R., Joshi, K., Pokharkar, V., and Sastry, M. (2006). Gold nanoparticles as carriers for efficient transmucosal insulin delivery. *Langmuir* 22, 300–305. doi: 10.1021/la051982u

Kajani, A. A., Bordbar, A.-K., Zarkesh Esfahani, S. H., and Razmjou, A. (2016). Gold nanoparticles as potent anticancer agent: green synthesis, characterization, and in vitro study. *RSC Adv.* 6, 63973–63983. doi: 10.1039/C6RA09050H

Kasthuri, J., Veerapandian, S., and Rajendiran, N. (2008). Biological synthesis of silver and gold nanoparticles using apiin as reducing agent. *Colloids Surf. B Biointerfaces* 68, 55–60. doi: 10.1016/j.colsurfb.2008.09.021

Kawata, S., Ichimura, T., Taguchi, A., and Kumamoto, Y. (2017). Nano-raman scattering microscopy: resolution and enhancement. *Chem. Rev.* 117, 4983–5001. doi: 10.1021/acs.CheMrev.6b00560

Khan, I., Saeed, K., and Khan, I. (2017). Nanoparticles: properties, applications and toxicities. *Arab. J. Chem.* 12, 908–931. doi: 10.1016/j.arabjc.2017.05.011

Khan, T., Ullah, N., Khan, M. A., Mashwani, Z. R., and Nadhman, A. (2019). Plant-based gold nanoparticles: a comprehensive review of the decade-long research on synthesis, mechanistic aspects and diverse applications. *Adv. Colloid Int. Sci.* 272:102017. doi: 10.1016/j.cis.2019.102017

Khanna, P., Kaur, A., and Goyal, D. (2019). Algae-based metallic nanoparticles: synthesis, characterization and applications. *J. Microbiol. Methods* 163:105656. doi: 10.1016/j.mimet.2019.105656

Kim, D., Park, S., Lee, J. H., Jeong, Y. Y., and Jon, S. (2007). Antibiofouling polymer-coated gold nanoparticles as a contrast agent for in vivo X-ray computed tomography imaging. *J. Am. Chem. Soc.* 129, 7661–7665. doi: 10.1021/ja076341v

Kim, H. S., and Lee, D. Y. (2018). Near-infrared-responsive cancer photothermal and photodynamic therapy using gold nanoparticles. *Polymers* 10:961. doi: 10.3390/polym10090961

Klebowski, B., Depciuch, J., Parlińska-Wojtan, M., and Baran, J. (2018). Applications of noble metal-based nanoparticles in medicine. *Int. J. Mol. Sci.* 19:4031. doi: 10.3390/ijms19124031

Kumar, S. A., Chang, Y. T., Wang, S. F., and Lu, H. C. (2010). Synthetic antibacterial agent assisted synthesis of gold nanoparticles: characterization and application studies. *J. Phys. Chem. Solids* 71, 1484–1490. doi: 10.1016/j.jpcs.2010.07.015

Kwatra, D., Venugopal, A., and Anant, S. (2013). Nanoparticles in radiation therapy: a summary of various approaches to enhance radiosensitization in cancer. *Transl. Cancer Res.* 2, 330–342. doi: 10.3978/j.issn.2218-676X.2013.08.06

Le, G. M., Paquirissamy, A., Gargouri, D., Fadda, G., Testard, F., Aymes-Chodur, C., et al. (2019). Irradiation effects on polymer-grafted gold nanoparticles for cancer therapy. *ACS Appl. Bio Mater.* 2, 144–154. doi: 10.1021/acsabm.8b00484

Lee, J., Lee, S. Y., Lim, D. K., Ahn, D. J., and Lee, S. (2019). Antifreezing gold colloids. *J. Am. Chem. Soc.* 141, 18682–18693. doi: 10.1021/jacs.9b05526

Leff, D. V., Ohara, P. C., Heath, J. R., and Gelbart, W. M. (1995). Thermodynamic control of gold nanocrystal size: experiment and theory. *J. Phys. Chem.* 99, 7036–7041. doi: 10.1021/j100018a041

Leonov, A. P., Zheng, J., Clogston, J. D., Stern, S. T., Patri, A. K., and Wei, A. (2008). Detoxification of gold nanorods by treatment with polystyrenesulfonate. *ACS Nano* 2, 2481–2488. doi: 10.1021/nn800466c

Li, C., Hsieh, J. H., Hung, M., Huang, B. Q., Song, Y. L., Denayer, J., et al. (2004). Ultrasonic spray pyrolysis for nanoparticles synthesis. *J. Mater. Sci.* 9, 3647–3657. doi: 10.1023/b:jmsc.0000030718.76690.11

Li, H., Ma, X., Dong, J., and Qian, W. (2009). Development of methodology based on the formation process of gold nanoshells for detecting hydrogen peroxide scavenging activity. *Anal. Chem.* 81, 8916–8922. doi: 10.1021/ac901534b

Li, S., Zhang, L., Wang, T., Li, L., Wang, C., and Su, Z. (2015). The facile synthesis of hollow Au nanoflowers for synergistic chemo-photothermal cancer therapy. *Chem. Commun.* 51, 14338–14341. doi: 10.1039/C5CC05676D

Lin, X., Liu, S., Zhang, X., Zhu, R., and Yang, H. (2019). Ultrasound activated vesicle of janus au-mno nanoparticles for promoted tumor penetration and sono-chemodynamic therapy of orthotopic liver cancer. *Angew. Chem. Int. Ed. Engl.* 59, 1682–1688. doi: 10.1002/anie.201912768

Link, S., and El-Sayed, M. A. (2003). Optical properties and ultrafast dynamics of metallic nanocrystals. *Annu. Rev. Phys. Chem.* 54, 331–366. doi: 10.1146/annurev.physchem.54.011002.103759

Liu, C., Jia, Q., Yang, C., Qiao, R., Jing, L., and Wang, L. X. (2011). Lateral flow immunochromatographic assay for sensitive pesticide detection by using Fe3O4 nanoparticle aggregates as color reagents. *Anal. Chem.* 83, 6778–6784. doi: 10.1021/ac201462d

Liu, C., Li, S., Gu, Y., Xiong, H., Wong, W., and Sun, L. (2018). Multispectral photoacoustic imaging of tumor protease activity with a gold nanocage-based activatable probe. *Mol. Imaging Biol.* 20, 919–929. doi: 10.1007/s11307-018-1203-1

Loynachan, C., Soleimany, A. P., Dudani, J. S., Lin, Y., Najer, A., Bekdemir, A., et al. (2019). Renal clearable catalytic gold nanoclusters for in vivo disease monitoring. *Nat. Nanotechnol.* 14, 883–890. doi: 10.1038/s41565-019-0527-6

Lu, L., Sun, G., Zhang, H., Wang, H., Xi, S., Hu, J., et al. (2004). Fabrication of core-shell Au-Pt nanoparticle film and its potential application as catalysis and SERS substrate. *J. Mater. Chem.* 14, 1005–1009. doi: 10.1039/B314868H

Luo, J., Deng, W., Yang, F., Wu, Z., Huang, M., and Gu, M. (2018). Gold nanoparticles decorated graphene oxide/nanocellulose paper for NIR laser-induced photothermal ablation of pathogenic bacteria. *Carbohydr. Polymers* 198, 206–214. doi: 10.1016/j.carbpol.2018.06.074

Lusic, H., and Grinstaff, M. K. (2013). X-ray-Computed Tomography contrast agents. *Chem. Rev.* 113, 1641–1666. doi: 10.1021/cr200358s

Mackey, M. A., Ali, M. R. K., Austin, L. A., Near, R. D., and El-Sayed, M. A. (2014). The most effective gold nanorod size for plasmonic photothermal therapy: theory and in vitro experiments. *J. Phys. Chem. B* 118, 1319–1326. doi: 10.1021/jp409298f

Marquis, B. J., Love, S. A., Braun, K. L., and Haynes, C. L. (2009). Analytical methods to assess nanoparticle toxicity. *Analyst* 134, 425–439. doi: 10.1039/b818082b

Martinho, N., Damgé, C., and Reis, C. P. (2011). Recent advances in drug delivery systems. *J. Biomater. Nanobiotechnol.* 2, 510–526. doi: 10.4236/jbnb.2011.225062

McMahon, S. J., Hyland, W. B., Muir, M. F., Coulter, J. A., Jain, S., Butterworth, K. T., et al. (2011). Nanodosimetric effects of gold nanoparticles in megavoltage radiation therapy. *Radiother. Oncol.* 100, 412–416. doi: 10.1016/j.radonc.2011.08.026

Meir, R., and Popovtzer, R. (2018). Cell tracking using gold nanoparticles and computed tomography imaging. *Wiley Int. Rev. Nanomed. Nanobiotechnol.* 10:e1480. doi: 10.1002/wnan.1480

Morita, M., Tachikawa, T., Seino, S., Tanaka, K., and Majima, T. (2017). Controlled synthesis of gold nanoparticles on fluorescent nanodiamond via electron-beam-induced reduction method for dual-modal optical and electron bioimaging. *ACS Appl. Nano Mater.* 1, 355–363. doi: 10.1038/srep44495

Mubarakali, D., Thajuddin, N., Jeganathan, K., and Gunasekaran, M. (2011). Plant extract mediated synthesis of silver and gold nanoparticles and its antibacterial activity against clinically isolated pathogens. *Colloids Surf. B Biointerfaces* 85, 360–365. doi: 10.1016/j.colsurfb.2011.03.009

Murphy, C. J., Thompson, L. B., Alkilany, A. M., Sisco, P. N., Boulos, S. P., Stivapalan, S. T., et al. (2010). The many faces of gold nanorods. *J. Phys. Chem. Lett.* 1, 2867–2875. doi: 10.1021/Jz100992x

Natan, M. J., and Brown, K. R. (1998). Hydroxylamine seeding of colloidal au nanoparticles in solution and on surfaces. *Langmuir* 14, 726–728. doi: 10.1021/la970982u

Ni, C., Zhou, J., Kong, N., Bian, T., Zhang, Y., Huang, X., et al. (2019). Gold nanoparticles modulate the crosstalk between macrophages and periodontal ligament cells for periodontitis treatment. *Biomaterials* 206, 115–132. doi: 10.1016/j.biomaterials.2019.03.039

Nie, W., Zhang, Y., Yu, H., Li, R., He, R., Dong, N., et al. (2018). Plasmonic nanoparticles embedded in single crystals synthesized by gold ion implantation for enhanced optical nonlinearity and efficient Q-switched lasing. *Nanoscale* 10, 4228–4236. doi: 10.1039/C7NR07304F

Nishanthi, R., Malathi, S., Paul, J. S., and Palani, P. (2019). Green synthesis and characterization of bioinspired silver, gold and platinum nanoparticles and evaluation of their synergistic antibacterial activity after combining with different classes of antibiotics. *Mater. Sci. Eng. C* 96, 693–707. doi: 10.1016/j.msec.2018.11.050

O'Neal, D. P., Hirsch, L. R., Halas, N. J., Payne, J. D., and West, J. L. (2004). Photothermal tumor ablation in mice using near infrared-absorbing nanoparticles. *Cancer Lett.* 209, 171–176. doi: 10.1016/j.canlet.2004.02.004

Orendorff, C. J., Sau, T. K., and Murphy, C. J. (2006). Shape-dependent plasmon-resonant gold nanoparticles. *Small* 2, 636–639. doi: 10.1002/smll.200500299

Ou, J., Zhou, Z., Chen, Z., and Tan, H. (2019). Optical diagnostic based on functionalized gold nanoparticles. *Int. J. Mol. Sci.* 20:4346. doi: 10.3390/ijms20184346

Philip, A., Ankudze, B., and Pakkanen, T. T. (2018). Polyethylenimine-assisted seed-mediated synthesis of gold nanoparticles for surface-enhanced Raman scattering studies. *Appl. Surf. Sci.* 444, 243–252. doi: 10.1016/j.apsusc.2018.03.042

Piktel, E., Niemirowicz, K., Watek, M., Wollny, T., Deptuła, P., and Bucki, R. (2016). Recent insights in nanotechnology-based drugs and formulations designed for effective anti-cancer therapy. *J. Nanobiotechnol.* 14:39. doi: 10.1186/s12951-016-0193-x

Pissuwan, D., Camilla, G., Mongkolsuk, S., and Cortie, M. B. (2019). Single and multiple detections of foodborne pathogens by gold nanoparticle assays. *WIREs Nanomed. Nanobiotechnol.* 12:1584. doi: 10.1002/wnan.1584

Podsiadlo, P., Sinani, V. A., Bahng, J. H., Kam, N. W. S., Lee, J., and Kotov, N. A. (2008). Gold nanoparticles enhance the anti-Leukemia action of a 6-Mercaptopurine chemotherapeutic agent. *Langmuir* 24, 568–574. doi: 10.1021/la702782k

Poinern, G. E. J. (2014). *A Laboratory Course in Nanoscience and Nanotechnology*. Boca Raton, FL: CRC Press. doi: 10.1080/00107514.2015.1133713

Prema, P., Iniya, P. A., and Immanuel, G. (2015). Microbial mediated synthesis, characterization, antibacterial and synergistic effect of gold nanoparticles using *Klebsiella pneumoniae* (MTCC-4030). *RSC Adv.* 6, 4601–4607. doi: 10.1039/C5RA23982F

Quester, K., Avalos-Borja, M., and Castro-Longoria, E. (2013). Biosynthesis and microscopicstudy of metallic nanoparticles. *Micron* 54, 1–27. doi: 10.1016/j.micron.2013.07.003

Rahman, W. N., Geso, M., Yagi, N., Abdul Aziz, S. A., Corde, S., and Annabell, N. (2014). Optimal energy for cell radiosensitivity enhancement by gold nanoparticles using synchrotronbased monoenergetic photon beams. *Int. J. Nanomed.* 9, 2459–2467. doi: 10.2147/IJN.S59471

Ramalingam, V. (2019). Multifunctionality of gold nanoparticles: plausible and convincing properties. *Adv. Colloid Int. Sci.* 271:101989. doi: 10.1016/j.cis.2019.101989

Ramalingam, V., Raja, S., Sundaramahalingam, T. S., and Rajaram, R. (2019). Chemical fabrication of graphene oxide nanosheets attenuates biofilm formation of human clinical pathogens. *Bioorg. Chem.* 83, 326–335. doi: 10.1016/j.bioorg.2018.10.052

Ramalingam, V., Rajaram, R., Premkumar, C., Santhanam, P., Dhinesh, P., Vinothkumar, S., et al. (2014). Biosynthesis of silver nanoparticles from deep sea bacterium *Pseudomonas aeruginosa* JQ989348 for antimicrobial, antibiofilm, and cytotoxic activity. *J. Basic Microbiol.* 54, 928–936. doi: 10.1002/jobm.201300514

Ramalingam, V., Revathidevi, S., Shanmuganayagam, T. S., Muthulakshmi, L., and Rajaram, R. (2017). Gold nanoparticle induces mitochondria-mediated apoptosis and cell cycle arrest in nonsmall cell lung cancer cells. *Gold Bull.* 50, 177–189. doi: 10.1007/s13404-017-0208-x

Ray, T. R., Lettiere, B., De Rutte, J., and Pennathur, S. (2015). Quantitative characterization of the colloidal stability of metallic nanoparticles using uv-vis absorbance spectroscopy. *Langmuir* 31, 3577–3586. doi: 10.1021/la504511j

Retif, P., Pinel, S., Toussaint, M., Frochot, C., Chouikrat, R., Bastogne, T., et al. (2015). Nanoparticles for radiation therapy enhancement: the key parameters. *Theranostics* 5, 1030–1044. doi: 10.7150/thno.11642

Riedel, R., Mahr, N., Yao, C., Wu, A., Yang, F., and Hampp, N. (2020). Synthesis of gold-silica core-shell nanoparticles by pulsed laser ablation in liquid and their physico-chemical properties towards photothermal cancer therapy. *Nanoscale* 12, 3007–3018. doi: 10.1039/C9NR07129F

Rigon, R. B., Oyafuso, M. H., Fujimura, A. T., Goncalez, M. L., do Prado, A. H., Daflon-Gremiao, M. P., et al. (2015). Nanotechnology-based drug delivery systems for melanoma antitumoral therapy: a review. *Biomed Res. Int.* 2015:841817. doi: 10.1155/2015/841817

Riley, M. K., and Vermerris, W. (2017). Recent advances in nanomaterials for gene delivery-a review. *Nanomaterials* 7:94. doi: 10.3390/nano7050094

Rodriguez-Fernandez, J., Perez-Juste, J., Garcia de Abajo, F. J., and Liz-Marzan, L. M. (2006). Seeded growth of submicron Au colloids with quadrupole plasmon resonance modes. *Langmuir* 22, 7007–7010. doi: 10.1021/la060990n

Roduner, E. (2006). Size matters: why nanomaterials are different. *Chem. Soc. Rev.* 35, 583–592. doi: 10.1039/b502142c

Rossi, A., Donati, S., Fontana, L., Porcaro, F., Battocchio, C., Proietti, E., et al. (2016). Negatively charged gold nanoparticles as a dexamethasone carrier: stability in biological media and bioactivity assessment *in vitro*. *RSC Adv.* 6, 99016–99022. doi: 10.1039/C6RA19561J

Sabella, S., Carney, R. P., Brunetti, V., Malvindi, M. A., Al-Juffali, N., Vecchio, G., et al. (2014). A general mechanism for intracellular toxicity of metal-containing nanoparticles. *Nanoscale* 6, 7052–7061. doi: 10.1039/c4nr01234h

Saha, B., Bhattacharya, J., Mukherjee, A., Ghosh, A. K., Santra, C. R., Dasgupta, A. K., et al. (2007). *In vitro* structural and functional evaluation of gold nanoparticles conjugated antibiotics. *Nanoscale Res. Lett*. 2, 614–622. doi: 10.1007/s11671-007-9104-2

Sant, S., Tao, S. L., Fisher, O. Z., Xu, Q., Peppas, N. A., and Khademhosseini, A. (2012). Microfabrication technologies for oral drug delivery. *Adv. Drug. Deliv. Rev.* 64, 496–507. doi: 10.1016/j.addr.2011.11.013

Shah, M., Fawcett, D., Sharma, S., Tripathy, S. K., and Poinern, G. E. J. (2015). Green synthesis of metallic nanoparticles via biological entities. *Materials* 8, 7278–7308. doi: 10.3390/ma8115377

Shahbazi, R., Sghia-Hughes, G., Reid, J. L., Kubek, S., Haworth, K. G., Humbert, O., et al. (2019). Targeted homology-directed repair in blood stem and progenitor cells with CRISPR nanoformulations. *Nat. Mater.* 18, 1124–1132. doi: 10.1038/s41563-019-0385-5

Sharifi, M., Attar, F., Saboury, A. A., Akhtari, K., Hooshmand, N., Hasan, A., et al. (2019). Plasmonic gold nanoparticles: optical manipulation, imaging, drug delivery and therapy. *J. Control. Release* 31, 170–189. doi: 10.1016/j.jconrel.2019.08.032

Sharma, A., Sharma, S., Sharma, K., Chetri, S. P., Vashishtha, A., Singh, P., et al. (2016). Algae as crucial organisms in advancing nanotechnology: a systematic review. *J. Appl. Phycol.* 28, 1759–1774. doi: 10.1007/s10811-015-0715-1

Shukla, A. K., and Iravani, S. (2017). Metallic nanoparticles: green synthesis and spectroscopic characterization. *Environ. Chem. Lett.* 15, 223–231. doi: 10.1007/s10311-017-0618-2

Shukla, R., Bansal, V., Chaudhary, M., Basu, A., Bhonde, R. R., and Sastry, M. (2005). Biocompatibility of gold nanoparticles and their endocytotic fate inside the cellular compartment: a microscopic overview. *Langmuir* 21, 10644–10654. doi: 10.1021/la0513712

Singaravelu, G., Arockiamary, J. S., Kumar, V. G., and Govindaraju, K. (2007). Anovel extracellular synthesis of monodisperse gold nanoparticles using marine alga, Sargassum wightii Greville. *Colloids Surf. B Biointerfaces* 57, 97–101. doi: 10.1016/j.colsurfb.2007.01.010

Singh, A. K., Senapati, D., Wang, S., Griffin, J., Neely, A., Candice, P., et al. (2009). Gold nanorod based selective identification of *Escherichia coli* bacteria using two-photon Rayleigh scattering spectroscopy. *ACS Nano* 3, 1906–1912. doi: 10.1021/nn9005494

Singh, P., Kim, Y. J., Wang, C., Mathiyalagan, R., and Yang, D. C. (2016a). The development of a green approach for the biosynthesis of silver and gold nanoparticles by using *Panax ginseng* root extract, and their biological applications. *Artif. Cells Nanomed. Biotechnol.* 44, 1150–1157. doi: 10.3109/21691401.2015.1011809

Singh, P., Pandit, S., Mokkapati, V. R. S. S., Garg, A., Ravikumar, V., and Mijakovic, I. (2018). Gold nanoparticles in diagnostics and therapeutics for human cancer. *Int. J. Mol. Sci.* 19:1979. doi: 10.3390/ijms19071979

Singh, P., Singh, H., Kim, Y. J., Mathiyalagan, R., Wang, C., and Yang, D. C. (2016b). Extracellular synthesis of silver and gold nanoparticles by *Sporosarcina koreensis* DC4 and their biological applications. *Enzyme Microb. Technol.* 86, 75–83. doi: 10.1016/j.enzmictec.2016.02.005

Singh, R. K., Kurian, A. G., Patel, K. D., Mandakhbayar, N., Knowles, J. C., Kim, H. W., et al. (2020). Label-free fluorescent mesoporous bioglass for drug delivery, optical triple-mode imaging, and photothermal/photodynamic synergistic cancer therapy. *ACS Appl. Bio Mater.* 2020, 2218–2229. doi: 10.1021/acsabm.0c00050

Singh, R. K., Patel, K. D., Leong, K. W., and Kim, H. W. (2017). Progress in nanotheranostics based on mesoporous silica nanomaterial platforms. *ACS Appl. Mater Inter.* 9, 10309–10337. doi: 10.1021/acsami.6b16505

Sivaraj, M., Mukherjee, A., Mariappan, R., Mariadoss, A. V., and Jeyaraj, M. (2018). Polyorganophosphazene stabilized gold nanoparticles for intracellular drug delivery in breast carcinoma cells. *Process Biochem.* 72, 152–161. doi: 10.1016/j.procbio.2018.06.006

Slocik, J. M., Stone, M. O., and Naik, R. R. (2005). Synthesis of gold nanoparticles using multifunctional peptides. *Small* 1, 1048–1052. doi: 10.1002/smll.200500172

Smitha, S. L., Philip, D., and Gopchandran, K. G. (2009). Green synthesis of gold nanoparticles using *Cinnamomum zeylanicum* leaf broth. *Spectrochim. Acta Part A* 74, 735–739. doi: 10.1016/j.saa.2009.08.007

Sztandera, K., Gorakiewicz, M., and Klajnert-Maculewicz, B. (2019). Gold nanoparticles in cancer treatment. *Mol. Pharm.* 16, 1–23. doi: 10.1021/acs.molpharmaceut.8b00810

Tahir, K., Nazir, S., Li, B., Khan, A. U., Khan, Z. U. H., Gong, P. Y., et al. (2015). Nerium oleander leaves extract mediated synthesis of gold nanoparticles and its antioxidant activity. *Mater. Lett.* 156, 198–201. doi: 10.1016/j.matlet.2015.05.062

Tao, C., An, Q., Zhu, W., Yang, H., Li, W., Lin, C. X., et al. (2011). Cucurbit[n]urils as a SERS hot-spot nanocontainer through bridging gold nanoparticles. *Chem. Commun.* 47, 9867–9869. doi: 10.1039/C1CC12474A

Tayo, L. L. (2017). Stimuli-responsive nanocarriers for intracellular delivery. *Biophys. Rev.* 9, 931–940. doi: 10.1007/s12551-017-0341-z

Terentyuk, G., Panfilova, E., Khanadeev, V., Chumakov, D., Genina, E., Bashkatov, A., et al. (2014). Gold nanorods with a hematoporphyrin-loaded silica shell for dual-modality photodynamic and photothermal treatment of tumors *in vivo*. *Nano Res.* 7, 325–337. doi: 10.1007/s12274-013-0398-3

Tian, Y., Zhang, Y., Teng, Z., Tian, W., Luo, S., Kong, X., et al. (2017). PH-dependent transmembrane activity of peptide-functionalized gold nanostars for computed tomography/photoacoustic imaging and photothermal therapy. *ACS Appl. Mater. Interfaces* 9, 2114–2122. doi: 10.1021/acsami.6b13237

Turkevich, J., Stevenson, P. C., and Hillier, J. (1951). A study of the nucleation and growth processes in the synthesis of colloidal gold. *Dis. Fara Soc.* 11, 55–75. doi: 10.1039/DF9511100055

Ullah, H., Khan, I., Yamani, Z. H., and Qurashi, A. (2017). Sonochemical-driven ultrafast facile synthesis of SnO2nanoparticles: growth mechanism structural electrical and hydrogen gas sensing proper-ties. *Ultrason. Sonochem.* 34, 484–490. doi: 10.1016/j.ultsonch.2016.06.025

Venditti, I. (2017). Gold nanoparticles in photonic crystals applications: a review. *Materials* 10:97. doi: 10.3390/ma10020097

Venditti, I. (2019). Engineered gold-based nanomaterials: morphologies and functionalities in biomedical applications. A mini review. *Bioengineering* 6:53. doi: 10.3390/bioengineering6020053

Venkatesan, R., Pichaimani, A., Hari, K., Balasubramanian, P. K., Kulandaivel, J., and Premkumar, K. (2013). Doxorubicin conjugated gold nanorods: a sustained drug delivery carrier for improved anticancer therapy. *J. Mater. Chem. B* 1, 1010–1018. doi: 10.1039/C2TB00078D

Vinod, M., Jayasree, R. S., and Gopchandran, K. G. (2017). Synthesis of pure and biocompatible gold nanoparticles using laser ablation method for SERS and photothermal applications. *Curr. Appl. Phys.* 17, 1430–1438. doi: 10.1016/j.cap.2017.08.004

Walters, G., and Parkin, P. I. (2009). The incorporation of noble metal nanoparticles into host matrix thin films: synthesis, characterisation and applications. *J. Mater. Chem.* 19, 574–590. doi: 10.1039/B809646E

Wang, B., Wang, J.-H., Liu, Q., Huang, H., Chen, M., Li, K., et al. (2014). Rose-Bengal-conjugated gold nanorods for in vivo photodynamic and photothermal oral cancer therapies. *Biomaterials* 35, 1954–1966. doi: 10.1016/j.biomaterials.2013.11.066

Wang, Z., Chen, Q., Zhong, Y., Yu, X., Wu, Y., and Fu, F. (2020). A multicolor immunosensor for sensitive visual detection of breast cancer biomarker based on sensitive nadh-ascorbic-acid-mediated growth of gold nanobipyramids. *Anal. Chem.* 92, 1534–1540. doi: 10.1021/acs.analchem.9b04828

Wani, I. A., and Ahmad, T. (2013). Size and shape dependant antifungal activity of gold nanoparticles: a case study of Candida. *Colloids Surf. B Biointerfaces* 101, 162–170. doi: 10.1016/j.colsurfb.2012.06.005

Wieder, M. E., Hone, D. C., Cook, M. J., Handsley, M. M., Gavrilovic, J., and Russell, D. A. (2006). Intracellular photodynamic therapy with photosensitizer-nanoparticle conjugates: cancer therapy using a 'Trojan horse.'. *Photochem. Photobiol. Sci.* 5, 727–734. doi: 10.1039/b602830f

Wójcik, M., Lewandowski, W., Król, M., Pawłowski, K., Mieczkowski, J., Lechowski, R., et al. (2015). Enhancing anti-tumor efficacy of doxorubicin by non-covalent conjugation to gold nanoparticles-in vitro studies on feline fibrosarcoma cell lines. *PLoS One* 10:e0124955. doi: 10.1371/journal.pone.0124955

Wu, Y., Wang, H., Gao, F., Xu, Z., Dai, F., and Liu, W. (2018). An injectable supramolecular polymer nanocomposite hydrogel for prevention of breast cancer recurrence with theranostic and mammoplastic functions. *Adv. Funct. Mater.* 28:1801000. doi: 10.1002/adfm.201801000

Xiao, T., Huang, J., Wang, D., Meng, T., and Yang, X. (2019). Au and Au-Based nanomaterials: synthesis and recent progress in electrochemical sensor applications. *Talanta* 206:120210. doi: 10.1016/j.talanta.2019.120210

Xu, X., Chong, Y., Liu, X., Fu, H., Yu, C., Huang, J., et al. (2019). Multifunctional nanotheranostic gold nanocages for photoacoustic imaging guided radio/photodynamic/photothermal synergistic therapy. *Acta Biomater.* 84, 328–338. doi: 10.1016/j.actbio.2018.11.043

Yang, J., Wang, Z., Zong, S., Song, C., Zhang, R., and Cui, Y. (2012). Distinguishing breast cancer cells using surface-enhanced Raman scattering. *Anal. Bioanal. Chem.* 402, 1093–1100. doi: 10.1007/s00216-011-5577-z

Yang, Y., Hu, Y., Du, H., Ren, L., and Wang, H. (2018). Colloidal plasmonic gold nanoparticles and gold nanorings: shape-dependent generation of singlet oxygen and their performance in enhanced photodynamic cancer therapy. *Int. J. Nanomed.* 13, 2065–2078. doi: 10.2147/IJN.S156347

Yin, D., Li, X., Ma, Y., and Liu, Z. (2017). Targeted cancer imaging and photothermal therapy via monosaccharide-imprinted gold nanorods. *Chem. Commun.* 53, 6716–6719. doi: 10.1039/c7cc02247f

Yokoyama, M. (2014). Polymeric micelles as drug carriers: their lights and shadows. *J. Drug Target.* 22, 576–583. doi: 10.3109/1061186X.2014.934688

Yu, Q., Li, J., Zhang, Y., Wang, Y., Liu, L., and Li, M. (2016). Inhibition of gold nanoparticles (AuNPs) on pathogenic biofilm formation and invasion to host cells. *Sci. Rep.* 6:26667. doi: 10.1038/srep26667

Yu, S., Wen, R., Wang, H., Zha, Y., Qiu, L., Li, B., et al. (2019). Chitosan-graft-poly(L-lysine) dendron-assisted facile self-assembly of Au nanoclusters for enhanced X-ray computer tomography imaging and precise MMP-9 plasmid shRNA delivery. *Chem. Mater.* 31, 3992–4007. doi: 10.1021/acs.chemmater.9b00507

Yun, S. H., Sohn, B. H., Jumg, J. C., Zin, W. C., Ree, M., and Park, J. W. (2006). Micropatterning of a single layer of nanoparticles by lithographical methods with diblock copolymer micelles. *Nanotechnology* 17, 450–454. doi: 10.1088/0957-4484/17/2/018

Zheng, J., Peng, C., Xu, J., Yu, M., Ning, X., Huang, Y., et al. (2019). Tuning in vivo transport of anticancer drugs with renal-clearable gold nanoparticles. *Angew. Chem. Int. Ed. Engl.* 58, 8479–8483. doi: 10.1002/anie.201903256

Zheng, Y., Zhang, Y., Zhang, T., Cai, H., Xie, X., Yang, Y., et al. (2020). AuNSs@Glycopolymer-ConA hybrid nanoplatform for photothermal therapy of hepatoma cells. *Chem. Eng. J.* 389:124460. doi: 10.1016/j.cej.2020.124459

Zhou, J., Cao, Z., Panwar, N., Hu, R., Wang, X., Qu, J., et al. (2017). Functionalized gold nanorods for nanomedicine: past, present and future. *Coordin. Chem. Rev.* 352, 15–66. doi: 10.1016/j.ccr.2017.08.020

Conflict of Interest: The authors declare that the research was conducted in the absence of any commercial or financial relationships that could be construed as a potential conflict of interest.

frontiers
in Bioengineering and Biotechnology

ORIGINAL RESEARCH
published: 18 August 2020
doi: 10.3389/fbioe.2020.00888

Strontium Modified Calcium Sulfate Hemihydrate Scaffold Incorporating Ginsenoside Rg1/Gelatin Microspheres for Bone Regeneration

Peng Luo[1,2†], Lan Yu[3†], Qiang Lin[4], Changde Wang[5], Dazhi Yang[1,2*] and Shuo Tang[6*]

[1] Department of Orthopaedics, Huazhong University of Science and Technology Union Shenzhen Hospital (Nanshan Hospital), Shenzhen, China, [2] Department of Orthopaedics, The 6th Affiliated Hospital of Shenzhen University Health Science Center, Shenzhen, China, [3] Department of Laboratory, Huazhong University of Science and Technology Union Shenzhen Hospital (Nanshan Hospital), Shenzhen, China, [4] Department of Orthopaedics, Guangdong Hospital of Traditional Chinese Medicine, Guangzhou, China, [5] Department of Geriatric Orthopeadics, Shenzhen Pingle Orthopaedic Hospital, Shenzhen, China, [6] Department of Orthopaedics, The Eighth Affiliated Hospital, Sun Yat-sen University, Shenzhen, China

Edited by:
Gang Wu,
VU University Amsterdam, Netherlands

Reviewed by:
Shun Duan,
Beijing University of Chemical Technology, China
Wei Wang,
Tianjin University, China

***Correspondence:**
Dazhi Yang
dazhiyang@email.szu.edu.cn
Shuo Tang
tangshuo1205@163.com

† These authors have contributed equally to this work

Specialty section:
This article was submitted to Biomaterials, a section of the journal Frontiers in Bioengineering and Biotechnology

Received: 18 March 2020
Accepted: 10 July 2020
Published: 18 August 2020

Citation:
Luo P, Yu L, Lin Q, Wang C, Yang D and Tang S (2020) Strontium Modified Calcium Sulfate Hemihydrate Scaffold Incorporating Ginsenoside Rg1/Gelatin Microspheres for Bone Regeneration. Front. Bioeng. Biotechnol. 8:888. doi: 10.3389/fbioe.2020.00888

The aim of this study was to prepare a promising biomaterial for bone tissue repair and regeneration. The Strontium – calcium sulfate hemihydrate (Sr-α-CaS) scaffold incorporating gelatin microspheres (GMs) encapsulated with Ginsenoside Rg1 (Rg1) was designed. The scaffolds of Rg1/GMs/Sr-α-CaS showed sustained release of Rg1, good biocompatibility and ability of promoting osteogenic differentiation and angiogenesis *in vitro*. The scaffolds were implanted into animal model of cranial bone defect to characterize bone tissue repair and regeneration *in vivo*. From the images of Micro-CT, it was obvious that the most bone tissue was formed in Rg1/GMs/Sr-α-CaS group in 12 weeks. New bone structure, collagen and mineralization were analyzed with staining of HE, Masson and Safranin O-Fast green and showed good distribution. The expression of osteocalcin of Rg1/GMs/Sr-α-CaS indicated new bone formation in defect site. The results revealed that synergy of Rg1 and Sr showed the best effect of bone repair and regeneration, which provided a new candidate for bone defect repair in clinic.

Keywords: Ginsenoside Rg1 (Rg1), gelatin microspheres, strontium (Sr), calcium sulfate hemihydrate (α-CaS), bone defect

INTRODUCTION

Large bone defect caused by trauma and tumor resection is still a severe problem in clinic for the limited self-repair capability and absence of transplant. Tissue engineering provides a feasible method for bone repair and regeneration (Porter et al., 2009). Compatible mechanical strength and good biocompatibility are especially important for ideal substitute of bone tissue. Inorganic biomaterials of hydroxyapatite, β-Tricalcium phosphate, and calcium sulfate has been reported widely (Gotterbarm et al., 2014; Ramesh et al., 2018; Meng et al., 2019). Calcium sulfate has been used as a bone defect filling and repairing material for over a 100 years. It has good biocompatibility and can be degraded and absorbed into the body without immune reaction (Kutkut and Andreana, 2010). Commercial medical calcium sulfate products such as Osteoset (Wright, United States) are used into clinic, which change $CaSO_4·2H_2O$ into $CaSO_4·0.5H_2O$ and can be degraded within 6–8 weeks *in vivo* (Winn and Hollinger, 2000). α-$CaSO_4·0.5H_2O$ loading bone morphogenetic proteins-2 (BMP-2) peptide was reported to repair a critical defect in the femoral condyle of rabbit (Liu et al., 2015b). The rapid solidification of α-$CaSO_4·0.5H_2O$ make it a candidate as bone cement. α-$CaSO_4 \cdot 0.5H_2O$ was mixed with bioactive glasses and the mixture had potential used as the substitute of bone implant (Zheng et al., 2018b).

Strontium (Sr) is an alkaline earth metal element and plays an important physiological function in human body. Strontium ranelate is used to treat severe osteoporosis in postmenopausal women authorized by the European Union (Barenholdt et al., 2009). Sr is also used widely in bone tissue engineering. Sr can substitute Calcium (Ca) for their similar ion diameter, and when the concentration of Sr > 0.2 mol L^{-1}, it would induce partial conversion of Calcium sulfate dihydrate to hemihydrate (Feldmann and George, 2013). Sr also has bone-seeking properties, and it can replace Ca to strength mechanical behaviors (Jimenez et al., 2019). The cement of Sr-containing α-calcium sulfate hemihydrate was reported with enhanced osteoblastic differentiation, new bone and new blood vessel formation in critical-sized calvarial defects *in vivo* (Yang et al., 2017). In our previous study, Sr substituted hydroxyapatite/silk fibroin scaffold loading BMP-2 increased bone mineral density (BMD) and improved new bone regeneration (Yan et al., 2018). For mesenchymal stem cells (MSCs), it was found that Sr activated Wnt/Catenin signaling to promote osteogenic differentiation *in vitro* and *vivo* (Yang et al., 2011). Sr also enhanced osteoblast activity and inhibited osteoclast activity (Wornham et al., 2014).

Ginsenoside Rg1 extracted from dry root of Panax ginseng C. A. Mey has many physiological functions for the antioxidant and anti-inflammatory properties (Gao et al., 2017b; Ghaeminia et al., 2018). For bone repair and regeneration, Rg1 was demonstrated to have protective effects on BMSCs apoptosis by activating mir-494-3p. ROCK-1. Bcl-2 signaling pathway in male rat (Zheng et al., 2018a). Rg1 was also reported to promote osteogenic differentiation with activated GR/BMP-2 signaling pathway *in vitro* and enhance bone calcification to accelerate the fracture healing *in vivo* (Gu et al., 2016). For osteonecrosis lesion, Rg1 stimulated capillary vessel formation and increased BMD (Heng et al., 2019). Furthermore, Rg1-loaded alginate-chitosan microspheres were prepared, and the controllable release of Rg1 promoted proliferation and differentiation and suppressed apoptosis of bone marrow stromal cells (hBMSCs) (Guo et al., 2017).

In this study, we designed a scaffold of Rg1/GMs/Sr-α-CaS to repair calvarial bone injury, which has not been reported before. Sr-α-CaS provided mechanical support, and Rg1 and Sr were released to repair bone defect. To avoid the burst release of drug, we introduced gelatin microspheres as drug carriers and prepared Rg1/GMs. We evaluated the structure and composition, biocompatibility, and the ability to induce osteogenic differentiation *in vitro* and tissue repair and regeneration monitored by Micro-CT *in vivo*. The expression of osteocalcin (OCN) and osteogenesis were evaluated.

MATERIALS AND METHODS

Ginsenoside Rg1 (>98%, Aladdin, China); Gelatin (Porcine skin, Type A, Sigma-Aldrich, United States); Span 80 (Aladdin, China); Olive oil (Aladdin, China); $SrCl_2 \cdot 6H_2O$ (Aladdin, China); Gibco MEM α, Nucleosides (Thermo Fisher Scientific, United States); Fetal bovine serum (FBS, Sigma-Aldrich, United States); Anti-Osteocalcin (Anti-OCN, Santa Cruz Biotechnology, United States); CCK-8 Kit (Beyotime, China); ALP Kit (Beyotime, China); RNeasy Mini Kit (Qiagen, United States); cDNA synthesis Kit (Beyotime, China); Bulge-LoopTM miRNA qRT-PCR kit (Ribobio, Guangzhou, China); Hematoxylin and Eosin Staining Kit (Beyotime, China); Masson's Trichrome Stain Kit (MKbio, Shanghai, China); and Safranin O-Fast green Stain Kit (Servicebio, Wuhan, China).

Cell Culture

MC3T3-E1 cells (Biowit Biotech, Shenzhen, China) were cultured in MEMα culture medium supplemented with 10% FBS and 1% Penicillin-Streptomycin at 37°C, 5% CO_2 humidified atmosphere. The medium was changed every 2 days for further experiment.

Preparation of Rg1 Loaded Gelatin Microspheres (Rg1/GMs)

Gelatin microspheres (GMs) were prepared with an emulsion solvent evaporation method with a slight modification (Yang et al., 2009). 0.1 g sorbitol oleate (Span-80) was added to 100 mL olive oil, heating in a water bath at 60°C for 0.5 h at 400 rpm. After mixing evenly, add 10 mL gelatin solution of 10 wt% drop by drop. After stirring for 3 h, transfer the mixed solution to the ice bath and keep the rotation speed for 30 min. Then, 0.1 mL of 25 wt% aqueous solution of glutaraldehyde was added. After 2 h stirring, add 30 mL acetone at 4°C and stir for 30 min. The product was placed into 10 mL acetone for further curing for about 24 h at 4°C. Then, the microspheres were gained and soaked into 1 mol/L aminoacetic acid for 30 min and washed alternately by ethanol and isopropyl alcohol for three times. Finally, freeze-drying to obtain GMs. Rg1/GMs were prepared similarly. 10 mg Rg1 was dispersed into 10 mL gelatin solution of 10 wt%. Then, the mixture was added in olive oil with Span-80, and repeat the methods as above. Rg1 was loaded into GMs to form Rg1/GMs. The microspheres with different mass ratio of Rg1 and GMs were prepared, and cell proliferation of MC3T3-E1 was used to evaluate the best dosage of Rg1.

Preparation of Rg1/GMs/Sr-α-CaS Scaffold

α-$CaSO_4 \cdot 0.5H_2O$ (α-CaS) calcium sulfate hemihydrate was synthesized first (Li et al., 2014). The composite crystallizer was prepared using sodium citrate, aluminum sulfate and succinic acid with a mass ratio of 1:1:1. Solution of $CaCl_2$ and K_2SO_4 was evenly stirred with molar mass ratio of 1:1 in a sealed hydrothermal reaction vessel, and then adding composite crystallizer into vessel with dosage at 5% of the total mass of $CaCl_2$ and K_2SO4. Dilute HCl was used to keep pH 5. Hydrothermal reaction was conducted for 4 h at 80°C, 300 r/min. The product was washed with hot water for three times and soaked in absolute ethanol to stop the reaction. After filtering, dry product in a vacuum oven for 4 h and at 105°C and get

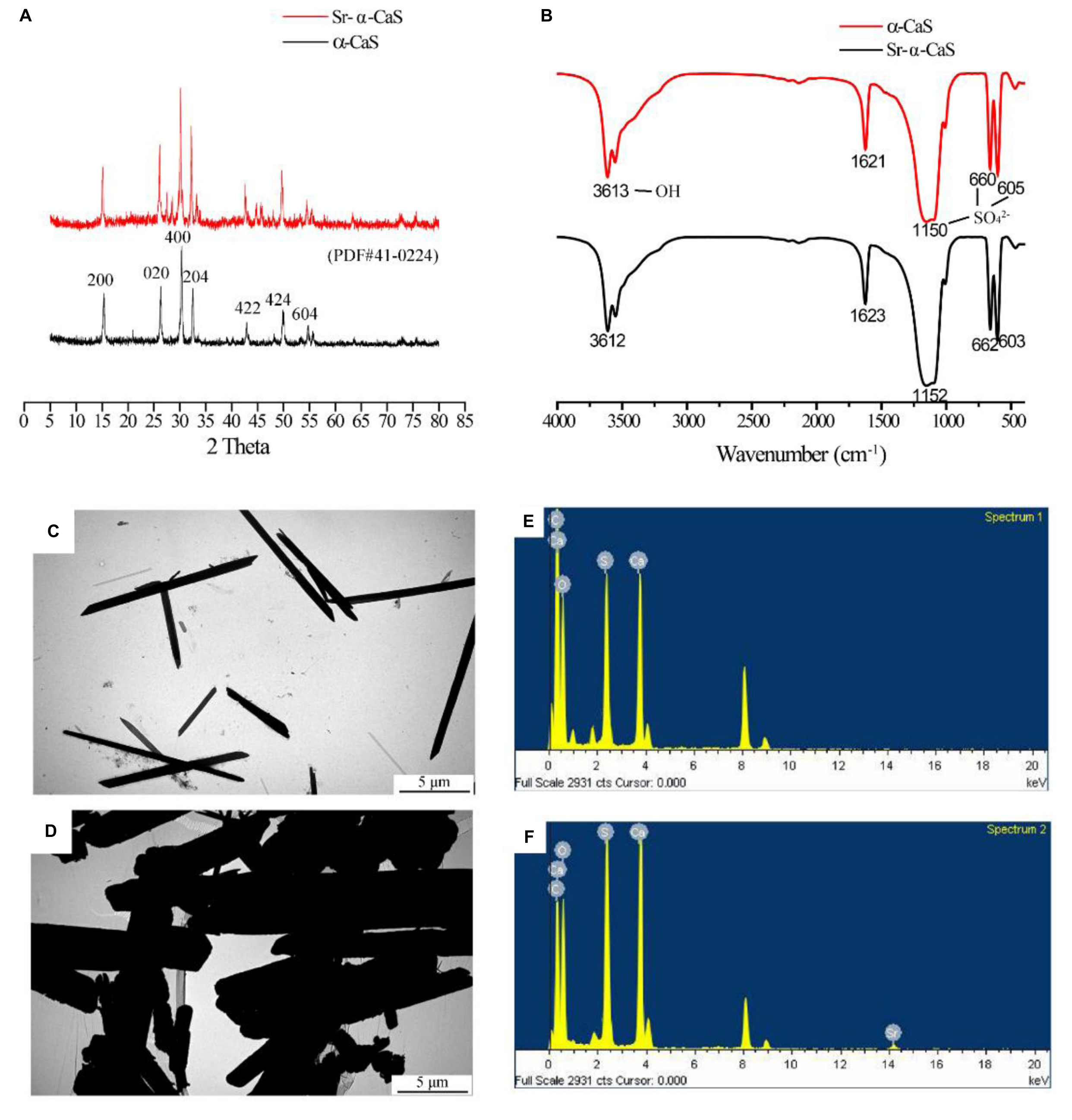

FIGURE 1 | XRD pattern **(A)**, FTIR spectrum **(B)** and TEM image of α-CaS **(C)** and Sr-α-CaS **(D)**, EDS of α-CaS **(E)** and Sr-α-CaS **(F)**.

the final product of α-CaS. α-CaS was fully ground and sealed for next use. Sr-α-CaS was prepared as above. $SrCl_2 \cdot 6H_2O$ and $CaCl_2$ were dissolved and mixed with a molar ratio of 1:6. Then add K_2SO_4 solution and keep the molar ratio at 1: 1 ($m_{Sr}{}^{2+}$& Ca^{2+}: $m_{SO4}{}^{2-}$). Repeat the above steps to get Sr-α-CaS. Rg1/GMs and Sr-α-CaS were fully mixed up with a mass ratio of 1: 100 by a planetary mixer (Nova, Shanghai, China) at 50–200 r/min. The homogeneous powder was pressed into a sheet-like scaffold with a tableting machine (Lvyi, Shanghai, China) under 10–20 MPa.

Characterization of Rg1/GMs/Sr-α-CaS Scaffold

Morphology of gelatin microspheres was measured by scanning electron microscope (SEM, Philips XL-30; Philips, Netherlands). Crystal structure of α-CaS and Sr-α-CaS was tested by X-ray diffractometer (XRD, Gemini S Ultra, Oxford Diffraction Ltd., Japan). The infrared (IR) spectra were obtained by Fourier transform infrared spectroscope (FTIR, VERTEX70, Bruker, Germany). The size and shape of α-CaS were determined

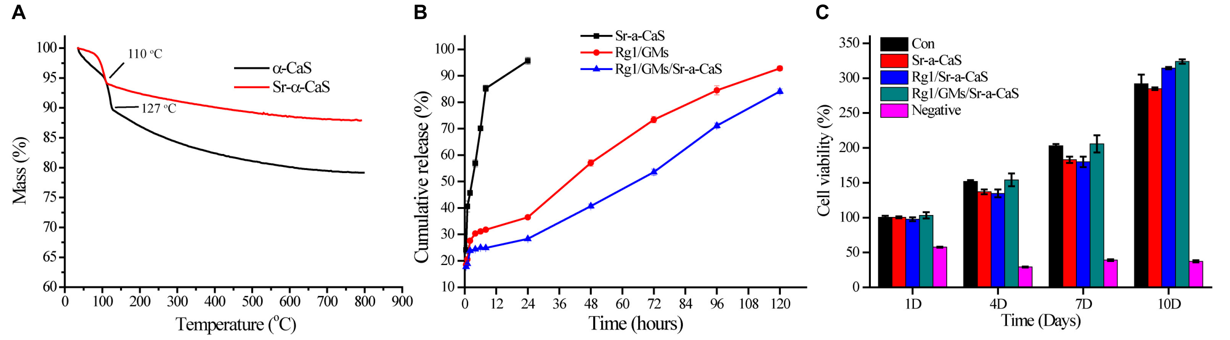

FIGURE 2 | TG **(A)** of α-CaS and Sr-α-CaS; cumulative release curve **(B)** of Ginsenoside Rg1 of Rg1/Sr-α-CaS, Rg1/GMs and Rg1/GMs/Sr-α-CaS; MC3T3-E1 cell viability **(C)** on different scaffolds.

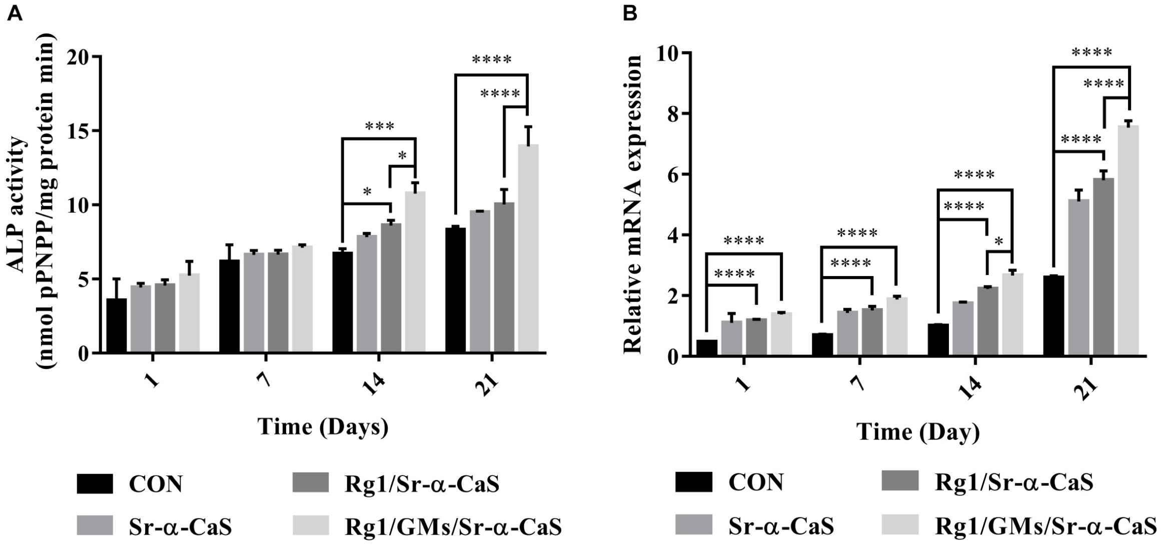

FIGURE 3 | The ALP **(A)** and VEGF **(B)** assay of MC3T3-E1 cultured on different scaffolds. $^*p < 0.05$, $^{**}p < 0.01$, $^{***}p < 0.001$, $^{****}p < 0.0001$.

by Transmission electron microscopy (TEM, Philips Tecnai-10; Philips, Netherlands) and quantitative analysis of elements was performed by Energy Dispersive Spectrometer (TEM-EDS). Composition was detected by Thermogravimetric analyzer (TG, TG 209; NETZSCH, Germany).

Loading Rate and Release of Rg1 *in vitro*

The quantification of Rg1 was detected by High performance liquid chromatography (HPLC, UltiMate 3000; Thermo Fisher Scientific, United States). The mobile phase was composed with acetonitrile (mobile phase) and 0.05% Na_2HPO_4 (PB, pH: 7, mobile phase B). The detection wavelength was selected at 203 nm. The standard Rg1 solution of 1 mg/mL was prepared and diluted into different concentrations. The HPLC assay was processed. Draw the standard curve of Rg1 and calculate the loading rate of Rg1/GMs. Scaffolds of Rg1/Sr-α-CaS and Rg1/GMs/Sr-α-CaS and 10 mg microspheres of Rg1/GMs were soaked into 10 mL PBS with pH 7.4 at 37°C. At the set time, 0.5 mL supernatant was collected and replaced by 0.5 mL fresh PBS. The collected supernatant was stored at −20°C. After all the samples were collected, the HPLC assay was carries out at 203 nm as above. The cumulative release of Rg1 was calculated via standard curve line. All experiments repeated in triplicate for each time interval and draw the cumulative release curve.

Cytotoxicity Assay *in vitro*

Leaching solution of each scaffold of Sr-α-CaS, Rg1/Sr-α-CaS and Rg1/GMs/Sr-α-CaS was prepared according to international standard. In brief, scaffolds were soaked into ethanol of 75% and conducted UV radiation for 30 min, respectively. Then, wash scaffolds with PBS for 2–3 times. Add medium with ten times the mass of scaffolds and incubate for 24 h at 37°C. MC3T3-E1 cells in logarithmic growth phase were digested and adjusted to 5×10^4/ mL. 100 μL cell suspension was added to 96-well plates. After growth for 24 h, replace the medium with leaching solution and continue to culture cells for 1, 4, 7, and 10 days. CCK-8 Kit was used to evaluate cell viability. Add CCK-8 reagent with a volume ratio of 1:9 (V_{medium}: V_{CCK-8} = 1:9) and incubate

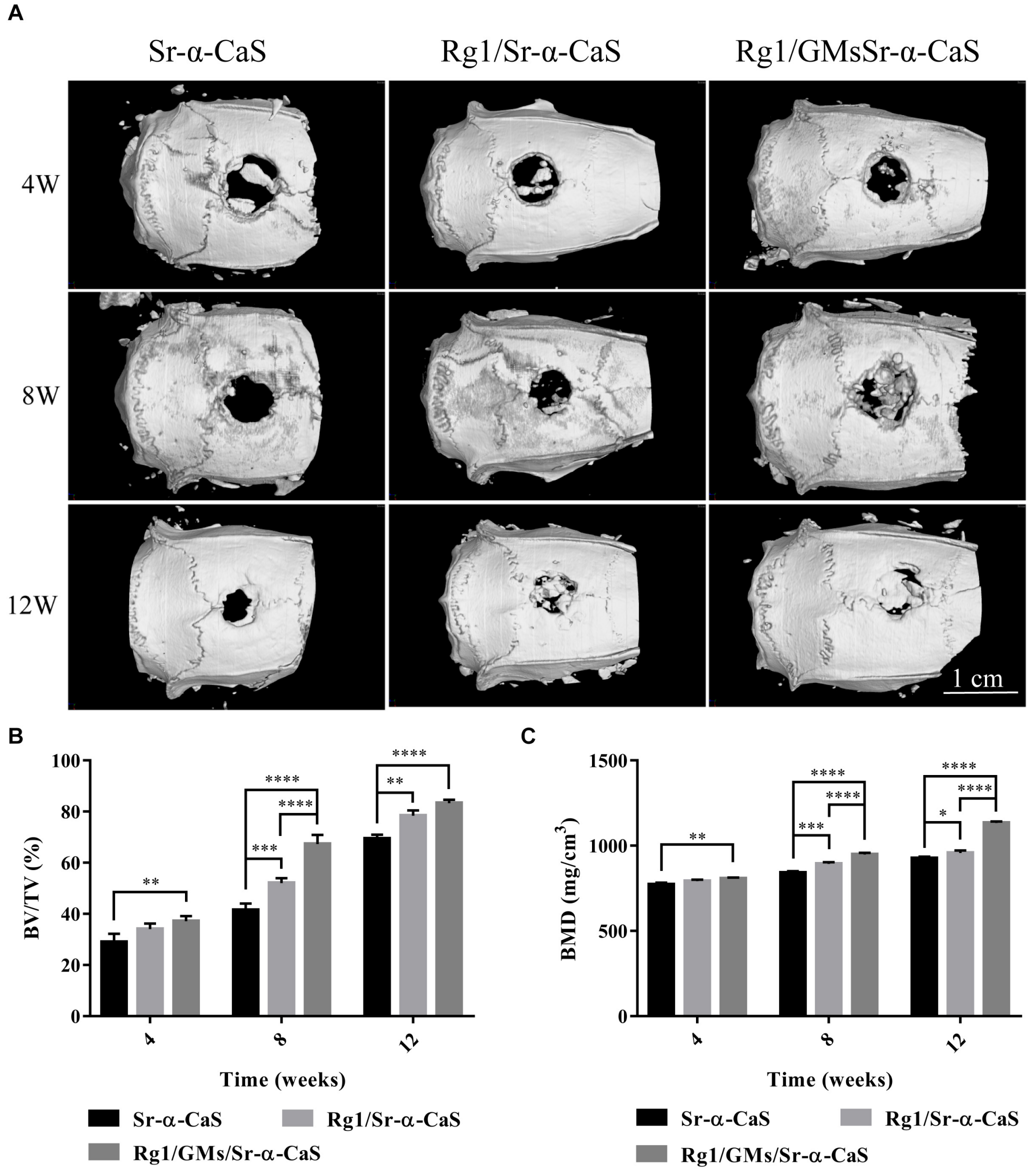

FIGURE 4 | Micro-CT images **(A)** of different scaffolds in rat calvarial defects; Micro-CT analysis of BT/TV **(B)** and BMD **(C)** in the rat calvarial defects. $*p < 0.05$, $**p < 0.01$, $***p < 0.001$, $****p < 0.0001$.

for 30 min according to manufacturer's instruction. Test the absorbance wavelength at 450 nm of each well using a microplate reader (MM-58938-00, Molecular Devices, United States) and calculate the cell viability.

Alkaline Phosphatase (ALP) *in vitro*

The osteogenic differentiation of MC3T3-E1 was evaluated with ALP activity test, which was a distinct feature of osteoblast differentiation. MC3T3-E1 cells were digested and adjusted to 3×10^4/mL, and 500 μL cell suspension was adding to 24-well plates. After incubating for 24 h, replace medium with 500 μL leaching solution. While culturing for 1, 7, 14, and 21 days, wash cells with PBS for three times and add 500 μL cell lysates. Cells were disrupted using an ultrasonic cell disrupter (Fisher Scientific 50, Thermo Fisher Scientific, United States) at 4°C. Centrifugate and collect supernatants, add 500 μL ALP substrate reaction solution. The reaction was carried out for 30 min at 37°C. 500 μL of 0.1 M NaOH was added to terminate the reaction. The UV absorption at 405 nm was then determined using ultraviolet-visible spectrophotometer (UV-2550, Shimadzu, Japan). ALP activity was calculated according to instructions. Each group of scaffolds at each time point was tested at least three times in parallel.

VEGF Expression *in vitro*

MC3T3-E1 cells were cultured with leaching solution in 24-well plates as above for 1, 4, 7, and 21 days. The cells were collected and total RNA was extracted with RNeasy Mini Kit.

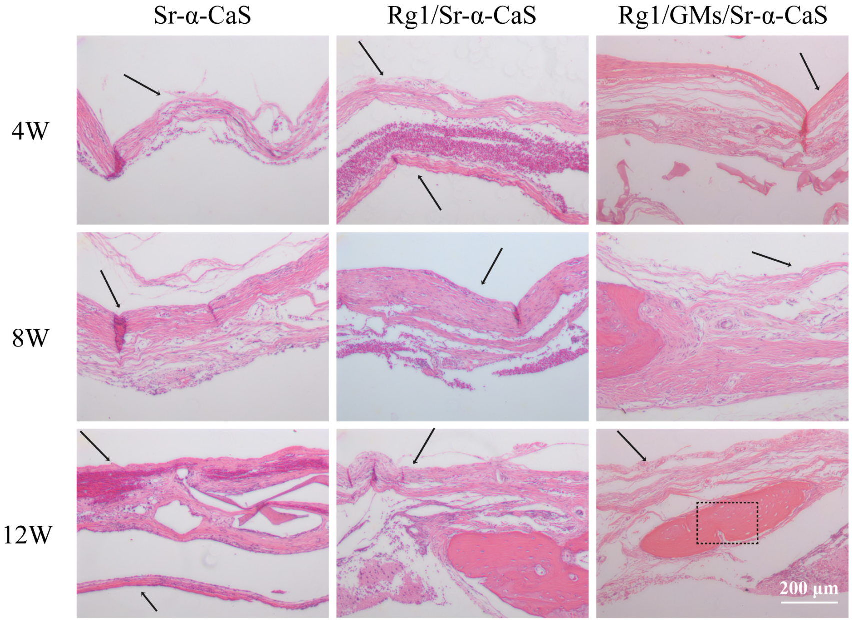

FIGURE 5 | Hematoxylin and eosin (H&E) staining photomicrographs of Sr-α-CaS, Rg1/Sr-α-CaS and Rg1/GMS/Sr-α-CaS groups (Magnification = 100×, black arrow: trabeculae, black rectangle: bone tissue).

Reverse transcription of total RNA to obtain cDNA according manufacture instruction. cDNAs and equal amounts of forward and reverse primers were added into a SYBR reaction mixture. The qPCR conditions were 2 min at 50°C, 10 min at 95°C, 50 cycles at 95°C for 15 s, and 1 min at 60°C. miRNA qRT-PCR was detected by the Bulge-LoopTM miRNA qRT-PCR kit. VEGF forward primers: 5′-ACAGAAGGGGAGCAGAAAGCCCAT-3′; Reverse primer: 5′-CGCTCTGACCAAGGCTCACAGT-3′; GAP DH forward primer: 5′-AGGTCGGTGTCAACGGATTT and reverse primer: 3′-CCTTCCACGATGCCAAAGTT.

Animal Model of Cranial Bone Defect

All animal experiments were strictly carried out in accordance with the regulations of the Animal Research Center of Sun Yat-sen University. 18 SD rats (200–250 g) were divided into three groups ($n = 6$): Sr-α-CaS, Rg1/Sr-α-CaS and Rg1/GMs/Sr-α-CaS. The scaffold (diameter: 8 mm, weight: 183.3 mg) implantation into calvarial defect was shown in **Supplementary Figure S5**. Before the operation, sodium pentobarbital solution of 1% was intraperitoneally injected into SD rats at a dose of 30 mg/kg. Remove the hair of the rat brain, and cut a 3 cm long scalp in the middle of the rat's head. At the same time, the subcutaneous tissue on both sides was peeled off. After removing the periosteum, a calvarial defect model with a diameter of 6 mm was constructed using a dental drill in the middle of the rat's parietal bone. Take care during the operation to maintain the integrity of the dura mater. The sterilized scaffolds were sequentially implanted into the calvarial defects as shown in **Supplementary Figure S5C**, and the periosteum and scalp were sutured (**Supplementary Figure S5D**). After 4, 8, and 12 weeks of implantation, the rats were sacrificed and the skulls were dissected and placed in a 4% paraformaldehyde solution for subsequent histological characterization.

Micro-CT *in vivo*

After 4, 8, and 12 weeks postoperatively, the rats were anesthetized, and then the defect was analyzed using the Micro-CT imaging system (BRUKER Micro-CT Sky Scan 1176, Bruker, United States). The parameters of the device were set: the layer thickness: 48 μm; the spacing between the layers: 48 μm; the pixel size: 48 μm and it was also set to high voltage mode. The bone volume and bone density of regenerated bone tissue were calculated using the software provided by Micro-CT.

Histological Analysis

After 4, 8, and 12 weeks, the removed samples were collected and soaked into 4% solution of paraformaldehyde at room temperature for 24 h. Subsequently, the fixed samples were immersed in 10% EDTA solution for decalcification of about 45 days, and the decalcification solution was changed every 3 days until the bone tissue needle can pass smoothly. Then, different concentrations of ethanol solution were used for dehydration. The samples were subjected to lateral paraffin embedding, and sliced vertically with 5 μm thickness. Finally, staining of hematoxylin-eosin (H&E), Masson's trichrome and Safranin/solid green were performed to characterize the bone tissue repair and regeneration.

Immunohistochemistry

Osteocalcin was a protein formed by osteoblasts to constitute new bone. The antibody of anti-OCN was used to evaluate

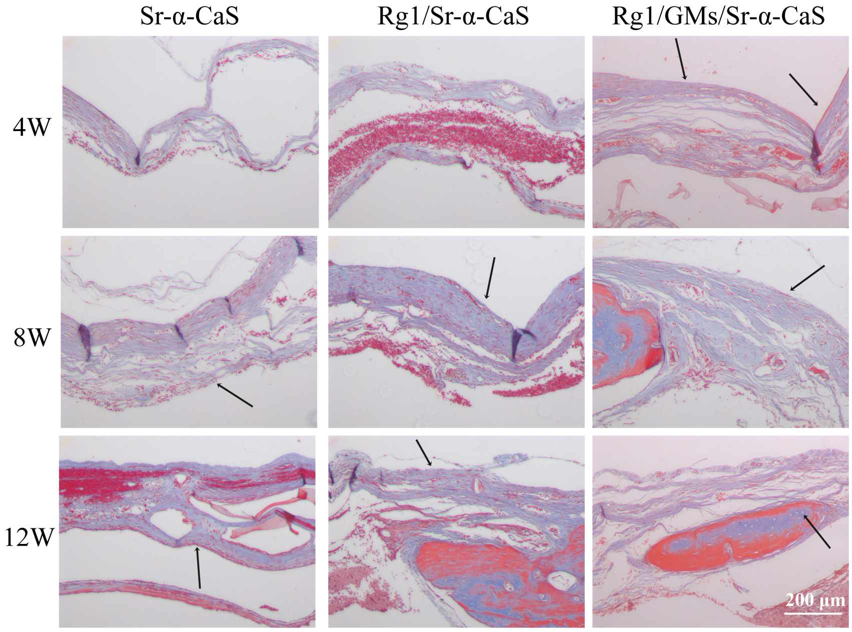

FIGURE 6 | Masson staining of Sr-α-CaS, Rg1/Sr-α-CaS and Rg1/GMS/Sr-α-CaS (Magnification = 100×, black arrow: collagen fibers).

the regeneration of bone tissue. The samples were prepared into sections as above. Sections were incubated with anti-OCN primary antibody (1: 200) overnight at 4°C. Then, add a secondary antibody (1: 500) to incubate for 2 h at room temperature. Diaminobenzidine (DAB) coloring agent was to perform protein distribution and observe OCN expression with light microscope (Olympus IX71, Japan).

Statistical Analysis

The data of this study were averaged ± standard deviation (SD) of statistical data using SPSS software (version 16.0; SPSS, Chicago, IL, United States). At least three parallel samples ($n = 3$) were set for all experiments. * indicates $p < 0.05$, ** indicates $p < 0.01$, and the smaller the p-value, the more the corresponding * is, the difference of $p < 0.05$ is considered to be statistically significant.

RESULTS

Characteristics of Scaffolds

The XRD diffraction patterns were shown in **Figure 1A**, the diffraction peaks of α-CaS at 15.1° (200), 26.2° (020), 30.5° (400), 32.6° (204), 43.0° (422), 50.1° (424), and 54.8° (604) were consistent with standard α-$CaSO_4 \cdot 0.5H_2O$ (PDF#41-0224). Sr-α-CaS had similar characteristic peaks with α-CaS, and diffraction peaks of Sr^{2+} presented at 27.5° and 28.5° (Li et al., 2014). FTIR spectrum of α-CaS was in **Figure 1B**. Characteristic absorption peaks at 1150, 660, and 605 cm^{-1} presented asymmetric stretching vibration and bending vibration of ${SO_4}^{2-}$ and characteristic peak at 3613 cm^{-1} was vibration of O-H. The results of XRD and FTIR of α-CaS indicated α-$CaSO_4 \cdot 0.5H_2O$ was successfully synthesized, and with the incorporation of Sr, the crystal structure of α-CaS was not significantly affected. TEM images was showed in **Figures 1C,D**. Whisker of α-CaS can be observed while Sr-α-CaS appeared larger particle and size thicker rod, which may be caused by the different growth rate of Sr^{2+} in the length direction and diameter direction of whisker surface. Elemental analysis from EDS in **Figures 1E,F** and **Table 1** showed the content of Sr was 16.1%. The composition of Sr-α-CaS was also tested by TG in **Figure 2A**. As temperature rise, both mass of α-CaS and Sr-α-CaS declined, and content of Sr was about 8.7%. Calcium sulfate hemihydrate containing 16.1% Sr (Sr-α-CaS) was prepared successfully. The SEM of gelatin microspheres was in **Supplementary Figure S1**, and the average diameter was 9.24 ± 0.87 μm, surface area was 268.09 ± 50.48 μm^2. The average diameter of pores in microspheres was also measured, which was 0.59 ± 0.06 μm. The SEM images of scaffolds were in **Supplementary Figure S2**. Compared with Sr-α-CaS, Rg1/GMs/Sr-α-CaS scaffolds showed rougher surface and round gelatin microspheres can be observed. Cell proliferation of MC3T3-E1 cells cultured with different ratio of Rg1/GMs was shown in **Supplementary Figure S3**. While Rg1/GMs ratio was 10:1, the highest proliferation rate can be obtained.

Loading Rate and Release of Rg1 *in vitro*

The standard curve of Rg1 was in **Supplementary Figure S4**, regression equation was $Y = 0.00426X - 0.0002835$, $R^2 = 0.9993$, linear range was 3.125–50.000 mg/L, which showed good correlation in the linear range. The loading rate of Rg1/GMs was obtained by calculating the peak area in chromatograms, and it was 2.51% (w/w). Cumulative release curve of Rg1 was in **Figure 2B**, which was calculated using the standard

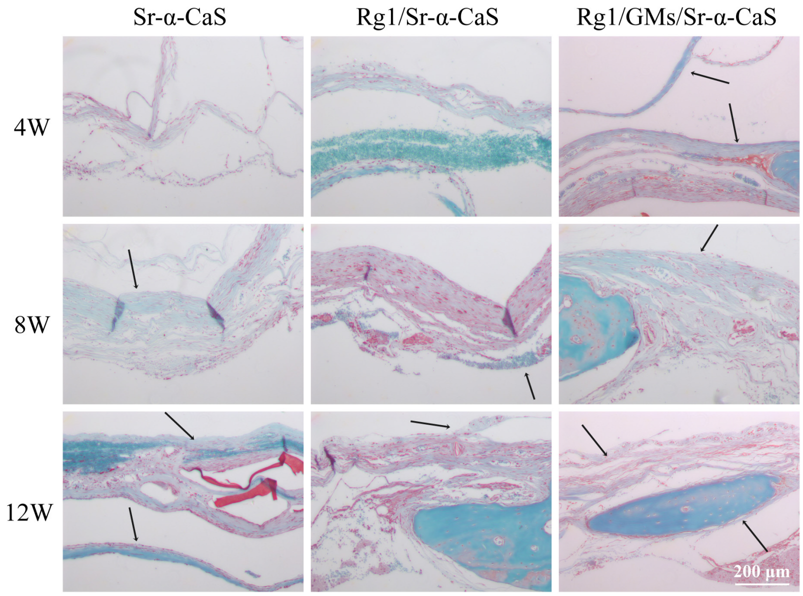

FIGURE 7 | Safranin O and Fast Green staining photomicrographs of calvarial defect sites treated with Sr-α-CaS, Gim/Sr-α-CaS and Gim/GMS/Sr-α-CaS (Magnification = 100×, black arrow: bone tissue).

TABLE 1 | The element weight of different α-CaS and Sr-α-CaS.

	C	O	S	Sr	Ca	Sr/(Sr+Ca)
	Weight (%)	Weight (%)	Weight (%)	Weight (%)	Weight (%)	Weight (%)
α-CaS	49.29	21.12	13.80	0	15.79	0
10% Sr-α-CaS	30.82	24.26	20.38	16.1	22.93	6.56

curve. In first 36 h, Rg1 was almost completely released from Rg1/Sr-α-CaS. However, for Rg1/GMs and Rg1/GMs/Sr-α-CaS, release rate decreased significantly and Rg1 showed sustained release without drug burst. Compared with Rg1/GMs, release rate of Rg1/GMs/Sr-α-CaS was always slower, and cumulative release of Rg1/GMs was 92% while it was 85% in Rg1/GMs/Sr-α-CaS within 120 h. Although the scaffolds of Sr-α-CaS had good degradability, GMs can be used as drug carriers to maintain sustained release of Rg1, which caused the above results. It demonstrated that Rg1/GMs/Sr-α-CaS can provide Rg1 stably to repair bone defect *in vivo*.

Cytotoxicity *in vitro*

To evaluate biocompatibility of scaffolds, cytotoxicity was conducted and 0.5wt% phenol was used as negative group. After culturing MC3T3-E1 cells for 1, 4, 7, and 10 days with leaching solution, cell viability was measured by CCK-8 assay in **Figure 2C**. Compared with control group, all the scaffolds showed good biocompatibility, and cell viability was more than 90%. The results demonstrated Sr-α-CaS was safe and incorporation of Sr did not affect the biocompatibility of scaffolds. What's more, Rg1/GMs/Sr-α-CaS showed the highest cell viability and it may be caused by slight release of Rg1.

ALP *in vitro*

The expression of ALP in **Figure 3A** indicated the osteogenic differentiation of MC3T3-E1. After culturing for 1, 7, 14, and 21 days, ALP activity gradually increased with time, and all scaffolds presented higher ALP activity than control group, which indicated each scaffold can provide support for osteogenic differentiation of MC3T3-E1. Scaffolds with Sr and Rg1 showed higher ALP expression in 14 and 21 days. Therefore, synergistic effect of Rg1 and Sr prompted osteogenic differentiation. However, compared with Rg1/Sr-α-CaS group, ALP activity of Rg1/GMs/Sr-α-CaS showed significant increase at 14 and 21 days. Due to sustained release of Rg1 from GMs, concentration of Rg1 in leaching solution of Rg1/Sr-α-CaS was higher than Rg1/GMs/Sr-α-CaS group, which was consistent with the result of cumulative release curve. Therefore, it was inferred that low concentration of Rg1 was more conducive to osteogenic differentiation.

VEGF Expression *in vitro*

VEGF expression was related to blood vessel formation, and it was measured by RT-qPCR at 1, 7, 14, and 21 days. In **Figure 3B**, all the scaffold groups showed significant increase in VEGF expression. Scaffolds with Sr and Rg1 also showed higher expression of VEGF than other group in 14 and 21 days. But compared with Rg1/Sr-α-CaS, VEGF expression of Rg1/GMs/Sr-α-CaS was increased obviously, which was consistent with results of ALP expression. It was also inferred that low concentration of Rg1 can effectively promote vascularization.

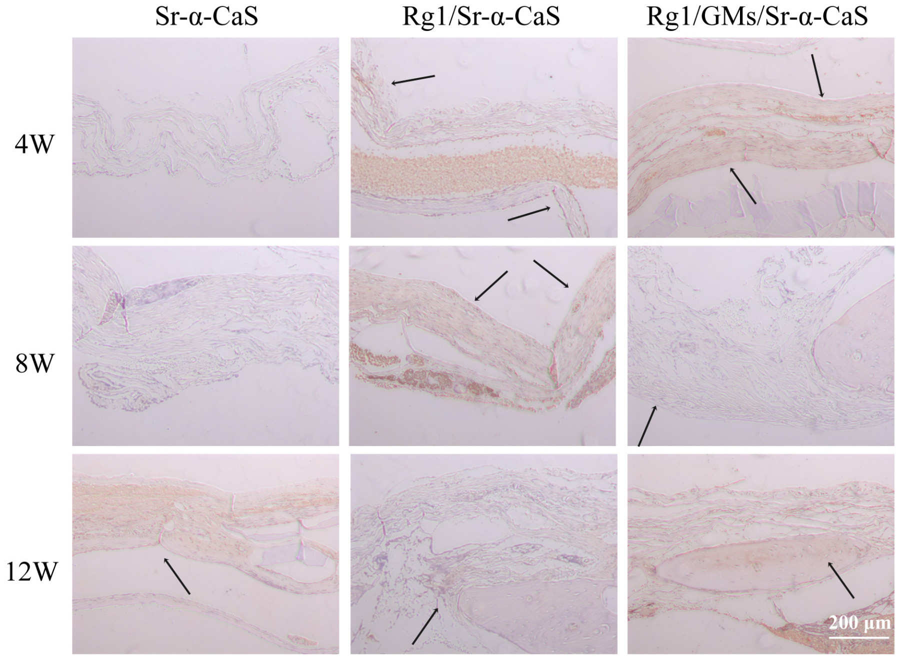

FIGURE 8 | OCN expression of Sr-α-CaS, Rg1/Sr-α-CaS and Rg1/@GMS/Sr-α-CaS group (Magnification = 100×, black arrow: OCN).

Micro-CT

Scaffolds of Sr-α-CaS, Rg1/Sr-α-CaS, and Rg1/GMs/ Sr-α-CaS were implanted into skull defect. The repair and regeneration in defect site were evaluated by Micro-CT in **Figure 4A**. It was obvious that more bone tissue was observed in scaffolds with Sr and Rg1 for 12 weeks. Compared with Rg1/Sr-α-CaS group, more bone tissue was formed in Rg1/GMs/ Sr-α-CaS group for 8 weeks, thus sustained Rg1 and Sr appeared the highest efficiency of cranial bone repair. New bone volume and BMD was calculated in **Figures 4B,C**. The volume of new bone increased with time for each scaffold, and Rg1/GMs/Sr-α-CaS group always showed the most bone volume. At 12 week, the BV/TV of Rg1/GMs/Sr-α-CaS rise up to 83% while it was only 78% in Rg1/Sr-α-CaS and 69% in Sr-α-CaS. BMD also increased with time. Scaffolds with Rg1 showed higher BMD than Sr-α-CaS, and Rg1/GMs/Sr-α-CaS group always had the highest BMD *in vivo*. It revealed that Rg1 and Sr promoted new bone formation with enhanced bone volume and BMD.

Histology

HE staining of bone tissues in defect site for 4, 8, and 12 weeks of was exhibited in **Figure 5**. After 4 week of implantation, no obvious inflammatory response was found in all groups and a small amount of bone trabecula (black arrows) was observed in Rg1/GMs/Sr-α-CaS group. After 8 week, bone trabecula and fibrous tissue in defect site were found. For 12 week, the trabecular bone became thicker and a large number of new bone formation was observed in all groups, and the morphology of newborn bone tissue (black rectangle) in Rg1/GMs/Sr-α-CaS was similar with normal tissue.

The formation of collagen fibers in 4, 8, and 12 weeks showed in **Figure 6** and **Supplementary Figure S6A**. From the result of Masson staining in 4 week, there was no significant difference between Sr-α-CaS and Rg1/Sr-α-CaS, but for Rg1/GMs/Sr-α-CaS group, fiber tissue (black arrows) can be observed. After 8 week of transplantation, filamentous collagen fibers formed at the defect for all groups. After 12 week, the new tissue of Rg1/ GMs/Sr-α-CaS was the most closet with normal bone tissue and the most collagen fiber was observed. The results of Safranin O-Fast green Staining was in **Figure 7** and **Supplementary Figure S6B**. Green newborn bone tissue (black arrows) was not apparent in 4 weeks. After 8 weeks, fibrous new bone trabecular was formed in all groups. After 12 week of transplantation, a large number of new bones was observed, and bone in Rg1/GMs/Sr-α-CaS also showed closet structure with normal bone tissue, which was consistent with the staining results of HE and Masson. Therefore, scaffold of Rg1/GMs/Sr-α-CaS showed good cranial bone repair, which accelerated the formation of collagen and bone.

Immunohistochemistry

Osteocalcin, a structural protein from osteoblast, played an important role in regulating bone calcium metabolism and was processed to produce carboxylate osteocalcin to participate bone development. In **Figure 8** and **Supplementary Figure S6C**, every scaffold showed low expression of OCN at 4 week. Rg1 loaded scaffolds showed higher OCN expression (black arrows) at 8 weeks, which was more obvious at 12 weeks. Therefore, sustained release of Rg1 accelerated bone regeneration *in vivo*.

DISCUSSION

Biomaterials of Sr modified calcium sulfate hemihydrate have been reported in bone repair. The scaffold of Sr-CaS showed good biocompatibility and repair in tibia bone defect of SD rats, which activated TGF-β/Smad signaling pathway to improve bone formation (Liu et al., 2019). Traditional Chinese medicine recently has become a hot research topic in life sciences. As a precious medicine, Panax ginseng C. A. has always been regarded as the king of herbs. Ginsenosides are considered to be active ingredients in ginseng (Lee and Kim, 2014; Biswas et al., 2017; Mohanan et al., 2018). The dose of Ginsenosides Rg1 was reported to have influence on cell growth and tissue differentiation such as adipose-derived stromal cells (ASCs) (Liang et al., 2019), neural stem cells (Li et al., 2015; Gao et al., 2017a), and human dental pulp cells (hDPCs) (Wang et al., 2012). For the cartilage repair and regeneration, the dosage of Rg1 was related to cell proliferation and chondrogenic phenotype differentiation of breast adipose-derived stem cells HBASCs (Xu et al., 2015). The dose-effect of Rg1 was also found in human periodontal ligament stem cells (hPDLSCs), and concentration from 10 to 100 μmol/L was investigated. Rg1 at 10 μmol/ L significantly enhanced the proliferation and osteogenic differentiation of hPDLSCs while 100 μmol/L Rg1 caused cytotoxicity (Yin et al., 2015).

In this study, we firstly introduced Rg1 to Sr-α-CaS scaffold, and both of Rg1 and Sr accelerated repair and regeneration of cranial bone. To avoid drug burst release, Rg1 was loaded to gelatin microspheres. From the results of Micro-CT in Rg1/GMs/Sr-α-CaS group, the new bone volume was about 83.3% in 12 weeks and BMD increased to 1133 mg/cm^3. Scaffolds also need to provide mechanical support and the mechanical properties should be as close as possible to normal tissue. As we knew, single calcium sulfate hemihydrate scaffolds were absorbed and metabolized too quickly for its rapid degradation. With the incorporation of Sr and Rg1/GMs, mechanical properties were improved and the Rg1 release was prolonged, which made scaffold of Rg1/GMs/Sr-α-CaS a promising candidate for bone repair. The main components of natural bone are hydroxyapatite and collagen. In order to match the degradation rate and mechanical properties with the natural bone, we are considering to prepare composite scaffolds with cross-linked natural biomaterials. To mimic the structure and function of natural bone tissue, natural biomaterials such as collagen, silk fibroin, and chitosan have been reported to add to calcium sulfate hemihydrate (Liu et al., 2015a, 2018; Chen et al., 2016).

Furthermore, dose of Rg1 also influenced the osteogenic differentiation and angiogenesis of MC3T3-E1 *in vitro*. In **Figures 3A,B**, Rg1/GMs/Sr-α-CaS group always showed higher expression of ALP and VEGF than Rg1/Sr-α-CaS. However, due to the degradation of scaffolds and sustained release of gelatin microspheres, the amount of Rg1 in leaching solution of Rg1/Sr-α-CaS was more than Rg1/GMs/Sr-α-CaS. The low concentration of Rg1 accelerated the osteogenic differentiation and vascularization of MC3T3-E1 *in vitro* while it was not obvious at high concentration. In future research, we would explore the effect of Rg1 concentration on cell proliferation and differentiation *in vitro* and tissue repair and regeneration *in vivo*.

In summary, this study prepared a novel Rg1/GMs/Sr-α-CaS scaffold to repair and regenerate cranial bone tissue. The scaffolds showed good biocompatibility and promoted osteogenic differentiation and vascularization *in vitro* and *in vivo*. The Rg1/GMs/Sr-α-CaS scaffolds combined traditional Chinese medicine with modern science and technology, and provided a possible way to study traditional herbs and a potential approach for bone repair and regeneration in clinic.

DATA AVAILABILITY STATEMENT

All datasets presented in this study are included in the article/**Supplementary Material**.

ETHICS STATEMENT

All experimental protocols were approved by the Ethics Committee in the Nanshan Hospital (protocol # 2018-C-106).

AUTHOR CONTRIBUTIONS

DY and ST designed the experiment. PL and QL completed the experiment and obtained the data. LY and CW also made substantial contributions to the experiment including the study design, *in vitro* and *in vivo* study, the acquisition, analysis, and interpretation of data for the work. All authors contributed to the article and approved the submitted version.

FUNDING

This study was supported financially by the Science and Technology Project of Shenzhen (Nos. JCYJ20190808102203649 and 20190802113709023), the Medical Science and Technology Foundation of Guangdong (No. A2020600), and the Science and Technology Project of Shenzhen Nanshan District (No. 2018050).

SUPPLEMENTARY MATERIAL

The Supplementary Material for this article can be found online at: https://www.frontiersin.org/articles/10.3389/fbioe.2020.00888/full#supplementary-material

REFERENCES

Barenholdt, O., Kolthoff, N., and Nielsen, S. P. (2009). Reply to Letter Re: "Effect of long term treatment with strontium ranelate on bone strontium content" by Barenholdt et al. (Bone, 2009). *Bone* 45, 1026–1027. doi: 10.1016/j.bone.2009.07.003

Biswas, T., Mathur, A. K., and Mathur, A. (2017). A literature update elucidating production of Panax ginsenosides with a special focus on strategies enriching the anti-neoplastic minor ginsenosides in ginseng preparations. *Appl. Microbiol. Biot.* 101, 4009–4032. doi: 10.1007/s00253-017-8279-4

Chen, Y. R., Zhou, Y. L., Yang, S. Y., Li, J. J., Li, X., and Ma, Y. F. (2016). Novel bone substitute composed of chitosan and strontium-doped alpha-calcium sulfate hemihydrate: Fabrication, characterisation and evaluation of biocompatibility. *Mat. Sci. Eng. C-Mater.* 66, 84–91. doi: 10.1016/j.msec.2016.04.070

Feldmann, T., and George, P. (2013). Demopoulos. influence of impurities on crystallization kinetics of calcium sulfate dihydrate and hemihydrate in strong HCl-CaCl2 solutions, *Ind. Eng. Chem. Res.* 52, 6540–6549. doi: 10.1021/ie302933v

Gao, J., Wan, F., Tian, M., Li, Y. Y., Li, Y. X., Li, Q., et al. (2017a). Si, effects of ginsenoside-Rg1 on the proliferation and glial-like directed differentiation of embryonic rat cortical neural stem cells in vitro. *Mol. Med. Rep.* 16, 8875–8881. doi: 10.3892/mmr.2017.7737

Gao, Y., Chu, S. F., Zhang, Z., and Chen, N. H. (2017b). Hepataprotective effects of ginsenoside Rg1-A review. *J. Ethnopharmacol.* 206, 178–183. doi: 10.1016/j.jep.2017.04.012

Ghaeminia, M., Rajkumar, R., Koh, H. L., Dawe, G. S., and Tan, C. H. (2018). Ginsenoside Rg1 modulates medial prefrontal cortical firing and suppresses the hippocampo-medial prefrontal cortical long-term potentiation. *J. Ginseng Res.* 42, 298–303. doi: 10.1016/j.jgr.2017.03.010

Gotterbarm, T., Breusch, S. J., Jung, M., Streich, N., Wiltfang, J., Vilei, S. B., et al. (2014). Complete subchondral bone defect regeneration with a tricalcium phosphate collagen implant and osteoinductive growth factors: a randomized controlled study in gottingen minipigs. *J. Biomed. Mater Res. B* 102, 933–942. doi: 10.1002/jbm.b.33074

Gu, Y. Q., Zhou, J. C., Wang, Q., Fan, W. M., and Yin, G. Y. (2016). Ginsenoside Rg1 promotes osteogenic differentiation of rBMSCs and healing of rat tibial fractures through regulation of GR-dependent BMP-2/SMAD signaling. *Sci. Rep.-Uk* 6:25282.

Guo, Y. H., Zhao, S., Du, Y. X., Xing, Q. J., Chen, B. L., and Yu, C. Q. (2017). Effects of ginsenoside Rg1-loaded alginate-chitosan microspheres on human bone marrow stromal cells. *Biosci. Rep.* 37:BSR20160566.

Heng, K., Zhu, Y. X., Geng, Q. H., Yin, G. Y., and Han, X. (2019). Ginsenoside Rg1 protects steroid-induced osteonecrosis of the femoral head in rats by suppressing oxidative stress and adipogenesis. *Int J. Clin. Exp. Med.* 12, 304–315.

Jimenez, M., Abradelo, C., San Roman, J., and Rojo, L. (2019). Bibliographic review on the state of the art of strontium and zinc based regenerative therapies. Recent developments and clinical applications. *J. Mater. Chem. B* 7, 1974–1985. doi: 10.1039/c8tb02738b

Kutkut, A., and Andreana, S. (2010). Medical-grade calcium sulfate hemihydrate in clinical implant dentistry: a review. *J. Long Term Eff. Med. Implants* 20, 295–301. doi: 10.1615/jlongtermeffmedimplants.v20.i4.40

Lee, C. H., and Kim, J. H. (2014). A review on the medicinal potentials of ginseng and ginsenosides on cardiovascular diseases. *J. Ginseng Res.* 38, 161–166. doi: 10.1016/j.jgr.2014.03.001

Li, X., Xu, P., Hou, Y. L., Song, J. Q., Cui, Z., and Wang, S. N. (2014). A novel resorbable strontium-containing alpha-calcium sulfate hemihydrate bone substitute: a preparation and preliminary study. *Biomed. Mater.* 9, 045010. doi: 10.1088/1748-6041/9/4/045010

Li, Y. B., Wang, Y., Tang, J. P., Chen, D., and Wang, S. L. (2015). Neuroprotective effects of ginsenoside Rgl-induced neural stem tell transplantation on hypwdc-ischemic encephalopathy. *Neural. Regen. Res.* 10, 753–759.

Liang, Z. J., Lu, X., Zhu, D. D., Yi, X. L., Wu, F. X., and He, N. (2019). Ginsenoside Rg1 accelerates paracrine activity and adipogenic differentiation of human breast adipose-derived stem cells in a dose-dependent manner in vitro. *Cell Transplant.* 28, 286–295. doi: 10.1177/0963689719825615

Liu, J. H., Mao, K. Z., Wang, X. M., Guo, W. G., Zhou, L., and Xu, J. (2015a). Calcium sulfate Hemihydrate/Mineralized collagen for bone tissue engineering: in vitro release and in vivo bone regeneration studies. *J. Biomater. Tiss Eng.* 5, 267–274. doi: 10.1166/jbt.2015.1308

Liu, J. H., Zhou, L., Zhang, L. C., Mao, K. Z., Xu, J., Shi, T., et al. (2015b). Bone morphogenetic Protein-2 derived peptide loaded calcium sulfate hemihydrate scaffold for enhanced bone tissue regeneration. *J. Biomater. Tiss Eng.* 5, 864–871. doi: 10.1166/jbt.2015.1371

Liu, S. C., Lian, X. J., Xu, R., Shi, Z. D., Du, M. M., Zhang, S. R., et al. (2018). Silk Nanofibers/Calcium sulfate composite: preparation and properties on infective bone repair. *Chinese J. Inorg. Chem.* 34, 490–498.

Liu, Z., Yu, Z. W., Chang, H., Wang, Y., Xiang, H. B., Zhang, X. R., et al. (2019). Strontium-containing alpha-calcium sulfate hemihydrate promotes bone repair via the TGF-beta/Smad signaling pathway. *Mol. Med. Rep.* 20, 3555–3564.

Meng, Z. L., Wu, Z. Q., Shen, B. X., Li, H. B., Bian, Y. Y., Zeng, D. L., et al. (2019). Reconstruction of large segmental bone defects in rabbit using the Masquelet technique with alpha-calcium sulfate hemihydrate. *J. Orthop. Surg. Res.* 14:192.

Mohanan, P., Subramaniyam, S., Mathiyalagan, R., and Yang, D. C. (2018). Molecular signaling of ginsenosides Rb1. Rg1, and Rg3 and their mode of actions, *J. Ginseng Res.* 42, 123–132. doi: 10.1016/j.jgr.2017.01.008

Porter, J. R., Ruckh, T. T., and Popat, K. C. (2009). Bone tissue engineering: a review in bone biomimetics and drug delivery strategies. *Biotechnol. Progr.* 25, 1539–1560.

Ramesh, N., Moratti, S. C., and Dias, G. J. (2018). Hydroxyapatite-polymer biocomposites for bone regeneration: a review of current trends. *J. Biomed. Mater. Res. B* 106, 2046–2057. doi: 10.1002/jbm.b.33950

Wang, P., Wei, X., Zhou, Y., Wang, Y. P., Yang, K., Zhang, F. J., et al. (2012). Effect of ginsenoside Rg1 on proliferation and differentiation of human dental pulp cells in vitro. *Aust. Dent. J.* 57, 157–165. doi: 10.1111/j.1834-7819.2012.0\break1672.x

Winn, S. R., and Hollinger, J. O. (2000). An osteogenic cell culture system to evaluate the cytocompatibility of Osteoset, a calcium sulfate bone void filler. *Biomaterials* 21, 2413–2425. doi: 10.1016/s0142-9612(00)00109-5

Wornham, D. P., Hajjawi, M. O., Orriss, I. R., and Arnett, T. R. (2014). Strontium potently inhibits mineralisation in bone-forming primary rat osteoblast cultures and reduces numbers of osteoclasts in mouse marrow cultures. *Osteoporosis. Int.* 25, 2477–2484. doi: 10.1007/s00198-014-2791-5

Xu, F. T., Li, H. M., Zhao, C. Y., Liang, Z. J., Huang, M. H., Li, Q., et al. (2015). Characterization of chondrogenic gene expression and cartilage phenotype differentiation in human breast adipose-derived stem cells promoted by ginsenoside rg1 in vitro. *Cell Physiol. Biochem.* 37, 1890–1902. doi: 10.1159/000438550

Yan, S. N., Feng, L. B., Zhu, Q. Y., Yang, W., Lan, Y., Li, D., et al. (2018). Controlled release of BMP-2 from a heparin-conjugated strontium-substituted nanohydroxyapatite/silk fibroin scaffold for bone regeneration. *Acs. Biomater. Sci. Eng.* 4, 3291–3303. doi: 10.1021/acsbiomaterials.8b00459

Yang, F., Wu, S. G., Pan, Y. F., Song, F. L., and Li, T. (2009). Preparation and characteristics of erythromycin microspheres for lung targeting. *Drug Dev. Ind. Pharm.* 35, 639–645. doi: 10.1080/03639040802512243

Yang, F., Yang, D. Z., Tu, J., Zheng, Q. X., Cai, L. T., and Wang, L. P. (2011). Strontium enhances osteogenic differentiation of mesenchymal stem cells and in vivo bone formation by activating wnt/catenin signaling. *Stem Cells* 29, 981–991. doi: 10.1002/stem.646

Yang, S. Y., Wang, L., Feng, S. B., Yang, Q. M., Yu, B., and Tu, M. (2017). Enhanced bone formation by strontium modified calcium sulfate hemihydrate in ovariectomized rat critical-size calvarial defects. *Biomed Mater.* 12:035004. doi: 10.1088/1748-605x/aa68bc

Yin, L. H., Cheng, W. X., Qin, Z. S., Sun, K. M., Zhong, M., Wang, J. K., et al. (2015). Effects of ginsenoside Rg-1 on the proliferation and osteogenic differentiation of human periodontal ligament stem cells. *Chin. J. Integr. Med.* 21, 676–681. doi: 10.1007/s11655-014-1856-9

Zheng, H. Z., Fu, X. K., Shang, J. L., Lu, R. X., Ou, Y. F., and Chen, C. L. (2018a). Ginsenoside Rg1 protects rat bone marrow mesenchymal stem cells against ischemia induced apoptosis through miR-494-3p and ROCK-1. *Eur. J. Pharmacol.* 822, 154–167. doi: 10.1016/j.ejphar.2018.01.001

Zheng, Y. Y., Xiong, C. D., Zhang, D. J., and Zhang, L. F. (2018b). In vitro bioactivity evaluation of alpha-calcium sulphate hemihydrate and bioactive glass composites for their potential use in bone regeneration. *B Mater. Sci.* 41:59.

Conflict of Interest: The authors declare that the research was conducted in the absence of any commercial or financial relationships that could be construed as a potential conflict of interest.

frontiers
in Bioengineering and Biotechnology

ORIGINAL RESEARCH
published: 26 August 2020
doi: 10.3389/fbioe.2020.00971

Production and Characterization of an Integrated Multi-Layer 3D Printed PLGA/GelMA Scaffold Aimed for Bile Duct Restoration and Detection

Yang Xiang[1,2], Weijia Wang[3], Yuanhui Gao[4], Jianquan Zhang[1], Jing Zhang[5], Zhiming Bai[2], Shufang Zhang[4] and Yijun Yang[1]**

[1] Department of Hepatobiliary Surgery, Affiliated Haikou Hospital of Xiangya Medical College, Central South University, Haikou, China, [2] Department of Urology Surgery, Affiliated Haikou Hospital of Xiangya Medical College, Central South University, Haikou, China, [3] School of Metallurgy and Environment, Central South University, Changsha, China, [4] Central Laboratory, Affiliated Haikou Hospital of Xiangya Medical College, Central South University, Haikou, China, [5] Department of Obstetrics and Gynecology, Affiliated Haikou Hospital of Xiangya Medical College, Central South University, Haikou, China

Edited by:
Gang Wu,
VU University Amsterdam,
Netherlands

Reviewed by:
Liangju Kuang,
Harvard Medical School,
United States
Liming Bian,
The Chinese University of Hong Kong,
China

****Correspondence:***
Shufang Zhang
haikouyiyuan@126.com
Yijun Yang
dryyj@163.com

Specialty section:
This article was submitted to
Biomaterials,
a section of the journal
Frontiers in Bioengineering and
Biotechnology

Received: *15 March 2020*
Accepted: *27 July 2020*
Published: *26 August 2020*

Citation:
Xiang Y, Wang W, Gao Y, Zhang J, Zhang J, Bai Z, Zhang S and Yang Y (2020) Production and Characterization of an Integrated Multi-Layer 3D Printed PLGA/GelMA Scaffold Aimed for Bile Duct Restoration and Detection. Front. Bioeng. Biotechnol. 8:971. doi: 10.3389/fbioe.2020.00971

We successfully fabricated artificial bile duct via 3D printing technique which was composed of poly (lactic-co-glycolic acid) (PLGA) and gelatin methacrylate (GelMA). The PLGA-inner layer provided sufficient strength to support the bile duct contraction, the GelMA-outer layer possessed good biocompatibility to provide a good living environment for the cells. Moreover, IKVAV laminin peptide (Ile-Lys-Val-Ala-Val) and ultrasmall superparamagnetic iron oxide (USPIO) were used to regulate scaffold cell adhesion and magnetic resonance imaging (MRI) detection, respectively. After BMSCs co-culture with IKVAV at a certain concentration, the survival rate and adhesion of BMSCs was increased obviously. Meanwhile, the fabricated scaffold exhibited the tensile modulus in the range of 17.19 – 29.05 MPa and the compressive modulus in the range of 0.042 – 0.066 MPa, which could meet the needs of human implantation. In an animal experiment *in vivo* pig bile duct regeneration, PLGA/GelMA/IKVAV/USPIO duct conduits could promote bile duct regeneration and enhance cytokeratin 19 (CK19) expression. In summary, the composite bile duct scaffold with excellent MRI imaging function and biocompatibility could be used to develop bioactive artificial bile ducts.

Keywords: 3D printing, IKVAV, hydrogel, bile duct, magnetic resonance imaging (MRI)

INTRODUCTION

In the current treatment of extrahepatic bile ducts affected by tumors or stenosis, surgical resection and reconstruction often cause postoperative complications, such as biliary leakage, bile duct strictures and bile leakage (Zografakis et al., 2003; Vieira-Silva et al., 2019). Clinical treatment, such as intrabiliary stent placement, percutaneous transhepatic biliary drainage (PTBD) and biliary anastomosis, has been used to relieve obstruction of the common bile duct and repair damaged bile ducts. However, different types of complications using metal and plastic stents (polyethylene, polyvinyl chloride, and polyurethane) have been reported, particularly in association with biofilm accumulation, clogging, and bacterial infection (Bege et al., 2012; Ogura et al., 2019). Therefore, if an artificial bile duct could be obtained that is completely consistent with the function of natural organs, artificial bile duct could be implanted to replace the pathological bile duct to prevent bile flow disorder and avoid the occurrence of liver transplantation. During the process of excellent bile duct preparation, two major factors should be considered.

Material selection is a key factor for bile duct restoration. Among them, poly (L-lactide-co-glycolide) (PLGA) and polycaprolactone (PCL) was a biocompatible (Reid et al., 2013), degradable (Lee et al., 2012), non-toxic material (Li et al., 2015). It has many successful applications in bile duct regeneration (Zong et al., 2017). PLGA could provide sufficient support strength to prevent bile duct contraction and narrowness. Moreover, it has good mechanical properties. In addition, proper flexibility and rigidity could facilitate cell migration. Recently, an emerging photo-cross linkable gelatin methacrylate (GelMA) have recently attracted increasing research interest in tissue engineering (Mccoul et al., 2017; O'Bryan et al., 2017; Grosskopf et al., 2018; Gao et al., 2019), which was not only owing to their biocompatibility of gelatin, but also because of easy cross-linking under UV light irradiation.

The second factor is surface modification and scaffold fabrication (Li et al., 2019). Although numerous materials have been exploited for artificial bile ducts, such as gelatin (Yan et al., 2018), poly (L-lactide-co-glycolide) (PLGA) (Zong et al., 2017), and polycaprolactone (PCL) (Bloise et al., 2020), few studies reported bilayered scaffold for bile duct tissue engineering. Li et al. (2020) reported a novel 3D printing PCL/GelMA scaffold containing USPIO for MRI, which could achieve MRI imaging and be beneficial to the proliferation of cells on the scaffolds, but there was poor cell adhesion properties. As a key factor in bile duct tissue engineering, an ideal scaffold would support cell adhesion, proliferation and differentiation, and act as physical reservoir to support bile flow and load bioactive substances. However, a scaffold composed of one material makes it difficult to strike a balance between the requirements to support bile flow and new tissue formation. Therefore, PLGA tube modification is critical for optimal biocompatibility. Nucleic acids (Kang et al., 2015), polypeptides (Han et al., 2010), and cells (Lee et al., 2015) were commonly used for surface coatings. IKVAV laminin peptide have good hydrophilicity and good biochemical properties, can improve cell adhesion, and is a substrate for bioactive scaffold materials. Therefore it was widely used in the field of tissue engineering. Laminin was found as an extracellular matrix (ECM) molecule in basement membranes, was the key substance for cell adhesion and polarization, widely used in neuroengineering (Silva et al., 2014). Prior study reported that laminin could promote bile duct cell polarization to form bile ducts (Tanimizu et al., 2007). However, there were no studies on the interaction between IKVAV and bile duct cells.

3D bioprinting technology hold great promise in the field of tissue engineering and regenerative medicine (Patel et al., 2017; Roh et al., 2017). This technology has been widely utilized to prepared arbitrary-shape three-dimensional tissues and organs including bile duct-like structures. Herein, layer-by-layer freeform production was used to encapsulate cells within microstructure of biocompatible hydrogel mixtures. Narayanan et al. reported that hydrogels are composed of human adipose-derived stem cells, PLA fibers and sodium alginate to print into a meniscus shape through extrusion bioprinting (Narayanan et al., 2016). Lozano et al. (2015) used a coaxial nozzle extrusion device to print neuron cells into a brain-like structure, and the results showed that the printed nerve cells can stretch and grow synapses. However, the degradation and repair of the 3D printing stent *in vivo* could not be detected in real time. Diagnostic tools, including computed tomography (CT) and magnetic resonance imaging (MRI), were employed to combination with the 3D scaffold to achieve a dual effect of diagnosis and treatment (Wang et al., 2017).

In this study, we innovatively designed a novel bilayered bile duct scaffold by layer by layer casting (LBLC) method as **Scheme 1**. The inner layer consist of PLGA, which exhibited appropriate mechanical properties, slow degradation kinetics and good biocompatibility. GelMA as matrix to incorporate IKVAV and ultrasmall superparamagnetic iron oxide (USPIO) was used for the outer, which would be conducive to formation of new tissue due to its rapid degradation. To further demonstrate the application, we tested the bioactivity and adhesion of IKVAV and examined the effects of the IKVAV on BMSCs cells. Meanwhile, we evaluated the ability of scaffold for bile duct regeneration *in vivo* pig bile duct defect model. Our engineered scaffold could be used in the construction of an artificial bile duct, due to its high flexibility, suitable mechanical strength and biocompatibility.

MATERIALS AND METHODS

Reagents and Materials

Gelatin (Gel, derived from pig skin, adhesive strength ∼300 g bloom) and methacrylate anhydride (MA) were obtained from Aladdin Reagent Company (Shanghai, China). The initiator lithium phenyl-2,4,6-trimethylbenzoylphosphinate (LAP) was purchased from Yinchang New Material Co., Ltd. (Shanghai, China). IKVAV peptides ($C_{16}H_{31}$O-NH-AAAGGGGEIKVAV-COOH, purity at >98%) was purchased from Apeptide Bio-Technology Co., Ltd. (Shanghai, China). Poly (lactic-co-glycolic acid) (PLGA, lactide: glycolide = 75:25, $M_w = 66 \sim 107$ kDa) was purchased from shanghai Ding Biological Technology Co., Ltd. (Shanghai, China). USPIO (average particle size = 20 nm) were obtained from Sino Biomaterials Co., Ltd. (Shanghai, China). The other reagents were listed as follows: Dulbecco's modified Eagle's medium (DMEM)/F12 with Glutamax (Invitrogen, Carlsbad, CA, United States) and fetal bovine serum (FBS, Gibco, United States), penicillin/streptomycin solution (Gibco, United States), Cell Counting Kit-8 (CCK-8, Dojindo, Japan). All other reagents were analytical reagent grade.

Synthesis of GelMA

Gelatin (10 g) was dissolved in 100 mL distilled water. After being dissolved at 50°C, 15 mL of methacrylate anhydride was added

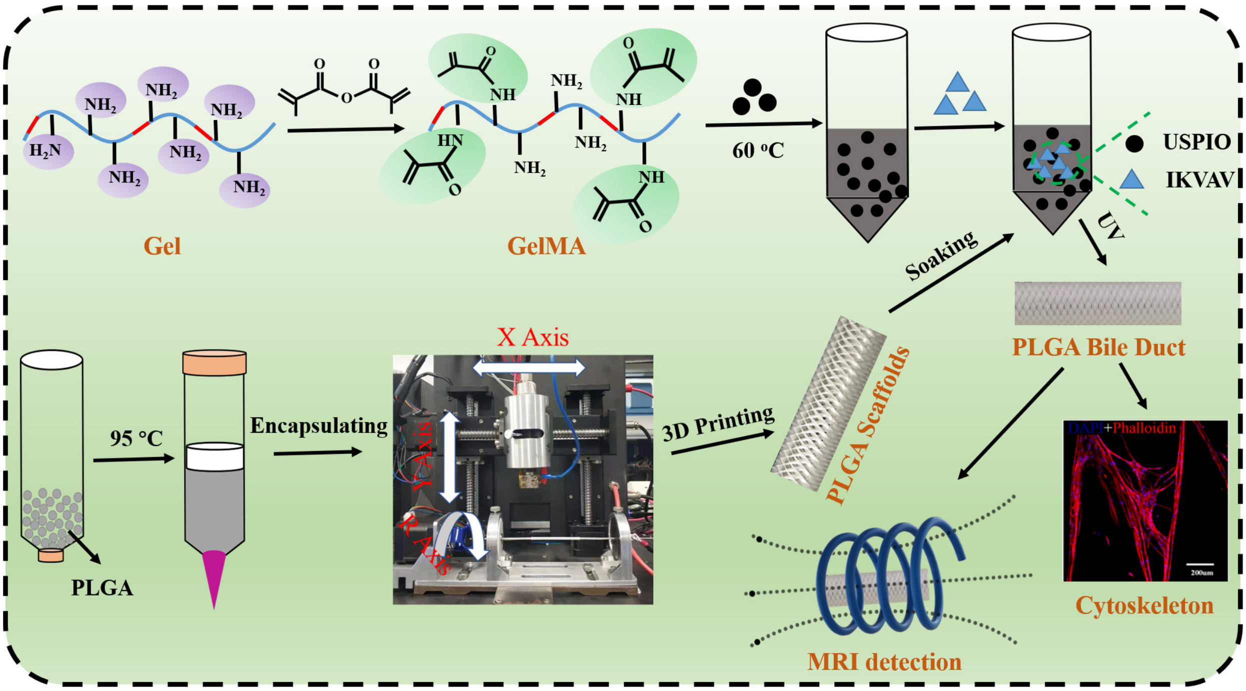

SCHEME 1 | Schematic of GelMA and the schematic illustration of PCL bile duct with LBLC method.

and reacted at 50°C for 4 h. Then dialysis with dialysis bags (molecular weight cutoff: 1000) for 2–3 days and then lyophilized at 80°C to obtain methacrylate gelatin (GelMA).

Fabrication of the PLGA Bile Duct Scaffold

All printings were carried out using a customized 3D printer (EFL-BP-6800, Suzhou, China) equipped with a nozzle temperature controller and a chamber temperature controller (Park et al., 2017). Firstly, PLGA particles were put into the barrel of a high-pressure near-field direct writing 3D printer, then set the extrusion temperature to 95°C and the bed temperature to 70°C for 2 h. After the PLGA was melted, air pressure was set to 7 kPa while applying voltage at 4 kV. Finally, the PLGA bile duct model was printed on a metal rotating shaft of 5 mm diameter by using default speed of 1000 mm/min, and the total number of layers was set to 100.

Fabrication of the PLGA/GelMA/IKVAV/USPIO Composite Bile Duct Scaffold

5 wt% GelMA and 0.5 wt% LAP was dissolved in PBS at 37°C. The IKVAV peptide (200 μg) was then added to the GelMA solution. Finally, GelMA/IKVAV solution and USPIO were mixed in accordance with a different mass/volume (g/L) ratio and fully mixed using a vortex mixer to prepare the final GelMA/IKVAV/USPIO scaffold for subsequent use. The PLGA tubular stent was fully infiltrated with the GelMA/IKVAV/USPIO solution, and then the GelMA/IKVAV/USPIO solution was crosslinked by a 405 nm ultraviolet (UV) lamp with a light intensity of 3.0 mW/cm^2 for 50 s, and finally the PLGA/GelMA/IKVAV/USPIO solution composite tubular stent was prepared.

Preparation of Cell-Scaffold Constructs

The bone marrow mesenchymal stem cell (BMSCs) were cultured in stem cell medium supplemented with DMEM/F12 with GlutaMAX and 10% fetal bovine serum, and were cultured under 5% carbon dioxide at 37°C. BMSCs were harvested after they reached approximately 80% confluence. The PLGA/GelMA/IKVAV/USPIO composite scaffold was successively soaked in 75% alcohol (Dashti et al., 2016), sterile PBS and sterile DMEM/F12 with GlutaMAX for 1 h, respectively. Then, the BMSCs cells with a density of 1 × 10^5 cells/ml were directly seeded onto the outside surface of sterilized PLGA/GelMA/IKVAV/USPIO composite tubular scaffold for routine cell culture.

Characterization of GelMA

The infrared (IR) spectra of the Gel and GelMA was detected by Fourier transform infrared spectroscope (FTIR, TENSOR 27; Bruker, Germany). Rheological tests of GelMA hydrogel at different concentrations were performed using a strain-controlled rheometer (MCR 302, Anton Paar, Japan) equipped with a parallel-plate (25 mm) geometry. The storage modulus (G′) and loss modulus (G″) were both measured in this study. Oscillation time sweep was measured with 1 Hz frequency at 25°C for 600 s. Additionally, frequency sweep test was conducted from a function angular frequency of 0.1–10 Hz with 0.1% strain.

Scanning Electron Microscope (SEM) Analysis

The micromorphology of the 3D structure scaffolds before and after incubating with GelMA hydrogel was observed by SEM (J SIRION-100; Eindhoven Netherlands) at 10 kV accelerating voltage. The samples were sputter coated with gold for 10 s before SEM observation.

Mechanical Testing

The mechanical properties of PLGA/GelMA/IKVAV/USPIO scaffold (60 mm in length) was measured by a universal material testing machine (Instron 5543A, Massachusetts, United States) with a crosshead speed of 30 mm/min. Rectangular specimens of PLGA/GelMA/IKVAV/USPIO scaffold (20 mm in height) were measured at the compressive velocity of 1 mm/min. The compressive modulus was measured from 2 to 10% of linear curve fit from the compressive curve. At least three samples were recorded for final statistical evaluation.

Swelling Testing

Swelling of the 3D print PLGA/GelMA/IKVAV/USPIO scaffold was investigated by the gravimetry method (Xue and Falcon, 2019). Briefly, lyophilized scaffold was weighed (W_d) before being immersed in 2 ml PBS at 37°C until the equilibrium swelling was reached, after which the scaffold were removed. Excess surface water on the scaffolds was gently wiped with filter paper before the swollen scaffold was finally weighed (W_s). The equilibrium swelling ratio was calculated using the following equation

$$\text{Swelling ratio} = (W_s - W_d)/W_d \times 100\%$$

In vitro Biodegradation

The degradation studies of the fabricated 3D printing scaffolds (PLGA and PLGA/GelMA/IKVAV/USPIO) were conducted in PBS with or without lysozyme (Hu et al., 2019). Briefly, the tested scaffold samples (Wi) were immersed into 10 mL of PBS with or without lysozyme, followed by incubation at 37°C with a stirring rate of 60 rpm. At predetermined time points, the weights (Wc) of degraded samples were recorded after distilled water washing and freeze-drying.

The degradation rate was determined using the following equation:

$$\text{Degradation} = (\text{Wi} - \text{Wc})/\text{Wi} \times 100\%$$

where Wi is the weight of the scaffold at day 0, and Wc is the weight of the scaffold at each time point.

MRI

First, the PLGA/GelMA/IKVAV/USPIO composite scaffold was placed in the centrifugal tube, and then all the composite tubular stents were performed T2 weighted imaging (T2WI) in clinical 3T whole body magnetic resonance scanner (SENSE-flex-M; Philips, Best, The Netherlands) using a small extremity coil. The parameters of T2WI were as follows: TR = 5000ms, TE = 5.8 ms, FOV = 8mm × 8mm, matrix size = 64 × 64, in-plane resolution = 125 mm × 125 mm, slice thickness = 0.8 mm.

Effect of IKVAV on BMSCs

Effect of IKVAV on Adhesion Rate of BMSCs

The IKVAV were dissolved in PBS, at five concentrations (80, 100, 200, 400, and 800 μg/mL) to be used. Soak the round cover glass slides in 75% ethanol for 4 h, dry them in a 12-well plate, and coating in several different concentrations of IKVAV solutions. After incubated for 4 h in incubator and washed with PBS. 0.5 mM Laminin was used as positive control group, and the untreated group served as the negative control. BMSCs cells were inoculated into 12-well plate with 4×10^5 per well. After 24 h, the cells were digested, counted, and statistical analysis was made. Cell adhesion rate was calculated according to the following formula:

$$\text{The cell adhesion rate (\%)} = \left(\text{the adhesive cells}\right) / \left(\text{the total cell}\right) \times 100\%$$

BMSCs cells were inoculated into 96 plates at a density of 2×10^4/ml for 24 h. Then, different concentrations of IKVAV solution (80, 100, 200, 400, and 800 μg/mL) were added, and three multiple holes were set up. At the period's time point (1, 2, and 3 days), the OD value of cells was measured by CCK-8 kit to directly reflect the proliferation of cells. Cell viability was calculated according to the following formula:

$$\text{Cell viability (\%)} = \left(\text{OD}_{\text{sample}} - \text{OD}_{\text{blank}}\right) / \left(\text{OD}_{\text{control}} - \text{OD}_{\text{blank}}\right) \times 100\%$$

Effect of USPIO of BMSCs

The GelMA hydrogels containing different concentrations of USPIO were prepared with a different mass/volume (g/L) ratio (USPIO: GelMA = 1:1, 2:1, 3:1, 4:1, 5:1, 6:1, 7:1, 8:1, 9:1, 10:1). Then, BMSC cells with the cell density of 1×10^4 cells/mL were cultured and inoculated into 96-well plate. After the cells adhered to the wall, GelMA hydrogels with different concentrations of USPIO were added. After 24 h of culture, the medium was replaced with the DMEM solution containing 10% CCK-8, and the culture continued for 2–4 h. Under the condition of 450 nm wavelength, the absorbance of each hole was read by enzyme labeling instrument.

Cell Proliferation Analysis

CCK-8 was used to assess the cell proliferation according to the instructions. BMSCs cultured with 10% fetal bovine serum and 1% penicillin/streptomycin at 37°C, 5% CO_2 condition. Before culturing the cells, the PLGA/GelMA/IKVAV/USPIO scaffolds were soaked in 75% ethanol for 1 h, washed with PBS for 3 times, and then cultured overnight in a 24-well petri dish. The naked GelMA, PLGA scaffold and PLGA/GelMA/USPIO were used as control. On days 1, 4, 7, and 10 of culture, samples were washed 3 times with PBS. Then, the DMEM medium containing 10% volume of CCK-8 were added to each well, and incubated for another 3 h. Finally, the OD of each solution were evaluated by microplate reader among at wavelength of 450 nm.

Live and dead cells were further visualized by LIVE/DEAD cell kit. The activity of intracellular esterase and the integrity of plasma membrane were measured by Calcein AM and Ethidium homodimer-1, respectively. They were mixed with phosphate buffer saline (DPBS) of Dulbecco and added to media-free cells/scaffolds, and the cells on scaffolds were observed by an inverted fluorescence microscope.

Cell Morphology Analysis

The morphology of cells was observed by cytoskeleton staining, including phalloidin staining and DAPI staining. Briefly, BMSCs cells were inoculated into PLGA/GelMA/IKVAV/USPIO scaffolds with an initial density of $4 \times 10^4/\text{cm}^2$ for 3 days. Then, the scaffold was taken out of the wells, fixed with 4% paraformaldehyde for 30 min, and washed with PBS. Finally, cells on the scaffold were counterstained by the F-actin with Phalloidin and nuclei with dye diamidino-2-phenylindole (DAPI). Finally, cells on the scaffold were observed by a confocal laser microscope (Leica, Wetzlar, Germany).

Animal Experiments

The animal experiments were performed with the permission of the Institutional Animal Care and Use Committee (IACUC) of Central South University. The male inbred Wuzhishan miniature pigs at 8 months of age weighing 30 ± 2.5 kg were Haikou Peoples Hospital (Hainan, China). All animals were maintained under 12-h light/dark conditions and fed a standard commercially available pig feed. Animals were divided into two groups (Normal and PLGA/GelMA/IKVAV/USPIO composite tubular scaffold treated) of six animals each. Before surgery, animals were fasted overnight for 12 h with access to water only. The pigs were fasted overnight for 12 h prior to surgery, and were provided with oral antibiotics (300 mg of cephalexin) following surgery. All pigs were anesthetized, placed in ventral recumbency, and laparotomized via a midline incision in the upper abdomen to expose the extrahepatic bile duct (EHBD) (**Figure 9A**). The lower EHBD was transected and the artificial PLGA/GelMA/IKVAV/USPIO composite bile duct scaffold was anastomosed end-to-end to the proximal and distal ends of the EHBD with interrupted 4.0 Ethilon sutures (**Figure 9B**). We further confirmed adequate bile drainage through the anastomosed bile duct scaffold during the surgery, the abdominal cavity was irrigated with warm saline and closed following surgery. For histological analysis, fresh tissues obtained from the pig bile duct were fixed with 10% formalin followed by paraffin embedding. Samples were sectioned at 4 μm and stained with hematoxylin and eosin (H&E). For immunohistochemistry, sections were blocked with 5% bovine serum albumin (BSA) in PBS for 30 min and incubated overnight with the primary antibody CK19 (BA4154, 1: 400, Boster) in PBS containing 1% BSA at 4°C.

Statistical Analysis

All of the experiments were carried out at least in triplicate. All data were presented as mean result ± standard deviation (SD). One-way analysis of variance (ANOVA) evaluated the differences between groups. $P < 0.05$ considered statistically significant, with $* = p < 0.05$; $** = p < 0.01$; $*** = p < 0.001$.

RESULTS AND DISCUSSION

Characterization of GelMA

To form the hydrogel for bile duct restoration, we synthesized the photocrosslinkable GelMA polymer by reacting methacrylic anhydride with gelatin according to methods previously described (Sun et al., 2018; Aldana et al., 2019b). The FTIR spectra of gelatin, MA and GelMA were shown in **Figure 1A**. The main bands of gelatin included a strong broad overlapping peak of 3252 cm^{-1}, attributed to the stretching of O–H (Topkaya, 2015). In addition, the characteristic absorption bands of GelMA were observed 1697 cm^{-1} (amide I, the stretching of C=O bond), 1542 cm^{-1} (amide II, bending of N-H bond) and 1458 cm^{-1} (amide III, plane vibration of C–N and N–H), respectively (Aldana et al., 2019a). Meanwhile, N–H stretching (amide A) was observed at 3284 cm^{-1}, demonstrating that MA was successfully grafted onto the gelatin chains.

To demonstrate the feasibility of the formed bioink for 3D printing, the rheological behaviors were carried out. The gelation behavior of different concentrations of GelMA was monitored by rheological analysis. As shown in **Figure 1B**, the storage modulus (G') also surpassed the loss modulus (G'') with the frequency from 0.1 to 10 Hz, which indicated that the photo-crosslinked GelMA hydrogel had enhanced resistance to deformation. As shown in **Figure 1C**, the time-sweep oscillation experiment shows the storage modulus G' of hydrogels was increased with an increase in the concentration of the GelMA. There was no significant difference between the G' of 15% GelMA and the G' of 10% GelMA. However, GelMA hydrogels at concentrations of 2 and 3% (w/v) with low G' (∼100 Pa) was insufficient to enhance the mechanical strength of the PLGA scaffold. Noticeably, GelMA hydrogels with a concentration of 10% and 15% (w/v) have a high G' (∼500 Pa), which is similar to a previous study (Athirasala et al., 2017).

Characterization of the Scaffold

An ideal hydrogel-based scaffold for usage in tissue engineering and regenerative medicine should have the following characteristics, such as sufficient mechanical properties, appropriate swelling ratio and biodegradation ratio *in vivo*, and good biocompatibility (Kim et al., 2016). Therefore, we systematically studied the effect of adding GelMA on the performance of these scaffolds. Here, a conduit with the fiber diameter of ∼50 μm was created using microneedles. After curing, the microneedles and the rolling tube mold were removed. The morphology of the 3D printing conduit was characterized using optical imaging and scanning electron microscopy (SEM). As shown in **Figures 2A–D**, the PLGA tubular scaffold has a uniform rhombohedral porous structure, and the wire diameter was uniform, about 5–7 μm, which was beneficial to the adhesion and growth of cells. The GelMA/IKVAV/USPIO gel uniformly fills the pores of the PLGA tubular scaffold. As shown in **Figures 2E–H**, the surface of

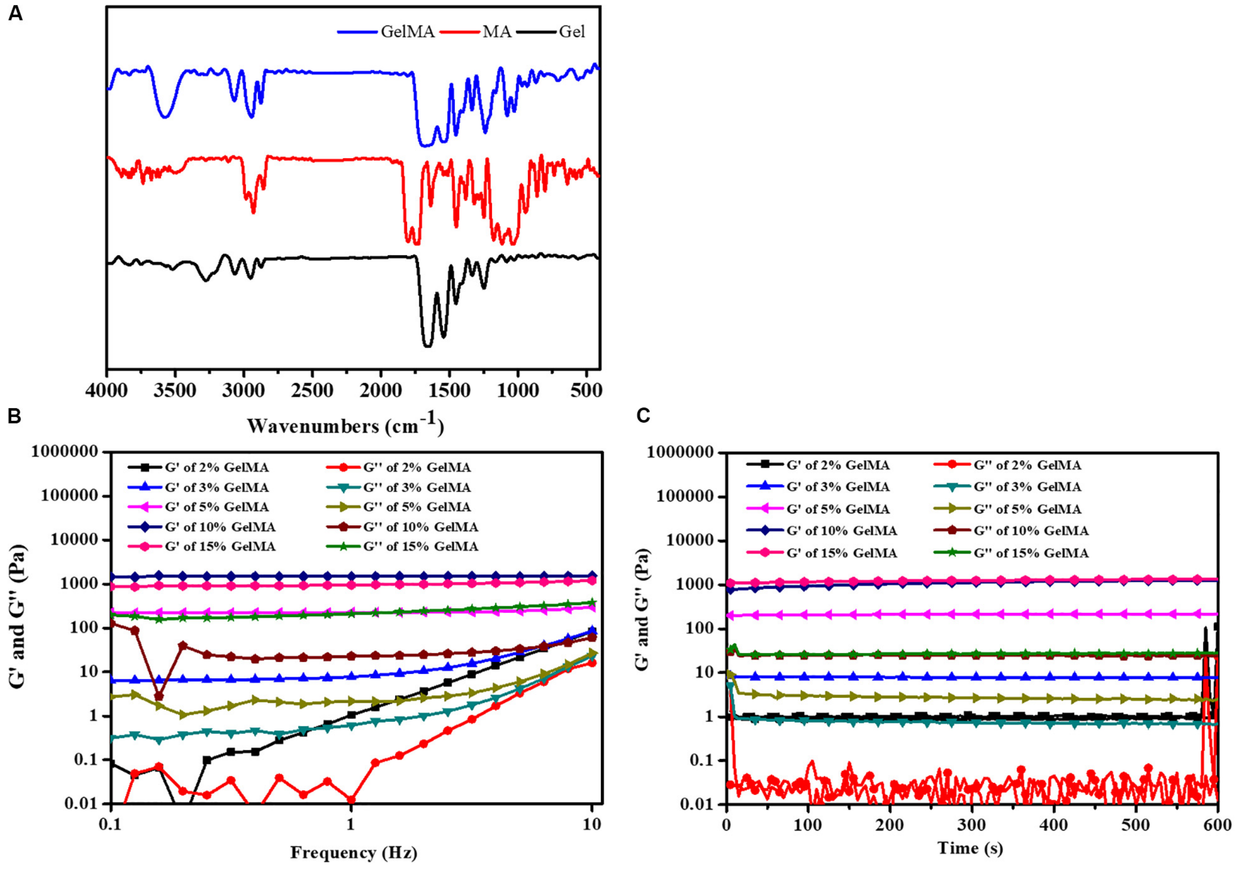

FIGURE 1 | (A) FTIR spectrum of GelMA. **(B)** The gel viscosity with frequency ranging from 0.1 to 10 Hz. **(C)** Rheological properties.

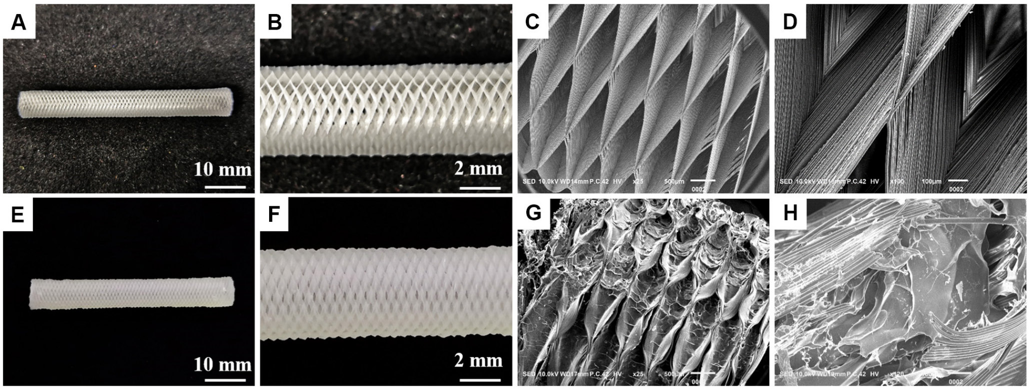

FIGURE 2 | Digital image of PLGA **(A,B)** and **(E,F)** PLGA/GelMA/IKVAV/USPIO tubular scaffold. Low- and high-magnification SEM image of PLGA **(C,D)** and PLGA/GelMA/IKVAV/USPIO **(G,H)**.

PLGA/GelMA/IKVAV/USPIO composite tubular scaffold has a microporous structure, which was beneficial to cell adhesion and growth (Shkarina et al., 2018).

Mechanical Properties of the Scaffolds

An ideal scaffold should equip with good mechanical properties to keep its integrity during use. The mechanical properties of the prepared scaffolds were evaluated by the tensile modulus and compressive modulus. As shown in **Figure 3**, the tensile modulus of the scaffold was measured to be in the range of 17.19 – 29.05 MPa and the compressive modulus in the range of 0.042 – 0.066 MPa. The mechanical properties were also tested in 37°C water bath to simulate the bile flow environment *in vivo*. The measured tensile modulus of the multi-layer

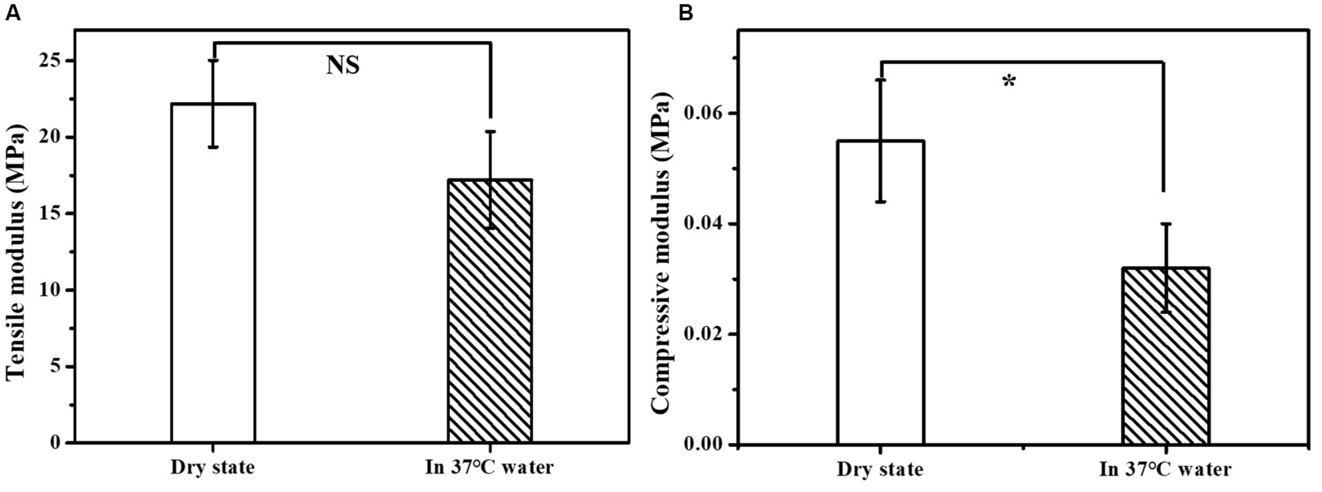

FIGURE 3 | Mechanical properties of the composite tubular scaffold. **(A)** Tensile modulus and **(B)** compression modulus of PLGA/GelMA/IKVAV/USPIO composite tubular scaffold in dry state (air environment) and wet state (37°C water bath).

3D-fabrication of PLGA/GelMA/IKVAV/USPIO scaffold was in the range of 14.05 – 20.37 MPa and the compressive modulus in the range of 0.024 – 0.04 MPa, which was suitable for bile duct implantation. Previous research also reported that the mechanical strength of the pure PLGA scaffold was similar to a real bile duct (Zong et al., 2017). The mechanical test indicated that the PLGA/GelMA/IKVAV/USPIO 3D conduit has both flexibility and toughness, which provide a supporting structure and allow duct regeneration. Furthermore, the designed bilayered scaffold has porous structure and improved mechanical stability. Additionally, the bilayered scaffold can be used to design artificial arteries and intestines (Zong et al., 2017).

Swelling Study

As shown in **Figure 4A**, the time-dependent swelling ratio was investigated by using water uptake experiment. The Swelling ratio of the GelMA were around 498.7 ± 11.8%, which was related to the high hydrophilicity of GelMA and porous structure of scaffold. The swelling ratio of PLGA/GelMA and PLGA/GelMA/IKVAV/USPIO scaffold was 351.7 ± 11.5%, 355.2 ± 17.0%, respectively. The relatively low swelling ratio may be related to the presence of PLGA and USPIO which has hydrophobic groups could decrease water adsorption. Meanwhile, PLGA and USPIO layer changed the internal structure and decrease the proportion of micropore, resulting in low swelling ratio. This low swelling ratio will not cause collateral damage to normal tissues.

Stability of Bilayered Bile Duct Scaffold

Recently, most of the bile duct stents used in clinic were non-degradable scaffolds, but as a long-term foreign material, non-degradable scaffolds were easy to cause inflammation, restenosis and other phenomena, resulting in secondary implantation difficulties. In addition, patients have to endure the pain of scaffold removal. Therefore, an increasing amount of scaffolds for bile duct repair were reported (Miyazawa et al., 2005). However, few studies on bilayered bile duct scaffolds have been reported at this time. Here, a kind of PLGA/GelMA bilayered bile duct scaffold was designed and fabricated. The PLGA inner layer exhibited a smooth and compact surface, which will promote the bile acid flow and avoid the bile leakage or cholestasis after implantation. The GelMA outer layer was able to effectively support cells adhesion and growth, load bioactive substances and accelerate the formation of new tissue. It would require as long as 2 years to fully degrade the entire PLGA scaffold *in vivo* (Sun et al., 2006). However, prior study indicated that GelMA hydrogel were completely degraded in PBS after 2 weeks (Yu et al., 2020). As shown in **Figure 4B**, weight retention rate of the PLGA/GelMA/USPIO/IKVAV scaffold either in PBS alone or PBS contained lysozyme decreased gradually with the incubation time increased. Despite the fact that enzyme do not exist in PBS, the hydrogel discs might be degraded by hydrolysis. The degradation of hydrogel were due to a combination of enzymolysis and hydrolysis. Moreover, the prepared scaffold shown a faster degradation behavior in PBS with lysozyme. The PLGA/GelMA/IKVAV/USPIO scaffold degraded ∼40% after 10 days, the fast degradation rate was associated with lysozyme. Prior study reported that lysozyme could degrade natural degradation sites for collagenases and matrix metalloproteinases (MMPs) in GelMA (Yu et al., 2020).

MRI

The composite scaffold was visualized by incorporating USPIO as contrast agent. As shown in **Figure 4C**, the different concentration of USPIO in PLGA/GelMA/IKVAV/USPIO composite tubular scaffold showed different degree of T2-weighted MRI imaging. MRI displayed a uniform signal at the boundary regions, which could intuitively see the original shape and status of the composite scaffold. Moreover, it can be seen that with the concentration of USPIO increases, the more obvious the imaging effect becomes. Hence the position changes of the fluorescence of USPIO can be used to monitor

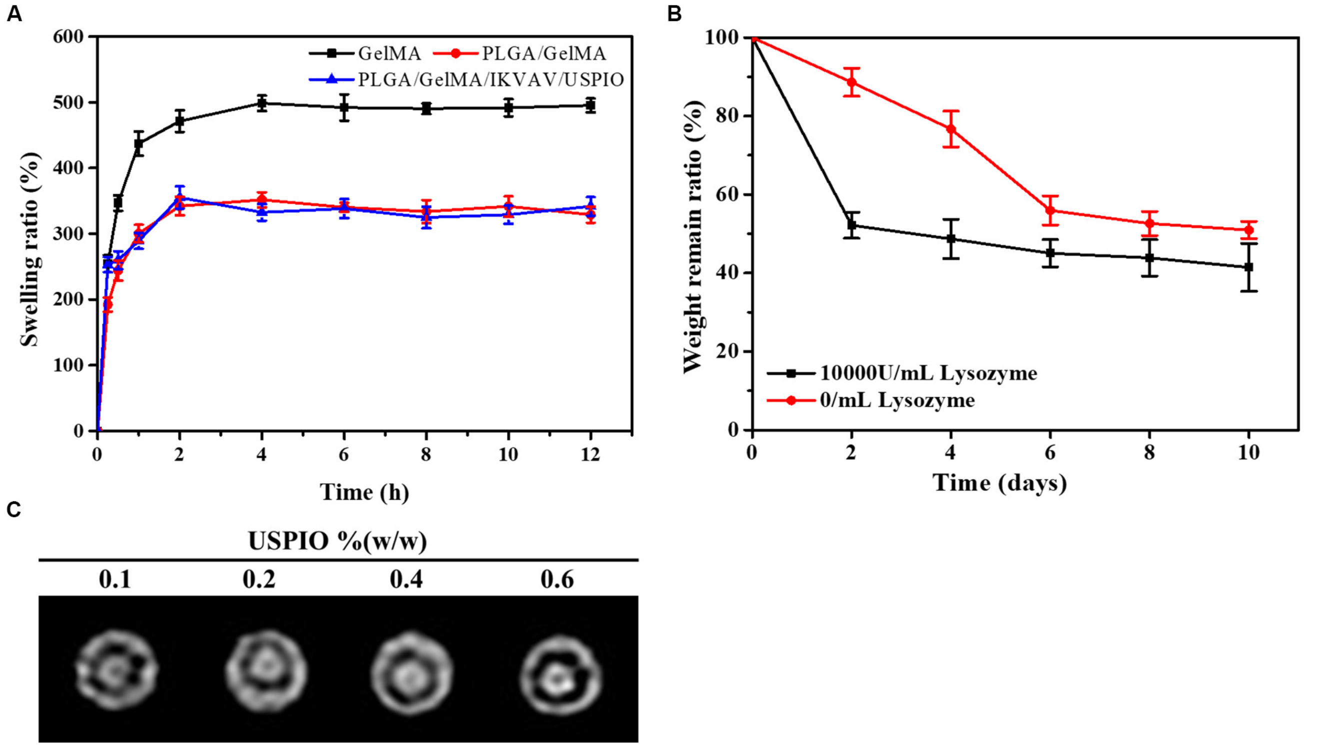

FIGURE 4 | Physical properties of the composite tubular scaffold. **(A)** Swelling ratio of GelMA, PLGA/GelMA, and PLGA/GelMA/IKVAV/USPIO. **(B)** Weight loss rate of the PLGA/GelMA/IKVAV/USPIO scaffolds in PBS with or without 10000 U/mL lysozyme. **(C)** *In vitro* MRI imaging of PLGA/GelMA/IKVAV/USPIO composite tubular scaffold.

degradation of scaffold in real time (Lei et al., 2017). Previous research also reported that T2-weighted MRI imaging was stable and reasonable, USPIO-labeled scaffcan be monitored in real time (Chen et al., 2018).

Effect of IKVAV of BMSCs

Effect of IKVAV on Adhesion Rate of BMSCs

The surface modification of biomedical scaffolds can enhance the adhesion of cells to materials and the biocompatibility of tissues and materials. One way to enhance cell adhesion was to use bioactive peptides such as collagen, fibronectin and laminin, which exist in extracellular matrix, which promote cell adhesion. For example, P15, a polypeptide from collagen, can promote cell adhesion and modulate a variety of genes (Carinci et al., 2004; Lucidarme et al., 2004; Funfak et al., 2019). The peptide has been integrated into a dental implant material and achieved good results. Other peptides that also promote cell adhesion include RGD, YIGSR and IKVAV, from laminin and peptides from laminin, which can directly promote cell adhesion (Kang et al., 2019). The effect of IKVAV on adhesion rate of BMSCs was shown as **Figure 5A**. Through the statistics of cell count at several time points, it can be seen intuitively that although the treatment of IKVAV was not as strong as that of Laminin, it was significantly higher than that of the negative control group, indicating that it still has the effect of promoting cell adhesion to a certain extent. In addition, it can also be seen that the cell adhesion rate at 400 μg/mL was higher than that of other concentrations, and the cell survival rate at this concentration was higher, second only to the positive group.

Effect of IKVAV on Proliferation of BMSCs

The effects of IKVAV on the proliferation of BMSCs were measured by CCK-8 and the results as shown in **Figure 5B**. At the same time point, the cell survival rate increased with the increase of polypeptide concentration, but when the concentration was higher than 400 μg/mL. On the contrary, the survival rate of cells decreased. In addition, it can also be seen that at the same concentration, the survival rate increases with the increase of time.

Effect of USPIO on BMSCs

As shown in **Figure 6A**, when the volume ratio of GelMA: USPIO was 5: 1, the cells have the highest survival rate, and when the volume ratio was less than 5: 1, the cells showed toxic effects. The higher concentration of USPIO, the better the MRI imaging effect. Therefore, under the condition of guaranteeing cell survival, GelMA hydrogel with a large concentration of USPIO was selected, that is, the preferred GelMA and USPIO volume ratio was 5:1.

Cell Proliferation Analysis

The biocompatibility of the developed scaffold was assessed by measuring the proliferative state of BMSCs on the surface

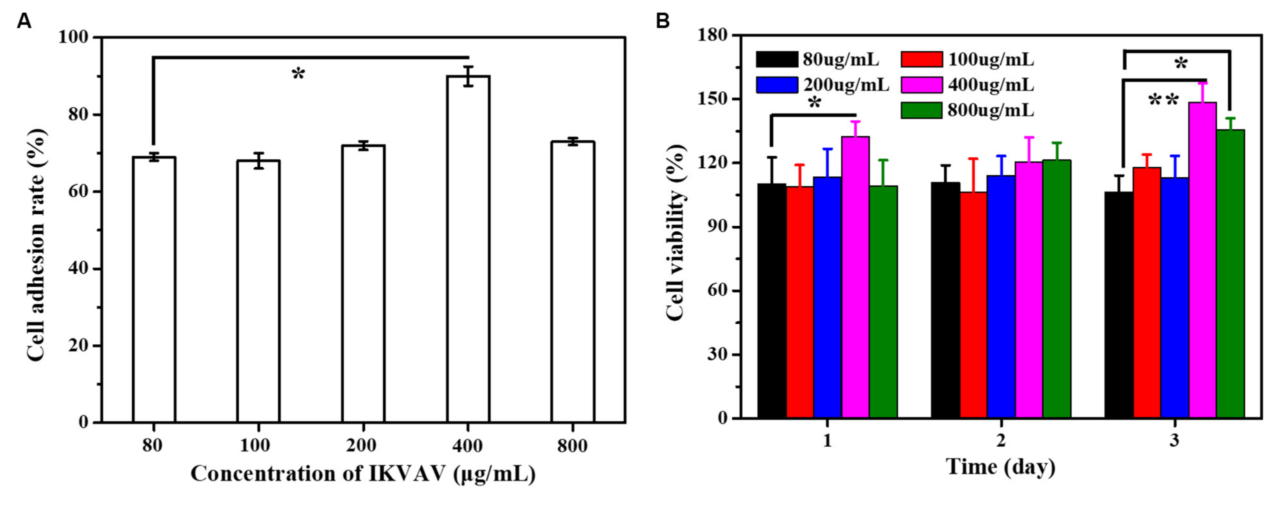

FIGURE 5 | (A) The adhesion rate of the cells with different IKVAN concentrations. **(B)** The cell viability with different IKVAV concentrations.

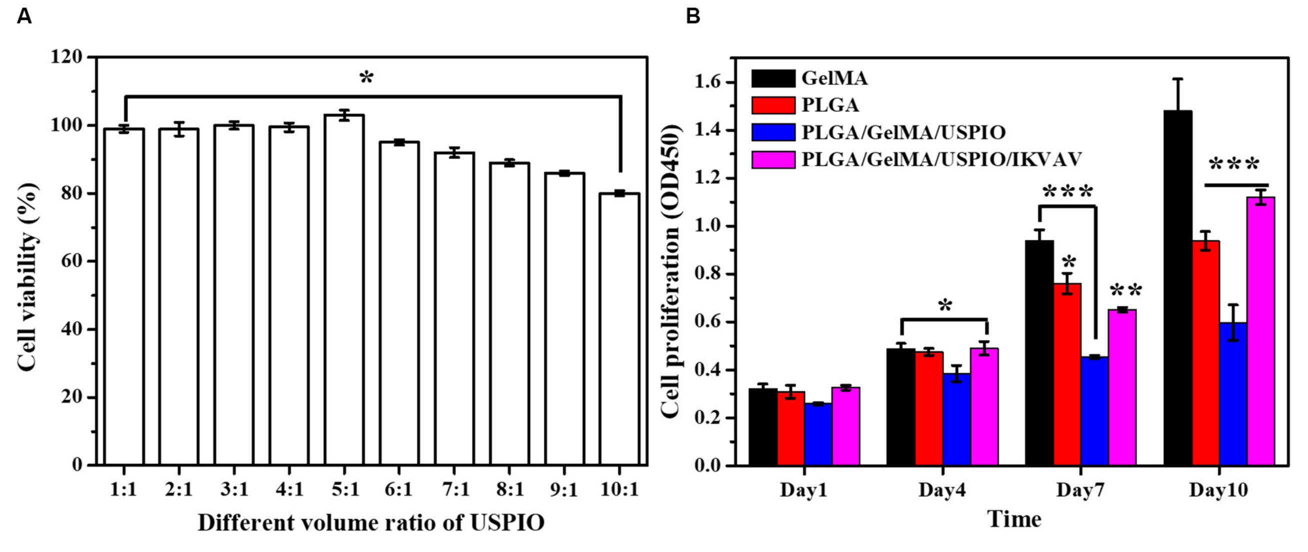

FIGURE 6 | *In vitro* biocompatibility evaluation of the composite tubular scaffold. **(A)** The cell viability of GelMA/USPIO with different USPIO concentrations. **(B)** Proliferation of BMSCs seeded on various composite scaffolds at day 1, 4, 7, and 10.

of scaffold. The cell viability and proliferation of different scaffold for 1, 4, 7, and 10 days as quantitatively examined by CCK-8. As shown in **Figure 6B**, the cell proliferation of pure GelMA group increased significantly from day 1 to day 10. Noticeably, PLGA and PLGA/GelMA/USPIO group showed a relatively lower cell proliferation rate than the GelMA group at day 7 and day 10. It was mainly due to the interaction of PLGA and USPIO with the cells. However, PLGA/GelMA/USPIO/IKVAV showed a higher proliferation than the PLGA and PLGA/GelMA/USPIO group at day 10, which attributed to the positive effect of GelMA and IKVAV modified PLGA in cell proliferation. Based on these results, it was concluded that the PLGA/GelMA/IKVAV/USPIO composite tubular scaffold have excellent biocompatibility to be favorable for BMSCs growth and proliferation.

Moreover, the proliferation of BMSCs on the surface of various scaffolds were further quantitatively visualized by Live/Dead staining at day 10. As shown in **Figure 7**, most of the cells were alive in PLGA/GelMA/IKVAV/USPIO composite tubular scaffold. Moreover, PLGA/GelMA/IKVAV/USPIO group exhibited high cell density and survival rate of over 90%, which was consistent with the results of cell proliferation. Hence, we designed 3D printed scaffolds to improve both cellular distribution and proliferation efficiencies of cells within the scaffold. Therefore, GelMA based 3D printed scaffolds with a satisfied cell density have a great potential for tissue engineering.

Cell Morphology Analysis

As shown in **Figure 8**, BMSCs presents a large cytoskeleton (red stained by Phalloidin reagent) and a small dotted nucleus (blue

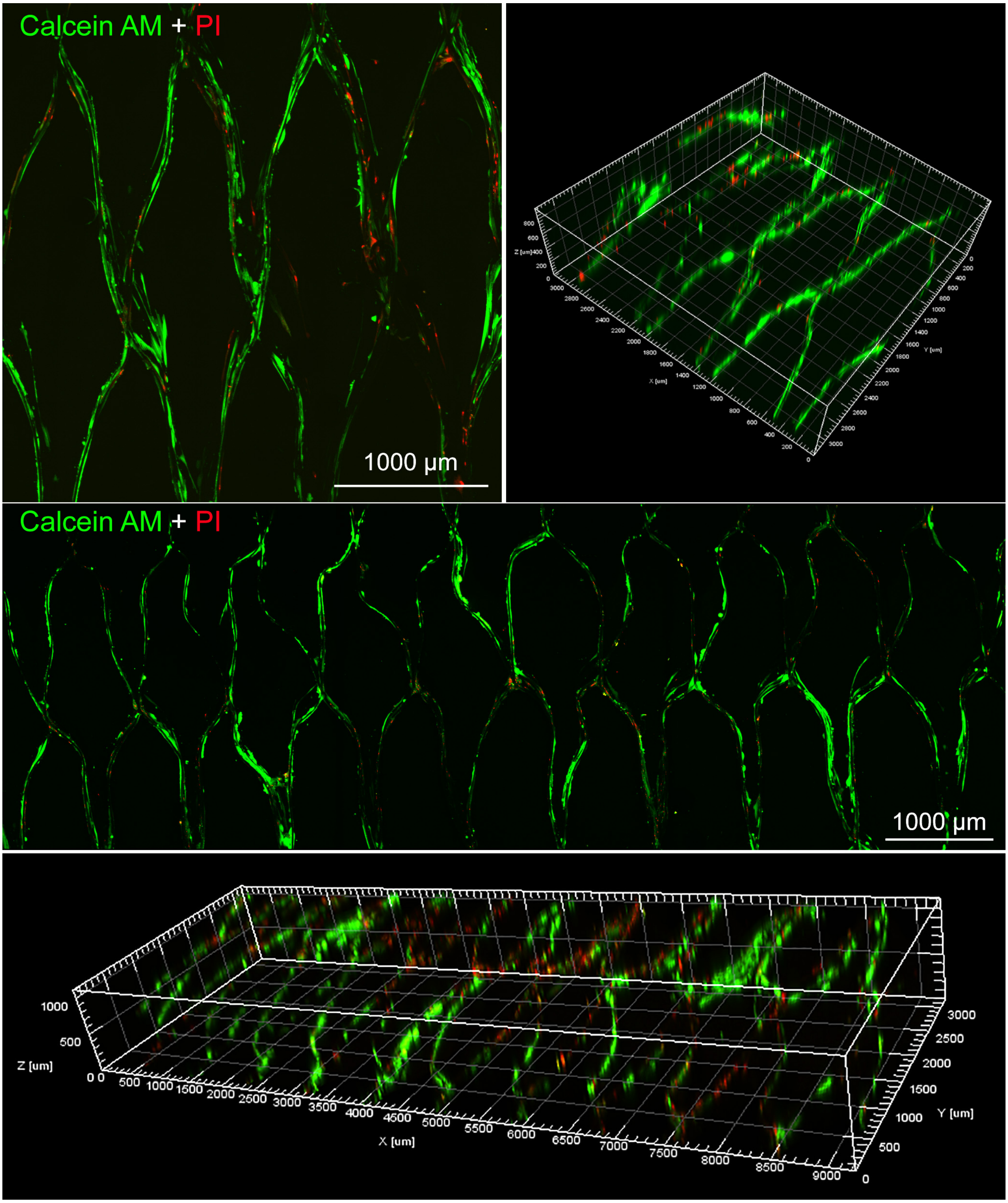

FIGURE 7 | Live/dead staining images of BMSCs seeded on PLGA/GelMA/IKVAV/USPIO composite scaffold at day 10.

stained by DAPI reagent). After 13 days in culture, the cells can be well adhered and spread in PLGA/GelMA/IKVAV/USPIO composite tubular scaffold. In addition, the cells can be seen sticking out on the material and adhering to the surface of the material. Meanwhile, a large number of cells grown into the internal fiber of composite tubular scaffold. The results showed that PLGA/GelMA/IKVAV/USPIO composite tubular scaffold can provide larger surface areas for cell adhesion.

In vivo Pig Bile Duct Defect Model

Histological analysis was performed on the surgically treated bile duct with hematoxylin and eosin (H&E). As shown in **Figure 9C**, the normal common bile duct showed that the histological structure was similar to that of human tissue. The bile duct wall was divided into three layers (mucous layer, muscular layer and adventitia layer) from inside to outside, and the boundary of each layer was not very clear. The surface was lined with a single layer of columnar mucosal epithelium and the basement membrane

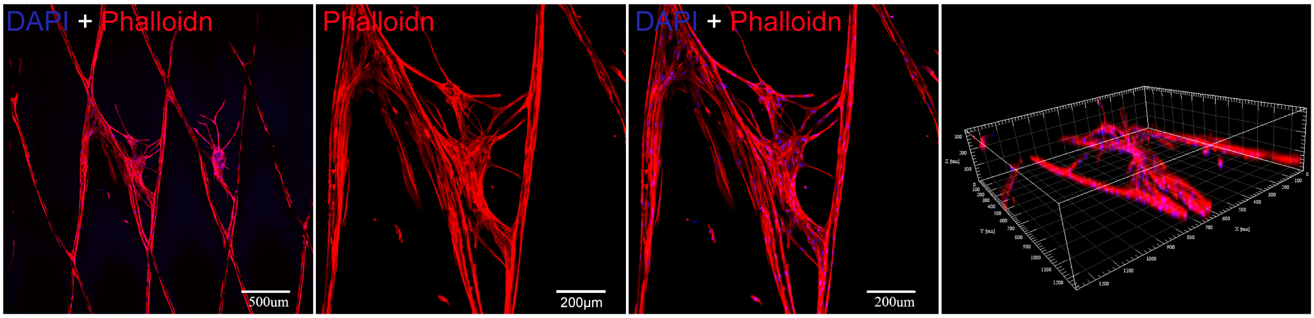

FIGURE 8 | Cytoskeleton fluorescence staining image of BMSCs seeded on a PLGA/GelMA/IKVAV/USPIO composite scaffold at day 13.

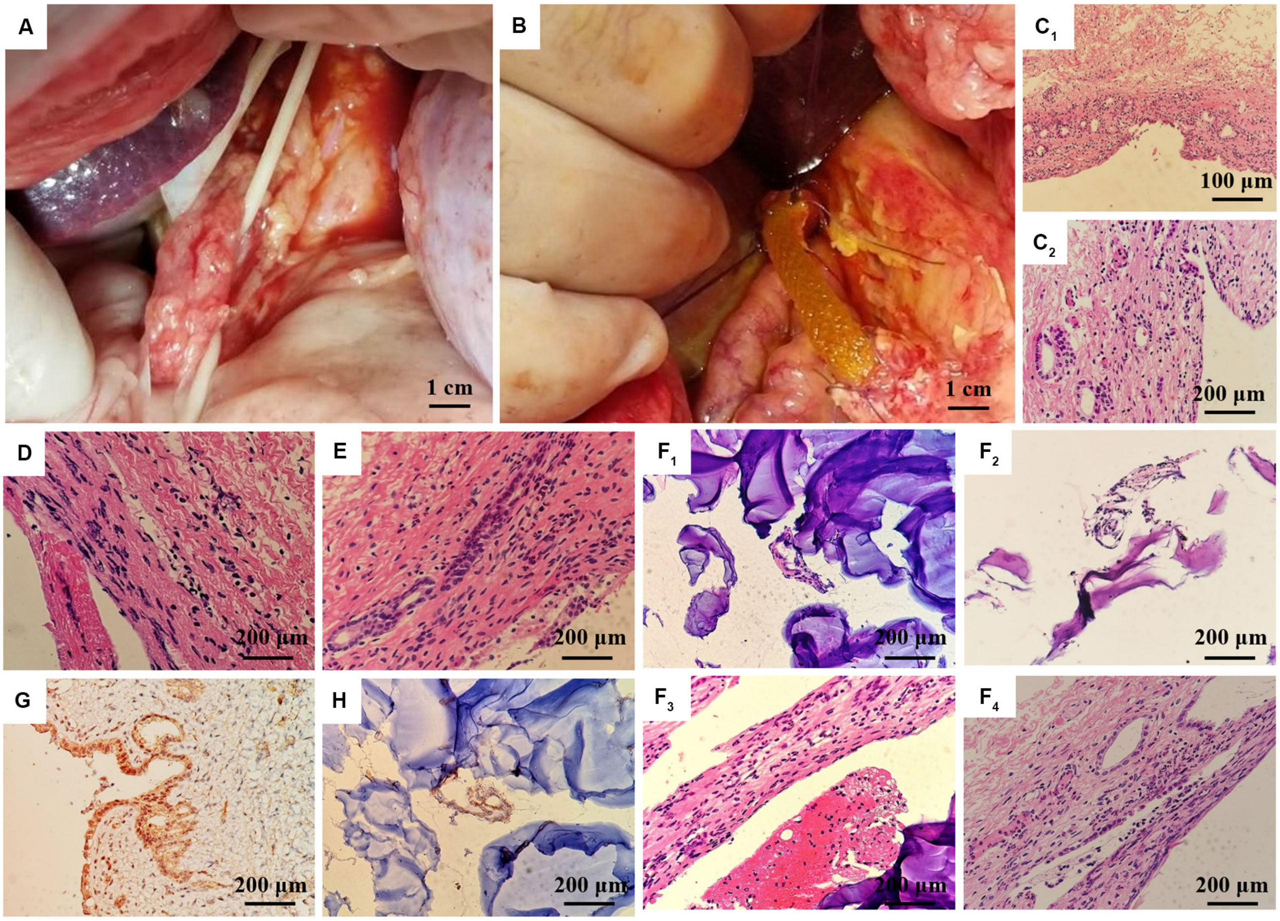

FIGURE 9 | *In vivo* regeneration of pig bile duct. **(A)** Free bile duct of inbred wuzhishan miniature pig. **(B)** PLGA/GelMA/IKVAV/USPIO composite stent implantation procedure. **(C)** HE staining of common bile duct of normal inbred (**C1**: 200×, **C2**: 400×). HE staining of common bile duct in the experimental group **(D)** and the sham operation group **(E)** at 14 days after surgery. **(F)** HE staining of common bile duct and PLGA/GelMA/IKVAV/USPIO composite scaffolds at 14 days after surgery. **(G)** Normal bile duct epithelial cytoplasm and **(H)** composite scaffolds immunohistochemical staining of bile duct CK19 at 14 days after surgery.

was not obvious. The lamina propria is dense fibrous connective tissue, which contains a lot of collagen and elastic fibers, and small blood vessels, in which a few single tubular submucosal glands can be seen. The distribution of smooth muscle in each segment of bile duct was different. The smooth muscle in the upper part of the bile duct was scattered or absent, while the smooth muscle bundles in the lower part of the bile duct were continuous or intermittent, and the middle part was between them, and the muscle bundles were mainly fibrous connective tissue. The adventitia is loose connective tissue including lymphatic vessels, nerve fibers and ganglion cells.

At 14 days after operation, HE staining PLGA/GelMA/IKVAV/USPIO composite tubular scaffold group showed that the morphology and structure of bile duct was normal, the small vessels in the lamina propria of bile duct were dilated, neutrophils and lymphocytes were infiltrated, and inflammatory cellulose-like exudate was seen on the surface of the stent (**Figures 9E,F**). A mild meutrophil and lymphocyte infiltration, epithelioid cell and multinucleated giant cell infiltration were seen on the surface of the scaffold. HE staining in control group showed normal morphology and structure of bile duct and infiltration of neutrophils and lymphocytes in the control group (**Figure 9D**).

At 14 days after operation, the immunohistochemical staining showed that the expression of CK19 in bile duct epithelial cells was positive. The expression of CK19 in bile duct epithelial cells was positive in normal group (**Figure 9G**). CK19 positive cells could be seen in the anastomotic site and inside the PLGA/GelMA/IKVAV/USPIO composite tubular scaffold, indicating the formation of bile duct-like epithelial cells (**Figure 9G**). A small amount of CK19 positive tissue with tubular arrangement could be seen on the composite scaffold, indicating the regeneration of tubular tissue (bile duct).

CONCLUSION

This study presents a novel 3D printing PLGA/GelMA/IKVAV/USPIO duct conduits through the layer by layer casting (LBLC) method. Different from traditional electrospinning fabrication of duct conduit, 3D printing technique avoided many disadvantages, such as the inconsistencies of temperature control, poor mechanical strength and gaps between nanofibers. Moreover, 3D printed scaffold can be used for real-time non-invasive detection of bile duct repair and scaffold degradation through MRI. The IKVAV were uniformly distributed on the duct conduit by the LBLC method to assure the good biocompatibility for duct regeneration. *In vivo* pig bile duct defect model, the tailored shape of the artificial duct PLGA/GelMA/IKVAV/USPIO duct conduits proved that its feasible and practicability in surgery. HE and immunohistochemistry showed that a mild meutrophil and lymphocyte infiltration, epithelioid cell and multinucleated giant cell infiltration with no evidence of bile leakage into the surrounding tissue, and the presence of CK19 expression. The finding of this study demonstrates that the prepared bilayered PLGA/GelMA/IKVAV/USPIO conduits can be used as a promising candidate for bile duct restoration and detection. Moreover, the present strategy provides a new method in the field of bilayered conduits for cell culture and tissue engineering.

DATA AVAILABILITY STATEMENT

All datasets generated for this study are included in the article/supplementary material.

ETHICS STATEMENT

The animal study was reviewed and approved by the Institutional Animal Care and Use Committee (IACUC) of Central South University.

AUTHOR CONTRIBUTIONS

YX carried out development of hydrogels, rheology, and 3D-fabrication of PLGA, and performed the mechanical testing. YX and WW carried out evaluation of scaffolds. YX and YY carried out the cell studies. All authors contributed to the article and approved the submitted version.

FUNDING

This study was supported financially by the Finance Science and Technology Project of Hainan Province (Grant No. ZDYF2018104), the Natural Science Foundation of Hainan Province (Grant No. 81760138), and the Natural Science Foundation of Hainan Province (Grant No. 2017CXTD010).

REFERENCES

Aldana, A. A., Malatto, L., Rehman, M. A. U., Boccaccini, A. R., and Abraham, G. A. (2019a). Fabrication of gelatin methacrylate (GelMA) scaffolds with nano- and micro-topographical and morphological features. *Nanomaterials* 9:120. doi: 10.3390/nano9010120

Aldana, A. A., Rial-Hermida, M. I., Abraham, G. A., Concheiro, A., and Alvarez-Lorenzo, C. (2019b). Temperature-sensitive biocompatible IPN hydrogels based on poly(NIPA-PEGdma) and photocrosslinkable gelatin methacrylate. *Soft. Mater.* 15, 341–349. doi: 10.1080/1539445x.2017.1378677

Athirasala, A., Lins, F., Tahayeri, A., Hinds, M., Smith, A. J., Sedgley, C., et al. (2017). A novel strategy to engineer pre-vascularized full-length dental pulp-like tissue constructs. *Sci. Rep.* 7:3323.

Bege, N., Steinmüller, S. O., Kalinowski, M., Reul, R., Klaus, S., Petersen, H., et al. (2012). Drug eluting stents based on Poly(ethylene carbonate): optimization of the stent coating process. *Eur. J. Pharm. Biopharm.* 80, 562–570. doi: 10.1016/j.ejpb.2011.12.006

Bloise, N., Rountree, I., Polucha, C., Montagna, G., Visai, L., Coulombe, K. L. K., et al. (2020). Engineering immunomodulatory biomaterials for regenerating the infarcted myocardium. *Front. Bioeng. Biotechnol.* 8:292. doi: 10.3389/fbioe.2020.00292

Carinci, F., Pezzetti, F., Volinia, S., Laino, G., Arcelli, D., Caramelli, E., et al. (2004). P-15 cell-binding domain derived from collagen: analysis of MG63 osteoblastic-cell response by means of a microarray technology. *J. Periodontol.* 75, 66–83. doi: 10.1902/jop.2004.75.1.66

Chen, Z., Yan, C., Yan, S., Liu, Q., Hou, M., Xu, Y., et al. (2018). Non-invasive monitoring of in vivo hydrogel degradation and cartilage regeneration by multiparametric MR imaging. *Theranostics* 8, 1146–1158. doi: 10.7150/thno.22514

Dashti, D. C., Johnson, J., and Betancourt, A. M. (2016). Development of an "off-the-shelf" implantable and absorbable electrospun polycaprolactone-chitosan (PCL-CS) device to regenerate damaged esophageal tissue. *Front. Bioeng. Biotechnol.* 4:880. doi: 10.3389/conf.fbioe.2016.01.00880

Funfak, A., Bouzhir, L., Gontran, E., Minier, N., Dupuis-Williams, P., and Gobaa, S. (2019). Biophysical control of bile duct epithelial morphogenesis in natural and synthetic scaffolds. *Front. Bioeng. Biotechnol.* 7:417. doi: 10.3389/fbioe.2019.00417

Gao, Q., Niu, X., Shao, L., Zhou, L., Lin, Z., Sun, A., et al. (2019). 3D printing of complex GelMA-based scaffolds with nanoclay. *Biofabrication* 11:035006. doi: 10.1088/1758-5090/ab0cf6

Grosskopf, A., Truby, R., Kim, H., Perazzo, A., Lewis, J. A., and Stone, H. A. (2018). Viscoplastic matrix materials for embedded 3D printing. *Acs Appl. Mater. Inter.* 10, 23353–23361. doi: 10.1021/acsami.7b19818

Han, T. H., Lee, W. J., Lee, D. H., Kim, J. E., Choi, E. Y., and Kim, S. O. (2010). Peptide/graphene hybrid assembly into core/Shell nanowires. *Adv. Mater. Weinh.* 22, 2060–2064. doi: 10.1002/adma.200903221

Hu, S., Cai, X., Qu, X., Yu, B., Yan, C., Yang, J., et al. (2019). Preparation of biocompatible wound dressings with long-term antimicrobial activity through covalent bonding of antibiotic agents to natural polymers. *Int. J. Biol. Macromol.* 123, 1320–1330. doi: 10.1016/j.ijbiomac.2018.09.122

Kang, H., Yang, B., Zhang, K., Pan, Q., Yuan, W., Li, G., et al. (2019). Immunoregulation of macrophages by dynamic ligand presentation via ligand-cation coordination. *Nat. Commun.* 10:1696.

Kang, S. H., Wan, S. H., Lin, Z., Kwon, S. H., and Hong, S. W. (2015). A robust highly aligned DNA nanowire array-enabled lithography for graphene nanoribbon transistors. *Nano Lett.* 15, 7913–7920. doi: 10.1021/acs.nanolett.5b02946

Kim, W. J., Lee, H., Kim, Y. B., Chang, H. C., and Kim, G. H. (2016). Versatile design of hydrogel-based scaffolds with manipulated pore structure for hard-tissue regeneration. *Biomed. Mater.* 11:055002. doi: 10.1088/1748-6041/11/5/055002

Lee, B. K., Ju, Y. M., Cho, J. G., Jackson, J. D., Lee, S. J., Atala, A., et al. (2012). End-to-side neurorrhaphy using an electrospun PCL/collagen nerve conduit for complex peripheral motor nerve regeneration. *Biomaterials* 33, 9027–9036. doi: 10.1016/j.biomaterials.2012.09.008

Lee, W. C., Lim, C. H., Kenry, Su, C., and Lim, C. T. (2015). Cell-assembled graphene biocomposite for enhanced chondrogenic differentiation. *Small* 11, 963–969. doi: 10.1002/smll.201401635

Lei, K., Chen, Y., Wang, J., Peng, X., Yu, L., and Ding, J. (2017). Non-invasive monitoring of in vivo degradation of a radiopaque thermoreversible hydrogel and its efficacy in preventing post-operative adhesions. *Acta Biomater.* 55, 396–409. doi: 10.1016/j.actbio.2017.03.042

Li, H., Yin, Y., Xiang, Y., Liu, H., and Guo, R. (2020). A novel 3D printing PCL/GelMA scaffold containing USPIO for MRI-guided bile duct repair. *Biomed. Mater.* 15:045004. doi: 10.1088/1748-605x/ab797a

Li, R., Lin, S., Zhu, M., Deng, Y., Chen, X., Wei, K., et al. (2019). Synthetic presentation of noncanonical Wnt5a motif promotes mechanosensing-dependent differentiation of stem cells and regeneration. *Sci. Adv.* 5:eaaw3896. doi: 10.1126/sciadv.aaw3896

Li, X., Yang, C., Li, L., Xiong, J., Xie, L., Yang, B., et al. (2015). A therapeutic strategy for spinal cord defect: human dental follicle cells combined with aligned PCL/PLGA electrospun material. *Biomed. Res. Int.* 2015: 197183.

Lozano, R., Stevens, L., Thompson, B. C., Gilmore, K. J., Gorkin, R., Stewart, E. M., et al. (2015). 3D printing of layered brain-like structures using peptide modified gellan gum substrates. *Biomaterials* 67, 264–273. doi: 10.1016/j.biomaterials.2015.07.022

Lucidarme, O., Nguyen, T., Kono, Y., Corbeil, J., Choi, S. H., Varner, J., et al. (2004). Angiogenesis model for ultrasound contrast research1. *Acad. Radiol.* 11, 4–12. doi: 10.1016/s1076-6332(03)00575-0

Mccoul, D., Rosset, S., Schlatter, S., and Shea, H. (2017). Inkjet 3D printing of UV and thermal cure silicone elastomers for dielectric elastomer actuators. *Smart Mate. Struct.* 26:125022. doi: 10.1088/1361-665x/aa9695

Miyazawa, M., Torii, T., Toshimitsu, Y., Okada, K., Koyama, I., and Ikada, Y. (2005). A tissue-engineered artificial bile duct grown to resemble the native bile duct. *Am. J. Transplant.* 5, 1541–1547. doi: 10.1111/j.1600-6143.2005.00845.x

Narayanan, L. K., Huebner, P., Fisher, M. B., Spang, J. T., Starly, B., and Shirwaiker, R. A. (2016). 3D-bioprinting of polylactic acid (PLA) nanofibers-alginate hydrogel bioink containing human adipose-derived stem cells. *Acs Biomater. Sci. Eng.* 2, 1732–1742. doi: 10.1021/acsbiomaterials.6b00196

O'Bryan, C. S., Bhattacharjee, T., Hart, S., Kabb, C. P., and Angelini, T. E. (2017). Self-assembled micro-organogels for 3D printing silicone structures. *Sci. Adv.* 3:e1602800. doi: 10.1126/sciadv.1602800

Ogura, T., Takenaka, M., Shiomi, H., Goto, D., Tamura, T., Hisa, T., et al. (2019). Long-term outcomes of EUS-guided transluminal stent deployment for benign biliary disease: multicenter clinical experience (with videos). *Endosc. Ultrasound* 8, 398–403.

Park, S. H., Kang, B. K., Lee, J. E., Chun, S. W., Jang, K., Kim, Y. H., et al. (2017). Design and fabrication of a thin-walled free-form scaffold on the basis of medical image data and a 3D printed template: its potential use in bile duct regeneration. *ACS Appl. Mater. Inter.* 9, 12290–12298. doi: 10.1021/acsami.7b00849

Patel, D. K., Sakhaei, A. H., Layani, M., Zhang, B., Ge, Q., and Magdassi, S. (2017). Highly stretchable and UV curable elastomers for digital light processing based 3D printing. *Adv. Mater.* 29:1606000. doi: 10.1002/adma.201606000

Reid, A. J., De Luca, A. C., Faroni, A., Downes, S., Sun, M., Terenghi, G., et al. (2013). Long term peripheral nerve regeneration using a novel PCL nerve conduit. *Neurosci. Lett.* 544, 125–130. doi: 10.1016/j.neulet.2013.04.001

Roh, S., Parekh, D. P., Bharti, B., Stoyanov, S. D., and Velev, O. D. (2017). 3D printing by multiphase silicone/water capillary inks. *Adv. Mater.* 29:1701554. doi: 10.1002/adma.201701554

Shkarina, S., Shkarin, R., Weinhardt, V., Melnik, E., Vacun, G., Kluger, P. J., et al. (2018). 3D biodegradable scaffolds of polycaprolactone with silicate-containing hydroxyapatite microparticles for bone tissue engineering: high-resolution tomography and in vitro study. *Sci. Rep.* 8, 8907–8907.

Silva, G. A., Czeisler, C., Niece, K. L., Beniash, E., Harrington, D. A., Kessler, J. A., et al. (2014). Selective differentiation of neural progenitor cells by high-epitope density nanofibers. *Science* 303, 1352–1355. doi: 10.1126/science.1093783

Sun, H., Mei, L., Song, C., Cui, X., and Wang, P. (2006). The in vivo degradation, absorption and excretion of PCL-based implant. *Biomaterials* 27, 1735–1740. doi: 10.1016/j.biomaterials.2005.09.019

Sun, M., Sun, X., Wang, Z., Guo, S., Yu, G., and Yang, H. (2018). Synthesis, properties, and biomedical applications of gelatin methacryloyl (GelMA) hydrogels. *Polymers* 10:2090.

Tanimizu, N., Miyajima, A., and Mostov, K. E. (2007). Liver progenitor cells develop cholangiocyte-type epithelial polarity in three-dimensional culture. *Mol. Biol. Cell* 18, 1472–1479. doi: 10.1091/mbc.e06-09-0848

Topkaya, S. N. (2015). Gelatin methacrylate (GelMA) mediated electrochemical DNA biosensor for DNA hybridization. *Biosens. Bioelectron.* 64, 456–461. doi: 10.1016/j.bios.2014.09.060

Vieira-Silva, S., Sabino, J., Valles-Colomer, M., Falony, G., Kathagen, G., Caenepeel, C., et al. (2019). Quantitative microbiome profiling disentangles inflammation-and bile duct obstruction-associated microbiota alterations across PSC/IBD diagnoses. *Nat. Microbiol.* 4, 1826–1831. doi: 10.1038/s41564-019-0483-9

Wang, K., Ho, C., Zhang, C., and Wang, B. J. E. (2017). A review on the 3D printing of functional structures for medical phantoms and regenerated tissue and organ applications. *Engineering* 3, 653–662. doi: 10.1016/j.eng.2017.05.013

Xue, X., and Falcon, D. M. (2019). The role of immune cells and cytokines in intestinal wound healing. *Int. J. Mol. Sci.* 20:6097. doi: 10.3390/ijms20236097

Yan, M., Lewis, P. L., and Shah, R. N. (2018). Tailoring nanostructure and bioactivity of 3D-printable hydrogels with self-assemble peptides amphiphile (PA) for promoting bile duct formation. *Biofabrication* 10:035010. doi: 10.1088/1758-5090/aac902

Yu, J. R., Janssen, M., Liang, B. J., Huang, H. C., and Fisher, J. P. (2020). A liposome/gelatin methacrylate nanocomposite hydrogel system for delivery of stromal cell-derived factor-1α and stimulation of cell migration. *Acta Biomater.* 108, 67–76. doi: 10.1016/j.actbio.2020.03.015

Zografakis, J. G., Jones, B. T., Ravichardran, P., Evancho-Chapman, M. M., and Gingras, P. (2003). Endoluminal reconstruction of the canine common biliary duct. *Curr. Sur.* 60, 437–441. doi: 10.1016/s0149-7944(02)00726-2

Zong, C., Wang, M., Yang, F., Chen, G., Chen, J., Tang, Z., et al. (2017). A novel therapy strategy for bile duct repair using tissue engineering technique: PCL/PLGA bilayered scaffold with hMSCs. *J. Tissue Eng. Regen. Med.* 11, 966–967.

Conflict of Interest: The authors declare that the research was conducted in the absence of any commercial or financial relationships that could be construed as a potential conflict of interest.

frontiers
in Bioengineering and Biotechnology

ORIGINAL RESEARCH
published: 25 September 2020
doi: 10.3389/fbioe.2020.575365

Targeting Fluorescence Imaging of RGD-Modified Indocyanine Green Micelles on Gastric Cancer

Jun Shao[1†], Xiaoming Zheng[1†], Longbao Feng[2], Tianyun Lan[3], Dongbing Ding[1], Zikai Cai[1], Xudong Zhu[1], Rongpu Liang[1] and Bo Wei[1*]

[1] Department of Gastrointestinal Surgery, The Third Affiliated Hospital of Sun Yat-sen University, Guangzhou, China, [2] Department of Biomedical Engineering, Ji'nan University, Guangzhou, China, [3] Central Laboratory, The Third Affiliated Hospital of Sun Yat-sen University, Guangzhou, China

Edited by:
Zhengwei Mao,
Zhejiang University, China

Reviewed by:
Haihua Xiao,
Chinese Academy of Sciences (CAS),
China
Jennifer Patterson,
KU Leuven, Belgium

***Correspondence:**
Bo Wei
weibo3@mail.sysu.edu.cn

†These authors have contributed equally to this work

Specialty section:
This article was submitted to
Biomaterials,
a section of the journal
Frontiers in Bioengineering and
Biotechnology

Received: 23 June 2020
Accepted: 09 September 2020
Published: 25 September 2020

Citation:
Shao J, Zheng X, Feng L, Lan T, Ding D, Cai Z, Zhu X, Liang R and Wei B (2020) Targeting Fluorescence Imaging of RGD-Modified Indocyanine Green Micelles on Gastric Cancer. Front. Bioeng. Biotechnol. 8:575365. doi: 10.3389/fbioe.2020.575365

Early diagnosis and complete resection of the tumor is an important way to improve the quality of life of patients with gastric cancer. In recent years, near-infrared (NIR) materials show great potential in fluorescence-based imaging of the tumors. To realize a satisfying intraoperative fluorescence tumor imaging, there are two pre-requirements. One is to obtain a stable agent with a relatively longer circulation time. The second is to make it good biocompatible and specific targeting to the tumor. Here, we developed an RGD-modified Distearyl acylphosphatidyl ethanolamine-polyethylene glycol micelle (DSPE-PEG-RGD) to encapsulate indocyanine green (ICG) for targeting fluorescence imaging of gastric cancer, aimed at realizing tumor-targeted accumulation and NIR imaging. ^{1}H NMR spectroscopy confirmed its molecular structure. The characteristics and stability results indicated that the DSPE-PEG-RGD@ICG had a relatively uniform size of $<$200 nm and longer-term fluorescence stability. RGD peptides had a high affinity to integrin $\alpha_V\beta_3$ and the specific targeting effect on SGC7901 was assessed by confocal microscopy *in vitro*. Additionally, the results of cytotoxicity and blood compatibility *in vitro* were consistent with the acute toxicity test *in vivo*, which revealed good biocompatibility. The biodistribution and tumor targeting image of DSPE-PEG-RGD@ICG were observed by an imaging system in tumor-bearing mice. DSPE-PEG-RGD@ICG demonstrated an improved accumulation in tumors and longer circulation time when compared with free ICG or DSPE-PEG@ICG. In all, DSPE-PEG-RGD@ICG demonstrated ideal properties for tumor target imaging, thus, providing a promising way for the detection and accurate resection of gastric cancer.

Keywords: gastric cancer, micelles, RGD, indocyanine green, targeting

INTRODUCTION

Gastric cancer (GC) is a common malignant tumor and ranks the second leading cause of cancer-related death in the world, making it a serious threat to human health and quality of life. According to GLOBACAN statistics, approximately 1,033,000 new cases are diagnosed and 783,000 deaths are estimated worldwide in 2018, the majority of which are diagnosed middle and advanced tumors (at stage II or III) (Bray et al., 2018; Son et al., 2019). Thus, accurate and early diagnosis of GC remains a significant clinical challenge. Recently, endoscopic procedures such as endoscopic mucosal resection (EMR) and endoscopic submucosal dissection (ESD), have been performed to treat GC in the early stage (Ban et al., 2018; Dahan et al., 2019). Meanwhile, laparoscopic gastrectomy has been widely accepted as a minimally invasive procedure for the treatment of GC (Zou et al., 2014; Itatani et al., 2019). Nevertheless, many questions remain unsolved. No or mild typical signs lead to great difficulty in the diagnosis of the early stage of GC. Also, due to the lack of tactile perception (haptic feedback), surgeons may have misjudgments about early lesions in laparoscopic surgery. The diagnosis of the small tumor, the accurate resection of the tumor, etc. Those seriously affect the quality of life and survival of patients with GC.

In the World Molecular Imaging Conference 2009, Roger Y. Tsien reported how to use the fluorescence microscope imaging system to guide the removal of fluorescence-modified tumor tissue in mice, which laid the foundation of the optical molecular imaging technology applied in the field of surgical navigation (Nguyen et al., 2010). Compared with traditional imaging techniques, intraoperative fluorescence imaging has several advantages, such as high contrast, high sensitivity, low cost, and visualization of tissues (Chen et al., 2017). To achieve a satisfying intraoperative fluorescence imaging, there are two prerequisites. One is to synthesize a stable agent with a relatively longer circulation time. The second is to make it good biocompatible and specific targeting to the tumor.

To date, many fluorescence imaging agents have been designed for tumor imaging and/or therapy, such as radionuclide, iron nanoparticles, and near-infrared (NIR) agents (Kotagiri et al., 2018; Lu et al., 2018). Among all the imaging agents, indocyanine green (ICG) is the only NIR agent approved for clinical use by Food and Drug Administration (FDA) (Hwang et al., 2017). It has been widely used for the determination of liver function and liver blood flow, cardiac output, and ophthalmic angiography (Hwang et al., 2017; Lee et al., 2019). However, there also exist several intrinsic drawbacks limiting the development of ICG, such as instability and self-aggregation in the liquid solution, resulting in fluorescence quenching, a short half-time in body, and a lack of tumor-targeted ability (Zhang et al., 2017). To address these challenges, numbers of carriers are introduced to encapsulate ICG that protect it from non-specific binding of plasma protein, provide enhanced stability and tumor targeting (i.e., permeability and retention effect, EPR). Nevertheless, in some solid tumors such as GC, since the interstitial fluid pressure is often increased (Yonucu et al., 2017; Hansem et al., 2019), it's hard for these nanoparticles to permeate from leak tumor endothelial cells and largely transfer to the tumor sites. Therefore, challenges remain to improve the ability to penetration and targeting of the tumor.

Integrins, consisting of one α- and one β- submit, are a family of cell surface adhesion receptors that transmit bidirectional signals across the plasma membrane (Nieberler et al., 2017; Raab-Westphal et al., 2017). Now more and more evidence shows that integrins expressed by endothelial cells regulate cell migration and survival during angiogenesis, while integrins expressed by cancer cells enhance metastasis by promoting invasion and movement across blood vessels (Weis and Cheresh, 2011; Nieberler et al., 2017). Integrin $\alpha_v\beta_3$ is over-expressed on neoplastic tumor blood vessels and some tumor cells, playing an important role in proliferation, metastasis, and invasion of cancer cells (Kwakwa and Sterling, 2017; Lin et al., 2018). A study on integrin $\alpha_v\beta_3$ in GC cancer reveals that it is expressed widely in at least one tumor component and may be helpful in the routine classification of GC subtypes (Boger et al., 2015). The tripeptide Arg–Gly–Asp (RGD) can specifically bind to the integrin $\alpha_v\beta_3$ and it is one of the most studied targeting molecules for cancer precision diagnosis and treatment. Several studies have shown that RGD linked to fluorescent molecules or radionuclides possess the function of tumor-targeted imaging, such as FITC, ^{99m}Tc, etc. (Zitzmann et al., 2002; Fang et al., 2011). However, because of the small molecular weight, such modified probes are too short-lived in circulation to be widely spread in clinical application.

Nowadays, nanocarriers, such as liposomes, polymer micelles, and nanoparticles, are widely applied in the drug delivery system (DDS) to achieve the maximum bioavailability and therapeutic effect (Repenko et al., 2017; Peng et al., 2018; Li et al., 2019). Lipid micelles are biocompatible, non-toxic, and stable *in vivo* (Xu et al., 2019). For example, PEGlyation has been largely used to modify the surface of nanocarriers for the purpose of stabilizing the DDS, weakening the interaction with plasma proteins, and reducing the clearance of reticuloendothelial system during the biological circulation (Gref et al., 2012). In this article, with the aim of tumor-targeted accumulation and NIR imaging, we designed and synthesized an RGD modified micelle to encapsulate ICG. As shown in **Scheme 1**, first, DSPE-PEG-RGD was obtained based on the Michael addition reaction between RGD peptide and DSPE-PEG-Mal. Second, the NIR agent ICG was encapsulated by the DSPE-PEG-RGD matrix via the self-assembly method. DSPE-PEG-Mal is an amphiphilic polymer. PEG serves as a hydrophilic unit to form the shell while DSPE is a hydrophobic unit to form the hydrophobic cavity with ICG in the core. The synthesis and Characteristics of DSPE-PEG-RGD@ICG were analyzed, including ^{1}H NMR spectroscopy, transmission electron microscope (TEM), and so on. Then, the cellular uptake and biocompatibility were assessed. In addition, by using an optical imaging system, we observed the biodistribution and improved accumulation of DSPE-PEG-RGD@ICG in the tumor. The results of this study may provide a promising nanocarrier to realize the future clinical application of optical molecular imaging in early diagnosis and accurate resection of GC.

MATERIALS AND METHODS

Materials and Reagents

Distearyl acylphosphatidyl ethanolamine – polyethylene glycol – maleimide (DSPE-PEG-Mal, Kw = 2,000) was bought from

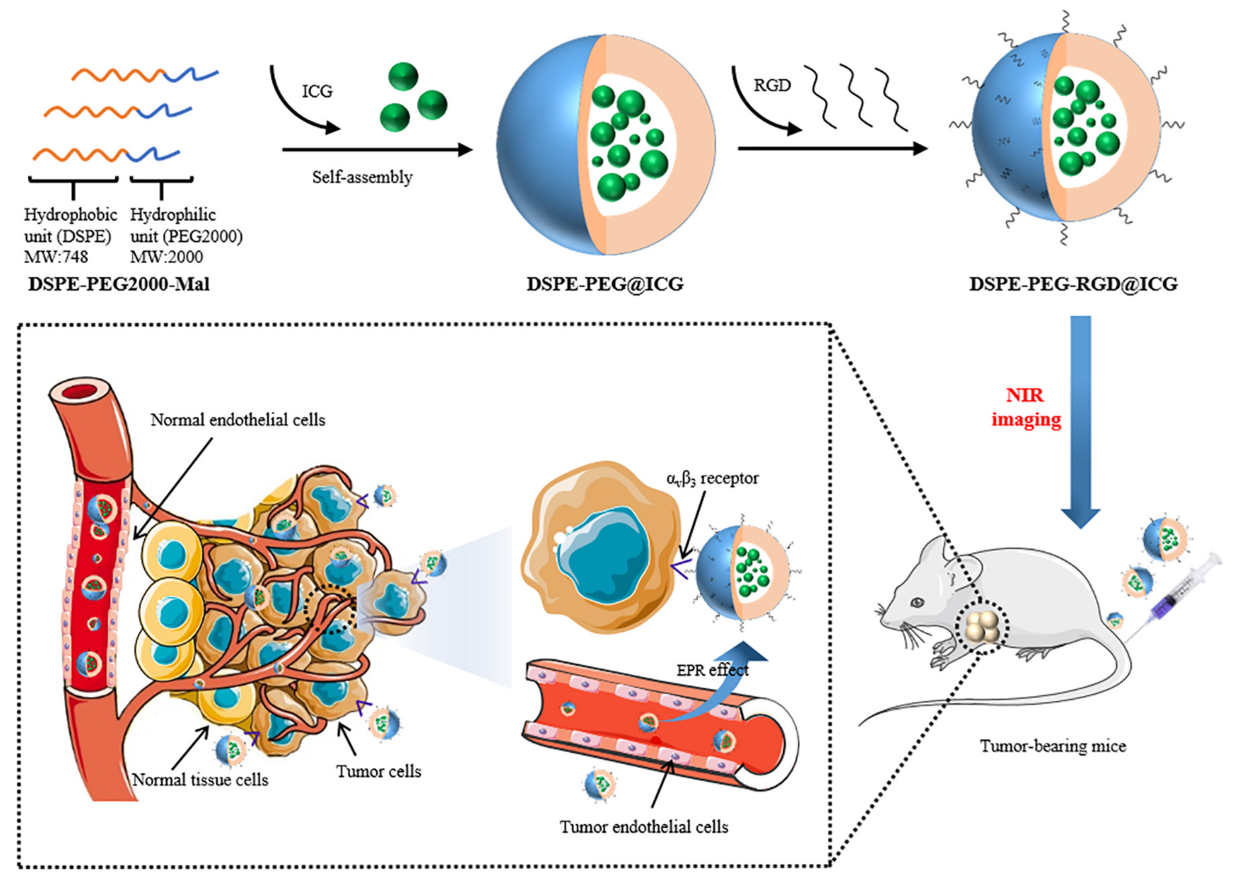

SCHEME 1 | Schematic illustration of RGD targeted DSPE-PEG@ICG micelles for gastric cancer monitor.

Shanghai Yare Biotechnology Co., Ltd. (Shanghai, China). ICG and dimethylsulfoxide (DMSO) were bought from Shanghai Macklin Biochemical Technology Co., Ltd. (Shanghai, China). RGD peptide was purchased from Shanghai Apeptide Co., Ltd. (Shanghai, China). Tetrahydrofuran (THF) was obtained from Damao Chemical Reagent Factory (Tianjin, China). RPMI 1640, cell culture reagents including Dulbecco's modified Eagle's medium (DMEM), fetal bovine serum (FBS), trypsin, and antibiotics were all bought from Gibco (Gaithersburg, MD, United States). Cell counting kit-8 (CCK-8) was obtained from Kaiji Bio-tech Co., Ltd. (Jiangsu, China). Human GC SGC7901 cells, mouse fibroblastic cells L929 were purchased from Beogene Biotechnology Co., Ltd. (Guangzhou, China). Live/Dead cell staining kits were obtained from BestBio Bio-Technology Co., Ltd. (Shanghai, China). All other reagents were of analytical grade unless otherwise noted.

Synthesis of DSPE-PEG-RGD

Attachment of RGD peptide to DSPE-PEG was based on a reported method in the literature via the Michael addition reaction between RGD and DSPE-PEG-Mal, with a slight adjustment (Cureton et al., 2017). Generally, 20 mg of DSPE-PEG-Mal was dissolved in 5 ml of ultra-pure water and mixed with 6 mg RGD polypeptide. Then, gently stir the mixture for 4 h and followed by dialyzed in a dialysis bag (MWCO: 1,000 Da) for 24 h against ultra-pure water. The final product was obtained by freeze-drying and stored at −20°C.

Synthesis of DSPE-PEG-RGD@ICG

DSPE-PEG-Mal was a long-chain polymer. PEG (MW: 2,000) served as a hydrophilic unit to form the shell while DSPE (MW: 748) was a hydrophobic unit to form the hydrophobic cavity with ICG in the core. DSPE-PEG-RGD@ICG was synthesized through the self-assembly method. In brief, 20 mg of DSPE-PEG-RGD and 6.7 mg of ICG were dissolved in 3 ml of THF and sonicated to ensure adequate dissolution and uniformity, followed by slowly adding 20 ml of ultra-pure water. Continuous sonicate for half an hour and dialyze the mixture in a dialysis bag (MWCO: 3,500 Da) for 24 h. The final product was obtained by freeze-drying and stored at −20°C. According to the same scheme, non-targeted DSPE-PEG@ICG was prepared by DSPE-PEG and ICG.

Characteristics of DSPE-PEG-RGD@ICG

First, nuclear magnetic resonance (^{1}H. NMR) spectrometer (AVANCE III 500M, Bruker, Germany) was performed to analyze the chemical structure of DSPE-PEG-RGD@ICG. Deuterated DMSO was used as a solvent. The morphology of

DSPE-PEG@ICG and DSPE-PEG-RGD@ICG was illustrated by TEM (JEM-2010F, JEOL Ltd., Tokyo, Japan). The mean hydrodynamic diameter and size distribution of the micelles with or without RGD modified were measured by Zetasizer Nano-ZS90 (Malvern Instruments Ltd., Worcestershire, United Kingdom) at 25°C. Each sample was repeated three times for each measurement, and the average value was taken.

Drug Loading Capacity and Encapsulation Efficiency

The encapsulation efficiency (EE) and drug loading capacity (LD) in both formulations were measured by UV-vis spectrometer (UV-3100PC, Mapada Instruments, Shanghai, China). Set the λ_{max} at 794 nm. The standard absorption curve of ICG in ultra-water was obtained and the formulas used were as follows:

$$\mathrm{EE}\ (\%) = \frac{\textit{Weight of ICG in micelles}}{\textit{Weight of feed ICG}} \times 100\%$$

$$\mathrm{LD}\ (\%) = \frac{\textit{Weight of ICG in micelles}}{\textit{Weight of micelles}} \times 100\%$$

In vivo Stability Evaluation

The absorption and fluorescence emission spectra were used to assess the stability of free ICG and DSPE-PEG-RGD@ICG in the liquid solution. Store the prepared samples in the dark at 4°C for 4 days. At the scheduled time points (0, 24, 48, 72, and 96 h), a UV-vis spectrometer was used to examine the absorption spectra and a fluorescence spectrometer (HR2000+, Ocean Optics) was used to analyze the fluorescence spectra.

Cell Lines and Mice

Human GC SGC7901 cells, mouse fibroblastic cells L929 were used in this paper. SGC7901 cells were cultured in RPMI 1640 while L929 cells were cultured in DMEM at 37°C in a humidified atmosphere containing 5% CO_2. All of the media were supplemented with 10% FBS, 1% penicillin, and 1% streptomycin. Male BALB/c (nu/nu) nude mice (6–8 weeks) were purchased from Beijing Virton Li Hua Experimental Animal Technology Co., Ltd. (Beijing, China). All mice experiments were approved by the Ethics Committee of the Institutional Animal Care and Use Subcommittee of the Third Hospital of Sun Yat-sen University. Before experimentation, all mice were raised for 1 week to acclimatize to the laboratory environment.

Cellular Uptake

The internalization and distribution of cells were observed by a laser confocal fluorescence microscope. Briefly, SGC7901 cells were seeded in 35-mm cell petri dishes (Nest, 801002) and cultured 24 h for cell attachment. The cell density per dish was 5×10^4. Next, replace the media with new serum-free media containing DSPE-PEG@ICG and DSPE-PEG-RGD@ICG, respectively (an equivalent ICG concentration: 1 mg/ml). After incubated for 4 and 12 h, the cells were washed with PBS and fixed with 4% paraformaldehyde. Afterward, the cells were stained with 10 μg/ml DAPI for 10 min and washed with PBS. Finally, a laser confocal fluorescence microscope (Zeiss LSM 710, Germany) was used for observing the binding and internalization of the micelles. The parameters were set at λ_{ex} 405 nm for the nuclei and λ_{ex} 633 nm for ICG.

For further quantitative analysis, 1×10^5 SGC7901 cells were seeded in 12-well plates per well and cultured with serum-free media containing DSPE-PEG@ICG and DSPE-PEG-RGD@ICG (an equivalent ICG concentration: 1 mg/ml) for 12 h. At predetermined times, the cells were harvested and washed with PBS. Then, the cells were re-suspended in PBS and immediately quantitatively analyzed by Accuri flow cytometry (BD, United States).

In vitro Cytotoxicity

For the cell viability assessment, Cell Counting Kit (CCK-8) assay and live/dead staining assay were performed. Generally, SGC7901 and L929 cells in the logarithmic phase were harvested, resuspended, and seeded into 96-well at the density of 5×10^3/ml. The cells were incubated overnight for adherents and replaced the media with new media containing the micelles with or without RGD peptide modified at different concentrations, respectively. Continue to incubate the cells for 24 h and assess the cell viability by CCK-8 assay. The absorbance value was measured at $\lambda = 490$ nm. Cell death was detected by the live/dead staining assay. In brief, SGC7901 cells were cultured with micelles with or without RGD peptide modified for 24 h, then stained with a mixed solution of calcein-AM and PI and observed under the fluorescence microscope. The images were acquired at 490 nm for calcein-AM and 545 nm for PI, respectively.

In vitro Blood Compatibility Test

This section includes two parts: hemolysis assay of erythrocytes and blood clotting analysis (Huang et al., 2016). For hemolysis assay (Skalickova et al., 2017), the fresh blood sample was collected from a 6-week-old nude mouse and red blood cells (RBCs) were obtained by centrifuged at 5,000 rpm for 5 min, followed by purified and re-suspended in PBS. The final concentration of the RBCs solution was adjusted to 16% (v:v) diluted with PBS. Then, DSPE-PEG-RGD@ICG samples at different concentrations (0.1, 0.5, and 1.0 mg/ml) in 1 ml PBS were added to the RBCs solutions (50 μl) and incubated for a period of time (0.25, 0.5, 1, 2, 3, 6, 12, and 24 h). RBCs incubated with ultra-pure water and PBS solution with the same volume were respectively set as negative and positive controls. At the end of the experiment, centrifuged the mixed solutions at 1,000 rpm for 5 min and detected the absorbance of the supernatants containing lysed erythrocytes at 540 nm, which stood for the effect of DSPE-PEG-RGD@ICG on the dissolution of erythrocytes.

Next, activated partial thromboplastin time (APTT) and prothrombin time (PT) were adopted to assess the effect of DSPE-PEG-RGD@ICG micelles on the coagulation system (Pyataev et al., 2019). Briefly, fresh blood samples were collected as mentioned above and stabilized with sodium citrate. Centrifuged at 1,000 g for 10 min and the plasma was obtained. A total of 360 μl plasma was collected and mixed with 40 μl DSPE-PEG-RGD@ICG PBS solution (concentration: 0.1, 0.2, 0.5, and 1 mg/ml). Meanwhile, the same volume of plasma mixed with normal saline was set as a negative control. Added the detection reagents and analyzed the APTT and PT utilizing an automatic coagulation analyzer (STAR Evolution, Diagnostica Stago, Assiernes, France).

In vivo Acute Toxicity Test

An acute toxicity test was performed for safety assessment *in vivo* (Paradossi et al., 2019). Twelve healthy male nude mice were allocated to four groups ($n = 3$) randomly and intravenously injected with DSPE-PEG-RGD@ICG at different does (an equivalent ICG dose: 0, 1, 2, and 4 mg/kg), respectively. Continue feeding the mice for one week and observe the death, diet, coat color, activity, and other conditions of the mice. Harvest blood samples via the retro-orbital vein on the 8th day and then kill the mice. The main organs were extracted immediately for sectioning and hematoxylin-eosin (H&E) staining. Histopathological analysis was conducted to assess organ toxicity. Blood samples were kept at 2–8°C. Use whole blood for cell count (RBC, WBC, and blood platelet) and serum for liver (ALT and AST) and kidney (Cr) function test to evaluate the effect of DSPE-PEG-RGD@ICG on bone marrow hematopoietic system and liver and kidney function in nude mice.

In vivo Fluorescence Imaging and Distribution

To develop the tumor-bearing mice model, 5×10^6 SGC7901 cells in PBS (0.2 ml) were injected into the left armpit subcutaneous areas of the male nude mice. The size of tumors was measured twice or three times a week and the volume was calculated ($V = \text{length} \times (\text{width})^2/2$). When the tumor size reached ≈150–200 mm^3, allocate the mice to three groups ($n = 3$) randomly, followed by treated with DSPE-PEG-RGD@ICG, DSPE-PEG@ICG or free ICG via tail vein (an equivalent ICG dose: 2 mg/kg), respectively. Mice were anesthetized with a mixture of 2% isoflurane and air. At selected time points of 0, 1, 3, 6, 24, and 48 h post-injection, the fluorescence signals were acquired with *Bruker in vivo Xtreme* imaging system (Billerica, MA, United States) with $\lambda_{ex} = 730$ nm and $\lambda_{em} = 830$ nm. After 48h imaging, all the experimental mice were immediately killed for isolating and visualizing tumors and main organs under the same conditions as described above. Last, *Bruker* molecular imaging software was used to quantify the fluorescence intensity at selected ROIs.

Statistical Analysis

In this study, quantitative data was demonstrated as mean ± SD, and the statistical analysis was conducted utilizing SPSS 21.0 software (Chicago, IL, United States). *T*-test was applied for comparisons between two groups whereas a one-way analysis of variance (ANOVA) was used for comparisons among multiple groups. The differences were considered significant when $^*P < 0.05$, and very significant when $^{**}P < 0.01$.

RESULTS AND DISCUSSION

Synthesis and Characterization of the DSPE-PEG-RGD@ICG

The preparation process of DSPE-PEG-RGD@ICG was shown in **Scheme 1** and its molecular structure was further verified by ^{1}H-NMR spectroscopy. As shown in **Supplementary Figure S1**, resonance peak at ∼3.4 ppm corresponded to δa ($-CH_2O-$) of PEG, and resonance peak at ∼3.5 ppm represented δb ($-OCH_2-CH_2-$), both of which were unaffected by the reaction with RGD peptide. Resonance peak at ∼7.0 ppm corresponded to δc ($-CO-CH=$) of the Mal group, which nearly disappeared in the spectrum of DSPE-PEG-RGD. The residual resonance peak might be due to the residual impurities in the sample. Thus, the Mal groups of DSPE-PEG-Mal had successfully reacted with the thiol groups of RGD peptide (Mozhi et al., 2020).

We further characterized the obtained micelles. The average size and surface potential were characterized by dynamic light scattering (DLS). The mean size of DSPE-PEG@ICG and DSPE-PEG-RGD@ICG were respectively 133.2 ± 4.2 nm and 147.6 ± 3.9 nm with a polydispersity index (PDI) of 0.21 and 0.28, as shown in **Figures 1A,B**, indicating slightly changes after the conjugation with RGD. Previous studies had revealed that particles with a <200 nm size increased drug accumulation ability in solid tumors through the EPR effect (Gao et al., 2009; Du et al., 2017). Meanwhile, the TEM image (**Figures 1C,D**) revealed that the morphology of the micelles was approximately circular and homogeneously distributed. The results were similar to that of DLS. The standard absorption curve of ICG in ultra-pure water was shown in **Supplementary Figure S2**. The LD and EE are crucial properties in drug delivery. In our study, the LD and EE of ICG were 11.4 and 34.2%, which were lower compared with previous studies (Xu et al., 2018). Similar results of micelles with or without RGD modifications were obtained.

Spectral Properties and Stability

The spectral properties of ICG and DSPE-PEG-RGD@ICG were showed in **Figures 2A,D**. The UV absorption and FL emission of DSPE-PEG-RGD@ICG were similar to that of ICG dissolved in pure water. In detail, the peak absorbance of DSPE-PEG-RGD@ICG had a slight red shift (≈7 nm), which verified that ICG had been encapsulated into the micelles successfully. Moreover, a shift toward longer wavelengths would lead to a remarkable decrease in the background signal during detection, making it an improved signal-to-noise ratio *in vivo* (Proulx et al., 2010).

Previous studies have demonstrated that ICG is unstable in aqueous solutions due to the saturation of the double bonds in the conjugated chain. When the concentration of ICG exceeds 3.9 mg/ml, it aggregates to form dimers and oligomers, leading to fluorescence self-quenching and simultaneous decrease of fluorescence and absorption spectrum (Saxena et al., 2003). After reserved in the dark at 4°C for 4 days, the absorption and fluorescence spectrum of free ICG decreased by 60 and 90%, respectively (**Figures 2B,E**). On the contrary, the absorption and fluorescence spectrum of DSPE-PEG-RGD@ICG declined by 50

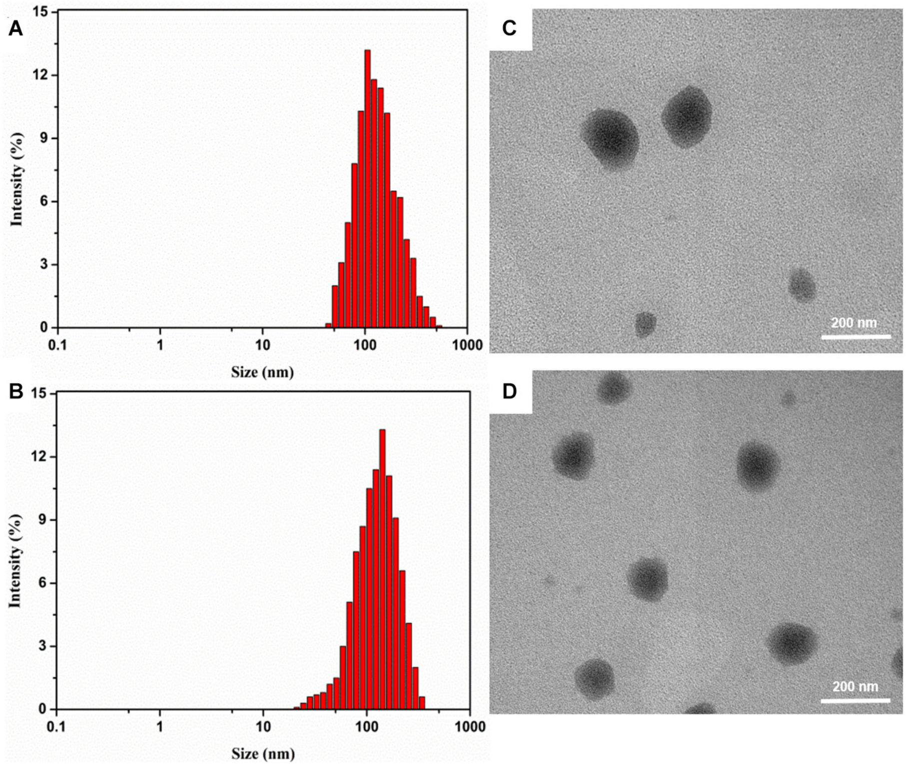

FIGURE 1 | The size distribution and TEM result of DSPE-PEG@ICG **(A, B)** and DSPE-PEG-RGD@ICG **(C, D)**.

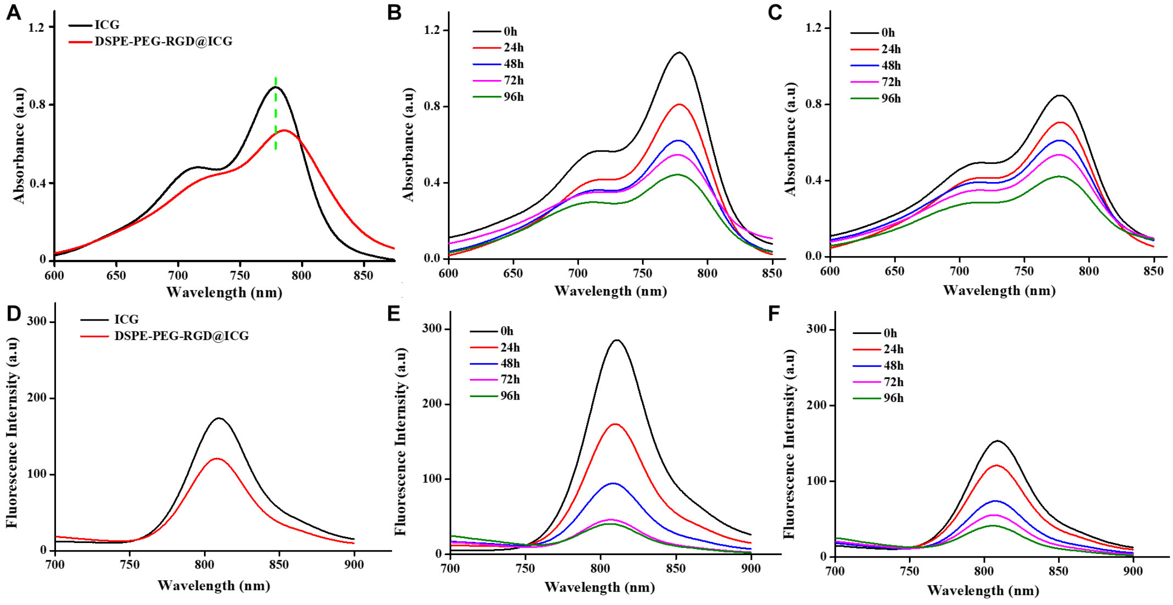

FIGURE 2 | UV–vis absorption spectra **(A)** and fluorescence emission spectra **(D)** of free ICG and DSPE-PEG-RGD@ICG. Stability assessment of free ICG **(B, E)** and DSPE-PEG-RGD@ICG **(C, F)** for 4 days.

and 75%, respectively (**Figures 2C,F**). Obviously, when ICG was encapsulated in DSPE-PEG-RGD@ICG, the hydrophobic lipid end could prevent their aggregation, thus improving the stability of ICG in aqueous solution. In addition, previous studies have shown that the interaction between lipids and ICG can improve the NIR imaging performance of ICG and make it have deeper tissue penetration (Kraft and Ho, 2014). At the same time, in order to achieve effective tumor imaging and accumulation, it is necessary to maintain the fluorescence stability of ICG.

In vitro Cellular Uptake

Integrin $\alpha_v\beta_3$ is widely expressed and maybe a putative prognostic biomarker in GC tissues according to a large-scale study conducted by Boger et al. (2015). Human GC SGC7901 cells were also overexpressed integrin $\alpha_v\beta_3$ (Cheng et al., 2017). In this section, in order to investigate the targeting ability of micelles with or without RGD, SGC7901 cells were incubated with micelles with or without RGD peptide modified for 4 and 12 h, respectively. Confocal microscopy was employed to observe the precise internalization procession. Nuclei represented blue fluorescence and ICG exhibited red fluorescence (**Figures 3A,C**). After incubated with DSPE-PEG-RGD@ICG for 4 or 12 h, the red fluorescence signal from the SGC7901 cells was significantly stronger than the cells incubated with DSPE-PEG@ICG, indicating that DSPE-PEG-RGD@ICG were greatly internalized by SGC7901 cells when compared to DSPE-PEG@ICG. Further flow cytometry analysis (**Figures 3B,D**) shown that the fluorescence intensity for DSPE-PEG-RGD@ICG in SGC7901 cells was significantly higher than that for DSPE-PEG@ICG at 4 or 12 h. Given the fact that RGD peptides have a strong affinity to integrin $\alpha_v\beta_3$ and specifically target tumors, the attachment of RGD to micelles enhanced the cellular uptake. Additionally, previous researches have shown that cellular internalization largely relied on the reaction between RGD and its receptors on the cell surface. Wang et al. designed iRGD or RGD modified nanoparticles with enhancing tumor accumulation and penetration (Wang et al., 2014). Yan et al. (2016) demonstrated a higher cellular uptake of iRGD modified nanoparticles in breast cancer cells with higher expression level of integrin $\alpha_v\beta_3$. The higher expression level of integrin $\alpha_v\beta_3$, the more RGD modified nanocarriers tend to be phagocytosed.

In vitro Cytotoxicity

The prerequisite property for a well-designed agent for clinical application is fine biological compatibility. To evaluate the biocompatibility of micelles *in vitro*, SGC7901 cells and L929 cells were cultured with the micelles with or without RGD peptide modified respectively. The relative growth rates (RGR) of cells were obtained and demonstrated in **Figures 4A,C**. With the increase in the concentration of micelles, there was a slightly correlated influence on the cell viability with no significant difference ($P > 0.05$), indicating no obvious toxicity. Moreover, even when the concentration increased to 2,000 μg/ml, cell viability was still more than 80%. The results of Live/Dead staining were shown in **Figures 4B,D**. After 24 h, there were a great number of viable cells and little dead or later apoptosis cells no matter incubated with DSPE-PEG@ICG or DSPE-PEG-RGD@ICG. The results were consistent with the CCK-8 assay. Based on RGR Score and Grade standard, once the material is considered to be utilized in medical applications, the RGR should ≥75%, which implies low or no cytotoxicity (Xiao et al., 2019). PEGylated materials are considered to be promising drug carriers with low cytotoxicity, biodegradability, and biocompatibility (Allen and Cullis, 2004). Meanwhile, ICG is approved for clinical use by FDA, and RGD peptides are naturally present in a variety of extracellular matrices. The expected results indicated that

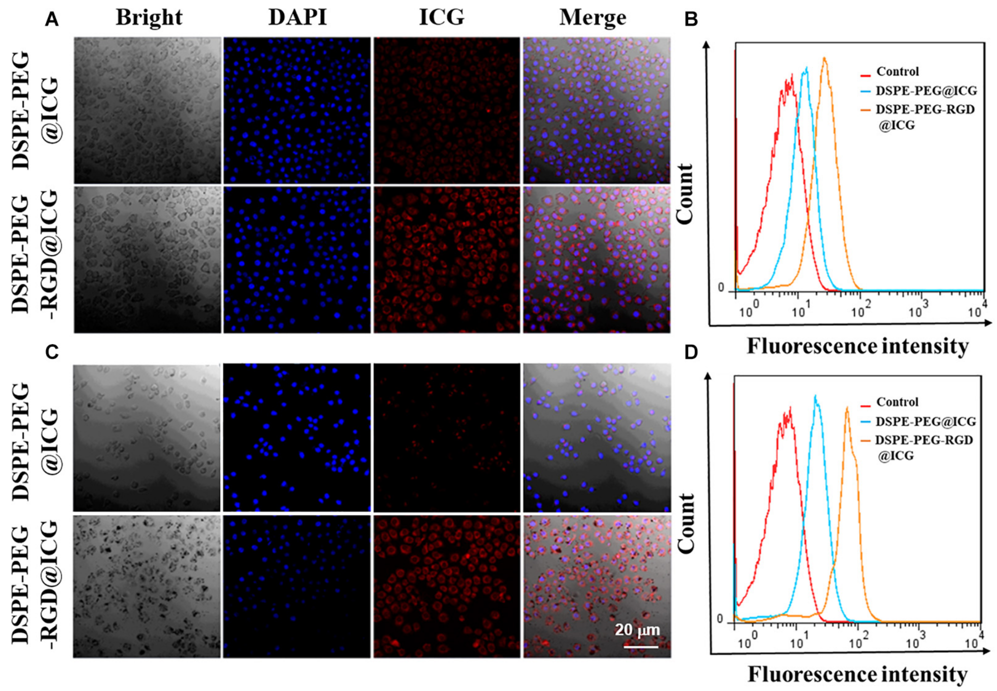

FIGURE 3 | Confocal images and flow cytometry analysis of DSPE-PEG@ICG or DSPE-PEG-RGD@ICG by SGC7901 cells at 4 h **(A, B)** and 12 h **(C, D)**, respectively.

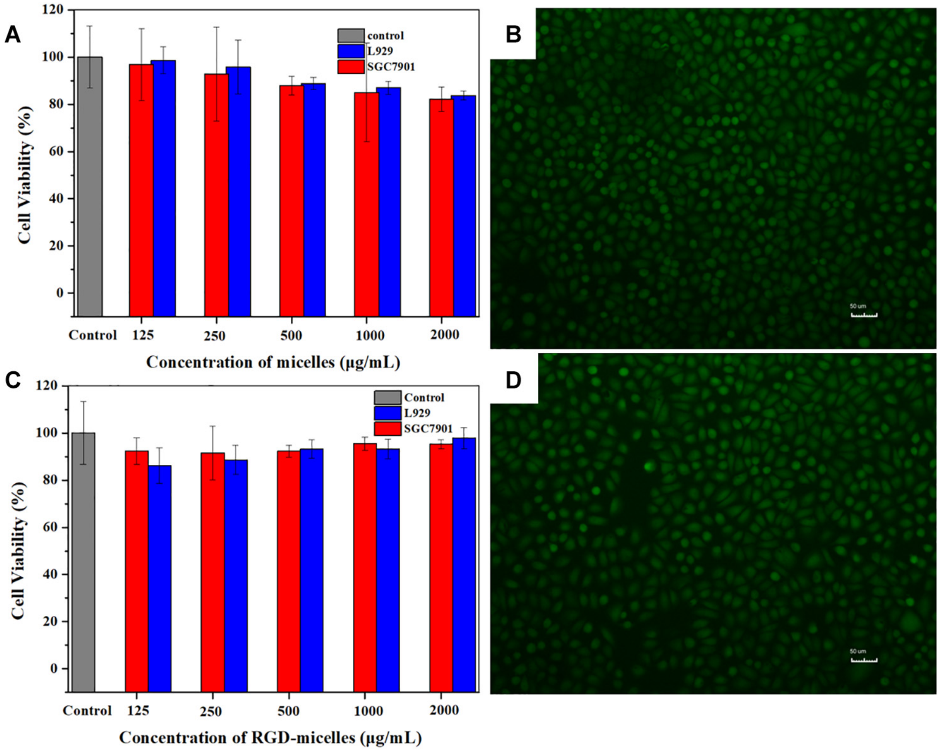

FIGURE 4 | CCK-8 analysis of the cell viability after incubated with **(A)** DSPE-PEG@ICG or **(C)** DSPE-PEG-RGD@ICG for 24 h. Fluorescence images of SGC7901 cells cultured with **(B)** DSPE-PEG@ICG or **(D)** DSPE-PEG-RGD@ICG after Live/Dead staining.

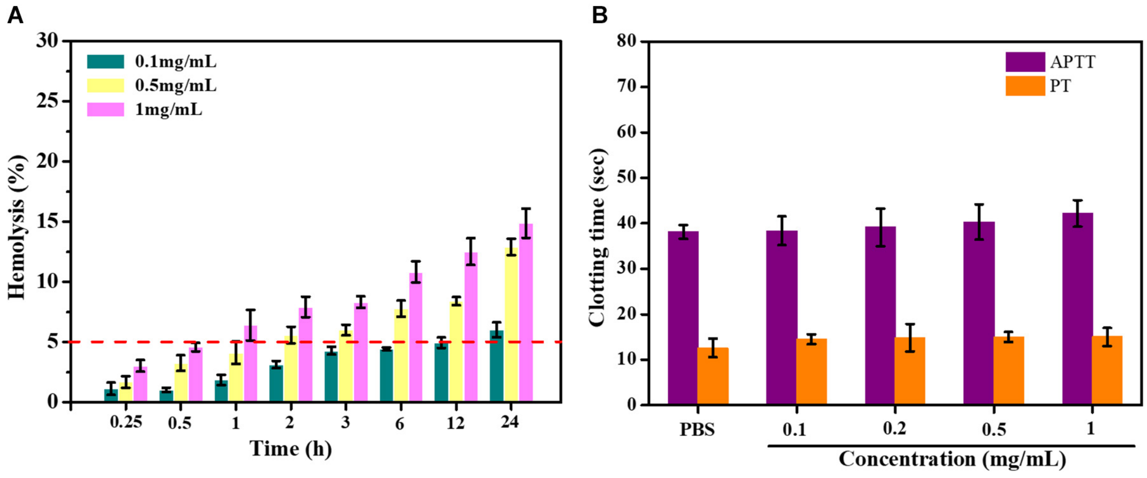

FIGURE 5 | **(A)** Hemolysis assay of erythrocytes and blood of DSPE-PEG-RGD@ICG; **(B)** effect of DSPE-PEG-RGD@ICG on APTT and PT.

even a high dose of micelles could be applied to cells with little cytotoxicity *in vitro*.

In vitro Blood Compatibility Test

Hemolysis is the rupture of RBCs releasing their contents (hemoglobin, etc.) into the surroundings. Hemolytic activity of erythrocytes is an alternative and reliable way to assess the blood compatibility of drugs for intravenous administration. The American Society for Testing and Materials (ASTM F756) divided the materials into three categories: non-hemolytic (hemolysis: 0–2%), slightly hemolytic (hemolysis: 2–5%), and hemolytic (hemolysis: >5%). As shown in **Figure 5A**, the hemolysis was nearly 5% within a certain concentration range of DSPE-PEG-RGD@ICG. The hemolytic activity of DSPE-PEG-RGD@ICG showed dose-depended hemolysis. As the concentration increased, more erythrocytes ruptured. The results of the hemolysis assay indicated that the hemolytic toxicity of DSPE-PEG-RGD@ICG was permissible within its normal concentration range.

Blood clotting results from the plasma coagulation cascade, which is activated by platelets. APTT and PT represent the intrinsic and extrinsic pathways of coagulation time, respectively.

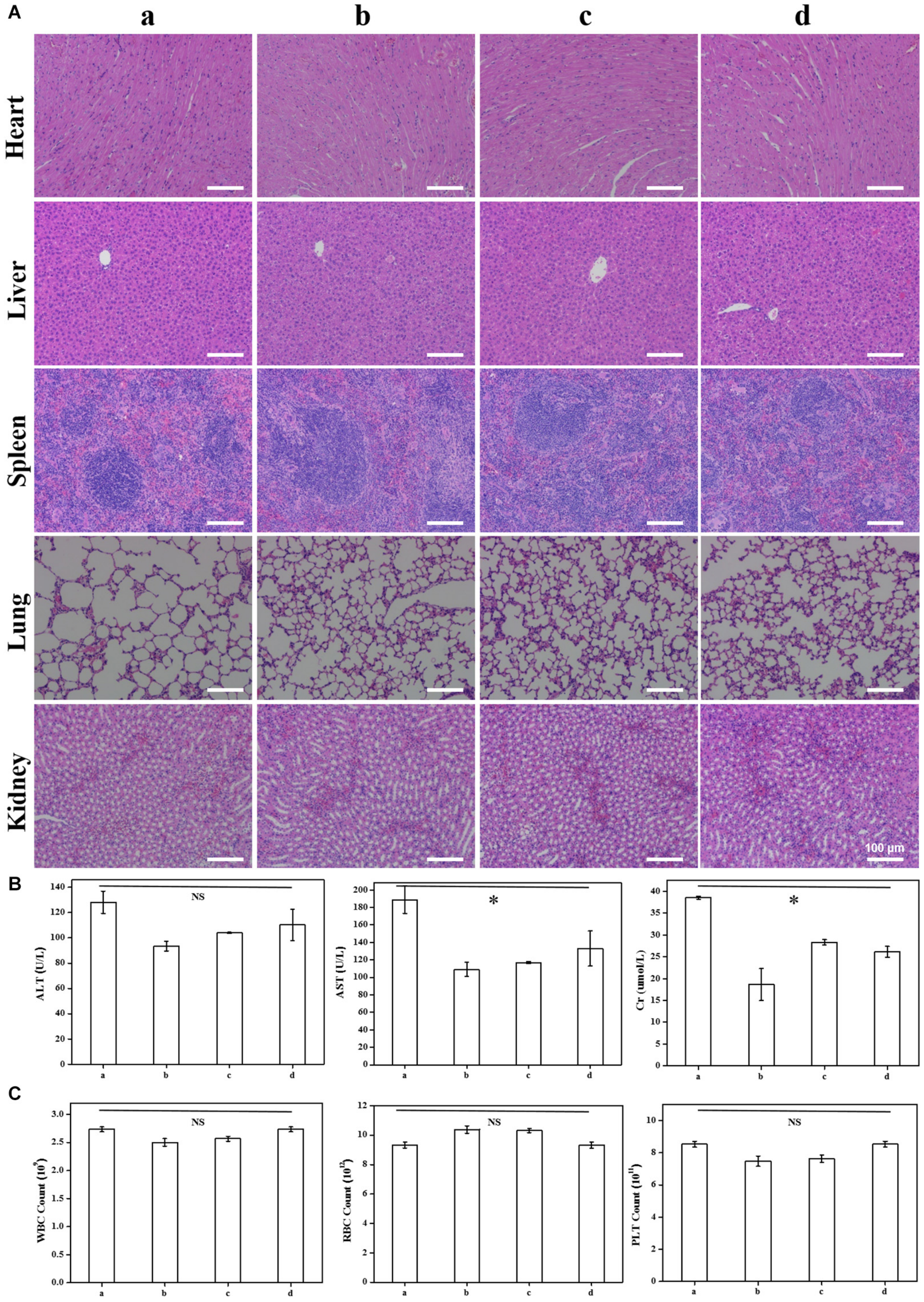

FIGURE 6 | H&E staining of the main organs 7 days after intravenous injection **(A)**; blood parameters for evaluating effects on liver (ALT and AST) and kidney (Cr) function **(B)** and bone marrow hematopoietic system (RBC, WBC, and platelet) **(C)** in nude mice. Note that **(a–d)** stand for intravenous injection of DSPE-PEG-RGD@ICG with different doses: 0 mg/kg **(a)**, 1 mg/kg **(b)**, 2 mg/kg **(c)**, and 4 mg/kg **(d)**. $^*P < 0.05$.

The normal physiological levels for APTT and PT were 25.1∼36.5 s and 9.4∼12.5 s, respectively (Huang et al., 2016). The impact of micelles on coagulation factors was assessed in this section. After being treated with DSPE-PEG-RGD@ICG micelles in different concentrations, the coagulation time of the platelet-poor plasma (PPP) mixed with different reagents was tested. The results were shown in **Figure 5B**. The APTT and PT values of the PBS group were 38.10 ± 1.52 s and 12.60 ± 2.03 s. Meanwhile, DSPE-PEG-RGD@ICG had no significant effect on coagulation time for the two pathways from low concentration (0.1 mg/ml) to relatively high concentration (1 mg/ml). The APTT and PT value of DSPE-PEG-RGD@ICG in 1 mg/ml were 42.18 ± 2.93 s and 15.00 ± 2.00 s. Thus, at the experimental concentration, the APTT and PT values of DSPE-PEG-RGD@ICG were both in the normal range and did not initiate the coagulation pathway, showing a good blood biocompatibility.

In vivo Acute Toxicity Test

Based on the above research *in vitro*, we carried out the study of toxicity *in vivo*. Briefly, twelve healthy male nude mice were treated with different doses of DSPE-PEG-RGD@ICG. No mortality or other abnormal signs were observed throughout the entire 7-day study period. On the 8th day, blood samples and the major organs were harvested for further histopathological analysis. **Figure 6A** shoed the H&E staining images of the major organs of mice. There was no obvious influence on the tissue structure and morphology of the major organs in all groups. Blood chemistry parameters for evaluating liver (ALT and AST) and kidney (Cr) function were tested, which showed no significant changes (**Figure 6B**). Additionally, the whole blood cell counts also illustrated no significant difference in WBC, RBC, and platelet when compared to the PBS group (**Figure 6C**). Therefore, our results indicated that DSPE-PEG-RGD@ICG micelles are safe and promising materials for GC fluorescence imaging *in vivo*.

In vivo Fluorescence Imaging and Distribution

In order to verify the specific active targeting efficiency of DSPE-PEG-RGD@ICG toward GC, the fluorescence imaging of tumor-bearing mice treated with different reagents was observed by an optic imaging system. After the injection of free ICG or micelles with or without RGD via tail vein for 48 h, the real-time distribution and tumor accumulation of different fluorescence agents were shown in **Figure 7A**. Obviously, at 1 h post-injection, the fluorescence signal could be obtained all over the body with the help of blood circulation in the three groups, mainly of which was concentrated in the liver. However, the fluorescence accumulation of the tumor and the location and edge of the tumor could be observed in the DSPE-PEG-RGD@ICG group

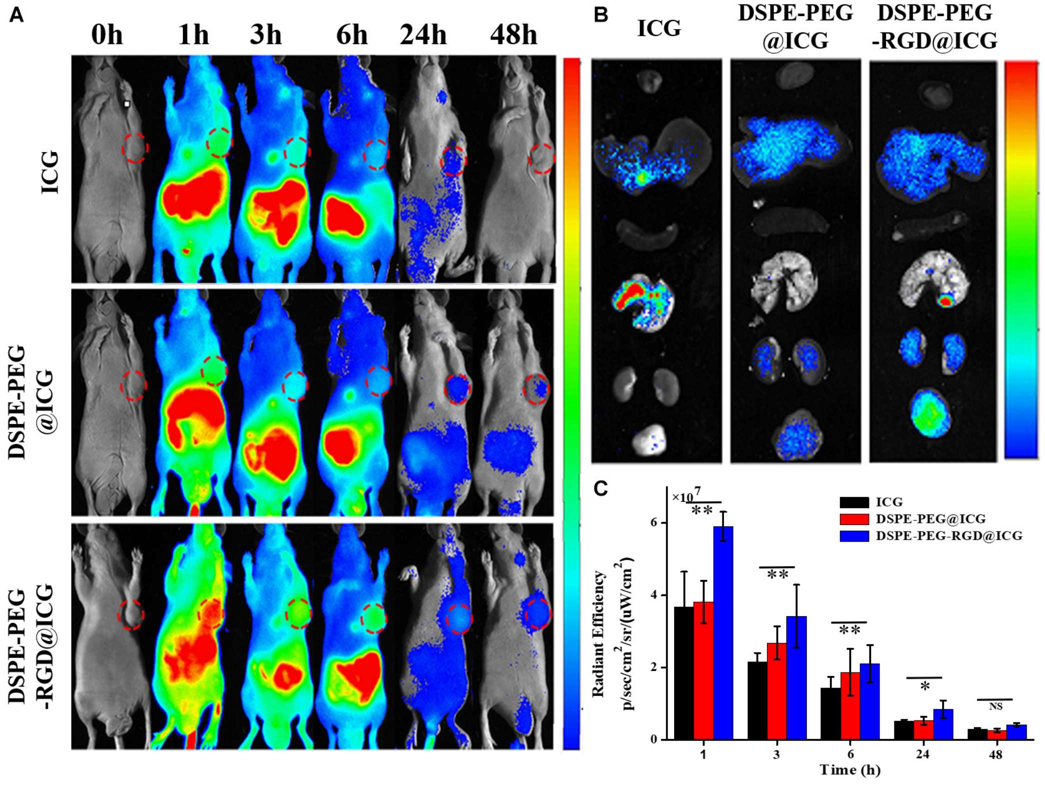

FIGURE 7 | (A) Fluorescence signal of experimental mice at different times treated with free ICG, DSPE-PEG@ICG and DSPE-PEG-RGD@ICG, respectively. The red circle represents the location of the tumor. **(B)** *In vitro* fluorescence signal of tumors and organs of the mice were observed at 48 h after injection. **(C)** Changes of the fluorescence signal intensity at the tumor site. $^{*}P < 0.05$ and $^{**}P < 0.01$.

at that point, but not obvious in DSPE-PEG@ICG or ICG treated mice. The fluorescence intensity of the three groups decreased gradually with the extension of time (**Figure 7C**). After 24 h, there was only a small amount of fluorescence signal remaining in the gastrointestinal tract and tumor in the mice receiving free ICG. Previous studies indicated that ICG binds to plasma proteins such as albumin and rapidly metabolized from the liver when introduced into the blood circulation (Han et al., 2018). Our experimental results were consistent with this point. On the contrary, there still existed fluorescence in the mice injected with DSPE-PEG@ICG or DSPE-PEG-RGD@ICG. Moreover, the tumor fluorescence could still be observed in the two groups even after 48 h post-injection, indicating a prolonged circulation time. It might be explained that the encapsulation of ICG into micelles prevented ICG from binding to plasma proteins. Additionally, the fluorescence intensity of mice receiving DSPE-PEG-RGD@ICG was higher than that of mice receiving DSPE-PEG@ICG at indicated time points. Thus, the attachment of RGD polypeptide to micelles increased the accumulation of ICG in tumors via the interaction between RGD peptide and Integrin $\alpha_v\beta_3$. After being imaged, all the tumor-bearing mice were immediately killed for isolating and visualizing the major organs and the tumors under the same conditions. As shown in **Figure 7B**, the *ex vivo* image conformed the obvious fluorescence accumulation in the tumors of the DSPE-PEG-RGD@ICG, but not the free ICG or DSPE-PEG@ICG. Interestingly, the fluorescence signals in the liver and spleen were also relatively high, which might be related to the natural phagocytosis of macrophages in these organs (Gref et al., 2012). So, how to minimize the nature internalization of micelles by the RES is a focus for the coming research. Thus, our results suggested that DSPE-PEG-RGD@ICG was an ideal fluorescence agent to higher accumulate in GC, and the EPR effect and RGD modification facilitated the targeting ability to tumors.

CONCLUSION

In this study, we attached RGD polypeptide to DSPE-PEG-Mal through the Michael addition reaction, and successfully encapsulated ICG to construct the targeting fluorescent agent delivery micelles DSPE-PEG-RGD@ICG, in which RGD was used for active targeting to GC, and micelles were used to extend the circulation time *in vivo*. The particle size less than 200 nm was conducive to the passive targeting to tumors via the EPR effect. Meanwhile, the toxicity was systematically evaluated. Cytotoxicity and blood compatibility *in vitro* were consistent with the acute toxicity test *in vivo*, which revealed good biocompatibility at the experimental concentration. Further biodistribution and tumor targeting image showed an improved accumulation in tumors and longer circulation time when compared with free ICG or DSPE-PEG@ICG. In a word, this targeting delivery micelles possessed marked biocompatibility and improved targeting accumulation in tumors, thus providing a promising strategy to realize an early diagnosis and complete resection of GCs.

DATA AVAILABILITY STATEMENT

All datasets presented in this study are included in the article/**Supplementary Material**.

ETHICS STATEMENT

The animal study was reviewed and approved by the Ethics Committee of the Institutional Animal Care and Use Subcommittee of the Third Hospital of Sun Yat-sen University.

AUTHOR CONTRIBUTIONS

BW designed the research. JS, XiZ, LF, TL, and DD performed the experiments. ZC, XuZ, and RL analyzed the data. JS and BW wrote the manuscript. All authors have read and approved the final submitted manuscript.

FUNDING

This work was supported in part by grants from Science and Technology Planning Project of Guangdong Province (2017B020227009 and 2017A010103009), and by the National Natural Science Foundation of China (81472825), by the Outstanding Young Talents Support Program of The Third Affiliated Hospital of Sun Yat-sen University.

ACKNOWLEDGMENTS

We are gratefully acknowledged Yang Shi (Uniklinik RWTH Aachen and Helmholtz Institute for Biomedical Engineering, Faculty of Medicine, RWTH Aachen University), Ning Zhu, and Lingzhi Zhao (Laboratory of Nanophotonic Functional Materials and Devices, South China Normal University) for helpful discussions.

SUPPLEMENTARY MATERIAL

The Supplementary Material for this article can be found online at: https://www.frontiersin.org/articles/10.3389/fbioe.2020.575365/full#supplementary-material

REFERENCES

Allen, T. M., and Cullis, P. R. (2004). Drug delivery systems: entering the mainstream. *Science* 303, 1818–1822. doi: 10.1126/science.1095833

Ban, H., Sugimoto, M., Otsuka, T., Murata, M., Nakata, T., Hasegawa, H., et al. (2018). Usefulness of the clip-flap method of endoscopic submucosal dissection: a randomized controlled trial. *World J. Gastroenterol.* 24, 4077–4085. doi: 10.3748/wjg.v24.i35.4077

Boger, C., Warneke, V. S., Behrens, H. M., Kalthoff, H., Goodman, S. L., Becker, T., et al. (2015). Integrins alphavbeta3 and alphavbeta5 as prognostic, diagnostic, and therapeutic targets in gastric cancer. *Gastric. Cancer* 18, 784–795. doi: 10.1007/s10120-014-0435-2

Bray, F., Ferlay, J., Soerjomataram, I., Siegel, R. L., Torre, L. A., and Jemal, A. (2018). Global cancer statistics 2018: globocan estimates of incidence and mortality worldwide for 36 cancers in 185 countries. *CA Cancer J. Clin.* 68, 394–424. doi: 10.3322/caac.21492

Chen, C., Song, Z., Zheng, X., He, Z., Liu, B., Huang, X., et al. (2017). AIEgen-based theranostic system: targeted imaging of cancer cells and adjuvant amplification of antitumor efficacy of paclitaxel. *Chem. Sci.* 8, 2191–2198. doi: 10.1039/c6sc03859j

Cheng, H., Chi, C., Shang, W., Rengaowa, S., Cui, J., Ye, J., et al. (2017). Precise integrin-targeting near-infrared imaging-guided surgical method increases surgical qualification of peritoneal carcinomatosis from gastric cancer in mice. *Oncotarget* 8, 6258–6272. doi: 10.18632/oncotarget.14058

Cureton, N., Korotkova, I., Baker, B., Greenwood, S., Wareing, M., Kotamraju, V. R., et al. (2017). Selective targeting of a novel vasodilator to the uterine vasculature to treat impaired uteroplacental perfusion in pregnancy. *Theranostics* 7, 3715–3731. doi: 10.7150/thno.19678

Dahan, M., Pauliat, E., Liva-Yonnet, S., Brischoux, S., Legros, R., Tailleur, A., et al. (2019). What is the cost of endoscopic submucosal dissection (ESD)? A medico-economic study. *United Eur. Gastroenterol. J.* 7, 138–145. doi: 10.1177/2050640618810572

Du, C., Qian, J., Zhou, L., Su, Y., Zhang, R., and Dong, C. M. (2017). Biopolymer-drug conjugate nanotheranostics for multimodal imaging-guided synergistic cancer photothermal-chemotherapy. *ACS Appl. Mater. Interfaces* 9, 31576–31588. doi: 10.1021/acsami.7b10163

Fang, W., He, J., Kim, Y. S., Zhou, Y., and Liu, S. (2011). Evaluation of 99mTc-labeled cyclic RGD peptide with a PEG4 linker for thrombosis imaging: comparison with DMP444. *Bioconjug. Chem.* 22, 1715–1722. doi: 10.1021/bc2003742

Gao, J., Zhong, W., He, J., Li, H., Zhang, H., Zhou, G., et al. (2009). Tumor-targeted PE38KDEL delivery via PEGylated anti-HER2 immunoliposomes. *Int. J. Pharm.* 374, 145–152. doi: 10.1016/j.ijpharm.2009.03.018

Gref, R., Domb, A., Quellec, P., Blunk, T., Müller, R. H., Verbavatz, J. M., et al. (2012). The controlled intravenous delivery of drugs using PEG-coated sterically stabilized nanospheres. *Adv. Drug. Deliv. Rev.* 64, 316–326.

Han, Y. H., Kankala, R. K., Wang, S. B., and Chen, A. Z. (2018). Leveraging engineering of indocyanine green-encapsulated polymeric nanocomposites for biomedical applications. *Nanomaterials* 8:360. doi: 10.3390/nano8060360

Hansem, L. M. K., Huang, R., Wegner, C. S., Simonsen, T. G., Gaustad, J. V., Hauge, A., et al. (2019). Intratumor heterogeneity in interstitial fluid pressure in cervical and pancreatic carcinoma xenografts. *Transl. Oncol.* 12, 1079–1085. doi: 10.1016/j.tranon.2019.05.012

Huang, H., Lai, W., Cui, M., Liang, L., Lin, Y., Fang, Q., et al. (2016). An evaluation of blood compatibility of silver nanoparticles. *Sci. Rep.* 6:25518. doi: 10.1038/srep25518

Hwang, Y., Yoon, H., Choe, K., Ahn, J., Jung, J. H., Park, J. H., et al. (2017). In vivo cellular-level real-time pharmacokinetic imaging of free-form and liposomal indocyanine green in liver. *Biomed. Opt. Express* 8, 4706–4716. doi: 10.1364/BOE.8.004706

Itatani, Y., Obama, K., Nishigori, T., Ganeko, R., Tsunoda, S., Hosogi, H., et al. (2019). Three-dimensional stereoscopic visualization shortens operative time in laparoscopic gastrectomy for gastric cancer. *Sci. Rep.* 9:4108. doi: 10.1038/s41598-019-40269-3

Kotagiri, N., Cooper, M. L., Rettig, M., Egbulefu, C., Prior, J., Cui, G., et al. (2018). Radionuclides transform chemotherapeutics into phototherapeutics for precise treatment of disseminated cancer. *Nat. Commun.* 9:275. doi: 10.1038/s41467-017-02758-9

Kraft, J. C., and Ho, R. J. (2014). Interactions of indocyanine green and lipid in enhancing near-infrared fluorescence properties: the basis for near-infrared imaging in vivo. *Biochemistry* 53, 1275–1283. doi: 10.1021/bi500021j

Kwakwa, K. A., and Sterling, J. A. (2017). Integrin alphavbeta3 signaling in tumor-induced bone disease. *Cancers* 9:84. doi: 10.3390/cancers9070084

Lee, K. M., Kim, J. M., Lee, E. J., and Kim, T. W. (2019). Anterior optic nerve head perfusion is dependent on adjacent parapapillary choroidal perfusion. *Sci. Rep.* 9:10999. doi: 10.1038/s41598-019-47534-5

Li, Y., Zhai, Y., Liu, W., Zhang, K., Liu, J., Shi, J., et al. (2019). Ultrasmall nanostructured drug based pH-sensitive liposome for effective treatment of drug-resistant tumor. *J. Nanobiotechnol.* 17:117. doi: 10.1186/s12951-019-0550-7

Lin, C. Y., Yang, S. T., Shen, S. C., Hsieh, Y. C., Hsu, F. T., Chen, C. Y., et al. (2018). Serum amyloid A1 in combination with integrin alphaVbeta3 increases glioblastoma cells mobility and progression. *Mol. Oncol.* 12, 756–771. doi: 10.1002/1878-0261.12196

Lu, S., Li, X., Zhang, J., Peng, C., Shen, M., and Shi, X. (2018). Dendrimer-stabilized gold nanoflowers embedded with ultrasmall iron oxide nanoparticles for multimode imaging-guided combination therapy of tumors. *Adv. Sci.* 5:1801612. doi: 10.1002/advs.201801612

Mozhi, A., Sunil, V., Zhan, W., Ghode, P. B., Thakor, N. V., and Wang, C. H. (2020). Enhanced penetration of pro-apoptotic and anti-angiogenic micellar nanoprobe in 3D multicellular spheroids for chemophototherapy. *J. Control Release* 323, 502–518. doi: 10.1016/j.jconrel.2020.05.005

Nguyen, Q. T., Olson, E. S., Aguilera, T. A., Jiang, T., Scadeng, M., Ellies, L. G., et al. (2010). Surgery with molecular fluorescence imaging using activatable cell-penetrating peptides decreases residual cancer and improves survival. *Proc. Natl. Acad. Sci. U.S.A.* 07, 4317–4322. doi: 10.1073/pnas.0910261107

Nieberler, M., Reuning, U., Reichart, F., Notni, J., Wester, H. J., Schwaiger, M., et al. (2017). Exploring the Role of RGD-recognizing integrins in cancer. *Cancers* 9:116. doi: 10.3390/cancers9090116

Paradossi, G., Oddo, L., Cerroni, B., Ben-Harush, C., Ariel, E., Di Meco, F., et al. (2019). In vivo toxicity study of engineered lipid microbubbles in rodents. *ACS Omega* 4, 5526–5533. doi: 10.1021/acsomega.8b03161

Peng, J., Xiao, Y., Li, W., Yang, Q., Tan, L., Jia, Y., et al. (2018). Photosensitizer micelles together with IDO inhibitor enhance cancer photothermal therapy and immunotherapy. *Adv. Sci.* 5:1700891. doi: 10.1002/advs.201700891

Proulx, S. T., Luciani, P., Derzsi, S., Rinderknecht, M., Mumprecht, V., Leroux, J. C., et al. (2010). Quantitative imaging of lymphatic function with liposomal indocyanine green. *Cancer Res.* 70, 7053–7062. doi: 10.1158/0008-5472.CAN-10-0271

Pyataev, N. A., Petrov, P. S., Minaeva, O. V., Zharkov, M. N., Kulikov, O. A., Kokorev, A. V., et al. (2019). Amylase-sensitive polymeric nanoparticles based on dextran sulfate and doxorubicin with anticoagulant activity. *Polymers* 11:921. doi: 10.3390/polym11050921

Raab-Westphal, S., Marshall, J. F., and Goodman, S. L. (2017). Integrins as therapeutic targets: successes and cancers. *Cancers* 9:110. doi: 10.3390/cancers9090110

Repenko, T., Rix, A., Ludwanowski, S., Go, D., Kiessling, F., Lederle, W., et al. (2017). Bio-degradable highly fluorescent conjugated polymer nanoparticles for bio-medical imaging applications. *Nat. Commun.* 8:470. doi: 10.1038/s41467-017-00545-0

Saxena, V., Sadoqi, M., and Shao, J. (2003). Degradation kinetics of indocyanine green in aqueous solution. *J. Pharm. Sci.* 92, 2090–2097. doi: 10.1002/jps.10470

Skalickova, S., Loffelmann, M., Gargulak, M., Kepinska, M., Docekalova, M., Uhlirova, D., et al. (2017). Zinc-modified nanotransporter of doxorubicin for targeted prostate cancer delivery. *Nanomaterials* 7:435. doi: 10.3390/nano7120435

Son, T., Sun, J., Choi, S., Cho, M., Kwon, I. G., Kim, H. I., et al. (2019). Multi-institutional validation of the 8th AJCC TNM staging system for gastric cancer: analysis of survival data from high-volume Eastern centers and the SEER database. *J. Surg. Oncol.* 120, 676–684. doi: 10.1002/jso.25639

Wang, K., Zhang, X., Liu, Y., Liu, C., Jiang, B., and Jiang, Y. (2014). Tumor penetrability and anti-angiogenesis using iRGD-mediated delivery of doxorubicin-polymer conjugates. *Biomaterials* 35, 8735–8747. doi: 10.1016/j.biomaterials.2014.06.042

Weis, S. M., and Cheresh, D. A. (2011). alphaV integrins in angiogenesis and cancer. *Cold Spring Harb. Perspect. Med.* 1:a006478. doi: 10.1101/cshperspect.a006478

Xiao, M., Zhang, N., Zhuang, J., Sun, Y., Ren, F., Zhang, W., et al. (2019). Degradable Poly(ether-ester-urethane)s based on well-defined aliphatic diurethane diisocyanate with excellent shape recovery properties at body temperature for biomedical application. *Polymers* 11:1002. doi: 10.3390/polym11061002

Xu, H. L., Shen, B. X., Lin, M. T., Tong, M. Q., Zheng, Y. W., Jiang, X., et al. (2018). Homing of ICG-loaded liposome inlaid with tumor cellular membrane to the homologous xenografts glioma eradicates the primary focus and prevents lung metastases through phototherapy. *Biomater. Sci.* 6, 2410–2425. doi: 10.1039/c8bm00604k

Xu, M., Zhang, C., Wu, J., Zhou, H., Bai, R., Shen, Z., et al. (2019). PEG-detachable polymeric micelles self-assembled from amphiphilic copolymers for tumor-acidity-triggered drug delivery and controlled release. *ACS Appl. Materi. Interfaces* 11, 5701–5713. doi: 10.1021/acsami.8b13059

Yan, F., Wu, H., Liu, H., Deng, Z., Liu, H., Duan, W., et al. (2016). Molecular imaging-guided photothermal/photodynamic therapy against tumor by iRGD-modified indocyanine green nanoparticles. *J. Control Release* 224, 217–228. doi: 10.1016/j.jconrel.2015.12.050

Yonucu, S., Yiotalmaz, D., Phipps, C., Unlu, M. B., and Kohandel, M. (2017). Quantifying the effects of antiangiogenic and chemotherapy drug combinations on drug delivery and treatment efficacy. *PLoS Comput. Biol.* 13:e1005724. doi: 10.1371/journal.pcbi.1005724

Zhang, C., Zhao, Y., Zhang, H., Chen, X., Zhao, N., Tan, D., et al. (2017). The application of heptamethine cyanine dye DZ-1 and indocyanine green for imaging and targeting in xenograft models of hepatocellular carcinoma. *Int. J. Mol. Sci.* 18, 1332. doi: 10.3390/ijms18061332

Zitzmann, S., Ehemann, V., and Schwab, M. (2002). Arginine-glycine-aspartic acid (RGD)-peptide binds to both tumor and tumor-endothelial cells in vivo. *Cancer Res.* 62, 5139–5143.

Zou, Z. H., Zhao, L. Y., Mou, T. Y., Hu, Y. F., Yu, J., Liu, H., et al. (2014). Laparoscopic vs open D2 gastrectomy for locally advanced gastric cancer: a meta-analysis. *World J. Gastroenterol.* 20, 16750–16764. doi: 10.3748/wjg.v20.i44.16750

Conflict of Interest: The authors declare that the research was conducted in the absence of any commercial or financial relationships that could be construed as a potential conflict of interest.

frontiers
in Bioengineering and Biotechnology

ORIGINAL RESEARCH
published: 08 October 2020
doi: 10.3389/fbioe.2020.573464

Antibacterial and Osteogenic Functionalization of Titanium With Silicon/Copper-Doped High-Energy Shot Peening-Assisted Micro-Arc Oxidation Technique

Xinkun Shen[1]†, Wenjia Hu[1]†, Linchao Ping[1], Chongxing Liu[1], Lili Yao[1]*, Zhennan Deng[1]* and Gang Wu[2,3]

[1] School and Hospital of Stomatology, Wenzhou Medical University, Wenzhou, China, [2] Department of Oral Implantology and Prosthetic Dentistry, Academic Centre for Dentistry Amsterdam (ACTA), Amsterdam Movement Science, University of Amsterdam and Vrije University Amsterdam, Amsterdam, Netherland, [3] Department of Oral and Maxillofacial Surgary/Pathology, Amsterdam UMC and Academic Centre for Dentistry Amsterdam (ACTA), Vrije Universitetit Amsterdam, Amsterdam Movement Science, Amsterdam, Netherlands

Edited by:
Changyou Gao,
Zhejiang University, China

Reviewed by:
Kui Cheng,
Zhejiang University, China
Saeid Kargozar,
Mashhad University of Medical Sciences, Iran

***Correspondence:**
Lili Yao
xan210@163.com
Zhennan Deng
dengzhennan@wmu.edu.cn

† These authors have contributed equally to this work

Specialty section:
This article was submitted to Biomaterials, a section of the journal Frontiers in Bioengineering and Biotechnology

Received: *17 June 2020*
Accepted: *07 September 2020*
Published: *08 October 2020*

Citation:
Shen X, Hu W, Ping L, Liu C, Yao L, Deng Z and Wu G (2020) Antibacterial and Osteogenic Functionalization of Titanium With Silicon/Copper-Doped High-Energy Shot Peening-Assisted Micro-Arc Oxidation Technique. Front. Bioeng. Biotechnol. 8:573464. doi: 10.3389/fbioe.2020.573464

Antibacterial and osteogenic functionalization of titanium (Ti) implants will greatly expand their clinical indications in immediate implant therapy, accelerate osteointegration, and enhance long-term prognosis. We had recently shown that the high-energy shot peening (HESP)-assisted micro-arc oxidation (MAO) significantly improved the bioactivity and coating stability of Ti-based substrates. In this study, we further functionalized Ti with antibacterial and osteogenic properties by doping silicon (Si) and/or copper (Cu) ions into HESP/MAO-treated coatings. Physicochemical characterization displayed that the doping of Si and Cu in HESP/MAO-treated coatings (Si/Cu-MAO) did not significantly change their surface topography, roughness, crystal structure, coating thickness, bonding strength, and wettability. The results of X-ray photoelectron spectroscopy (XPS) showed that Si and Cu in the Si/Cu-MAO coating was in the form of silicate radical ($SiO_3{}^{2-}$) and bivalent copper (Cu^{2+}), respectively. The total amounts of Si and Cu were about 13.5 and 5.8 μg/cm^2, which released about 33.2 and 31.3% within 14 day, respectively. Compared with the control group (MAO), Si doping samples (MAO-Si) significantly increased the cell viability, alkaline phosphatase (ALP) activity, mineralization and osteogenic genes (ALP, collagen I and osteocalcin) expression of MC3T3-E1 cells. Furthermore, the addition of Cu presented good bactericidal property against both *Staphylococcus aureus* and *Streptococcus mutans* (even under the co-culture condition of bacteria and MC3T3-E1 cells): the bacteriostatic rate of both bacteria was over 95%. In conclusion, the novel bioactive Si/Cu-MAO coating with antibacterial and osteogenic properties is a promising functionalization method for orthopedic and dental implants, especially in the immediate implant treatment with an infected socket.

Keywords: titanium, high-energy shot peening, micro-arc oxidation, antibacterial, osteogenesis

INTRODUCTION

Compared with conventional implantation, immediate implant surgery has been widely used in the restoration of tooth loss due to its advantages of fewer surgical procedures, shorter treatment time and better appearance. However, there are still some contraindications that restrict the clinical promotion of immediate implantation (Koh et al., 2010). At present, socket infection has been considered as one of the most commonly faced complications of immediate implantation (Rass, 2010; Narad et al., 2018). An incomplete pre-implantation curettage (conventional surgical treatment of infected socket before implantation) of infected tissues will leave residual bacteria around the implant which significantly increases the risk of multiple complications and ultimately results in implant failure (Narad et al., 2018). A published meta-analysis has shown that the implant failure rate increase by 116% when the implants are placed directly in a bacterial-infected socket compared with a normal socket (Zhao et al., 2016). Previous study has also shown that low immune resistance in the early post-implantation period will increase the susceptibility of infection, with only 100 bacteria per gram of tissue leading to infection around the implant (Mangram et al., 1999; Zimmerli and Sendi, 2011). The infected bacteria will form a dense biofilm on the surfaces of Ti-based implants in a very short time, which will further block the permeation of host immune cells (such as macrophages) and systemic antibiotics, thereby ensuring the survival of bacteria (Hoffman et al., 2005; Shen et al., 2019a). If not treated in time, infection and secondary inflammation will disrupt the osseointegration of the implant, cause local bone resorption, and finally cause loosening or falling off of implants. Therefore, an effective prevention and treatment of bacterial infection are crucial for the prognosis of long-term implant survivability.

Compared with oral and intravenous antimicrobial agents, a local antibacterial coating on the surface of implants is more preferred by researchers. These locally drug-releasing coatings can allow for low-dose and long-lasting drug therapy, and prevent side effects of the drug on normal tissues or organs (Maher et al., 2018). At present, the active antibacterial agents commonly used in the treatment of Ti-based implants include antibiotics, antimicrobial peptides, and metal ions (Liu et al., 2017; Ghosh et al., 2019; Shen et al., 2019a). However, long-term antibiotics usage may induce drug-resistant bacteria, furthermore, antimicrobial peptides are relatively expensive, so the metal ions-rich antibacterial coatings provide a more extensive application prospect.

In order to improve the bioactivity of titanium (Ti) implants, which are biological inertia, a variety of surface modification strategies have been developed (Szesz et al., 2014; Shen et al., 2019b; Wang et al., 2020). Among them, the bone-like porous coatings with ideal elastic modulus and wear resistance prepared by micro-arc oxidation (MAO) technology are favored and frequently used to prepare commercial Ti-based materials (Szesz et al., 2014; Guo et al., 2020). In our recent work, we have used high-energy shot peening (HESP) pretreatment to significantly improve the comprehensive properties of MAO-treated porous coatings and proved its superior application potential under normal conditions (Shen et al., 2020). However, although the HESP/MAO-prepared porous coatings have been proved to have good bioactivity, the osseointegration of the corresponding implants remains unsatisfactory when exposed to bacterial infection. In the process of MAO treatment, a large number of ion channels will be formed on the surface of Ti, and then suitable ions can be enriched in these porous coatings (Li G. et al., 2019; Shen et al., 2020). Thus, certain metal ions can be selected to further endow the HESP/MAO-treated samples with antibacterial properties. As an essential trace element, copper (Cu) is suitable for the development of antibacterial Ti implants due to its excellent broad-spectrum antibacterial activity against fungus, Gram-positive and Gram-negative bacteria (Macdonald et al., 2011; Xia et al., 2019). Other studies have also reported that application of Cu^{2+} with the appropriate concentration (MC3T3-E1 cells: $< 10\ \mu M$; human umbilical vein endothelial cells: $< 222\ \mu M$) can enhance multiple biological properties, which include the promotion of cell proliferation and angiogenesis (Shi et al., 2017; Huang et al., 2019; Li K. et al., 2019).

Furthermore, we add silicon (Si) to the HESP/MAO-prepared coatings to further enhance their osteoinductive potential. It has been reported that Si is located in the active calcification area of bone tissue (Kim et al., 2017) and the appropriate concentration (10–20 μM) of Si can significantly promote the secretion of type I collagen and the differentiation of osteoblasts (Reffitt et al., 2003). By adding Cu and Si to the porous coating concurrently, a new type of multifunctional coating with antibacterial ability and osteoinductive function can be achieved, which is more ideal for preventing implant-related infection and promoting osseointegration.

In this study, the Si/Cu composite porous coatings on HESP-pretreated titanium were successfully constructed for the first time via MAO. The antibacterial effect of Si/Cu doped coatings on *Staphylococcus aureus* (*S. aureus*) and *Streptococcus mutans* (*S. mutans*) were investigated with single and co-culture (bacteria/MC3T3-E1 cells) assays. Furthermore, the spreading, proliferation and differentiation of MC3T3-E1 cells on Si/Cu-added samples were also studied in detail.

MATERIALS AND METHODS

Materials

Ti substrates were obtained from Engineering Research Center for Biomaterials, Sichuan University. Glutaraldehyde, cetylpyridinium chloride, calcium acetate [$Ca(CH_3COO)_2 \cdot H_2O$], sodium silicate ($Na_2SiO_3 \cdot 9H_2O$), and β-glycerophosphate disodium salt ($C_3H_7Na_2O_6P \cdot 5H_2O$) were purchased from Aladdin Industrial Co. (Shanghai, China). Alizarin red, CCK8, and Live-Dead Cell Staining Kit were provided by Sigma Chemical Co. (MO, United States). LIVE/DEAD® BacLight^{TM} Bacterial Viability kit was received from Molecular Probes (CA, United States). Alkaline Phosphatase (ALP) Assay Kit, Bicinchoninic Acid Assay (BCA) Kit were obtained from Nanjing Jiancheng Biotechnology Institute (Nanjing, China). PrimeScript® RT Reagent Kit and SYBR Premix ExTMTaq II were purchased from Takara Bio Inc. (Kyoto, Japan). Other chemicals were provided by Dingsheng Medical Instrument Reagent Co. (Wenzhou, China).

Sample Preparation and Characterization

The HESP and MAO technologies were used to treat Ti for preparing target samples according to our previous study (Shen et al., 2020). Briefly, Ti substrates were first polished with gradient sandpapers, cleaned using detergent/alcohol and dried at 60°C. Then, the cleaned samples were treated for 100 s using a HESP device (Shot Peening Machine, Rösler, Germany) under 5 Mpa (pressure) and 0.1 mmA (strength). Glass beads with 0.25–0.3 mm in diameter were used as the shot. After that, HESP-pretreated specimens were further treated with different electrolytes (**Tables 1**, **2**) for 5 min at 480 V using a MAO device developed by Xi'an Technological University. Electrolytes of the target specimens (named as MAO, Si-MAO, Si/Cu-MAO, respectively) evaluated in detail by following cells/bacteria tests.

The surface and cross-sectional morphologies of different coatings (MAO, Si-MAO, Si/Cu-MAO) were measured by scanning electron microscopy (SEM, Inspect-F, FEI, United States). The thickness and bonding strength of different coatings were characterized by an eddy current thickness gauge (ED200, Tianxing Research Institute, China) and scratch tester (Revetest Scratch Tester, CSM Instruments, Switzerland), respectively. The surface roughness (Ra), crystalline phase, chemical compositions, chemical states, and water contact angle were further tested by surface roughness meter (Perthometer M1, Mahr, Germany), X-ray diffraction (XRD, X'Pert Pro MPD, Philips, Dutch), energy dispersive spectrometry (EDS, Oxford Instruments, United Kingdom), X-ray photoelectron spectroscopy (XPS, Model PHI 5400, Perkin Elmer, United States), and contact angle measuring instrument (DSA30, Kruss, Germany), respectively.

Release Profile of Cu^{2+}

The specimens were soaked in 6 mL of phosphate buffer saline (PBS) solution at 37°C. After 1, 4, 7, 10, and 14 day, we collected all the soaking solution and re-added another fresh PBS solution (6 mL). In addition, to determine the exact concentration of Si and Cu in the coatings, Si/Cu-MAO samples were soaked in 6 mL of hydrochloric acid (HCl, 3 mol/L) solution for 14 day under oscillatory conditions. The contents of Cu and Si in the PBS or HCl immersion solution were finally measured with an inductively coupled plasma emission spectrometer (ICAP-9000, Jarrell-Ash, United States).

TABLE 1 | Compositions of working solution used to construct Si-loaded substrates [MAO, Si1, Si2, and Si3 (Si-MAO)].

	Component contents (moL) in ddH_2O (1,000 mL)			
Working solution	$C_3H_7Na_2O_6P{\cdot}5H_2O$	Ca ($CH_3COO)_2{\cdot}H_2O$	$Na_2SiO_3{\cdot}9H_2O$	Prepared samples
1	0.05	0.10	0	Si0
2	0.05	0.10	0.02	Si1
3	0.05	0.10	0.04	Si2
4	0.05	0.10	0.08	Si4 (Si-MAO)

Bacterial Culture and Morphology

The *S. aureus* (ATCC 6538) and *S. mutans* (ATCC 25175) were provided by the State Key Laboratory of Oral Diseases. After the determination of no other bacterial contamination by Gram stain, a single colony was selected to be inoculated on TSB/LB plates via the streak plate method and continued to culture for 24 h. The individual colonies on the plate were further transferred to liquid medium for culture 10 h before the following bacterial tests.

For detecting the bacterial morphology, two bacteria (1 mL) were cultured on different specimens with a density of 1 × 10^6 Colony-Forming Units (CFU)/mL. After 24 h, the bacteria attached to the samples were cleaned 3 times with PBS solution, fixed by 2.5% glutaraldehyde for 30 min at 4°C, and then dehydrated with gradient ethanol (30, 50, 75, 85, 95, and 100%). Finally, the bacterial samples were sprayed with gold and observed by SEM.

Bacteriostasis Rate

The bacteriostasis rate of *S. aureus* and *S. mutans* on different substrates were determined by the attachment film method (referring to GB/T21510-2008). Briefly, 20 μL of bacterial solution (1 × 10^6 CFU/mL) was added to the surface of different specimens, covered with a cover glass, and cultured for 24 h at 37°C. Bacterial samples were then soaked in 20 mL of PBS solution for 5 min of vortex processing. After diluting 100 times, 0.1 mL of diluted bacteria solution was evenly coated on the agar plate and cultured for another 48 h. Finally, the colony was counted one by one and the bacteriostasis rate was statistically analyzed according to the following formula: Bacteriostasis rate (%) = (Bacterial number in MAO group - Bacterial number in experimental group) / Bacterial number in MAO group × 100%. The experimental group contained Si-MAO and Si/Cu-MAO in this study.

Live/Dead Staining of Bacteria

One milliliter of *S. aureus* or *S. mutans* (1 × 10^6 CFU/mL) were seeded on different samples for 24 h. After cleaning 3 times with PBS solution, bacteria were stained using a LIVE/DEAD® BacLight^{TM} Bacterial Viability kit. According to the kit instructions, 100 μL mixture solution of SYTO9 and PI were carefully added to the surface of different specimens and incubated for 15 min. Finally, the stained bacteria were observed using a confocal laser scanning microscope (CLSM, TCS SP2, LEICA, Germany). The final results were analyzed with Leica TCS SP2 Software and presented as 3D images.

Morphology and Viability of MC3T3-E1 Cells

MC3T3-E1 cells were cultured with low-sugar Dulbecco's modified Eagle medium (DMEM) supplemented with 10% fetal

TABLE 2 | Compositions of working solution used to construct Si/Cu-loaded substrates [Si-MAO, Si-Cu1, Si-Cu1 (Si/Cu-MAO), and Si-Cu3].

	Component contents (mol) in ddH_2O (1,000 mL)				
Working solution	$C_3H_7Na_2O_6P{\cdot}5H_2O$	$Ca(CH_3COO)_2{\cdot}H_2O$	$Na_2SiO_3{\cdot}9H_2O$	$Cu(CH_3COO)_2{\cdot}2H_2O$	**Prepared samples**
1	0.05	0.10	0	0	MAO
2	0.05	0.10	0.08	0	Si-MAO
3	0.05	0.10	0.08	0.025	Si/Cu1
4	0.05	0.10	0.08	0.05	Si/Cu2 (Si/Cu-MAO)
5	0.05	0.10	0.08	0.075	Si/Cu3

bovine serum. When the fusion reached 80–90%, cells were digested by 0.25% trypsin and seeded on different substrates at a density of 1×10^4 cells/cm^2. For morphology observation, cells cultured for 3 day were also fixed by 2.5% glutaraldehyde and dehydrated with gradient ethanol (30, 50, 75, 85, 95, and 100%). The dehydrated cells were further sprayed with gold and observed by SEM. In addition, for viability detection, Cell Counting Kit-8 (CCK8) assay was carried out. Briefly, cells at 1×10^4 cells/cm^2 were cultured on different substrates for 4 and 7 day. After removing the culture medium, the mixture of CCK-8 solution (30 μL) and DMEM medium (270 μL) was added to each well and incubated for 2 h. 200 μL of the final solution was transferred to a 96-well plate and detected at 450 nm using an enzyme-labeled instrument (Multiskan Spectrum, Thermo Fisher Scientific Inc., United States).

ALP Activity of MC3T3-E1 Cells

The activity of ALP in MC3T3-E1 cells was determined by spectrophotometry. After culturing for 4 and 7 day on different samples, MC3T3-E1 cells were collected with 0.25% trypsin, creaked by repeated freeze-thaw treatment, and then detected using a ALP Assay Kit. Briefly, 30 μL of sample lysates, phenol standard solution, or double-distilled water were added to a 96-well plate, respectively. Fifty microliter of buffer and 50 μL of matrix solution were then added to each well in turn. After incubation for 15 min at 37°C, 150 μL of color developer was added to each well and detected at 520 nm using an enzyme-labeled instrument. Meanwhile, the concentration of total protein in each group was determined with a BCA Kit at 570 nm to standardize the final ALP activity.

Mineralization Level of MC3T3-E1 Cells

After culturing for 7 and 14 day on MAO, Si-MAO, and Si/Cu-MAO substrates, MC3T3-E1 cells were fixed by 2.5% glutaraldehyde (30 min) and stained with commercial alizarin red staining solution (60 min). Then, the stained calcium nodule was dissolved using 10% cetylpyridinium chloride and measured at 540 nm.

Osteogenic Gene Expression

The expression of ALP, collagen I (Col I), and osteocalcin (OCN) genes was measured by real-time fluorescence quantitative PCR (RT-qPCR). After culturing for 7 day, the total RNA of MC3T3-E1 cells was extracted through the Trizol method. The mRNA was then reverse transcribed into complementary deoxyribonucleic acid (cDNA) and determined using a PrimeScript® RT Reagent Kit and SYBR Premix ExTMTaq II, respectively. MAO group was considered the control group in this study. The expression of target genes was standardized with the glyceraldehyde-3-phosphate dehydrogenase (GAPDH) gene. The primers were shown in **Table 3**.

Co-culture of MC3T3-E1 Cells and *S. mutans*

MC3T3-E1 cells (1×10^4 cells/cm^2) and *S. mutans* (5×10^5 cells/cm^2) were co-cultured on different specimens for 24 h. For SEM observation, the adherent cells were cleaned 3 times with PBS solution, fixed for 40 min with 2.5% glutaraldehyde, and then dehydrated with gradient ethanol (30, 50, 75, 85, 95, and 100%). The treated samples were sprayed with gold and observed by SEM. Next, to directly observe the living and dead MC3T3-E1 cells on different substrates, the adherent cells were stained with a commercial Live-Dead Cell Staining Kit for another 20 min. The stained cells were visualized using fluorescence microscope (IX71, OLYMPUS, Japan). In addition, the ALP activity and osteogenic genes (ALP and OCN) expression of the co-cultured MC3T3-E1 cells were further determined (refer to 2.8 and 2.10).

Statistical Analysis

All experiments were independently repeated 3 times. The data was represented by means ± standard deviation. SPSS20.0 packages were used for statistical analysis in this study. The one-way analysis of variance (ANOVA) and Student-Newman-Keuls (SNK) tests were used to determine the differences between different groups. $^*p < 0.05$ (confidence level: 95%)

TABLE 3 | Real-time polymerase chain reaction primers of osteogenic genes in MC3T3-E1 cells.

Target genes	Primers
ALP	F:5′-AGGGCTGTAAGGACATCGCCTACCA-3′ R:5′-GACTGCGCCTGGTAGTTGTTGTGAG-3′
COL I	F:5′-CCAGAAGAACTGGTACATCAGCAA-3′ R:5′-CGCCATACTCGAACTGGAATC-3′
OCN	F:5′-CCTCACACTCCTCGCCCTATTGG-3′ R:5′-GCTCACACACCTCCCTCCTGG-3′
GAPDH	F:5′-GGCATTGCTCTCAATGACAA-3′ R:5′-TGTGAGGGAGATGCTCAGTG-3′

and $^{**}p < 0.01$ (confidence level: 99%) indicated significant differences between groups.

RESULTS AND DISCUSSION

Concentration Selection of SiO_3^{2-} and Cu^{2+}

In order to obtain the best Si/Cu-doped porous structures, the initial concentrations of $Na_2SiO_3{\cdot}9H_2O$ and $Cu(CH_3COO)_2{\cdot}2H_2O$ in the electrolyte were investigated. We selected a concentration range of 0–0.08 moL/L for $Na_2SiO_3{\cdot}9H_2O$ to be used in this study, because higher concentration (>0.08 moL/L) would cause the electrolyte to be cloudy and affect the integrity of target coatings. From **Figure 1A**, it was found that the ability of the obtained samples to promote osteoblast proliferation increased gradually with the increase of initial SiO_3^{2-} (Si1 < Si2 < Si3). Therefore, Si3 (also named as Si-MAO) were selected to further prepare the target Si/Cu-doped materials. After adding different concentrations of Cu^{2+} to Si3, the biological activity of target samples was Cu^{2+} concentration-dependent (increasing at first and then decreasing, **Figure 1B**), which was consistent with previous studies (Cao et al., 2012; Li K. et al., 2019). Since the main reason for adding Cu^{2+} was to endow titanium with excellent antibacterial properties, Si/Cu2 (also named as Si/Cu-MAO) with similar bioactivity to Si-MAO was selected for follow-up studies.

Physicochemical Characterization

The key variables that play a role in affecting the biocompatibility of implant materials include surface morphology, roughness, chemical composition/state, crystalline structure, wettability, and coating stability (Chen et al., 2019; Abaricia et al., 2020). Hence, the in-depth surface characterization of MAO, Si-MAO, and Si/Cu-MAO were conducted. The SEM images (**Figure 2A**) showed no significant difference in the surface morphology of MAO, Si-MAO, and Si/Cu-MAO, which presented some porous structures (pore size: ∼4 μm). These pores were considered to be the channels for micro-arc discharges during MAO treatment. No obvious cracks were observed on these porous coatings, which was related to the pretreatment of HESP. In our previous study (Shen et al., 2020), we have demonstrated that the formation of coating cracks can be significantly inhibited by the residual compressive stress generated by the HESP treatment. In addition, the cross-sectional SEM images (**Figure 2A**) and eddy current thickness gauge result (**Figure 2B**) showed that that the porous coatings of MAO, Si-MAO, and Si/Cu-MAO (about 8.4 μm) were tightly bound to titanium substrates.

EDS results (**Table 4**) showed that the contents of Ca, P, Ti, and O in MAO samples were about 43.8 ± 0.4, 41.7 ± 0.4, 7.5 ± 0.3, and 7.1 ± 0.2 wt%, respectively. Furthermore, Si was also successfully detected in Si-MAO and Si/Cu-MAO groups (2.4 ± 0.2 and 2.3 ± 0.5 wt%), while Cu was only observed in the latter. The content of Cu (1.4 ± 0.1 wt%) in the Si/Cu-MAO coating was consistent with the range reported in the previous study (Yao et al., 2014).

XPS results (**Figure 3A**) further proved that Si and Cu were successfully doped in the Si/Cu-MAO coatings. By comparing with the NIST X-ray Photoelectron Spectroscopy Database, the fitting peak of Si2p near 102.5 eV was determined to be silicate radical (SiO_3^{2-}). The characteristic peaks of $CuSiO_3/Cu_3(PO_4)_2$ [Cu2p1/2 (955.0 eV) and Cu2p3/2 (934.7 eV)] and CuO [Cu2p1/2 (952.8 eV), Cu2p3/2 (933.0 eV), Cu2p3/2 sat (944.0 eV) and Cu2p3/2 sat (940.5 eV)] were also observed in the fitting curves of Cu2p, indicating that Cu existed in a bivalent form (Cu^{2+}).

XRD results (**Figure 3B**) showed that the three materials have similar patterns except for the difference of peak strength. Only the characteristic peaks of anatase (JCPDS 21-1272) and titanium (JCPDS 05-0682) were observed. This indicates that there was no change in the crystalline structure of MAO coating after the addition of Cu and Si. Furthermore, there was no significant differences observed in the surface roughness (∼2.2 μm, **Figure 2C**), critical loads (∼14 N,

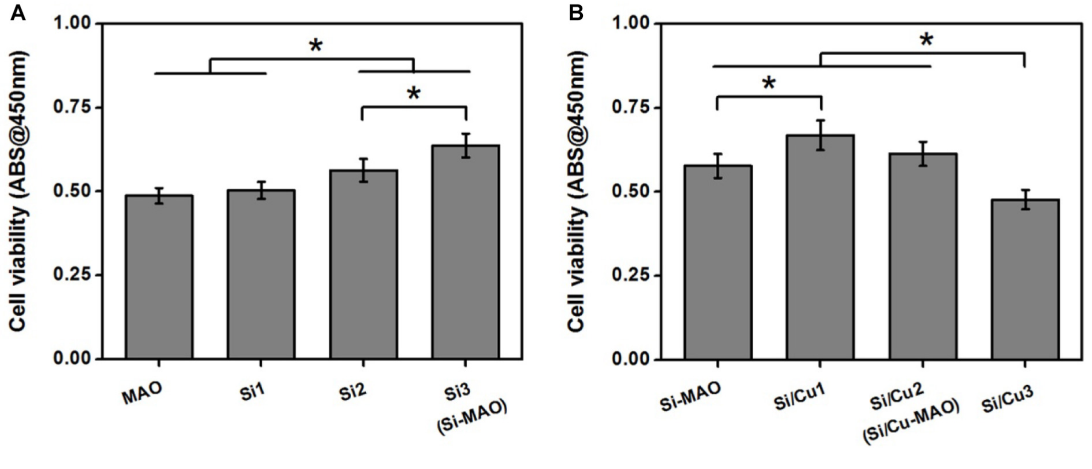

FIGURE 1 | (A) Cell viability of MC3T3-E1 cells on Si-loaded specimens [MAO, Si1, Si2, and Si3 (Si-MAO)] at 4 day. **(B)** cell viability of MC3T3-E1 cells on Si/Cu-loaded substrates [Si-MAO, Si-Cu1, Si-Cu1 (Si/Cu-MAO), and Si-Cu3] after 4 day. Error bars represent mean ± SEM for $n = 6$, $^{*}p < 0.05$.

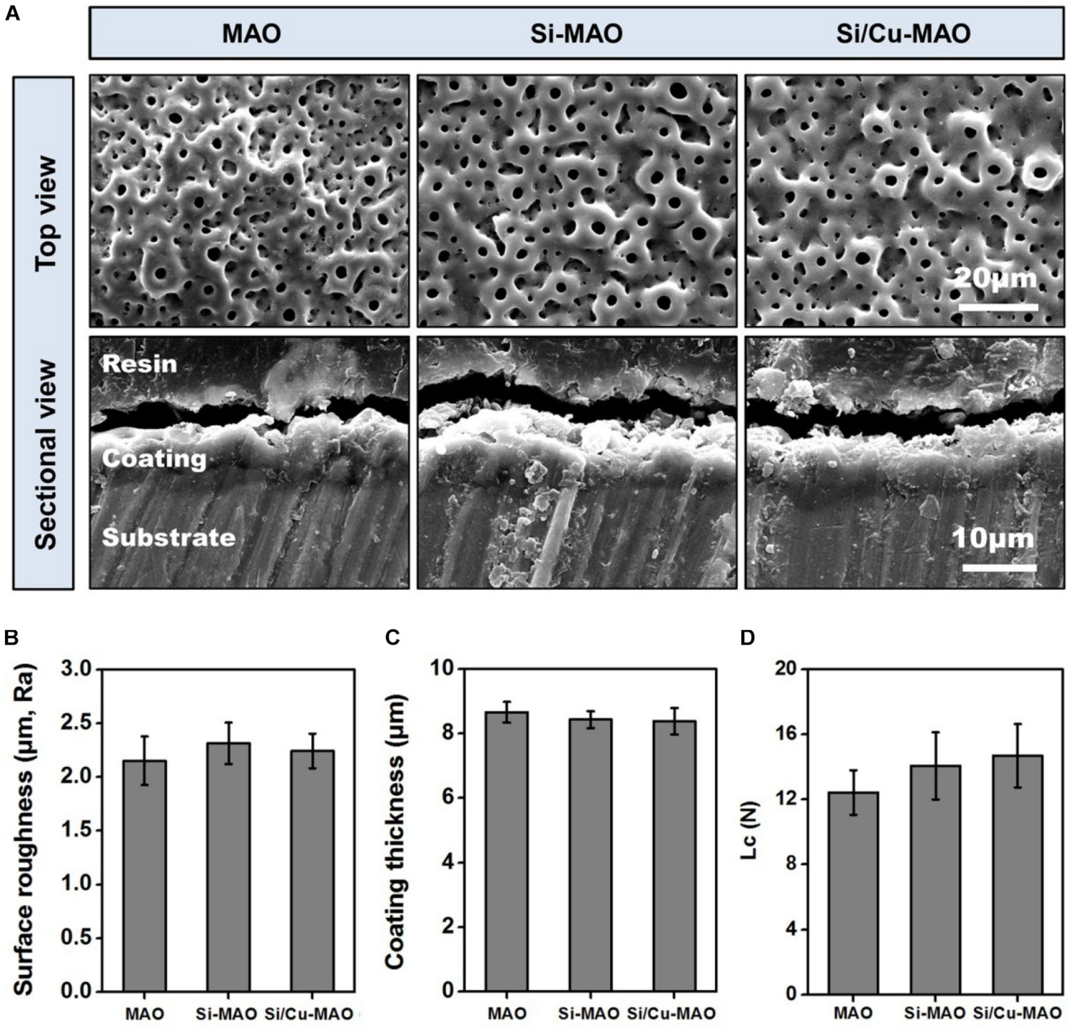

FIGURE 2 | (A) SEM images of MAO, Si-MAO, and Si/Cu-MAO samples (top and sectional views); statistics of coating thickness **(B)**, surface roughness **(C)**, and critical loads (Lc, **D**) of MAO, Si-MAO, and Si/Cu-MAO substrates.

TABLE 4 | Statistics of chemical compositions on the surface of MAO, Si-MAO, and Si/Cu-MAO substrates.

	Content of different elements (wt%)					
Samples	**Ti**	**O**	**P**	**Ca**	**Si**	**Cu**
MAO	43.8 ± 0.4	41.7 ± 0.4	7.5 ± 0.3	7.1 ± 0.2	0	0
Si-MAO	41.5 ± 0.6	41.8 ± 0.5	7.1 ± 0.2	7.1 ± 0.3	2.4 ± 0.2	0
Si/Cu-MAO	40.0 ± 0.4	39.3 ± 0.4	6.7 ± 0.2	10.3 ± 0.2	2.3 ± 0.5	1.4 ± 0.1

Figure 2D), and water contact angle (∼54°, **Figure 3C**) among the three materials.

Release Profile of Cu^{2+}

To detect the release behavior of Cu^{2+} and $SiO_3{}^{2-}$, Si/Cu-MAO substrates were soaked in PBS/HCl solution for 1, 4, 7, 10, and/or 14 day. **Figure 3D** showed that the total contents of Cu and Si in the Si/Cu-MAO coatings were about 5.8 and 13.5 μg/cm^2, respectively. Comparing the amount at different time, Cu^{2+} and $SiO_3{}^{2-}$ released on day 1 was the largest (reaching 0.51 ± 0.03 and 1.3 ± 0.10 μg). With the extension of the soaking time, the amount of Cu^{2+} and $SiO_3{}^{2-}$ gradually decreased: 0.42 ± 0.03 and 0.96 ± 0.09 μg (4 day), 0.32 ± 0.03 and 0.79 ± 0.04 μg (7 day), 0.30 ± 0.02 and 0.75 ± 0.03 μg (10 day), and 0.27 ± 0.03 (14 day) and 0.66 ± 0.04 μg, respectively. Further statistics showed that the release of Si and Cu accounted for about 33.2 and 31.3% of the total added ions within 14 day. The long-term slow-release property of the Cu^{2+} and $SiO_3{}^{2-}$ can endow

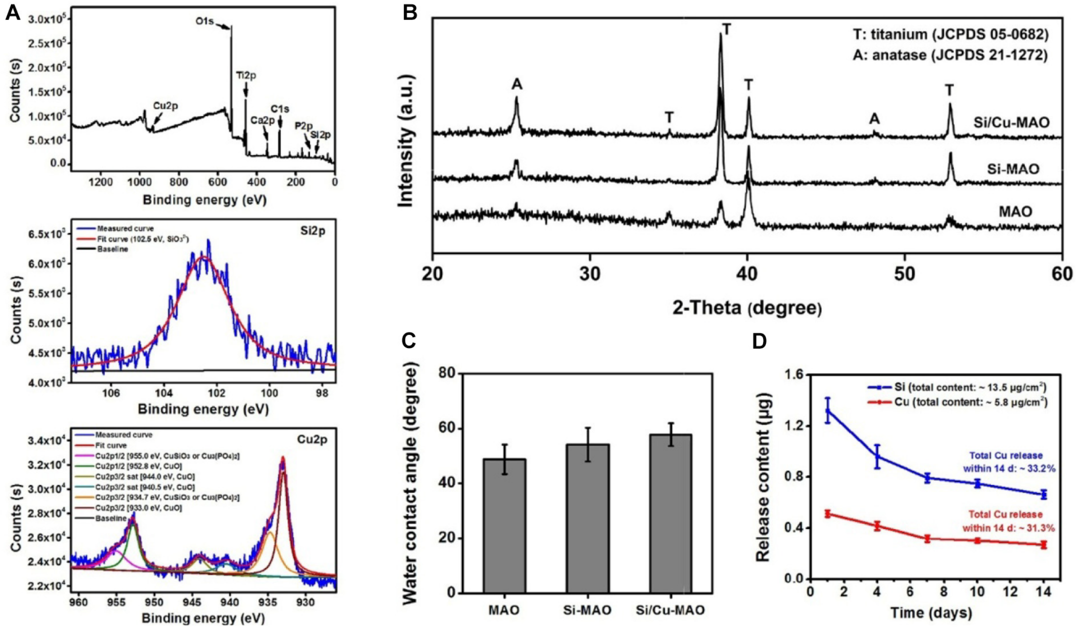

FIGURE 3 | (A) XPS pattern and the deconvoluted Si2p/Cu2p of Si/Cu-MAO samples; XRD patterns **(B)** and water contact angles **(C)** images of MAO, Si-MAO, and Si/Cu-MAO substrates; **(D)** release profile of Si and Cu from Si/Cu-MAO specimens at 1, 4, 7, 10, and 14 day.

Si/Cu-MAO specimens with longer antibacterial and osteogenic induction functions.

Bacteriostasis Rate

S. aureus is a common pathogen of implantable infection and has strong pathogenicity. Recent studies have confirmed that *S. aureus* is also a common cause of peri-implantitis (Ulu et al., 2018; Karthikeyan et al., 2019). Moreover, *S. mutans* in the oral cavity is also a common bacterium in inducing peri-implantitis, and can significantly increase the pathogenicity of other bacterial infections (Geremias et al., 2017; Lemos et al., 2019). Therefore, we have selected both *S. aureus* and *S. aureus* to be used for antibacterial studies of our target materials in this study. No significant difference in antibacterial activity was observed between MAO and Si-MAO groups (**Figure 3A**), which indicated no contribution of Si to antibacterial property. Compared to MAO and Si-MAO, Si/Cu-MAO samples showed a better bacteriostatic effect on *S. aureus* and *S. mutans*, and the antibacterial rate was about 99.1 ± 2.3% and 98.7 ± 3.5%, respectively. This was further confirmed by the Live/Dead staining results as shown in **Figure 5**. The staining images (**Figure 5A**) demonstrated the two types of bacteria on the surface of MAO and Si-MAO were stained green (living bacteria), while almost all bacteria on Si/Cu-MAO were stained red (dead bacteria). The dead/total rate (**Figure 5B**) of bacteria on Si/Cu-MAO substrates were 96.4 ± 3.2% (*S. aureus*) and 94.1 ± 3.9% (*S. mutans*), respectively. These results suggested that Si/Cu-MAO had an excellent broad-spectrum germicidal efficacy against the common oral bacteria.

Previous studies had demonstrated that copper substances/ions could harm the nucleic acid, protein, and lipid of bacteria by changing bacterial membrane potential or inducing excessive active oxygen production (Hong et al., 2012; Tambosi et al., 2018; Zhang et al., 2020). The antibacterial mechanism of Si/Cu-MAO to *S. aureus* and *S. mutans* might be also as follows: firstly, when bacteria attached to Si/Cu-MAO, the doped copper directly destroyed the membrane potential and induced the death of bacteria (contact bacteriostasis; Zhang et al., 2020); secondly, the released Cu^{2+} could bind to the sulfhydryl and amino groups in the bacterial membrane/protein, destroy the energy metabolism and respiratory system of the bacteria, resulting in bacterial death (release bacteriostasis; Tambosi et al., 2018). Therefore, the synergistic effect of contact and release modes endowed Si/Cu-MAO with broad-spectrum antibacterial effect.

Bacterial Morphology

The attachment of *S. aureus* and *S. mutans* to different substrates were observed through SEM, as shown in **Figure 4B**. A large number of *S. aureus* and *S. mutans* were observed on the surfaces of MAO and Si-MAO, indicating that the addition of $SiO_3{}^{2-}$ had no obvious antibacterial effects. Compared with MAO and Si-MAO groups, there was a significant reduction of both bacteria on the surfaces of Si/Cu-MAO samples indicated with red arrows (dead bacteria). This further showed that Si/Cu-MAO could inhibit the early adhesion and proliferation of *S. aureus* and *S. mutans*, which was confirmed by the above results of bacteriostasis rate (**Figures 4A**, **5**).

Cell Morphology and Viability

To determine the effects of additive $SiO_3{}^{2-}$ and Cu^{2+} on cell morphology and viability, SEM observation and CCK-8

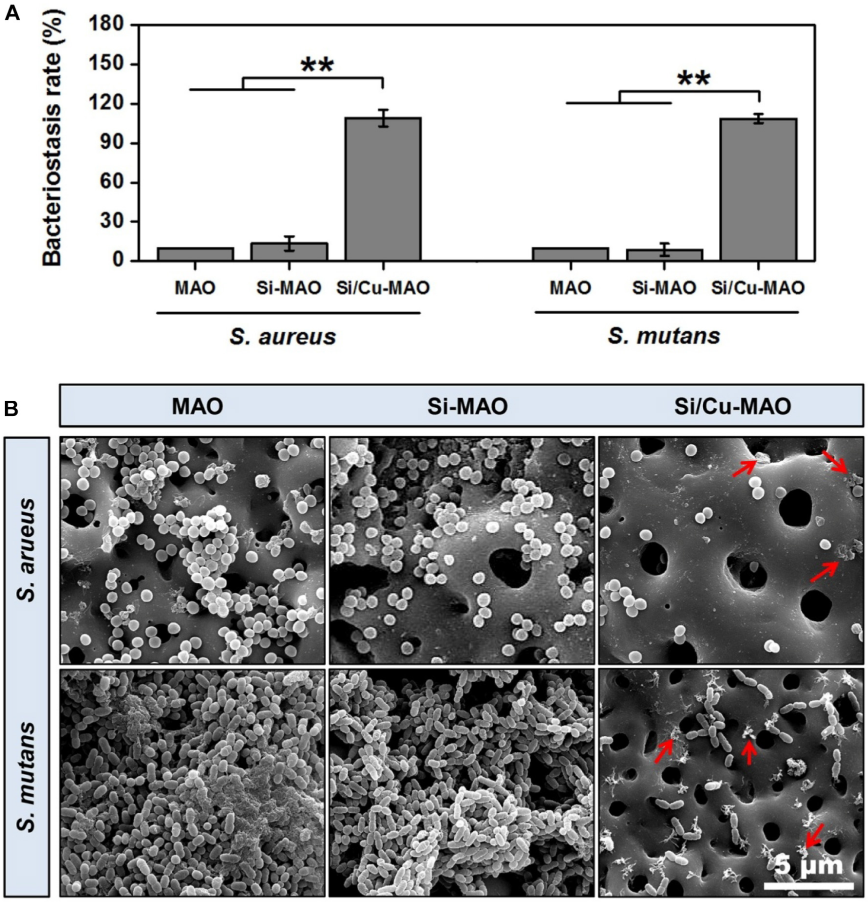

FIGURE 4 | (A) Bacteriostasis rate of MAO, Si-MAO, and Si/Cu-MAO samples against *S. aureus* and *S. mutans* at 24 h. Error bars represent mean ± SEM for $n = 6$, $^{**}p < 0.01$; **(B)** SEM images of two bacteria on MAO, Si-MAO, and Si/Cu-MAO substrates at 24 h (red arrows represent dead bacteria).

measurement were carried out. From SEM results (**Figure 6A**), it was found that all MC3T3-E1 cells adhered tightly to the surfaces of different materials after 3 day of culture. Compared with the MAO group, the cells on Si-MAO and Si/Cu-MAO groups produced more filamentous pseudopods (red arrows), which extended into the pore structures. The result (**Figure 6B**) of cell viability also showed that Si-MAO and Si/Cu-MAO significantly ($p < 0.05$ or 0.01) improved the proliferation of MC3T3-E1 cells compared with MAO group after culturing for 4 and 7 day. However, no significant difference of cell viability was observed between Si-MAO and Si/Cu-MAO groups.

In this study, to obtain the best bacteriostatic effect, we chose the highest concentration of Cu^{2+} that MC3T3-E1 cells could tolerate as the parameter of sample preparation (**Figure 1B**). Thus, the properties of Si-MAO and Si/Cu-MAO in promoting pseudopodia formation and cell proliferation were mainly caused by Si. It had been proved that Si had great potential to cause cell microenvironment alkalization and activate the Ca^{2+} channels to increase the Ca^{2+} influx, thus promoting the early cell adhesion and pseudopods formation (Liu et al., 2013; Wu et al., 2014). In addition, Si could also combine with O_2 to form silicate with three-dimensional network structures, then adsorb free proteins and interact with cell integrin, and finally promote the adhesion, proliferation and differentiation of osteoblasts (Henstock et al., 2015).

Cell Differentiation

As a non-specific phosphomonoesterase, ALP had been proved to greatly hydrolyze inorganic pyrophosphate and increase the formation of hydroxyapatite (Siller and Whyte, 2018; Yu et al., 2018). Thus, ALP activity was frequently selected as a typical early marker of osteoblast differentiation. In addition to ALP, the mineralization level of osteoblasts was also evaluated as a late indicator of osteogenic differentiation in previous researches (Yu et al., 2018; Su et al., 2020). After both 4 and 7 day of culture, the ALP activity of MC3T3-E1 cells in Si-MAO and Si/Cu-MAO groups was significantly ($p < 0.05$ or 0.01) higher than that in MAO group (**Figure 7A**). The mineralization results (**Figure 7B**) also confirmed that Si-MAO and Si/Cu-MAO substrates were more effective in promoting osteoblast differentiation. In addition, to further verify the osteoinductive potential of different samples at the molecular level, the expression of ALP, collagen I (Col I) and osteocalcin (OCN) gene was measured after 7 day. The expression trends (**Figure 7C**) of the three genes were similar

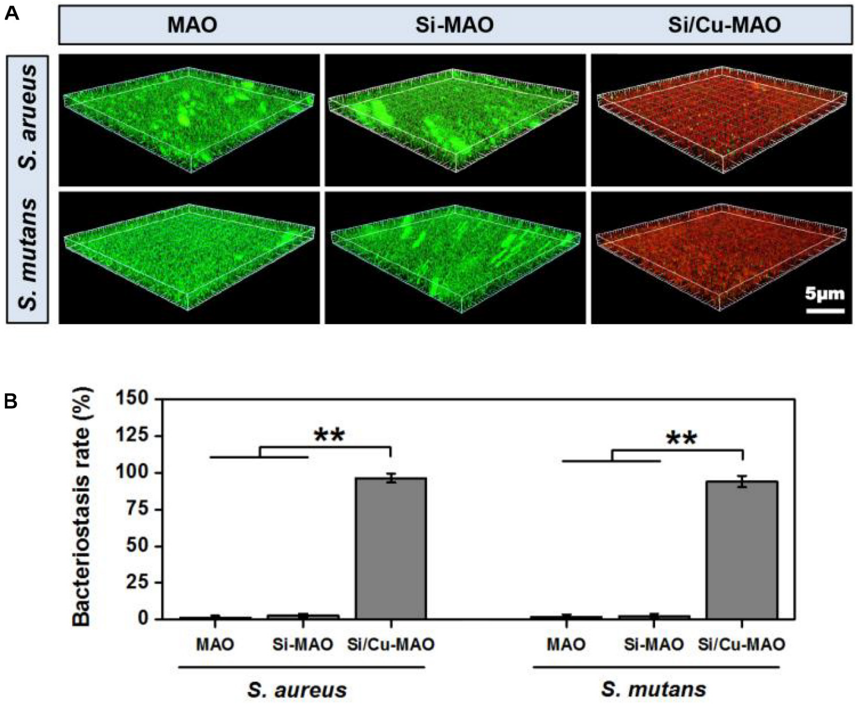

FIGURE 5 | 3D fluorescent images (Live/Dead staining, **A**) and dead/total rate **(B)** of two bacteria on MAO, Si-MAO, and Si/Cu-MAO substrates at 24 h. Error bars represent mean ± SEM for $n = 6$, $^{**}p < 0.01$.

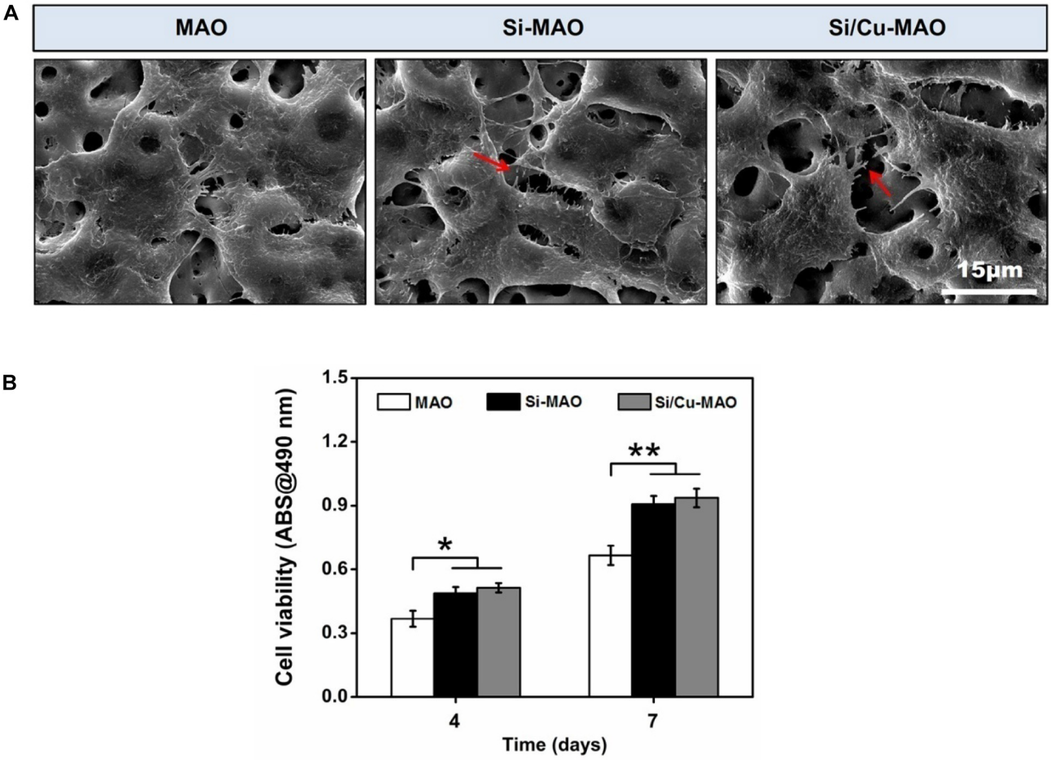

FIGURE 6 | (A) SEM images of MC3T3-E1 cells on MAO, Si-MAO, and Si/Cu-MAO samples (red arrows represent pseudopodia of MC3T3-E1 cells); **(B)** cell viability of MC3T3-E1 cells on MAO, Si-MAO, and Si/Cu-MAO substrates at 4 and 7 day. Error bars represent mean ± SEM for $n = 6$, $^{*}p < 0.05$, $^{**}p < 0.01$.

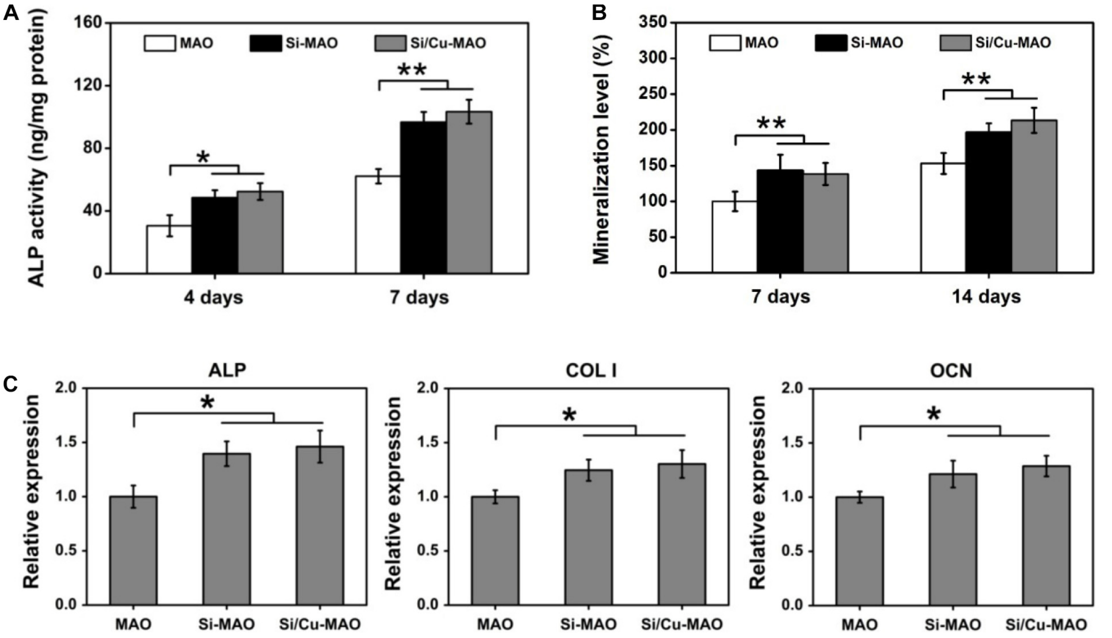

FIGURE 7 | ALP activity **(A)** and mineralization level **(B)** of MC3T3-E1 cells on MAO, Si-MAO, and Si/Cu-MAO substrates at 4, 7, and/or 14 day; **(C)** osteogenic gene expression of MC3T3-E1 cells on MAO, Si-MAO, and Si/Cu-MAO substrates at 7 day. Error bars represent mean ± SEM for $n = 6$, $^{*}p < 0.05$, $^{**}p < 0.01$.

to ALP activity and mineralization level: compared with MAO, both Si-MAO and Si/Cu-MAO significantly ($p < 0.05$) enhanced the gene expression of ALP, Col I, and OCN.

The aforementioned results of pseudopodia formation, cell proliferation, ALP activity, mineralization and gene expression showed that Si/Cu-MAO was slightly better than Si-MAO, but there was no significant difference between them. This indicated that the osteogenic effects of Si-MAO and Si/Cu-MAO was mainly attributed to Si rather than Cu. Sun et al. had reported that the Si-doped hydroxyapatite could promote the proliferation and differentiation of osteoblasts via up-regulating MAPK and Wnt signaling pathways (Sun et al., 2018). Dong et al. also claimed that SiO_3^{2-} could promote the Col I and OCN synthesis of MSCs by activating the BMP-2/Smad1/5/RUNX2 signaling pathway (Dong et al., 2016). Although Cu^{2+} also had superior biocompatibility, they were very dose-dependent (Lin et al., 2016; Li K. et al., 2019). High concentrations of Cu^{2+} would lead to significant cytotoxicity through the oxidative stress pathway (Cao et al., 2012; Li K. et al., 2019). The release of Cu^{2+} from Si/Cu-MAO was about 0.51 μg (~8 μM) at the first day, which had been close to its safe concentration (~10 μM) for MC3T3-E1 cells (Li K. et al., 2019). Therefore, compared with Si-MAO, Si/Cu-MAO did not significantly promote the spreading, proliferation and osteogenic differentiation of MC3T3-E1 cells, nor did it show obvious cytotoxicity in this study.

Co-culture of Bacteria and MC3T3-E1 Cells

Studies have shown that when bacteria are present, they competitively adhere to the implant surface with the host cells (Subbiahdoss et al., 2011). By forming a dense bacterial membrane or secreting a large amount of toxin, these adherent bacteria induce apoptosis of repair cells and ultimately prevent the formation of new bone (Hoffman et al., 2005; Subbiahdoss et al., 2011; Shen et al., 2019b). The ideal implantation material is expected to inhibit bacterial infection without affecting the normal physiological function of osteoblasts. Therefore, in this study, to further investigate the protective effects of different materials on surface cells in the presence of bacteria, MC3T3-E1 cells and *S. mutans* were further co-cultured for 24 h. The SEM images (**Figure 8A**) showed that MC3T3-E1 cells on the surfaces of MAO and Si-MAO were round, and many bacteria adhered to the cell surface (cell location images). Many bacteria were also observed in the empty spaces around the cells (bare location images). Compared with the above two groups, the number of bacteria in the cell and bare parts of the Si/Cu-MAO group decreased significantly. The cell spreading of MC3T3-E1 cells (red arrows) on the surface of Si/Cu-MAO group was almost unaffected by bacteria. Live/Dead staining images (**Figure 8A**) showed that there were a large number of dead cells (red color) on MAO and Si-MAO, and the remaining living cells (green color) also shriveled into a round shape. However, only a small number of cells died on Si/Cu-MAO substrates, indicating that it could ensure the survival of MC3T3-E1 cells effectively in the presence of *S. mutans*. Meanwhile, we found that the round living cells on MAO and Si-MAO appeared to be larger than those in Si/Cu-MAO group, most likely due to the presence of a large number of living bacteria (also appeared green) on the cell surface. **Figures 8B,C** further showed that only the

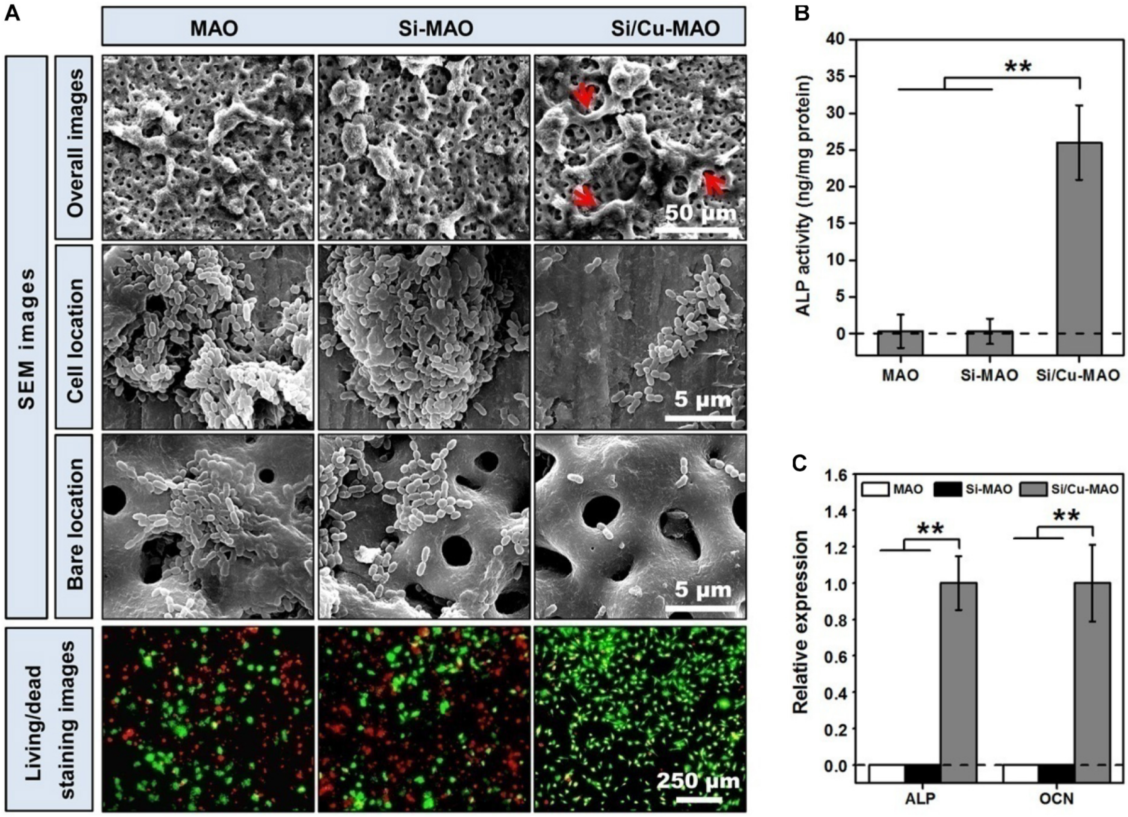

FIGURE 8 | (A) SEM (red arrows: spreading MC3T3-E1 cells) and Live/Dead staining (red color: dead MC3T3-E1cells; green color: living MC3T3-E1cells) images of co-cultured MC3T3-E1 cells and *S. mutans* on MAO, Si-MAO, and Si/Cu-MAO substrates at 24 h; ALP activity **(B,C)** osteogenic gene expression of co-cultured MC3T3-E1 cells on MAO, Si-MAO, and Si/Cu-MAO substrates at 7 day. Error bars represent mean ± SEM for $n = 6$, $^{**}p < 0.01$.

co-cultured MC3T3-E1 cells on Si/Cu-MAO substrates had significant ALP activity and genes (ALP and OCN) expression. The other two groups showed almost no enzyme activity and gene expression. These results further proved that Si/Cu-MAO substrates had good antibacterial activity and could maintain the normal biological behavior of surface osteoblasts under infection conditions.

CONCLUSION

In this study, we prepared three porous coatings (MAO, Si-MAO, and Si/Cu-MAO) with similar surface morphology and crystalline structure by HESP and MAO techniques. Excluding element composition, we have proven that there were no significant differences in the surface roughness (∼2.2 μm), coating thickness (∼8.4 μm) and bonding strength (∼14 N), and water contact angle (∼54°) of the three coatings. Furthermore, *in vitro* cell and bacterial results showed that Si-MAO and Si/Cu-MAO significantly promoted the spreading, proliferation and differentiation of MC3T3-E1 cells compared to the control group (MAO), but only the latter had a better bactericidal effect on both *S. aureus* (antibacterial rate: 99.1 ± 2.3%) and *S. mutans* (antibacterial rate: 98.7 ± 3.5%). All the findings show that the Si/Cu-MAO have excellent comprehensive properties, and has good application prospects in the immediate implant treatment for patients with socket infection.

DATA AVAILABILITY STATEMENT

All datasets generated for this study are included in the article.

AUTHOR CONTRIBUTIONS

XS and CL collated the data and wrote the original draft. WH, LP, and ZD designed the study and carried out the experiments. LY and GW reviewed and edited the manuscript. All authors have read and approved the final submitted manuscript.

FUNDING

This work was funded by the National Natural Science Foundation of China (81701016, 81870810, and 31700827), Scientific Research Fund of Zhejiang Provincial Education Department (Y201533871), Zhejiang Provincial Science and Technology Project for Public Welfare (No. LGF20H140002), Zhejiang Provincial Medical and Health Science and Technology Project (2020KY657) and Wenzhou Public Welfare Science and Technology Project (Y20160142 and Y20190099), Wenzhou Medical University Basic Scientific Research Operating Expenses (KYYW201905), and Open project of State Key Laboratory of Oral Diseases (SKLOD2020OF04).

ACKNOWLEDGMENTS

All the authors want to thank Kendrick HiiRuYie for his help of the language embellishment.

REFERENCES

Abaricia, J. O., Shah, A. H., Chaubal, M., Hotchkiss, K. M., and Olivaresnavarrete, R. (2020). Wnt signaling modulates macrophage polarization and is regulated by biomaterial surface properties. *Biomaterials* 243:119920. doi: 10.1016/j.biomaterials.2020.119920

Cao, B., Zheng, Y., Xi, T., Zhang, C., Song, W., Burugapalli, K., et al. (2012). Concentration-dependent cytotoxicity of copper ions on mouse fibroblasts in vitro: effects of copper ion release from TCu380A vs TCu220C intra-uterine devices. *Biomed. Microdev.* 14, 709–720. doi: 10.1007/s10544-012-9651-x

Chen, C., Hao, Y., Bai, X., Ni, J., Chung, S., Liu, F., et al. (2019). 3D printed porous Ti6Al4V cage: Effects of additive angle on surface properties and biocompatibility; bone ingrowth in Beagle tibia model. *Mat. Des.* 175:107824. doi: 10.1016/j.matdes.2019.107824

Dong, M., Jiao, G., Liu, H., Wu, W., Li, S., Wang, Q., et al. (2016). Biological silicon stimulates collagen type 1 and osteocalcin synthesis in human osteoblast-Like cells through the BMP-2/Smad/RUNX2 signaling pathway. *Biol. Trace Elem. Res.* 173, 306–315. doi: 10.1007/s12011-016-0686-3

Geremias, T. C., Montero, J. F., Magini, R. D., Filho, G. S., De Magalhaes, E. B., and Bianchini, M. A. (2017). Biofilm analysis of retrieved dental implants after different peri-implantitis treatments. *Case Rep. Dent.* 2017, 8562050–8562050. doi: 10.1155/2017/8562050

Ghosh, R., Swart, O., Westgate, S., Miller, B. L., and Yates, M. Z. (2019). Antibacterial copper-hydroxyapatite composite coatings via electrochemical synthesis. *Langmuir* 35, 5957–5966. doi: 10.1021/acs.langmuir.9b00919

Guo, Q., Xu, D., Yang, W., Guo, Y., Yang, Z., Li, J., et al. (2020). Synthesis, corrosion, and wear resistance of a black micro-arc oxidation coating on pure titanium. *Surf. Coat. Tech.* 386:125454. doi: 10.1016/j.surfcoat.2020.125454

Henstock, J. R., Canham, L. T., and Anderson, S. I. (2015). Silicon: the evolution of its use in biomaterials. *Acta Biomater.* 11, 17–26. doi: 10.1016/j.actbio.2014.09.025

Hoffman, L., D'Argenio, D., MacCoss, M., Zhang, Z., Jones, R., and Miller, S. (2005). Aminoglycoside antibiotics induce bacterial biofilm formation. *Nature* 436, 1171–1175. doi: 10.1038/nature03912

Hong, R., Kang, T. Y., Michels, C. A., and Gadura, N. (2012). Membrane lipid peroxidation in copper alloy-mediated contact killing of *Escherichia coli*. *Appl. Environ. Microb.* 78, 1776–1784. doi: 10.1128/AEM.07068-11

Huang, Q., Ouyang, Z., Tan, Y., Wu, H., and Liu, Y. (2019). Activating macrophages for enhanced osteogenic and bactericidal performance by Cu ion release from micro/nano-topographical coating on a titanium substrate. *Acta Biomater.* 100, 415–426. doi: 10.1016/j.actbio.2019.09.030

Karthikeyan, M., Ahila, S. C., and Kumar, B. M. (2019). The antibacterial influence of nanotopographic titanium, zirconium, and aluminum nanoparticles against Staphylococcus aureus and Porphyromonas gingivalis: an in vitro study. *Ind. J. Dent. Res.* 30, 37–42. doi: 10.4103/ijdr.IJDR_91_16

Kim, B., Yang, S., Yoon, J., and Lee, J. (2017). Enhanced bone regeneration by silicon-substituted hydroxyapatite derived from cuttlefish bone. *Clin. Oral Impl. Res.* 28, 49–56. doi: 10.1111/clr.12613

Koh, R. U., Rudek, I., and Wang, H. L. (2010). Immediate implant placement: positives and negatives. *Impl. Dent.* 19, 98–108. doi: 10.1097/ID.0b013e3181d47eaf

Lemos, J. A., Palmer, S. R., Zeng, L., Wen, Z. T., Kajfasz, J. K., Freires, I. D., et al. (2019). The biology of *Streptococcus mutans*. *Microbiol. Spectr.* 7, 435–448. doi: 10.1128/microbiolspec.GPP3-0051-2018

Li, G., Wang, Y., Zhang, S., Zhao, R., and Chen, C. (2019). Investigation on entrance mechanism of calcium and magnesium into micro-arc oxidation coatings developed on Ti-6Al-4V alloys. *Surf. Coat Tech.* 378:124951. doi: 10.3390/ma11030344

Li, K., Xia, C., Qiao, Y., and Liu, X. (2019). Dose-response relationships between copper and its biocompatibility/antibacterial activities. *J. Trace Elem. Med. Biol.* 55, 127–135. doi: 10.1016/j.jtemb.2019.06.015

Lin, Y., Xiao, W., Bal, B. S., and Rahaman, M. N. (2016). Effect of copper-doped silicate 13-93 bioactive glass scaffolds on the response of MC3T3-E1 cells in vitro and on bone regeneration and angiogenesis in rat calvarial defects in vivo. *Mater. Sci. Eng. C Mater. Biol. Appl.* 67, 440–452. doi: 10.1016/j.msec.2016.05.073

Liu, D., He, C., Liu, Z., and Xu, W. (2017). Gentamicin coating of nanotubular anodized titanium implant reduces implant-related osteomyelitis and enhances bone biocompatibility in rabbits. *Int. J. Nanomed.* 12, 5461–5471. doi: 10.2147/IJN.S137137

Liu, D., Yi, C., Wang, K., Fong, C., Wang, Z., Lo, P. K., et al. (2013). Reorganization of cytoskeleton and transient activation of Ca2+ channels in mesenchymal stem cells cultured on silicon nanowire arrays. *ACS Appl. Mater. Inter.* 5, 13295–13304. doi: 10.1021/am404276r

Macdonald, C. A., Clark, I., Zhao, F., Hirsch, P. R., Singh, B. K., and Mcgrath, S. P. (2011). Long-term impacts of zinc and copper enriched sewage sludge additions on bacterial, archaeal and fungal communities in arable and grassland soils. *Soil Biol. Biochem.* 43, 932–941. doi: 10.1016/j.soilbio.2011.01.004

Maher, S., Mazinani, A., Barati, M. R., and Losic, D. (2018). Engineered titanium implants for localized drug delivery: recent advances and perspectives of titania nanotubes arrays. *Exp. Opin. Drug Del.* 15, 1021–1037. doi: 10.1080/17425247.2018.1517743

Mangram, A. J., Horan, T. C., Pearson, M. L., Silver, L. C., and Jarvis, W. R. (1999). Guideline for prevention of surgical Site infection, 1999. *Am. J. Infect. Cont.* 27, 97–134. doi: 10.1016/S0196-6553(99)70088-X

Narad, C., Lingraj, J. B., Aulakh, K. K., Handa, K. K., Kotrashetti, S. M., and Pinto, P. X. (2018). Assessment of primary stability of the implant placed in prepared infected extraction sockets. *J. Oral Biol. Cran. Res.* 8, 154–157. doi: 10.1016/j.jobcr.2016.10.002

Rass, M. A. (2010). Interim endodontic therapy for alveolar socket bone regeneration of infected hopeless teeth prior to implant therapy. *J. Oral Implantol.* 36, 37–59. doi: 10.1563/AAID-JOI-D-09-00040

Reffitt, D., Ogston, N., Jugdaohsingh, R., Cheung, H. F., Evans, B. A., Thompson, R. P., et al. (2003). Orthosilicic acid stimulates collagen type 1 synthesis and osteoblastic differentiation in human osteoblast-like cells in vitro. *Bone* 32, 127–135. doi: 10.1016/s8756-3282(02)00950-x

Shen, X., Albaadani, M. A., He, H., Cai, L., Wu, Z., Yao, L., et al. (2019a). Antibacterial and osteogenesis performances of LL37-loaded titania nanopores in vitro and in vivo. *Int. J. Nanomed.* 14, 3043–3054. doi: 10.2147/IJN.S198583

Shen, X., Ping, L., Wang, L., Liu, C., Liu, J., and Deng, Z. (2020). Improving the stability and bioactivity of micro-arc oxidized calcium phosphate/titania porous coatings by high energy shot peening pretreatment. *Ceram. Int.* 46, 2041–2048. doi: 10.1016/j.ceramint.2019.09.183

Shen, X., Zhang, Y., Ma, P., Sutrisno, L., Luo, Z., Hu, Y., et al. (2019b). Fabrication of magnesium/zinc-metal organic framework on titanium implants to inhibit bacterial infection and promote bone regeneration. *Biomaterials* 212, 1–16. doi: 10.1016/j.biomaterials.2019.05.008

Shi, F., Liu, Y., Zhi, W., Xiao, D., Li, H., Duan, K., et al. (2017). The synergistic effect of micro/nano-structured and Cu2+-doped hydroxyapatite particles to promote osteoblast viability and antibacterial activity. *Biomed. Mater.* 12:035006. doi: 10.1088/1748-605X/aa6c8d

Siller, A. F., and Whyte, M. P. (2018). Alkaline phosphatase: discovery and naming of our favorite enzyme. *J. Bone. Miner. Res.* 33, 362–364. doi: 10.1002/jbmr.3225

Su, J., Du, Z., Xiao, L., Wei, F., Yang, Y., Li, M., et al. (2020). Graphene oxide coated titanium surfaces with osteoimmunomodulatory role to enhance osteogenesis. *Mat. Sci. Eng. C Mater.* 113:110983. doi: 10.1016/j.msec.2020.110983

Subbiahdoss, G., Saldarriaga Fernández, I. C., da Silva Domingues, J. F., Kuijer, R., van der Mei, H. C., and Busscher, H. J. (2011). In vitro interactions between bacteria, osteoblast-like cells and macrophages in the pathogenesis of biomaterial-associated infections. *PLoS One* 6:e24827. doi: 10.1371/journal.pone.0024827

Sun, T., Wang, M., Shao, Y., Wang, L., and Zhu, Y. (2018). The effect and osteoblast signaling response of trace silicon doping hydroxyapatite. *Biol. Trace Elem. Res.* 181, 82–94. doi: 10.1007/s12011-017-1031-1

Szesz, E., Souza, G., Lima, G., Silva, B., Kuromoto, N., and Lepienski, C. (2014). Improved tribo-mechanical behavior of CaP-containing TiO2 layers produced on titanium by shot blasting and micro-arc oxidation. *J. Mater. Sci. Mater. Med.* 25, 2265–2275. doi: 10.1007/s10856-014-5238-9

Tambosi, R., Liotenberg, S., Bourbon, M., Steunou, A., Babot, M., Durand, A., et al. (2018). Silver and copper acute effects on membrane proteins and impact on photosynthetic and respiratory complexes in bacteria. *mBio* 9:e01535. doi: 10.1128/mBio.01535-18

Ulu, M., Pekbagriyanik, T., Ibis, F., Enhos, S., and Ercan, U. K. (2018). Antibiofilm efficacies of cold plasma and er: YAG laser on *Staphylococcus aureus* biofilm on titanium for nonsurgical treatment of peri-implantitis. *Niger. J. Clin. Pract.* 21, 758–765. doi: 10.4103/njcp.njcp_261_17

Wang, L., Wang, W., Zhao, H., Liu, Y., Liu, J., and Bai, N. (2020). Bioactive effects of low-temperature argon-oxygen plasma on a titanium implant surface. *ACS Omega* 5, 3996–4003. doi: 10.1021/acsomega.9b03504

Wu, B., Kao, C., Huang, T., Hung, C., Shie, M., and Chung, H. (2014). Effect of verapamil, a calcium channel blocker, on the odontogenic activity of human dental pulp cells cultured with silicate-based materials. *J. Endodont.* 40, 1105–1111. doi: 10.1016/j.joen.2013.12.019

Xia, J., Wang, W., Hai, X., Shuang, E., Shu, Y., and Wang, J. (2019). Improvement of antibacterial activity of copper nanoclusters for selective inhibition on the growth of gram-positive bacteria. *Chin. Chem. Lett.* 30, 421–424. doi: 10.1016/j.cclet.2018.07.008

Yao, X., Zhang, X., Wu, H., Tian, L., Ma, Y., and Tang, B. (2014). Microstructure and antibacterial properties of Cu-doped TiO2 coating on titanium by micro-arc oxidation. *Appl. Surf. Sci.* 292, 944–947. doi: 10.1016/j.apsusc.2013.12.083

Yu, Y., Shen, X., Luo, Z., Hu, Y., Li, M., Ma, P., et al. (2018). Osteogenesis potential of different titania nanotubes in oxidative stress microenvironment. *Biomaterials* 167, 44–57. doi: 10.1016/j.biomaterials.2018.03.024

Zhang, X., Yang, C., and Yang, K. (2020). Contact killing of cu-bearing stainless steel based on charge transfer caused by the microdomain potential difference. *ACS Appl. Mater. Inter.* 12, 361–372. doi: 10.1021/acsami.9b19596

Zhao, D., Wu, Y., Xu, C., and Zhang, F. (2016). Immediate dental implant placement into infected vs. non-infected sockets: a meta-analysis. *Clin. Oral Impl. Res.* 27, 1290–1296. doi: 10.1111/clr.12739

Zimmerli, W., and Sendi, P. (2011). Pathogenesis of implant-associated infection: the role of the host. *Sem. Immunopathol.* 33, 295–306. doi: 10.1007/s00281-011-0275-7

Conflict of Interest: The authors declare that the research was conducted in the absence of any commercial or financial relationships that could be construed as a potential conflict of interest.

frontiers in Bioengineering and Biotechnology

ORIGINAL RESEARCH
published: 23 October 2020
doi: 10.3389/fbioe.2020.584410

Human Salivary Histatin-1 Promotes Osteogenic Cell Spreading on Both Bio-Inert Substrates and Titanium SLA Surfaces

Wei Sun[1,2,3†], Dandan Ma[3†], Jan G. M. Bolscher[3], Kamran Nazmi[3], Enno C. I. Veerman[3], Floris J. Bikker[3], Ping Sun[1,2], Haiyan Lin[4*‡] and Gang Wu[5,6*‡]

[1] The Affiliated Stomatology Hospital, Zhejiang University School of Medicine, Hangzhou, China, [2] Key Laboratory of Oral Biomedical Research of Zhejiang Province, Hangzhou, China, [3] Department of Oral Biochemistry, Academic Centre for Dentistry Amsterdam, University of Amsterdam and Vrije Universiteit Amsterdam, Amsterdam, Netherlands, [4] Savaid Stomatology School, Hangzhou Medical College, Hangzhou, China, [5] Department of Oral Implantology and Prosthetic Dentistry, Academic Centre for Dentistry Amsterdam, University of Amsterdam and Vrije Universiteit Amsterdam, Amsterdam, Netherlands, [6] Department of Oral and Maxillofacial Surgery/Pathology, Amsterdam UMC and Academic Center for Dentistry Amsterdam, Vrije Universiteit Amsterdam, Amsterdam Movement Science, Amsterdam, Netherlands

Edited by:
Malcolm Xing,
University of Manitoba, Canada

Reviewed by:
Kunyu Zhang,
Johns Hopkins University,
United States
Menekse Ermis Sen,
Middle East Technical University,
Turkey

***Correspondence:**
Haiyan Lin
lhaiyanlily@163.com
Gang Wu
g.wu@acta.nl

† These authors have contributed equally to this work
‡ These authors share last authorship

Specialty section:
This article was submitted to Biomaterials, a section of the journal Frontiers in Bioengineering and Biotechnology

Received: *17 July 2020*
Accepted: *22 September 2020*
Published: *23 October 2020*

Citation:
Sun W, Ma D, Bolscher JGM, Nazmi K, Veerman ECI, Bikker FJ, Sun P, Lin H and Wu G (2020) Human Salivary Histatin-1 Promotes Osteogenic Cell Spreading on Both Bio-Inert Substrates and Titanium SLA Surfaces. Front. Bioeng. Biotechnol. 8:584410. doi: 10.3389/fbioe.2020.584410

Promoting cell spreading is crucial to enhance bone healing and implant osteointegration. In this study, we investigated the stimulatory effect of human salivary histatin-1 (Hst-1) on the spreading of osteogenic cells *in vitro* as well as the potential signaling pathways involved. Osteogenic cells were seeded on bio-inert glass slides with or without the presence of Hst1 in dose-dependent or time-course assays. 1 scrambled and 6 truncated Hst1 variants were also evaluated. Cell spreading was analyzed using a well-established point-counting method. Fluorescent microscopy was adopted to examine the cellular uptake of fluorescently labeled Hst1 (F-Hst1) and also the cell spreading on sandblasted and acid etched titanium surfaces. Signaling inhibitors, such as U0126, SB203580, and pertussis toxin (PTx) were used to identify the potential role of extracellular-signal-regulated kinase, p38 and G protein-coupled receptor pathways, respectively. After 60 min incubation, Hst1 significantly promoted the spreading of osteogenic cells with an optimal concentration of 10 μM, while truncated and scrambled Hst1 did not. F-Hst1 was taken up and localized in the vicinity of the nuclei. U0126 and SB2030580, but not PTx, inhibited the effect of Hst1. 10 μM Hst1 significantly promoted the spreading of osteogenic cells on both bio-inert substrates and titanium SLA surfaces, which involved ERK and p38 signaling. Human salivary histatin-1 might be a promising peptide to enhance bone healing and implant osteointegration in clinic.

Keywords: salivary, peptide, osteogenic cells, cell spreading, osteoconductivity

INTRODUCTION

Large-volume bone defects (LVBD) can result from various diseases, such as congenital malformation, trauma, infection, inflammation and cancer (Hak, 2007; Mcallister and Haghighat, 2007; Chiapasco et al., 2009). Due to limited regenerative capacity of bone tissue, LVBD usually causes delayed repair or non-union—a permanent failure of healing, which may severely compromise aesthetics and musculoskeletal functions of patients. Hitherto, the repair of LVBD is still challenging in the fields of oral implantology, maxillofacial surgery and orthopedics. Autologous bone grafts are still regarded as the gold standard treatment for LVBD (Kneser et al., 2006). However, their applications are hindered by donor-site morbidity and limited availability. As alternatives to autologous bone, a large variety of medical devices, such as allografts, xenografts, synthetic materials have been developed and applied (Laurencin et al., 2006; Kumar et al., 2013). Most of these medical devices bear intrinsic osteoconductivity—the ability to support the attachment, spreading, migration and ingrowth of osteogenic cells within bone substitues (Albrektsson and Johansson, 2001). However, in general their osteoconductivity appears too limited to result in a completely osseous healing of LVBD. Besides, in dental implantology, continuous efforts are being made to enhance cell spreading on titanium implants so as to enhance osteointegration (Canullo et al., 2016) and re-osteointegration (Duske et al., 2012).

One viable option to promote the osteoconductivity of bone substitutes and metallic implants is to apply bioactive peptides (Lee et al., 2008; Pountos et al., 2016). An interesting candidate peptide in this respect is histatin-1 (Hst1), a member of a large histidine-rich peptide family that is present in human saliva. Various Hsts have been implicated in numerous protective functions in the mouth, such as detoxification (Yan and Bennick, 1995), antimicrobial activity (Xu et al., 1991; Kavanagh and Dowd, 2004) and inhibition of enamel demineralization (Yin et al., 2003). In our previous studies, we have demonstrated that Hst1 promotes the wound closure of human epithelial cells *in vitro* (Oudhoff et al., 2008, 2009a,b), putatively by the activation of G protein-coupled receptor (GPCR) and extracellular-signal-regulated kinase (ERK), but not p38 MAPK (mitogen-activated protein kinase) signaling pathways (Oudhoff et al., 2008, 2009b). Furthermore, it has been found that Hst1 promotes the adhesion and spreading of epithelial cells onto bio-inert glass, bio-inert substrate (Van Dijk et al., 2015) and on hydroxyapatite and sputtered titanium *in vitro* (Van Dijk et al., 2017a). Meanwhile, recent studies demonstrate that Hst1 also promotes the attachment of osteogenic cells on titanium SLA (sandblasted and acid etched) surfaces (Van Dijk et al., 2017a) as well as their migration (Castro et al., 2019), which suggests a promising application potential of Hst1 for promoting the osteoconductivity of various medical devices. However, the effect of Hst1 on the spreading of osteogenic cells on titanium SLA surfaces remains to be elucidated.

Hitherto, there is no report to systematically investigate the dose-dependent effect of Hst1 on the spreading of osteogenic cells and its potential molecular mechanisms. In the present study, we explored the effects of Hst1 and its truncated variants on the spreading of osteogenic cells, as well as the involvement of cell signaling pathway using specific inhibitors. As model surface it was chosen to use glass cover slips as they are widely adopted to investigate cell behaviors on bio-inert surfaces. Glass coverslips are also transparent and can thus be used to observe both live and fixed cells using light or fluorescent microscopy (Islam et al., 2016; Van Dijk et al., 2017a; Che et al., 2018). In addition, we also investigated the effect of Hst1 on cell spreading on titanium SLA surface — a most commonly used surface for dental implants.

MATERIALS AND METHODS

Cell Culture

Osteogenic cells [MC3T3-E1 mouse pre-osteoblast cell line, subclone 4, CRL-2593, American Type Culture Collection (ATCC)], was cultured in alpha-Minimum Essential Medium (α-MEM) (Gibco, Thermo Fisher Scientific). All media were supplemented with 10% fetal bovine serum (FBS, Thermo Fisher Scientific), 10 units/mL penicillin and 10 μg/mL streptomycin (Invitrogen, Thermo Fisher Scientific). Cells were cultured at 37°C in a moist atmosphere at 5% CO_2 and routinely tested for the presence of mycoplasm. In all experiments, cells from exponentially growing cultures were used.

Solid-Phase Peptide Synthesis

All peptides (**Table 1**) were manufactured by solid-phase peptide synthesis using 9-fluorenylmethoxycarbonyl (Fmoc)-chemistry as described previously (Bolscher et al., 2011; Van Dijk et al., 2015). The peptides were purified by High-Performance Liquid Chromatography (RF-HPLC, Dionex Ultimate 3000, Thermo Scientific, Breda, Netherlands) to a purity of at least 95%. The authenticity was confirmed by mass spectrometry with a Microflex LRF MALDI-TOF (Bruker Daltonik GmbH, Bremen, Germany) as previously described (Bolscher et al., 2011; Van Dijk et al., 2015). During synthesis, part of Hst1 was labeled with the fluorescent dye ATTO-647N (ATTO-TEC GmbH, Siegen, Germany). An equimolar amount of the dye was coupled to the ε-amino group of the side chain of lysine residue number 17 (lys17, K of Hst1 after removal of the specific protective (ivDde)-OH group by hydrazine (2% hydrazine hydrate).

Cell Spreading Assay

In this experiment, four groups of three wells each were set up each time in 12-well cell culture plates. Each experiment was repeated at least two times for statistical analysis, so $N = 6$ wells per group. Cells were serum deprived for 24 h, detached using 0.05% trypsin (Gibco), and suspended in culture

TABLE 1 | Amino acid sequences of Hst1, Scrambled Hst1 (Scr-Hst1), and Hst1 truncated variants.

Name	Amino acid sequence
Control	No peptide
Scr-Hst1	SDHSRHEEFKPRFHYHGGDYYRGRSKNFYHLEYKDHNH
Hst1 (1–38)	DSHEKRHHGYRRKFHEKHHSHREFPFYGDYGSNYLYDN
Hst1 (12–38)	..........................RKFHEKHHSHREFPFYGDYGSNYLYDN
Hst1 (16–34)	....................................EKHHSHREFPFYGDYGSNY.........
Hst1 (18–34)	....HHSHREFPFYGDYGSNY.........
Hst1 (20–34)	....SHREFPFYGDYGSNY.........
Hst1 (20–32)	....SHREFPFYGDYGS.............
Hst1 (20–30)	....SHREFPFYGDY...................

Double underlined K in Hst1 is labeled with a fluorescent molecule ATTO647.

medium containing 2% FBS to inactivate the trypsin and centrifuged at 200 g for 5 min at room temperature. Next, cells were re-suspended in their prescribed medium without serum and counted using a hemocytometer. Cells were seeded on glass coverslips (diameter, 12 mm, No. 1, VWR, Amsterdam, Netherlands) in 12-wells suspension cell culture plates (Greiner Bio-One, Alphen aan de Rijn, Netherlands) at a density of 6×10^4 cells/well, treated with 0–20 μM of the Hst1 or 10 μM truncated Hst1 or scrambled Hst1. Cells were imaged every 20 min during a 3 h period using an EVOS-FL microscope (Thermo Fisher Scientific) equipped with a LPlanFL PH2 20x using the phase contrast setting or the Cy5 light cube (628/40 and 692/40 nm, excitation and emission filters, respectively). For each well, 6 images were taken randomly with about 90–120 cells per image. Thereafter, we randomly selected 3 images for further analysis by measuring the surface area of cells' filopodia and lamellipodia (denoted in **Supplementary Figure 1** with the red circle) using a point-counting method (Gundersen and Jensen, 1987; **Supplementary Figure 1**). The surface area of cell was considered to quantitatively represent cell spreading.

Uptake and Localization of Hst1 in Osteogenic Cells

To analyze the uptake and localization of fluorescently labeled Hst1 (F-Hst1) by osteogenic cells, cells from a semi-confluent cell culture were transferred into a 48-wells plate at a density of about 3.5×10^4 cells/well and cultivated at 37°C for at least 24 h. Subsequently, the cells were washed once with DPBS (Dulbecco's PBS, Gibco) after which serum-free medium was added. Two micrometer F-Hst1 was added and after a 1 h period, the cells were washed four times with DPBS containing 0.9 mM Ca^{2+} and 0.5 mM Mg^{2+}. As a negative control, incubations without F-Hst1 were included. The cells were studied by the EVOS-FL microscope with a 20x objective with a phase contrast setting and a "Cy-5 light cube" with a 628/40 excitation filter and a 692/40 nm emission filter. Digital photographs were recorded by a computer integrated in the microscope.

To more precisely observe the uptake and localization of F-Hst1, the cells were further studied using a LEICA TCS SP8 confocal laser scanning microscopy (CLSM) system as previously described (Ma et al., 2020). Before incubation with F-Hst1, cell nuclei and membrane were stained with NucBlue^{TM} live cell stain (Life Technologies, Grand Island, NY) and PKH67GL (Sigma–Aldrich, MO, United States) respectively, following manufacturer's instructions.

Signaling Pathways for the Effects of Hst1

In our previous studies, we have demonstrated that Hst1 promotes the wound closure of human epithelial cells *in vitro* (Oudhoff et al., 2008, 2009a, b), putatively by the activation of GPCR and ERK1/2, but not p38 MAPK signaling pathways (Oudhoff et al., 2008, 2009b). To investigate the role of potential signaling pathways in the effects of Hst1 on the spreading of osteogenic cells, we applied the following signaling pathway-specific inhibitors of ERK1/2 (U0126, 10 μM; LC Laboratories, Woburn, MA, United States), GPCR (pertussis toxin (PTx), 200 ng/mL; LC Laboratories, Woburn, MA, United States), and p38 MAPK (SB203580, 10 μM; LC Laboratories, Woburn, MA, United States) using the cell spreading model on bio-inert glass.

Cell Spreading on Titanium SLA Surface

Commercially titanium (purity > 99.6%, 125 μm in thickness, ADVENT, United Kingdom) foil was cut into round discs (5 mm in diameter). To make SLA surface, the titanium discs were first sandblasted with large corundum grits. Thereafter, the discs were cleaned ultrasonically in alcohol and dH_2O for 15 min respectively, and then acid etched with a mixture of 37% HCL 25 ml, 98% H_2SO_4 25 mL and 50 mL dH_2O solution at 60℃ for 22 min in a stirring condition (100 rpm). Finally, the discs were cleaned ultrasonically in dH_2O for 15 min three times and dried overnight in oven. These discs were thereafter autoclaved for sterilization and kept in sterile condition. Cell spreading on titanium SLA surface was performed as described in the section of cell spreading assay. 1.5 h after seeding, cells on titanium discs were fixed, dehydrated and stained with DAPI and FITC-Phalloidin to stain nuclei and cell skeleton respectively. Fluorescent micrographs were randomly taken using a fluorescent microscope (Olympus BX61) with Excitation/Emission wavelengths (nm) of 358/461 and of 496/516, respectively. On the micrographs, spreading surface of each cell was estimated using the abovementioned point-counting method. More than 30 cells per group were calculated.

Statistical Analysis

All experiments were carried out at least three times and in quadruple. Data were plotted using Graphpad Prism (Graphpad Software version 6.0, La Jolla, CA, United States), analyzed using Student's *t*-test and one- way ANOVA with Bonferroni's *post hoc* test for multiple comparisons. For the data from different groups at different time points in **Figure 1D**, we used two-way ANOVA to analyze the data with Bonferroni's *post hoc* test for multiple comparisons. Results were reported as mean ± SD. A value of $P < 0.05$ was considered as statistical significance. $^{*}p < 0.05$; $^{**}p < 0.01$; $^{***}p < 0.001$.

RESULTS

Hst1 Promoted Spreading of Osteogenic Cells on Bio-Inert Glass

We first evaluated the dose-dependent effect of Hst1 on cell spreading. The presence of Hst1 promoted the spreading of osteogenic cells with larger lamellipodia and more filopodia in comparison with the control (no Hst1) (**Figure 1A**). Compared to the control, treatment with Hst1 at concentrations of 10 and 20 μM resulted in significantly larger spreading surface area (**Figure 1B**) 170 min post incubation. Thereafter, we assessed the dose-dependent effects of Hst1 on cell spreading. Cell treated with Hst1 for > 90 min, showed significantly higher spreading than the control (untreated cells) (**Figure 1C**). The spreading areas in Hst1 group were 1.46, 1.51, 1.93, and 2.02

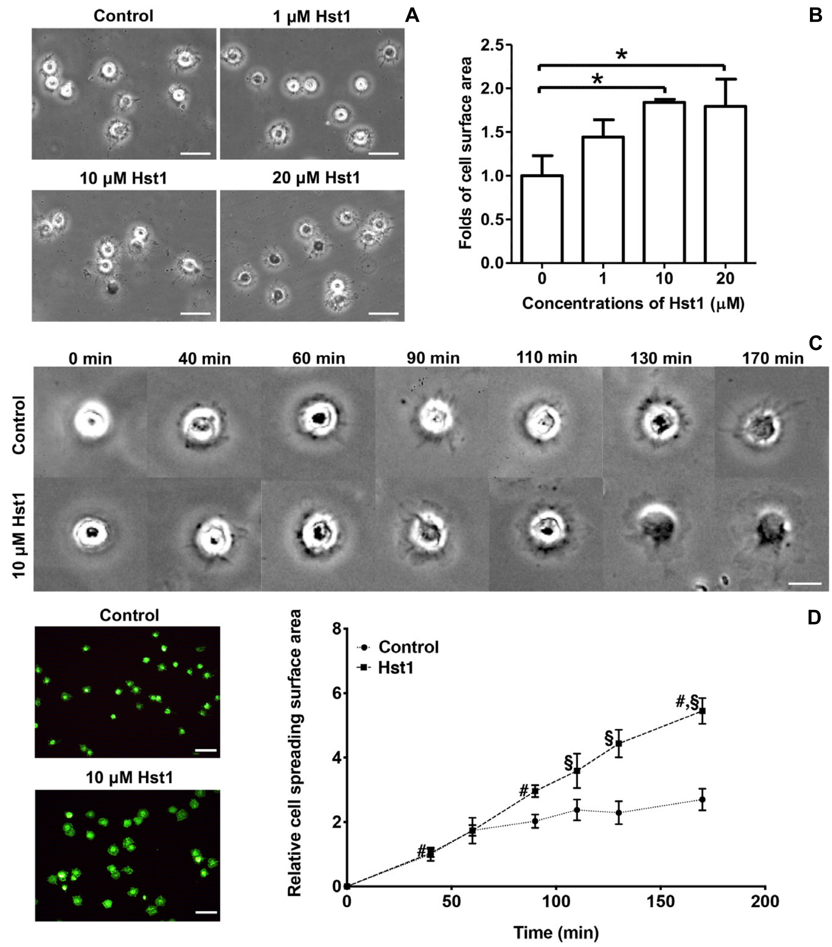

FIGURE 1 | Hst1 promoted the spreading of osteogenic cells on glass surfaces. **(A)** Light micrographs depicting the spreading of osteogenic cells in the absence or presence 1, 10, and 20 μM Hst1. Bar = 50 μm. **(B)** Folds of cell spreading surface area in the absence or presence or of 1, 10, and 20 μM Hst1. Data are shown as mean ± SD (*n* = 6). $^*p < 0.05$ **(C)** Light micrographs of the spreading of osteogenic cells in the absence or presence of 10 μM Hst1 on different time points. **(D)** Fluorescent micrographs depicting the spreading of osteogenic cells (stained with FITC-Phalloidin) in the presence or absence of 10 μM Hst1 on bio-inert glass surface. Time-dependent cell spreading surface area (expressed in folds with the value of the control group at first time point as 1) in the presence or absence of 10 μM Hst1. Data were shown as mean ± SD (*n* = 6). $^{\S}p < 0.05$ indicating a significant difference compared with the values in the control group at the same time point; $^{\#}p < 0.05$ indicating a significant difference compared with the value in the same treatment group at the earlier time point. Bar = 50 μm.

times those in control group at 90, 110, 130, and 170 min, respectively (**Figure 1D**).

Truncated Hst1 Variants Did Not Improve the Spreading of Osteogenic Cells on Bio-Inert Glass

Scrambled Hst1 did not promote spreading of osteogenic cells compared to the control. In order to determine the minimal domain of Hst1 required for cell spreading on bio-inert glass, we tested 6 truncated variants of Hst1. Since the *in vitro* wound-healing properties of Hst1 (amino acids 12–38) appeared comparable to those of the parent peptide Hst1 (Oudhoff et al., 2008), this peptide was used as a starting point for mapping the minimal active domain. To map the minimal active domain responsible for the cell spreading, a number of truncated variants of Hst1 were synthesized (encompassing amino acids 12–38, 16–34, 18–34, 20–34, 20–32, and 20–30) as previously reported (Oudhoff et al., 2009a). The relative spreading area of osteogenic cells under the stimulation of Hst1 (1–38), Hst1 (12–38), Hst1 (16–34), Hst1 (18–34), Hst1 (20–34), Hst1 (20–32), and Hst1 (20–30) were 1.76 ± 0.23, 1.35 ± 0.14, 1.20 ± 0.16, 1.24 ± 0.36, 0.68 ± 0.09, 1.01 ± 0.06, and 0.94 ± 0.18, respectively (**Figure 2**). However, except for Hst1 (1–38), none of these variants, significantly promoted the spreading of osteogenic cells on glass surface in comparison with the control (1.00 ± 0.19) (**Figure 2**).

Uptake and Localization of Hst1 by Osteogenic Cells

In order to study whether Hst1 is also taken up by osteogenic cells, MC3T3-E1 cells were incubated with F-Hst1 and microscopically analyzed. After a 1 h incubation, an intracellular bright, granular labeling pattern was observed in the vicinity

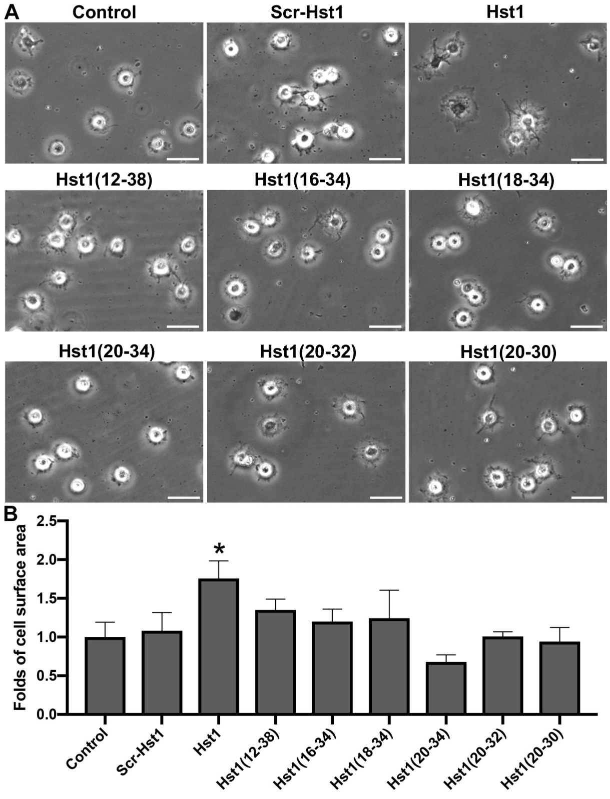

FIGURE 2 | The effect of truncated Hst1 variants on the spreading of osteogenic cells. **(A)** Light micrographs depicting the spreading of osteogenic cells in the presence or absence of scrambled Hst1 and 6 truncated variants of Hst1 on glass surfaces. Bar = 50 μm. **(B)** Folds of cell spreading surface area in the presence or absence of scrambled Hst1 and 6 truncated variants of Hst1 on glass. Data are shown as mean ± SD ($n = 6$). $^{*}p < 0.05$.

of nuclei (**Figure 3A**). CLSM micrographs showed that F-Hst1 (red) distributed between cell membrane (green) and nucleus (blue), while in the control group (no Hst1) red fluorescence was detected in intracellular space (**Figure 3B**).

Effects of Inhibitors of ERK1/2, P38 and GPCR on Hst1-Induced Cell Spreading

To reveal the potential involvement of signaling pathways in Hst1-induced spreading of osteogenic cells, we analyzed the effects of the ERK1/2 inhibitor (U0126), p38 MAPK inhibitor (SB203580) and PTx (an inhibitor of GPCR) on the Hst1-induced cell spreading. U0126 (10 μM) or SB203580 (10 μM) completely abolished the stimulating effects of Hst1 on the spreading of osteogenic cells (**Figures 4A–D**). In contrast, PTx did not show any significant effect (**Figures 4E,F**). The inhibitors had no effect on the basal cell spreading in the absence of Hst1.

Hst1 Enhanced the Osteogenic Cell Spreading on Titanium SLA Surface

In order to assess the promoting effect of Hst1 on osteogenic cells on titanium plates, MC3T3-E1 cells were seeded on the titanium plates with SLA surfaces in the absence or presence of 10 μM Hst1. To enable quantification of the cell-surface area by fluorescence microscopy, cellular actin was fluorescently labeled using FITC-Phalloidin (**Figure 5A**). Quantitative analysis indicated that the surface area per cell in the group of 10 μM Hst1 (713.26 ± 172.94 μm^2) was significantly higher than that without Hst1 (537.38 ± 108.19 μm^2) (**Figure 5B**).

DISCUSSION

The adhesion, spreading and migration of osteogenic cells on medical devices are indispensable for effective bone formation of LVBD and osteointegration of implants (Deligianni, 2014; Zhang et al., 2015). In this study, we demonstrated that Hst1 significantly promoted the spreading of osteogenic cells on bio-inert glass in dose- and time-dependent assays. It appeared that such effect of Hst1 was associated with ERK1/2 and p38 signaling as their specific inhibitors counteracted the Hst1 stimulation. We also showed that Hst1 significantly promoted the spreading of osteogenic cells on SLA titanium surface. Therefore, Hst1 bears an application potential to promote osteoconductivity, so as to enhance bone healing and osteointegration.

It is well established that cell-substrate contact area can determine cell activities, such as proliferation, quiescence or apoptosis (McGrath, 2007). When plated on glass, the cells go through three major phases from the unsuspended state to the flat and polarized state: (1) initial attachment; (2) a rapid increase in cell spreading area through depletion of membrane reservoirs; and (3) a slower spreading phase that includes periodic protrusion/retraction of the cell edge and an increase in membrane area (Dubin-Thaler et al., 2004; Giannone et al., 2004). The advantage of using the model system of cell spreading from the unattached state is that it is highly reproducible and the stages that the cell undergoes can be characterized and quantified in a time-dependent manner (Wolfenson et al., 2014). There exist many experimental methods to quantitatively evaluate cell spreading, such as the determination of relative cell spreading and calculation of the so called cell index (Van Dijk et al., 2015, 2017a). The later parameter qualifies the impedance of cells that proportionally correlate to, but not directly show, cell spreading extent. In contrast, in the current study, we adopted a point-counting method (Cruz-Orive and Weibel, 1990) to measure the surface area of spreading cells, which could directly reflect the newly formed cell-substrate contact area.

Hst1 has already been shown to be efficacious in promoting the adhesion, spreading and migration of various epithelial cells from skin (Oudhoff et al., 2009a), mucosal (Oudhoff et al., 2008, 2009b), gingival (Van Dijk et al., 2015, 2017a) and corneal origin (Shah et al., 2017). Hst1 bears a very broad pharmaceutical dosage. Hst1 is associated with no cytotoxicity and significantly enhanced metabolic activity of human corneal epithelial cells within 200 μM (Shah et al., 2017). In our recent study, we also show that 10 μM Hst1 significantly promotes metabolic activity of human oral mucosal epithelial cells, skin keratinocytes and gingival fibroblasts (Ma et al., 2020). These findings indicate

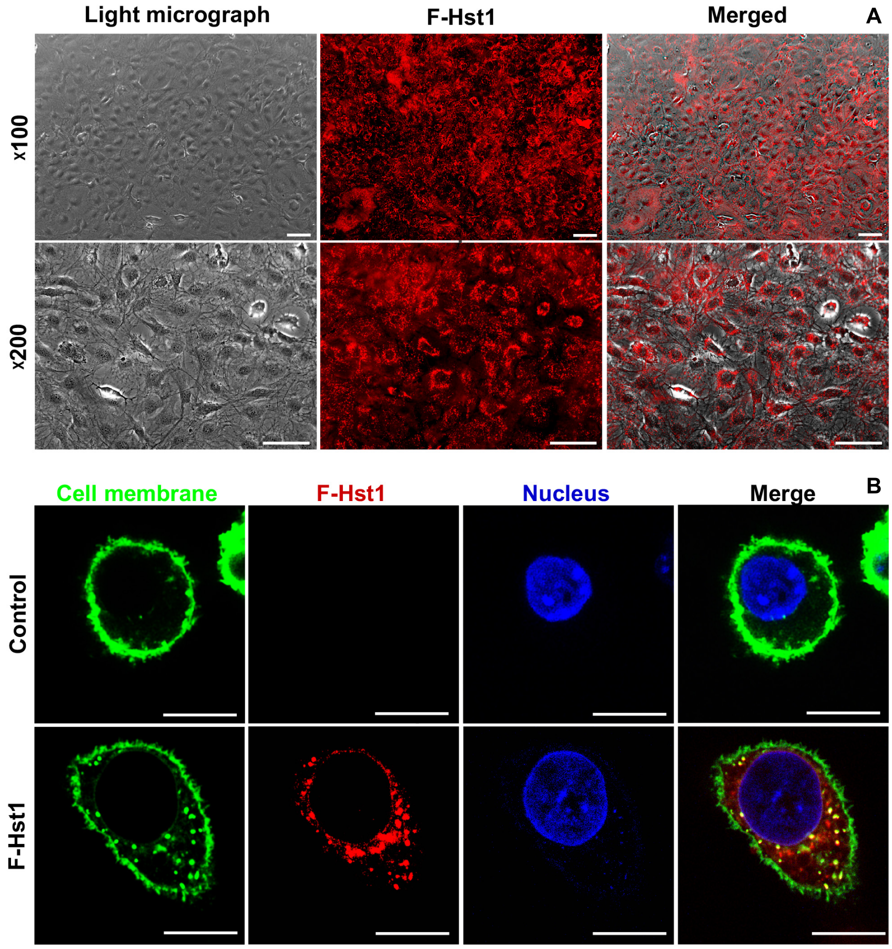

FIGURE 3 | The uptake and distribution of F-Hst1 in osteogenic cells. **(A)** Light (left column) and fluorescent (middle column) micrographs depicting the uptake of fluorescently labeled Hst1 (F-Hst1) (middle column) by osteogenic cells (left column) in lower (upper row) and higher (lower row) magnification. Bar = 100 μm. **(B)** Cellular uptake of the fluorescence (ATTO-647N)-labeled Hst1 (F-Hst1). CLSM images of F-Hst1 variants (in red) were taken up by osteogenic cells; cell membrane are stained in green; nuclei are stained in blue; Bar = 20 μm.

the good biocompatibility of Hst1. It remains unclear how Hst1 influences cellular metabolic activity. Our recent study shows that Hst1 can be quickly internalized and accumulate in cytoplasm (Ma et al., 2020). In the present study, we adopted CLSM and, for the first time, clearly showed the uptake of Hst1 by pre-osteoblasts. After being taken up, Hst1 is quickly targeted to mitochondria and endoplasmic reticulum (ER) (Ma et al., 2020), which suggests a potential role of mitochondria-ER contact in the modulating effects of Hst1 on cellular metabolic activity. However, hitherto, the intracellular signaling pathways and genes activated by Hst1 remains to be elucidated. Further studies should be performed to clarify these issues.

Consistent with these reports, it was observed that 10 μM of Hst1 optimally promoted the spreading of osteogenic cells *in vitro* 60 min post incubation. The time-dependent course of Hst1's effect was consistent with the previous findings on epithelial cells that the surface of fibroblasts increased remarkably after 60 min treated with Hst1 when compared to the control (Van Dijk et al., 2015, 2017a). Further publications also reported that Hst1 could promote endothelial cell adhesion, migration, and angiogenesis (Torres et al., 2017; Van Dijk et al., 2017b). Hst1 was also demonstrated to promote the attachment of osteogenic cells on the both sputtered smooth titanium surface and SLA surfaces (Van Dijk et al., 2017a). In the current study, we showed that Hst1 could also promote the spreading of osteogenic cells on both bio-inert glass surfaces as well as on titanium SLA surfaces. These findings suggested that Hst1 could improve cell-biomaterial interaction so as to promote bone healing and implant osteointegration. Furthermore, Hst1 is also shown to counteract the cytotoxic and anti-migratory effects of zoledronic acid on MC3T3-E1 osteogenic cells and endothelial cells (Castro et al., 2019). Zoledronic acid, the most frequent agent associated with bisphosphonate-related osteonecrosis of the jaw, has been reported as cytotoxic for bone and vascular cells (Aghaloo et al., 2015). It has been shown that Hst1 can protect cells from different adverse conditions by decreasing

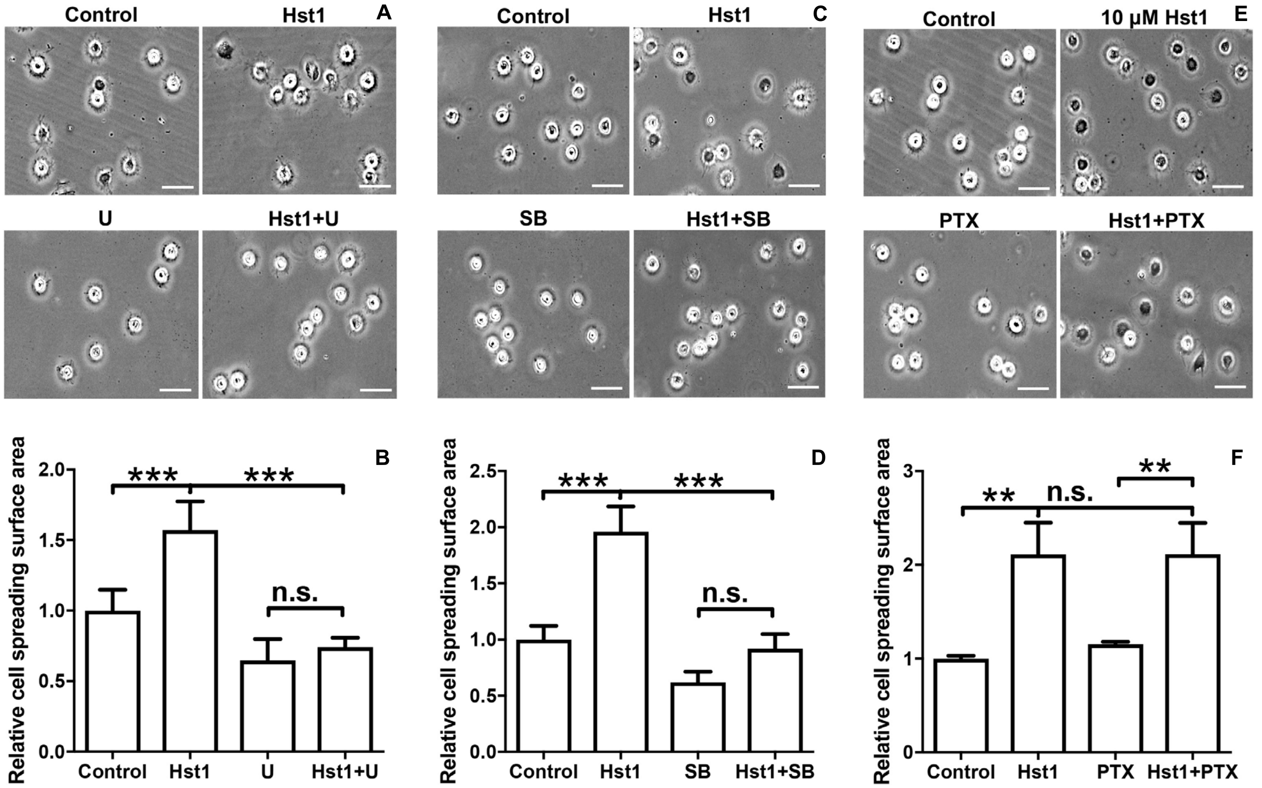

FIGURE 4 | The effects of signaling pathway inhibitors on Hst1-induced spreading of osteogenic cells. Light micrographs depicting the spreading of osteogenic cells that were treated with **(A)** extracellular-signal-regulated kinase (ERK) signaling (10 μM U0126), **(C)**: p38 signaling (10 μM SB203580) and **(E)** G protein-coupled receptor (GPCR) (200 ng/mL Pertussis toxin, PTx). Bar = 50 μm. Relative spreading surface area of osteogenic cells that were treated with Hst1 with or without the pretreatment with the inhibitors of **(B)** extracellular-signal-regulated kinase (ERK) signaling (10 μM U0126), **(D)** p38 signaling (10 μM SB203580) and **(F)** G protein-coupled receptor (GPCR) (200 ng/mL Pertussis toxin, PTx). Data are shown as mean ± SD (*n* = 6). $^{**}p < 0.01$, $^{***}p < 0.001$.

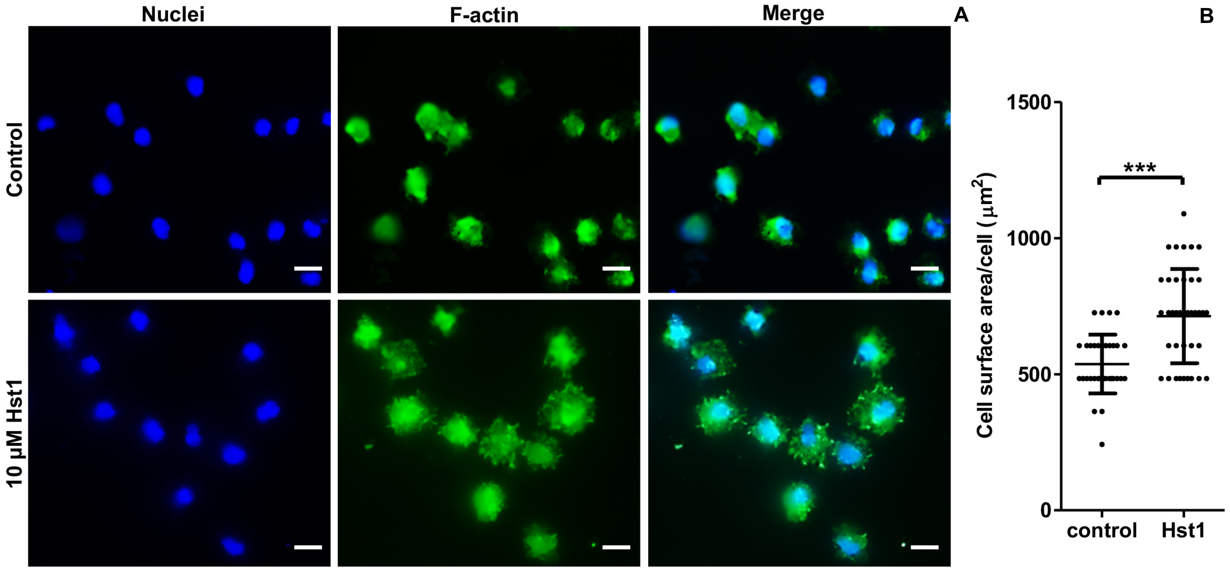

FIGURE 5 | Hst1 promoted the spreading of osteogenic cells on titanium SLA surfaces. Fluorescent micrographs **(A)** depicting the spreading of osteogenic cells that were stained by Dapi (for nuclei) (left column) and by FITC-Phalloidin (for F-actin) (middle column) Bar = 20 μm. **(B)** Graph depicting the quantitative analysis of the spreading of osteogenic cells. Data are shown as mean ± SD (*n* = 32). $^{***}p < 0.001$.

cell apoptosis (Aghaloo et al., 2015; Huang et al., 2018). These findings suggested that Hst1 has a great application potential in various bone diseases.

Titanium is widely used as implant material in case of e.g., cervical prosthetics, joint prosthetics, mini-plates, mini-screws, and dental implants (Giannasi et al., 2018). Continuous efforts have been made to enhance cell spreading on titanium implants with an aim to facilitate osteointegration (Canullo et al., 2016) and re-osteointegration (Duske et al., 2012). For this purpose, various peptides have also been attempted. For example, P15, a synthetic 15 amino acid peptide mimicking the cell-binding domain within the alpha-1 chain of human collagen, can significantly promote cell attachment, spreading and osteogenic gene expression (Liu et al., 2012). Peptide derived from another cell matrix laminin also promoted cell attachment of human osteoblast-like cells (Min et al., 2013). To exert such functions, most of these peptides still needs to be pre-attached onto the surface of titanium (Liu et al., 2012; Min et al., 2013). Different from the application pattern of these peptides, we showed that Hst1 could promote the attachment of osteogenic cells without the needs of pre-attachment to titanium surfaces. In this study, we investigated the effect of Hst1 on osteogenic cell spreading on titanium SLA surface, the most commonly used surface for dental implants. Consistent with the previous conclusion (Van Dijk et al., 2017a), we showed that Hst1 significantly enhanced the spreading of osteogenic cells on titanium SLA surfaces when compared to the control group. In our recent study, we showed that Hst1 could be quickly taken up and distribute in the vicinity of surrounding nuclei within epithelial cells and fibroblasts, which suggested an important role of subcellular targets (mitochondria and endoplasmic reticulum) in Hst1's functions (Ma et al., 2020). In this study, our data obtained using fluorescent microscopy showed that F-Hst1 was taken up by osteogenic cells and distributed intracellularly. CLSM results corroborated that Hst1 was distributed in the vicinity of the nucleus. These findings suggested that Hst1 did not act as an intermediate (coating) between substrate and cell, but rather induces a cellular response. With these properties, Hst1 can be used as convenient stimulatory molecule to promote osteointegration of titanium implants.

Hitherto, it is still unclarified by which exact molecular mechanism Hst1 promotes cell spreading. Our previous studies suggest that the promoting effect of Hst1 on the migration of epithelial cells is mediated by the GPCRs-ERK1/2 pathway, but not by the p38 pathway (Oudhoff et al., 2009a). Our recent study shows that co-administration of Hst1 with all-trans retinoic acid additively stimulates the spreading and osteogenicity of preosteoblasts on bio-inert glass surfaces *in vitro*, which can be abolished by specific inhibitors of retinoic acid receptors α (but not β or γ) (Sun W. et al., 2020). However, the signaling pathways accounting for the Hst1's effect on the pre-osteoblasts' adhesion remains to be clarified. In this study, we found that U0126, an inhibitor of ERK1/2 pathway, significantly inhibited the effect of Hst1. However, also the p38 inhibitor SB203580 abolished the effect of Hst1, suggesting that in the present system, both ERK1/2 and p38 pathways wound to be involved in mediating the effect of Hst1. This is incongruent with a previous study in which it was found that inhibition of ERK1/2, but not of p38, abrogated the stimulatory effects of Hst1 (Oudhoff et al., 2009a). Furthermore, in that study, it is found that Hst1 (20–32) (SHREFPFYGDYGS) is the minimal domain of Hst1 that promotes the migration of epithelial cells (Oudhoff et al., 2009a). Such a study is highly important to identify a minimal functional domain. Furthermore, a much shorter peptide would be very meaningful for its pharmaceutical application due to a significantly lower production cost. In the present study, we, for the first time, showed the effects of truncated Hst1 variants on the spreading of pre-osteoblasts. Inconsistent with the previous finding, our present study showed that none of truncated Hst1 variants had any effect on osteogenic cell spreading. Further studies are needed to clarify these apparent discrepancies, which may be caused by the use of different cell types (epithelial vs. osteogenic cells) from different species (human vs. mouse) in these studies. Although our data suggest the roles of ERK and p38 signaling in the promoting effects of Hst1 on cell adhesion, it remains unclear how these two signaling pathways interact with the cell skeleton-modulating signaling cascades, such as phosphatidylinositol 3 kinases, ERK1/2, 5'-AMP-activated protein kinase, members of the Rho GTPase family (RhoA, Rac, Cdc42), Rho guanine nucleotide exchange factors, Rho GTPase activating proteins, and Rho guanine nucleotide dissociation inhibitors (Moujaber and Stochaj, 2020). Further studies should be performed to clarify how Hst1 interacts with these signaling pathways.

On the other hand, ERK1/2 and p38 are proved to be involved in osteogenic differentiation (Guo and Wu, 2012). Under the stimulation of bone morphogenetic protein 2 (BMP2), the inhibition of p38 by SB203580 was associated with a significantly decreased alkaline phosphatase activity (an early osteogenic differentiation marker) and osteocalcin (OCN, a late osteogenic differentiation marker) in MC3T3-E1 pre-osteoblasts (Guicheux et al., 2003), while ERK signaling was barely activated, which indicates the importance of p38 but not ERK signaling in BMP2-induced osteogenic differentiation. On the other hand, icaritin, a hydrolytic product of icariin from the genus Epimedium, can significantly upregulate ERK and p38 signaling in its-induced osteogenic differentiation in MC3T3-E1 pre-osteoblasts. Furthermore, p38 antagonist SB203580 and ERK1/2 antagonist PD98059 markedly inhibit the icaritin-induced the mRNA expression of ALP, COL1 (encoding collagen type I), OCN and OPN (encoding osteopontin) (Wu et al., 2017). These results suggest that different ligands may stimulate different patterns of signaling. Since ERK and p38 seems to be involved in Hst1's effect, question may be raised whether Hst1 can promote *in vitro* osteogenic differentiation and *in vivo* osteogenesis, thereby contributing to osteoinductivity—another important property to heal LVBD and facilitate osteointegration. Hitherto, this issue is rarely reported. In our recent study, we show that Hst1 alone does not promote ALP activity (Sun W. et al., 2020). Additionally, our ongoing study shows that Hst1 does not further enhance BMP2-induced *in vitro* extracellular mineralization of MC3T3-E1 (data not shown). Therefore, although ERK and p38 signaling are involved in Hst1's effects on cell adhesion and spreading, they don't directly lead to osteogenic differentiation at least in MC3T3-E1 pre-osteoblasts. All these data suggest that Hst1 does not enhance osteogenic differentiation, thus bearing no osteoinductivity. On the other hand, in our recent *in vivo* study, Hst1 significantly promotes angiogenesis and osteogenesis under the stimulation of BMP2 in an ectopic bone induction model (Sun P. et al., 2020). Such an effect of Hst1 on osteogenesis may be attributed to the stimulating effect of Hst1 on angiogenesis (Torres et al., 2017) that favors bone regeneration (Grosso et al., 2017). However, caution should be always taken to completely exclude the direct stimulating effects of Hst1 on osteogenic differentiation because only a mouse partially osteogenically-committed cell line has been examined. Human primary mesenchymal stem cells, such as bone marrow stem cells, should be used in future study to further investigate the effects of Hst1 on osteogenic differentiation.

DATA AVAILABILITY STATEMENT

All datasets presented in this study are included in the article/**Supplementary Material**.

AUTHOR CONTRIBUTIONS

GW, HL, and EV: conceptualization. WS, GW, and DM: investigation. GW and JB: resources. WS and GW: formal analysis. KN and FB: data curation. WS, FB, and GW: writing—original draft preparation. PS, WS, DM, FB, JB, KN, HL, GW, and EV: editing. WS, GW, PS, HL, and EV: funding acquisition. All authors contributed to the article and approved the submitted version.

FUNDING

This work was supported by the Zhejiang Provincial Natural Science Foundation of China (grant no. LQ18H140003), the Foundation of Zhejiang Educational Committee, China (grant no. Y201636248), Zhejiang Provincial Natural Science Foundation of China (grant no. LQ Y17H140023), Zhejiang Provincial Basic Public Welfare Research Project (grant no. GJ19H140001), Science Technology Department of Zhejiang Province (grant no. 2017C33168). China's National Key R&D Programs (NKPs, grant no. 2018YFB0407204), and Eurostars project (grant no. STAR19104).

SUPPLEMENTARY MATERIAL

The Supplementary Material for this article can be found online at: https://www.frontiersin.org/articles/10.3389/fbioe.2020.584410/full#supplementary-material

REFERENCES

Aghaloo, T., Hazboun, R., and Tetradis, S. (2015). Pathophysiology of osteonecrosis of the jaws. *Oral. Maxillofac. Surg. Clin. North Am.* 27, 489–496. doi: 10.1016/j.coms.2015.06.001

Albrektsson, T., and Johansson, C. (2001). Osteoinduction, osteoconduction and osseointegration. *Eur. Spine J.* 10(Suppl. 2), S96–S101.

Bolscher, J. G., Oudhoff, M. J., Nazmi, K., Antos, J. M., Guimaraes, C. P., Spooner, E., et al. (2011). Sortase A as a tool for high-yield histatin cyclization. *FASEB J.* 25, 2650–2658. doi: 10.1096/fj.11-182212

Canullo, L., Genova, T., Tallarico, M., Gautier, G., Mussano, F., and Botticelli, D. (2016). Plasma of argon affects the earliest biological response of different implant surfaces: an *In vitro* comparative study. *J. Dent Res.* 95, 566–573. doi: 10.1177/0022034516629119

Castro, M., Torres, P., Solano, L., Cordova, L. A., and Torres, V. A. (2019). Histatin-1 counteracts the cytotoxic and anti-migratory effects of zoledronic acid in endothelial and osteoblast-like cells. *J. Periodontol.* 90, 766–774. doi: 10.1002/jper.18-0644

Che, X., Boldrey, J., Zhong, X., Unnikandam-Veettil, S., Schneider, I., Jiles, D., et al. (2018). On-chip studies of magnetic stimulation effect on single neural cell viability and proliferation on glass and nanoporous surfaces. *ACS Appl. Mater. Interfaces* 10, 28269–28278. doi: 10.1021/acsami.8b05715

Chiapasco, M., Casentini, P., and Zaniboni, M. (2009). Bone augmentation procedures in implant dentistry. *Int. J. Oral. Maxillofac. Implants* 24(Suppl.), 237–259.

Cruz-Orive, L. M., and Weibel, E. R. (1990). Recent stereological methods for cell biology: a brief survey. *Am. J. Physiol.* 258, L148–L156.

Deligianni, D. D. (2014). Multiwalled carbon nanotubes enhance human bone marrow mesenchymal stem cells' spreading but delay their proliferation in the direction of differentiation acceleration. *Cell Adh. Migr.* 8, 558–562. doi: 10.4161/cam.32124

Dubin-Thaler, B. J., Giannone, G., Dobereiner, H. G., and Sheetz, M. P. (2004). Nanometer analysis of cell spreading on matrix-coated surfaces reveals two distinct cell states and STEPs. *Biophys. J.* 86, 1794–1806. doi: 10.1016/s0006-3495(04)74246-0

Duske, K., Koban, I., Kindel, E., Schroder, K., Nebe, B., Holtfreter, B., et al. (2012). Atmospheric plasma enhances wettability and cell spreading on dental implant metals. *J. Clin. Periodontol.* 39, 400–407. doi: 10.1111/j.1600-051x.2012.01853.x

Giannasi, C., Pagni, G., Polenghi, C., Niada, S., Manfredi, B., Brini, A. T., et al. (2018). Impact of dental implant surface modifications on adhesion and proliferation of primary human gingival keratinocytes and progenitor cells. *Int. J. Periodontics Restorative Dent.* 38, 127–135. doi: 10.11607/prd.3304

Giannone, G., Dubin-Thaler, B. J., Dobereiner, H. G., Kieffer, N., Bresnick, A. R., and Sheetz, M. P. (2004). Periodic lamellipodial contractions correlate with rearward actin waves. *Cell* 116, 431–443. doi: 10.1016/s0092-8674(04)00058-3

Grosso, A., Burger, M. G., Lunger, A., Schaefer, D. J., Banfi, A., and Di Maggio, N. (2017). It takes two to tango: coupling of angiogenesis and osteogenesis for bone regeneration. *Front. Bioeng. Biotechnol.* 5:68. doi: 10.3389/fbioe.2017.00068

Guicheux, J., Lemonnier, J., Ghayor, C., Suzuki, A., Palmer, G., and Caverzasio, J. (2003). Activation of p38 mitogen-activated protein kinase and c-Jun-NH2-terminal kinase by BMP-2 and their implication in the stimulation of osteoblastic cell differentiation. *J. Bone Miner Res.* 18, 2060–2068. doi: 10.1359/jbmr.2003.18.11.2060

Gundersen, H. J., and Jensen, E. B. (1987). The efficiency of systematic sampling in stereology and its prediction. *J Microsc* 147, 229–263. doi: 10.1111/j.1365-2818.1987.tb02837.x

Guo, J., and Wu, G. (2012). The signaling and functions of heterodimeric bone morphogenetic proteins. *Cytokine Growth Factor Rev.* 23, 61–67. doi: 10.1016/j.cytogfr.2012.02.001

Hak, D. J. (2007). The use of osteoconductive bone graft substitutes in orthopaedic trauma. *J. Am. Acad. Orthop. Surg.* 15, 525–536. doi: 10.5435/00124635-200709000-00003

Huang, G. Q., Yi, G. G., Wu, L. W., Feng, S. F., Wu, W., Peng, L., et al. (2018). Protective effect of histatin 1 against ultraviolet-induced damage to human corneal epithelial cells. *Exp. Ther. Med.* 15, 679–684.

Islam, M., Atmaramani, R., Mukherjee, S., Ghosh, S., and Iqbal, S. M. (2016). Enhanced proliferation of PC12 neural cells on untreated, nanotextured glass coverslips. *Nanotechnology* 27:415501. doi: 10.1088/0957-4484/27/41/415501

Kavanagh, K., and Dowd, S. (2004). Histatins: antimicrobial peptides with therapeutic potential. *J. Pharm. Pharmacol.* 56, 285–289. doi: 10.1211/0022357022971

Kneser, U., Schaefer, D. J., Polykandriotis, E., and Horch, R. E. (2006). Tissue engineering of bone: the reconstructive surgeon's point of view. *J. Cell Mol. Med.* 10, 7–19. doi: 10.1111/j.1582-4934.2006.tb00287.x

Kumar, P., Vinitha, B., and Fathima, G. (2013). Bone grafts in dentistry. *J. Pharm. Bioallied Sci.* 5, S125–S127.

Laurencin, C., Khan, Y., and El-Amin, S. F. (2006). Bone graft substitutes. *Expert Rev. Med. Devices* 3, 49–57.

Lee, J. J., Ho, M. H., and Hsiao, S. W. (2008). Immobilization of peptides by ozone activation to promote the osteoconductivity of PLLA substrates. *J. Biomater. Sci. Polym. Ed.* 19, 1637–1648. doi: 10.1163/156856208786440497

Liu, Q., Limthongkul, W., Sidhu, G., Zhang, J., Vaccaro, A., Shenck, R., et al. (2012). Covalent attachment of P15 peptide to titanium surfaces enhances cell attachment, spreading, and osteogenic gene expression. *J. Orthop. Res.* 30, 1626–1633. doi: 10.1002/jor.22116

Ma, D., Sun, W., Nazmi, K., Veerman, E. C. I., Bikker, F. J., Jaspers, R. T., et al. (2020). Salivary histatin 1 and 2 are targeted to mitochondria and endoplasmic reticulum in human cells. *Cells* 9:795. doi: 10.3390/cells9040795

Mcallister, B. S., and Haghighat, K. (2007). Bone augmentation techniques. *J. Periodontol.* 78, 377–396.

McGrath, J. L. (2007). Cell spreading: the power to simplify. *Curr. Biol.* 17, R357–R358.

Min, S. K., Kang, H. K., Jang, D. H., Jung, S. Y., Kim, O. B., Min, B. M., et al. (2013). Titanium surface coating with a laminin-derived functional peptide promotes bone cell adhesion. *Biomed. Res. Int.* 2013:638348.

Moujaber, O., and Stochaj, U. (2020). The cytoskeleton as regulator of cell signaling pathways. *Trends Biochem. Sci.* 45, 96–107. doi: 10.1016/j.tibs.2019.11.003

Oudhoff, M. J., Bolscher, J. G., Nazmi, K., Kalay, H., Van 'T Hof, W., Amerongen, A. V., et al. (2008). Histatins are the major wound-closure stimulating factors in human saliva as identified in a cell culture assay. *FASEB J.* 22, 3805–3812. doi: 10.1096/fj.08-112003

Oudhoff, M. J., Kroeze, K. L., Nazmi, K., Van Den Keijbus, P. A., Van 'T Hof, W., Fernandez-Borja, M., et al. (2009a). Structure-activity analysis of histatin, a potent wound healing peptide from human saliva: cyclization of histatin potentiates molar activity 1,000-fold. *FASEB J.* 23, 3928–3935. doi: 10.1096/fj.09-137588

Oudhoff, M. J., Van Den Keijbus, P. A., Kroeze, K. L., Nazmi, K., Gibbs, S., Bolscher, J. G., et al. (2009b). Histatins enhance wound closure with oral and non-oral cells. *J. Dent Res.* 88, 846–850. doi: 10.1177/0022034509342951

Pountos, I., Panteli, M., Lampropoulos, A., Jones, E., Calori, G. M., and Giannoudis, P. V. (2016). The role of peptides in bone healing and regeneration: a systematic review. *BMC Med.* 14:103. doi: 10.1186/s12916-016-0646-y

Shah, D., Ali, M., Shukla, D., Jain, S., and Aakalu, V. K. (2017). Effects of histatin-1 peptide on human corneal epithelial cells. *PLoS One* 12:e0178030. doi: 10.1371/journal.pone.0178030

Sun, P., Shi, A., Shen, C., Liu, Y., Wu, G., and Feng, J. (2020). Human salivary histatin-1 (Hst1) promotes bone morphogenetic protein 2 (BMP2)-induced osteogenesis and angiogenesis. *FEBS Open Bio* 10, 1503–1515. doi: 10.1002/2211-5463.12906

Sun, W., Shi, A., Ma, D., Bolscher, J. G. M., Nazmi, K., Veerman, E. C. I., et al. (2020). All-trans retinoic acid and human salivary histatin-1 promote the spreading and osteogenic activities of pre-osteoblasts *in vitro*. *FEBS Open Bio* 10, 396–406. doi: 10.1002/2211-5463.12792

Torres, P., Diaz, J., Arce, M., Silva, P., Mendoza, P., Lois, P., et al. (2017). The salivary peptide histatin-1 promotes endothelial cell adhesion, migration, and angiogenesis. *FASEB J.* 31, 4946–4958. doi: 10.1096/fj.201700085r

Van Dijk, I. A., Beker, A. F., Jellema, W., Nazmi, K., Wu, G., Wismeijer, D., et al. (2017a). Histatin 1 enhances cell adhesion to titanium in an implant integration model. *J. Dent Res.* 96, 430–436. doi: 10.1177/0022034516681761

Van Dijk, I. A., Ferrando, M. L., Van Der Wijk, A. E., Hoebe, R. A., Nazmi, K., De Jonge, W. J., et al. (2017b). Human salivary peptide histatin-1 stimulates epithelial and endothelial cell adhesion and barrier function. *FASEB J.* 31, 3922–3933. doi: 10.1096/fj.201700180r

Van Dijk, I. A., Nazmi, K., Bolscher, J. G. M., Veerman, E. C. I., and Stap, J. (2015). Histatin-1, a histidine-rich peptide in human saliva, promotes cell-substrate and cell-cell adhesion. *Faseb J.* 29, 3124–3132. doi: 10.1096/fj.14-266825

Wolfenson, H., Iskratsch, T., and Sheetz, M. P. (2014). Early events in cell spreading as a model for quantitative analysis of biomechanical events. *Biophys. J.* 107, 2508–2514. doi: 10.1016/j.bpj.2014.10.041

Wu, Z., Ou, L., Wang, C., Yang, L., Wang, P., Liu, H., et al. (2017). Icaritin induces MC3T3-E1 subclone14 cell differentiation through estrogen receptor-mediated ERK1/2 and p38 signaling activation. *Biomed. Pharmacother.* 94, 1–9. doi: 10.1016/j.biopha.2017.07.071

Xu, T., Levitz, S. M., Diamond, R. D., and Oppenheim, F. G. (1991). Anticandidal activity of major human salivary histatins. *Infect. Immun.* 59, 2549–2554.

Yan, Q. Y., and Bennick, A. (1995). Identification of histatins as tannin-binding proteins in human saliva. *Biochem. J.* 311, 341–347. doi: 10.1042/bj3110341

Yin, A., Margolis, H. C., Grogan, J., Yao, Y., Troxler, R. F., and Oppenheim, F. G. (2003). Physical parameters of hydroxyapatite adsorption and effect on candidacidal activity of histatins. *Arch. Oral Biol.* 48, 361–368. doi: 10.1016/s0003-9969(03)00012-8

Zhang, Q., Dong, H., Li, Y., Zhu, Y., Zeng, L., Gao, H., et al. (2015). Microgrooved polymer substrates promote collective cell migration to accelerate fracture healing in an in vitro model. *ACS Appl. Mater. Interfaces* 7, 23336–23345. doi: 10.1021/acsami.5b07976

Conflict of Interest: The authors declare that the research was conducted in the absence of any commercial or financial relationships that could be construed as a potential conflict of interest.

frontiers
in Bioengineering and Biotechnology

REVIEW
published: 03 November 2020
doi: 10.3389/fbioe.2020.549089

Biotechnology and Biomaterial-Based Therapeutic Strategies for Age-Related Macular Degeneration. Part I: Biomaterials-Based Drug Delivery Devices

Nahla Jemni-Damer[1,2†], Atocha Guedan-Duran[1,2,3†], María Fuentes-Andion[1,2], Nora Serrano-Bengoechea[1,2,4], Nuria Alfageme-Lopez[1,2,4], Felix Armada-Maresca[5], Gustavo V. Guinea[4,6,7,8], José Pérez-Rigueiro[4,6,7,8], Francisco Rojo[4,6,7,8], Daniel Gonzalez-Nieto[4,6,8], David L. Kaplan[3] and Fivos Panetsos[1,2,4*]

[1] Neuro-Computing and Neuro-Robotics Research Group, Complutense University of Madrid, Madrid, Spain, [2] Innovation Group, Institute for Health Research San Carlos Clinical Hospital (IdISSC), Madrid, Spain, [3] Department of Biomedical Engineering, Tufts University, Medford, MA, United States, [4] Silk Biomed SL, Madrid, Spain, [5] Ophthalmology Service, La Paz University Hospital, Madrid, Spain, [6] Center for Biomedical Technology, Universidad Politécnica de Madrid, Madrid, Spain, [7] Department of Material Science, Civil Engineering Superior School, Universidad Politécnica de Madrid, Madrid, Spain, [8] Biomedical Research Networking Center in Bioengineering, Biomaterials and Nanomedicine (CIBER-BBN), Madrid, Spain

OPEN ACCESS

Edited by:
Zhengwei Mao,
Zhejiang University, China

Reviewed by:
Timothy Charles Hughes,
Commonwealth Scientific and Industrial Research Organisation (CSIRO), Australia
PaYaM ZarrinTaj,
Oklahoma State University, United States

***Correspondence:**
Fivos Panetsos
fivos@ucm.es

†These authors have contributed equally to this work

Specialty section:
This article was submitted to Biomaterials, a section of the journal Frontiers in Bioengineering and Biotechnology

Received: 04 April 2020
Accepted: 06 October 2020
Published: 03 November 2020

Citation:
Jemni-Damer N, Guedan-Duran A, Fuentes-Andion M, Serrano-Bengoechea N, Alfageme-Lopez N, Armada-Maresca F, Guinea GV, Pérez-Rigueiro J, Rojo F, Gonzalez-Nieto D, Kaplan DL and Panetsos F (2020) Biotechnology and Biomaterial-Based Therapeutic Strategies for Age-Related Macular Degeneration. Part I: Biomaterials-Based Drug Delivery Devices. Front. Bioeng. Biotechnol. 8:549089. doi: 10.3389/fbioe.2020.549089

Age-related Macular Degeneration (AMD) is an up-to-date untreatable chronic neurodegenerative eye disease of multifactorial origin, and the main causes of blindness in over 65 years old people. It is characterized by a slow progression and the presence of a multitude of factors, highlighting those related to diet, genetic heritage and environmental conditions, present throughout each of the stages of the illness. Current therapeutic approaches, mainly consisting of intraocular drug delivery, are only used for symptoms relief and/or to decelerate the progression of the disease. Furthermore, they are overly simplistic and ignore the complexity of the disease and the enormous differences in the symptomatology between patients. Due to the wide impact of the AMD and the up-to-date absence of clinical solutions, the development of biomaterials-based approaches for a personalized and controlled delivery of therapeutic drugs and biomolecules represents the main challenge for the defeat of this neurodegenerative disease. Here we present a critical review of the available and under development AMD therapeutic approaches, from a biomaterials and biotechnological point of view. We highlight benefits and limitations and we forecast forthcoming alternatives based on novel biomaterials and biotechnology methods. In the first part we expose the physiological and clinical aspects of the disease, focusing on the multiple factors that give origin to the disorder and highlighting the contribution of these factors to the triggering of each step of the disease. Then we analyze available and under development biomaterials-based drug-delivery devices (DDD), taking into account the anatomical and functional characteristics of the healthy and ill retinal tissue.

Keywords: retinal pigment epithelium, Bruch's membrane, retina, biomaterials, neuroprotection, ocular drug delivery, nanocarriers, VEGF

INTRODUCTION

Age-related macular degeneration is a chronic neurodegenerative eye disease of multifactorial origin, characterized by the appearance of alterations in the central part of the retina, the macula. According to the WHO, there are 196 million cases worldwide and are expected to reach 288 million by 2040, making AMD one of the leading causes of irreversible loss of vision in people over 65 years in developed countries (Evans et al., 2004; Ferris et al., 2005; Lim et al., 2012; Garcìa and Martinez, 2013; IAPB Vision Atlas, 2017; World Health Organization, 2018). In the United States there are more than 2 million people affected by AMD and it is estimated that they will exceed 4 million by 2030 (Friedman et al., 2004; Klein et al., 2011; Friedman et al., 2012; Degeneration et al., 2017). In Western Europe, the IAPB estimates 4.8 million cases of AMD for 2020, making it the second most common cause of eye disease, preceded only by cataracts (Damián et al., 2006; Casado, 2009; Klein et al., 2011; Degeneration et al., 2017; Jeffries et al., 2017).

Despite the great research efforts dedicated in the development of AMD therapies, nowadays available treatments only are able to treat symptomatology and/or slowing down the progression of the disease.

In the present paper we briefly analyze the biomolecular and cellular processes responsible for the development of the AMD, and we review available and under development biomaterials-based drug-delivery devices (DDD) for possible treatments of disease.

NATURAL HISTORY

Risk Factors

The pathogenesis mechanisms of AMD are heterogeneous and not yet understood (Lacour et al., 2002; Ambati and Fowler, 2012; Kabiesz and Nowak, 2015; Michalska-Małecka et al., 2015), however, it is known that one of the main risk factor for AMD is aging (Lacour et al., 2002; Ardeljan and Chan, 2013; Daneault et al., 2016). Other risk factors are sex (higher rates in women), race (higher rates in the Caucasian population) and environmental factors that increase oxidative stress in the RPE, such as: blue light exposure, smoking, alcohol consumption, obesity, low antioxidant diet (e.g., lack of vitamins A and E, zinc, lutein and omega-3 fatty acids) as well as systemic factors associated with cardiovascular risks (Thornton et al., 2005; Michalska-Małecka et al., 2015). The risk of AMD is also increased by ocular factors such as macular pigment optical density, iris pigmentation (less risk in dark eyes), cataract surgery and high refractive errors (Michalska-Małecka et al., 2015). In addition, several genetic factors have been reported (**Table 1**).

Clinical Aspects

An outline of the stages involved in the disease, and the fundus images of affected patients are shown in **Figures 1**, **2**, respectively. The early stages of AMD are detected by the presence of drusen between the basal membrane of the RPE and the Bruch's membrane (BrM). Drusen are lipids, cellular and metabolic debris that originate in the RPE and surrounding tissues. In more advanced stages of the disease, these deposits may be also found between the RPE and the neuroretina. In both cases, metabolic abnormalities in the RPE cells is one of the causes of the formation of drusen (Winkler et al., 1999; Anderson et al., 2002; McConnell and Silvestri, 2005; Damián et al., 2006; Nowak, 2006; Jager et al., 2008). Depending on the number and extension of the drusen and the degree of the macular atrophy, AMD is customarily classified into three stages (**Table 2**): Early AMD; characterized by the presence of a few, small or medium-sized (<124 μm) drusen and minimal RPE cell alterations leading to some pigmentary anomalies (hypo- and hyper-pigmentation). Patients are normally asymptomatic. Intermediate AMD; characterized by the presence of one or more large (>124 μm) drusen, together with geographic atrophy that does not reach the central area of the macula. Patients are either asymptomatic or complain of decreased contrast sensitivity, abnormal scotopic vision or blurred vision while

---

Abbreviations: A2E, *N*-retinyl-*N*-retinylidene ethanolamine; AC-H, alginate-chitosan hydrogels; Ac-HA, acylated hyaluronic acid; AMD, age-related macular degeneration; ARPE-19, human retinal pigment epithelial cell line-19; AuNPs, gold nanoparticles; BRB, blood–retinal barrier; BrM, Bruch's membrane; CPP, cell penetrating peptide; D-AMD, Dry Age-Related Macular Degeneration; DDD, drug delivery device; DEACM, 7-(diethylamino) coumarin-4-yl] methyl carboxyl; Dex-SH, thiol-functionalized polysaccharide dextran; EMA, European Medicines Agency; EPC, poly (ether ester urethane); ESHU, poly (ethylene glycol)-poly (serinol hexamethylene urethane); FDA, US Food and Drug Administration Agency; IAPB, International Agency for the Prevention of Blindness; IL, interleukins; IVT, intravitreally; MBA, *N*, *N*′-methylenebisacrylamide; MEMS, microelectromechanical system; mPEG-PLGA, methoxy-poly (ethylene glycol) block-poly lactic-co-glycolic acid; mPEG-PLGA-BOX, methoxy-poly (ethylene glycol)-block-poly (lactic-co-glycolic acid); PCL, polycaprolactone; PDMS, polydimethylsiloxane; PDS, port delivery system; PEG, poly (ethylene glycol); PEG-DA, polyethylene glycol diacrylate; PEG-PLA, poly (ethylene oxide)-poly (D, L-lactic acid); PEG-PLLA-DA, poly (ethylene glycol diacrylate)-co-(L-lactic acid); PEG-PLLA-DA/NIPAAm, poly (ethylene glycol) -co- (L-lactic-acid) diacrylate/*N*-isopropylacrylamide; PEOzPCL-PEOz, Poly (2-ethyl-2-oxazoline)-b poly (ε-caprolactone)-b-poly (2-ethyl-2-oxazoline); PGA, polyglycolic acid; PLA, polylactic acid; PLGA, poly(lactic-co-glycolic) acid; PLLA, poly (L-lactic acid); PLLA/PLGA, poly (L-lactic acid)/poly (lactic-co-glycolic acid); PLV, phospholipid vesicles or liposomes; PNIPAAm, Poly *N*-isopropylacrylamide; PPG, poly (propylene glycol); PVA, poly vinyl alcohol; RPE, retinal pigment epithelium; TKI, tyrosine kinase inhibitor; TRL, clinical trials; UV, ultraviolet; VEGF, vascular endothelium growth factor; VS-HA, vinylsulfone functionalized glycosaminoglycan hyaluronic acid; HA-VS/Dex-SH, thiolated functionalized hyaluronic acid and thiolated dextran; W-AMD, Wet Age-Related Macular Degeneration; WHO, World Health Organization.

TABLE 1 | List of possible genes that have a determining influence on AMD (Klein et al., 2005; Rivera et al., 2005; Zareparsi et al., 2005; Khan et al., 2006; Nozaki et al., 2006; Ratnapriya and Chew, 2013; Michalska-Małecka et al., 2015; Sergejeva et al., 2016).

Polymorphisms of the complement factor H	CFH
Age-related maculopathy susceptibility 2	ARMS2/LOC 387715
Genes of the complement pathway	C2, CFB, C3 and CFI
Genes encoding inflammatory factors	C-X-C motif chemokine receptor 1 - CXCR1-, toll-like receptor 3 - TLR3-, TLR4, human leukocyte antigen -HLA-
Cholesterol/lipid metabolism	Lipase C - LIPC-, cholesteryl ester transfer protein - CETP-, ATP-binding cassette A-subclass - ABCA1-, ABCA4, apolipoprotein E -APOE-
Collagen	COL10A1 and COL8A1
Extracellular matrix	Cystatin C - CST3-, matrix metalloproteinase -MMP- 9-, tissue inhibitor of metalloproteinases-3 - TIMP3-, fibulin
Angiogenesis regulation-involved factors	Vascular endothelial growth factor A -VEGFA-

reading. Advanced AMD; either manifested in dry (D-AMD) or wet (W-AMD) form. D-AMD is characterized by the presence of large white or yellow drusen, the RPE atrophy and the photoreceptors' deterioration. Patients suffer from a decreased visual acuity and metamorphopsias. W-AMD is characterized by choroidal neovascularization, macular edema, aneurysms, hemorrhages, RPE and/or retinal detachment and photoreceptors death. Patients present important loss of visual acuity or total blindness, metamorphopsias and photopsia.

Pathogenesis

Most pathways and causes of the AMD are very well-established. However, this fact does not imply a straightforward identification of the AMD-triggering mechanisms. Such identification is challenging because of the multifactorial and extremely complex etiology of this disease: (I) It is not still clear if all of them have been identified, (II) None of them has been proved as the sole cause of the disease, and (III) Synergistic relations between causes that determine each phase triggering of the disease has not yet been identified. As we have already mentioned, AMD is the result of several molecular and cellular processes of different origins that interact with each other. Oxidative stress and inflammation are at the origin of neovascularization processes. Neovascularization, in turn, affects the function of the retina and causes additional inflammation, establishing a vicious circle that encourages the progress of AMD.

Oxidative Stress

Oxidative stress refers to an imbalance between the number of oxidants (reactive oxygen species) produced in a cell and the capacity of different scavenging enzymes and other molecules with anti-oxidant properties to reduce such an imbalance (Winkler et al., 1999; Beatty et al., 2000; Lin and Beal, 2006; Ambati and Fowler, 2012; Jarrett and Boulton, 2012; Cuenca et al., 2014; Hanus et al., 2015; Tang and Le, 2016). The antioxidant effect is achieved by a cell defense reducing process, carried out by superoxide dismutase, peroxidase, and catalase enzymes.

At early and intermediate stages (I, II) of the disease, key factors for the development of AMD are increased levels of oxidative stress and toxin accumulation in the retina in connection with dysfunction and atrophy of RPE cells responsible for the elimination of toxic accumulations (Winkler et al., 1999; Ambati and Fowler, 2012; Jarrett and Boulton, 2012). Toxic accumulations in the retina can form intracellular remains (lipofuscin and oxidized mitochondria), extracellular waste (drusen) or reactive oxygen species, all of them being some of the multifactorial causes of AMD (Ambati and Fowler, 2012). Among the different waste products being accumulating as the retina ages and as the disease progresses, we would like to underlie the accumulations of lipofuscin -a mixture of oxidized proteins, lipids, carbohydrates, and other types of bioorganic molecules- in the RPE, similar to the accumulation of β-amyloid and tau-protein in other neurodegenerative diseases. The accumulation of these molecules seems to be related to a possible vulnerability of RPE cells to oxidative stress (Crouch et al., 2015; Handa et al., 2019).

Lipids accumulation is considered one of the causes of the inflammation process as well as of the accumulation of complement factors which occurs later. Particularly important is the cholesterol because of the lack of recycling and disposal processes of this type of molecule (Handa et al., 2019). Another component present in lipofuscin is A2E, a natural product of the visual cycle, which accumulates as the disease progresses (Crouch et al., 2015). Closely related to smoking habits, cadmium is another AMD-triggering accumulated molecule. It is one of the toxic products present in tobacco, and it is accumulated in the retinas during the evolution of the disease (Wills et al., 2008).

Altered Cell Functions

Atrophy and disfunction of RPE cells appear in the intermediate phase. These cells are responsible for the elimination of toxic accumulations in the retina, so their atrophy provokes uncontrolled growth of such cumuli which, in turn, generates positive feedback to the previous mechanism. In the dry stage, toxin accumulation also appears within the cells of the RPE (Ambati and Fowler, 2012; Kinnunen et al., 2012; Tarallo et al., 2012).

Also, local inflammation and functional deficits of retinal glial cells impede the development of the molecular processes that are responsible for retinal tissue repair (Cuenca et al., 2014; Tang and Le, 2016). Glia has a strong contribution to AMD development. Under physiological conditions

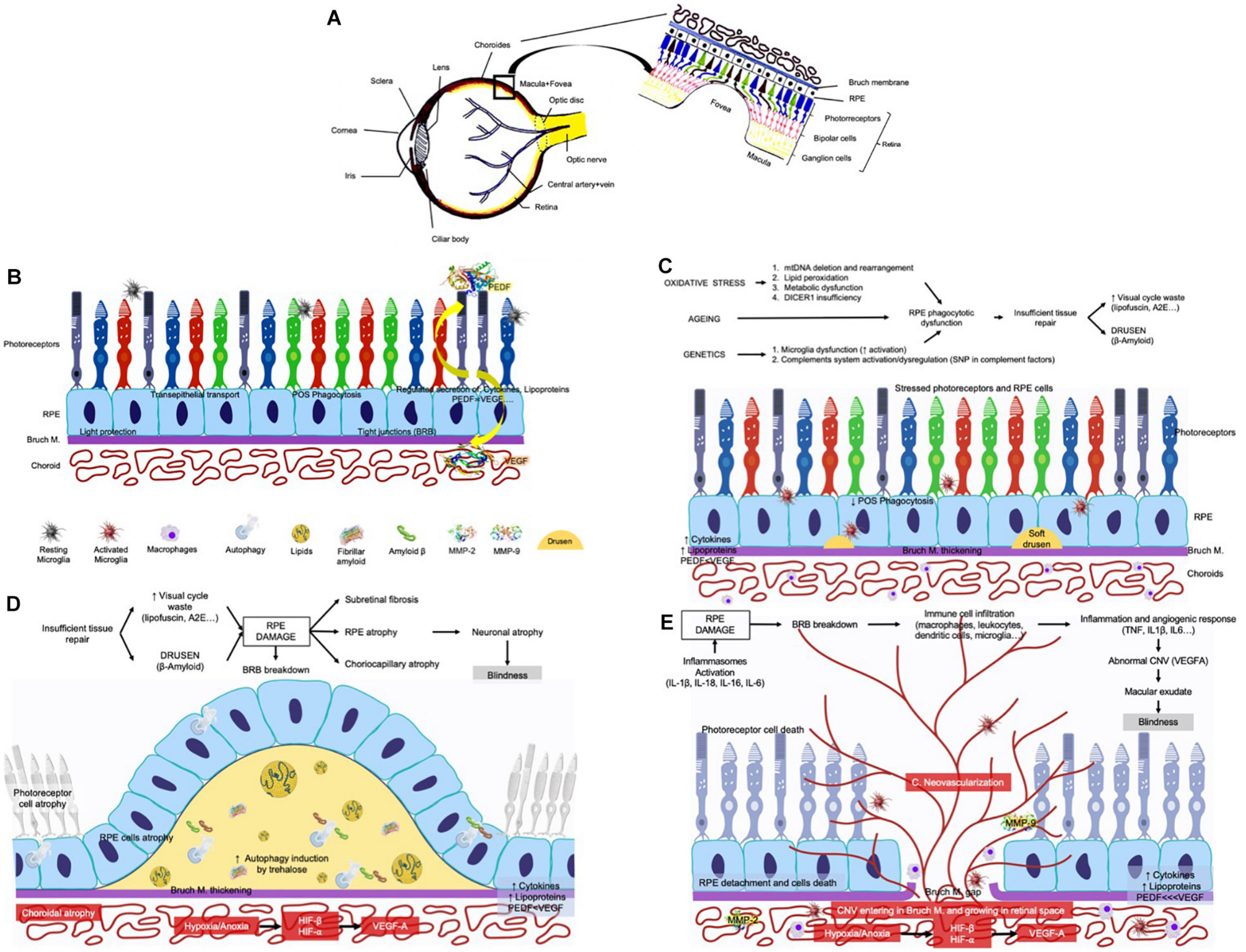

FIGURE 1 | Schematic representation of the eye and the stages of the AMD. **(A)** The eye and the retina. **(B)** Normal retina in a cross section of the eye where appear: the layer of the photoreceptors, the choroid, the RPE and the Bruch's membrane (BrM). The main functions of the normal RPE are: (1) transport of nutrients, ions, and water (2) absorption of light and protection against photooxidation, (3) re-isomerization of all-*trans*-retinal into 11-*cis*-retinal, which is a key element of the visual cycle, (4) phagocytosis of shed photoreceptor membranes, and (5) secretion of various essential factors for the structural integrity of the retina. POS, photoreceptors outer segment; BRB, blood–retinal barrier; PEDF, pigment epithelium-derived factor, the most potent inhibitor of angiogenesis in the mammalian eye; VEGF, vascular endothelial growth factor. VEGF is essential for development and maintenance of functionally efficient retinal vasculature as well as for integrity of the RPE, BrM, and choroidal endothelial cells. **(C)** Early and intermediate AMD phases in a cross section of the eye. Without apparent cause, debris from the RPE cells layer as well as from the surrounding tissues begin to accumulate between RPE and BrM forming clusters called drusen. **(D)** Progress of the dry AMD in a cross section of the eye where the clusters called drusen start growing in size and accumulate as the disease progresses. The accumulation of drusen and the degeneration of RPE provokes the beginning of photoreceptor's atrophy. **(E)** The progress of wet AMD. As drusen accumulate, they can cause inflammation. Inflammatory cells are then recruited by the retina, and these cells, together with the RPE begin to release vascular growth factors (mainly VEGF) that cause growth of the blood vessels. In this case, the degeneration is characterized by choroidal neovascularization, neovessels penetrating the BrM, presence of inflammatory cells, exudates of lipid content, hemorrhage, and the destruction of the RPE and photoreceptors (wet AMD).

microglia and macroglia (astrocytes and Müller cells) are in continuous communication, reporting on neural activity and maintaining immunomodulatory activity that is responsible for neuroprotection and regulation of cellular activity. In this way, the activation of microglial cells together with their immune response to the lesions contribute to the development and progression of the disease, provoking tissue degeneration, early changes in the pigmentation of the RPE and the formation of drusen (Polazzi and Monti, 2010; Marín-Teva et al., 2011; Cherry et al., 2014; Tang and Le, 2016; Vilhardt et al., 2017; Rathnasamy et al., 2019).

Finally, molecules damaged by oxidants and cellular deposits due to non-immune damage, induce macrophage infiltration and activation and deposition of complement fragments.

Neovascularization

In 10–20% of D-AMD cases, the pathology progresses and the subretinal space is invaded by blood vessels of choroidal origin (choroidal neovascularization) that break into the retinal tissue, provoke inflammation and macular edema, induce serum and/or hemorrhagic detachment of both, the RPE or the neural retina, and, eventually

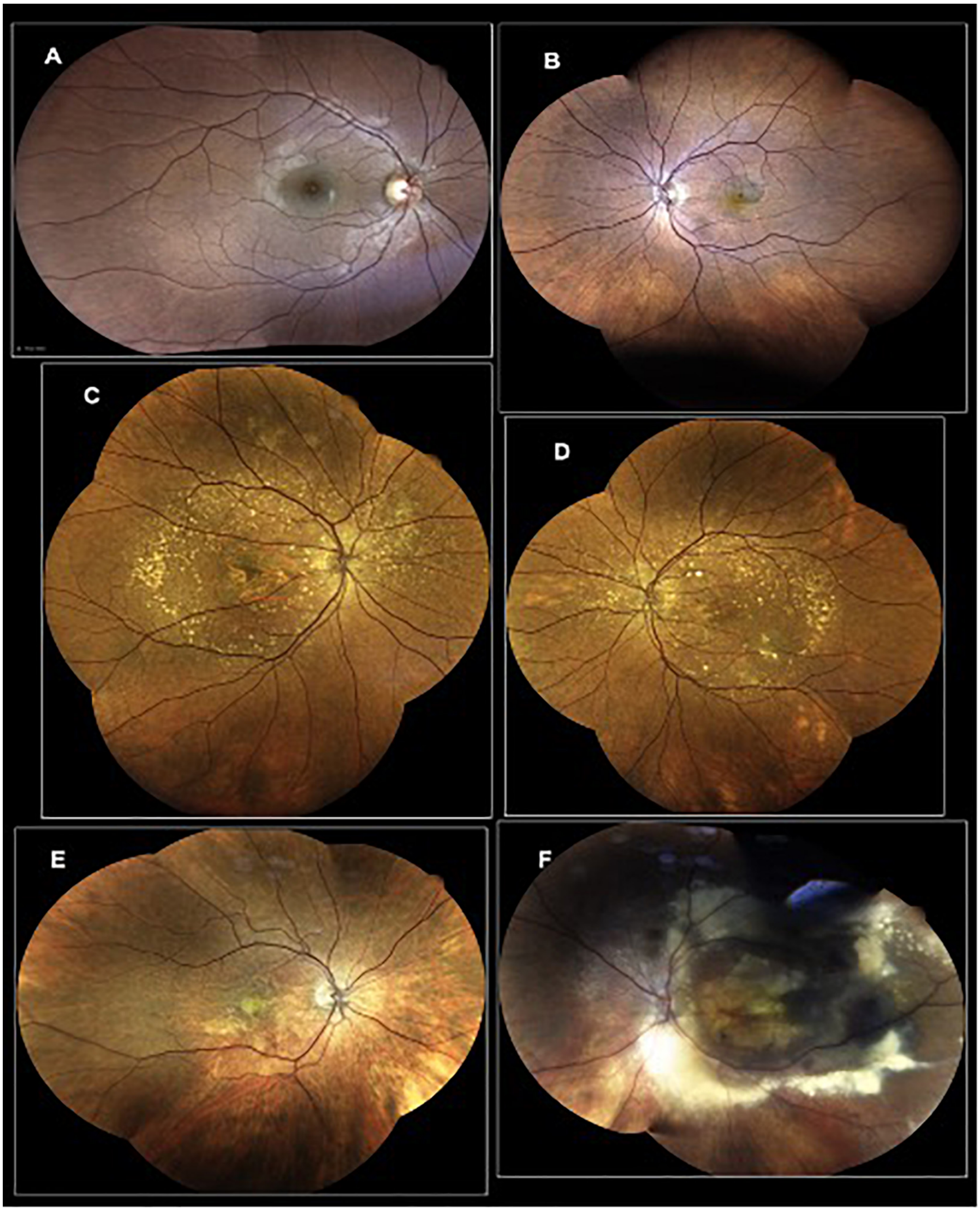

FIGURE 2 | Representative photographs of AMD-affected eyes. **(A)** Eye of a healthy subject; **(B)** AMD patient with macular hemorrhage and active exudation; **(C)** AMD patient with wide macular geographic atrophy and several druses in the back of the eye; **(D)** AMD patient with macular pigment changes, several druses as well as a macular hemorrhage secondary to an active neovascular complex; **(E)** patient with an active macular neovascular complex, secondary to an AMD; **(F)** AMD patient with an active AMD with a pseudo-tumoral lesion.

result in fibrovascular disciform scar-associated death of the photoreceptors (Jager et al., 2008; Ambati and Fowler, 2012). Neovascularization alters the geometry, the morphology and the structure of the retina at the macular level that leads to rapid and permanent loss of central vision. Such progression is called wet or exudative AMD (W-AMD). In the transition from D-AMD to W-AMD, the key factor is neovascularization of the retina (Ambati and Fowler, 2012; Cuenca et al., 2014; Tang and Le, 2016). Oxidative stress causes an increase of inflammatory and pro-angiogenic molecules in the subretinal space, which provokes rapid and uncontrolled angiogenesis in the choroid and an invasion of the subretinal space by neovascular vessels.

TABLE 2 | AMD stages: pathological characterization and clinical aspects.

Type of AMD	"Early" AMD	"Intermediate" AMD	"Advanced" AMD	
	No maculopathy	Dry/atrophic	Dry/atrophic	Wet/exudative
Incidence	–	–	80% cases	20% cases
Progression	Slow progression (lasting years)	Slow progression (lasting years)	Slow progression (lasting years)	Fast progression (lasting a few months)
Physiological changes/Clinical aspects	Small drusen (<124 μm). Minimal pigmentary anomalies.	One or more large drusen (>124 μm). Geographic atrophy not reaching the central area of the macula.	Large white or yellow drusen, cellular deterioration. Final Stage: Geographic atrophy, BrM thinning and disruption.	Choroidal neovascularization, Macular edema, aneurisms, hemorrhages, RPE and/or retinal detachment, photoreceptors death. Final Stage: Disciform scar, BrM thinning and disruption.
Impact on visual acuity	Normally asymptomatic	Normally asymptomatic, abnormal scotopic vision or blurred vision while reading	Decreased visual acuity and metamorphopsias	Important loss of visual acuity or total blindness, metamorphopsies and photopsia
Palliative Treatment	Regular medical observation for early detection	Antioxidant vitamin + zinc and mineral supplement	Antioxidant vitamin + zinc + mineral supplement. Complement factors' inhibitors (C3, C5). Visual cycle modulators (Fenretinide)	Pharmacological treatment (Anti-VEGF intravitreal injection). PDT – Photo-Dynamic Therapy with Verteporfin, Surgery

RPE, retinal pigment epithelium; CPZ, choriocapillary, pigmented zones; BrM, Bruch's membrane; VEGF, vascular endothelial growth factor.

Chronic inflammation has very important consequences in disease progression. This process triggers the secretion of pro-angiogenic factors by the RPE and other immune cells and also gives rise to further increases in oxidative stress. This increases due to the imbalance between generation and elimination of reactive-oxygen species that creates a toxic retinal microenvironment which eventually leads to the death of the pigment epithelium retinal cells through cell death mechanisms. Furthermore, due to their atrophy, retinal epithelium cells are no longer capable of activating/regulating certain biomolecules derived from the inflammatory process, such as complement factors C3a and C5a (chemotactic agents that cause an increase of leukocytes in the choroid) or some cytokines such as IL1 (Nozaki et al., 2006).

Neovascularization is triggered by increased expression of the vascular endothelial growth factor A (VEGF-A), in charge of increased vascular permeability and vascular endothelial cells recruitment, proliferation and migration. The increased number of macrophages attracted by lipofuscin, cause the secretion of proteolytic enzymes, such as collagenase and elastase (MMP2 and MMP9), which erode BrM, facilitating the penetration of the choroidal neovessels (Risau, 1997; Grossniklaus et al., 2002; Spaide, 2017). In addition, both, astrocytes and Müller cells participate in the development of neo-vessels, releasing angiogenic factors in response to pathogenic stimuli. Müller cells alter the blood-retina barrier, causing infiltration of several blood components including growth factors, cytokines, inflammatory factors and blood-derived immune cells; allowing the growing neo-vessels from the choroid to access the retina through the damaged Bruch's membrane and the RPE (Bringmann et al., 2009; Nash et al., 2011; Rathnasamy et al., 2019).

Age-related macular degeneration progression is often very slow in the early stages and accelerates in the wet phase. D-AMD usually takes about 5 years to evolve to the wet form (Nussenblatt and Ferris, 2007; Ardeljan and Chan, 2013; Fleckenstein et al., 2018). Although only 10–20% of patients develop W-AMD, this stage is the most important one because it is the origin of more than 80% of severe and very severe vision loss: approximately 40% of patients not correctly treated develop almost complete blindness.

Anti-VEGF Drugs

Even though there is no cure for neither form of AMD, there are several EMA/Food and Drug Administration (FDA)-approved therapeutic approaches focusing on symptomatology relief and on slowing down the progression of the disease, all of them exclusively dedicated to the "wet" form of the disease.

Among them, there are several drugs target directly or indirectly the vascular endothelial growth factor (VEGF). These drugs include pegaptanib, ranibizumab, aflibercept, and brolucizumab. Bevacizumab is another drug, non-FDA-approved for W-AMD treating, but it has been used off-label since 2005, with very good results (Martin et al., 2012). These drugs are IVT administered with monthly or bimonthly frequency (Freund et al., 2013) (anti-VEGF agents are summarized in **Table 3**). Frequent injections are necessary due to the limited volume of drugs that can be injected in the vitreous each time (Tabandeh et al., 2014) and their limited time of efficacy. The risk of bleeding, retinal detachment, endophthalmitis, cataracts, and infection increases with the number of IVT injections (Jager et al., 2004; Falavarjani and Nguyen, 2013).

An intent to overcome this problem was the development of new molecular drugs with different administration routes,

TABLE 3 | Drugs for AMD therapy.

Drug	Pegaptanib (Macugen)	Ranibizumab (Lucentis)	Bevacizumab (Avastin)	Aflibercept (Eylea)	Abicipar pegol (Allergan)	Brolucizumab (Novartis)
Characteristics	PEGylated synthetic RNA-based aptamer	Fragment of monoclonal humanized IgG1 antibody	Full monoclonal humanized IgG1 antibody	Recombinant fusion protein (VEGFR-1/2 fused with Fc portion of human IgG)	DARPin: Anti-VEGF designed ankyrin repeat protein	Humanized single-chain (scFv) antibody fragment
Inhibits	VEGF-A_{165} isoform	All VEGF-A isoforms	All VEGF-A isoforms	All VEGF-A isoforms, VEFG-B and PIGF	All VEGF-A isoforms	All VEGF-A isoforms
MW	50 kD	48 kD	149 kD	115 kD	~34 kD	26 kD
Half-life	8–14 days	6–10 days	4–5 days	7 days	>15 days	2–3 days
Doses	0.3 mg/dose every 2 months	0.5 mg/dose per month	1.25 mg/dose per month	2 mg/dose per month	2 mg/dose every 8–12 weeks	6 mg/dose every 8–12 weeks
Administration	Intravitreal	Intravitreal	Intravitreal	Intravitreal	Intravitreal	Intravitreal
Employment	Used	Used	Used	Used	TRL Phase III	TRL Phase III
FDA	2004	2006	2004*	2011	Declined	2019
EMA	2006	2007	2005*	2012	–	2020
Advantages	Suitable for all AMD types	Higher tissue penetration and affinity than Pegaptanib and Bevacizumab, more efficient than Pegaptanib	Low price. More efficient than Pegaptanib	Efficient up to 2.5 months after injection, Higher affinity than Ranibizumab, Efficient (inhibits more isoforms)	Smaller MW than Ranibizumab, Higher durability and affinity Ranibizumab, High specificity	Smaller MW than Ranibizumab, Higher durability and tissue penetration than Aflibercept and Ranibizumab, High specificity, Rapid systemic clearance
Disadvantages	Only inhibits one VEGF-A isoform Patients lose visual acuity	Fast pharmacokinetics. Only W-AMD. Expensive.	High MW, difficulties in penetrating the deepest layers of the eye, not approved for AMD, only for W-AMD	Only W-AMD, Expensive	Only W-AMD	Only W-AMD
Cost/dose (approx.)	Not anymore used	$1950 (United States) €700 (EU)	$50 (United States) €70 (EU)	$1850 (United States) €600 (EU)	–	$1850 (United States)

*IgG, immunoglobulin; VEGF, vascular endothelial growth factor; VEGFR, VEGF receptor; Fc, fragment crystallizable region; DARPin, designed ankyrin repeat proteins; scFv, single-chain variable fragment; PIGF, phosphatidylinositol-glycan biosynthesis class F protein; FDA, US Food and Drug Administration Agency; EMA, European Medicines Agency; TRL, clinical trials. *Approved for metastatic colorectal cancer. Used off-label for W-AMD since 2005.*

for example oral or topic, which are currently under test (McLaughlin et al., 2013; Jackson et al., 2017; Adams et al., 2018). Unfortunately, even though these routes are non-invasive (e.g., ocular drops), drug arrival to the targeted area, the posterior segment of the eye, is hindered by the several barriers the drugs have to cross (Patel et al., 2013), which severely limits drug bioavailability.

For this reason, work is currently underway to extend the IVT administration beyond 2 months by developing DDD (known also as drug delivery systems, or DDS) that allow a controlled release of the drug, widening its action window and thus lowering the number of interventions needed for AMD treatment per year. The ideal DDD should maintain effective levels of the drug for extended periods, reducing the necessary interventions.

Innovative DDD based on biomaterials in the form of hydrogels, liposomes, colloidal particles, nanoparticles, micelles, dendrimers, or combinations of either of them is currently being tested for the delivery of anti-VEGFs drugs to the posterior segment of the eye. Researchers are working with both, synthetic and natural materials, include hyaluronic acid (Awwad et al., 2019), dextran (Yu et al., 2019), Silk fibroin (Lovett et al., 2015), poly (lactic-co-glycolic acid) (PLGA) (Varshochian et al., 2015), poly(ethylene glycol) (PEG) (Yu et al., 2014), *N*-isopropyl acrylamide (NIPAAm) (Liu et al., 2019b), etc. Different materials have been modified or combined to create DDD sustainably releasing the drug through time, either right after injection, or on-demand, responding to precise external stimuli, such as light (Basuki et al., 2017; Jiang et al., 2019).

Age-related macular degeneration represents both a challenge and an opportunity for biologists, physicians and biomedical engineers, among others, since many of the processes that give rise to the disease could be controlled by new therapies employing advanced biomaterials-based carriers loaded with biomolecules or drugs that can be introduced into the eye. In the present paper we review the different biomaterial-based anti-angiogenic delivery systems developed and/or tested as AMD therapeutic strategies. We examine hydrogels, colloidal particles, nanoparticles, and implantable drug-delivery devices, with special attention to their capacity of preservation of drugs bioactivity within the biomaterial.

TECHNOLOGIES FOR CONTROLLED INTRAOCULAR DRUG-DELIVERY

As any other ocular disease treatment, AMD pharmacological therapy depends on the pharmacodynamics of the involved agents (molecular characteristics of the drug) which are conditioned by the specific tissue barriers (tear film barrier, corneal and conjunctival barrier, blood-aqueous barrier and finally the blood–retinal barrier-BRB), which in term determine the optimal administration route. Blood–retinal barrier (BRB) increase eye's resistance to exposure to foreign substances but also to pharmacological agents (Cunha-Vaz et al., 2011; Campbell and Humphries, 2013). There is little convection of molecules, since BRB has no cellular components and is selectively permeable to the most lipophilic molecules (Yasukawa et al., 2004; Kang-Mieler et al., 2020). To avoid BRB, medication to the anterior segment of the eye can be delivered topically and by sub-conjunctival or intracameral injections. In the case of the posterior segment, medication can be delivered topically, systemically, periocularly through the suprachoroidal space, and by IVT or subretinal injections (Kang-Mieler et al., 2014, 2020). As mentioned above, AMD treatments often require repeated IVT injections, whose frequency and duration depend on the course of the pathology in the individual patients, and the same occurs in all other eye degenerative diseases. Although certain benefits are obtained, the excessive repetition of the treatment leads to a worsening of the problem. To reduce that repeat burden we need minimally invasive pharma delivery systems, capable to maintain the necessary drug levels throughout several months or even years and this is precisely one of the actual research lines (Kang-Mieler et al., 2020).

Anti-VEGF molecules are proteins with fragile tertiary and quaternary structure, and they are very sensitive to environmental factors, like heat, pH changes, and proteolytic enzymes, so they require strong preservation measures along the administration route, to maintain intact their physical structure and, consequently, their pharmacological activity (Oo and Kalbag, 2016). Furthermore, since they cannot penetrate the structural barriers of the eye, they have to be IVT injected every 1–3 months (Edington et al., 2017).

Advances in biomaterial engineering and nanotechnology have fueled a growth of the research in prolonged DDD, made by biodegradable microparticles and nanoparticles, hydrogels or eye implanted devices, making them an attractive alternative to the frequent IVT injections (Kang-Mieler et al., 2020). Optimal biomaterials for sustained retinal drugs supply must meet the following properties [**Figures 3**, **4** (Seah et al., 2020)]:

- Be able to preserve the bioactivity of the molecule, protecting its tertiary and quaternary structure from denaturation, changes in pH or enzymatic degradation.
- Being able to deliver the molecules to the retina.
- Avoid raising intraocular pressure during administration. The biomaterial should be able to encapsulate a large amount of the drug in a minimal volume; in the case of an anti-VEGF, that means 0.5–2.0 mg of drug within a maximum volume of 0.05–0.1 ml.
- After inoculation, it should be able to maintain molecules' release for >1 month, thus avoiding frequent administrations.
- Be biocompatible and remain optically transparent within the vitreous humor to avoid any interference with vision.

Drug Delivery Devices (DDD)

Ganciclovir, for retinitis treatment by cytomegalovirus, was the first FDA-approved implantable DDD. With this implant, controlled release rates were obtained, which maintained active drug concentrations below toxic levels, while achieving high drug concentrations with limited systemic side effects (Yasukawa et al., 2004; Ebrahim et al., 2005). With the success of this implant,

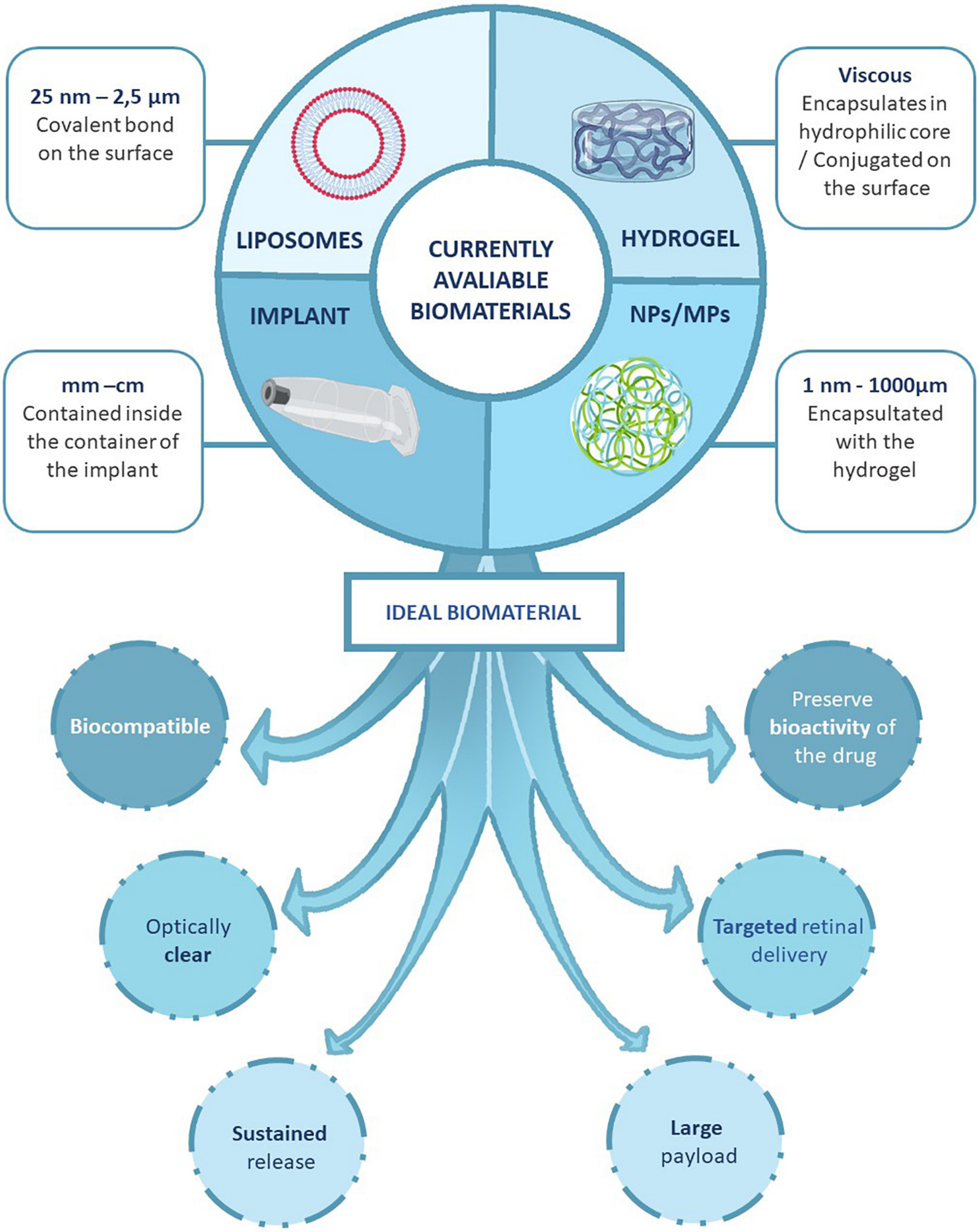

FIGURE 3 | Developing strategies for the sustained drug delivery to the retina. We describe the type of systems that can be used to encapsulate the different molecules can be classified based on the size. The nano-formulations allows the encapsulation of the drugs directly to a molecule that favors the administration and the survival of the substance. The bulk systems protect the drug and allows a progressive administration of the substance during longer periods of time. And, we also represent the ideal characteristics of a sustained drug delivery platform for AMD.

numerous biodegradable and non-biodegradable devices have been developed and many of them are in clinical use (Kang-Mieler et al., 2020). Implantable devices aim at providing structural/mechanical support for the localization of the drugs in the eyeball and to function as vehicles for controlled releases. Such DDD potentially locate therapeutic agents in the vitreous, lowering systemic exposure and, thus, reducing possible toxicity and/or side effects (Lim et al., 1999; Bourges et al., 2006; Kang-Mieler et al., 2020). They have many advantages over the more traditional administration methods since they improve the convenience, safety and efficacy of pharmacological therapies, bypass BRB and allow the sustained release of the drug directly

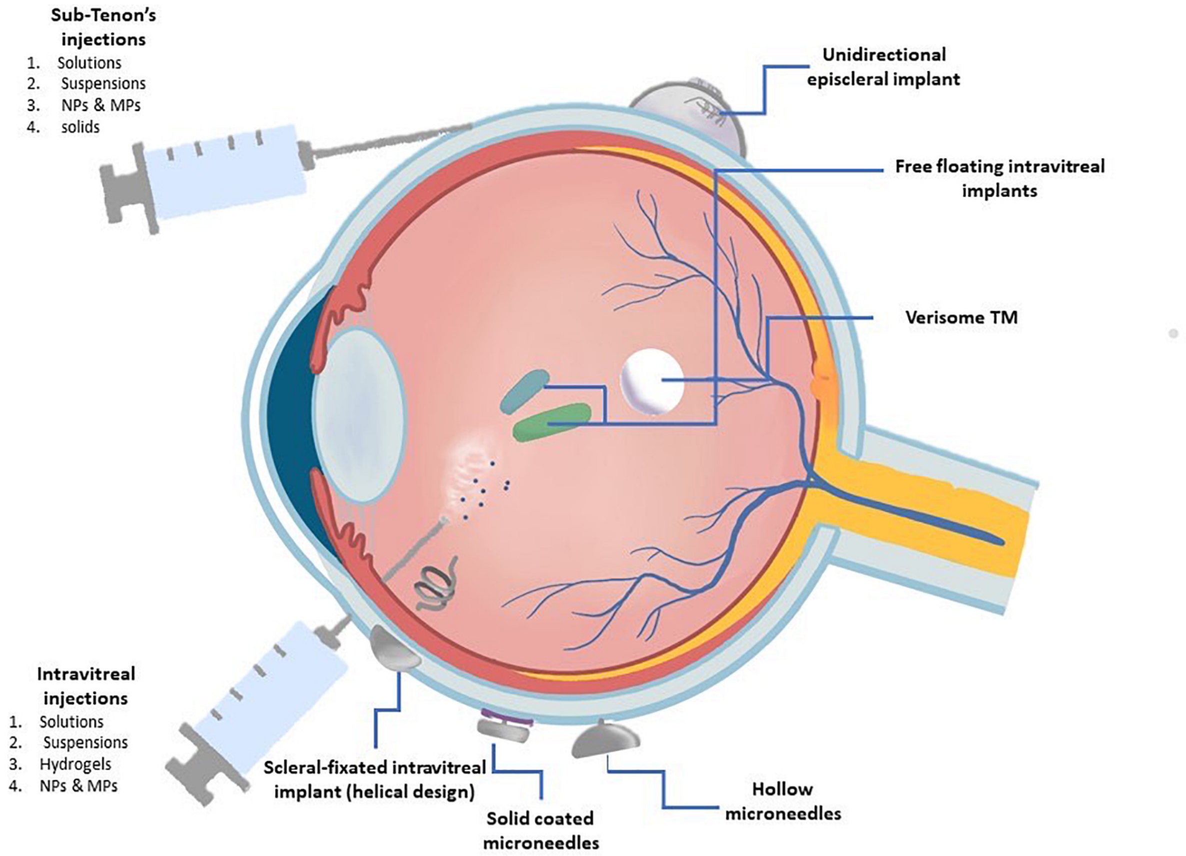

FIGURE 4 | Representation of the ocular drug delivery methods discussed on this review. The treatment of retinal diseases is challenging due to the anatomic barriers and physiological clearance mechanism of the eye. This figure represents the methods currently used in the clinical setting to treat posterior segments diseases classified by their administration route.

at the target site, while decreasing the risk of infection or retinal detachment.

Drug delivery devices can be either biodegradable [e.g., PCL, PLA, PGA, PLGA, among others; or non-biodegradable (e.g., silicone), the latter needing to be surgically removed post use]. Ordinarily, implants are placed in the vitreous cavity by surgical intervention, although newer models are placed periocularly (e.g., transsclerally or suprachoroidally) or by IVT injection (del Amo and Urtti, 2008; Gaudana et al., 2009; Patel et al., 2013; Journal et al., 2018). **Table 4** show currently available devices, the majority of them still in trial stages.

Intravitreally Injectable Devices

Durasert^{TM}, an EyePoint Pharmaceuticals (Watertown, MA, United States) is a 3.5 mm-long and Ø 0.37 mm solid polymer implant, IVT injectable with a small gauge needle and capable of up-to 3 years release of small molecules. It allows customization of release duration, linear release kinetics, and high drug loading (Callanan et al., 2008; Haghjou et al., 2011; Kang-Mieler et al., 2020). Durasert^{TM} gave origin to two different versions for the administration of Fluocinolone acetonide (Iluvien®) and Dexamethasone (Ozurdex®), as a plausible treatment for macular pathologies. Iluvien (Alimera Sciences, 2019) is a small non-biodegradable silicone implant to diffuse a low dose of fluocinolone acetonide (0.23–0.45 μg/day) for 18–36 months through a PVA capsule. The implant has to be removed surgically, it increases intraocular pressure, provokes cataract and is contraindicated for glaucoma patients (Jaffe et al., 2000; Kane et al., 2008; Ghasemi Falavarjani, 2009; Kuno and Fujii, 2010; Schmit-Eilenberger, 2015; Mandal et al., 2017; Alimera Sciences, 2019; ClinicalTrials.gov, 2020d,f). Iluvien was approved by the FDA in 2014 for the treatment of diabetic macular edema and by the United Kingdom Agency in 2012 for chronic diabetic macular edema-associated visual impairments (ILUVIEN)[1]. Ozurdex (Allergan) is a biodegradable poly lactic-co-glycolic acid (PLGA) solid implant which delivers dexamethasone. It permits long-lasting drug delivery, but it has serious collateral effects, like increased intraocular pressure, cataract formation and uveitis, due to the side effects of the corticosteroids and to the traction exerted to the vitreous humor. This system is contraindicated in patients with glaucoma. The device was approved by the FDA in 2009 and by the EMA in 2010 (Kuppermann et al., 2007; Haller

---

[1] ILUVIEN. *190 Micrograms Intravitreal Implant in Applicator - Summary of Product Characteristics (SmPC) - (emc).* Available online at: https://www.medicines.org.uk/emc/medicine/27636#AUTHDATE (accessed August 15, 2020).

TABLE 4 | Anti-VEGF intravitreally injectable and surgically implantable devices.

TABLE 4.1 | Anti-VEGF intravitreally injectable devices (AVEGF-IID).

Product	Active principle	Type	Description	Stage/TRL	Advantages	Disadvantages	Duration
Iluvien (Alimera Science) (Jaffe et al., 2000; Kane et al., 2008; Schmit-Eilenberger, 2015)	Fluocinolone acetonide	Silicone and PVA	Silicone and PVA membrane polyimide tube, encapsulating 0.19 mg fluocinolone acetonide	FDA approved (2014, for DME)	Long lasting drug delivery, drastically decreases injections frequency	Non-biodegradable, needs surgical removal, provokes high IOP and cataract, contraindicated in glaucoma	36 months
Ozurdex (Allergan) (Haller et al., 2010; Blumenkranz et al., 2011; Boyer et al., 2011; Bezatis et al., 2013; Querques et al., 2013; Whitcup and Robinson, 2015)	Dexamethasone	PLGA	PLGA drug delivery device containing micronized 0.7 mg dexamethasone	FDA approved (2009). EMA approved (2010)	Biodegradable	Contraindicated in presence of glaucoma, risk of implant migration to the anterior chamber	6 months
Brimonidine implant (Allergan) (Burke and Schwartz, 1996; Gao et al., 2002)	Brimonidine tartrate	Polymer matrix	Polymer matrix containing Brimonidine tartrate (alpha-2-selective adrenergic receptor agonist)	Phase II	Biodegradable	Limited amount of drug	6 months
ENV705 (Envisia Therapeutics) (Benjamin et al., 2014; Navratil et al., 2014)	Bevacizumab	PLGA	PLGA-made implant containing bevacizumab/trehalose; fabricated with PRINT technology	Pre-clinical rabbit	Biodegradable	Release kinetics often not ideal, risk of migration due to lack of fixation	6 months
Nano-porous film device (Desai and Bernards, 2014; Lance et al., 2015)	Ranibizumab	PCL nanopori	PDMS-made PCL/nanoporous film	Pre-clinical rabbit	Biodegradable	No serious side effects	4 months

Biomaterials-based solid implantable degradable devices. Principal characteristics, advantages and disadvantages. PVA, poly vinyl alcohol; IOP, increased intraocular pressure; PLGA, polylactic-co-glycolic acid; FDA, US Food and Drug Administration Agency; DDD, drug delivery device; DME, diabetic macular edema; PCL, polycaprolactone; PDS, port delivery system; PDMS, polydimethylsiloxane.

TABLE 4.2 | Surgically implantable devices.

Product	Active principle	Type	Description	TRL	Advantages	Disadvantages	Duration
PDS (Genetech/For Sight Vision 4) (Campochiaro et al., 2019)	Ranibizumab	PDS	*Trans*-scleral implantable device	Phase II	Long-lasting delivery, minimal to no burst or lag time, constant zero-order release, release controlled by diffusion	Non-biodegradable, surgically implanted and removed	Refillable
Microelectro-mechanical system (MEMS-based devices) (Lo et al., 2009; Humayun et al., 2014)	Any drug	PDMS	Flexible cannula forming a refillable reservoir, implantable sub-conjunctival	Humans	Variable delivery rates, reduces complications with repeated intraocular injections	Non-biodegradable, surgically implanted and removed	Refillable 3 m study

Biomaterials-based solid implantable refillable devices. Principal characteristics, advantages and disadvantages. PDS, port delivery system; PDMS, polydimethylsiloxane.

et al., 2010; Kuno and Fujii, 2010; Blumenkranz et al., 2011; Boyer et al., 2011; Bezatis et al., 2013; Querques et al., 2013; Whitcup and Robinson, 2015; Mandal et al., 2017).

Brimonidine (Allergan) is a biodegradable polymer matrix containing Brimonidine tartrate (alpha-2-selective adrenergic receptor agonist). This molecule is normally used in glaucoma but recent studies suggest it also provides protection of retinal cells from degeneration in AMD geographic atrophy (Burke and Schwartz, 1996; Gao et al., 2002; Ghasemi Falavarjani, 2009; Campochiaro et al., 2012; Lai, 2013). Brimonidine is efficient and lacks toxicity, however, the amount of drug that can be loaded is limited because of the size of the molecule. Additionally, the hydrophilic nature of the molecule limits the sustained-release possibilities. The drug has achieved Phase II clinical trials (ClinicalTrials.gov, 2020c).

ENV705 (Envisia Therapeutics) is an IVT injectable biodegradable implant made with PGA and fabricated with PRINT technology, which provides a sustained release of Bevacizumab for up to 6 months. This implant is capable of releasing effective therapeutic drug concentration, but the release kinetics are often not ideal. The drug is currently in preclinical trials (Benjamin et al., 2014; Navratil et al., 2014).

Zordera is a Ø 10 mm biodegradable nano-porous cylindric device for long-lasting sustained release of Ranibizumab. Made by sandwiched PCL films with millions of porous of the molecule size of the drugs (Bernards et al., 2012; Schlesinger et al., 2015). The device is IVT implanted by a syringe (Desai and Bernards, 2014; Lance et al., 2016). The device is still in preclinical phase (Radhakrishnan et al., 2017; Mandal et al., 2018).

Surgically Implantable Devices

Subconjunctivally implantable pumps are versatile and affordable alternatives, permitting long-lasting, sustained and well controlled drug releases that avoid the need for repeated surgical interventions. Pumps consist of a small reservoir connected to a cannula which is inserted through the sclera into the eye, and they are empowered with a valve to control both, number of the doses and doses volume, thus optimizing and personalizing drug release profiles. They are refillable through a thin needle.

Port Delivery Systems, PDS (Genentech/For sight Vision4, Inc.) is a semipermeable, non-biodegradable refillable transscleral port delivery system, surgically implanted through a 2–3 mm incision and fixed to the sclera to avoid migration. The device has been used for long-lasting sustained release of Ranibizumab. Because of the sclera surface this device permits easy and low invasive transscleral drug delivery with increased absorption rate. However, serious adverse effects were reported, including endophthalmitis and persistent vitreous hemorrhage (Mainardes et al., 2005; Shah et al., 2010; Kim et al., 2017; Mandal et al., 2017; Campochiaro et al., 2019). Phase II clinical trials showed that 15 months recharge frequency with drug concentration of 100 mg/ml have equivalent visual and anatomical effects to patients treated with monthly IVT ranibizumab injections (Campochiaro et al., 2019). Also, implant insertion and reloading procedures were well tolerated by patients. The system is now under Phase III trials, expecting to reach 3 years implants with recharges every 6 months: PORTAL (NCT03683251) and ARCHWAY (NCT03677934) trials, expected to end in January 2022 and April 2022, respectively (ClinicalTrials.gov, 2020b,e).

Replenish® is a sub-conjunctival refillable, non-biodegradable MEMS for long-lasting sustained drug release. It is a sub-conjunctively placed PDMS 0.6 ml refillable reservoir with a flexible cannula and a valve. The cannula is inserted through the sclera and fixed with sutures (Lo et al., 2009). It is refillable up to 10 times with a thin needle. Replenish, Inc., was planning to start Clinical trials for AMD treatment (Lo et al., 2009; Gutiérrez-Hernández et al., 2014; Humayun et al., 2014).

Injectable Hydrogels

To overcome some of the limitations of implantable DDD and to avoid surgeries, injectable hydrogels have emerged as an alternative for IVT drug administration using different biomaterial formats.

A hydrogel is a three-dimensional network of hydrophilic polymers that can swell in water and retain a large amount of H_2O molecules while maintaining its solid state (Li and Mooney, 2016). Despite the high solubility of hydrophilic polymers (in water), hydrogels resist dissolution and even interact favorably with H_2O molecules, because their hydrophilic polymer chains form a strongly crosslinked network (Li and Mooney, 2016). Their high H_2O percentage (>10% of the total weight) make them easy-to-manipulate, flexible materials. Furthermore, their porous structure makes them suitable for encapsulation of drugs, biomolecules, or even stem cells. Hydrogels are highly biocompatible and can undergo a volume phase, or gel-sol phase transition, either spontaneously after injection (*in situ*-forming hydrogels) or triggered by specific external stimuli (changes of pH, temperature, pressure, light intensity, etc.) (Bahram et al., 2016; Chang et al., 2019). Injected into the eye, hydrogels provide both, structural support and long-term sustained release of the incorporated drugs, molecules or stem cells' secretome (Alexander et al., 2014; Kirchhof et al., 2015a; Su et al., 2015; Yu et al., 2015; Seah et al., 2020).

The employed polymers can be natural, synthetic or hybrid. Natural polymers (cellulose, chitosan, alginate, hyaluronic acid, silk fibroin, etc.) are degraded by the enzymes of the body, so their biodegradation rate cannot be adjusted (Lovett et al., 2015; Yu et al., 2015). Synthetic polymers (PCL, PEG, PLGA, PLLA, NIPAAm, etc.) properties such as porosity, swelling capacity, stability, mechanical resistance and biocompatibility can be adjustable by varying their chemical composition and preparation methods. Within this group, we find both biodegradable polymers such as PEG (Anwary et al., 2018), PLGA (Arranz-Romera et al., 2019), etc. which can be degraded by the action of biological factors such as changes in pH, increase in temperature, enzymatic activity or by the immune system itself; and non-biodegradable polymers such as PDMS (Pirmoradi et al., 2011; Humayun et al., 2014). Hybrid polymers display the characteristics of their individual components (Yu et al., 2015, 2019; Osswald and Kang-Mieler, 2016; Awwad et al., 2019). Incorporation of therapeutic agents (e.g., anti-VEGF drugs) to a hydrogel strongly depends on the crosslinking of gel's polymers. Molecules incorporation to a covalently crosslinked gel requires chemical actions, which often result in modification and/or inactivation of the bioactive molecule as well as in increased toxicity (Kang Derwent and Mieler, 2008; Matanović et al., 2014; Awwad et al., 2018, 2019; Seah et al., 2020). On the other side, molecules incorporation to a non-covalently crosslinked gel needs an *ad hoc* tuning of the manufacturing parameters, so important characteristics of the gel (e.g., gelation time and diffusion rate) become difficult to predict (Seah et al., 2020).

Injectable hydrogels allow reducing drug administration frequency and, even more important, avoid eye procedures-associated complications, including blurred vision or irritation However, hydrogels require IVT administration, show poor penetrability and specificity, and present difficulties for correct sterilization (Alexander et al., 2014; Kirchhof et al., 2015a; Su et al., 2015; Yu et al., 2015; Galante et al., 2018; Seah et al., 2020).

Several hydrogels have been used for drug delivery in different non-ocular pathologies, with favorable results (Sharpe et al., 2014). Despite their theoretical advantages, hydrogels for the ocular route face serious difficulties to meet safety, tolerability, manufacturability, degradability, and facility of administration requirements, while maintaining the bioactivity and clinical effectiveness of the desired drug (Chang et al., 2019). To our knowledge, no hydrogel has been approved by FDA or EMA and only one of them has reached clinical trials stage (Ocular Therapeutix), all other being still in a preclinical stage, **Table 5**).

Using a bioabsorbable hydrogel (OTX-TKI), Ocular Therapeutix (Bedford, MA, United States) developed a TKI implant, capable to supply TKI for up to 12 months (Jarrett et al., 2017). OTX-TKI is under Phase I clinical study in Australia, to test its safety, durability and tolerability (Eyewire News, 2020). The same company in collaboration with Regeneron (Tarrytown, NY, United States), is developing an injectable version of OTX-IVT to provide sustained aflibercept release for 4–6 months (OTX-IVT, 2020).

Poly (2-ethyl-2-oxazoline)-b poly (ε-caprolactone)-b-poly (2-ethyl-2-oxazoline) (PEOzPCL-PEOz) copolymer-based thermosensitive biodegradable hydrogels for prolonged releases of bevacizumab were shown to be biocompatible *in vitro* and *in vivo* with a human retinal pigment cell line and in a lagomorph model, respectively, for 2 months (Wang et al., 2012).

Hydrogels of PEG synthesized via thiol-maleimide reaction from PEG-Mal and PEG-SH, loaded with bevacizumab did not generate cytotoxicity after 7 days of incubation and maintained a sustained drug release for 14 days *in vitro*, reaching 70% release in this time interval (Yu et al., 2014). Maintenance of drug bioactivity was not tested.

Long-term bevacizumab release from a ESHU hydrogel *in vivo* was well tolerated, without inflammation and without intraocular pressure alterations in rabbit retinas for 9 weeks. ESHU maintained continuous release with no initial burst and drug concentrations 4.7 times higher than free bevacizumab injections (Rauck et al., 2013).

A thermosensitive poly (*N*-isopropylacrylamide) hydrogel (PNIPAAm) made by crosslinking PNIPAAm with poly (ethylene glycol) diacrylate (PEG-DA) or poly (ethylene glycol diacrylate)-co-(L-lactic acid) (PEG-PLLA-DA) was capable of locally releasing bevacizumab or ranibizumab for 1 month, without inducing long-term effects on retinal function (Turturro et al., 2011; Drapala et al., 2014).

Silk fibroin hydrogels were studied for bevacizumab sustained delivery in a rabbit model for 3 months showing higher concentrations in day 90 than those in day 30 after direct injections and the gels started to biodegrade after 3 months (Lovett et al., 2015).

Yu et al., 2015 assessed the biocompatibility and release of bevacizumab of an *in situ* gelling hydrogel made by thiolated functionalized hyaluronic acid and thiolated dextran (HA-VS/Dex-SH) maintained relevant therapeutic concentrations, over 100 times higher than the freely injected drug, 6 months after injection and without inducing pathologies, in a lagomorph model (Yu et al., 2015). In primates, no cytotoxic effects were observed 21 weeks post-injection (Yu et al., 2019).

A thermosensitive hydrogel of methoxy-poly (ethylene glycol)-block-poly (lactic-co-glycolic acid) (mPEG-PLGA-BOX) released bevacizumab, with no burst release nor cytotoxicity and maintaining drug activity during 35 days in a rabbit model (Hu et al., 2019).

NIPAAM and Ac-HA hydrogel combined with bevacizumab was performed in the PK-Eye^{TM} model, an *in vitro* ocular flow model developed by Awwad et al. (2015) that simulates the times protein clearance at the posterior chamber of the human eye. This hydrogel formulation bevacizumab release for at least 50 days, maintaining a therapeutic dose in the posterior cavity of the eye model and with zero order kinetics post 5 days (Awwad et al., 2019).

Bevacizumab and aflibercept have also been encapsulated in a multiblock EPC thermoresponsive hydrogel consisting of PEG, poly (propylene glycol) (PPG) and poly(ε-caprolactone) (PCL) (Xue et al., 2019). Both anti-VEGF were released similarly and almost linearly for up to 40 days, remaining bioactive in a HUVECs cellular line model *in vitro*, as well as inhibiting vessel outgrowth in rat *ex vivo* choroidal explants. In an *in vivo* retinal neovascularization rabbit model, aflibercept anti-angiogenic bioactivity was maintained for 28 days and animals showed a reduction of vascular leakage.

An injectable polysaccharide cross-linked hydrogel (Alginate-Chitosan) was developed for Bevacizumab delivery and tested *in vitro*. It achieved a 3-days sustained with 4-h initial bursting (Xu et al., 2013).

Diels-Alder hydrogels synthesized and functionalized with [furyl (-Fur) and maleimide groups (-Mal)] for bevacizumab delivery showed >6 weeks *in vitro* release (Kirchhof et al., 2015b).

Colloidal Particles

Colloidal systems (liquid suspensions with nanometric carriers) including nanosuspensions, micro/nanoparticles, liposomes, dendrimers and hydrogels have been postulated as promising alternatives for AMD therapy. They are micro/nanosized particles, based on either natural or synthetic materials and composed of highly stable lipophilic, hydrophilic or amphiphilic molecules, loaded with drug molecules (Kandatsu et al., 2005). These particles improve drugs solubility and act as reservoirs for long-term sustained release or for enhanced transport of proteins

TABLE 5 | Injectable hydrogels.

Product	Active principle	Description	Model	Gelation time	Advantages	Disadvantages	Release
Hyaluronic acid/Dextran (Yu et al., 2019)	Bevacizumab	VS-HA chemically crosslinked to a Dex-SH *in situ*-forming hydrogel	Monkey	30 s	Non-toxic, transparent, biocompatible, good mechanical strength, easy functionalization	Initial burst release	5–6 months
Silk Fibroin (Lovett et al., 2015)	Bevacizumab/Ranibizumab	Crosslinked silkworm silk fibroin	Rabbit	Modifiable	Non-toxic, biocompatible, good mechanical strength, controllable degradation, sustained drug release rate	Initial burst release	∼90 days
ESHU (Rauck et al., 2013)	Bevacizumab	PU coupled with PEG	Rabbit	3 m at 37°C	Thermo-responsive polymer, no initial burst release, no significant inflammation	–	9 weeks
OTX-TKI (Jarrett et al., 2017)	Tyrosine kinase inhibitor	Micronized TKI particles in hydrogel	Rabbit	–	Bioabsorbable, safe, sustained drug release and tolerability	–	24 weeks
(PEOzPCL-PEOz) copolymer (Wang et al., 2012)	Bevacizumab	(PEOzPCL-PEOz) copolymer thermosensitive biodegradable hydrogels	Rabbit	60 s	Reversible sol-gel transition, intraocular biocompatibility, extended drug release rate	Low initial drug concentration (loading dose)	8 weeks
mPEG-PLGA-BOX (Hu et al., 2019)	Bevacizumab	Thermosensitive polymer mPEG-PLGA with BOX as linker	Rabbit		No initial burst release. Biocompatibility and reduction of angiogenesis.	–	5 weeks
EPC (Xue et al., 2019)	Bevacizumab/Aflibercept	Polymer synthetized from PEG, PPG and PCL diol using HMDI as coupling agent	Rabbit	–	Thermo-responsive polymer.	Initial burst release	4 weeks
PNIPAAm/PEG-DA (Alexander et al., 2014; Drapala et al., 2014)	Bevacizumab/Ranibizumab	Cross-linking PNIPAAm with PEG-DA thermosensitive hydrogel.	Rat	Once injected	Synthetic, biocompatible, thermo-responsive polymer, good mechanical strength	Initial burst release. No improvement	<4 weeks
(PEOzPCL-PEOz) copolymer (Wang et al., 2012)	Bevacizumab	(PEOzPCL-PEOz) copolymer thermosensitive biodegradable hydrogels	*In vitro*	60 s	Thermosensitive reversible sol-gel transition. 90% viability of cultured cells	Low initial drug concentration (loading dose)	8 weeks
NIPAAm/Ac-HA (Awwad et al., 2019)	Bevacizumab	Cross-linking NIPAAm gel with Ac-HA	*In vitro*	–	Thermo-responsive polymer, sustained drug release	Initial burst release	7 weeks
EPC (Xue et al., 2019)	Bevacizumab/Aflibercept	Polymer synthetized from PEG, PPG and PCL diol using HMDI as coupling agent	*In vitro*	–	Thermo-responsive polymer. Pharmaco-hydrogel inhibits the growth of angiogenic cells	Initial burst release	6 weeks
Diels-Alder hydrogel (Kirchhof et al., 2015b)	Bevacizumab	PEG macro-monomer chemically crosslinked by Diels-Alder reaction	*In vitro*	14–171 m	Good mechanical strength, controllable degradation, sustained drug release rate	Initial burst release	<6 weeks
PEG thiol/maleimide (Yu et al., 2014)	Bevacizumab	*In situ*-gelling hydrogel chemically cross-linked by thiol-maleimide reaction	*In vitro*	95–210 s	Predictable degradation, modifiable release rate by crosslinking density	Initial burst release	2 weeks

(Continued)

TABLE 5 | Continued

Product	Active principle	Description	Model	Gelation time	Advantages	Disadvantages	Release
PEG thiol/maleimide (Santhanam et al., 2016)	Bevacizumab	*In situ*-gelling hydrogel chemically cross-linked by thiol-maleimide reaction	*In vitro*	90–120 s	Predictable degradation	Initial burst release	2 weeks
mPEG-PLGA-BOX (Hu et al., 2019)	Bevacizumab	mPEG-PLGA with BOX as linker	*In vitro*	–	No initial burst release, thermo-responsive polymer. Non-toxic		<2 weeks
Alginate-Chitosan (Xu et al., 2013)	Bevacizumab	Polysaccharides cross-linked hydrogel	*In vitro*	2 m at 37°C	Transparent, tailored degradation rate, modifiable release rate	Initial burst release	3 days
Hyaluronic acid/Dextran (Yu et al., 2015)	Bevacizumab	VS-HA chemically crosslinked to a Dex-SH *in situ*-forming hydrogel	*In vitro*	30 s	Non-toxic, transparent, and cytocompatibility. 99%Cytocompatibility of hydrogel	Initial burst release	1 day

In vitro and in vivo trials of hydrogels-integrated injectable drugs. VS-HA, vinylsulfone functionalized glycosaminoglycan hyaluronic acid; Dex-SH, thiol-functionalized polysaccharide, dextran; PNIPAAm, Poly N-isopropylacrylamide; PEG-DA, poly ethylene glycol diacrylate; Ac-HA, acrylated hyaluronic acid; PEG, poly(ethylene glycol); mPEG-PLGA-BOX, methoxy-poly (ethylene glycol)-block-poly (lactic-co-glycolic acid); ESHU, poly(ethylene glycol)-poly-(serinol hexamethylene urethane); PU, polyurethane; EPC, poly(ether ester urethane); PPG, poly(propylene glycol); PCL, poly(ε-caprolactone); PEOzPCL-PEOz, poly (2-ethyl-2-oxazoline)-b poly (ε-caprolactone)-b-poly (2-ethyl-2-oxazoline). APRPG, liposomes modified with Ala-Pro-Arg-Pro-Gly. SU5416, 3-([2,4-dimetilpirrhol-5-il] metilidenil)-indolin-2-ona. SFN, silk fibroin nanoparticles. Bev-MVL, Bevacizumab-loaded multivesicular liposomes. OCCNP, oligochitosan coated cerium oxide nanoparticles.

through the eye barriers (Hora et al., 1990; Herrero-Vanrell and Refojo, 2001; Medina et al., 2009; Li, 2012; Varshochian et al., 2013, 2015; Yandrapu et al., 2013; Ye et al., 2015; Imperiale et al., 2018). Such particles are usually composed of PLA, PLLA, PLGA, PEG, PEG-DA, alginate-chitosan and PLV and are injected IVT; being completely degradable, they do not require subsequent extraction surgery (Mi et al., 2002; Kang-Mieler et al., 2020).

Micro/nanoparticles capacity for tissue penetration, protection capabilities against proteolysis and prolonged drug-release periods depend on the characteristics of their external layer, which in turn depend on the polymer these micro/nanoparticles are made of Sakurai et al. (2001), Sahoo et al. (2008), Honda et al. (2013) and Seah et al. (2020).

Fluorescein-labeled polystyrene micro/nanoparticles studies in a lagomorph model showed that IVT microparticles are transported to the vitreous cavity and to the trabecular meshwork, while nanoparticles are transported to the retinal tissue (Sakurai et al., 2001).

Micro/nanoparticles provide several benefits as drug carriers for posterior ocular drug delivery, but the main one is that they are capable of increasing drug penetration across the conjunctival and corneal epithelia by temporarily altering the tight junctions when administered topically (Hans and Lowman, 2002). In addition to their ability to increase *trans*-corneal penetration, the ability to improve solubility of lipophilic drugs may play an important role in increasing IVT half-life and thus bioavailability of lipophilic drugs. This approach also provides sustained release of the encapsulated molecules. In cases with low encapsulation efficiency where it is difficult to establish or control the conditions of drug release, the systems can be modified for tissue-specific uptake and to protect the therapeutic molecules from degradation. Despite its advantages, there are limitations associated with formulation stability, high initial burst release, protein denaturation, clearance by the immune system, control of particle size, control of drug release rate and large-scale manufacturing of sterile preparations (Sakurai et al., 2001; Hans and Lowman, 2002; Kang-Mieler et al., 2020; Seah et al., 2020). Still, many of these particles are being evaluated preclinically for the administration of drugs into the posterior segment of the eye as carriers of anti-VEGF factors for AMD.

Intravitreal injections of PLGA microspheres-encapsulated bevacizumab in a lagomorph model showed higher concentrations in the vitreous and aqueous humor than of freely-injected drug, and a maintenance of their pharmacological activity for over 42 days (Ye et al., 2015). However, authors did not determine drug's ability to reach the target tissue, neither its long-lasting effects.

PLGA-albumin nanoparticles for sustained supply of bevacizumab, made from a double water-in-oil-in-water emulsion showed bioactive IVT concentrations (>500 ng/ml) for 8 weeks after IVT injection in a rabbit model (Varshochian et al., 2015). More recently, PLGA nanospheres-encapsulated fenofibrate showed full biocompatibility and attenuation of both, VEGF expression and vascular tissue disruption for up to 60 weeks after IVT injection in a rat W-AMD model, a diabetic retinopathy rat model and a very low-density lipoprotein receptor knockout (Vldlr–/–) mouse model (Qiu et al., 2019).

Despite PLGA's good biodegradability and biocompatibility, one of the main problems is that PLGA degeneration causes an accumulation of lactic and glycolic acid in the sphere, which provokes a decrease of the pH and a consequent denaturation of the drug (Liu et al., 2019a,b; Qiu et al., 2019). A possible solution to this problem is the manufacture of monomer conjugated PLGA microspheres which prevent rapid degradation of the biomaterial and preserve the biocompatibility of the drug for a longer time.

Silk fibroin abilities as nanocarrier for anti-VEGF particles has been tested by encapsulating bovine serum albumin (BSA, macromolecular model with similar weight to the antibodies that are usually used in AMD) showing a prolonged retention compared to free BSA solution and better distribution in *in vitro* studies with ARPE-19 and *in vivo* studies in a rabbit model (Yang et al., 2019).

The biggest limitation of the use of micro/nanoparticles is the small amount of drug that they are able to encapsulate inside, therefore, prolonged treatments require frequent IVT injections that can cause discomfort to the patient and even eye damage during the procedure (Seah et al., 2020).

Another colloidal system used today are liposomes (Abrishami et al., 2009; Shah et al., 2010; Patel et al., 2013; Davis et al., 2014; Ameeduzzafar et al., 2016), vesicles consisting of a phospholipid bilayer membrane incorporating water-soluble and lipid-soluble drugs in aqueous and lipid phases, respectively. Compared to nanoparticles, liposomes usually have low immunological reactivity or toxicity since phospholipids are easily metabolized once the liposome is degraded (Seah et al., 2020).

These vesicles provide sustained release of drugs with decreased frequency of dosing. The systems also allow for modifications of the rate of drug release and the ability to provide stimulus-sensitive drug release. However, these vesicles present some limitations including blurred vision after injection of the liposomal suspension into the vitreous body, low reproducibility, instability of the macromolecules during production, variable size distribution and storage conditions specific to the composition of the drug and liposome.

Numerous animal studies have shown that IVT injected liposomal drugs release their aqueous contents slowly, protecting the intercalated substances from degradation and clearance. This process avoids the toxicity from the high peak concentrations normally seen after injection of free drug. Therefore, the liposomal drug release formulations may lead to greater clinical efficacy by maintaining therapeutic concentrations for longer time intervals. Liposomal applications in the posterior segment provide longer clearance times, less toxicity, and specific delivery.

Furthermore, the surface of the liposomes can be functionalized to improve penetration through the different tissues and to reach the target tissue. In a study by Davis et al. (2014), the liposome surface was modified using annexin-A5 with the aim of improving the administration of Bevacizumab through the epithelial barriers of the cornea (Davis et al., 2014). This study verified that annexin functionalization allowed liposomes to reach the retina more easily (however, the results still require improvement since only 1% of the dose reached the target).

In other studies, such as Honda et al. (2013) in which the effects of Semaxanib-SU5416 (VEGF receptor proteinTKI, an angiogenesis inhibitor) were evaluated, it was demonstrated that the use of liposomes allowed to decrease choroidal neovascularization (CNV) activity in animal model compared to the control group. That is, liposomes allowed the drug to reach the target tissue more easily than the drug alone (Honda et al., 2013).

Studies have shown that the release of anti-VEGF drugs in liposomes can be maintained for more than a month without causing cytotoxicity (Mu et al., 2018). In the latter study, they demonstrated that changing the aqueous/lipid ratio improved the encapsulation efficiency of the drug (Bevacizumab) in Brown-Norway rats with laser-induced choroidal neovascularization. IVT liposome-treated eyes with bevacizumab in rabbits maintained high drug levels for >56 days.

The limitations that exist in the use of liposomes as a drug transport system must be taken into account. One of the main limitations of this colloidal system is the lack of studies that exist today. Drug release from liposomes to target tissue is highly dependent on environmental conditions such as pH or enzyme activity (Villegas et al., 2017). Because there are so many factors that can affect liposome stability, it is difficult to predict drug release. Therefore, although liposomes have structural characteristics that allow effective administration of the drug and degradation of the transport system that does not cause toxicity, a more exhaustive study of the environmental factors that cause the degradation of liposomes is necessary.

A slightly different device is Verisome IBI-20089 (Icon bioscience), actually in Phase I/II clinical trials (ClinicalTrials.gov, 2020a), consisting of a biodegradable non-polymer injectable liquid (carbonates, tocopherols, and citrate ester) that forms small spherules once injected into the vitreous. It has been formulated to deliver intravitreal injections of triamcinolone acetonide (TA) in combination with ranibizumab in W-AMD for >1 year, showing good safety and efficacy (Lim et al., 2015).

Table 6 summarizes some of the colloidal systems (micro/nanoparticles and liposomes) for AMD therapies.

Compound Particles-Hydrogels Drug Delivery Technologies

Despite the already discussed advantages of injectable polymeric micro/nanoparticles, one of their main limitations is locating them at the injection site of the eye. A normal eye can eliminate microparticles in 50 days and vitrectomized ones in 14 days (Morirero et al., 1991). As a solution to limit the movement of these particles, the use of injectable particles-hydrogels has been proposed, to provide a prolonged and localized release of the drug after injection (Kang-Mieler et al., 2017). These compound systems offer advantages over each of the two platforms separately, by reducing the initial explosion and extending the release time (Osswald and Kang-Mieler, 2015, 2016).

TABLE 6 | Injectable colloidal particles.

Product	Active principle	Format	Description	Model	Advantages	Disadvantages	Release
Verisome IBI-20089 (Icon Bioscience) (Lim et al., 2015)	Triamcinolone acetonide + Ranibizumab	Small spherules	DDD that forms small spherules once injected into the vitreous	Phase I/II	Biodegradable, decreases injection frequency	Damages the choroid and destroys retinal layers (at high densities)	<12 months
PLGA-Albumin NPs (Varshochian et al., 2015)	Bevacizumab	NP	Fabricated by w/o/w double emulsion in presence of albumin as a stabilizer. Particle size, 197 nm	Rabbit	Stable, sterile	Initial burst release	16 weeks
PLV (Abrishami et al., 2009)	Bevacizumab	Liposome	EPC-Chol and DPC-Chol liposomes formed by dehydration and rehydration followed by freeze drying	Rabbit	Prolonged drug residency	No demonstrated efficiency	6 weeks
Anexine 5 on PLV (Davis et al., 2014)	Bevacizumab	Peptide-conjugated liposome	PC-PS-Chol-Toc liposomes made by dehydration and rehydration, coated with annexin. Particle size 100 nm	Rabbit	Enhanced bioavailability. Transscleral delivery	No demonstrated efficiency	1 week
PLGA MPs (Ye et al., 2015)	Bevacizumab	MP	Fabricated by solid-in-oil-in-hydrophilic oil. Particle size, 2–7 μm	Rabbit	–	Initial burst release	>2 weeks
SFN (Yang et al., 2019)	BSA	NP	Regenerated silk fibroin	Rabbit	Accumulated distribution and extended retention	Loading capacity might be limited by its physico-chemical properties	1–2 weeks
Bev-MVL (Mu et al., 2018)	Bevacizumab	Liposome (multivesicular)	Bev-MVLs with high encapsulation efficiency. Prepared by double emulsification technique	Rabbit/rat	Sustained release. High retention time in the vitreous	–	2 months
PLGA-NPs (Qiu et al., 2019)	Fenofibrato	NP	NP are prepared using an emulsification method with PLGA and fenobibrato fenofibrate. Particle Size, 250 nm	Mouse/rat	Sustained therapeutic effects. Prolonged release. Potentially reduced injection frequency	Need to optimize effective drug loading of Pheno-NP and release kinetics	32 months
APRPG (Honda et al., 2013)	SU5416	Liposome	Liposomes were prepared using the thin-film hydration method	Rat	Significant reduction of the CNV area	VEGF inhibition could affect normal and angiogenic vessels	1–2 weeks
Silica-based hydrogel (William et al., 2012)	Bevacizumab	NP	NP synthesized by electrochemical etching and oxidation of silicon wafer in hydrofluoric acid. Particle size, 100 nm	*In vitro*	Drug release by matrix erosion, can deliver any type of drug	Initial burst release, hydrogel formed in a syringe	~12 months
PEG-PLLA-DA/NIPAAm (Liu et al., 2019b)	Ranibizumab	PLGA microspheres in NIPAAm crosslinked with PEG-PLLA-DA	Microparticles are synthesized and charged by double emulsion solvent evaporation technique	*In vitro*	Thermo-responsive polymer, modifiable release rate, sustained release	Initial burst release	6 months
Alginate-Chitosan/PLGA (Xu et al., 2013)	Bevacizumab/Ranibizumab	PLGA microspheres encapsulated into AC-H	Synthesis of different systems of hydrogel for drug release	*In vitro*	Biocompatible, controlled degradation rate, sustained drug release	Initial burst release	<6 months
PEG-PLA (Li, 2012)	Bevacizumab	MP	Fabricated by Double emulsion. Particle size, 2-10 um	*In vitro*	–	Initial burst release	3 months
mPEG-PLGA (Pan et al., 2011)	Bevacizumab	MP	mPEG-PLGA-made multiblock copolymer hydrogel by 2,2-bis 2-oxazoline. Particle size, 2–10 μm	*In vitro*	–	Initial burst release	1 month

(Continued)

TABLE 6 | Continued

Product	Active principle	Format	Description	Model	Advantages	Disadvantages	Release
PLGA (Pandit et al., 2017)	Bevacizumab	PLGA nanoparticles covered with chitosan/alginate	Bevacizumab loaded CS-coated PLGA NPs was prepared by double emulsion solvent evaporation method	*In vitro*	Stable and sustained drug release	–	3 days
OCCNP (Wang et al., 2018)	Cerium Oxide	NP/Alginate-hydrogel	Cerium oxide- oligo-chitosan NP/alginate-hydrogel that have antibacterial and anti-inflammatory functions	*In vitro*	Strong antioxidant, O2 radical absorption. Anti-inflammatory. VEGF inhibition	–	2 days

*In vitro and in vivo trials of colloidal particles-integrated injectable drugs. PLGA, polylactic-co-glycolic acid; AC-H, alginate-chitosan hydrogels; MP, microparticles; NP, nanoparticles; mPEG-PLGA: methoxy-poly (ethylene glycol)block-poly lactic-co-glycolic acid; EPC-Chol, egg phosphatidylcholine-cholesterol; DPC-chol, 1,2 dipalmitoyl-sn-glycero-3-phosphocholine; Ac-HA, acrylated hyaluronic acid; PEG, poly(ethylene glycol); PEG-PLLA-DA/NIPAAm, poly(ethylene glycol)-co-(*L*-lactic-acid) diacrylate/N-isopropylacrylamide; BSA, bovine serum albumin.*

A thermosensitive biodegradable hydrogel-microspheres fabricated by suspending, poly (lactic-co-glycolic acid) (PLGA) microspheres with ranibizumab within a poly (ethylene glycol)-co-(L-lactic-acid) diacrylate/*N*-isopropylacrylamide (PEG-PLLA-DA/NIPAAm) hydrogel, achieved a controlled release of ranibizumab and aflibercept for 6 months (Liu et al., 2019b,c), while efficacy was tested *in vivo* in a rodent choroidal neovascularization model (Osswald et al., 2017; Liu et al., 2019c).

The anti-angiogenic and anti-inflammatory properties of cerium oxide nanoparticles coated with oligo-chitosan in alginate hydrogel were studied in an *in vitro* model of human retinal pigment epithlium-19 (ARPE-19) and umbilical endothelial cell lines. Sustained nanoparticles release and controlled hydrogel degradation with strong antioxidant properties and reduction of apoptosis were observed for 2 months. Furthermore, in the same model, they suppress bacterial lipopolysaccharides-induced inflammatory responses, inhibit VEGF expression and reduced cell apoptosis (Wang et al., 2018).

Externally Light-Triggered Drug Release Hydrogels or Nanoparticles

Extending the half-life of the therapeutic agent can reduce dosage, costs and injections frequency. Alternative strategies to increase the half-life of anti-angiogenic drugs after IVT injection without losing effectiveness include nanotechnology-based DDD, for example hydrogels, liposome, microsphere, micro/nanoparticles, etc. (Fuchs and Igney, 2017; Machinaga et al., 2018; Nayak and Misra, 2018). Nevertheless, none of them allows an external control of the timing of the release.

To overcome this drawback several photoactive biomaterials have been developed which release the drug after being exposed to an external ultraviolet (UV) or visible light stimulus. Light-responsive systems can be classified into three categories according to the light-triggering mechanism for drug release: (1) photochemical, where light breaks a covalent bond (2) photoisomerization, where light induces conformational changes, and (3) photothermal, where light produces heat after photoexcitation to selectively affect thermally modulated components of the system (Linsley and Wu, 2017). This is a well-known technology, mainly tested in cancer therapy, translated to posterior segment eye diseases due to the transparency of the cornea, which allow easy light stimulation of the back of the eye. Nevertheless, very few studies have been dedicated to AMD treatment (**Table 7**).

We have identified two systems with photochemical and two with photothermal activation of drug release for AMD treatment.

A nanoparticle storage platform for on-demand drug delivery, based on a UV ultra-degradable polymer, which releases drug after a brief exposure to 365 nm UV light (Fomina et al., 2010; Huu et al., 2015). This polymer contains a fraction of *o*-nitrobenzyl in each monomer, responding to the absorption of UV by degrading into fragments and small molecules through quinone-methide rearrangements. The system releases drug for >30 weeks post-injection and authors reported light-induced release of Nintedanib, an angiogenesis inhibitor, as well as

TABLE 7 | *In vitro* and *in vivo* trials of light triggered biomaterials-integrated drugs.

Product	Active principle	Wavelength (nm)	Description	Model	Advantages	Disadvantages	Release
NP/UVSP (Huu et al., 2015)	Nintedanib	365	PLGA NP in light-degradable polymer DMN-based	Rat	Biocompatible NP and irradiation safe for the eye. Non-cytotoxic	Initial burst release	<30 weeks
NP-CPP (Wang et al., 2019)	Doxorubicin	400	PEG-PLA chains modified by CPP and binded to DEACM	Mouse	Biocompatible and irradiation safe for the eye. Non-cytotoxic	Initial burst release. >90% of the drug is released in 48h	1 week
Agarose-AuNPs (Basuki et al., 2017)	Bevacizumab	400–500	Polymer-functionalized gold nanoparticles in agarose hydrogel	*In vitro*	Modifiable release rates by changes in hydrogel composition	–	15 days (9 cycles)
NIPAM-AuNR (Jiang et al., 2019)	Doxorubicin and curcumin	808	AuNRs in polymerizated NIPAM with nanogels as crosslinker	*In vitro*	Lineal release of the drug in each irradiation cycle	–	70 months (10 cycles)

*NP, nanoparticles; UVSP, ultraviolet-sensitive polymer; PLGA, polylactic-co-glycolic acid; DMN, 4,5-Dimethoxy-2-nitrobenzyl; NP-CPP, nanoparticles modified with cell penetrating peptide; PEG-PLA, poly(ethylene oxide)-poly(*D, L*-lactic acid) block copolymer; DEACM, 7-(diethylamino)coumarin-4-yl]methyl carboxyl; AuNPs, polymer-functionalized gold nanoparticles; NIPAM, N-Isopropylacrylamide; AuNR, gold nanorod.*

suppression of choroidal neovascularization in rats for >10 weeks (Huu et al., 2015).

A nanoparticles-based DDD which, injected intravenously, can release the drug into the eye by 400 nm light activation was developed and tested by Wang et al. (2019). Nanoparticles (NP-CPP) were composed of poly (ethylene oxide)-poly (D, L-lactic acid) (PEG-PLA) chains modified with Tat-C peptide (CPP), that allows their entry into cells. CPP is reversely binded by a covalent bond to a DEACM group that prevents entry into cells. After the exposure to light, DEACM releases CPP, which migrates from the center of the nanoparticle to the surface, activating it. Toxicity and biocompatibility of the system were tested both, *in vitro* and *in vivo*. Irradiation of the eyes after intravenous injection provoked NP-CPP accumulation in mouse neovascular lesions. Doxorubicin-loaded NP-CPP significantly reduced the size of the neovascular lesion, the majority of the drug being released 48 h post-irradiation.

Chromophores coupled with a thermally responsive drug-releasing materials gave origin to two different photothermal DDD (Basuki et al., 2017; Jiang et al., 2019).

The former is based on a photo-thermal interaction of polymer-coated AuNPs within an agarose hydrogel. Stimulation by 400–500 nm-light radiation increases local temperature which in turn causes a reversible softening of the hydrogel matrix and a consequent release of the drug. Release profile is adjusted by modifying AuNPs and agarose concentrations, light intensity and exposure time. Bevacizumab was showed to maintain affinity for binding to recombinant human VEGF-165 up to 15 days *in vitro* (Basuki et al., 2017).

A dual drug release system, acting by near-infrared light (808 nm) stimulation was developed and tested by Jiang et al. (2019). Nanogel-crosslinked thermosensitive hydrogels, embedded in gold nanorods (AuNR) were prepared by the precipitation polymerization of poly (*N*-isopropylacrylamide) (NIPAAm) with MBA as crosslinker and the hydrogels were prepared by radical polymerization of NIPAM with nanogels as crosslinker. Two types of drugs are encapsulated, one in the nanogel (doxorubicin) and the other in the AuNR-enriched hydrogel (curcumin). NIR light provokes a heating effect in the AuNRs, which induces a volume phase transition of the hydrogel. As a result, the drugs are released. In the first cycle, 19% of curcumin and 10% of doxorubicin were released. Curcumin is released first, and doxorubicin is released second (Jiang et al., 2019).

Drug Administration

Non-invasive drug administration methods represent a very worthy objective but in clinical ophthalmology this is very long-term challenge. For eye treatment, these methods need to strongly improve tissue penetrability and targeting while reducing drug dispersion levels. As stated above, the structural complexity of the eye is a serious obstacle, especially when drugs have to reach the back segment. On the other side, eye barriers exclude several types of treatments, like the topically administered ones.

Anti-VEGF IVT injections, although less aggressive against drugs' structural conformation, necessary for the effectiveness of their therapeutic principles, are not efficient. This is due to the small percentage of the drug capable of reaching the target tissue, mainly due to its dispersion and a rapid deterioration in the aqueous medium. Furthermore, IVT injections are associated with multiple complications, like infections, which can cause permanent loss of vision (Mason et al., 2008; Bhavsar et al., 2009). Consequently, multiple injections (monthly or bimonthly) are necessary to treat chronic eye diseases, which ultimately increases infection risks, patients' discomfort and caregiving complexity.

Biomaterial-based drugs administration to extend the time between injections is the most promising approach for short-term and mid-term clinical solutions. In recent years, the use of biomaterials has been widely studied and characterized as a transport vehicle for drug administration in the eye, especially for non-biodegradable implants, colloidal systems and hydrogels. Solid carriers improve visual recovery speed, with lower vision loss risk, and avoiding multiple injections-associated side effects. However, they can increase intraocular pressure as well as to induce local adverse effects and cataract progression due to traction exerted on the vitreous humor. Solid carriers have also an inherent risk of tissue damage. As mentioned above, an ideal biomaterial for drug delivery must be able (i) to preserve physical and chemical integrity of the transporting substance (ii) to prevent its dispersion in the eye tissues/media (iii) to make it reach the target tissue and (iv) to encapsulate a large amount of drug in the smallest possible volume.

Retention of Bioactivity Within Drug Delivery Depots

Most of the molecules employed in AMD treatment formulations are sensible to external factors such as temperature, pH, and enzymatic activity (Oo and Kalbag, 2016), and, like conventional drugs formulations, they exhibit chemical stability problems. If we focus on macromolecules, such as proteins, chemical stability challenges pairs with physical stability problems related to their tertiary structure, the maintenance of which is determines the bioactivity of the molecule (Rakesh, 2019). Chemical stability is disrupted when covalent bonds are broken and/or created in the molecule; in contrast, physical degradation occurs when non-covalent forces required to maintain the secondary, tertiary, or quaternary structure of the molecule are broken (Deb et al., 2018). Encapsulating drugs on biomaterials avoid some of these stability problems, which prevents an initial exposure of the drug to the external environment. Drug encapsulation has other benefits like the controlled drug release and decreased need for new doses administration. Moreover, the porosity of the material provides a high surface area-to-volume ratio, enhancing drug loading capacity and improving drug release profile. Nevertheless, drug encapsulation compromises bioactivity stability, with many drugs losing it when formulated in a drug delivery depot (Koerselman et al., 2020).

Large molecules are more prone to lose bioactivity via cleavage or conformational changes when encapsulated. This loss of bioactivity can be influenced by the distribution of the drug within a fibrous material (Tang, 2015). An adequate distribution of the drug far from the surface, within the material, also avoids burst release profiles (Awwad et al., 2018). Moreover, the methods used in the encapsulation process play a great role in the preservation of the bioactivity. For instance, hydrosoluble molecules are more like to maintain their bioactivity if they are exposed to less organic solvents during the process (Wilkinson et al., 2017). Another strategy that has proven to preserve drug bioactivity is to embed drugs in electrospun fibers, with hydrophilic solution core (Saraf et al., 2009). Besides, coaxial fibers fabricated by coaxial electrospinning (Qin, 2017), have shown greater potential in maintaining bioactivity and extended-release of drugs than conventional electrospun fibers (Saraf et al., 2009). Activity preservation faces other challenges in drug encapsulation in nanofibrous scaffolds. Here, drug suspension has to have good solubility, be as homogeneous as possible, be regularly immobilized in the material, and be capable to maintain its bioactivity. Needless to say, these requirements are difficult to meet, and both, pre- and post-fabrication methods need a radical improvement to reach the goals (Tiwari and Tiwari, 2013).

The principal challenges of refillable non-biodegradable implants capable for prolonged drug delivery periods [among the most advanced DDD, currently under clinical trials (Seah et al., 2020)] are to increase the volume capacity of the devices and, at the same time, to achieve a slow and uniform release speed. The idea is to dispose of large amounts of drug, to prevent the dispersion of drug molecules, as well as to slow down drug spreading and degradation rate and, consequently, to reduce interventions frequency to <1/year (Bansal et al., 2016; Rupenthal, 2017; Shen et al., 2018). Functionalize biomaterials by embedding specific drug molecules can provide a sustained, diffusion-independent drug release format (Bansal et al., 2016; Rupenthal, 2017; Shen et al., 2018), adaptable to the desired release kinetics by adjusting the degradation dynamics of the employed scaffold.

Port delivery system and micropumps have been efficient in both, preclinical and clinical trials for chronic retinopathies' treatments (Campochiaro et al., 2011; Haghjou et al., 2011; Pirmoradi et al., 2011; Kang-Mieler et al., 2020), respectively. PDS systems are one of the very few transport systems that have been able to successfully complete clinical trials, with controlled long-term diffusion of the drug: a 220 patients Phase II clinical trial with Ranibizumab reported good PDS tolerance and maintenance of the therapeutic levels during the 9 months of the study (Campochiaro et al., 2019). However, benefits are counterbalanced by collateral risks, either related to the surgical processes or to the non-biodegradability of the implant which may lead to inflammatory processes. Indeed, in the above trial, about 5% of the patients developed surgery-originated vitreous hemorrhage.

Technological Solutions

Hydrogels are very promising materials for sustained ophthalmic drug delivery. Their high-water content makes them very biocompatible and transparent and their porous structure acts as a protective barrier against denaturant environmental agents while allowing a large amount of drug to be loaded (Kang Derwent and Mieler, 2008; Matanović et al., 2014; Anwary et al., 2018). "Intelligent" hydrogels are able to specifically react in presence of external environmental factors like pH or temperature (Kang Derwent and Mieler, 2008; Matanović et al., 2014; Seah et al., 2020).

Several preclinical and clinical trials provided evidence for sustained drug supply, improvement of lesions and retinal functionality, with little or no toxicity of the biomaterials (Turturro et al., 2011; Agrawal et al., 2012; Drapala et al., 2014; Yu et al., 2015; OTX-IVT, 2020). However, hydrogels present several disadvantages like sterilization difficulties, risk of harm to biopharmaceuticals due to chemical crosslinking reactions, risk of toxic effects caused by polymerization initiator, presence of toxic residuals after polymerization, and difficulties in the control of drug release rate and degradation kinetics due to water absorption during swelling (Kanjickal et al., 2008; Karajanagi et al., 2011; Hammer et al., 2015; Kirchhof et al., 2015a; Baino and Kargozar, 2020).

Colloidal biofunctionalized materials have been designed to provide a format independent sustained drug release (Bansal et al., 2016; Rupenthal, 2017; Shen et al., 2018). Administration route, release rate and diffusion of the drug into the tissue directly depend on the size, structure and stability of the employed molecule (Seah et al., 2020). Drug release can also be tuned to the desired kinetics by adjusting the degradation dynamics of the scaffolding biomaterial.

Liposomes can incorporate either hydrophobic or hydrophilic compounds (e.g., anti-VEGF). They have adjustable drug release kinetics, phospholipids are metabolized as the liposome is being degraded and, compared to polymeric microparticles, they have longer half-time and lower immunogenicity and toxicity (Seah et al., 2020). Furthermore, their surface can be modified with proteins or polymers, providing additional functionalities, such as light or chemical activation, allowing specific and precise pharmacological release (Baino and Kargozar, 2020). Verteporfin was the first liposome-based drug used for photodynamic therapy of neovascular AMD, improving the topical release of bevacizumab with the use of surface-modified liposomes (Bressler et al., 2002; Fenton and Perry, 2006; Lajavardi et al., 2007). In animal models, several IVT- administered liposomes-formulated DDD have reached >1 month sustained anti-VEGF release rates (Abrishami et al., 2009; Mu et al., 2018). However, it is still unknown how liposomes interact with physiological processes, being difficult to predict the duration of sustained supply (Honda et al., 2013). For example, their stability can be compromised by the enzymatic activity or the pH of the eye, while liposomes themselves can be destabilized and ingested by macrophages (Yatvin et al., 1980; Moghimi et al., 1989). Furthermore, they have a limited drug encapsulation capability; complications with sterilization procedures and they present a risk of blurred vision after IVT injections is high (Baino and Kargozar, 2020).

Nanoparticles can encapsulate molecules, proteins, peptides and vaccines, as well as hydrophilic and hydrophobic biological macromolecules and their low cytotoxicity makes them good candidates for safe eye DDD. Their physical and chemical characteristics can be modified to fit specific pharmacological objectives (Hans and Lowman, 2002).

They have achieved several weeks of slow and sustained drug release, with some therapeutic effects, like a reduction of neovascularization damages and some improvement of the visual function (Varshochian et al., 2013, 2015; Tanetsugu et al., 2017; Narvekar et al., 2019; Qiu et al., 2019).

Despite their advantages, these systems have a low protein encapsulation efficiency (<60% for microparticles and <30% for nanoparticles), high initial release rates (20–50% of the drug in 24 h), incomplete release and loss of bioactivity of the drug during release (Yeo and Park, 2004; Manoharan and Singh, 2009; Herrero-Vanrell et al., 2014). Movement of microparticles has also been observed from the target site (Morirero et al., 1991). To limit such movement it has been proposed the simultaneous use of injectable hydrogels, to limit particles' mobility and allow a prolonged drug release (Kang-Mieler et al., 2017). These particulate-hydrogel systems offer advantages over each of the platforms separately, as the release time is extended and the initial burst of the drug is reduced (Osswald and Kang-Mieler, 2015, 2016). Besides, since the number of microspheres suspended in the hydrogel can be controlled, the total amount of drug delivered can be controlled without changing the volume and injectability of the system (Osswald and Kang-Mieler, 2015, 2016; Bhatt et al., 2019; Liu et al., 2019c). Also, these hydrogels combined with microparticles are biocompatible and inhibit the expression of VEGF (Wang et al., 2018). However, studies to date only consist of *in vitro* and *in vivo* preclinical trials, so studies in patients have not yet been achieved. Finally, unlike other PLGA-based applications which have been proven to be safe, the small size of the micro/nanoparticles systems has, to date, limited a through test of biocompatibility and safety of the materials (Sakurai et al., 2001).

CONCLUSION

To date, AMD is an untreatable neurodegenerative disease that represents a major and growing worldwide public health burden. The use of biomaterials for the sustained administration of drugs in the treatment of AMD is a promising methodology but it needs a long personal-, material- and time-effort to approximate clinical application. The immense majority of the biomaterials are still far from performing clinical trials. One of the main problems of the proposed therapies is their limited capacity for drug storage. IVT injectable and surgically implantable devices are the less elegant and oldest technology DDD, not lacking serious side effect consequences. However, they are the only available therapeutic offer for AMD patients, and they will continue to be in the near future. Improvement of these technologies is and will be extremely important for both, AMD suffering persona and for the pharma industry. Hydrogels are promising candidates due to the number of biodegradable and biocompatible components, in addition to their structural characteristics (resistance, transparency, water-holding capacity, etc.). Colloid particles are postulated as better candidates, but the development of real alternatives is still in the beginning. Probably the best therapies will combine several of the above materials and strategies to increase therapeutic effects, to reduce interventions frequency and to decrease the risks associated with such interventions.

AUTHOR CONTRIBUTIONS

NJ-D and AG-D: bibliographic research and information synthesis, AMD course, writing the manuscript, equal contribution. MF-A, NS-B, and NA-L: bibliographic research and information synthesis. FA-M: clinical aspects. JP-R, FR, GG, and DK: biomaterials aspects. DG-N: biomaterials, cell and tissue therapy. GG, JP-R, DK, and DG-N: manuscript revision. FP: manuscript design, information synthesis, supervision, writing the manuscript. All authors contributed to the article and approved the submitted version.

FUNDING

The authors gratefully acknowledge financial support received from the Spanish Ministerio de Economía y Competitividad through grants MAT2016-76847-R, MAT2016-79832-R and MAT2015-66666-C3-3-R; from the Comunidad de Madrid, Spain through grants Neurocentro-B2017/BrMD-3760 and IND2018/BrMD-9804, from the National Institutes of Health (P41EB002520); and predoctoral FPI grant from the Spanish Ministerio de Economía y Competitividad (AG-D) and research contract from the Comunidad de Madrid, Spain (MF-A).

REFERENCES

Abrishami, M., Zarei-Ghanavati, S., Soroush, D., Rouhbakhsh, M., Jaafari, M. R., and Malaekeh-Nikouei, B. (2009). Preparation, characterization, and in vivo evaluation of nanoliposomes-encapsulated bevacizumab (avastin) for intravitreal administration. *Retina* 29, 699–703. doi: 10.1097/IAE.0b013e3181a2f42a

Adams, C. M., Anderson, K., Artman, G., Bizec, J. C., Cepeda, R., Elliott, J., et al. (2018). The Discovery of N-(1-Methyl-5-(trifluoromethyl)-1H-pyrazol-3-yl)-5-((6- ((methylamino)methyl)pyrimidin-4-yl)oxy)-1H-indole-1-carboxamide (Acrizanib), a VEGFR-2 inhibitor specifically designed for topical ocular delivery, as a therapy for neovascular age-. *J. Med. Chem.* 61, 1622–1635. doi: 10.1021/acs.jmedchem.7b01731

Agrawal, A. K., Das, M., and Jain, S. (2012). In situ gel systems as "smart" carriers for sustained ocular drug delivery. *Expert Opin. Drug Deliv.* 9, 383–402. doi: 10.1517/17425247.2012.665367

Alexander, A., Ajazuddin, Khan, J., Saraf, S., and Saraf, S. (2014). Polyethylene glycol (PEG)–Poly(N-isopropylacrylamide) (PNIPAAm) based thermosensitive injectable hydrogels for biomedical applications. *Eur. J. Pharm. Biopharm.* 88, 575–585. doi: 10.1016/J.EJPB.2014.07.005

Alimera Sciences (2019). *Alimera Sciences*. Available online at: https://alimerasciences. com/ (accessed March 19, 2019).

Ambati, J., and Fowler, B. J. (2012). Mechanisms of age-related macular degeneration. *Neuron* 75, 26–39. doi: 10.1016/j.neuron.2012.06.018

Ameeduzzafar, A., Ali, J., Fazil, M., Qumbar, M., Khan, N., and Ali, A. (2016). Colloidal drug delivery system: amplify the ocular delivery. *Drug Deliv.* 23, 710–726. doi: 10.3109/10717544.2014.923065

Anderson, D. H., Mullins, R. F., Hageman, G. S., and Johnson, L. V. (2002). A role for local inflammation in the formation of drusen in the aging eye. *Am. J.Ophthalmol.* 134, 411–431.

Anwary, M., Kumar, P., du Toit, L. C., Choonara, Y. E., and Pillay, V. (2018). Polymeric, injectable, intravitreal hydrogel devices for posterior segment applications and interventions. *Artif. Cells Nanomed. Biotechnol.* 46, 1074–1081.

Ardeljan, D., and Chan, C.-C. (2013). Aging is not a disease: distinguishing age-related macular degeneration from aging. *Prog. Retin. Eye Res.* 37, 68–89. doi: 10.1016/j.preteyeres.2013.07.003

Arranz-Romera, A., Davis, B. M., Bravo-Osuna, I., Esteban-Pérez, S., Molina-Martínez, I. T., Shamsher, E., et al. (2019). Simultaneous co-delivery of neuroprotective drugs from multi-loaded PLGA microspheres for the treatment of glaucoma. *J. Control. Release* 297, 26–38. doi: 10.1016/j.jconrel.2019.01.012

Awwad, S., Abubakre, A., Angkawinitwong, U., Khaw, P. T., and Brocchini, S. (2019). In situ antibody-loaded hydrogel for intravitreal delivery. *Eur. J. Pharm. Sci.* 137:104993. doi: 10.1016/j.ejps.2019.104993

Awwad, S., Al-Shohani, A., Khaw, P. T., and Brocchini, S. (2018). Comparative study of in situ loaded antibody and PEG-Fab NIPAAM Gels. *Macromol. Biosci.* 18:1700255. doi: 10.1002/mabi.201700255

Awwad, S., Lockwood, A., Brocchini, S., and Khaw, P. T. (2015). The PK-Eye?: a novel in vitro ocular flow model for use in preclinical drug development. *J. Pharm. Sci.* 104, 3330–3342. doi: 10.1002/jps.24480

Bahram, M., Mohseni, N., and Moghtader, M. (2016). "An introduction to hydrogels and some recent applications," in *Emerging Concepts in Analysis and Applications of Hydrogels*, ed. S. B. Majee (London: InTech), doi: 10.5772/64301

Baino, F., and Kargozar, S. (2020). Regulation of the ocular cell/tissue response by implantable biomaterials and drug delivery systems. *Bioengineering* 7, 1–30. doi: 10.3390/bioengineering7030065

Bansal, P., Garg, S., Sharma, Y., and Venkatesh, P. (2016). Posterior segment drug delivery devices: current and novel therapies in development. *J. Ocular Pharmacol. Ther.* 32, 135–144. doi: 10.1089/jop.2015.0133

Basuki, J. S., Qie, F., Mulet, X., Suryadinata, R., Vashi, A. V., Peng, Y. Y., et al. (2017). Photo-modulated therapeutic protein release from a hydrogel depot using visible light. *Angew. Chem, Int. Ed.* 56, 966–971. doi: 10.1002/anie.201610618

Beatty, S., Koh, H., Phil, M., Henson, D., and Boulton, M. (2000). The role of oxidative stress in the pathogenesis of age-related macular degeneration. *Survey Ophthalmol.* 45, 115–134. doi: 10.1016/s0039-6257(00)00140-5

Benjamin, M., Garcia, A., Tully, J., Owens, G., Robeson, R., Navratil, T., et al. (2014). Development of precisely-engineered biodegradable drug delivery systems for posterior ocular drug delivery: PRINT® PLGA extended release implants for anti-VEGF biologics. *Invest. Ophthalmol. Vis. Sci.* 55:5269.

Bernards, D. A., Lance, K. D., Ciaccio, N. A., and Desai, T. A. (2012). Nanostructured thin film polymer devices for constant-rate protein delivery NIH public access. *Nano Lett.* 12, 5355–5361. doi: 10.1021/nl302747y

Bezatis, A., Spital, G., Höhn, F., Maier, M., Clemens, C. R., Wachtlin, J., et al. (2013). Functional and anatomical results after a single intravitreal Ozurdex injection in retinal vein occlusion: a 6-month follow-up – The SOLO study. *Acta Ophthalmol.* 91, e340–e347. doi: 10.1111/AOS.12020

Bhatt, P., Narvekar, P., Lalani, R., Chougule, M. B., Pathak, Y., and Sutariya, V. (2019). An in vitro assessment of thermo-reversible gel formulation containing sunitinib nanoparticles for neovascular age-related macular degeneration. *AAPS PharmSciTech* 20:281. doi: 10.1208/s12249-019-1474-0

Bhavsar, A. R., Googe, J. M., Stockdale, C. R., Bressler, N. M., Brucker, A. J., Elman, M. J., et al. (2009). Risk of endophthalmitis after intravitreal drug injection when topical antibiotics are not required: the diabetic retinopathy clinical research network laser-ranibizumab-triamcinolone clinical trials. *Arch. Ophthalmol.* 127, 1581–1583. doi: 10.1001/archophthalmol.2009.304

Blumenkranz, M. S., Chan, L.-S., and Leung, M. S. (2011). Critical appraisal of the clinical utility of the dexamethasone intravitreal implant (Ozurdex&reg) for the treatment of macular edema related to branch retinal vein occlusion or central retinal vein occlusion. *Clin. Ophthalmol.* 5:1043. doi: 10.2147/OPTH.S13775

Bourges, J. L., Bloquel, C., Thomas, A., Froussart, F., Bochot, A., Azan, F., et al. (2006). Intraocular implants for extended drug delivery: therapeutic applications. *Adv. Drug Deliv. Rev.* 58, 1182–1202. doi: 10.1016/j.addr.2006.07.026

Boyer, D. S., Faber, D., Gupta, S., Patel, S. S., Tabandeh, H., Li, X.-Y., et al. (2011). Dexamethasone intravitreal implant for treatment of diabetic macular edema in vitrectomized patients. *Retina* 31, 915–923. doi: 10.1097/IAE.0b013e318206d18c

Bressler, N. M., Arnold, J., Benchaboune, M., Blumenkranz, M. S., Fish, G. E., Gragoudas, E. S., et al. (2002). Verteporfin therapy of subfoveal choroidal neovascularization in patients with age-related macular degeneration additional information regarding baseline lesion composition's impact on vision outcomes-TAP Report No. 3 treatment of age-related macular degeneration with photodynamic therapy (TAP) study group*. *Arch. Oftalmol.* 120, 1443–1454.

Bringmann, A., Iandiev, I., Pannicke, T., Wurm, A., Hollborn, M., Wiedemann, P., et al. (2009). Cellular signaling and factors involved in Müller cell gliosis: neuroprotective and detrimental effects. *Prog. Retin. Eye Res.* 28, 423–451. doi: 10.1016/j.preteyeres.2009.07.001

Burke, J., and Schwartz, M. (1996). Preclinical evaluation of brimonidine. *Survey Ophthalmol.* 41(Suppl. 1), S9–S18.

Callanan, D. G., Jaffe, G. J., Martin, D. F., Pearson, P. A., and Comstock, T. L. (2008). Treatment of posterior uveitis with a fluocinolone acetonide implant three-year clinical trial results. *Arch Ophthalmol.* 126, 1191–1201.

Campbell, M., and Humphries, P. (2013). The blood-retina barrier tight junctions and barrier modulation. *Adv. Exp. Med. Biol.* 763, 70–84. doi: 10.1007/978-1-4614-4711-5_3

Campochiaro, P. A., Brown, D. M., Pearson, A., Chen, S., Boyer, D., Ruiz-Moreno, J., et al. (2012). Sustained delivery fluocinolone acetonide vitreous inserts provide benefit for at least 3 years in patients with diabetic macular Edema. *Ophthalmology* 119, 2125–2132. doi: 10.1016/j.ophtha.2012.04.030

Campochiaro, P. A., Brown, D. M., Pearson, A., Ciulla, T., Boyer, D., Holz, F. G., et al. (2011). Long-term benefit of sustained-delivery fluocinolone acetonide vitreous inserts for diabetic macular edema. *Ophthalmology* 118, 626.e2–635.e2. doi: 10.1016/j.ophtha.2010.12.028

Campochiaro, P. A., Marcus, D. M., Awh, C. C., Regillo, C., Adamis, A. P., Bantseev, V., et al. (2019). The port delivery system with ranibizumab for neovascular age-related macular degeneration: results from the randomized phase 2 ladder clinical trial. *Ophthalmology* 126, 1141–1154. doi: 10.1016/j.ophtha.2019.03.036

Casado, J. M. (2009). Origin of the diseases suffered by the aged, today: behavior, life style, diet, greater life expectancy. *Servir* 57, 46–56.

Chang, D., Park, K., and Famili, A. (2019). Hydrogels for sustained delivery of biologics to the back of the eye. *Drug Discov. Today* 24, 1470–1482. doi: 10.1016/j.drudis.2019.05.037

Cherry, J. D., Olschowka, J. A., and O'Banion, M. (2014). Neuroinflammation and M2 microglia: the good, the bad, and the inflamed. *J. Neuroinflamm.* 11:98. doi: 10.1186/1742-2094-11-98

ClinicalTrials.gov (2020a). 20089 TA+Lucentis Combo Intravitreal Injections for Treatment of Neovascular Age-related Macular Degeneration (AMD) - Full Text View. Available online at: https://clinicaltrials.gov/ct2/show/NCT01175395?term=IBI-20089&draw=2&rank=1 (accessed August 6, 2020).

ClinicalTrials.gov (2020b). *A Phase III Study to Evaluate the Port Delivery System With Ranibizumab Compared With Monthly Ranibizumab Injections in Participants With Wet Age-Related Macular Degeneration - Full Text View*. Available online at: https://clinicaltrials.gov/ct2/show/NCT03677934 (accessed August 6, 2020).

ClinicalTrials.gov (2020c). *A Safety, and Efficacy Study of Brimonidine Intravitreal Implant in Geographic Atrophy Secondary to Age-related Macular Degeneration - Full Text View*. Available online at: https://clinicaltrials.gov/ct2/show/NCT02087085?term=Brimonidine+Implant&draw=2&rank=1 (accessed August 6, 2020).

ClinicalTrials.gov (2020d). *Combined Ranibizumab, and Iluvien for Diabetic Macular Oedema - Full Text View*. Available online at: https://clinicaltrials.gov/ct2/show/NCT03784443 (accessed August 6, 2020).

ClinicalTrials.gov (2020e). *Extension Study for the Port Delivery System With Ranibizumab(Portal) - Full Text View*. Available online at: https://clinicaltrials.gov/ct2/show/NCT03683251 (Accessed August 6, 2020).

ClinicalTrials.gov (2020f). *Fluocinolone Acetonide in Diabetic Macular Edema (FAME) Extension Study - Full Text View*. Available online at: https://clinicaltrials.gov/ct2/show/NCT01304706 (accessed August 6, 2020).

Crouch, R. K., Koutalos, Y., Kono, M., Schey, K., and Ablonczy, Z. (2015). Chapter twenty-six - A2E and lipofuscin. *Prog. Mol. Biol. Transl. Sci.* 134, 449–463. doi: 10.1016/bs.pmbts.2015.06.005

Cuenca, N., Fernández-Sánchez, L., Campello, L., Maneu, V., De la Villa, P., Lax, P., et al. (2014). Cellular responses following retinal injuries and therapeutic approaches for neurodegenerative diseases. *Prog. Retin. Eye Res.* 43, 17–75. doi: 10.1016/j.preteyeres.2014.07.001

Cunha-Vaz, J., Bernardes, R., and Lobo, C. (2011). Blood-retinal barrier. *Eur. J. Ophthalmol.* 21, 3–9. doi: 10.5301/EJO.2010.6049

Damián, J., Pastor, R., Armadá, F., and Arias, L. (2006). Epidemiología de la degeneración macular asociada con la edad. Situación en España. *Aten. Primaria* 38, 51–57. doi: 10.1157/13090016

Daneault, V., Dumont, M., Massé, É, Vandewalle, G., and Carrier, J. (2016). Light-sensitive brain pathways and aging. *J. Physiol. Anthropol.* 35:9. doi: 10.1186/s40101-016-0091-9

Davis, B. M., Normando, E. M., Guo, L., Turner, L. A., Nizari, S., O'Shea, P., et al. (2014). Topical delivery of avastin to the posterior segment of the eye in vivo using annexin A5-associated liposomes. *Small* 10, 1575–1584. doi: 10.1002/smll.201303433

Deb, P. K., Al-Attraqchi, O., Jaber, A. Y., Amarji, B., and Tekade, R. K. (2018). "Physicochemical aspects to be considered in pharmaceutical product development," in *Dosage Form Design Considerations*, Vol. I, ed. R. K. Tekade (Amsterdam: Elsevier), 57–83. doi: 10.1016/B978-0-12-814423-7.00002-2

Degeneration, A. M., Jonas, J. B., Ming, C., and Cheung, G. (2017). Updates on the epidemiology of age-related macular degeneration. *Asia Pacific J. Ophthalmol.* 6, 493–497. doi: 10.22608/apo.2017251

del Amo, E. M., and Urtti, A. (2008). Current and future ophthalmic drug delivery systems: a shift to the posterior segment. *Drug Discov. Today* 13, 135–143. doi: 10.1016/J.DRUDIS.2007.11.002

Desai, T., and Bernards, D. A. (2014). *Zordera*. Available online at: www.ondrugdelivery.com (accessed March 19, 2019).

Drapala, P. W., Jiang, B., Chiu, Y. C., Mieler, W. F., Brey, E. M., Kang-Mieler, J. J., et al. (2014). The effect of glutathione as chain transfer agent in PNIPAAm-based thermo-responsive hydrogels for controlled release of proteins. *Pharm. Res.* 31, 742–753. doi: 10.1007/s11095-013-1195-0

Ebrahim, S., Peyman, G. A., and Lee, P. J. (2005). Applications of liposomes in ophthalmology. *Surv. Ophthalmol.* 50, 167–182. doi: 10.1016/j.survophthal.2004.12.006

Edington, M., Connolly, J., and Chong, N. V. (2017). Pharmacokinetics of intravitreal anti-VEGF drugs in vitrectomized versus non-vitrectomized eyes. *Expert Opin. Drug Metab. Toxicol.* 13, 1217–1224. doi: 10.1080/17425255.2017.1404987

Evans, J. R., Fletcher, A. E., and Wormald, R. P. (2004). Causes of visual impairment in people aged 75 years and older in Britain: an add-on study to the MRC Trial of Assessment and Management of Older People in the Community. *Br. J. Ophthalmol.* 88, 365–370.

Eyewire News (2020). *Ocular Therapeutix Announces Dosing of First Patient in Phase 1 Clinical Trial for the Treatment of Wet AMD*. Available online at: https://eyewire.news/articles/ocular-therapeutix-announces-dosing-of-first-patient-in-phase-1-clinical-trial-for-the-treatment-of-wet-amd/ (accessed June 28, 2020).

Falavarjani, K. G., and Nguyen, Q. D. (2013). Adverse events and complications associated with intravitreal injection of anti-VEGF agents: a review of literature. *Eye* 27, 787–794. doi: 10.1038/eye.2013.107

Fenton, C., and Perry, C. M. (2006). Verteporfin: a review of its use in the management of subfoveal choroidal neovascularisation. *Drugs Aging* 23, 421–445. doi: 10.2165/00002512-200623050-00006

Ferris, F. L., Davis, M. D., Clemons, T. E., Lee, L. Y., Chew, E. Y., Lindblad, A. S., et al. (2005). A simplified severity scare for age-related macular degeneration: AREDS Report no.18. *Arch Ophthalmol.* 123, 1570–1574.

Fleckenstein, M., Mitchell, P., Freund, K. B., Sadda, S., Holz, F. G., Brittain, C., et al. (2018). The progression of geographic atrophy secondary to age-related macular degeneration. *Ophthalmology* 125, 369–390. doi: 10.1016/j.ophtha.2017.08.038

Fomina, N., McFearin, C., Sermsakdi, M., Edigin, O., and Almutairi, A. (2010). UV and near-IR triggered release from polymeric nanoparticles. *J. the Am. Chem. Soc.* 132, 9540–9542. doi: 10.1021/ja102595j

Freund, K. B., Mrejen, S., and Gallego-Pinazo, R. (2013). An update on the pharmacotherapy of neovascular age-related macular degeneration. *Expert Opin. Pharm.* . 14, 1017–1028. doi: 10.1517/14656566.2013.787410

Friedman, D., O'Colmain, B., Tomany, S., McCarty, C., de Jong, P., Nemesure, B., et al. (2004). Prevalence of age-related macular degeneration in the US population. *Arch. Ophthalmol.* 122, 564–572.

Friedman, D. S., O'Colmain, B., and Mestril, I. (2012). *Vision Problems in the U.S*, 5th Edn. Washington DC: Prevent Blindness America.

Fuchs, H., and Igney, F. (2017). Binding to ocular albumin as a half-life extension principle for intravitreally injected drugs: evidence from mechanistic rat and rabbit studies. *J. Ocul. Pharmacol. Ther.* 33, 115–122. doi: 10.1089/jop.2016.0083

Galante, R., Pinto, T. J. A., Colaço, R., and Serro, A. P. (2018). Sterilization of hydrogels for biomedical applications: a review. *J. Biomed. Mater. Res.Part B Appl. Biomater.* 106, 2472–2492. doi: 10.1002/jbm.b.34048

Gao, H., Qiao, X., Cantor, L. B., and WuDunn, D. (2002). Up-regulation of brain-derived neurotrophic factor expression by brimonidine in rat retinal ganglion cells. *Arch. Ophthalmol.* 120, 797–803.

Garcìia, M. A., and Martinez, S. E. (2013). Degeneracioìn macular asociada a la edad (DMAE). Guiìa cliìnica optomeìtrica, a partir de estudios basados en la evidencia. *Gaceta de Optometriìa y Oìptica Oftaìlmica* 487, 24–30.

Gaudana, R., Jwala, J., Boddu, S. H. S., and Mitra, A. K. (2009). Recent perspectives in ocular drug delivery. *Pharm. Res.* 26, 1197–1216. doi: 10.1007/s11095-008-9694-0

Ghasemi Falavarjani, K. (2009). Implantable posterior segment drug delivery devices; novel alternatives to currently available treatments. *J. Ophthalmic Vis. Res.* 4, 191–193.

Grossniklaus, H. E., Ling, J. X., Wallace, T. M., Dithmar, S., Lawson, D. H., Cohen, C., et al. (2002). Macrophage and retinal pigment epithelium expression of angiogenic cytokines in choroidal neovascularization. *Mol. Vis.* 8, 119–126.

Gutiérrez-Hernández, J.-C., Caffey, S., Abdallah, W., Calvillo, P., González, R., Shih, J., et al. (2014). One-year feasibility study of replenish micropump for intravitreal drug delivery: a pilot Study. *Transl. Vis. Sci. Technol.* 3:8. doi: 10.1167/tvst.3.4.1

Haghjou, N., Soheilian, M., and Abdekhodaie, M. J. (2011). Sustained release intraocular drug delivery devices for treatment of uveitis. *J. Ophthalmic Vis. Res.* 6, 317–319.

Haller, J. A., Bandello, F., Belfort, R., Blumenkranz, M. S., Gillies, M., Heier, J., et al. (2010). Randomized, sham-controlled trial of dexamethasone intravitreal implant in patients with macular edema due to retinal vein occlusion. *Ophthalmology* 117, 1134.e3–1146.e3. doi: 10.1016/j.ophtha.2010.03.032

Hammer, N., Brandl, F. P., Kirchhof, S., Messmann, V., and Goepferich, A. M. (2015). Protein compatibility of selected cross-linking reactions for hydrogels. *Macromol. Biosci.* 15, 405–413. doi: 10.1002/mabi.201400379

Handa, J. T., Bowes Rickman, C., Dick, A. D., Gorin, M. B., Miller, J. W., Toth, C. A., et al. (2019). A systems biology approach towards understanding and treating non-neovascular age-related macular degeneration. *Nat. Commun.* 10:3347. doi: 10.1038/s41467-019-11262-1

Hans, M. L., and Lowman, A. M. (2002). Biodegradable nanoparticles for drug delivery and targeting. *Curr. Opin. Solid State Mater. Sci.* 6, 319–327. doi: 10.1016/S1359-0286(02)00117-1

Hanus, J., Anderson, C., and Wang, S. (2015). RPE necroptosis in response to oxidative stress and in AMD. *Ageing Res. Rev.* 24, 286–298. doi: 10.1016/j.arr.2015.09.002

Herrero-Vanrell, R., Bravo-Osuna, I., Andrés-Guerrero, V., Vicario-de-la-Torre, M., and Molina-Martínez, I. T. (2014). The potential of using biodegradable microspheres in retinal diseases and other intraocular pathologies. *Prog. Retin. Eye Res.* 42, 27–43. doi: 10.1016/j.preteyeres.2014.04.002

Herrero-Vanrell, R., and Refojo, M. F. (2001). Biodegradable microspheres for vitreoretinal drug delivery. *Adv. Drug Deliv. Rev.* 52, 5–16. doi: 10.1016/S0169-409X(01)00200-9

Honda, M., Asai, T., Oku, N., Araki, Y., Tanaka, M., and Ebihara, N. (2013). Liposomes and nanotechnology in drug development: focus on ocular targets. *Int. J. Nanomed.* 8, 495–504. doi: 10.2147/IJN.S30725

Hora, M. S., Rana, R. K., Nunberg, J. H., Tice, T. R., Gilley, R. M., and Hudson, M. E. (1990). Release of human serum albumin from poly(lactide-co-glycolide) microspheres. *Pharm. Res.* 7, 1190–1194.

Hu, C. C., Chiu, Y. C., Chaw, J. R., Chen, C. F., and Liu, H. W. (2019). Thermo-responsive hydrogel as an anti-VEGF drug delivery system to inhibit retinal angiogenesis in Rex rabbits. *Technol Health Care* 27, 153–163. doi: 10.3233/THC-199015

Humayun, M., Santos, A., Altamirano, J. C., Ribeiro, R., Gonzalez, R., de la Rosa, A., et al. (2014). Implantable micropump for drug delivery in patients with diabetic macular edema. *Transl. Vis. Sci. Technol.* 3:5. doi: 10.1167/tvst.3.6.5

Huu, V. A. N., Luo, J., Zhu, J., Zhu, J., Patel, S., Boone, A., et al. (2015). Light-responsive nanoparticle depot to control release of a small molecule angiogenesis inhibitor in the posterior segment of the eye. *J. Control. Release?* 200, 71–77. doi: 10.1016/j.jconrel.2015.01.001

IAPB Vision Atlas (2017*). *Global Vision Database Maps. Global Vision Database Maps*. London: IAPB Vision Atlas.

Imperiale, J. C., Acosta, G. B., and Sosnik, A. (2018). Polymer-based carriers for ophthalmic drug delivery. *J. Control. Release* 285, 106–141. doi: 10.1016/j.jconrel.2018.06.031

Jackson, T. L., Boyer, D., Brown, D. M., Chaudhry, N., Elman, M., Liang, C., et al. (2017). Oral tyrosine kinase inhibitor for neovascular age-related macular degeneration: a phase 1 dose-escalation study. *JAMA Ophthalmol.* 135, 761–767. doi: 10.1001/jamaophthalmol.2017.1571

Jaffe, G. J., Yang, C. H., Guo, H., Denny, J. P., Lima, C., and Ashton, P. (2000). Safety and pharmacokinetics of an intraocular fluocinolone acetonide sustained delivery device. *Inves. Ophthalmol. Vis. Sci.* 41, 3569–3575.

Jager, R. D., Aiello, L. P., Patel, S. C., and Cunningham, E. T. (2004). Risks of intravitreous injection: a comprehensive review. *Retina* 24, 676–698. doi: 10.1097/00006982-200410000-00002

Jager, R. D., Mieler, W. F., and Miller, J. W. (2008). Age-related macular degeneration. *N. Engl. J. Med.* 358, 2606–2617. doi: 10.1056/NEJMra0801537

Jarrett, S. G., and Boulton, M. E. (2012). Consequences of oxidative stress in age-related macular degeneration. *Mol. Aspects Med.* 33, 399–417. doi: 10.1016/j.mam.2012.03.009

Jarrett, T., Elhayek, R. F., Lattrell, Z., McGrath, M., Takach, S., Jarrett, P. K., et al. (2017). Pharmacokinetics of a 6 month sustained hydrogel delivery system for tyrosine kinase inhibitors in dutch belted rabbits. *Invest. Ophthalmol. Vis. Sci.* 58:1984.

Jeffries, A. M., Killian, N. J., and Pezaris, J. S. (2014). Mapping the primate lateral geniculate nucleus: a review of experiments and methods. *J. Physiol. Paris* 108, 3–10. doi: 10.1016/j.jphysparis.2013.10.001

Jiang, S., Wang, K., Dai, Y., Zhang, X., and Xia, F. (2019). Near-infrared light-triggered dual drug release using gold nanorod-embedded thermosensitive nanogel-crosslinked hydrogels. *Macromol. Mater. Eng.* 304:1900087. doi: 10.1002/mame.201900087

Journal, A. I., Anwary, M., Kumar, P., Toit, L. C., and Choonara, Y. E. (2018). Polymeric, injectable, intravitreal hydrogel devices for posterior segment applications and interventions. *Artif. Cells Nanomed. Biotechnol.* 46, 1074–1081. doi: 10.1080/21691401.2018.1478845

Kabiesz, A., and Nowak, M. (2015). Age related macular degeneration – challenge for future?: pathogenesis and new perspectives for the treatment. *Eur. Geriatr. Med.* 6, 69–75. doi: 10.1016/j.eurger.2014.09.007

Kandatsu, N., Nan, Y.-S., Feng, G.-G., Nishiwaki, K., Hirokawa, M., Ishikawa, K., et al. (2005). Opposing effects of isoflurane and sevoflurane on neurogenic pulmonary edema development in an animal model. *Anesthesiology* 102, 1182–1189. doi: 10.1097/00000542-200506000-00018

Kane, F. E., Burdan, J., Cutino, A., and Green, K. E. (2008). Iluvien TM?: a new sustained delivery technology for posterior eye disease. *Expert Opin. Drug Deliv.* 5, 1039–1046. doi: 10.1517/17425247.5.9.1039

Kang Derwent, J. J., and Mieler, W. F. (2008). Thermoresponsive hydrogels as a new ocular drug delivery platform to the posterior segment of the eye. *Trans. Am. Ophthalmol. Soc.* 106, 206–213. discussion 213-4

Kang-Mieler, J. J., Dosmar, E., Liu, W., and Mieler, W. F. (2017). Extended ocular drug delivery systems for the anterior and posterior segments: biomaterial options and applications. *Expert Opin. Drug Deliv.* 14, 611–620. doi: 10.1080/17425247.2016.1227785

Kang-Mieler, J. J., Osswald, C. R., and Mieler, W. F. (2014). Advances in ocular drug delivery: emphasis on the posterior segment. *Expert Opin. Drug Deliv.* 11, 1647–1660. doi: 10.1517/17425247.2014.935338

Kang-Mieler, J. J., Rudeen, K. M., Liu, W., and Mieler, W. F. (2020). Advances in ocular drug delivery systems. *Eye* 34, 1371–1379. doi: 10.1038/s41433-020-0809-0

Kanjickal, D., Lopina, S., Evancho-Chapman, M. M., Schmidt, S., and Donovan, D. (2008). Effects of sterilization on poly(ethylene glycol) hydrogels. *J. Biomed. Mater. Res. Part A* 87, 608–617. doi: 10.1002/jbm.a.31811

Karajanagi, S. S., Yoganathan, R., Mammucari, R., Park, H., Cox, J., Zeitels, S. M., et al. (2011). Application of a dense gas technique for sterilizing soft biomaterials. *Biotechnol. Bioeng.* 108, 1716–1725. doi: 10.1002/bit.23105

Khan, J. C., Thurlby, D. A., Shahid, H., Clayton, D. G., Yates, J. R. W., Bradley, M., et al. (2006). Smoking and age related macular degeneration: the number of pack years of cigarette smoking is a major determinant of risk for both geographic atrophy and choroidal neovascularisation. *Br. J. Ophthalmol.* 90, 75–80. doi: 10.1136/bjo.2005.073643

Kim, C. E., Lee, J. H., Yeon, Y. K., Park, C. H., and Yang, J. (2017). Effects of silk fibroin in murine dry eye. *Nat. Publ. Group* 7:44364. doi: 10.1038/srep44364

Kinnunen, K., Petrovski, G., Moe, M. C., and Kaarniranta, K. (2012). Molecular mechanisms of retinal pigment epithelium damage and development of age-related macular degeneration. *Acta Ophthalmol.* 90, 299–309. doi: 10.1111/j.1755-3768.2011.02179.x

Kirchhof, S., Goepferich, A. M., and Brandl, F. P. (2015a). Hydrogels in ophthalmic applications. *Eur. J. Pharm. Biopharm.* 95, 227–238. doi: 10.1016/j.ejpb.2015.05.016

Kirchhof, S., Gregoritza, M., Messmann, V., Hammer, N., Goepferich, A. M., and Brandl, F. P. (2015b). Diels–Alder hydrogels with enhanced stability: first step toward controlled release of bevacizumab. *Eur. J. Pharm. Biopharm.* 96, 217–225. doi: 10.1016/J.EJPB.2015.07.024

Klein, R., Chou, C.-F., Klein, B. E. K., Zhang, X., Meuer, S. M., and Saaddine, J. B. (2011). Prevalence of age-related macular degeneration in the us population. *Arch. Ophthalmol.* 129, 75–80. doi: 10.1001/archophthalmol.2010.318

Klein, R. J., Zeiss, C., Chew, E. Y., Tsai, J.-Y., Sackler, R. S., Haynes, C., et al. (2005). Complement factor H polymorphism in age-related macular degeneration. *Science* 308, 385–389. doi: 10.1126/science.1109557

Koerselman, M., Warmink, K., Korthagen, N. M., van Midwoud, P., Verrips, T., Weinans, H. H., et al. (2020). Intra-articular drug depots for controlled release of heavy chain only antibodies blocking joint inflammation. *Osteoarthr. Cartil.* 28:S37. doi: 10.1016/j.joca.2020.02.061

Kuno, N., and Fujii, S. (2010). Biodegradable intraocular therapies for retinal disorders. *Drugs Aging* 27, 117–134. doi: 10.2165/11530970-000000000-00000

Kuppermann, B. D., Blumenkranz, M. S., Haller, J. A., Williams, G. A., Weinberg, D. V., Chou, C., et al. (2007). Randomized controlled study of an intravitreous dexamethasone drug delivery system in patients with persistent macular edema. *Arch. Ophthalmol.* 125, 309–317. doi: 10.1001/archopht.125.3.309

Lacour, M., Kiilgaard, J. F., and Nissen, M. H. (2002). Age-related macular degeneration. *Drugs Aging* 19, 101–133. doi: 10.2165/00002512-200219020-00003

Lai, J.-Y. (2013). Influence of solvent composition on the performance of carbodiimide cross-linked gelatin carriers for retinal sheet delivery. *J. Mater. Sci.* 24, 2201–2210. doi: 10.1007/s10856-013-4961-y

Lajavardi, L., Bochot, A., Camelo, S., Goldenberg, B., Naud, M. C., Behar-Cohen, F., et al. (2007). Downregulation of endotoxin-induced uveitis by intravitreal injection of vasoactive intestinal peptide encapsulated in liposomes. *Invest. Ophthalmol. Vis. Sci.* 48, 3230–3238. doi: 10.1167/iovs.06-1305

Lance, K. D., Bernards, D. A., Ciaccio, N. A., Good, S. D., Mendes, T. S., Kudisch, M., et al. (2016). In vivo and in vitro sustained release of ranibizumab from a nanoporous thin-film device. *Drug Deliv. Transl. Res.* 6, 771–780. doi: 10.1007/s13346-016-0298-7

Lance, K. D., Good, S. D., Mendes, T. S., Ishikiriyama, M., Chew, P., Estes, L. S., et al. (2015). In vitro and in vivo sustained zero-order delivery of rapamycin (Sirolimus) from a biodegradable intraocular device. *Invest. Opthalmol. Vis. Sci.* 56:7331. doi: 10.1167/iovs.15-17757

Li, F. (2012). Controlled release of bevacizumab through nanospheres for extended treatment of age-related macular degeneration. *Open Ophthalmol. J.* 6, 54–58. doi: 10.2174/1874364101206010054

Li, J., and Mooney, D. J. (2016). Designing hydrogels for controlled drug delivery. *Nat. Rev. Mater.* 1:16071. doi: 10.1038/natrevmats.2016.71

Lim, J. H., Wickremasinghe, S. S., Xie, J., Chauhan, D. S., Baird, P. N., Robman, L. D., et al. (2012). Delay to treatment and visual outcomes in patients treated with anti-vascular endothelial growth factor for age-related macular degeneration. *Am. J. Ophthalmol.* 153, 678–686.

Lim, J. I., Niec, M., and Wong, V. (2015). One year results of a phase 1 study of the safety and tolerability of combination therapy using sustained release intravitreal triamcinolone acetonide and ranibizumab for subfoveal neovascular AMD. *Br. J. Ophthalmol.* 99, 618–623. doi: 10.1136/bjophthalmol-2014-306002

Lim, J. I., Wolitz, R. A., Dowling, A. H., Bloom, H. R., Irvine, A. R., and Schwartz, D. M. (1999). Visual and anatomic outcomes associated with posterior segment complications after ganciclovir implant procedures in patients with AIDS and cytomegalovirus retinitis. *Am. J. Ophthalmol.* 127, 288–293.

Lin, M. T., and Beal, M. F. (2006). Mitochondrial dysfunction and oxidative stress in neurodegenerative diseases. *Nature* 443, 787–795. doi: 10.1038/nature05292

Linsley, C. S., and Wu, B. M. (2017). Recent advances in light-responsive on-demand drug-delivery systems. *Ther. Deliv.* 8, 89–107. doi: 10.4155/tde-2016-0060

Liu, J., Li, S., Li, G., Li, X., Yu, C., Fu, Z., et al. (2019a). Highly bioactive, bevacizumab-loaded, sustained-release PLGA/PCADK microspheres for intravitreal therapy in ocular diseases. *Int. J. Pharm.* 563, 228–236. doi: 10.1016/j.ijpharm.2019.04.012

Liu, W., Borrell, M. A., Venerus, D. C., Mieler, W. F., and Kang-Mieler, J. J. (2019b). Characterization of biodegradable microsphere-hydrogel ocular drug delivery system for controlled and extended release of ranibizumab. *Transl. Vis. Sci. Technol.* 8:12. doi: 10.1167/tvst.8.1.12

Liu, W., Lee, B. S., Mieler, W. F., and Kang-Mieler, J. J. (2019c). Biodegradable microsphere-hydrogel ocular drug delivery system for controlled and extended release of bioactive aflibercept in vitro. *Curr. Eye Res.* 44, 264–274. doi: 10.1080/02713683.2018.1533983

Lo, R., Li, P.-Y., Saati, S., Agrawal, R. N., Humayun, M. S., and Meng, E. (2009). A passive MEMS drug delivery pump for treatment of ocular diseases. *Biomed. Microdev.* 11, 959–970. doi: 10.1007/s10544-009-9313-9

Lovett, M. L., Wang, X., Yucel, T., York, L., Keirstead, M., Haggerty, L., et al. (2015). Silk hydrogels for sustained ocular delivery of anti-vascular endothelial growth factor (anti-VEGF) therapeutics. *Eur. J. Pharm. Biopharm.* 95, 271–278. doi: 10.1016/J.EJPB.2014.12.029

Machinaga, N., Ashley, G. W., Reid, R., Yamasaki, A., Tanaka, K., Nakamura, K., et al. (2018). A controlled release system for long-acting intravitreal delivery of small molecules. *Transl. Vis. Sci. Technol.* 7:21. doi: 10.1167/tvst.7.4.21

Mainardes, R. M., Urban, M. C. C., Cinto, P. O., Khalil, N. M., Chaud, M. V., Evangelista, R. C., et al. (2005). Colloidal carriers for ophthalmic drug delivery. *Curr.Drug Targ.* 6, 363–371.

Mandal, A., Bisht, R., Rupenthal, I. D., and Mitra, A. K. (2017). Polymeric micelles for ocular drug delivery?: from structural frameworks to recent preclinical studies. *J. Control. Release* 248, 96–116. doi: 10.1016/j.jconrel.2017.01.012

Mandal, A., Pal, D., Agrahari, V., Trinh, H. M., Joseph, M., and Mitra, A. K. (2018). Ocular delivery of proteins and peptides: challenges and novel formulation approaches. *Adv. Drug Deliv. Rev.* 126, 67–95. doi: 10.1016/j.addr.2018.01.008

Manoharan, C., and Singh, J. (2009). Insulin loaded PLGA microspheres: effect of zinc salts on encapsulation, release, and stability. *J. Pharm. Sci.* 98, 529–542. doi: 10.1002/jps.21445

Marín-Teva, J. L., Cuadros, M. A., Martín-Oliva, D., and Navascués, J. (2011). Microglia and neuronal cell death. *Neuron Glia Biol.* 7, 25–40. doi: 10.1017/S1740925X12000014

Martin, D. F., Maguire, M. G., Fine, S. L., Ying, G., Jaffe, G. J., Grunwald, J. E., et al. (2012). Ranibizumab and bevacizumab for treatment of neovascular age-related macular degeneration. *Ophthalmology* 119, 1388–1398. doi: 10.1016/j.ophtha.2012.03.053

Mason, J. O., White, M. F., Feist, R. M., Thomley, M. L., Albert, M. A., Persaud, T. O., et al. (2008). Incidence of acute onset endophthalmitis following intravitreal bevacizumab (avastin) injection. *Retina* 28, 564–567. doi: 10.1097/IAE.0b013e3181633fee

Matanović, M. R., Kristl, J., and Grabnar, P. A. (2014). Thermoresponsive polymers: insights into decisive hydrogel characteristics, mechanisms of gelation, and promising biomedical applications. *Int. J. Pharm.* 472, 262–275. doi: 10.1016/j.ijpharm.2014.06.029

McConnell, V., and Silvestri, G. (2005). Age-related macular degeneration. *Ulster Med. J.* 74, 82–92.

McLaughlin, M. M., Paglione, M. G., Slakter, J., Tolentino, M., Ye, L., Xu, C. F., et al. (2013). Initial exploration of oral pazopanib in healthy participants and patients with age-related macular degeneration. *JAMA Ophthalmol.* 131, 1595–1601. doi: 10.1001/jamaophthalmol.2013.5002

Medina, C., Santos-Martinez, M. J., Radomski, A., Corrigan, O. I., and Radomski, M. W. (2009). Nanoparticles: pharmacological and toxicological significance. *Br. J. Pharmacol.* 150, 552–558. doi: 10.1038/sj.bjp.0707130

Mi, F.-L., Lin, Y.-M., Wu, Y.-B., Shyu, S.-S., and Tsai, Y.-H. (2002). Chitin/PLGA blend microspheres as a biodegradable drug-delivery system: phase-separation, degradation and release behavior. *Biomaterials* 23, 3257–3267.

Michalska-Małecka, K., Kabiesz, A., Nowak, M., and Śpiewak, D. (2015). Age related macular degeneration – challenge for future: pathogenesis and new perspectives for the treatment. *Eur. Geriatr. Med.* 6, 69–75. doi: 10.1016/J.EURGER.2014.09.007

Moghimi, S. M., Patel, H. M., and Patel, H. M. (1989). Serum opsonins and phagocytosis of saturated and unsaturated phospholipid liposomes. *Biochim. Biophys. Acta* 984, 384–387.

Morirero, T., Ogura, Y., Hondo, Y., Suong-Hyu Hyoaf, R. W., and Ikadaf, Y. (1991). Microspheres of Biodegradable Polymers as a Drug-Delivery System in the Vitreous. *Invest. Ophthalmol. Vis. Sci.* 32, 1785–1790.

Mu, H., Wang, Y., Chu, Y., Jiang, Y., Hua, H., Chu, L., et al. (2018). Multivesicular liposomes for sustained release of bevacizumab in treating laser-induced choroidal neovascularization. *Drug Deliv.* 25, 1372–1383. doi: 10.1080/10717544.2018.1474967

Narvekar, P., Bhatt, P., Fnu, G., and Sutariya, V. (2019). Axitinib-loaded Poly(Lactic-Co-Glycolic Acid) nanoparticles for age-related macular degeneration: formulation development and in vitro characterization. *Assay Drug Dev. Technol.* 17, 167–177. doi: 10.1089/adt.2019.920

Nash, B., Ioannidou, K., and Barnett, S. C. (2011). Astrocyte phenotypes and their relationship to myelination. *J. Anat.* 219, 44–52. doi: 10.1111/j.1469-7580.2010.01330.x

Navratil, T., Maynor, B., and Yerxa, B. (2014). Improving outcomes: in ophthalmology via sustained drug delivery. *ONdrugDelivery* 48, 10–13.

Nayak, K., and Misra, M. (2018). Biomedicine & Pharmacotherapy A review on recent drug delivery systems for posterior segment of eye. *Biomed. Pharmacother.* 107, 1564–1582. doi: 10.1016/j.biopha.2018.08.138

Nowak, J. Z. (2006). Age-related macular degeneration (AMD): pathogenesis and therapy. *Pharmacol. Rep.* 58, 353–363.

Nozaki, M., Raisler, B. J., Sakurai, E., Sarma, J. V., Barnum, S. R., Lambris, J. D., et al. (2006). Drusen complement components C3a and C5a promote choroidal neovascularization. *Proc. Natil. Acad. Sci. U.S.A.* 103, 2328–2333. doi: 10.1073/pnas.0408835103

Nussenblatt, R. B., and Ferris, F. (2007). Age-related macular degeneration and the immune response: implications for therapy. *Am. J. Ophthalmol.* 144, 618–626. doi: 10.1016/j.ajo.2007.06.025

Oo, C., and Kalbag, S. S. (2016). Leveraging the attributes of biologics and small molecules, and releasing the bottlenecks: a new wave of revolution in drug development. *Expert Rev. Clin. Pharmacol.* 9, 747–749. doi: 10.1586/17512433.2016.1160778

Osswald, C. R., Guthrie, M. J., Avila, A., Valio, J. A., Mieler, W. F., and Kang-Mieler, J. J. (2017). In vivo efficacy of an injectable microsphere-hydrogel ocular drug delivery system. *Curr. Eye Res.* 42, 1293–1301. doi: 10.1080/02713683.2017.1302590

Osswald, C. R., and Kang-Mieler, J. J. (2015). Controlled and extended release of a model protein from a microsphere-hydrogel drug delivery system. *Ann. Biomed. Eng.* 43, 2609–2617. doi: 10.1007/s10439-015-1314-7

Osswald, C. R., and Kang-Mieler, J. J. (2016). Controlled and extended in vitro release of bioactive anti-vascular endothelial growth factors from a microsphere-hydrogel drug delivery system. *Curr. Eye Res.* 41, 1216–1222. doi: 10.3109/02713683.2015.1101140

OTX-IVT (2020). *(anti-VEGF antibody implant) – Ocular Therapeutix*. Available online at: https://www.ocutx.com/research/otx-ivt/ (accessed June 28, 2020).

Pan, C. K., Durairaj, C., Kompella, U. B., Agwu, O., Oliver, S. C. N., Quiroz-Mercado, H., et al. (2011). Comparison of long-acting bevacizumab formulations in the treatment of choroidal neovascularization in a rat model. *J. Ocul. Pharmacol. Ther.* 27, 219–224. doi: 10.1089/jop.2010.0158

Pandit, J., Sultana, Y., and Aqil, M. (2017). Chitosan-coated PLGA nanoparticles of bevacizumab as novel drug delivery to target retina: optimization, characterization, and *in vitro* toxicity evaluation. *Artif. Cells Nanomed. Biotechnol.* 45, 1397–1407. doi: 10.1080/21691401.2016.1243545

Patel, A., Cholkar, K., Agrahari, V., and Mitra, A. K. (2013). Ocular drug delivery systems: an overview. *World J. Pharmacol.* 2, 47–64. doi: 10.5497/wjp.v2.i2.47

Pirmoradi, F. N., Jackson, J. K., Burt, H. M., and Chiao, M. (2011). On-demand controlled release of docetaxel from a battery-less MEMS drug delivery device. *Lab Chip* 11, 2744–2752. doi: 10.1039/c1lc20134d

Polazzi, E., and Monti, B. (2010). Microglia and neuroprotection: from in vitro studies to therapeutic applications. *Prog. Neurobiol.* 92, 293–315. doi: 10.1016/j.pneurobio.2010.06.009

Qin, X. (2017). "Coaxial electrospinning of nanofibers," in *Electrospun Nanofibers*, ed. M. Afshari (Amsterdam: Elsevier Inc), 41–71. doi: 10.1016/B978-0-08-100907-9.00003-9

Qiu, F., Meng, T., Chen, Q., Zhou, K., Shao, Y., Matlock, G., et al. (2019). Fenofibrate-loaded biodegradable nanoparticles for the treatment of experimental diabetic retinopathy and neovascular age-related macular degeneration. *Mol. Pharm.* 16, 1958–1970. doi: 10.1021/acs.molpharmaceut.8b01319

Querques, L., Querques, G., Lattanzio, R., Gigante, S. R., Del Turco, C., Corradetti, G., et al. (2013). Repeated intravitreal dexamethasone implant (ozurdex®) for retinal vein occlusion. *Ophthalmologica* 229, 21–25. doi: 10.1159/000342160

Radhakrishnan, K., Sonali, N., Moreno, M., Nirmal, J., Fernandez, A. A., Venkatraman, S., et al. (2017). Protein delivery to the back of the eye: barriers, carriers and stability of anti-VEGF proteins. *Drug Discov. Today* 22, 416–423. doi: 10.1016/j.drudis.2016.10.015

Rakesh, T. (2019). "Advances in pharmaceutical product development and research," in *Biomaterials and Bionanotechnology*, 1st Edn, ed. T. Rakesh (Amsterdam: Elsevier).

Rathnasamy, G., Foulds, W. S., Ling, E.-A., and Kaur, C. (2019). Retinal microglia – A key player in healthy and diseased retina. *Prog. Neurobiol.* 173, 18–40. doi: 10.1016/j.pneurobio.2018.05.006

Ratnapriya, R., and Chew, E. Y. (2013). Age-related macular degeneration-clinical review and genetics update. *Clin. Genet.* 84, 160–166. doi: 10.1111/cge.12206

Rauck, B. M., Friberg, T. R., Medina Mendez, C. A., Park, D., Shah, V., Bilonick, R. A., et al. (2013). Biocompatible reverse thermal gel sustains the release of intravitreal bevacizumab in vivo. *Invest. Ophthalmol. Vis. Sci.* 55, 469–470. doi: 10.1167/iovs.13-13120

Risau, W. (1997). Mechanisms of angiogenesis. *Nature* 386, 671–674. doi: 10.1038/386671a0

Rivera, A., Fisher, S. A., Fritsche, L. G., Keilhauer, C. N., Lichtner, P., Meitinger, T., et al. (2005). Hypothetical LOC387715 is a second major susceptibility gene for age-related macular degeneration, contributing independently of complement factor H to disease risk. *Hum. Mol. Genet.* 14, 3227–3236. doi: 10.1093/hmg/ddi353

Rupenthal, I. D. (2017). Drug-device combination approaches for delivery to the eye. *Curr. Opin. Pharmacol.* 36, 44–51. doi: 10.1016/j.coph.2017.08.003

Sahoo, S. K., Dilnawaz, F., and Krishnakumar, S. (2008). Nanotechnology in ocular drug delivery. *Drug Discov. Today* 13, 144–151. doi: 10.1016/j.drudis.2007.10.021

Sakurai, E., Ozeki, H., Kunou, N., and Ogura, Y. (2001). Effect of particle size of polymeric nanospheres on intravitreal kinetics. *Ophthalmic Res.* 33, 31–36. doi: 10.1159/000055638

Santhanam, S., Liang, J., Struckhoff, J., Hamilton, P. D., and Ravi, N. (2016). Biomimetic hydrogel with tunable mechanical properties for vitreous substitutes. *Acta Biomater.* 43, 327–337. doi: 10.1016/j.actbio.2016.07.051

Saraf, A., Lozier, G., Haesslein, A., Kasper, F. K., Raphael, R. M., Baggett, L. S., et al. (2009). Fabrication of nonwoven coaxial fiber meshes by electrospinning. *Tissue Eng. Part C*15, 333–344. doi: 10.1089/ten.tec.2008.0422

Schlesinger, E., Ciaccio, N., and Desai, T. A. (2015). Polycaprolactone thin-film drug delivery systems: empirical and predictive models for device design. *Mater. Sci. Eng. C* 57, 232–239. doi: 10.1016/j.msec.2015.07.027

Schmit-Eilenberger, V. (2015). A novel intravitreal fluocinolone acetonide implant (Iluvien®) in the treatment of patients with chronic diabetic macular edema that is insufficiently responsive to other medical treatment options: a case series. *Clin. Ophthalmol.* 9, 801–811. doi: 10.2147/OPTH.S79785

Seah, I., Zhao, X., Lin, Q., Liu, Z., Su, S. Z. Z., Yuen, Y., et al. (2020). Use of biomaterials for sustained delivery of anti-VEGF to treat retinal diseases. *Eye* 34, 1341–1356. doi: 10.1038/s41433-020-0770-y

Sergejeva, O., Botov, R., Liutkevièienë, R., and Kriauèiûnienë, L. (2016). Genetic factors associated with the development of age-related macular degeneration. *Medicina* 52, 79–88. doi: 10.1016/j.medici.2016.02.004

Shah, S. S., Denham, L. V., Elison, J. R., Bhattacharjee, P. S., Clement, C., Huq, T., et al. (2010). Drug delivery to the posterior segment of the eye for pharmacologic therapy. *Expert Rev. Ophthalmol.* 5, 75–93. doi: 10.1586/eop.09.70

Sharpe, L. A., Daily, A. M., Horava, S. D., and Peppas, N. A. (2014). Therapeutic applications of hydrogels in oral drug delivery. *Expert Opin. Drug Deliv.* 11, 901–915. doi: 10.1517/17425247.2014.902047

Shen, J., Lu, G. W., and Hughes, P. (2018). Targeted ocular drug delivery with pharmacokinetic/pharmacodynamic considerations. *Pharm. Res.* 35:217. doi: 10.1007/s11095-018-2498-y

Spaide, R. F. (2017). Choroidal neovascularization. *Retina* 37, 609–610. doi: 10.1097/IAE.0000000000001575

Su, X., Tan, M. J., Li, Z., Wong, M., Rajamani, L., Lingam, G., et al. (2015). Recent progress in using biomaterials as vitreous substitutes. *Biomacromolecules* 16, 3093–3102. doi: 10.1021/acs.biomac.5b01091

Tabandeh, H., Boscia, F., Sborgia, A., Ciracì, L., Dayani, P., Mariotti, C., et al. (2014). Endophthalmitis associated with intravitreal injections. *Retina* 34, 18–23. doi: 10.1097/IAE.0000000000000008

Tanetsugu, Y., Tagami, T., Terukina, T., Ogawa, T., Ohta, M., and Ozeki, T. (2017). Development of a sustainable release system for a ranibizumab biosimilar using Poly(lactic-co-glycolic acid) biodegradable polymerbased microparticles as a platform. *Biol. Pharm. Bull.* 40, 145–150.

Tang, B. (2015). *Electrospinning: Principles, Practice and Possibilities*. Available online at: https://books.google.es/books?hl=es&lr=&id=znMoDwAAQBAJ&oi=fnd&pg=PP1&dq=Tang,+B.+Z.+(2015).+Electrospinning:+principles,+practice+and+possibilities.+Royal+Society+of+Chemistry.&ots=UdRDF2txrB&sig=y-iwskx-KpMKRAIvoKDMrtd8sAE (accessed July 9, 2020).

Tang, Y., and Le, W. (2016). Differential roles of M1 and M2 microglia in neurodegenerative diseases. *Mol. Neurobiol.* 53, 1181–1194. doi: 10.1007/s12035-014-9070-5

Tarallo, V., Hirano, Y., Gelfand, B. D., Dridi, S., Kerur, N., Kim, Y., et al. (2012). DICER1 Loss and Alu RNA induce age-related macular degeneration via the NLRP3 Inflammasome and MyD88. *Cell* 149, 847–859. doi: 10.1016/j.cell.2012.03.036

Thornton, J., Edwards, R., Mitchell, P., Harrison, R. A., Buchan, I., and Kelly, S. P. (2005). Smoking and age-related macular degeneration: a review of association. *Eye* 19, 935–944. doi: 10.1038/sj.eye.6701978

Tiwari, A., and Tiwari, A. (2013). *Nanomaterials in Drug Delivery, Imaging, and Tissue Engineering*. Hoboken, NJ: John Wiley & Sons.

Turturro, S. B., Guthrie, M. J., Appel, A. A., Drapala, P. W., Brey, E. M., Pérez-Luna, V. H., et al. (2011). The effects of cross-linked thermo-responsive PNIPAAm-based hydrogel injection on retinal function. *Biomaterials* 32, 3620–3626. doi: 10.1016/j.biomaterials.2011.01.058

Varshochian, R., Jeddi-Tehrani, M., Mahmoudi, A. R., Khoshayand, M. R., Atyabi, F., Sabzevari, A., et al. (2013). The protective effect of albumin on bevacizumab activity and stability in PLGA nanoparticles intended for retinal and choroidal neovascularization treatments. *Eur. J. of Pharm. Sci.* 50, 341–352. doi: 10.1016/j.ejps.2013.07.014

Varshochian, R., Riazi-Esfahani, M., Jeddi-Tehrani, M., Mahmoudi, A. R., Aghazadeh, S., Mahbod, M., et al. (2015). Albuminated PLGA nanoparticles containing bevacizumab intended for ocular neovascularization treatment. *J. Biomed. Mater. Res. Part A* 103, 3148–3156. doi: 10.1002/jbm.a.35446

Vilhardt, F., Haslund-Vinding, J., Jaquet, V., and McBean, G. (2017). Microglia antioxidant systems and redox signalling. *Br. J. Pharmacol.* 174, 1719–1732. doi: 10.1111/bph.13426

Villegas, V. M., Aranguren, L. A., Kovach, J. L., Schwartz, S. G., and Flynn, H. W. (2017). Current advances in the treatment of neovascular age-related macular degeneration. *Expert Opin. Drug Deliv.* 14, 273–282. doi: 10.1080/17425247.2016.1213240

Wang, C. H., Hwang, Y. S., Chiang, P. R., Shen, C. R., Hong, W. H., and Hsiue, G. H. (2012). Extended release of bevacizumab by thermosensitive biodegradable and biocompatible hydrogel. *Biomacromolecules* 13, 40–48. doi: 10.1021/bm2009558

Wang, K., Mitra, R. N., Zheng, M., and Han, Z. (2018). Nanoceria-loaded injectable hydrogels for potential age-related macular degeneration treatment. *J. Biomed. Mater. Res. Part A* 106, 2795–2804. doi: 10.1002/jbm.a.36450

Wang, Y., Liu, C. H., Ji, T., Mehta, M., Wang, W., Marino, E., et al. (2019). Intravenous treatment of choroidal neovascularization by photo-targeted nanoparticles. *Nat. Commun.* 10:804. doi: 10.1038/s41467-019-08690-4

Whitcup, S. M., and Robinson, M. R. (2015). Development of a dexamethasone intravitreal implant for the treatment of noninfectious posterior segment uveitis. *Ann. N. Y. Acad. Sci.* 1358, 1–12. doi: 10.1111/nyas.12824

Wilkinson, C., Schachat, A., Hinton, D., Freund, K. B., Sarraf, D., and Wiedemann, P. (2017). *Ryan's Retina* -, 6th Edn, ed. S. V. Sadda (Amsterdam: Elsevier).

William, F. R., Sailor, M., Chen, M., and Cheng, L. (2012). Nanostructured porous silicon dioxide microparticles as an intravitreal injectable drug delivery system for avastin (Bevacizumab) lasting six months. *Invest. Ophthalmol. Vis. Sci.* 53:456.

Wills, N. K., Ramanujam, V. M. S., Chang, J., Kalariya, N., Lewis, J. R., Weng, T. X., et al. (2008). Cadmium accumulation in the human retina: effects of age, gender, and cellular toxicity. *Exp. Eye Res.* 86, 41–51. doi: 10.1016/j.exer.2007.09.005

Winkler, B. S., Boulton, M. E., Gottsch, J. D., and Sternberg, P. (1999). Oxidative damage and age-related macular degeneration. *Mol. Vis.* 5:32.

World Health Organization (2018). *Priority Eye Diseases*. Geneva: World Health Organization.

Xu, X., Weng, Y., Xu, L., and Chen, H. (2013). Sustained release of avastin§from polysaccharides cross-linked hydrogels for ocular drug delivery. *Int. J. Biol.Macromol.* 60, 272–276. doi: 10.1016/j.ijbiomac.2013.05.034

Xue, K., Zhao, X., Zhang, Z., Qiu, B., Tan, Q. S. W., Ong, K. H., et al. (2019). Sustained delivery of anti-VEGFs from thermogel depots inhibits angiogenesis without the need for multiple injections. *Biomater. Sci.* 7, 4603–4614. doi: 10.1039/c9bm01049a

Yandrapu, S. K., Upadhyay, A. K., Petrash, J. M., and Kompella, U. B. (2013). Nanoparticles in porous microparticles prepared by supercritical infusion and pressure quench technology for sustained delivery of bevacizumab. *Mol. Pharm.* 10, 4676–4686. doi: 10.1021/mp400487f

Yang, P., Dong, Y., Huang, D., Zhu, C., Liu, H., Pan, X., et al. (2019). Silk fibroin nanoparticles for enhanced bio-macromolecule delivery to the retina. *Pharm. Dev. Technol.* 24, 575–583. doi: 10.1080/10837450.2018.1545236

Yasukawa, T., Ogura, Y., Tabata, Y., Kimura, H., Wiedemann, P., and Honda, Y. (2004). Drug delivery systems for vitreoretinal diseases. *Prog. Retin. Eye Res.* 23, 253–281. doi: 10.1016/j.preteyeres.2004.02.003

Yatvin, M. B., Kreutz, W., Horwitz, B. A., and Shinitzky, M. (1980). pH-sensitive liposomes: possible clinical implications. *Science* 210, 1253–1255. doi: 10.1126/science.7434025

Ye, Z., Ji, Y.-L., Ma, X., Wen, J.-G., Wei, W., and Huang, S.-M. (2015). Pharmacokinetics and distributions of bevacizumab by intravitreal injection of bevacizumab-PLGA microspheres in rabbits. *Int. J. Ophthalmol.* 8, 653–658. doi: 10.3980/j.issn.2222-3959.2015.04.02

Yeo, Y., and Park, K. (2004). Control of encapsulation efficiency and initial burst in polymeric microparticle systems. *Arch. Pharm. Res.* 27, 1–12.

Yu, J., Xu, X., Yao, F., Luo, Z., Jin, L., Xie, B., et al. (2014). In situ covalently cross-linked PEG hydrogel for ocular drug delivery applications. *Int. J. Pharm.* 470, 151–157. doi: 10.1016/j.ijpharm.2014.04.053

Yu, Y., Lau, L. C. M., Lo, A. C., and Chau, Y. (2015). Injectable chemically crosslinked hydrogel for the controlled release of bevacizumab in vitreous: a 6-month in vivo study. *Transl. Vis. Sci. Technol.* 4:5. doi: 10.1167/tvst.4.2.5

Yu, Y., Lin, X., Wang, Q., He, M., and Chau, Y. (2019). Long-term therapeutic effect in nonhuman primate eye from a single injection of anti-VEGF controlled release hydrogel. *Bioeng. Transl. Med.* 4:e10128. doi: 10.1002/btm2.10128

Zareparsi, S., Branham, K. E. H., Li, M., Shah, S., Klein, R. J., Ott, J., et al. (2005). Strong association of the Y402H variant in complement factor h at 1q32 with susceptibility to age-related macular degeneration. *Am. J. Hum. Genet.* 77, 149–153. doi: 10.1086/431426

Conflict of Interest: The authors declare that the research was conducted in the absence of any commercial or financial relationships that could be construed as a potential conflict of interest.

frontiers
in Bioengineering and Biotechnology

REVIEW
published: 10 December 2020
doi: 10.3389/fbioe.2020.588014

Biotechnology and Biomaterial-Based Therapeutic Strategies for Age-Related Macular Degeneration. Part II: Cell and Tissue Engineering Therapies

*Nahla Jemni-Damer[1,2†], Atocha Guedan-Duran[1,2,3†], María Fuentes-Andion[1,2], Nora Serrano-Bengoechea[1,2,4], Nuria Alfageme-Lopez[1,2,4], Félix Armada-Maresca[5], Gustavo V. Guinea[4,6,7,8], José Perez-Rigueiro[4,6,7,8], Francisco Rojo[4,6,7,8], Daniel Gonzalez-Nieto[4,6,8], David L. Kaplan[3] and Fivos Panetsos[1,2,4]**

[1] Neuro-computing and Neuro-robotics Research Group, Complutense University of Madrid, Madrid, Spain, [2] Innovation Group, Institute for Health Research San Carlos Clinical Hospital, Madrid, Spain, [3] Department of Biomedical Engineering, Tufts University, Medford, MA, United States, [4] Silk Biomed SL, Madrid, Spain, [5] Ophthalmology Service, La Paz University Hospital, Madrid, Spain, [6] Center for Biomedical Technology, Universidad Politécnica de Madrid, Pozuelo de Alarcon, Spain, [7] Department of Material Science, Civil Engineering Superior School, Universidad Politécnica de Madrid, Madrid, Spain, [8] Biomedical Research Networking Center in Bioengineering, Biomaterials and Nanomedicine, Madrid, Spain

OPEN ACCESS

Edited by:
Zhengwei Mao,
Zhejiang University, China

Reviewed by:
PaYaM ZarrinTaj,
Oklahoma State University,
United States
Jindan Wu,
Zhejiang Sci-Tech University, China

***Correspondence:**
Fivos Panetsos
fivos@ucm.es

†These authors have contributed equally to this work

Specialty section:
This article was submitted to Biomaterials,
a section of the journal
Frontiers in Bioengineering and Biotechnology

Received: 28 July 2020
Accepted: 19 November 2020
Published: 10 December 2020

Citation:
Jemni-Damer N, Guedan-Duran A, Fuentes-Andion M, Serrano-Bengoechea N, Alfageme-Lopez N, Armada-Maresca F, Guinea GV, Perez-Rigueiro J, Rojo F, Gonzalez-Nieto D, Kaplan DL and Panetsos F (2020) Biotechnology and Biomaterial-Based Therapeutic Strategies for Age-Related Macular Degeneration. Part II: Cell and Tissue Engineering Therapies. Front. Bioeng. Biotechnol. 8:588014. doi: 10.3389/fbioe.2020.588014

Age-related Macular Degeneration (AMD) is an up-to-date untreatable chronic neurodegenerative eye disease of multifactorial origin, and the main causes of blindness in over 65 y.o. people. It is characterized by a slow progression and the presence of a multitude of factors, highlighting those related to diet, genetic heritage and environmental conditions, present throughout each of the stages of the illness. Current therapeutic approaches, mainly consisting on intraocular drug delivery, are only used for symptoms relief and/or to decelerate the progression of the disease. Furthermore, they are overly simplistic and ignore the complexity of the disease and the enormous differences in the symptomatology between patients. Due to the wide impact of the AMD and the up-to-date absence of clinical solutions, Due to the wide impact of the AMD and the up-to-date absence of clinical solutions, different treatment options have to be considered. Cell therapy is a very promising alternative to drug-based approaches for AMD treatment. Cells delivered to the affected tissue as a suspension have shown poor retention and low survival rate. A solution to these inconveniences has been the encapsulation of these cells on biomaterials, which contrive to their protection, gives them support, and favor their retention of the desired area. We offer a two-papers critical review of the available and under development AMD therapeutic approaches, from a biomaterials and biotechnological point of view. We highlight benefits and limitations and we forecast forthcoming alternatives based on novel biomaterials and biotechnology methods. In this second part we review the preclinical and clinical cell-replacement approaches aiming at the development of efficient AMD-therapies, the employed cell types, as well as the cell-encapsulation and cell-implant systems. We discuss their advantages and disadvantages and how they could improve the survival and integration of the implanted cells.

Keywords: retinal pigment epithelium, Bruch's membrane, photoreceptors, biomaterials, cell therapy, tissue engineering, biotechnology, cell replacement

INTRODUCTION

Age-Related Macular Degeneration

Age-Related Macular Degeneration (AMD) is a multifactorial degenerative eye disease, estimated to affect nearly 290 million people by 2040 (Wong et al., 2014). It is characterized by the deterioration of the central retinal area in the elderly population leading to vision deterioration and even blindness [see Therapeutic Strategies for Age-Related Macular Degeneration Part I and Part II, also (Hoon et al., 2014; Wong et al., 2014)].

The retina is the inner component of the eyeball (**Figure 1**). It is a 10-layers complex structure, where a several types of neural cells, photoreceptors, bipolar, horizontal, amacrine and retinal ganglion cells, are tightly interconnected by means of chemical and electrical synapses to form a network. Visual perception starts at photoreceptors, highly specialized retinal neurons which convert light into electric signals. Retina's outer sheet, the Photoreceptors, lies over three non-neural layers: choroid, Bruch's membrane (BrM) and retinal pigment epithelium (RPE), all of them strongly involved in the development of the AMD (**Figure 1**; Hoon et al., 2014; Wong et al., 2014). Retina's inner layer is in contact with the vitreous humor, a non-vascularized transparent gelatinous medium that fills the interior of the eyeball, whose function is to maintain the shape of the eye and smooth the retinal surface to form sharp images.

The choroid is a vascularized layer that supplies oxygen and nutrients to the whole retina. Additionally, it serves as physical support and it also contributes to the maintenance of the intraocular pressure and the regulation of eye's temperature (Marmor and Wolfensberger, 1998; Michalska-Małecka et al., 2015). BrM is a 2–5 μm-thick acellular sheet, mainly composed of elastin, collagen I-V, laminin and fibronectin and it is divided into five layers: the choriocapillary basement membrane, the outer collagenous layer, the central band of elastic fibers, the inner collagenous layer and the RPE basement membrane (**Figure 2**; Hogan et al., 1971; Booij et al., 2010). It gives physical support to the RPE cells and regulates the exchange of molecules, oxygen, nutrients and metabolic residues between the choroid and the RPE (Hogan et al., 1971; Booij et al., 2010). RPE is a monolayer of highly specialized hexagonal cells that are in direct contact with the outer segment of the photoreceptors. It is dedicated to the absorption of scattered light, to the secretion of growth factors, the transport of nutrients from the choroid to the neural cells, the phagocytosis of the outer segment of the photoreceptors and, together with BrM, to the formation of the blood-retinal barrier (**Figure 2**; Cunha-Vaz, 1997; Campbell and Humphries, 2013). RPE cells play a key role in the maintenance of the visual function and the survival of the photoreceptors (Hoon et al., 2014; Wong et al., 2014) and, similarly to what happens to the neural cells, RPE cells cannot regenerate after birth (Marmor and Wolfensberger, 1998; Bharti et al., 2006; Cunha-Vaz et al., 2011; Jin et al., 2019).

Since choroid, BrM and RPE provide physical support for the neural retina, and since they are in charge for both, the interchange of the metabolic molecules and the correct physiological functioning of the photoreceptors, any degenerative pathology affecting one of these layers, would also impair or even kill the photoreceptors with the consequent visual impairment or even blindness. In AMD, BrM weakens and thickens, thus losing its permeability and diffusive properties (Booij et al., 2010). Low permeability and diffusion capability provoke an accumulation of the lipids and the cellular/metabolic residues that are originated in the RPE and the surrounding tissue, giving rise to drusen formation between RPE and BrM. In turn, these changes cause loss of the integrity of the external blood-retinal barrier as well as death of the RPE cells (Marmor and Wolfensberger, 1998; Booij et al., 2010). Due to RPE extensive interactions with the photoreceptors and because RPE cells are unable to regenerate after birth, RPE dysfunction or dead can cause permanent loss of vision capabilities (Marmor and Wolfensberger, 1998; Bharti et al., 2006; Cunha-Vaz et al., 2011; Jin et al., 2019). When alterations occur in the choroid, they give origin to the most aggressive form of AMD, the wet one (W-AMD): choriocapillar alterations provoke uncontrolled angiogenesis, sub-choroidal neovessels penetrate the subretinal space through existing BrM/RPE defects and destroy the morphology and cellular structure of the retinal tissue (Marmor and Wolfensberger, 1998; Michalska-Małecka et al., 2015).

In the human eye, there are approximately 137 million photoreceptors: 7 million cones and 130 million rods. Cones are concentrated in the center of the eye (in the fovea) and their density decreases radially from the center to the periphery. Rods are concentrated at about 20° from the center (approx. 6 mm from the fovea) and their density also decreases toward the periphery but, slower than the cones. Photoreceptors' degeneration is irreversible because all cellular regeneration and repair processes are inhibited by the unfavorable molecular conditions that prevail throughout the central nervous system. Among them, the absence or inappropriate concentration of neurotrophic and/or neurotropic factors, the appearance of inflammatory processes, astrocytic reactions and inhibitory molecular signals (myelin binding proteins or excess of neurotransmitters and ions), as well as the presence of myelin-associated factors and/or glial scar

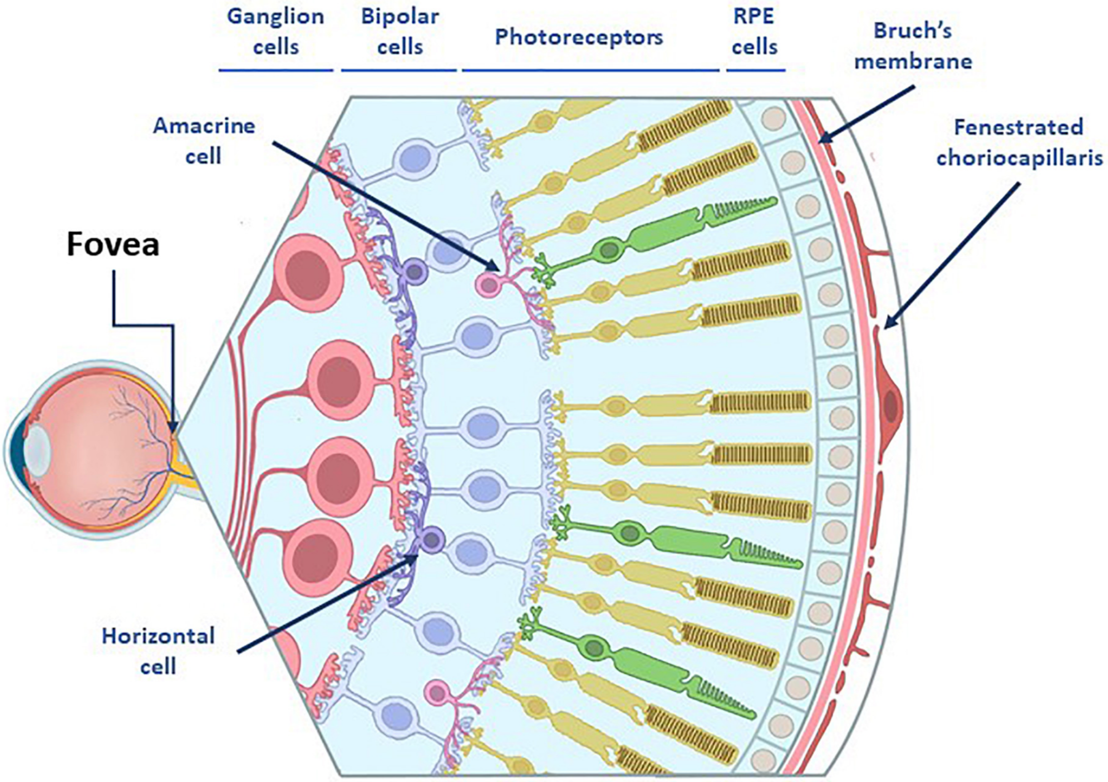

FIGURE 1 | Representation of the eye anatomy. The retina consists on 3 nuclear layers: (I) tanner nuclear layer which consists of ganglion cells bodies whose axons will form the optic nerve (II) the middle nuclear layer which are located the bipolar cell bodies and (III) the outer nuclear layer which includes photoreceptors, those cells lies over three non-neural layers: Choroid, Bruch's membrane (BrM) and retinal pigment epithelium (RPE) cells. In between the nuclear cell layers are two plexiform layers which contain amacrine and horizontal cells whose function is the modulation of the activity in the bipolar and ganglion cells via lateral inhibition.

(Bray et al., 1987; Aguayo et al., 1991; Sauve and Gaillard, 1995; Liu et al., 2006).

Drugs, molecules and factors' administration are the prevalent therapeutic options today, none of them being a therapy for the disease. They only contribute to slow down the progression of the pathology, with the aggravating factor that they are effective in only a small percentage of patients (Gehrs et al., 2006; Sabel et al., 2011; Irisvision, 2020). For this reason, in the last decades, serious efforts have been done to develop new, more effective treatments based either on the implant of stem cells that are used as micro-factories producing *in situ* neuroprotective and neuroregenerative biomolecules (Emerich and Thanos, 2008; Augustin et al., 2012; Guerrero-Naranjo et al., 2013; Barar et al., 2016), or on the replacement of damaged cells by autologous or allogeneic cell transplants (Gaillard and Sauvé, 2007; MacLaren and Pearson, 2007; Singh and MacLaren, 2011; Bharti et al., 2014; Singh et al., 2020).

The Immunoprivileged State of the Eye

The inflammatory response in the eye is regulated by its own immunosuppressive microenvironment, a series of complex regulatory systems which include vasoactive peptides (α-melanocyte-stimulating hormone, a regulator of the adaptive immune response, and calcitonin gene-related peptide), macrophage migration-inhibitory factor, and soluble CD95L (which regulates the innate immune response) (Taylor, 2016). Furthermore, the eye complement system plays an important role in the production of inflammatory cytokines (Goslings et al., 1998). Multiple complement factors have been described in the eye of both, human and mice (Anderson et al., 2010; Luo et al., 2011), which can be regulated by the CD46, CD55, CD59, and Crry proteins, expressed by microglia and RPE cells.

However, at the same time, the eye is one of the few immunoprivileged tissues, characterized by the presence of negative regulators which prevent the activation of local inflammatory processes (Medawar, 1948) and where implants can survive for an extended period of time (Streilein, 2003). The biological role of this immunological privilege is to avoid vision deterioration in case of overreaction of the immune system (Sandhu et al., 2019).

Immunoprivileged conditions are the result of a synergy of physical, molecular and cellular barriers (Taylor, 2016) implemented by inflammation suppressors and down-regulators

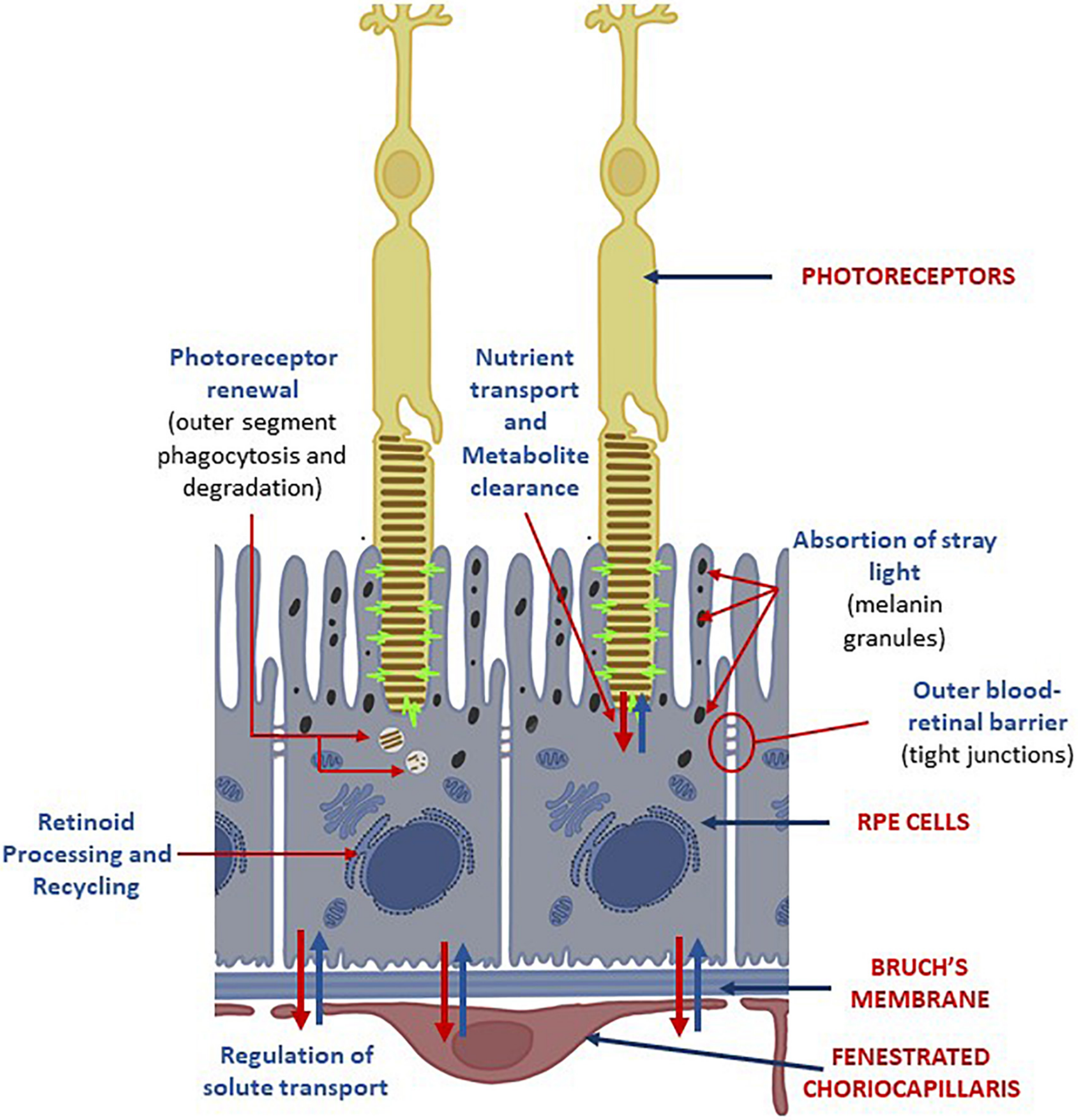

FIGURE 2 | Choroid-RPE-Photoreceptors interactions. RPE cells are located between the light-sensitive outer segments of the photoreceptors and the fenestrated choriocapillaris from the choroid. Its apical membrane faces the subretinal space and it's specialized to enable interactions between the monolayer of RPE and the outer segments of the photoreceptors. The functions of RPE cells on the neural retina are: (I) absorption of tray light by its abundant melanin granules; (II) retinoid processing and recycling; (III) transport of nutrients and metabolites: (IV) degradation of photoreceptors' outer segments. Its basolateral membrane is in contact with the Bruch's membrane. The tight junctions between RPE cells create a selective blood-retinal barrier that regulates the flow of nutrients, metabolic waste products, ions, proteins and water into and out the retina.

of the immune system, located either on cell membrane or the extracellular tissue (Taylor and Ng, 2018).

Blood-retina barrier and the indirect draining of the ocular microenvironment by the lymphatic system constitute the physical barriers. Blood-retina barrier is formed by the endothelial junctions of RPE cells which impede immune system cells to leak into the eye (Niederkorn et al., 1981). The indirect draining of the eye eliminates the necessity of a channel to the interior of the eye, which increases the difficulty for the immune system to reach the ocular tissue and enhances the efficiency of the blood-retina barrier. TGF-β2 and other soluble immunomodulatory molecules present in the aqueous humor constitute the molecular barrier, whose role is to attack and neutralize the cells of the immune system and to control inflammation (Taylor, 2016). Three antigen-presenting cell types, microglia, perivascular macrophages and dendritic cells, are believed to form the cellular barrier (Forrester and Xu, 2012): macrophages participate in the maintenance of vascular homeostasis in the retina and are believed to be capable of antigen presentation, although microglia is the primary antigen-presenting cell type of the eye.

Age-related macular degeneration-originated damages of the RPE alter this state of the eye. Cellular and tissue engineering AMD therapy procedures, either injections or surgical implants, also contribute to the worsening of the situation.

CELL AND TISSUE ENGINEERING THERAPIES

The retina, the tissue most severely by AMD is an easy target for cell and tissue engineering therapeutical approaches, because of its location and its small size, which allow easy surgical accessibility and transplantation of smaller amounts of replacement cells compared to other organs. Besides, the availability of a large number of clinical variables for the assessment of the visual function, facilitated the precise evaluation of the effectiveness of novel AMD therapies (Bennett et al., 2019) and fostered the development of several regenerative approaches based on BrM, RPE and photoreceptor cells replacement (Chichagova et al., 2018).

Biomolecules can be used for therapeutic reasons on a neural tissue, through two, non-mutually exclusive mechanisms. On one side, through the application of neuroprotective and neuroregenerative factors (directly injected to the neural tissue or secreted from implanted stem cells) which diffuse into the host tissue and rescue the degenerating cells. On the other, by implanting healthy cells into the host tissue and replacing the damaged/degenerated cells by the new ones. In the first case, to avoid molecules/cells dispersion into the host tissue, encapsulation can be employed. Porous materials permits the signals of the damaged environment to reach the implanted cells and stimulate the production of neuroprotective biomolecules, as well as to allow the diffusion of the secreted molecules to the damaged tissue (Battler and Leor, 2006; Weiner, 2008; Seiler and Aramant, 2012; Lin et al., 2017; Fernández-García et al., 2018; González-Nieto et al., 2018). However, although neuroprotective factors could protect retinal cells before apoptosis occurrence, their application is not a viable solution for many patients with advanced retinal pathologies. In the second case, cell replacement strategies get advantage of the encapsulation of therapeutic cells in biomaterial formats with an optimal mesh size to obtain a functional connection of donor cells with host tissue; however, this strategy faces the risk of a higher exposition to inflammatory responses that can be detrimental for the grafted cells as well as the risk of rejection of the allogenic material by the host tissue (**Figure 3**).

Cell Sources for Retinal Implants

Cells source is a key component to the success of any cell therapy. We can identify three main sources for retinal implants:

Embryonic or Fetal-Derived Stem Cells

They represent an attractive source due to their ability to self-renew and differentiate into any type of cell in the body (pluripotent). However, they also present serious disadvantages, e.g., difficult and expensive cell differentiation and cell expansion protocols, complex bioengineering processes, tumor formation risks, rejection risks, possibility of harboring donor's genetic defects, possible ethical challenges, etc. (Arnhold et al., 2004; Aoki et al., 2009; Lu et al., 2009; Falkner-Radler et al., 2011; Schwartz et al., 2012; Carr et al., 2013; Gonzalez-Cordero et al., 2013; Jayakody et al., 2015; Lu and Barnstable, 2017).

Adult Tissue-Derived Stem Cells

They are a source of autologous multipotent cells. However, these cells could be hard to obtain and they could harbor the genetic cause of the disease (West et al., 2009; Ballios and van der Kooy, 2010; Mead et al., 2013, 2015; Hertz et al., 2014; Park et al., 2017).

Induced Pluripotent Stem Cells

They are a relatively new source of stem cells developed by directly reprogramming adult somatic cells to transit to a pluripotent state. The use of iPSCs is exciting because iPSCs can be derived from the patient's own tissue and are associated with fewer ethical concerns than ESCs. Using a combination of soluble factors, iPSCs can be expanded and differentiated into various types of retinal cells, including rods, cones, and retinal ganglion cells. They present a very low rejection risk, however, they could conserve epigenetic characteristics of the original cells, harbor the disease genes from the donor and lead to tumor formation (Rowland et al., 2012; Kamao et al., 2014; Clegg et al., 2015; Mead et al., 2015; Fields et al., 2016; Rajala and Gardner, 2016; Bhattacharya et al., 2017; Bracha et al., 2017). The positive outcomes of early-phase trials postulate iPSCs as the most promising choice (**Table 1**; Chichagova et al., 2018).

Encapsulation of Biomolecule-Producing Stem Cells

At the present, cell encapsulation represents the preferred therapeutic approach since direct injection of cells has been proven to be suboptimal, due to cell losses from the rapid dispersion into the host tissue, along with glia and host immune system attacks.

In vitro Studies

In their attempt to create artificial BrM, (McCormick et al., 2020) generated a poly (ethylene terephthalate) (PET) scaffold with poly (lactic acid-co-glycolic acid) (PLGA) or poly (glycolic acid) (PGA) degradable nanoparticles that exhibited a continuous release of a fluorescent dye from PLGA particles for 2 weeks and from PGA particles for 1 day.

For cell encapsulation Bhatt et al. (2019) focused on composites by encapsulating retinal pigment epithelial cell line-19 model (ARPE-19) in PLGA nanoparticles of sunitinib malate, which in turn were included in thermosensitive hydrogels (from methoxy poly (ethylene glycol)-b-copolymers of polycaprolactone (mPEG-PCL)), to increase the residence time of the particles in the vitreous humor. In an *in vitro* study they showed that their device had better drug absorption, increased antiangiogenic potential, and prolonged inhibition of vascular endothelial growth factor (VEGF) activity compared to the free drug solution (Bhatt et al., 2019).

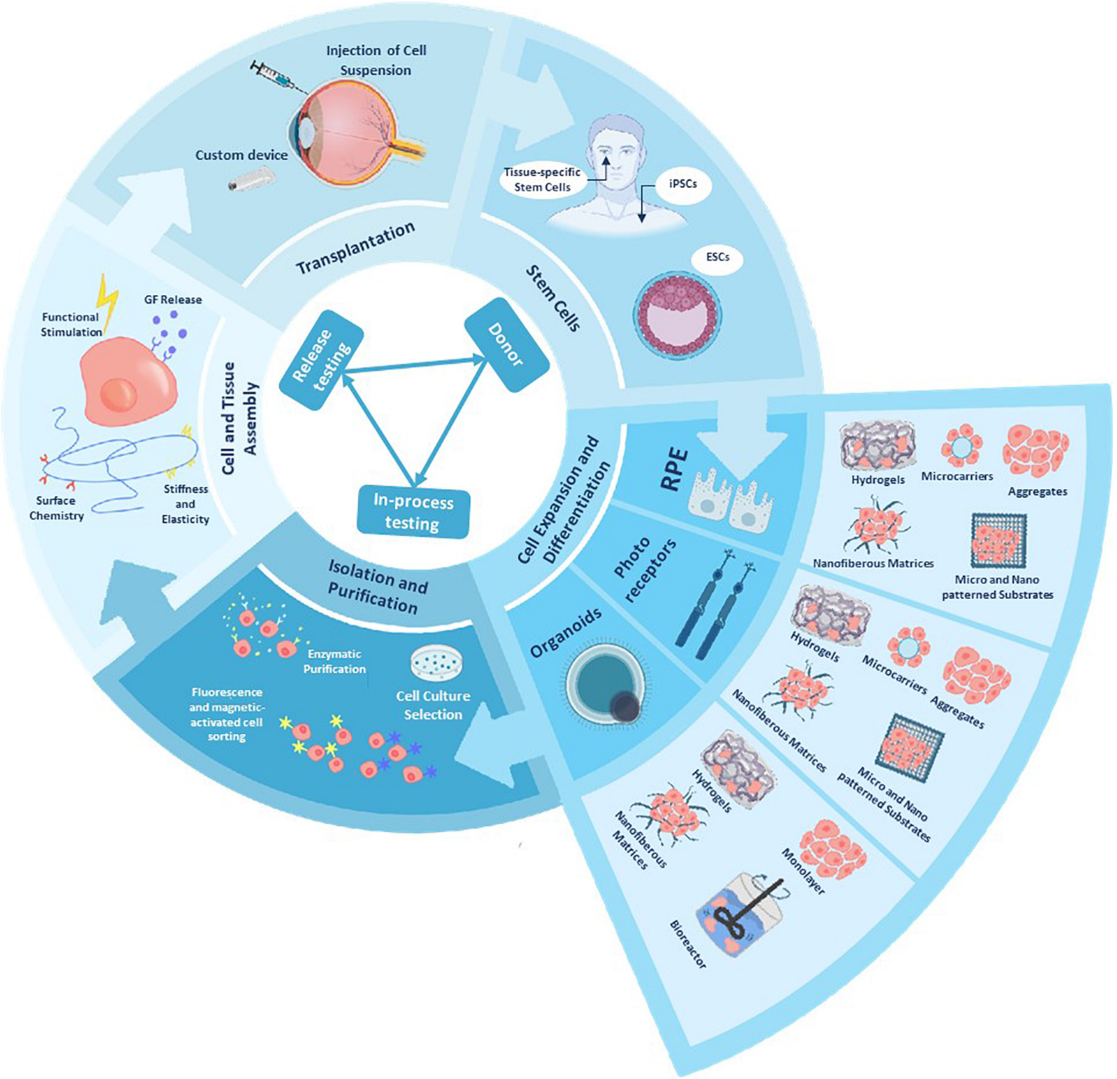

FIGURE 3 | Schematic representation of a tissue bioengineering model, applied to cell and tissue manufacture and delivery. Manipulating and differentiating stem cells into different retinal cells is a challenging with common goals as achieving manufacturing standard and testing for each clinical stage as well achieving an efficient manufacturing and banking. Bioengineering approaches can provide us with scalable 3D cell culture systems that allow differentiation into different retinal cells, biomanufacturer and bioassembly of functional eye tissues and delivery vehicles for an *in vivo* model [after (Stern et al., 2018)].

Clinical Trials

NT-501, NT-503 and iTrack275 Microcatheter, three products developed for the encapsulation of biomolecule-producing stem cells, are aiming at obtaining Food and Drug Administration (FDA) approval for AMD treatment (**Table 2**):

NT-501 (Renexus, Neurotech Pharma) is a non-biodegradable polysulfone scaffold to encapsulate genetically engineered human RPE cells. The device is injected intravitreally and provides a sustained delivery of ciliary neurotrophic factor for months. The device is sutured into the sclera by a titanium loop to avoid migration risks and requires surgery to get removed. The device is in Phase III clinical trials and it has been effective for up to 18 months providing photoreceptor protection (Tao et al., 2002; Bush et al., 2004; Sieving et al., 2006; Emerich and Thanos, 2008; Kuno et al., 2011; Birch et al., 2013; Bisht et al., 2017; U.S. National Library of Medicine, 2020b,g).

NT-503 (Neurotech Pharma) is a non-biodegradable polyethylene terephthalate semipermeable hollow fiber membrane that encapsulates genetically engineered human RPE cells that synthesize and secrete a VEGF receptor fragment crystallizable region. This device is implanted intravitreally through a peritomy and subsequent 3 mm sclerotomy and it has been shown to maintain therapeutic effects for 12 months in W-AMD and was 20 times more efficient than injections of Ranibizumab. As with NT-501, the device gets fixed to the sclera to avoid migration and also requires surgery to be removed.

TABLE 1 | Cellular types employed in AMD cell therapy.

Cell Type	Source	Advantages	Disadvantages
Autologous ocular tissue [1]	IPE cells, peripheral RPE patch or as suspension, Bruch membrane	Derived from the same embryonic cell line, can be easily collected	Can retain original epigenetic features, harbors donor's disease genes
Adult TDSC [2]	Bone marrow-derived mSC, adipose-derived cells, neural progenitor SC, umbilical tissue cells, RPE cells, Müller cells, ciliary margin zone SC	Multipotent, no rejection risks, source of factors providing neuroprotection	Hard to harvest, can harbor donor's disease genes
Fetal or early postnatal retinal progenitor cells [3]	Neuroretina, RPE sheet, combined RPE and retinal sheet, retinal progenitor cells	Feasible source of cell, low immunogenicity and not always rejected	Ethically challenging, likely to be rejected, harbors donor's disease genes
ESCs [4]	Inner cell mass of blastocyst	Pluripotent, self-renew ability, differentiated to all retinal cell types	Likely to be rejected, harbors donor's disease genes, risk of tumor formation, ethically challenging
iPSC [5]	Somatic cell (e.g., skin fibroblast) with factor- based reprogramming	Pluripotent, easy to grow, low rejection risk, differentiated to all retinal cell types	Can retain original epigenetic features, harbor donor's disease genes

IPE, iris pigment epithelium; RPE, retinal pigment epithelium; TDSC, tissue-derived stem cells; mSC, mesenchymal stem cells; SC, stem cells; ESCs, embryonic- or fetal-derived stem cells; iPSC, induced pluripotent stem cells; PR, photoreceptors. [1] (Crafoord et al., 2002; Falkner-Radler et al., 2011; van Zeeburg et al., 2012); [2] (Salero et al., 2012; Davis et al., 2017); [3] (Seaton et al., 1994; Little et al., 1998; Das et al., 1999); [4] (Schwartz et al., 2012); [5] (Carr et al., 2009).

TABLE 2 | Cell encapsulation technologies for solid implantable devices integrating stem cells for *in situ* production of therapeutic biomolecules.

Product	Secretome	Type	Description	TRL	Advantages	Disadvantages	Duration
Renexus NT-501 [1]	CNTF	Polysulfone	Polysulfone scaffold with hRPE cells, intravitreally injected	II/III	No immune response, no risk of implant migration, no serious side effects	Needs surgical removal, no improvement	18 m
NT-503 [2]	VEGFR-Fc	PET membrane	Semipermeable PET membrane containing hRPE cells, intravitreally injected	II	No immune response, no risk of implant migration	Needs surgical removal, no serious side effects	12 m
iTrack275 [3]	Bevacizumab/Stem cells (CNTO 2476)	Microcatheter + optic fiber + pump	Supra-choroidally injected	II	Controlled delivery of drugs and human stem cells	Surgically implanted and removed, no serious side effects	Refillable

CNTF, ciliary neurotrophic factor; RPE, retinal pigment epithelium; VEGF, vascular endothelium growth factor; VEGFR-Fc, VEGF receptor fragment crystallizable region; PET, polyethylene terephthalate. All devices are non-biodegradable. [1] (Neurotech Pharma) (Sieving et al., 2006; Emerich and Thanos, 2008; Birch et al., 2013); [2] (Neurotech Pharma) (Guerrero-Naranjo et al., 2013; Neurotech, 2020); [3] (Johnson and Johnson/iScience, Inc.) (Ho et al., 2017; U.S. National Library of Medicine, 2020a).

This device is in Phase II clinical trials (Sieving et al., 2006; Guerrero-Naranjo et al., 2013; Rupenthal, 2017; U.S. National Library of Medicine, 2020u).

iTrack275 Microcatheter (iScience Interventional) is a micro-calibrated pump for supra-choroidal drug/cell delivery, surgically inserted through a non-biodegradable microcatheter that includes an optical fiber illuminator to guide the insertion of the device. This suprachoroidal pump allows an improved supply of drugs, a longer duration and a greater penetration into the tissue due to the proximity to the choroid and the BrM, with the consequent avoidance of blurred vision, changes in the lens and in the vitreous (traction exerted), compared to pharmacological delivery by intravitreal or periocular injection. The device has been used in combination with Bevacizumab in advanced AMD and with cells derived from human umbilical tissue (CNTO 2476) for dry-AMD (D-AMD), showing good safety and efficacy with no serious complications (Kuno et al., 2011; Augustin et al., 2012; Pearce et al., 2015; Bansal et al., 2016; Rupenthal, 2017). Phase I/IIa trials were performed with CNTO 2476 using iTrack275, for the administration of a single subretinal dose. Although, it was associated with a high rate of retinal perforations and retinal detachments, when the cells were "sequestered" by the subretinal space, it was well tolerated and was associated with some improvement in visual acuity. Larger studies are required to confirm these results (Ho et al., 2017; U.S. National Library of Medicine, 2020a).

In situ Cell Replacement

BrM-RPE Transplantation

Early attempts

Early attempts of AMD tissue reconstruction consisted of either autologous (translocated explants) or allogenic (fetal origin) RPE transplants, to replace the damaged retinal tissue (Steindl and Binder, 2008) by substituting the whole choroid-BrM-RPE complex (Ruysch's complex) via an RPE-choroid explant or by an RPE layer alone. Despite some promising results on the autologous strategy in a small portion of patients (van Zeeburg et al., 2012) aiming at slowing the progression of the pathology and/or improving visual capability, these therapeutic approaches were abandoned due to a number of serious drawbacks. The most significant problems were the limited availability of autologous tissue and the maintenance of genetic risks to develop the disease. Even though allogenic transplants showed better results, today, RPE transplants with natural membranes have been totally replaced by implants based on biomaterials and eye/stem cells. However, the beneficial effects of these autologous and allogenic transplants served as a proof-of-principle for the subsequent cell therapy strategies (Hynes and Lavik, 2010; Yao et al., 2011; Kim et al., 2012; Tam et al., 2014).

In vitro and pre-clinical trials

Retinal pigment epithelium degeneration can lead to the development of more advanced AMD stages so, transplants of healthy RPE cells have been considered as candidates for the deceleration of the disease (Ambati and Fowler, 2012). Vision improvement of AMD patients subject to RPE cell transplantation supported this approach (van Zeeburg et al., 2012). The specific requirements for improving physiological functions and fostering the survival of RPE cells, are thickness, flexibility, permeability and biodegradability of the implant, as well as easiness to handle during surgical intervention (Hynes and Lavik, 2010). Artificial BrM needs to be biocompatible while promoting and maintaining a proper RPE phenotype. Good integration with the choroid is also sought. In addition, artificial membranes must be porous, thin (less than 10 μm, mimicking BrM) and mechanically competent to withstand manipulation during surgery. Since damaged BrM can also compromise the success of cell transplantation, several researchers dedicated their efforts to the development of artificial membranes allowing successful transplantation of RPE cells (Srivastava et al., 2011; Hu et al., 2012; Warnke et al., 2013; McHugh et al., 2014; Stanzel et al., 2014; Ilmarinen et al., 2015; Peng et al., 2016; Calejo et al., 2017; Harris et al., 2019; McCormick et al., 2020).

A number of artificial scaffolds seeded with RPE cells, mimicking a healthy BrM-RPE complex, have been investigated. Collagen has been one of the most experimented materials because it is one of the fundamental components of BrM: (Lu et al., 2007) cultured human ARPE-19 cells in 2.4 μm-thick collagen films confirming cell attachment and viability at 25 days and a suitable cell phenotype. Other polymeric substrates have been tested *in vitro* and/or *in vivo* with comparable results: gelatin (Del Priore et al., 2004; Lai, 2013; Rose et al., 2014), poly-methyl-methacrylate (PMMA) (Tao et al., 2007), modified polytetrafluoroethylene (PTFE) (Maminishkis et al., 2016), polyethylene terephthalate (PET) (Kamao et al., 2014; Liu et al., 2014, 2018; Jin et al., 2018), polyester matrix membranes (Liu et al., 2014; Stanzel et al., 2014), poly-caprolactone (PCL) (Redenti et al., 2008; McHugh et al., 2014; Tam et al., 2014), poly(L-lactic acid) blends (PLLA/PLGA) (Giordano et al., 1997; Lu et al., 1998; Hadlock et al., 1999; Warnke et al., 2013), polyethylene glycol di-methacrylate (PEGDMA) (Singh et al., 2001), polydimethylsiloxane (PDMS) (Peng et al., 2016). Silk fibroin was also used as a versatile material for scaffolds since it has a number of functional groups that can react with biomolecules of interest like arginine–glycine–aspartic acid (RGD) (Chirila et al., 2008, 2015; Wenk et al., 2011; Kundu et al., 2013; Xiang et al., 2014; Zhang et al., 2015), all of them in experimental phase.

Synthetic BrMs consisting of PET scaffolds and degradable nanoparticles were developed by McCormick et al. (2020). ARPE-19 cells cultured on these scaffolds were able to form monolayers and were maintained for up to 3 months without any cytotoxic effect. This proof-of-concept showed the potential of this nanoparticle-scaffold system for future RPE transplantation. In another synthetic BrM, composed of collagen type I and PLGA, cultured human RPE (hRPE) showed polarity, phagocytic activity, and native RPE characteristic morphology and they were maintained alive for at least 11 days (Warnke et al., 2013). Calejo et al. (2017) developed microporous films comprised of copolymer 96/4 L-lactide/D-lactide with deposited layers of collagen type I and IV. These films simulated BrM characteristics and acted as a support for cultured human embryonic stem cell-derived RPE (hESCs-RPE) cells. These cells were maintained alive for 8 weeks and revealed good adhesion, morphology, and expressed RPE markers. In a different study, fetal human RPE (fhRPE) cultured on porous PCL scaffolds for 8 weeks showed positive results regarding survival, mature and functional RPE markers expression, barrier function, etc. (McHugh et al., 2014). Plasma-modified PDMS with laminin (PDMS-PmL) scaffolds were also used as an artificial BrM. Pluripotent differentiated RPE (dRPE) cells cultured on these scaffolds revealed good adhesion, proliferation, polarization, maturation, and functionality. Also, PDMS-PmL could sustain a multilayer of dRPE cells and precursors of photoreceptors. Furthermore, the PDMS-PmL-RPE subretinal implant *in vivo* in porcine eyes confirmed the biocompatibility of the material for a 2-year period (Peng et al., 2016). In another study, films made of elastin-like recombinamers (ELRs) were investigated: ARPE-19 cells cultured with a bioactive sequence (RGD), maintained their phenotype for up to 5 days and no cytotoxicity was detected (Srivastava et al., 2011).

Stanzel et al. (2014) tested the viability of a subretinal transplant of hESCs-derived RPE cells on a polyester matrix in rabbits. 1-month post-implantation, hESCs-derived RPE remained viable, maintaining their polarization and monolayer structure. hESCs-derived RPE cultured on ultrafine porous polyimide (PI) membranes survived for 6 weeks after subretinal injection in rats, which also showed some functional rescue of electroretinography signal (Ilmarinen et al., 2015). hESCs-RPE on PI transplanted subretinally into rabbit's eyes showed good membrane tolerability but low RPE cells survival (Ilmarinen et al., 2015).

Spider silk, a very promising biomaterial for artificial BrM, was also tested *in vitro*. This silk fibroin-based membrane allowed ARPE-19 cells to develop a morphology and physiology very similar to those of native RPE cells, as it was shown by the morphological studies and the analysis of their protein expression profiles. This native-like phenotype remained in the silk fibroin films for up to 7 days (Harris et al., 2019). In a very recent study (Jemni Damer et al., 2020) built a multilayer 3D biohybrid retina with RPE, Müller and retinal neural cells on silkworm silk fibroin biofilms, glued with silk fibroin hydrogels. Both, RPE and neural retinal cells survived *in vitro* for the 7 days of the experiment.

In addition to the above substrates, expanded PTFE (ePTFE)-modified membranes were developed to serve as a substrate for RPE growth (Krishna et al., 2011). The surface of the membranes was modified by an ammonia gas plasma treatment, which resulted in ARPE-19 cells attachment and enhanced proliferation. ARPE-19 cells grew in a monolayer and displayed phagocytic capacity. Parylene polymer has also been used as support for the growth and subretinal implantation of hESCs-RPE cells in rats, allowing post-implant cell survival (Hu et al., 2012).

Hsiung et al. (2015) showed that RPE cells derived from hESCs, implanted in the subretinal space within a supporting biomaterial, had higher survival rates than injections of cell suspensions. Previous studies testing artificial RPE strata built with hESCs growing on thin polymeric sheets obtained good results (Redenti et al., 2008; Liu et al., 2012, 2013). Functional integration into the host system is not easy, as it requires migration to the target nuclei, differentiation into the correct cell type for integration into the existing circuitry, and restoration of long-term function. All these steps have to be done by the stem cells while exposed to the hostile conditions of the degenerating retina. Almost all current tissue reconstruction approaches are in the experimental phase, either *in vitro* or *in vivo*, with only a few of these are in clinical trials (see **Tables 3**, **4**).

Clinical trials

Clinical trials of RPE transplantation include both, injections of suspensions of RPE cells to the posterior segment of the eye and implants of RPE monolayers (alone or in a substrate) between the retina and the native RPE cells.

Safety and tolerability of subretinally transplanted hESC-RPE cells in suspension in patients with advanced D-AMD has been assessed in a Phase I/II trial (U.S. National Library of Medicine, 2020m). The transplanted cells were well tolerated up to 4 months post-injection (Schwartz et al., 2012) and no adverse effects were detected in the patients in the next 22 months (Schwartz et al., 2015). Another Phase I/II Trial with the same objective is currently recruiting patients (U.S. National Library of Medicine, 2020k).

Regarding RPE monolayers transplantation, a Phase I Trial tested the safety of an ESCs-RPE patch on a vitronectin-coated polyester membrane subretinally implanted in two patients affected by W-AMD (U.S. National Library of Medicine, 2020c). Implants were well tolerated and resulted in a gain in visual acuity in both patients (da Cruz et al., 2018). A Phase I/II Trial to assess the safety and tolerability of subretinally implanted hESCs-RPE on a non-degradable Parylene membrane in D-AMD patients is underway (U.S. National Library of Medicine, 2020m).

Parylene and PLGA membranes are in Phases I/II and Phase I/II Clinical Trials, respectively (Liu et al., 2012; Lu et al., 2012; Diniz et al., 2013; U.S. National Library of Medicine, 2020m). A Phase I/II Trial to assess the safety and tolerability of subretinally implanted hESCs-RPE on a non-degradable Parylene membrane in D-AMD patients is underway (U.S. National Library of Medicine, 2020m). Also, Phase I/II Trial for the subretinal implant of a PLGA biodegradable scaffold, carrying autologous iPSC-derived RPEs in patients affected by AMD-associated geographic atrophy is currently recruiting patients (U.S. National Library of Medicine, 2020d).

It is worthy to state that a sheet of iPSC-derived RPE implanted in a W-AMD patient after removal of the neovascular membrane did not show visual acuity improvement and provoked a macular edema 1 year after surgery (Mandai et al., 2017a), while a Japanese Phase I Trial of RPE monolayers of iPSC-derived RPE cells, implanted as strips with no substrate, began in early 2014 was suspended in that same year.

Resuming, up to now, both, RPE cells injected in suspension and implanted as monolayers on artificial BrMs showed good preliminary results in terms of safety and tolerability. RPE cells injected in suspension have several drawbacks such as the necessity to migrate from the injection site and the tendency of suspended RPE to de-differentiate, problems not present in implanted scaffolded RPE monolayers. No positive results are available in terms of AMD therapy and visual acuity recovery.

Photoreceptors' Transplantation

General considerations

Different types of cells have been used for neural retinal cell replacement, including photoreceptor precursor cells (PPCs), photoreceptors, and retinal stem cells (RSCs) (see (Lakowski et al., 2011; Tucker et al., 2011; Eberle et al., 2012, 2014; Pearson et al., 2012; Barnea-Cramer et al., 2016) for the former, (Yang et al., 2010; Gust and Reh, 2011; Pearson et al., 2012; Singh et al., 2013; Gagliardi et al., 2018; Garita-Hernandez et al., 2019; Lorach et al., 2019) for the second and (Singh et al., 2020) for the latter. The sources of RSCs can be either endogenous, including neuronal stem cells, or exogenous, including ESCs and iPSCs (Tu et al., 2019).

Similarly to other types of cells, also photoreceptors can be transplanted, either to secret immunomodulatory and/or neuroprotective factors that foster the protection and recovery of the damaged cells or to replace the damaged photoreceptors by new ones (Singh et al., 2020). Photoreceptors' replacement can be a good therapeutic strategy when, in advanced AMD stages, this type of cells become dysfunctional and eventually die as a result of RPE cells' deterioration and death (Bhutto and Lutty, 2012). Fortunately, there is a wide time-window for therapeutic interventions, because inner retinal layers' neurons can survive for prolonged periods of time after photoreceptors degeneration, offering the possibility for cell transplantation to be successful (Medeiros and Curcio, 2001; Jones et al., 2003). However, to make synapses with the bipolar cells and to reverse the synaptic

TABLE 3 | Biohybrids/TI, Biomaterials-encapsulated RPE cells, *in vitro* studies.

Product	**Cell types**	**Description**	**Format**	**Cell survival**
Collagen-PLGA [1]	Human RPE cells	RPE cells formed a monolayer, showed polarity and native-like morphology could phagocytose	film	<2 w
Collagen [2]	Human RPE cell line (ARPE-19)	RPE cells formed a monolayer with appropriate phenotype and could phagocytose photoreceptors outer segments	scaffold	>1 w
Collagen [3]	Human RPE cell line (ARPE-19)	RPE cells formed a monolayer on both materials, collagen demonstrated upregulation of angiogenic molecule	scaffold	0.5 w
Gelatin [4]	Human RPE cell line (ARPE-19)	RPE cells formed a monolayer with carbodiimide cross-linked gelatin membrane	film	0.5 w
Elastin-like recombinamers (ELRs) [5]	Human RPE cell line (ARPE-19)	ELRs were not toxic, ARPE-19 proliferated well and maintained their phenotype	film	<1w
Microphotodiode array (SiO2, Si3N4, Pt, MPDA-Pt) [6]	Porcine RPE cells	RPE cells formed a monolayer with appropriate phenotype, biocompatible and non-toxic	film	<2 w
PLC [7]	Fetal human RPE	RPE cells on nanopatterned porous PLC showed better pigmentation, increased cell density, superior barrier function, up-regulation of RPE-specific genes, etc., than on porous PCL, non-porous PCL, or Costar porous polyester transwells	scaffold	>8 w
PDMS-PmL [8]	Pluripotent cell differentiated RPE cells	dRPE revealed good adhesion, proliferation, polarization, maturation and functionality cultured on PDMS-PmL	scaffold	>3 w
PEGDMA [9]	Adult human RPE; porcine RPE	Over 90% viability; confluent cells expressed F-actin and tight junction	film	1 w
PET/PLGA-PGA NP [10]	Adult human RPE stem cell (hRPESC)	RPE cells formed a monolayer, the scaffold and NP showed no cytotoxicity	scaffold	12 w
PLLA/PLGA [11]	Fetal human RPE	Good properties, cell attachment, and proliferation	film	1 w
PLLA/PLGA [12]	Human primary RPE cells/Porcine RPE cells	RPE cells formed a monolayer, good properties, cell attachment and proliferation	film	2 w
PLDLA/Collagen [13]	Human embryonic stem cell derived RPE cells	Supported cell growth, hESCs-RPE showed good adhesion, morphology and maintained phagocytic capacity	film	8 w
PLGA/PEG/PLA [14]	Human RPE cell line (D407)	Micropatterned synthetic biodegradable polymer film that control RPE cell morphology, allows cell-cell interactions and higher cell adhesion	film	1 w
Polyimide (PI) [15]	Adult human RPE stem cell (hRPESC)	Cells established hexagonal, cobblestone morphology with strong pigmentation, expressed RPE specific markers, and phagocytosed photoreceptor outer segments	scaffold	–
Polytetrafluoroethylene-modified surface [16]	Human RPE cell line (ARPE-19)	ARPE-19 cells grew in a monolayer, showed phagocytic capacity. The film was not toxic.	film	2 w
Silk Fibroin/PLC/Gelatin [17]	Human primary RPE cells	Higher cell growth rate and higher expression of characteristic RPE genes compared to PCL and PCL-silk scaffolds	scaffold	>12 w
Silk fibroin [17] [18]	Human RPE cell line (ARPE-19)	RPE cells formed a monolayer, the material showed biocompatibility and no toxicity	film	>16 w
Spider silk proteins [19]	Human RPE cell line (ARPE-19)	RPE cells formed a monolayer with appropriate phenotype and began to exhibit barrier function properties	film	1 w

ESC, embryonic stem cells; dRPE, pluripotent differentiated RPE; RPE, retinal pigment epithelium; hESCs-RPE, human embryonic stem cell-derived RPE cells; ARPE-19, human retinal pigment epithelial cell line-19; PCL, poly caprolactone; PET, poly(ethylene terephthalate); PLGA, poly(lactic acid-co-glycolic acid); PGA, poly(glycolic acid); NP, nanoparticles; PLDLA, copolymer 96/4 L-lactide/D-lactide; PLLA, poly(L-lactic acid); PLA, poly(DL-lactic acid); PEGDMA polyethylene glycol dimethacrylate; PDMS-PmL, plasma modified polydimethylsiloxane coated with laminin. [1] (Warnke et al., 2013); [2] (Lu et al., 2007); [3] (Imai et al., 2007); [4] (Lai, 2013): [5] (Redenti et al., 2009); [6] (Guenther et al., 1999; Wu et al., 2007); [7] (McHugh et al., 2014); [8] (Peng et al., 2016); [9] (Singh et al., 2001); [10] (McCormick et al., 2020); [11] (Giordano et al., 1997); [12] (Hadlock et al., 1999); [13] (Calejo et al., 2017); [14] (Lu et al., 2001); [15] (Subrizi et al., 2012); [16] (Krishna et al., 2011); [17] (Xiang et al., 2014); [18] (Chirila et al., 2015); [19] (Harris et al., 2019).

remodeling that takes place after photoreceptors degeneration, implanted photoreceptors need to be functional, a very hard to achieve condition (Jones et al., 2012; Mandai et al., 2017a).

Although post-mitotic transplanted photoreceptors have been proved to be able to regain relative vision functionality (Pearson et al., 2012; Barber et al., 2013), to date no one has achieved a significant restoration of visual function.

In vitro and pre-clinical trials

Photoreceptor transplantation without biomaterials. Similarly to RPE cells, photoreceptors transplantation to the diseased eye can be done either by injection of dissociated cells suspension (see **Table 5**) (Gust and Reh, 2011; Pearson et al., 2012; Barber et al., 2013; Gagliardi et al., 2018; Garita-Hernandez et al., 2019) or by implanting them as a sheet of tissue, cultivated on a biomaterial

TABLE 4 | Biohybrids/TI, Biomaterials-encapsulated RPE cells, *in vivo* studies.

Product	Cell types	Description	Format	Model	Cell survival
Collagen [1]	Human RPE cells	Non-crosslinked collagen + supported RPE integrated with host RPE over crosslinked collagen	scaffold	rabbit	<6 w
Fibrinogen [2]	Human fetal RPE	RPE cells with crosslinked fibrinogen particles survived after transplantation into the subretinal space, retinal degeneration was noted in areas of particles	particles	rabbit	4 w
Gelatin [3]	RPE grafts	Subretinal transplant of an allogeneic RPE grafts embedded in gelatin, no infiltration of the graft site with inflammatory cells	film	pig	12 w
Parylene [4]	hESCs-derived RPE	hESCs-derived RPE survived post-implantation	film	rat	–
Parylene-C [5]	hESC-derived RPE cells	Safe and useful implantation of synthetic sheets seeded with organized retinal cells	film	rat	>1 w
PDMS-PmL [6]	iPSC derived RPE	Subretinal scaffold showed biocompatibility and preserved macular function up to 2 years after implantation with no inflammation	scaffold	pig	*
PET or P(LA-co-CL) [7]	hESC-derived RPE cells	Showed subretinal biocompatibility, some migration of native RPE cells into nanofibers, reactive gliosis with some photoreceptor degeneration	film	rabbit	>2 w
Polyester [8]	hESCs-derived RPE	hESCs-derived RPE maintained their structure and polarity on polyester matrix	matrix	rabbit	4 w
Polyester (PET) [7] [9]	Adult human RPE stem cell (hRPESC) and fetal human RPE stem cells	Subretinal implantation of a polarized monolayer of adult hRPESC-derived RPE, after implantation cells survived and maintained key properties, no graft proliferation.	film	rabbit	>4 w
Polyimide (PI) [10]	hESCs-derived RPE	Membrane well tolerated but hESCs-derived RPE showed loss of pigmentation over time	scaffold	rabbit	–
Silk Fibroin/PLC/Gelatin [11]	Human primary RPE cells	Subscleral implantation with no inflammation or rejection	scaffold	rabbit	>12 w

*ESC, embryonic stem cells; RPE, retinal pigment epithelium; hESCs-RPE, human embryonic stem cell-derived RPE cells; iPSC, induced pluripotent stem cell; PDMS-PmL, plasma modified polydimethylsiloxane coated with laminin; PET, poly(ethylene terephthalate); P(LA-co-CL), poly(l-lactide-co-ε-caprolactone); PCL, poly caprolactone. [1] (Bhatt et al., 1994); [2] (Oganesian et al., 1999); [3] (Del Priore et al., 2004): [4] (Hu et al., 2012); [5] (Liu et al., 2012; Lu et al., 2012; Diniz et al., 2013); [6] (Peng et al., 2016); [7] (Liu et al., 2014); [8] (Giordano et al., 1997); [9] (Stanzel et al., 2014); [10] (Ilmarinen et al., 2015) [11] (Xiang et al., 2014). *no cell viability assay performed after implantation.*

substrate (Yang et al., 2010). If the outer nuclear layer, the layer of the retina formed by the bodies of rods and cones, has already degenerated, the latter strategy would be preferable due to the difficulty of the injected cells to get integrated to the damaged tissue and reconstruct a new layer.

Subretinal injection of a suspension of photoreceptors from embryonic-postnatal mice showed that donor cells integrated well in the host retina and the morphology and marker expression of donor cells were similar to those of the photoreceptors of the host retina (Gust and Reh, 2011).

Early postnatal rat photoreceptors implanted as a sheet to a model of dominant retinitis pigmentosa slowed cone loss 6 months after surgery (Yang et al., 2010). Rod precursors from postnatal mice injected as dissociated cells formed synaptic connections with bipolar and horizontal cells in the retina of Gnat12/2 mice (congenital stationary night blindness model) and responded to light stimuli (Pearson et al., 2012). Also, early postnatal mice rod-photoreceptors, transplanted as a cell suspension into 6 different mice models of retinal degeneration, got integrated into the host tissue with better results in the Prph2$^{+/\Delta 307}$ model (retinitis pigmentosa model) (Barber et al., 2013). hiPSC-derived CD73+ photoreceptors isolated and injected in clusters in the eyes of immunosuppressed rats survived, and matured for 10 weeks (Gagliardi et al., 2018). Rat RPE/photoreceptors' grafts transplanted in a retinal degeneration rat model protected the host photoreceptor layer from degeneration 6 months after surgery. The graft integrated well with the host tissue and created synapses with the bipolar cells (Lorach et al., 2019).

An interesting approach was taken by Garita-Hernandez et al. (2019). They introduced a hyperpolarizing microbial opsin in photoreceptors extracted from P4 mice and transplant them as a cell suspension into transgenic blind mice lacking the whole layer of photoreceptors (Cpfl1/Rho-/- and C3H rd/rd mice) who recovered their visual function. The same authors obtained hiPSCs-derived cones expressing NpHR (Natronomonas pharaonis halorhodopsin); blind mice that received them also as cell suspension, displayed signs of retinal repair 4 weeks post-injection (Garita-Hernandez et al., 2019).

Photoreceptor transplantation with biomaterials. Both synthetic polymers and biological materials can be used in the fabrication of scaffolding structures for photoreceptors implants: natural materials like alginate, collagen, etc., are suitable for imitating natural architectures (Ramakrishna et al., 2001); synthetic polymers, such as poly-caprolactone (PCL) and poly (lactic-co-glycolic) acid (PLGA), offer higher mechanical strength and controllable degradation rates (Chen et al., 2011) although the latter usually cause less biological activity (Yang et al., 2017).

TABLE 5 | Transplanted photoreceptors.

Source	Cell type	Description	Format	Model	Cell survival
E12.5-P28 days mice [1]	photoreceptors	Cells integrated well in the host retina and expressed equal markers	dissociated cells	mouse	2 w
hiPSCs [2]	photoreceptors	Photoreceptors survived and matured in the host eye	injected in clusters	rat	10 w
P4 mice/hiPSCs [3]	photoreceptors	Blind mice recovered visual function/mice showed signs of retinal repair	cell suspension	mouse	4 w
P4-8 mice [4]	Rod precursors	Rod precursors stablished synaptic connection with cells in retina of Gnat12/2 mice and were light-responsive	dissociated cells	mouse	6 w
P6-8 mice [5]	photoreceptors	Prph2$^{+/\Delta 307}$ model showed higher integration of rods	cell suspension	mouse	4 w
P8 rat [6]	photoreceptors	Transplantation reduced cone loss 6 months after surgery	sheet	rat	24 w
Adult rats [7]	Full-thickness retina with attached RPE	well-preserved host photoreceptor layer and RPE integrated well	graft	rat	–

E, embryonic day; P, postnatal day; Gnat12/2 mice, a model of congenital stationary night blindness; hiPSCs, human induced pluripotent stem cells; Prph2$^{+/\Delta 307}$, model of retinitis pigmentosa. [1] (Gust and Reh, 2011); [2] (Gagliardi et al., 2018); [3] (Garita-Hernandez et al., 2019); [4] (Pearson et al., 2012); [5] (Barber et al., 2013); [6] (Yang et al., 2010); [7] (Lorach et al., 2019).

Scaffolds for retinal progenitor cells (RPCs) transplants can be cylindrical, mimicking the vertical disposition of cells in the retina, fibrous, mimicking the microstructure of the extracellular matrix or made by hydrogels, to mimic the mechanical properties of the retina (Kador and Goldberg, 2012). The employment of 2D–3D scaffolds has been proved to be an efficient strategy to overcome the limitations of free cell injections, like low survival, low cell integration at the injection site and difficulty to maintain the injected cells in the target areas (Behtaj et al., 2020).

A 3D biodegradable poly-caprolactone (PCL)-microfabricated scaffold promoted good RPCs retention *in vitro* (Sodha et al., 2011). Another biodegradable PCL scaffold, in this case subretinally implanted in porcine eyes, showed good tolerability without retinal neither choroid inflammation (Christiansen et al., 2012). PCL scaffolds with varying surface topographies enhanced mice RPCs differentiation toward photoreceptor phenotype *in vitro*. Transplanted RPCs-PCL integrated well into the host retina and expressed specific markers of photoreceptors (Yao et al., 2015). And (Lawley et al., 2015) found that vitronectin-simulating peptides into a PCL film increased hRPCs adhesion, inhibited hRPCs proliferation and induced differentiation to photoreceptors phenotypes. Transplanted cells into mice degenerating retina, migrated to the outer nuclear layer and survive for 3 weeks.

In a multiple substrates study, RPCs showed good adhesion on poly-l-lysine, fibronectin, laminin, hyaluronic acid, and matrigel substrates *in vitro* (Thakur et al., 2018).

The fabrication of hybrids has also been explored. Poly-caprolactone (PCL)-retinal extracellular matrix hybrids allowed adhesion of the hRPCs cells and helped their differentiation toward the photoreceptor phenotype *in vitro* (Baranov et al., 2014). Interphotoreceptor matrix employed as a scaffolding material for hRPCs showed good cellular attachment absence of cytotoxicity and hRPCs differentiation toward the photoreceptor phenotype *in vitro* (Kundu et al., 2018). Tucker et al. (2010) tested a biodegradable cell delivery platform made of pre-activated MMP2 into a poly(lactic-co-glycolic) acid polymer *in vitro* and *in vivo*. Active MMP2 was released in a controlled manner and allowed RPCs to migrate into the outer nuclear layer and adopt a photoreceptor phenotype.

Jung et al. (2018) developed a 3D cup-shaped scaffold with μm-sized structures in ultrathin biocompatible elastomer films. These films were composed of a non-biodegradable part plasma-modified polydimethylsiloxane (PDMS) and a biodegradable part poly (glycerol-sebacate) (PGS) and were designed to deliver photoreceptors in a polarized manner. hPSCs-PRs showed polarization and robust survival *in vitro* 3 months post-seed in the scaffold.

Table 6 shows the most relevant studies for biomaterials-encapsulated progenitor cells/photoreceptors.

Clinical trials

Although preclinical studies have shown that all, RPCs, photoreceptor precursors and mature photoreceptors could potentially replace damaged retinal cells, clinical trials for these approaches are limited.

A Phase II study in which human fetal neural retinal tissue and RPE were transplanted together in a group of AMD patients, showed promising results (Radtke et al., 2008; U.S. National Library of Medicine, 2020o). Interestingly, the vision improvement observed in treated patients began 6 months after transplantation, the time predicted for the fetal cells to differentiate into mature photoreceptors. Another phase I/II study used HuCNS-SC® (human central nervous system stem cells) injected subretinally in AMD patients (U.S. National Library of Medicine, 2020r). This study was completed in 2015 but no results have been posted yet. Besides, a long-term follow-up safety study from the same sponsor has terminated based on, as posted, a business decision unrelated to safety concerns (U.S. National Library of Medicine, 2020i). Another clinical trial using HuCNS-SC® was terminated due to the same reason (U.S. National Library of Medicine, 2020q).

Bone marrow-derived stem cells have also got promising results in a Phase I/II Trial: NCT01920867 (Weiss et al., 2015; U.S. National Library of Medicine, 2020p). Another Phase I/II Trial testing bone marrow-derived stem cells, proved their safety: NCT01518127 (Cotrim et al., 2017; U.S. National Library of Medicine, 2020h).

Three ongoing clinical trials are using fetal-derived RPC for photoreceptor's replacement in retinitis pigmentosa patients.

TABLE 6 | Biohybrids/TI.

Product	Cell types	Description	Format	Model	Cell survival
Hyaluronic acid/methylcellulose [1]	RSC-derived rods	Improved cell survival, integration and migration, improved rod survival and visual function	hydrogel	mouse	3 w
Hyaluronic acid/methylcellulose [2]	RSCs	Superior cell distribution in subretinal space	hydrogel	mouse	4 w
IPM [3]	hRPCs	hRPCs attached well and differentiated into photoreceptors IPM showed no cytotoxicity	scaffold	*in vitro*	1 w
MMP2–PLGA polymer [4]	RPCs	RPCs differentiated into photoreceptors	scaffold	*in vitro*	2 w
MMP2–PLGA polymer [4]	RPCs	RPCs differentiated into photoreceptors and migrated to the outer nuclear layer of mice retina	scaffold	mouse	2 w
PCL [5]	Primary mouse embryonic RPCs	Localized to the outer nuclear layer and expressed appropriate photoreceptor markers	film	mouse	–
PCL [6]	Primary mouse embryonic RPCs	Supported cell growth, some migration and differentiation	scaffold	mouse	>4 w
PCL-extracellular matrix of the retina [7]	hRPCs	hRPCs adhered well and differentiated to photoreceptors	scaffold	*in vitro*	1 w
PLLA/PLGA [8]	GFP+ mouse RPCs	RPCs-seeded demonstrated effectiveness and increasing progenitor cell survival	scaffold	mouse	4 w
Polycaprolactone [9]	RPCs	Scaffold showed good retention of cells and good permeability	scaffold	*in vitro*	1 w
Polycaprolactone [10]	RPCs	RPCs integrated well in the outer nuclear layer and showed photoreceptor fate markers	scaffold	mouse	3 w
Polydimethylsiloxane and poly(glycerol-sebacate) [11]	hPSCs-PRs	Good polarization of PRs and robust survival 3 months post-seed	scaffold	*in vitro*	12 w
Poly (glycerol sebacate) [12]	Primary mouse embryonic RSPC	Transplanted cell migration into retina and maturation	scaffold	mouse	4 w
Poly-L-lysine, fibronectin, laminin, hyaluronic acid, and matrigel [13]	RPCs	RPCs showed good adhesion in the named substrates	scaffold/matrix	*in vitro*	–
Poly (methyl methacrylate) (PMMA) [14]	GFP+ mouse RSPC	PMMA scaffolds and transplanted into the sub-retinal space, biocompatible and non-toxic, retained RPE cells better during transplant, integrated cells expressed mature and immature markers	scaffold	mouse	1 w
Vitronectin- PCL [15]	hRPCs	hRPCs differentiated into photoreceptors and migrated to the outer nuclear layer of mice retina	film/scaffold	mouse	3 w

Biomaterials-encapsulated progenitor cells/photoreceptors. RPE, retinal pigment epithelium; RSCs, retinal stem cells; hRPCs, human retinal progenitor cells; RPCs, retinal progenitor cells; IPM, interphotoreceptor matrix; MMP2, matrix metallopeptidase 2; PLGA, poly(lactic acid-co-glycolic acid); PCL, poly caprolactone; PLLA, poly(L-lactic acid); PMMA, poly(methyl methacrylate); GFP, green fluorescent protein; hPSCs-PRs, human progenitor stem cells-derived photoreceptors. [1] (Shoichet et al., 2015); [2] (Ballios et al., 2010); [3] (Kundu et al., 2018): [4] (Tucker et al., 2010); [5] (Yao et al., 2015); [6] (Redenti et al., 2008); [7] (Baranov et al., 2014); [8] (Tomita et al., 2005); [9] (Sodha et al., 2011); [10] (Yao et al., 2015); [11] (Liu et al., 2014; Stanzel et al., 2014); [12] (Redenti et al., 2009); [13] (Thakur et al., 2018); [14] (Tao et al., 2007); [15](Lawley et al., 2015).

ReNeuron is carrying a phase I/II trial to evaluate the safety, tolerability and preliminary efficacy of hRPCs, administered as a suspension by a single subretinal injection (U.S. National Library of Medicine, 2020l). An already completed phase I/II study testing hRPCs injected intravitreally, showed that hRPCs were safe and well-tolerated at doses up to 3 million cells (U.S. National Library of Medicine, 2020n). A phase IIb clinical trial designed to assess efficacy of hRPCs is currently active (U.S. National Library of Medicine, 2020j). A phase I study to determine the safety of CD34+ marrow-derived stem cells injected intravitreally into the eye as a treatment for patients with various retinal conditions started in 2012 (U.S. National Library of Medicine, 2020f). Not results have been posted regarding the enrolled AMD patients. Future results from these studies may be extrapolated to AMD patients.

Retinal Organoids and 3D Structures Transplantation

Retinal cells' transplantation low success rates are due to the above mentioned adverse retinal environmental conditions, but also to the complexity of the interactions between photoreceptors and other retinal cell types as well as to the structural complexity of the photoreceptors themselves (Llonch et al., 2018). Particularly critical are the interactions RPE-photoreceptors since RPE cells are the responsible for the recycling of the visual pigment, for the phagocytosis of photoreceptors' external segment as well as for the secretion of growth factors (Strauss, 2005). Indeed, co-culture studies, attempting at de-differentiating mesenchymal stem cells, showed that RPE cells determine both, cell differentiation and connectivity of the differentiated cells (Salero et al., 2012). Unfortunately, during culture passages, RPE cells easily undergo an epithelial-mesenchymal transition (EMT), losing their characteristic cell polarity and cell-cell adhesion, necessary for the survival and functional integration of the photoreceptors (Sonoi et al., 2017). Furthermore, RPE cell cultures should be prepared exclusively with macular RPE cells because of phenotypes' differences between cells located in the peripheral part and cells located in the posterior part -macula- of the eye (cell shape and size, proliferation capacity, maturation time, granule content, growth potential, timing for the formation of tight junctions, etc. (Burke and Hjelmeland, 2005; Haderspeck et al., 2019). Non-homogeneous cultures would lead to retinal-type tissues, with structure vulnerable to degenerative retinal diseases (Burke and Hjelmeland, 2005).

Due to the above-mentioned complications and to the biological limitations of the available cells, researchers started to build artificial retinal tissues, with structural complexity and functionality mimicking the natural ones. As a consequence, retinal organoids have been built from either ESCs or iPSCs, by differentiating retinal cells through complex experimental protocols in 3D cell cultures (Eiraku et al., 2011; Nakano et al., 2012; Llonch et al., 2018).

The main benefits of 3D cultures are a high diversity of cell types, better tissue survival, functional interaction between the different types of cells, and the achievement of retinal layers thanks to the self-organizing capabilities of the PSCs. In addition to their use for therapeutic purposes, 3D cultures represent a model of great interest for the study of retinogenesis, a non-animal model of retinal diseases and a perfect tissue for drug screening. The main limitations of these types of models are the lack of vascularization, which leads to long-term necrosis in the innermost areas of the organoid, the lack of interaction between the RPE and photoreceptors' layer, the maturation of the different cell types which does not reach an adult state and the absence of some types of important cells, like microglia (Achberger et al., 2019). Furthermore, all organoids have a characteristic folded structure that not only makes implantation difficult but also causes greater cell death in the internal layers of this artificial tissue. The use of biomaterials could help in developing flat vascularized organoid retinas that would favor the interaction with the host tissue as well as the acceptance and survival of the transplanted cells (Singh D. et al., 2018). Advanced biomaterials could also facilitate artificial tissues manipulation and implant in a specific place in the host retina (Singh R. et al., 2018).

Tables 7, **8** resume up-to-day research in retinal organoids.

DISCUSSION

Functional Integration of the Implanted Cells

Cell therapy, and in particular stem cell-based therapy, is gaining strength as a potential therapeutic approach for untreatable retinal degeneration diseases (Bharti, 2018; Singh et al., 2020). It consists either in the use of ocular multipotent or RPCs, administered in a non-polarized way (cell suspension), to provide non-selective neuroprotective and/or neuromodulator factors, or in the implant of layered constructs of cells aiming at replacing the damaged or degenerated retinal tissue. In both cases, therapeutic effects are conditioned by the limited cell survival within the harmful ocular environment (Singh et al., 2020).

In the majority of the preclinical trials with dissociated cells suspensions for photoreceptor regeneration, the transplanted cells fail to survive or to functionally integrate with the host tissue; despite some positive results none of the attempted approaches achieved a significant restoration of the visual function (Gamm and Wong, 2015; Canto-Soler et al., 2016; Zarbin, 2016). Furthermore, it is not known to which extent the observed improvements are due to the capability of the grafted cells of replacing the lost retinal tissue; to the secretion of protective and regenerative factors that protect the retinal neurons, or by both of them (Liu et al., 2020).

Regarding RPE, there are several investigations on the inoculation of suspensions of this type of cells. However, up-to-now evidence suggests that suspension-injected RPEs do not consistently form a monolayer and do not survive in the long term (Hu et al., 2012; Diniz et al., 2013). Since RPE cells' therapeutic effects are conditioned by the polarization of the implanted cells as well as by their spatial arrangement in a monolayer settled in the subretinal space, there is a great challenge for injections of suspended cells (Miyagishima et al., 2016, 2017). Injected in suspension RPE cells loose most of their morphological and functional properties as proved by the low efficiency of this therapy in both, preclinical and clinical trials (Singh et al., 2020). The most promising studies focus on tissue transplantation or patches of RPE.

Promising results in both, feasibility and functionality, have been obtained in preclinical and clinical trials using functional RPE derived from both iPSCs (Bracha et al., 2017; Mandai et al., 2017b) and ESC cells (Klimanskaya et al., 2004; Bharti et al., 2006; Idelson et al., 2009; Miyagishima et al., 2016; May-Simera et al., 2018), as well as RPESC (Salero et al., 2012; Blenkinsop et al., 2013; Miyagishima et al., 2016; Mandai et al., 2017b). However, the use of iPSCs and ESC cells can lead to abnormal cell growth in the retina. Moreover, the differentiation toward a specific cell type (RPE) may not be complete or efficient, thus hindering their integration in the host retina. On their side, RPESC, although being fully committed to the RPE lineage, they are extracted from cadavers, which can lead to the retention of endophenotypes of aging and disease. Unlike cell suspensions, where the characteristics of RPE are lost, cell patches are capable of maintaining many of the typical cell functions (Miyagishima et al., 2016, 2017) which makes autologous choroid-RPE transplant surgical procedures a good candidate for AMD treatment (Joussen et al., 2006; Maaijwee K. et al., 2007; Maaijwee K.J.M. et al., 2007; Maaijwee et al., 2008).

Recent studies on subretinal injection of a suspension of photoreceptor precursors derived from mouse or human ESC/iPSC in rodent models of photoreceptor degeneration, suggested that the implanted cells are capable of getting integrated into the host retina, of achieving a morphological and

TABLE 7 | *In vitro* studies of 3D structures/organoids.

References	Product	Cell type	Description	Cell survival
Eiraku and Sasai, 2012	Matrigel	mESC	Organoid model to obtain a 3D retinal model.	>3 w
Hiler et al., 2015	–	miPSC	Model obtained from iPSC derived from different sources to study retinogenesis.	4 w
Hasegawa et al., 2016	Collagen	mESC	Organoid gel model to study retinogenesis.	>1 w
Völkner et al., 2016	Matrigel	mESC	Model to study retinogenesis.	3 w
Chen et al., 2016	–	mESC miPSC	Model to study morphogenesis of the photoreceptors.	5 w
Lamba et al., 2006	Matrigel	hESC	Model to obtain neural precursors and co-culture with retinal explant.	3 w
Osakada et al., 2008	–	mESC monkey ESC hESC	Model to obtain retinal cells. Co-culture with retinal explants to study interaction.	mESC-PR: >4 w monkey ESC-RPE:13 w monkey ESC- PR: 18 w hESC- RPE: 17 w hESC – PR: 28 w
Ohlemacher et al., 2015	Matrigel	hPSC	Model to study development of retinal tissue and drug screening.	10 w
Fligor et al., 2018	Matrigel	hPSC	Model to study development of retinal tissue and retinal ganglion cells growth.	6 w
Zhong et al., 2014	Matrigel	hiPSC	Modeling of diseases and to obtain retinal cells.	13 w
Nakano et al., 2012	–	hESC	Model to obtain and store retinal cells.	18 w
Lowe et al., 2016	Matrigel	hESC	Organoid model.	2 w
Achberger et al., 2019	Agarose Polydimethylsiloxane and Polyethylene terephthalate	iPSC	Development of vascularization in an organoid matrix and membrane models.	2 w
Thangaraj et al., 2011	–	Chicken retina	Organotypic culture. Retinal development model.	3 w
Engelsberg et al., 2008	Millicell inserts	Human retina	Organotypic culture. Development of neuronal and glial cells.	6 w
Niyadurupola et al., 2011	Millicell inserts	Human retina	Organotypic culture. Model for retinal ganglion cell degeneration.	0.5 w
Osborne et al., 2016	–	Human retina	Organotypic culture. Model for retinal ganglion cell degeneration.	4 w
Curatola et al., 2005	–	Mice retina	Organotypic culture. Vascularization of the 3d culture.	2 w
Caffé et al., 2002	–	Mouse retina	Organotypic culture. Retinal development.	4 w
Ghosh et al., 2009	–	Rat retina	Organotypic culture. Isolation of photoreceptors.	2 w
Wang et al., 2002	–	Mice retina	Organotypic culture. Introduction of genes. Study cellular differentiation.	1 w
Subrizi et al., 2012	Polyimide	hESC	Development of retinal pigment epithelium in a polyimide membrane. Coculture with rat retinal explants.	hESC-RPE: 2–8 w Coculture: <0.5 w
Johnson et al., 2016	–	Mice retina	Organotypic culture. Neuroprotection studies.	1 w
Engelsberg et al., 2005	–	Porcine retina	Organotypic culture.	6 w
Taylor et al., 2013	–	Porcine retina	Organotypic culture. Study the effect of the neurotrophic factors in retinal survival.	1.5 w
Taylor et al., 2014	polycarbonate	Porcine retina	Organotypic culture in a polycarbonate membrane. Study the effect of the biomaterial in the structure of the retina.	1.5 w
Huang et al., 2000	–	Rabbit retina	Organotypic culture. Developmental study.	1 w
Koizumi et al., 2007	–	Rabbit retina	Organotypic culture. Model for genetic manipulation.	1 w

mESC, mouse embryonic stem cell; miPSC, mouse induced pluripotent stem cell; hESC, human embryonic stem cell; hiPSC, human induced pluripotent stem cell.

TABLE 8 | textitIn vivo studies of 3D structures/organoids transplantation.

References	Product	Cell type	Description	Animal	Cell survival
Gonzalez-Cordero et al., 2013	–	mESC	Transplantation of photoreceptors from an organoid model.	Mouse	3 w
Assawachananont et al., 2014	Matrigel	mESC miPSC	Transplantation of retinal sheet into a degenerative model.	Mouse	2–24 w
Decembrini et al., 2014	–	mESC	Organoid model for retinal cells transplantation.	Mouse	3 w
Mandai et al., 2017a	–	miPSC	Retinal tissue transplant in a degenerative model.	Mouse	4 w
Johnson and Martin, 2008	–	Rat retina h-müller cells	Organotypic culture. Transplant of cells in an ocular hypertension model.	Rat	>2 w
Santos-Ferreira et al., 2016a	Matrigel	mESC	Organoid model. Transplantation of photoreceptors into mouse models.	Mouse	4–24 w
Santos-Ferreira et al., 2016b	Matrigel	mESC	Organoid model. Transplantation of photoreceptors into mouse models.	Mouse	10 w
Singh D. et al., 2018	Gelatin Chondroitin Sulfate Hyaluronic Acid	hESC	Biomaterials are used to develop a flat sponge retinal organoid that improves implantation and interaction with host tissue. Subretinal implant.	Mouse	12 w
Julien et al., 2011	Polyimide, gelatin	Rat retina	Subretinal implantation of organotypic layers in a biofunctionalized membrane maintaining a laminated format (Foils).	Rat	1 w (*in vitro*) 9 w (*in vivo*)
McLelland et al., 2018	–	hESC	Subretinal implantation or retinal sheets from organoids integrate in the host tissue.	Rat	8–43 w
Singh et al., 2019	–	hESC	Subretinal implantation or retinal tissue.	Cat	4–9 w
Koss et al., 2016	Parylene C	hESC	Subretinal implantation of a layer of RPE on mesh.	Yucatan minipig	4 w
Xian et al., 2019	Poly (Lactic-Co-Glycolic) (PLGA)	hiPSC	Epiretinal transplantation of retinal organoids using PLGA-composites.	Monkey	8 w
Mandai et al., 2017b	–	hiPSC	Transplantation of a retinal pigment epithelial cells sheet in a AMD model.	Human	52 w

mESC, mouse embryonic stem cell; miPSC, mouse induced pluripotent stem cell; hESC, human embryonic stem cell; hiPSC, human induced pluripotent stem cell.

functional differentiation similar to the native photoreceptors as well as of restoring some visual abilities (Lamba et al., 2009; Gonzalez-Cordero et al., 2013; Homma et al., 2013; Decembrini et al., 2014; Barnea-Cramer et al., 2016; Santos-Ferreira et al., 2016b). However, only a low proportion of transplanted cells can get integrated into the retina. What really happens is an exchange of intercellular materials between the immense majority of the native photoreceptors and the transplanted cells (Pearson et al., 2016; Santos-Ferreira et al., 2016b; Singh et al., 2016). This material transfer is bidirectional and, interestingly, it is independent of the source of implanted stem cells (Singh et al., 2016; Ortin-Martinez et al., 2017; Waldron et al., 2018). It seems that the therapeutic effects are due more to neurotrophic and neuroprotective function, rather than functional integration in the diseased retina (Liu et al., 2020). These facts raise the need to reevaluate all up-to-day photoreceptor transplant studies, characterizing the relative contribution to vision restoration based on material transfer and donor integration.

The recent development of 3D technology for the culture and differentiation of ESC/iPSC in retinal tissue has allowed several groups to test the viability of transplanting retinal sheets derived from this type of stem cell (Assawachananont et al., 2014; Shirai et al., 2016; Mandai et al., 2017a; Iraha et al., 2018). These ESC/iPSC-derived retinal sheets, derived from both mice and humans, are capable of surviving in the host retina for up to 6 months after transplantation in the subretinal space, in animal models of end-stage photoreceptor degeneration. In addition, they manage to generate all types of neural cells in the retina, i.e., photoreceptors, bipolar, amacrine, and retinal ganglion cells. In particular, the photoreceptors achieved a high degree of maturity, expressing opsins, synaptic proteins and formation of inner and outer segments (Assawachananont et al., 2014; Iraha et al., 2018). However, it has been revealed that in these grafts it is not possible to maintain an adequate laminar organization; instead, they generate a disorganized histoarchitecture (Assawachananont et al., 2014; Shirai et al., 2016; Mandai et al., 2017a; Iraha et al., 2018). 3D-culture techniques and implantation of retinal sheets suppose an expectation of providing photoreceptors in the form of tissue, providing them with an improved physical and physiological microenvironment, increasing their survival and functional integration capabilities. However, this area of cell therapy research has only just begun, so there are many emerging challenges and limitations that need to be addressed.

Regarding retinal organoids, despite the great advances achieved in this field, a number of serious limitations impede the employment of this technology for real AMD therapies: (1)

lack of vascularization, which leads to long-term necrosis in the innermost areas of the organoid (2) lack of interaction between RPE and photoreceptor layer, essential for the proper functioning of the neurons (3) impossibility of the different cell types to reach an adult state, despite the complex differentiation protocols that are carried out and (4) lack of some essential cell types, such as microglia, despite presenting a high number of cell types (Achberger et al., 2019).

The lack of certain cell types during the development of the 3D culture may be due, among other causes, to the lack of sufficient physical and environmental signals, also causing high variability between the various retinal organoid models. A possible solution to some of the limitations mentioned above in relation to this type of culture could be the use of biomaterials as a support for the organoid's growth and differentiation and their biofunctionalization to make them able to generate the adequate physical and chemical signals (molecules of the extracellular matrix) to stimulate the correct differentiation of the cells (Hynes and Lavik, 2010). Biomaterials could also allow interaction between the various layers of the retina, increasing connectivity and synaptogenesis, favoring obtaining a functional and complete retina (Singh R. et al., 2018).

Summarizing, despite the promising results obtained in several studies, long-term viability of cell implants has not yet been achieved, neither significant functional integration in the host retina nor improvement of long-term visual capabilities. Up-to-day photoreceptors integration in the host retina is clearly insufficient and/or inadequate. AMD cellular therapy has three main unanswered questions: (1) RPE plays a critical role in the maintenance and function of photoreceptors but very few studies consider the interdependence between RPE cells and photoreceptors (Bhutto and Lutty, 2012; Handa, 2012; Handa et al., 2017) which could be one of the reasons long-term maintenance of RPE and photoreceptor transplantation has not yet been achieved. In this case, a possible solution would be the joint transplantation of the two sheets of cell, either sequentially or at the same time. (2) The mechanisms involved in the development and integration of photoreceptors in the retinal circuit remain unknown (Gamm and Wong, 2015). It has been observed expression of specific synaptic proteins in the terminal bar of the implanted photoreceptors; it has also been observed expression of postsynaptic proteins of the host bipolar cells in contact with the donor cells; and it has been observed a certain improvement of visual function. However, evaluation of the neural function of these transplants are very few and clearly insufficient (Singh et al., 2013). (3) Detailed mechanisms for material exchange between donor and host cells are almost unknown (Lluis and Cosma, 2010; Sanges et al., 2016). Most of the cells identified as integrated donor photoreceptors in the most recent studies could actually be host photoreceptors with exchanged material (Pearson et al., 2016; Santos-Ferreira et al., 2016b; Singh et al., 2016; Ortin-Martinez et al., 2017; Waldron et al., 2018).

Addressing these problems could allow us to identify those factors that could be used to promote cellular viability, synaptogenesis and integration of the donor cells to the host tissue. Further questions regard the safety of the transplants (depending on their origin), possibility of transferring of the pathology to the implanted healthy cells, etc. It should be noticed that the most promising results have been obtained in tissue transplantation of retinal sheets and RPE patches.

Maintenance of the Immunoprivileged State of the Eye

Several subfoveal RPE implantation techniques have been employed in AMD patients. Most often, excision at sub-macular level is necessary for transplantation of the monolayer of fetal or adult RPE. This procedure can lead to acute tissue inflammation and a consequent eye damage that can impair the visual route, or even a higher immune reaction if the implant comes from another organism. Therefore, knowledge of the immunosuppression mechanisms is necessary to prevent rejection of RPE layers (Tezel et al., 2007), and it has been postulated that the low success rate of RPE monolayers transplants is due to alterations of the immunoprivileged state of the eye (indeed, rejection rate of retina transplants is higher than of other tissues, such as heart or skin (Streilein, 2003; Niederkorn and Kaplan, 2007; Sandhu et al., 2019)). Clinical studies of RPE transplants in patients undergoing immunosuppressive therapy, suggest that the immune system could destroy the transplanted cells without involving any inflammatory process (Schwartz et al., 2015). On the other hand, a higher survival of photoreceptor transplants has been observed in preclinical studies when some type of immune suppression was used after the surgery (Sandhu et al., 2019). Combined RPE-photoreceptors transplants showed that the use of immunosuppressants could improve the cellular integrity of the graft (Radtke et al., 2002, 2008). However, these results have not yet been replicated. In other preclinical studies, it was observed that only 0.5% of photoreceptors got integrated into the retina (Pearson et al., 2016; Santos-Ferreira et al., 2016a). It is not clear if the effects of photoreceptors transplantation in mice are the result of cell integration and synapse formation, rather than cytoplasmic exchange between donor and host cells. However, we can conclude that the use of immunosuppressants in human retinal transplants may lead to a higher success rate.

Biomaterials and Improvement of Cell Survival

2D – 3D scaffolding approaches have been shown to be efficient for overcoming limitations like low cell survival, lack of cell integration at the transplant site or keeping the injected cells in the target area (Behtaj et al., 2020). However, it is important to mention that the majority of the biomaterials developed for retinal regeneration has not been tested *in vivo*.

Biodegradable polymer scaffolds for the transplantation of retinal stem cells increase survival cell rate (Schubert et al., 2014). On the other hand, the dimensional conformation or porosity of the scaffold seems to promote the union and subsequent differentiation and orientation of the RPCs (Lee Ventola, 2014). Other studies defend the idea that scaffold topography influences orientation, because of its positive influence on differentiation, morphology, proliferation, migration and adhesion of the cells (Ramakrishna et al., 2001; Kador et al., 2016; Yang et al., 2017).

Scaffolds can actively interact with different cellular components. Furthermore, biomaterials can include biological cues (e.g., cellular ligands) to promote cell adhesion or physical clues (e.g., scaffold topography) to favor cell alignment and morphology. Scaffolds can also serve as supplier or repository for excitatory growth signals to accelerate tissue regeneration (Chan and Leong, 2008). Biomaterials with a sophisticated chemical and morphological structure to allow the survival, proliferation and differentiation of RPE cells and the consequent successful transplantation into the degenerated retina have also been pursued (Chichagova et al., 2018). For the encapsulation of iPSC and hESC, optimal and standardized culture media and good bioengineering processes are needed to achieve the desired expansion and differentiation, processes that are currently under investigation (Bracha et al., 2017; Mandai et al., 2017b; U.S. National Library of Medicine, 2020c).

Biomaterials should be biocompatible, biologically inert and sterilizable, not triggering cytotoxic processes neither inflammatory responses while promoting the proliferation, survival and migration of the implanted cells. Significant challenges are the risk of immune reactions at the implant site as well as the long-term survival and functionality of the transplanted cells.

A very promising biomaterial is silkworm silk fibroin, because it fulfills all the above requirements. The encapsulation of mesenchymal stem cells in silk fibroin hydrogels promotes a substantial release of anti-inflammatory and anti-oxidant molecules with marked neuroregenerative and neuroprotective properties that could be used in AMD treatment (Martín-Martín et al., 2019; Jemni Damer et al., 2020).

Current research of cell and tissue engineering approaches focuses on the preservation of photoreceptors by replacing the damaged retinal pigment epithelium since this technique has been shown to slow the degeneration of photoreceptors and even restore partial visual functions (Aboutaleb Kadkhodaeian et al., 2019; Jin et al., 2019; McGill et al., 2019; Zarbin, 2019). The development of physical substrates for artificial RPE sheets is the main objective for biomaterials engineers. It is worth noting that actual focusing on photoreceptor's preservation is partly due to the current difficulties to maintain functional photoreceptors alive before they could get transplanted, as well as to integrate the transplanted photoreceptors to the neural retina and functionally replace those already lost. In culture, photoreceptors can be maintained alive for 24–48 h, depending on the age of the donor (Fontaine et al., 1998) and less than 20% survive after transplantation (Sortwell et al., 2000). It is unclear how many of these alive cells are functional photoreceptors. State-of-the-art 3D scaffolds have been used to build a polarized photoreceptor monolayer capable to can get integrated into the neural retina, but also to facilitate the differentiation of progenitors of photoreceptor (Jung et al., 2018).

Good results on biomaterials and RPE cells have been obtained from both, *in vitro* and *in vivo* studies (Warnke et al., 2013; McHugh et al., 2014; Stanzel et al., 2014; Ilmarinen et al., 2015; Peng et al., 2016; Calejo et al., 2017; Jemni Damer et al., 2020) although how long the transplanted cells could survive has still to be determined. The scaffolds on which they are placed may be designed to act either as supporting devices or as artificial BrMs, showing the latter the best viability of RPE cells. In clinical trials, RPE cells have been injected in suspension, as a monolayer and also on biomaterials (Schwartz et al., 2015; da Cruz et al., 2018; U.S. National Library of Medicine, 2020s). Unfortunately, these clinical trials are very few and are in very early stages of development, so their results should be analyzed accordingly.

In conclusion, the use of biomaterials to generate implantable biohybrid tissue may be a potential solution to the main problems of cell transplantation, increasing the survival of implanted cells and improving their integration capacity.

CONCLUSION

Cell replacement, either by using cell suspensions or by integrating cell's sheets on a scaffolding material to promote the survival of the transplanted cells, is a promising treatment for advanced AMD stages. Pioneering studies have provided a proof-of-concept for RPE and photoreceptors transplantation as a plausible therapeutic strategy.

The effective integration of the transplanted cells into the damaged retina is the principal limitation of cell therapy. The development of advanced biomaterials to support the *in vitro* development of artificial 3D retinal tissues, as well as the implantation and the functional integration of these constructs into the damaged retina represents the most promising therapeutic approach. Indeed, there is evidence that retinal cells on supporting biomaterials, implanted in the posterior segment of the eye, achieve a better but limited integration than injections of free cells in the same region, and slightly improve vision capabilities in different experimental models.

To obtain clinically relevant therapeutic solutions, a good effectiveness of the proposed treatment must be achieved. And the key factor to increase the effectiveness of retinal implant therapies is the accomplishment of a substantial integration of the implanted cells. In this aspect an immense amount of work is still needed: the discovery of the exchange of genetic material between native and implanted photoreceptors suggests that the integration of these neurons to the host retina, reported in up-to-date studies, is probably not real, putting on the table the need to verify and reevaluate these studies. It is still unknown whether the therapeutic effect of cell transplants is due to an improvement in functionality by integration or due to production of protective factors. The elucidation of the involved mechanisms is essential for the accomplishment of this goal. Furthermore, functionality analysis of the integrated implants has to be performed.

AUTHOR CONTRIBUTIONS

NJ-D and AG-D: bibliographic research and information synthesis, AMD course, wrote the manuscript, and equal contribution. MF-A, NS-B, and NA-L: bibliographic research and information synthesis. FA-M: clinical aspects. GG, JP-R, FR, and DK: biomaterials aspects. DG-N: biomaterials and cell and tissue therapy. GG, JP-R, DK, DG-N: manuscript revision. FP: manuscript design, information synthesis, supervision, and wrote the manuscript. All authors contributed to the article and approved the submitted version.

FUNDING

The authors gratefully acknowledge financial support received from the Spanish Ministerio de Economía y Competitividad through grants MAT2016-76847-R, MAT2016-79832-R, and MAT2015-66666-C3-3-R; from the Comunidad de Madrid, Spain through grants Neurocentro-B2017/BrMD-3760 and IND2018/BrMD-9804, and from the National Institutes of Health (P41EB002520); predoctoral FPI grant from the Spanish Ministerio de Economía y Competitividad (AGD) and research contract from the Comunidad de Madrid, Spain (MFA).

REFERENCES

Aboutaleb Kadkhodaeian, H., Tiraihi, T., Ahmadieh, H., Ziaei, H., Daftarian, N., and Taheri, T. (2019). Generation of retinal pigmented epithelium-like cells from pigmented spheres differentiated from bone marrow stromal cell-derived neurospheres. *Tissue Eng. Regen. Med.* 16, 253–263. doi: 10.1007/s13770-019-00183-1

Achberger, K., Probst, C., Haderspeck, J. C., Bolz, S., Rogal, J., Chuchuy, J., et al. (2019). Merging organoid and organ-on-a-chip technology to generate complex multi-layer tissue models in a human retina-on-a-chip platform. *Elife* 8:e46188. doi: 10.7554/eLife.46188

Aguayo, A. J., Rasminsky, M., Bray, G. M., Carbonetto, S., and Mckerracher, L. (1991). Degenerative and regenerative responses of injured neurons in the central nervous system of adult mammals. *Philos. Trans. R Soc. Lond. B Biol. Sci.* 331, 337–343. doi: 10.1098/rstb.1991.0025

Ambati, J., and Fowler, B. J. (2012). Mechanisms of age-related macular degeneration. *Neuron* 75, 26–39. doi: 10.1016/j.neuron.2012.06.018

Anderson, D. H., Radeke, M. J., Gallo, N. B., Chapin, E. A., Johnson, P. T., Curletti, C. R., et al. (2010). The pivotal role of the complement system in aging and age-related macular degeneration: hypothesis re-visited. *Prog. Retin. Eye Res.* 29, 95–112. doi: 10.1016/j.preteyeres.2009.11.003

Aoki, H., Hara, A., Niwa, M., Yamada, Y., and Kunisada, T. (2009). In vitro and in vivo differentiation of human embryonic stem cells into retina-like organs and comparison with that from mouse pluripotent epiblast stem cells. *Dev. Dyn.* 238, 2266–2279. doi: 10.1002/dvdy.22008

Arnhold, S., Klein, H., Semkova, I., Addicks, K., and Schraermeyer, U. (2004). Neurally selected embryonic stem cells induce tumor formation after long-term survival following engraftment into the subretinal space. *Invest. Opthalmol. Vis. Sci.* 45, 4251–4255. doi: 10.1167/iovs.03-1108

Assawachananont, J., Mandai, M., Okamoto, S., Yamada, C., Eiraku, M., Yonemura, S., et al. (2014). Transplantation of embryonic and induced pluripotent stem cell-derived 3D retinal sheets into retinal degenerative mice. *Stem Cell Rep.* 2, 662–674. doi: 10.1016/j.stemcr.2014.03.011

Augustin, C., Augustin, A., Tetz, M., and Rizzo, S. (2012). Suprachoroidal drug delivery – a new approach for the treatment of severe macular diseases. *Eur. Ophthalmic Rev.* 06:25. doi: 10.17925/EOR.2012.06.01.25

Ballios, B. G., Cooke, M. J., van der Kooy, D., and Shoichet, M. S. (2010). A hydrogel-based stem cell delivery system to treat retinal degenerative diseases. *Biomaterials* 31, 2555–2564. doi: 10.1016/j.biomaterials.2009.12.004

Ballios, B. G., and van der Kooy, D. (2010). Biology and therapeutic potential of adult retinal stem cells. *Can. J. Ophthalmol.* 45, 342–351. doi: 10.3129/i10-070

Bansal, P., Garg, S., Sharma, Y., and Venkatesh, P. (2016). Posterior segment drug delivery devices: current and novel therapies in development. *J. Ocul. Pharmacol. Ther.* 32, 135–144. doi: 10.1089/jop.2015.0133

Baranov, P., Michaelson, A., Kundu, J., Carrier, R. L., and Young, M. (2014). Interphotoreceptor matrix-poly(ϵ-caprolactone) composite scaffolds for human photoreceptor differentiation. *J. Tissue Eng.* 5:2041731414554139. doi: 10.1177/2041731414554139

Barar, J., Aghanejad, A., Fathi, M., and Omidi, Y. (2016). Advanced drug delivery and targeting technologies for the ocular diseases. *BioImpacts* 6, 49–67. doi: 10.15171/bi.2016.07

Barber, A. C., Hippert, C., Duran, Y., West, E. L., Bainbridge, J. W. B., Warre-Cornish, K., et al. (2013). Repair of the degenerate retina by photoreceptor transplantation. *Proc. Natl. Acad. Sci. U.S.A.* 110, 354–359. doi: 10.1073/pnas.1212677110

Barnea-Cramer, A. O., Wang, W., Lu, S. J., Singh, M. S., Luo, C., Huo, H., et al. (2016). Function of human pluripotent stem cell-derived photoreceptor progenitors in blind mice. *Sci. Rep.* 6:29784. doi: 10.1038/srep29784

Battler, A., and Leor, J. (2006). *Stem Cell and Gene-Based Therapy: Frontiers in Regenerative Medicine*. Berlin: Springer. doi: 10.1007/1-84628-142-3

Behtaj, S., Öchsner, A., Anissimov, Y. G., and Rybachuk, M. (2020). Retinal tissue bioengineering, materials and methods for the treatment of glaucoma. *Tissue Eng. Regen. Med.* 17, 253–269. doi: 10.1007/s13770-020-00254-8

Bennett, C. R., Bex, P. J., Bauer, C. M., and Merabet, L. B. (2019). The assessment of visual function and functional vision. *Semin. Pediatr. Neurol.* 31, 30–40. doi: 10.1016/j.spen.2019.05.006

Bharti, K. (2018). Patching the retina with stem cells. *Nat. Biotechnol.* 36, 311–313. doi: 10.1038/nbt.4118

Bharti, K., Nguyen, M. T. T., Skuntz, S., Bertuzzi, S., and Arnheiter, H. (2006). The other pigment cell: specification and development of the pigmented epithelium of the vertebrate eye. *Pigment Cell Res.* 19, 380–394. doi: 10.1111/j.1600-0749.2006.00318.x

Bharti, K., Rao, M., Hull, S. C., Stroncek, D., Brooks, B. P., Feigal, E., et al. (2014). Developing cellular therapies for retinal degenerative diseases. *Invest. Ophthalmol. Vis. Sci.* 55, 1191–1201. doi: 10.1167/iovs.13-13481

Bhatt, N. S., Newsome, D. A., Fenech, T., Hessburg, T. P., Diamond, J. G., Miceli, M. V., et al. (1994). Experimental transplantation of human retinal pigment epithelial cells on collagen substrates. *Am. J. Ophthalmol.* 117, 214–221. doi: 10.1016/S0002-9394(14)73079-X

Bhatt, P., Narvekar, P., Lalani, R., Chougule, M. B., Pathak, Y., and Sutariya, V. (2019). An in vitro assessment of thermo-reversible gel formulation containing sunitinib nanoparticles for neovascular age-related macular degeneration. *AAPS PharmSciTech* 20:280. doi: 10.1208/s12249-019-1474-0

Bhattacharya, S., Gangaraju, R., and Chaum, E. (2017). Recent advances in retinal stem cell therapy. *Curr. Mol. Biol. Rep.* 3, 172–182. doi: 10.1007/s40610-017-0069-3

Bhutto, I., and Lutty, G. (2012). Understanding age-related macular degeneration (AMD): relationships between the photoreceptor/retinal pigment epithelium/Bruch's membrane/choriocapillaris complex. *Mol. Aspects Med.* 33, 295–317. doi: 10.1016/j.mam.2012.04.005

Birch, D. G., Weleber, R. G., Duncan, J. L., Jaffe, G. J., Tao, W., and Ciliary Neurotrophic Factor Retinitis Pigmentosa Study Groups (2013). Randomized trial of ciliary neurotrophic factor delivered by encapsulated cell intraocular implants for retinitis pigmentosa. *Am. J. Ophthalmol.* 156, 283.e1–292.e1. doi: 10.1016/j.ajo.2013.03.021

Bisht, R., Jaiswal, J. K., and Rupenthal, I. D. (2017). Nanoparticle-loaded biodegradable light-responsive in situ forming injectable implants for effective peptide delivery to the posterior segment of the eye. *Med. Hypotheses* 103, 5–9. doi: 10.1016/j.mehy.2017.03.033

Blenkinsop, T. A., Salero, E., Stern, J. H., and Temple, S. (2013). The culture and maintenance of functional retinal pigment epithelial monolayers from adult human eye. *Methods Mol. Biol.* 945, 45–65. doi: 10.1007/978-1-62703-125-7_4

Booij, J. C., Baas, D. C., Beisekeeva, J., Gorgels, T. G. M. F., and Bergen, A. A. B. (2010). The dynamic nature of Bruch's membrane. *Prog. Retin. Eye Res.* 29, 1–18. doi: 10.1016/j.preteyeres.2009.08.003

Bracha, P., Moore, N. A., and Ciulla, T. A. (2017). Induced pluripotent stem cell-based therapy for age-related macular degeneration. *Expert Opin. Biol. Ther.* 17, 1113–1126. doi: 10.1080/14712598.2017.1346079

Bray, G. M., Villegas-Pérez, M. P., Vidal-Sanz, M., and Aguayo, A. J. (1987). The use of peripheral nerve grafts to enhance neuronal survival, promote growth and permit terminal reconnections in the central nervous system of adult rats. *J. Exp. Biol.* 132, 5–19.

Burke, J. M., and Hjelmeland, L. M. (2005). Mosaicism of the retinal pigment epithelium: seeing the small picture. *Mol. Interv.* 5, 241–249. doi: 10.1124/mi.5.4.7

Bush, R. A., Lei, B., Tao, W., Raz, D., Chan, C.-C., Cox, T. A., et al. (2004). Encapsulated cell-based intraocular delivery of ciliary neurotrophic factor in normal rabbit: dose-dependent effects on ERG and retinal histology. *Invest. Ophthalmol. Vis. Sci.* 45, 2420–2430. doi: 10.1167/iovs.03-1342

Caffé, A. R., Ahuja, P., Holmqvist, B., Azadi, S., Forsell, J., Holmqvist, I., et al. (2002). Mouse retina explants after long-term culture in serum free medium. *J. Chem. Neuroanat.* 22, 263–273. doi: 10.1016/S0891-0618(01)00140-5

Calejo, M. T., Ilmarinen, T., Vuorimaa-Laukkanen, E., Talvitie, E., Hakola, H. M., Skottman, H., et al. (2017). Langmuir-Schaefer film deposition onto honeycomb porous films for retinal tissue engineering. *Acta Biomater.* 54, 138–149. doi: 10.1016/j.actbio.2017.02.035

Campbell, M., and Humphries, P. (2013). The blood-retina barrier tight junctions and barrier modulation introduction: general anatomy of the human eye. *Adv. Exp. Med. Biol.* 763, 70–84. doi: 10.1007/978-1-4614-4711-5_3

Canto-Soler, V., Flores-Bellver, M., and Vergara, M. N. (2016). Stem cell sources and their potential for the treatment of retinal degenerations. *Invest. Ophthalmol. Vis. Sci.* 57, ORSFd1–ORSFd9. doi: 10.1167/iovs.16-19127

Carr, A. F., Smart, M. J. K., Ramsden, C. M., Powner, M. B., Cruz, L., and Coffey, P. J. (2013). Development of human embryonic stem cell therapies for age-related macular degeneration. *Trends Neurosci.* 36, 385–395. doi: 10.1016/j.tins.2013.03.006

Carr, A.-J., Vugler, A. A., Hikita, S. T., Lawrence, J. M., Gias, C., Chen, L. L., et al. (2009). Protective effects of human ips-derived retinal pigment epithelium cell transplantation in the retinal dystrophic rat. *PLoS One* 4:e8152. doi: 10.1371/journal.pone.0008152

Chan, B. P., and Leong, K. W. (2008). Scaffolding in tissue engineering: general approaches and tissue-specific considerations. *Eur. Spine J.* 4(Suppl. 4), 467–479. doi: 10.1007/s00586-008-0745-3

Chen, H. Y., Kaya, K. D., Dong, L., and Swaroop, A. (2016). Three-dimensional retinal organoids from mouse pluripotent stem cells mimic in vivo development with enhanced stratification and rod photoreceptor differentiation. *Mol. Vis.* 22, 1077–1094.

Chen, M., Le, D. Q. S., Baatrup, A., Nygaard, J. V., Hein, S., Bjerre, L., et al. (2011). Self-assembled composite matrix in a hierarchical 3-D scaffold for bone tissue engineering. *Acta Biomater.* 7, 2244–2255. doi: 10.1016/j.actbio.2010.12.031

Chichagova, V., Hallam, D., Collin, J., Zerti, D., Dorgau, B., Felemban, M., et al. (2018). Cellular regeneration strategies for macular degeneration: past, present and future. *Eye* 32, 946–971. doi: 10.1038/s41433-018-0061-z

Chirila, T., Barnard, Z., Zainuddin, Harkin, D. G., Schwab, I. R., and Hirst, L. (2008). Bombyx mori silk fibroin membranes as potential substrata for epithelial constructs used in the management of ocular surface disorders. *Tissue Eng. A* 14, 1203–1211. doi: 10.1089/ten.tea.2007.0224

Chirila, T. V., Shadforth, A. M. A., Richardson, N. A., Suzuki, S., Harkin, D. G., and Theodoropoulos, C. (2015). A Bruch's membrane substitute fabricated from silk fibroin supports the function of retinal pigment epithelial cells in vitro. *J. Tissue Eng. Regen. Med.* 11, 1915–1924. doi: 10.1002/term.2089

Christiansen, A. T., Tao, S. L., Smith, M., Wnek, G. E., Prause, J. U., Young, M. J., et al. (2012). Subretinal implantation of electrospun, short nanowire, and smooth poly(ε-caprolactone) Scaffolds to the Subretinal Space of Porcine Eyes. *Stem Cells International.* 2012:454295. doi: 10.1155/2012/454295

Clegg, D. O., Hinton, D. R., Falabella, P., Rowland, T., Kashani, A. H., Humayun, M. S., et al. (2015). Stem cell based therapies for age-related macular degeneration: the promises and the challenges. *Prog. Retin. Eye Res.* 48, 1–39. doi: 10.1016/j.preteyeres.2015.06.004

Cotrim, C. C., Toscano, L., Messias, A., Jorge, R., and Siqueira, R. C. (2017). Intravitreal use of bone marrow mononuclear fraction containing CD34+ stem cells in patients with atrophic age-related macular degeneration. *Clin. Ophthalmol.* 11, 931–938. doi: 10.2147/OPTH.S133502

Crafoord, S., Geng, L., Seregard, S., and Algvere, P. V. (2002). *Photoreceptor Survival in Transplantation of Autologous Iris Pigment Epithelial Cells to the Subretinal Space*. Available online at: https://onlinelibrary.wiley.com/doi/pdf/10.1034/j.1600-0420.2002.800408.x (accessed May 19, 2019).

Cunha-Vaz, J., Bernardes, R., and Lobo, C. (2011). Blood-retinal barrier. *Eur. J. Ophthalmol.* 21, 3–9. doi: 10.5301/EJO.2010.6049

Cunha-Vaz, J. G. (1997). The blood-ocular barriers: past, present, and future. *Doc. Ophthalmol.* 93, 149–157. doi: 10.1007/BF02569055

Curatola, A. M., Moscatelli, D., Norris, A., and Hendricks-Munoz, K. (2005). Retinal blood vessels develop in response to local VEGF-A signals in the absence of blood flow. *Exp. Eye Res.* 81, 147–158. doi: 10.1016/j.exer.2005.06.001

da Cruz, L., Fynes, K., Georgiadis, O., Kerby, J., Luo, Y. H., Ahmado, A., et al. (2018). Phase 1 clinical study of an embryonic stem cell–derived retinal pigment epithelium patch in age-related macular degeneration. *Nat. Biotechnol.* 36, 328–337. doi: 10.1038/nbt.4114

Das, T., del Cerro, M., Jalali, S., Rao, V. S., Gullapalli, V. K., Little, C., et al. (1999). The transplantation of human fetal neuroretinal cells in advanced retinitis pigmentosa patients: results of a long-term safety study. *Exp. Neurol.* 157, 58–68. doi: 10.1006/exnr.1998.6992

Davis, R. J., Alam, N. M., Zhao, C., Müller, C., Saini, J. S., Blenkinsop, T. A., et al. (2017). The developmental stage of adult human stem cell-derived retinal pigment epithelium cells influences transplant efficacy for vision rescue. *Stem Cell Rep.* 9, 42–49. doi: 10.1016/j.stemcr.2017.05.016

Decembrini, S., Koch, U., Radtke, F., Moulin, A., and Arsenijevic, Y. (2014). Derivation of traceable and transplantable photoreceptors from mouse embryonic stem cells. *Stem Cell Rep.* 2, 853–865. doi: 10.1016/j.stemcr.2014.04.010

Del Priore, L. V., Tezel, T. H., and Kaplan, H. J. (2004). Survival of allogeneic porcine retinal pigment epithelial sheets after subretinal transplantation. *Invest. Opthalmol. Vis. Sci.* 45, 985–992. doi: 10.1167/iovs.03-0662

Diniz, B., Thomas, P., Thomas, B., Ribeiro, R., Hu, Y., Brant, R., et al. (2013). Subretinal implantation of retinal pigment epithelial cells derived from human embryonic stem cells: improved survival when implanted as a monolayer. *Invest. Opthalmol. Vis. Sci.* 54, 5087–5096. doi: 10.1167/iovs.12-11239

Eberle, D., Kurth, T., Santos-Ferreira, T., Wilson, J., Corbeil, D., and Ader, M. (2012). Outer segment formation of transplanted photoreceptor precursor cells. *PLoS One* 7:e46305. doi: 10.1371/journal.pone.0046305

Eberle, D., Santos-Ferreira, T., Grahl, S., and Ader, M. (2014). Subretinal transplantation of MACS purified photoreceptor precursor cells into the adult mouse retina. *J. Vis. Exp.* 84:e50932. doi: 10.3791/50932

Eiraku, M., and Sasai, Y. (2012). Mouse embryonic stem cell culture for generation of three-dimensional retinal and cortical tissues. *Nat. Protoc.* 7, 69–79. doi: 10.1038/nprot.2011.429

Eiraku, M., Takata, N., Ishibashi, H., Kawada, M., Sakakura, E., Okuda, S., et al. (2011). Self-organizing optic-cup morphogenesis in three-dimensional culture. *Nature* 472, 51–56. doi: 10.1038/nature09941

Emerich, D. F., and Thanos, C. G. (2008). NT-501: an ophthalmic implant of polymer-encapsulated ciliary neurotrophic factor-producing cells. *Curr. Opin. Mol. Ther.* 10, 506–515.

Engelsberg, K., Ehinger, B., and Ghosh, F. (2008). Early development of retinal subtypes in long-term cultures of human embryonic retina. *Curr. Eye Res.* 33, 185–191. doi: 10.1080/02713680701843784

Engelsberg, K., Johansson, K., and Ghosh, F. (2005). Development of the embryonic porcine neuroretina in vitro. *Ophthalmic Res.* 37, 104–111. doi: 10.1159/000084252

Falkner-Radler, C. I., Krebs, I., Glittenberg, C., Povazay, B., Drexler, W., Graf, A., et al. (2011). Human retinal pigment epithelium (RPE) transplantation: outcome after autologous RPE-choroid sheet and RPE cell-suspension in a randomised clinical study. *Br J. Ophthalmol.* 95, 370–375. doi: 10.1136/bjo.2009.176305

Fernández-García, L., Pérez-Rigueiro, J., Martinez-Murillo, R., Panetsos, F., Ramos, M., Guinea, G. V., et al. (2018). Cortical reshaping and functional recovery induced by silk fibroin hydrogels-encapsulated stem cells implanted in stroke animals. *Front. Cell. Neurosci.* 12:296. doi: 10.3389/fncel.2018.00296

Fields, M., Cai, H., Gong, J., and Del Priore, L. (2016). Potential of induced pluripotent stem cells (iPSCs) for treating age-related macular degeneration (AMD). *Cells* 5:44. doi: 10.3390/cells5040044

Fligor, C. M., Langer, K. B., Sridhar, A., Ren, Y., Shields, P. K., Edler, M. C., et al. (2018). Three-dimensional retinal organoids facilitate the investigation of retinal ganglion cell development, organization and neurite outgrowth from human pluripotent stem cells. *Sci. Rep.* 8:14520. doi: 10.1038/s41598-018-32871-8

Fontaine, V., Kinkl, N., Sahel, J., Dreyfus, H., and Hicks, D. (1998). Survival of purified rat photoreceptors in vitro is stimulated directly by fibroblast growth factor-2. *J. Neurosci.* 18, 9662–9672. doi: 10.1523/JNEUROSCI.18-23-09662.1998

Forrester, J. V., and Xu, H. (2012). Good news-bad news: the yin and yang of immune privilege in the eye. *Front. Immunol.* 3:338. doi: 10.3389/fimmu.2012.00338

Gagliardi, G., Ben, M., Barek, K., Chaffiol, A., Slembrouck-Brec, A., Conart, J. B., et al. (2018). Characterization and transplantation of CD73-positive photoreceptors isolated from human iPSC-derived retinal organoids. *Stem Cell Rep.* 11, 665–680. doi: 10.1016/j.stemcr.2018.07.005

Gaillard, F., and Sauvé, Y. (2007). Cell-based therapy for retina degeneration: the promise of a cure. *Vis. Res.* 47, 2815–2824. doi: 10.1016/j.visres.2007.06.018

Gamm, D. M., and Wong, R. (2015). Report on the national eye institute audacious goals initiative: photoreceptor regeneration and integration workshop. *Transl. Vis. Sci. Technol.* 4:2. doi: 10.1167/tvst.4.6.2

Garita-Hernandez, M., Lampič, M., Chaffiol, A., Guibbal, L., Routet, F., Santos-Ferreira, T., et al. (2019). Restoration of visual function by transplantation of optogenetically engineered photoreceptors. *Nat. Commun.* 10:4524. doi: 10.1038/s41467-019-12330-2

Gehrs, K. M., Anderson, D. H., Johnson, L. V., and Hageman, G. S. (2006). Age-related macular degeneration – Emerging pathogenetic and therapeutic concepts. *Ann. Med.* 38, 450–471. doi: 10.1080/07853890600946724

Ghosh, F., Arnér, K., and Engelsberg, K. (2009). Isolation of photoreceptors in the cultured full-thickness fetal rat retina. *Invest. Ophthalmol. Vis. Sci.* 50, 826–835. doi: 10.1167/iovs.08-2389

Giordano, G. G., Thomson, R. C., Ishaug, S. L., Mikos, A. G., Cumber, S., Garcia, C. A., et al. (1997). Retinal pigment epithelium cells cultured on synthetic biodegradable polymers. *J. Biomed. Mater. Res.* 34, 87–93. doi: 10.1002/(SICI)1097-4636(199701)34:1<87::AID-JBM12>3.0.CO;2-M

Gonzalez-Cordero, A., West, E. L., Pearson, R. A., Duran, Y., Carvalho, L. S., Chu, C. J., et al. (2013). Photoreceptor precursors derived from three-dimensional embryonic stem cell cultures integrate and mature within adult degenerate retina. *Nat. Biotechnol.* 31, 741–747. doi: 10.1038/nbt.2643

González-Nieto, D., Fernández-García, L., Pérez-Rigueiro, J., Guinea, G. V., and Panetsos, F. (2018). Hydrogels-assisted cell engraftment for repairing the stroke-damaged brain: chimera or reality. *Polymers* 10:184. doi: 10.3390/polym10020184

Goslings, W. R., Prodeus, A. P., Streilein, J. W., Carroll, M. C., Jager, M. J., and Taylor, A. W. (1998). A small molecular weight factor in aqueous humor acts on C1q to prevent antibody-dependent complement activation. *Invest Ophthalmol Vis Sci.* 39, 989–995.

Guenther, E., Tröger, B., Schlosshauer, B., and Zrenner, E. (1999). Long-term survival of retinal cell cultures on retinal implant materials. *Vis. Res.* 39, 3988–3994. doi: 10.1016/S0042-6989(99)00128-5

Guerrero-Naranjo, J. L., Quiroz-Mercado, H., Sanchez-Bermudez, G., Schoonewolff, F., Salinas Longoria, S., Romero Vera, R., et al. (2013). Safety of implantation of the NT-503 device in patients with choroidal neovasculariza- tion secondary to age-related macular degeneration. *Assoc. Res. Vis. Ophthalmol.* 54:3298.

Gust, J., and Reh, T. A. (2011). Adult donor rod photoreceptors integrate into the mature mouse retina. *Invest. Ophthalmol. Vis. Sci.* 52, 5266–5272. doi: 10.1167/iovs.10-6329

Haderspeck, J. C., Chuchuy, J., Kustermann, S., Liebau, S., and Loskill, P. (2019). Organ-on-a-chip technologies that can transform ophthalmic drug discovery and disease modeling. *Exp. Opin. Drug Discov.* 14, 47–57. doi: 10.1080/17460441.2019.1551873

Hadlock, T., Singh, S., Vacanti, J. P., and McLaughlin, B. J. (1999). Ocular cell monolayers cultured on biodegradable substrates. *Tissue Eng.* 5, 187–196. doi: 10.1089/ten.1999.5.187

Handa, J. T. (2012). How does the macula protect itself from oxidative stress? *Mol. Aspects Med.* 33, 418–435. doi: 10.1016/j.mam.2012.03.006

Handa, J. T., Cano, M., Wang, L., Datta, S., and Liu, T. (2017). Lipids, oxidized lipids, oxidation-specific epitopes, and Age-related Macular Degeneration. *Biochim. Biophys. Acta* 1862, 430–440. doi: 10.1016/j.bbalip.2016.07.013

Harris, T. I., Paterson, C. A., Farjood, F., Wadsworth, I. D., Caldwell, L., Lewis, R. V., et al. (2019). Utilizing recombinant spider silk proteins to develop a synthetic bruch's membrane for modeling the retinal pigment epithelium. *ACS Biomater. Sci. Eng.* 5, 4023–4036. doi: 10.1021/acsbiomaterials.9b00183

Hasegawa, Y., Takata, N., Okuda, S., Kawada, M., Eiraku, M., and Sasai, Y. (2016). Emergence of dorsal-ventral polarity in ESC-derived retinal tissue. *Development* 143, 3895–3906. doi: 10.1242/dev.134601

Hertz, J., Qu, B., Hu, Y., Patel, R. D., Valenzuela, D. A., and Goldberg, J. L. (2014). Survival and integration of developing and progenitor-derived retinal ganglion cells following transplantation. *Cell Transplant.* 23, 855–872. doi: 10.3727/096368913X667024

Hiler, D., Chen, X., Hazen, J., Kupriyanov, S., Carroll, P. A., Qu, C., et al. (2015). Quantification of retinogenesis in 3d cultures reveals epigenetic memory and higher efficiency in iPSCs derived from rod photoreceptors. *Cell Stem Cell* 17, 101–115. doi: 10.1016/j.stem.2015.05.015

Ho, A. C., Chang, T. S., Samuel, M., Williamson, P., Willenbucher, R. F., and Malone, T. (2017). Experience with a subretinal cell-based therapy in patients with geographic atrophy secondary to age-related macular degeneration. *Am. J. Ophthalmol.* 179, 67–80. doi: 10.1016/j.ajo.2017.04.006

Hogan, M. J., Alvarado, J. A., and Weddell, J. E. (1971). *Histology of the Human Eye; An Atlas and Textbook*. Philadelphia, PA: Saunders.

Homma, K., Okamoto, S., Mandai, M., Gotoh, N., Rajasimha, H. K., Chang, Y. S., et al. (2013). Developing rods transplanted into the degenerating retina of Crx-knockout mice exhibit neural activity similar to native photoreceptors. *Stem Cells* 31, 1149–1159. doi: 10.1002/stem.1372

Hoon, M., Okawa, H., Della Santina, L., and Wong, R. O. L. (2014). Functional architecture of the retina: development and disease. *Prog. Retin. Eye Res.* 42, 44–84. doi: 10.1016/j.preteyeres.2014.06.003

Hsiung, J., Zhu, D., and Hinton, D. R. (2015). Polarized human embryonic stem cell-derived retinal pigment epithelial cell monolayers have higher resistance to oxidative stress-induced cell death than nonpolarized cultures. *Stem Cells Transl. Med.* 4, 10–20. doi: 10.5966/sctm.2014-0205

Hu, Y., Liu, L., Lu, B., Zhu, D., Ribeiro, R., Diniz, B., et al. (2012). A novel approach for subretinal implantation of ultrathin substrates containing stem cell-derived retinal pigment epithelium monolayer. *Ophthalmic Res.* 48, 186–191. doi: 10.1159/000338749

Huang, B. O., Mitchell, C. K., and Redburn-Johnson, D. A. (2000). GABA and GABA a receptor antagonists alter developing cone photoreceptor development in neonatal rabbit retina. *Vis. Neurosci.* 17, 925–935. doi: 10.1017/S0952523800176126

Hynes, S. R., and Lavik, E. B. (2010). A tissue-engineered approach towards retinal repair: scaffolds for cell transplantation to the subretinal space. *Graefes Arch. Clin. Exp. Ophthalmol.* 248, 763–778. doi: 10.1007/s00417-009-1263-7

Idelson, M., Alper, R., Obolensky, A., Ben-Shushan, E., Hemo, I., Yachimovich-Cohen, N., et al. (2009). Directed differentiation of human embryonic stem cells into functional retinal pigment epithelium cells. *Cell Stem Cell* 5, 396–408. doi: 10.1016/j.stem.2009.07.002

Ilmarinen, T., Hiidenmaa, H., Kööbi, P., Nymark, S., Sorkio, A., Wang, J. H., et al. (2015). Ultrathin polyimide membrane as cell carrier for subretinal transplantation of human embryonic stem cell derived retinal pigment epithelium. *PLoS One* 10:e0143669. doi: 10.1371/journal.pone.0143669

Imai, H., Honda, S., Kondo, N., Ishibashi, K., Tsukahara, Y., and Negi, A. (2007). The upregulation of angiogenic gene expression in cultured retinal pigment epithelial cells grown on type I collagen. *Curr. Eye Res.* 32, 903–910. doi: 10.1080/02713680701604749

Iraha, S., Tu, H. Y., Yamasaki, S., Kagawa, T., Goto, M., Takahashi, R., et al. (2018). Establishment of immunodeficient retinal degeneration model mice and functional maturation of human ESC-derived retinal sheets after transplantation. *Stem Cell Rep.* 10, 1059–1074. doi: 10.1016/j.stemcr.2018.01.032

Irisvision (2020). *Age Related Macular Degeneration Guidelines – IrisVision*. Available online at: https://irisvision.com/age-related-macular-degeneration/ (accessed July 22, 2020).

Jayakody, S. A., Gonzalez-Cordero, A., Ali, R. R., and Pearson, R. A. (2015). Cellular strategies for retinal repair by photoreceptor replacement. *Prog. Retin. Eye Res.* 46, 31–66. doi: 10.1016/j.preteyeres.2015.01.003

Jemni Damer, N., Guedan Duran, A., Cichy, J., Lozano-Picazo, P., Gonzalez-Nieto, D., Pérez-Rigueiro, J., et al. (2020). First steps for the development of silk fibroin-based 3D biohybrid retina for age-related macular degeneration (AMD). *J. Neural Eng.* 17:055003. doi: 10.1088/1741-2552/abb9c0

Jin, Z., Gao, M., Deng, W., Wu, K., Sugita, S., Mandai, M., et al. (2018). Stemming retinal regeneration with pluripotent stem cells. *Prog. Retin. Eye Res.* 69, 38–56. doi: 10.1016/j.preteyeres.2018.11.003

Jin, Z.-B., Gao, M.-L., Deng, W.-L., Wu, K.-C., Sugita, S., Mandai, M., et al. (2019). Stemming retinal regeneration with pluripotent stem cells. *Prog. Retin. Eye Res.* 69, 38–56.

Johnson, T. V., and Martin, K. R. (2008). Development and characterization of an adult retinal explant organotypic tissue culture system as an in vitro intraocular stem cell transplantation model. *Invest. Ophthalmol. Vis. Sci.* 49, 3503–3512. doi: 10.1167/iovs.07-1601

Johnson, T. V., Oglesby, E. N., Steinhart, M. R., Cone-Kimball, E., Jefferys, J., and Quigley, H. A. (2016). Time-lapse retinal ganglion cell dendritic field degeneration imaged in organotypic retinal explant culture. *Invest. Opthalmol. Vis. Sci.* 57, 253–264. doi: 10.1167/iovs.15-17769

Jones, B. W., Kondo, M., Terasaki, H., Lin, Y., McCall, M., and Marc, R. E. (2012). Retinal remodeling. *Jap. J. Ophthalmol.* 56, 289–306. doi: 10.1007/s10384-012-0147-2

Jones, B. W., Watt, C. B., Frederick, J. M., Baehr, W., Chen, C. K., Levine, E. M., et al. (2003). Retinal remodeling triggered by photoreceptor degenerations. *J. Comp. Neurol.* 464, 1–16. doi: 10.1002/cne.10703

Joussen, A. M., Heussen, F. M. A., Joeres, S., Llacer, H., Prinz, B., Rohrschneider, K., et al. (2006). autologous translocation of the choroid and retinal pigment epithelium in age-related macular degeneration. *Am. J. Ophthalmol.* 142, 17–30. doi: 10.1016/j.ajo.2006.01.090

Julien, S., Peters, T., Ziemssen, F., Arango-Gonzalez, B., Beck, S., Thielecke, H., et al. (2011). Implantation of ultrathin, biofunctionalized polyimide membranes into the subretinal space of rats. *Biomaterials* 32, 3890–3898. doi: 10.1016/j.biomaterials.2011.02.016

Jung, Y. H., Phillips, M. J., Lee, J., Xie, R., Ludwig, A. L., Chen, G., et al. (2018). 3D Microstructured Scaffolds to Support Photoreceptor Polarization and Maturation. *Adv. Mater.* 30:e1803550. doi: 10.1002/adma.201803550

Kador, K. E., and Goldberg, J. L. (2012). Scaffolds and stem cells: delivery of cell transplants for retinal degenerations. *Exp. Rev. Ophthalmol.* 7, 459–470. doi: 10.1586/eop.12.56

Kador, K. E., Grogan, S. P., Dorthé, E. W., Venugopalan, P., Malek, M. F., Goldberg, J. L., et al. (2016). Control of retinal ganglion cell positioning and neurite growth: combining 3D printing with radial electrospun scaffolds. *Tissue Eng. A* 22, 286–294. doi: 10.1089/ten.tea.2015.0373

Kamao, H., Mandai, M., Okamoto, S., Sakai, N., Suga, A., Sugita, S., et al. (2014). Characterization of human induced pluripotent stem cell-derived retinal pigment epithelium cell sheets aiming for clinical application. *Stem Cell Rep.* 2, 205–218. doi: 10.1016/j.stemcr.2013.12.007

Kim, H., Cooke, M. J., and Shoichet, M. S. (2012). Creating permissive microenvironments for stem cell transplantation into the central nervous system. *Trends Biotechnol.* 30, 55–63. doi: 10.1016/j.tibtech.2011.07.002

Klimanskaya, I., Hipp, J., Rezai, K. A., West, M., Atala, A., and Lanza, R. (2004). Derivation and comparative assessment of retinal pigment epithelium from human embryonic stem cells using transcriptomics. *Cloning Stem Cells* 6, 217–245. doi: 10.1089/clo.2004.6.217

Koizumi, A., Zeck, G., Ben, Y., Masland, R. H., and Jakobs, T. C. (2007). Organotypic culture of physiologically functional adult mammalian retinas. *PLoS One* 2:e221. doi: 10.1371/journal.pone.0000221

Koss, M. J., Falabella, P., Stefanini, F. R., Pfister, M., Thomas, B. B., Kashani, A. H., et al. (2016). Subretinal implantation of a monolayer of human embryonic stem cell-derived retinal pigment epithelium: a feasibility and safety study in Yucatán minipigs. *Graefes Arch. Clin. Exp. Ophthalmol.* 254, 1553–1565. doi: 10.1007/s00417-016-3386-y

Krishna, Y., Sheridan, C., Kent, D., Kearns, V., Grierson, I., and Williams, R. (2011). Expanded polytetrafluoroethylene as a substrate for retinal pigment epithelial cell growth and transplantation in age-related macular degeneration. *Br. J. Ophthalmol.* 95, 569–573. doi: 10.1136/bjo.2009.169953

Kundu, B., Rajkhowa, R., Kundu, S. C., and Wang, X. (2013). Silk fi broin biomaterials for tissue regenerations. *Adv. Drug Deliv. Rev.* 65, 457–470. doi: 10.1016/j.addr.2012.09.043

Kundu, J., Michaelson, A., Baranov, P., Chiumiento, M., Nigl, T., Young, M. J., et al. (2018). Interphotoreceptor matrix based biomaterial: impact on human retinal progenitor cell attachment and differentiation. *J. Biomed. Mater. Res. B Appl. Biomater.* 106, 891–899. doi: 10.1002/jbm.b.33901

Kuno, N., Fujii, S., Kuno, N., and Fujii, S. (2011). Recent advances in ocular drug delivery systems. *Polymers* 3, 193–221. doi: 10.3390/polym3010193

Lai, J.-Y. (2013). Influence of solvent composition on the performance of carbodiimide cross-linked gelatin carriers for retinal sheet delivery. *J. Mater. Sci.* 24, 2201–2210. doi: 10.1007/s10856-013-4961-y

Lakowski, J., Han, Y. T., Pearson, R. A., Gonzalez-Cordero, A., West, E. L., Gualdoni, S., et al. (2011). Effective transplantation of photoreceptor precursor cells selected via cell surface antigen expression. *Stem Cells* 29, 1391–1404. doi: 10.1002/stem.694

Lamba, D. A., Gust, J., and Reh, T. A. (2009). Transplantation of human embryonic stem cell-derived photoreceptors restores some visual function in Crx-deficient mice. *Cell Stem Cell* 4, 73–79. doi: 10.1016/j.stem.2008.10.015

Lamba, D. A., Karl, M. O., Ware, C. B., and Reh, T. A. (2006). Efficient generation of retinal progenitor cells from human embryonic stem cells. *Proc. Natl. Acad. Sci. U.S.A.* 103, 12769–12774. doi: 10.1073/pnas.0601990103

Lawley, E., Baranov, P., and Young, M. (2015). Hybrid vitronectin-mimicking polycaprolactone scaffolds for human retinal progenitor cell differentiation and transplantation. *J. Biomater. Appl.* 29, 894–902. doi: 10.1177/0885328214547751

Lee Ventola, C. (2014). Medical applications for 3D printing: current and projected uses. *P T* 39, 704–711.

Lin, T. C., Seiler, M. J., Zhu, D., Falabella, P., Hinton, D. R., Clegg, D. O., et al. (2017). Assessment of safety and functional efficacy of stem cell-based therapeutic approaches using retinal degenerative animal models. *Stem Cells Int.* 2017:9428176. doi: 10.1155/2017/9428176

Little, C. W., Cox, C., Wyatt, J., del Cerro, C., and del Cerro, M. (1998). Correlates of Photoreceptor Rescue by Transplantation of Human Fetal RPE in the RCS Rat. *Exp. Neurol.* 149, 151–160. doi: 10.1006/exnr.1997.6642

Liu, B. P., Cafferty, W. B. J., Budel, S. O., and Strittmatter, S. M. (2006). Extracellular regulators of axonal growth in the adult central nervous system. *Philos. Trans. R. Soc. Lond. B Biol. Sci.* 361, 1593–1610. doi: 10.1098/rstb.2006.1891

Liu, L., Johnson, L. V., Hikita, S. T., Hinton, D. R., Ribeiro, R., Lu, B., et al. (2012). A novel approach for subretinal implantation of ultrathin substrates containing stem cell-derived retinal pigment epithelium monolayer. *Ophthalmic Res.* 48, 186–191.

Liu, X., Chen, F., Chen, Y., Lu, H., Lu, X., Peng, X., et al. (2020). Paracrine effects of intraocularly implanted cells on degenerating retinas in mice. *Stem Cell Res. Ther.* 11:142. doi: 10.1186/s13287-020-01651-5

Liu, Y., Wang, R., Zarembinski, T. I., Doty, N., Jiang, C., Regatieri, C., et al. (2013). The application of hyaluronic acid hydrogels to retinal progenitor cell transplantation. *Tissue Eng. A* 19, 135–142. doi: 10.1089/ten.tea.2012.0209

Liu, Y., Xu, H. W., Wang, L., Li, S. Y., Zhao, C. J., Hao, J., et al. (2018). Human embryonic stem cell-derived retinal pigment epithelium transplants as a potential treatment for wet age-related macular degeneration. *Cell Discov.* 4:50. doi: 10.1038/s41421-018-0053-y

Liu, Z., Yu, N., Holz, F. G., Yang, F., and Stanzel, B. V. (2014). Enhancement of retinal pigment epithelial culture characteristics and subretinal space tolerance of scaffolds with 200 nm fiber topography. *Biomaterials* 35, 2837–2850. doi: 10.1016/j.biomaterials.2013.12.069

Llonch, S., Carido, M., and Ader, M. (2018). Organoid technology for retinal repair. *Dev. Biol.* 433, 132–143. doi: 10.1016/j.ydbio.2017.09.028

Lluis, F., and Cosma, M. P. (2010). Cell-fusion-mediated somatic-cell reprogramming: a mechanism for tissue regeneration. *J. Cell. Physiol.* 223, 6–13. doi: 10.1002/jcp.22003

Lorach, H., Kang, S., Bhuckory, M. B., Trouillet, A., Dalal, R., Marmor, M., et al. (2019). Transplantation of mature photoreceptors in rodents with retinal degeneration. *Transl. Vis. Sci. Technol.* 8:30. doi: 10.1167/tvst.8.3.30

Lowe, A., Harris, R., Bhansali, P., Cvekl, A., and Liu, W. (2016). Intercellular adhesion-dependent cell survival and ROCK-regulated actomyosin-driven forces mediate self-formation of a retinal organoid. *Stem Cell Rep.* 6, 743–756. doi: 10.1016/j.stemcr.2016.03.011

Lu, A. Q., and Barnstable, C. J. (2017). Generation of photoreceptor precursors from mouse embryonic stem cells. *Stem Cell Rev. Rep.* 14, 247–261. doi: 10.1007/s12015-017-9773-x

Lu, B., Malcuit, C., Wang, S., Girman, S., Francis, P., Lemieux, L., et al. (2009). Long-term safety and function of RPE from human embryonic stem cells in preclinical models of macular degeneration. *Stem Cells* 27, 2126–2135. doi: 10.1002/stem.149

Lu, B., Zhu, D., Hinton, D., Humayun, M. S., and Tai, Y.-C. (2012). Mesh-supported submicron parylene-C membranes for culturing retinal pigment epithelial cells. *Biomed. Microdevices* 14, 659–667. doi: 10.1007/s10544-012-9645-8

Lu, J. T., Lee, C. J., Bent, S. F., Fishman, H. A., and Sabelman, E. E. (2007). Thin collagen film scaffolds for retinal epithelial cell culture. *Biomaterials* 28, 1486–1494. doi: 10.1016/j.biomaterials.2006.11.023

Lu, L., Garcia, C. A., and Mikos, A. G. (1998). Retinal pigment epithelium cell culture on thin biodegradable poly(DL-lactic-co-glycolic acid) films. *J. Biomater. Sci. Polym. Ed.* 9, 1187–1205. doi: 10.1163/156856298X00721

Lu, L., Nyalakonda, K., Kam, L., Bizios, R., Göpferich, A., and Mikos, A. G. (2001). Retinal pigment epithelial cell adhesion on novel micropatterned surfaces fabricated from synthetic biodegradable polymers. *Biomaterials* 22, 291–297. doi: 10.1016/S0142-9612(00)00179-4

Luo, C., Chen, M., and Xu, H. (2011). Complement gene expression and regulation in mouse retina and retinal pigment epithelium/choroid. *Mol. Vis.* 17, 1588–1597.

Maaijwee, K., Heimann, H., Missotten, T., Mulder, P., Joussen, A., and van Meurs, J. (2007). Retinal pigment epithelium and choroid translocation in patients with exudative age-related macular degeneration: long-term results. *Graefes Arch. Clin. Exp. Ophthalmol.* 245, 1681–1689. doi: 10.1007/s00417-007-0607-4

Maaijwee, K. J. M., Van Meurs, J. C., Kirchhof, B., Mooij, C. M., Fischer, J. H., Mackiewicz, J., et al. (2007). Histological evidence for revascularisation of an autologous retinal pigment epithelium-choroid graft in the pig. *Br. J. Ophthalmol.* 91, 546–550. doi: 10.1136/bjo.2006.103259

Maaijwee, K., Joussen, A. M., Kirchhof, B., and Van Meurs, J. C. (2008). Retinal pigment epithelium (RPE)-choroid graft translocation in the treatment of an RPE tear: preliminary results. *Br. J. Ophthalmol.* 92, 526–529. doi: 10.1136/bjo.2007.131383

MacLaren, R. E., and Pearson, R. A. (2007). Stem cell therapy and the retina. *Eye* 21, 1352–1359. doi: 10.1038/sj.eye.6702842

Maminishkis, A., Al-Nawaiseh, S., Wolschendorf, M., Liu, Z., Braun, N., Brinken, R., et al. (2016). A step by step protocol for subretinal surgery in rabbits. *J. Vis. Exp.* 13:53927. doi: 10.3791/53927

Mandai, M., Fujii, M., Hashiguchi, T., Sunagawa, G. A., Ito, S., Sun, J., et al. (2017a). iPSC-derived retina transplants improve vision in rd1 end-stage retinal-degeneration mice. *Stem Cell Rep.* 8, 69–83. doi: 10.1016/j.stemcr.2016.12.008

Mandai, M., Watanabe, A., Kurimoto, Y., Hirami, Y., Morinaga, C., Daimon, T., et al. (2017b). Autologous induced stem-cell-derived retinal cells for macular degeneration. *N. Engl. J. Med.* 376, 1038–1046. doi: 10.1056/NEJMoa1608368

Marmor, M. F., and Wolfensberger, T. J. (1998). *The Retinal Pigment Epithelium: Function and Disease*. Oxford: Oxford University Press. doi: 10.1007/978-94-011-5137-5_1

Martín-Martín, Y., Fernández-García, L., Sanchez-Rebato, M. H., Marí-Buyé, N., Rojo, F. J., Pérez-Rigueiro, J., et al. (2019). Evaluation of neurosecretome from mesenchymal stem cells encapsulated in silk fibroin hydrogels. *Sci. Rep.* 9:8801. doi: 10.1038/s41598-019-45238-4

May-Simera, H. L., Wan, Q., Jha, B. S., Hartford, J., Khristov, V., Dejene, R., et al. (2018). Primary cilium-mediated retinal pigment epithelium maturation is disrupted in ciliopathy patient cells. *Cell Rep.* 22, 189–205. doi: 10.1016/j.celrep.2017.12.038

McCormick, R., Pearce, I., Kaye, S., and Haneef, A. (2020). Optimisation of a novel bio-substrate as a treatment for atrophic age-related macular degeneration. *Front. Bioeng. Biotechnol.* 8:456. doi: 10.3389/fbioe.2020.00456

McGill, T. J., Osborne, L., Lu, B., Stoddard, J., Huhn, S., Tsukamoto, A., et al. (2019). Subretinal transplantation of human central nervous system stem cells stimulates controlled proliferation of endogenous retinal pigment epithelium. *Transl. Vis. Sci. Technol.* 8:43. doi: 10.1167/tvst.8.3.43

McHugh, K. J., Tao, S. L., and Saint-Geniez, M. (2014). Porous poly(ε-caprolactone) scaffolds for retinal pigment epithelium transplantation. *Invest. Ophthalmol. Vis. Sci.* 55, 1754–1762. doi: 10.1167/iovs.13-12833

McLelland, B. T., Lin, B., Mathur, A., Aramant, R. B., Thomas, B. B., Nistor, G., et al. (2018). Transplanted hESC-derived retina organoid sheets differentiate, integrate, and improve visual function in retinal degenerate rats. *Invest. Ophthalmol. Vis. Sci.* 59, 2586–2603. doi: 10.1167/iovs.17-23646

Mead, B., Berry, M., Logan, A., Scott, R. A. H., Leadbeater, W., and Scheven, B. A. (2015). Stem cell treatment of degenerative eye disease. *Stem Cell Res.* 14, 243–257. doi: 10.1016/j.scr.2015.02.003

Mead, B., Logan, A., Berry, M., Leadbeater, W., and Scheven, B. A. (2013). Intravitreally transplanted dental pulp stem cells promote neuroprotection and axon regeneration of retinal ganglion cells after optic nerve injury. *Invest. Opthalmol. Vis. Sci.* 54, 7544–7556. doi: 10.1167/iovs.13-13045

Medawar, P. B. (1948). Immunity to homologous grafted skin; the fate of skin homografts transplanted to the brain, to subcutaneous tissue, and to the anterior chamber of the eye. *Br. J. Exp. Pathol.* 29, 58–69.

Medeiros, N. E., and Curcio, C. A. (2001). Preservation of ganglion cell layer neurons in age-related macular degeneration. *Invest. Ophthalmol. Vis. Sci.* 42, 795–803.

Michalska-Małecka, K., Kabiesz, A., Nowak, M., and Śpiewak, D. (2015). Age related macular degeneration – challenge for future: pathogenesis and new perspectives for the treatment. *Eur. Geriatr. Med.* 6, 69–75. doi: 10.1016/j.eurger.2014.09.007

Miyagishima, K. J., Wan, Q., Corneo, B., Sharma, R., Lotfi, M. R., Boles, N. C., et al. (2016). In pursuit of authenticity: induced pluripotent stem cell-derived retinal pigment epithelium for clinical applications. *Stem Cells Transl. Med.* 5, 1562–1574. doi: 10.5966/sctm.2016-0037

Miyagishima, K. J., Wan, Q., Miller, S. S., and Bharti, K. (2017). A basis for comparison: sensitive authentication of stem cell derived RPE using physiological responses of intact RPE monolayers. *Stem Cell Transl. Investig.* 4:e1497.

Nakano, T., Ando, S., Takata, N., Kawada, M., Muguruma, K., Sekiguchi, K., et al. (2012). Self-formation of optic cups and storable stratified neural retina from human ESCs. *Cell Stem Cell.* 10, 771–785. doi: 10.1016/j.stem.2012.05.009

Neurotech (2020). *NC-503 ECT*. Available online at: http://www.neurotechusa.com/nc-503-ect.html (accessed July 21, 2020).

Niederkorn, J., Streilein, J. W., and Shadduck, J. A. (1981). Deviant immune responses to allogeneic tumors injected intracamerally and subcutaneously in mice. *Invest Ophthalmol Vis Sci.* 20, 355–363.

Niederkorn, J. Y., and Kaplan, H. J. (2007). Rationale for immune response and the eye. *Chem. Immunol. Allergy* 92, 1–3. doi: 10.1159/000099234

Niyadurupola, N., Sidaway, P., Osborne, A., Broadway, D. C., and Sanderson, J. (2011). The development of human organotypic retinal cultures (HORCs) to study retinal neurodegeneration. *Br. J. Ophthalmol.* 95, 720–726. doi: 10.1136/bjo.2010.181404

Oganesian, A., Gabrielian, K., Ernest, J. T., and Patel, S. C. (1999). A new model of retinal pigment epithelium transplantation with microspheres. *Arch. Ophthalmol.* 117, 1192–1200. doi: 10.1001/archopht.117.9.1192

Ohlemacher, S. K., Iglesias, C. L., Sridhar, A., Gamm, D. M., and Meyer, J. S. (2015). Generation of highly enriched populations of optic vesicle-like retinal cells from human pluripotent stem cells. *Curr. Protoc. Stem Cell Biol.* 32, 1H.8.1–1H.8.20. doi: 10.1002/9780470151808.sc01h08s32

Ortin-Martinez, A., Tsai, E. L. S., Nickerson, P. E., Bergeret, M., Lu, Y., Smiley, S., et al. (2017). A reinterpretation of cell transplantation: gFP transfer from donor to host photoreceptors. *Stem Cells* 35, 932–939. doi: 10.1002/stem.2552

Osakada, F., Ikeda, H., Mandai, M., Wataya, T., Watanabe, K., Yoshimura, N., et al. (2008). Toward the generation of rod and cone photoreceptors from mouse, monkey and human embryonic stem cells. *Nat. Biotechnol.* 26, 215–224. doi: 10.1038/nbt1384

Osborne, A., Hopes, M., Wright, P., Broadway, D. C., and Sanderson, J. (2016). Human organotypic retinal cultures (HORCs) as a chronic experimental model for investigation of retinal ganglion cell degeneration. *Exp. Eye Res.* 143, 28–38. doi: 10.1016/j.exer.2015.09.012

Park, S. S., Moisseiev, E., Bauer, G., Anderson, J. D., Grant, M. B., Zam, A., et al. (2017). *Advances in Bone Marrow Stem Cell Therapy for Retinal Dysfunction*. Amsterdam: Elsevier Ltd, doi: 10.1016/j.preteyeres.2016.10.002

Pearce, W., Hsu, J., and Yeh, S. (2015). Advances in drug delivery to the posterior segment. *Curr. Opin. Ophthalmol.* 26, 233–239. doi: 10.1097/ICU.0000000000000143

Pearson, R. A., Barber, A. C., Rizzi, M., Hippert, C., Xue, T., West, E. L., et al. (2012). Restoration of vision after transplantation of photoreceptors. *Nature* 485, 99–103. doi: 10.1038/nature10997

Pearson, R. A., Gonzalez-Cordero, A., West, E. L., Ribeiro, J. R., Aghaizu, N., Goh, D., et al. (2016). Donor and host photoreceptors engage in material transfer following transplantation of post-mitotic photoreceptor precursors. *Nat. Commun.* 7:13029. doi: 10.1038/ncomms13029

Peng, C. H., Chuang, J. H., Wang, M. L., Jhan, Y. Y., Chien, K. H., Chung, Y. C., et al. (2016). Laminin modification subretinal bio-scaffold remodels retinal pigment epithelium-driven microenvironment in vitro and in vivo. *Oncotarget* 7, 64631–64648. doi: 10.18632/oncotarget.11502

Radtke, N. D., Aramant, R. B., Petry, H. M., Green, P. T., Pidwell, D. J., and Seiler, M. J. (2008). Vision improvement in retinal degeneration patients by implantation of retina together with retinal pigment epithelium. *Am. J. Ophthalmol.* 146, 172–182. doi: 10.1016/j.ajo.2008.04.009

Radtke, N. D., Seiler, M. J., Aramant, R. B., Petry, H. M., and Pidwell, D. J. (2002). Transplantation of intact sheets of fetal neural retina with its retinal pigment epithelium in retinitis pigmentosa patients. *Am. J. Ophthalmol.* 133, 544–550. doi: 10.1016/S0002-9394(02)01322-3

Rajala, R. V. S., and Gardner, T. W. (2016). Burning fat fuels photoreceptors patient iPSCs: a new discovery tool for Smith-Lemli-Opitz syndrome. *Nat. Med.* 22, 342–343. doi: 10.1038/nm.4080

Ramakrishna, S., Mayer, J., Wintermantel, E., and Leong, K. W. (2001). Biomedical applications of polymer-composite materials: a review. *Compos. Sci. Technol.* 61, 1189–1224. doi: 10.1016/S0266-3538(00)00241-4

Redenti, S., Neeley, W. L., Rompani, S., Saigal, S., Yang, J., Klassen, H., et al. (2009). Engineering retinal progenitor cell and scrollable poly(glycerol-sebacate) composites for expansion and subretinal transplantation. *Biomaterials* 30, 3405–3414. doi: 10.1016/j.biomaterials.2009.02.046

Redenti, S., Tao, S., Yang, J., Gu, P., Klassen, H., Saigal, S., et al. (2008). Retinal tissue engineering using mouse retinal progenitor cells and a novel biodegradable, thin-film poly(e-caprolactone) nanowire scaffold. *J. Ocul. Biol. Dis. Infor.* 1, 19–29. doi: 10.1007/s12177-008-9005-3

Rose, J. B., Pacelli, S., Haj, A. J., El, Dua, H. S., Hopkinson, A., et al. (2014). Gelatin-based materials in ocular tissue engineering. *Materials* 7, 3106–3135. doi: 10.3390/ma7043106

Rowland, T. J., Buchholz, D. E., and Clegg, D. O. (2012). Pluripotent human stem cells for the treatment of retinal disease. *J. Cell. Physiol.* 227, 457–466. doi: 10.1002/jcp.22814

Rupenthal, I. D. (2017). Drug-device combination approaches for delivery to the eye. *Curr. Opin. Pharmacol.* 36, 44–51. doi: 10.1016/j.coph.2017.08.003

Sabel, B. A., Henrich-Noack, P., Fedorov, A., and Gall, C. (2011). Vision restoration after brain and retina damage: the ‘residual vision activation theory. *Prog. Brain Res.* 192, 199–262. doi: 10.1016/B978-0-444-53355-5.00013-0

Salero, E., Blenkinsop, T. A., Corneo, B., Harris, A., Rabin, D., Stern, J. H., et al. (2012). Adult human RPE can be activated into a multipotent stem cell that produces mesenchymal derivatives. *Cell Stem Cell* 10, 88–95. doi: 10.1016/j.stem.2011.11.018

Sandhu, H., Adeniran, J. M. F., and Kaplan, H. J. (2019). “Transplantation immunology: retinal cell-based therapy,” in *Cell-Based Therapy for Degenerative Retinal Disease. Stem Cell Biology and Regenerative Medicine*, eds M. Zarbin, M. Singh, and R. Casaroli-Marano (Cham: Humana Press), 141–156. doi: 10.1007/978-3-030-05222-5_8

Sanges, D., Simonte, G., Di Vicino, U., Romo, N., Pinilla, I., Nicolás, M., et al. (2016). Reprogramming Müller glia via in vivo cell fusion regenerates murine photoreceptors. *J. Clin. Invest.* 126, 3104–3116. doi: 10.1172/JCI85193

Santos-Ferreira, T., Llonch, S., Borsch, O., Postel, K., Haas, J., and Ader, M. (2016a). Retinal transplantation of photoreceptors results in donor-host cytoplasmic exchange. *Nat. Commun.* 7:13028. doi: 10.1038/ncomms13028

Santos-Ferreira, T., Völkner, M., Borsch, O., Haas, J., Cimalla, P., Vasudevan, P., et al. (2016b). Stem cell-derived photoreceptor transplants differentially integrate into mouse models of cone-rod dystrophy. *Invest. Ophthalmol. Vis. Sci.* 57, 3509–3520. doi: 10.1167/iovs.16-19087

Sauve, Y., and Gaillard, F. (1995). *Regeneration in the Visual System of Adult Mammals*. Available online at: http://www.ncbi.nlm.nih.gov/pubmed/21413374 (accessed July 8, 2020).

Schubert, C., Van Langeveld, M. C., and Donoso, L. A. (2014). Innovations in 3D printing: a 3D overview from optics to organs. *Br. J. Ophthalmol.* 98, 159–161. doi: 10.1136/bjophthalmol-2013-304446

Schwartz, S. D., Hubschman, J.-P., Heilwell, G., Franco-Cardenas, V., Pan, C. K., Ostrick, R. M., et al. (2012). Embryonic stem cell trials for macular degeneration: a preliminary report. *Lancet* 379, 713–720. doi: 10.1016/S0140-6736(12)60028-2

Schwartz, S. D., Regillo, C. D., Lam, B. L., Eliott, D., Rosenfeld, P. J., Gregori, N. Z., et al. (2015). Human embryonic stem cell-derived retinal pigment epithelium in patients with age-related macular degeneration and Stargardt’s macular dystrophy: follow-up of two open-label phase 1/2 studies. *Lancet* 385, 509–516. doi: 10.1016/S0140-6736(14)61376-3

Seaton, A. D., Sheedlo, H. J., and Turner, J. E. (1994). A primary role for RPE transplants in the inhibition and regression of neovascularization in the RCS rat. *Invest. Ophthalmol. Vis. Sci.* 35, 162–169.

Seiler, M. J., and Aramant, R. B. (2012). Cell replacement and visual restoration by retinal sheet transplants. *Prog. Retin. Eye Res.* 31, 661–687. doi: 10.1016/j.preteyeres.2012.06.003

Shirai, H., Mandai, M., Matsushita, K., Kuwahara, A., Yonemura, S., Nakano, T., et al. (2016). Transplantation of human embryonic stem cell-derived retinal tissue in two primate models of retinal degeneration. *Proc. Natl. Acad. Sci. U.S.A.* 113, E81–E90. doi: 10.1073/pnas.1512590113

Shoichet, M. S., van der Kooy, D., Cooke, M. J., Morshead, C. M., Coles, B. L. K., Donaldson, L., et al. (2015). A hyaluronan-based injectable hydrogel improves the survival and integration of stem cell progeny following transplantation. *Stem Cell Rep.* 4, 1031–1045. doi: 10.1016/j.stemcr.2015.04.008

Sieving, P. A., Caruso, R. C., Tao, W., Coleman, H. R., Thompson, D. J. S., Fullmer, K. R., et al. (2006). Ciliary neurotrophic factor (CNTF) for human retinal degeneration: phase I trial of CNTF delivered by encapsulated cell intraocular implants. *Proc. Natl. Acad. Sci. U.S.A.* 103, 3896–3901. doi: 10.1073/pnas.0600236103

Singh, D., Wang, S., Bin, Xia, T., Tainsh, L., Ghiassi-Nejad, M., et al. (2018). A biodegradable scaffold enhances differentiation of embryonic stem cells into a thick sheet of retinal cells. *Biomaterials* 154, 158–168. doi: 10.1016/j.biomaterials.2017.10.052

Singh, R., Cuzzani, O., Binette, F., Sternberg, H., West, M. D., and Nasonkin, I. O. (2018). Pluripotent stem cells for retinal tissue engineering: current status and future prospects. *Stem Cell Rev. Rep.* 14, 463–483. doi: 10.1007/s12015-018-9802-4

Singh, M. S., Balmer, J., Barnard, A. R., Aslam, S. A., Moralli, D., Green, C. M., et al. (2016). Transplanted photoreceptor precursors transfer proteins to host photoreceptors by a mechanism of cytoplasmic fusion. *Nat. Commun.* 7:13537. doi: 10.1038/ncomms13537

Singh, M. S., Issa, P. C., Butler, R., Martin, C., Lipinski, D. M., Sekaran, S., et al. (2013). Reversal of end-stage retinal degeneration and restoration of visual function by photoreceptor transplantation. *Proc. Natl. Acad. Sci. U.S.A.* 110, 1101–1106. doi: 10.1073/pnas.1119416110

Singh, M. S., and MacLaren, R. E. (2011). Stem cells as a therapeutic tool for the blind: biology and future prospects. *Proc. R. Soc. B Biol. Sci.* 278, 3009–3016. doi: 10.1098/rspb.2011.1028

Singh, M. S., Park, S. S., Albini, T. A., Canto-Soler, M. V., Klassen, H., MacLaren, R. E., et al. (2020). Retinal stem cell transplantation: balancing safety and potential. *Prog. Retin. Eye Res.* 75:100779. doi: 10.1016/j.preteyeres.2019.100779

Singh, R. K., Occelli, L. M., Binette, F., Petersen-Jones, S. M., and Nasonkin, I. O. (2019). Transplantation of human embryonic stem cell-derived retinal tissue in the subretinal space of the cat eye. *Stem Cells Dev.* 28, 1151–1166. doi: 10.1089/scd.2019.0090

Singh, S., Woerly, S., and McLaughlin, B. J. (2001). Natural and artificial substrates for retinal pigment epithelial monolayer transplantation. *Biomaterials* 22, 3337–3343. doi: 10.1016/S0142-9612(01)00171-5

Sodha, S., Wall, K., Redenti, S., Klassen, H., Young, M. J., and Tao, S. L. (2011). Microfabrication of a three-dimensional polycaprolactone thin-film scaffold for retinal progenitor cell encapsulation. *J. Biomater. Sci. Polym. Ed.* 22, 443–456. doi: 10.1163/092050610X487738

Sonoi, R., Kim, M. H., Yamada, K., and Kino-oka, M. (2017). Phenotypic heterogeneity of human retinal pigment epithelial cells in passaged cell populations. *J. Biosci. Bioeng.* 124, 227–233. doi: 10.1016/j.jbiosc.2017.03.008

Sortwell, C. E., Pitzer, M. R., and Collier, T. J. (2000). Time course of apoptotic cell death within mesencephalic cell suspension grafts: implications for improving grafted dopamine neuron survival. *Exp. Neurol.* 165, 268–277. doi: 10.1006/exnr.2000.7476

Srivastava, G. K., Martín, L., Singh, A. K., Fernandez-Bueno, I., Gayoso, M. J., Garcia-Gutierrez, M. T., et al. (2011). Elastin-like recombinamers as substrates for retinal pigment epithelial cell growth. *J. Biomed. Mater. Res. A* 97, 243–250. doi: 10.1002/jbm.a.33050

Stanzel, B. V., Liu, Z., Somboonthanakij, S., Wongsawad, W., Brinken, R., Eter, N., et al. (2014). Human RPE stem cells grown into polarized RPE monolayers on a polyester matrix are maintained after grafting into rabbit subretinal space. *Stem Cell Rep.* 2, 64–77. doi: 10.1016/j.stemcr.2013.11.005

Steindl, K., and Binder, S. (2008). Retinal degeneration processes and transplantation of retinal pigment epithelial cells: past, present and future trends. *Spektrum der Augenheilkunde* 22, 357–361. doi: 10.1007/s00717-008-0292-7

Stern, J. H., Tian, Y., Funderburgh, J., Pellegrini, G., Zhang, K., Goldberg, J. L., et al. (2018). Regenerating eye tissues to preserve and restore vision. *Cell Stem Cell* 22, 834–849. doi: 10.1016/j.stem.2018.05.013

Strauss, O. (2005). The retinal pigment epithelium in visual function. *Physiol. Rev.* 85, 845–881. doi: 10.1152/physrev.00021.2004

Streilein, J. W. (2003). Ocular immune privilege: the eye takes a dim but practical view of immunity and inflammation. *J. Leukocyte Biol.* 74, 179–185. doi: 10.1189/jlb.1102574

Subrizi, A., Hiidenmaa, H., Ilmarinen, T., Nymark, S., Dubruel, P., Uusitalo, H., et al. (2012). Generation of hESC-derived retinal pigment epithelium on biopolymer coated polyimide membranes. *Biomaterials* 33, 8047–8054. doi: 10.1016/j.biomaterials.2012.07.033

Tam, R. Y., Fuehrmann, T., Mitrousis, N., and Shoichet, M. S. (2014). Regenerative therapies for central nervous system diseases: a biomaterials approach. *Neuropsychopharmacology* 39, 169–188. doi: 10.1038/npp.2013.237

Tao, S., Young, C., Redenti, S., Zhang, Y., Klassen, H., Desai, T., et al. (2007). Survival, migration and differentiation of retinal progenitor cells transplanted on micro-machined poly(methyl methacrylate) scaffolds to the subretinal space. *Lab Chip* 7, 695–701. doi: 10.1039/b618583e

Tao, W., Wen, R., Goddard, M. B., Sherman, S. D., O'Rourke, P. J., Stabila, P. F., et al. (2002). Encapsulated cell-based delivery of CNTF reduces photoreceptor degeneration in animal models of retinitis pigmentosa. *Invest. Ophthalmol. Vis. Sci.* 43, 3292–3298.

Taylor, A. W. (2016). Ocular immune privilege and transplantation. *Front. Immunol.* 7:37. doi: 10.3389/fimmu.2016.00037

Taylor, A. W., and Ng, T. F. (2018). Negative regulators that mediate ocular immune privilege. *J. Leukoc. Biol.* 103, 1179–1187. doi: 10.1002/JLB.3MIR0817-337R

Taylor, L., Arner, K., Engelsberg, K., and Ghosh, F. (2013). Effects of glial cell line-derived neurotrophic factor on the cultured adult full-thickness porcine retina. *Curr. Eye Res.* 38, 503–515. doi: 10.3109/02713683.2013.763989

Taylor, L., Arnér, K., Holmgren Taylor, I., and Ghosh, F. (2014). Feet on the ground: physical support of the inner retina is a strong determinant for cell survival and structural preservation in vitro. *Invest. Ophthalmol. Vis. Sci.* 55, 2200–2213. doi: 10.1167/iovs.13-13535

Tezel, T. H., Del Priore, L. V., Berger, A. S., and Kaplan, H. J. (2007). Adult retinal pigment epithelial transplantation in exudative age-related macular degeneration. *Am. J. Ophthalmol.* 143, 584–595. doi: 10.1016/j.ajo.2006.12.007

Thakur, A., Mishra, S., Pena, J., Zhou, J., Redenti, S., Majeska, R., et al. (2018). Collective adhesion and displacement of retinal progenitor cells upon extracellular matrix substrates of transplantable biomaterials. *J. Tissue Eng.* 9:2041731417751286. doi: 10.1177/2041731417751286

Thangaraj, G., Greif, A., and Layer, P. G. (2011). Simple explant culture of the embryonic chicken retina with long-term preservation of photoreceptors. *Exp. Eye Res.* 93, 556–564. doi: 10.1016/j.exer.2011.07.011

Tomita, M., Lavik, E., Klassen, H., Zahir, T., Langer, R., and Young, M. J. (2005). Biodegradable Polymer Composite Grafts Promote the Survival and Differentiation of Retinal Progenitor Cells. *Stem Cells* 23, 1579–1588. doi: 10.1634/stemcells.2005-0111

Tu, H. Y., Watanabe, T., Shirai, H., Yamasaki, S., Kinoshita, M., Matsushita, K., et al. (2019). Medium- to long-term survival and functional examination of human iPSC-derived retinas in rat and primate models of retinal degeneration. *EBioMedicine* 39, 562–574. doi: 10.1016/j.ebiom.2018.11.028

Tucker, B. A., Park, I. H., Qi, S. D., Klassen, H. J., Jiang, C., Yao, J., et al. (2011). Transplantation of adult mouse iPS cell-derived photoreceptor precursors restores retinal structure and function in degenerative mice. *PLoS One* 6:e18992. doi: 10.1371/journal.pone.0018992

Tucker, B. A., Redenti, S. M., Jiang, C., Swift, J. S., Klassen, H. J., Smith, M. E., et al. (2010). The use of progenitor cell/biodegradable MMP2-PLGA polymer constructs to enhance cellular integration and retinal repopulation. *Biomaterials* 31, 9–19. doi: 10.1016/j.biomaterials.2009.09.015

U.S. National Library of Medicine (2020a). *A Safety Study of CNTO 2476 in Patients With Age-Related Macular Degeneration – Tabular View – ClinicalTrials.gov*. Available online at: https://clinicaltrials.gov/ct2/show/record/NCT01226628 (accessed July 21, 2020).

U.S. National Library of Medicine (2020b). *A Study of an Encapsulated Cell Technology (ECT) Implant for Patients With Atrophic Macular Degeneration – Full Text View – ClinicalTrials.gov*. Available online at: https://clinicaltrials.gov/ct2/show/NCT00447954 (accessed July 22, 2020).

U.S. National Library of Medicine (2020c). *A Study Of Implantation Of Retinal Pigment Epithelium In Subjects With Acute Wet Age Related Macular Degeneration – Full Text View – ClinicalTrials.gov*. Available online at: https://clinicaltrials.gov/ct2/show/NCT01691261 (accessed July 22, 2020).

U.S. National Library of Medicine (2020d). *Autologous Transplantation of Induced Pluripotent Stem Cell-Derived Retinal Pigment Epithelium for Geographic Atrophy Associated With Age-Related Macular Degeneration – Full Text View – ClinicalTrials.gov*. Available online at: https://clinicaltrials.gov/ct2/show/NCT04339764 (accessed July 22, 2020).

U.S. National Library of Medicine (2020f). *Clinical Trial of Autologous Intravitreal Bone-marrow CD34+ Stem Cells for Retinopathy – Full Text View – ClinicalTrials.gov*. Available online at: https://clinicaltrials.gov/ct2/show/NCT01736059 (accessed July 22, 2020).

U.S. National Library of Medicine (2020g). *Evaluation of Safety of Ciliary Neurotrophic Factor Implants in the Eye – Full Text View – ClinicalTrials.gov*. Available online at: https://clinicaltrials.gov/ct2/show/NCT00063765 (accessed July 22, 2020).

U.S. National Library of Medicine (2020h). *Intravitreal Bone Marrow-Derived Stem Cells in Patients With Macular Degeneration – Full Text View – ClinicalTrials.gov*. Available online at: https://clinicaltrials.gov/ct2/show/NCT01518127 (accessed July 22, 2020).

U.S. National Library of Medicine (2020i). *Long-Term Follow-up Safety Study of Human Central Nervous System Stem Cells in Subjects With Geographic Atrophy of Age-Related Macular Degeneration – Full Text View – ClinicalTrials.gov*. Available online at: https://clinicaltrials.gov/ct2/show/NCT02137915 (accessed July 22, 2020).

U.S. National Library of Medicine (2020j). *Safety and Efficacy of Intravitreal Injection of Human Retinal Progenitor Cells in Adults With Retinitis Pigmentosa – Full Text View – ClinicalTrials.gov*. Available online at: https://clinicaltrials.gov/ct2/show/NCT03073733 (accessed July 22, 2020).

U.S. National Library of Medicine (2020k). *Safety and Efficacy Study of OpRegen for Treatment of Advanced Dry-Form Age-Related Macular Degeneration – Full Text View – ClinicalTrials.gov*. Available online at: https://clinicaltrials.gov/ct2/show/NCT02286089 (accessed July 8, 2020).

U.S. National Library of Medicine (2020l). *Safety and Tolerability of hRPC in Retinitis Pigmentosa – Full Text View – ClinicalTrials.gov*. Available online at: https://clinicaltrials.gov/ct2/show/NCT02464436 (accessed July 22, 2020).

U.S. National Library of Medicine (2020m). *Safety and Tolerability of Sub-retinal Transplantation of hESC Derived RPE (MA09-hRPE) Cells in Patients With Advanced Dry Age Related Macular Degeneration – Full Text View – ClinicalTrials.gov*. Available online at: https://clinicaltrials.gov/ct2/show/NCT01344993 (accessed July 8, 2020).

U.S. National Library of Medicine (2020n). *Safety of a Single, Intravitreal Injection of Human Retinal Progenitor Cells (jCell) in Retinitis Pigmentosa – Study Results – ClinicalTrials.gov*. Available online at: https://clinicaltrials.gov/ct2/show/results/NCT02320812 (accessed July 22, 2020).

U.S. National Library of Medicine (2020o). *Safety Study in Retinal Transplantation for Dry Age Related Macular Degeneration. – Full Text View – ClinicalTrials.gov*. Available online at: https://clinicaltrials.gov/ct2/show/NCT00346060 (accessed July 22, 2020).

U.S. National Library of Medicine (2020p). *Stem Cell Ophthalmology Treatment Study – Full Text View – ClinicalTrials.gov*. Available online at: https://www.clinicaltrials.gov/ct2/show/NCT01920867 (accessed July 22, 2020]

U.S. National Library of Medicine (2020q). *Study of HUCNS-SC Subretinal Transplantation in Subjects With GA of AMD – Full Text View – ClinicalTrials.gov*. Available online at: https://clinicaltrials.gov/ct2/show/NCT02467634 (accessed July 22, 2020).

U.S. National Library of Medicine (2020r). *Study of Human Central Nervous System Stem Cells (HuCNS-SC) in Age-Related Macular Degeneration (AMD) – Full Text View – ClinicalTrials.gov*. Available online at: https://clinicaltrials.gov/ct2/show/NCT01632527 (accessed July 22, 2020).

U.S. National Library of Medicine (2020s). *Study of Subretinal Implantation of Human Embryonic Stem Cell-Derived RPE Cells in Advanced Dry AMD – Full Text View – ClinicalTrials.gov*. Available online at: https://clinicaltrials.gov/ct2/show/NCT02590692 (accessed July 8, 2020).

U.S. National Library of Medicine (2020u). *Study of the Intravitreal Implantation of NT-503-3 Encapsulated Cell Technology (ECT) for the Treatment of Recurrent Choroidal Neovascularization (CNV) Secondary to Age-Related Macular Degeneration (AMD) – Full Text View – ClinicalTrials.gov*. Available online at: https://clinicaltrials.gov/ct2/show/NCT02228304 (accessed July 22, 2020).

van Zeeburg, E. J. T., Maaijwee, K. J. M., Missotten, T. O. A. R., Heimann, H., and van Meurs, J. C. (2012). A free retinal pigment epithelium–choroid graft in patients with exudative age-related macular degeneration: results up to 7 years. *Am. J. Ophthalmol.* 153, 120.e2–127.e2. doi: 10.1016/j.ajo.2011.06.007

Völkner, M., Zschätzsch, M., Rostovskaya, M., Overall, R. W., Busskamp, V., Anastassiadis, K., et al. (2016). Retinal organoids from pluripotent stem cells efficiently recapitulate retinogenesis. *Stem Cell Rep.* 6, 525–538. doi: 10.1016/j.stemcr.2016.03.001

Waldron, P. V., Di Marco, F., Kruczek, K., Ribeiro, J., Graca, A. B., Hippert, C., et al. (2018). Transplanted donor- or stem cell-derived cone photoreceptors can both integrate and undergo material transfer in an environment-dependent manner. *Stem Cell Rep.* 10, 406–421. doi: 10.1016/j.stemcr.2017.12.008

Wang, S. W., Mu, X., Bowers, W. J., and Klein, W. H. (2002). Retinal ganglion cell differentiation in cultured mouse retinal explants. *Methods* 28, 448–456. doi: 10.1016/S1046-2023(02)00264-5

Warnke, P. H., Alamein, M., Skabo, S., Stephens, S., Bourke, R., Heiner, P., et al. (2013). Primordium of an artificial Bruch's membrane made of nanofibers for engineering of retinal pigment epithelium cell monolayers. *Acta Biomater.* 9, 9414–9422. doi: 10.1016/j.actbio.2013.07.029

Weiner, L. P. (2008). Definitions and criteria for stem cells. *Methods Mol. Biol.* 438, 3–8. doi: 10.1007/978-1-59745-133-8_1

Weiss, J. N., Levy, S., and Malkin, A. (2015). Stem cell ophthalmology treatment study (SCOTS) for retinal and optic nerve diseases: a preliminary report. *Neural Regen. Res.* 10, 982–988. doi: 10.4103/1673-5374.158365

Wenk, E., Merkle, H. P., and Meinel, L. (2011). Silk fibroin as a vehicle for drug delivery applications. *J. Control. Release* 150, 128–141. doi: 10.1016/j.jconrel.2010.11.007

West, E. L., Pearson, R. A., MacLaren, R. E., Sowden, J. C., and Ali, R. R. (2009). *Cell Transplantation Strategies for Retinal Repair*. Amsterdam: Elsevier, doi: 10.1016/S0079-6123(09)17501-5

Wong, W. L., Su, X., Li, X., Cheung, C. M. G., Klein, R., Cheng, C.-Y., et al. (2014). Global prevalence of age-related macular degeneration and disease burden projection for 2020 and 2040: a systematic review and meta-analysis. *Lancet Glob. Health* 2, e106–e116. doi: 10.1016/S2214-109X(13)70145-1

Wu, H. J., Li, X. X., Dong, J. Q., Pei, W. H., and Chen, H. D. (2007). Effects of subretinal implant materials on the viability, apoptosis and barrier function of cultured RPE cells. *Graefes Arch. Clin. Exp. Ophthalmol.* 245, 135–142. doi: 10.1007/s00417-006-0296-4

Xian, B., Luo, Z., Li, K., Li, K., Tang, M., Yang, R., et al. (2019). Dexamethasone Provides Effective Immunosuppression for Improved Survival of Retinal Organoids after Epiretinal Transplantation. *Stem Cells Int.* 2019:7148032. doi: 10.1155/2019/7148032

Xiang, P., Wu, K.-C., Zhu, Y., Xiang, L., Li, C., Chen, D.-L., et al. (2014). A novel Bruch's membrane-mimetic electrospun substrate scaffold for human retinal pigment epithelium cells. *Biomaterials* 35, 9777–9788. doi: 10.1016/j.biomaterials.2014.08.040

Yang, T. C., Chuang, J. H., Buddhakosai, W., Wu, W. J., Lee, C. J., Chen, W. S., et al. (2017). Elongation of axon extension for human iPSC-derived retinal ganglion cells by a nano-imprinted scaffold. *Int. J. Mol. Sci.* 18:2013. doi: 10.3390/ijms18092013

Yang, Y., Mohand-Said, S., Léveillard, T., Fontaine, V., Simonutti, M., and Sahel, J. A. (2010). Transplantation of photoreceptor and total neural retina preserves cone function in p23h rhodopsin transgenic rat. *PLoS One* 5:e13469. doi: 10.1371/journal.pone.0013469

Yao, J., Ko, C. W., Baranov, P. Y., Regatieri, C. V., Redenti, S., Tucker, B. A., et al. (2015). Enhanced differentiation and delivery of mouse retinal progenitor cells using a micropatterned biodegradable thin-film polycaprolactone scaffold. *Tissue Eng. Part A* 21, 1247–1260. doi: 10.1089/ten.tea.2013.0720

Yao, J., Tao, S. L., Young, M. J., Yao, J., Tao, S. L., and Young, M. J. (2011). Synthetic polymer scaffolds for stem cell transplantation in retinal tissue engineering. *Polymers* 3, 899–914. doi: 10.3390/polym3020899

Zarbin, M. (2016). Cell-based therapy for degenerative retinal disease. *Trends Mol. Med.* 22, 115–134. doi: 10.1016/j.molmed.2015.12.007

Zarbin, M. (2019). Cell-based therapy for retinal disease: the new frontier. *Methods Mol. Biol.* 1834, 367–381. doi: 10.1007/978-1-4939-8669-9_23

Zhang, D., Ni, N., Chen, J., Yao, Q., Shen, B., Zhang, Y., et al. (2015). Electrospun SF/PLCL nanofibrous membrane: a potential scaffold for retinal progenitor cell proliferation and differentiation. *Sci. Rep.* 5:14326. doi: 10.1038/srep14326

Zhong, X., Gutierrez, C., Xue, T., Hampton, C., Vergara, M. N., Cao, L. H., et al. (2014). Generation of three-dimensional retinal tissue with functional photoreceptors from human iPSCs. *Nat. Commun.* 5:4047. doi: 10.1038/ncomms5047

Conflict of Interest: The authors declare that the research was conducted in the absence of any commercial or financial relationships that could be construed as a potential conflict of interest.

APPENDIX I

Abbreviations List

AMD, Age-Related Macular Degeneration
ARPE-19, human retinal pigment epithelial cell line-19
BrM, Bruch's membrane
CNTF, ciliary neurotrophic factor
CNV, choroidal neovascularization
D-AMD, Dry Age-Related Macular Degeneration
dRPE, Pluripotent differentiated RPE
ECT, encapsulated cell technology
ELRs, elastin-like recombinamers
ESCs, embryonic- or fetal- derived stem cells
ePTFE, expanded polytetrafluoroethylene
fhRPE, fetal human RPE
FDA, US Food and Drug Administration Agency
GFP, green fluorescent protein
Gnat12/2 mice, model of congenital stationary night blindness
hESCs, human embryonic stem cells
hESCs-RPE cells, human embryonic stem cell-derived RPE cells
hiPSC, human induced pluripotent stem cells
hPSCs-PRs, human pluripotent stem cells-derived photoreceptors
hRPCs, human retinal progenitor cells
hRPE, human RPE
IPE, iris pigment epithelium
IPM, interphotoreceptor matrix
iPSC, induced pluripotent stem cell
mESC, mouse embryonic stem cell
miPSC, mouse induced pluripotent stem cell
MMP2, matrix metallopeptidase 2
mPEG-PLGA, methoxy-poly (ethylene glycol) block-poly lactic-co-glycolic acid
mPEG-PCL, methoxy poly (ethylene glycol) -b-copolymers of polycaprolactone
mSC, mesenchymal stem cell
NP, nanoparticles
NpHR, Natronomonas pharaonis halorhodopsin
PCL, poly(caprolactone)
PDMS, plasma-modified polydimethylsiloxane
PDMS-PmL, plasma-modified polydimethylsiloxane (PDMS) with laminin
PEGDMA, polyethylene glycol dimethacrylate
PEG, poly (ethylene glycol)
PET, polyethylene terephthalate
PGA, polyglycolic acid
PGS, poly(glycerol-sebacate)
PI, polyimide
PLA, poly (DL-lactic acid)
P(LA-co-CL), poly(l-lactide-co-ε-caprolactone)
PLDLA, copolymer 96/4 L-lactide/D-lactide
PLGA, poly(lactic-co-glycolic) acid
PLLA, poly (L-lactic acid)
PLLA/PLGA, poly (L-lactic acid)/poly (lactic-co-glycolic acid)
PMMA, poly (methyl methacrylate)
PPCs, photoreceptor precursor cells
PR, photoreceptors
Prph2+/Δ307, model of retinitis pigmentosa
PSCs, pluripotent stem cells
PTFE, Polytetrafluoroethylene
RGD, arginine–glycine–aspartic acid
RPCs, retinal progenitor cell
RPE, retinal pigment epithelium
RPESC, retinal pigment epithelium stem cells
RSCs, retinal stem cells
SC, stem cell
TDSC, tissue-derived stem cells
TRL, clinical trials
VEGF, vascular endothelium growth factor
VEGF-Fc, VEGF receptor fragment crystallizable region
W-AMD, Wet Age-Related Macular Degeneration

frontiers in Materials

ORIGINAL RESEARCH
published: 11 December 2020
doi: 10.3389/fmats.2020.598057

Icaritin Enhancing Bone Formation Initiated by Sub-Microstructured Calcium Phosphate Ceramic for Critical Size Defect Repair

Haitao Peng[1†], Jianxiao Li[2†], Yanan Xu[3] and Guoyu Lv[1]*

[1]*College of Physics, Sichuan University, Chengdu, China,* [2]*Department of Orthopedics, The First Affiliated Hospital of Chongqing Medical University, Chongqing, China,* [3]*Department of Trauma Surgery, Emergency Medical Center of Chongqing, Chongqing, China*

Adequate bone tissue regeneration has been challenging to achieve at critical-sized bone defects caused by disease. Bone tissue engineering using a combination of scaffolds and bioactive factors provides new hope for the treatment of this extreme condition. Icaritin, a herb-derived chemical, has shown its ability to enhance bone formation both *in vitro* and *in vivo*, and it has been found that sub-micron surface structure instructs bone formation in calcium phosphate ceramics (CaPs). Here, we evaluated the possibility of using a submicron surface structured CaP ceramic as the carrier of icaritin for bone tissue regeneration in critical-sized bone defects. Icaritin, an herb-derived chemical, was loaded into a submicron surface structured porous calcium phosphate ceramic (Ø12.8 × 3 mm) to get samples with 0, 10, 50, 250, and 1,250 μg icaritin per CaP disc (M0, M10, M50, M250, M1250 groups, respectively). *In vitro* evaluation with the certain dosages correlated to those released from the samples showed a dose-dependent enhancement of osteogenic differentiation and mineralization of human bone marrow stromal cells with the presence of osteogenic factors in the culture medium, indicating icaritin is an osteopromotive factor. After intramuscular implantation of the samples in dogs for 8 weeks, a dose-dependent of bone formation was seen with enhanced bone formation at the dosage of 50 and 250 μg. To evaluate the *in vivo* osteogenic potentials of icaritin-containing CaP ceramic scaffolds in the orthopedic site, a 12.8 mm calvarial defect model in rabbits was established. Micro-computed tomography (micro-CT) and histology results at weeks 4, 8 and 12 post-surgery showed more newly formed bone in M250 group, with correspondingly more new vessel ingrowth. The results presented herein suggested that being osteopromotive, icaritin could enhance bone formation initiated by sub-microstructured CaP ceramics and the CaP ceramics scaffold incorporating icaritin is a promising biomaterial for the treatment of critical-sized defect.

Keywords: icaritin, submicron surface structure, calcium phosphate ceramic, critical-sized bone defect, bone regeneration

Edited by:
Gang Wu,
VU University Amsterdam,
Netherlands

Reviewed by:
Janos Kanczler,
University of Southampton,
United Kingdom
Dongxia Ye,
University of Rochester, United States

***Correspondence:**
Guoyu Lv
lgy929@126.com

[†]*These authors have contributed equally to this work*

Specialty section:
This article was submitted to Biomaterials, a section of the journal Frontiers in Materials

Received: *23 August 2020*
Accepted: *30 October 2020*
Published: *11 December 2020*

Citation:
Peng H, Li J, Xu Y and Lv G (2020) Icaritin Enhancing Bone Formation Initiated by Sub-Microstructured Calcium Phosphate Ceramic for Critical Size Defect Repair. Front. Mater. 7:598057. doi: 10.3389/fmats.2020.598057

INTRODUCTION

The orthopedic critical-sized defect due to traumatic injuries or tumor resection is still a significant challenge. Pursuing alternatives to autologous bone grafts has always been a goal of biomaterial engineering. Allowing bone formation on their surface and form chemical bonding to the new bone, calcium phosphate (CaP) ceramics have been widely used as bone graft substitutes (Hench and Wilson, 1984; Damien and Parsons, 1991; Bohner et al., 2012). However, compared with autogenous bone, the capacity of CaP ceramics for repairing critical-sized defects still seems to be insufficient.

Surface modification may improve the bone regeneration ability of CaP ceramics. When the surface structure of CaP ceramics decreased from micron to submicron scale, it induced bone formation in the muscle of dogs (Davison et al., 2014b; Zhang et al., 2014)and under the skin of FVB mouse (Davison et al., 2014a). Having the osteoinductive property, calcium phosphate ceramics not only enhanced bone regeneration in non-critically sized bone defects (Habibovic et al., 2004; Yuan et al., 2006) but also could repair critical-sized defects (Yuan et al., 2010) and enhance bone formation in the spinal environment (van Dijk et al., 2018).

Besides, osteogenic factors can also exert considerable bone repair effects when combined with scaffolds (McMillan et al., 2018). Icaritin, an exogenous semi-synthesized small phytomolecule, is an intestinal metabolite of herbal epimedium-derived flavonoids (Zhang et al., 2007; Qin et al., 2008), and has shown to affect various biological processes. For instance, it inhibited both thrombosis and lipid-deposition reducing thus the incidence of steroid-associated osteonecrosis (Zhang et al., 2009), and it exhibited *in vitro* anti-inflammatory effects on the mouse peritoneal macrophages (Lai et al., 2013). Most recently, the roles of icaritin in bone metabolism were also found. It enhanced the differentiation and proliferation of osteoblasts, facilitated matrix calcification (Qin et al., 2008; Yao et al., 2012), and enhanced bone regeneration in an ovariectomized rat osseous model (Zhang et al., 2008; Peng et al., 2013).

Although icaritin exhibits bone-enhancing effects in PLGA/TCP scaffolds (Chen et al., 2012; Chen et al., 2013), there is no report on the combination of icaritin and inorganic ceramics to repair the critical-sized defect. More notably, when icaritin was loaded on a special submicron structured CaP scaffold, it is unknown whether the bone regeneration ability of CaP ceramics is enhanced.

We hypothesized that the combination of chemicals enhancing bone formation and osteoinductive calcium phosphate ceramics would result in bone substitutes with improved bone regeneration capacity for critical-sized defect repair. Considering the possible bone-enhancing function of icaritin as previously shown, we introduced icaritin into sub-micron surface structured tricalcium phosphate ceramic and characterized the resulting materials concerning for their physicochemical properties and icaritin release. Following the *in vitro* evaluation of icaritin released with hBMSCs, we investigated the bone-forming ability of the materials after intramuscular implantation in a canine model. According to previous research, rabbit calvarial defect is a mature model for evaluating the bone repairability of biological scaffolds, but the critical defect size rarely exceeds 10 mm (Xu et al., 2008; Lee et al., 2018). In this study, we designed a 12.8 mm critical bone defect to investigate the bone repair effect of the materials by micro-computed tomography (micro-CT) and histology. With results showing, the sub-microstructured CaP ceramics scaffold incorporating icaritin could be a promising biomaterial for the treatment of critical-sized defect.

MATERIALS AND METHODS

Preparation and Physico-chemical Properties of CaP Ceramics With Sub-micron Scale Surface Structure

CaP powder was synthesized by neutralization reaction method at Ca/P ratio of 1.5. H_3PO_4 solution was dropped into a $Ca(OH)_2$ suspension to get CaP powder. The porous CaP green bodies were obtained using H_2O_2 (1%) and wax particles and then sintered at 1,050°C for 8 h to form ceramics (Yuan et al., 2010; Zhang et al., 2014; Zhang et al., 2015). Microporous discs (Ø12.8 × 3 mm) were machined from the ceramic bodies using a lathe and a diamond saw microtome (Leica SP1600). Discs were ultrasonically cleaned in successive baths of acetone, ethanol, and deionized water, and then dried at 60°C.

X-ray diffraction (XRD; Rigaku, Tokyo, Japan) was used to analyze the crystal structure of CaP powder. The grain, micropore size and surface topography was detected by scanning electron microscope (XL30, ESEMFEG, Philips, Eindhoven, The The Netherlands). Especially, the grain and micropore was selected randomly from the image and the vertical lengths crossing the center of each grain and micropore were considered to be the grain and pore size. Mercury intrusion was used to obtain the ceramics' total porosity, microporosity and micropore size distribution.

In vitro Release of Icaritin by CaP Scaffold in Calcium Medium

CaP discs were sterilized with autoclave at 121°C for 30 min. Icaritin solutions of 0, 40, 200, 1 and 5 mg/ml were prepared with methyl alcohol and sterilized with 0.2 μm filter (Acrodisc® 13 CR PTFE 0.2 μm, Gelman Pall). Under sterile condition, 250 μL of each icaritin solution was loaded onto CaP disc. Thereafter, methyl alcohol was evaporated in sterile conditions at 50°C with ventilation for seven days to obtain samples containing 0 μg icaritin per disc (M0), 10 μg icaritin per disc (M10), 50 μg icaritin per disc (M50), 250 μg icaritin per disc (M250) and 1,250 μg icaritin per disc (M1250) respectively. Then, samples ($n = 3$) were individually incubated in 3 ml of culture medium containing *a*-MEM (Lonza), 10% FBS (Gibco) and 1% antibiotics (100 U/ml penicillin and 100 μg/ml streptomycin, Invitrogen) at 37°C and 5% CO_2. Culture medium was refreshed at day 1, 2, 4, 7, 14, 21, 28, 35, 42, 49 and day 56 respectively. The medium collected at each refreshment point were stored at −20°C before further use.

Icaritin concentration in medium was detected with an HPLC-MS/MS system (TSQ Quantum Ultra, ThermoFisher Scientific, Co. Ltd., USA) equipped with a surveyor Autosampler, a mass pump and a triple quadrupole mass spectrometer. Six standard icaritin solutions in culture medium (i.e., 2, 5, 50, 100, 250, and 500 ng/ml) were prepared for a calibration line. The icaritin concentration in the samples was calculated according to the calibration line, while the remaining icaritin was calculated by subtracting the cumulative icaritin release from the original loading.

To determine the solubility of icaritin in water and culture medium, icaritin was directly added to water and culture medium at 37°C overnight and centrifuged at 5,000 rpm for 5 min. The supernatants (n = 3) were subjected to HPLC-MS/MS assay.

In vitro Evaluation With Human Bone Marrow Stromal cells (hBMSC)

Medium Preparation

Basic medium (BM), Growth medium (GM) and Osteogenic medium (OM) were used in the *in vitro* cell culture. Basic medium was *a*-MEM (Invitrogen, United Kingdom) supplemented with 10% FBS (Lonza, Germany), 2 mM L-Glutamine (Invitrogen, United Kingdom), 0.2 mM L-Ascorbic acid 2-phosphate (AsAP, Sigma), 100 IU/ml penicillin (Invitrogen, United Kingdom) and 100 g/ml streptomycin (Invitrogen, United Kingdom), growth medium was basic medium supplemented with 1 ng/ml basic fibroblasts growth factors (bFGF, Instruchemie, the The Netherlands), and osteogenic medium was basic medium supplemented with 10 nM dexamethasone (Sigma) and 10 mM-glycerophosphate (Sigma) (Luo et al., 2014).

Icaritin was added to BM and OM according to the saturated concentration of icaritin in culture medium with/without the presence of CaP ceramic discs (e.g., 2,000 and 4,300 ng/ml, as obtained from icaritin release test), thus both BM and OM containing 0, 20, 200, 2,000 and 4,300 ng/ml icaritin were prepared by first dissolving 5 mg icaritin in 10 ml methyl alcohol as the stock solution, followed by diluting this stock solution with either BM or OM. Specifically, additional methyl alcohol was added to each medium to keep the methyl alcohol concentration in all medium consistent.

Human Bone Marrow Stromal Cells (hBMSC) Cultivation

hBMSc (Passage 3, D307, Lonza) were expanded in cell culture flasks with GM under a humidified atmosphere of 5% CO_2 at 37°C until 80% confluence. Then GM was removed, and cells were harvested with 0.25% trypsin (Invitrogen, United Kingdom). 5,000 cells/well were seeded in 48-well cell culture plates (n = 5 per condition at each time point) and cultured with various medium prepared as described above. The medium was refreshed twice a week accordingly, and cells were harvested after 1, 4, 7, 14, and 21 days for further assays.

Cell Morphology

By day 14, cells were rinsed once with 37°C phosphate-buffered saline (PBS) and fixed with 4% formaldehyde solution at room temperature for 10 min. Afterwards, the fixation solution was removed and cells were rinsed again with PBS and stained with 1% methylene blue solution for 1 min. Cell morphology was visualized using a Nikon SMZ800 stereomicroscope equipped with a Nikon camera.

Calcium Deposition

By day 14, 21, cells were rinsed once with 37°C phosphate-buffered saline (PBS) and fixed with 4% formaldehyde solution at room temperature for 10 min. Afterwards, the fixation solution was removed, and cells were rinsed once with PBS, twice with distilled water and stained with 2% alizarin red staining for 1 min. Excessive staining was rinsed twice with distilled water. Staining was visualized using a Nikon SMZ800 stereomicroscope equipped with a Nikon camera.

Cell Proliferation and Osteogenic Differentiation Assay

By day 1,4,7,14,21, cells were frozen at −80°C for 24 h after rinsed once with 37°C phosphate-buffered saline (PBS). The proliferation of hBMSCs was analyzed with a CyQuant cell proliferation assay kit (Invitrogen). Briefly, to obtain the cell lysate, 150 μL CyQuant lysis buffer was added to each well after cell culture plates were thawed at room temperature, followed by shooking at 400 rpm for 5 min. Then GR reagent was diluted 400 times by CyQuant lysis buffer. After 100 μL diluted reagent was incubated with 100 μL cell lysate for 5 min in the dark at room temperature, the fluorescence was detected using a spectrophotometer (Anthos Zenyth 3100) at wavelength of 480 nm for excitation and 520 nm for emission.

By using AttoPhos® AP fluorescent substrate system (catalog S1000, Promega), the amount of 2-[2-benzothiazoyl]-6-hydroxybenzothiazole (BBT) produced during the reaction was used to present the Alkaline phosphatase (ALP) activity. Briefly, 90 μL substrate reagent was incubated with 10 μL cell lysate for 15 min in dark at room temperature. The fluorescence signal was then collected using a spectrophotometer (Anthos Zenyth 3100).

Ectopic Implantation

To study the influence of icaritin on bone formation, the icaritin-CaP discs (M0, M10, M50, M250, M1250) were evaluated in canine and rabbit ectopic models. All the animal experiments were followed the "Guidance Suggestions for the Care and Use of Laboratory Animals" by the National Science and Technology Committee of the People's Republic of China in order No. 2, 2006. Icaritin-CaP discs were implanted in the para-spinal muscles of five adult male beagles (body weight 14–17 kg) for 8 weeks. The surgeries were performed under general anesthesia by abdominal injection of sodium pentobarbital (30 mg/kg body weight) under sterile conditions. Following the surgeries, penicillin (40 mg/kg body weight) was injected intramuscularly for three consecutive days to prevent infection. After operation, all animals were allowed to bear full weight and received a normal diet.

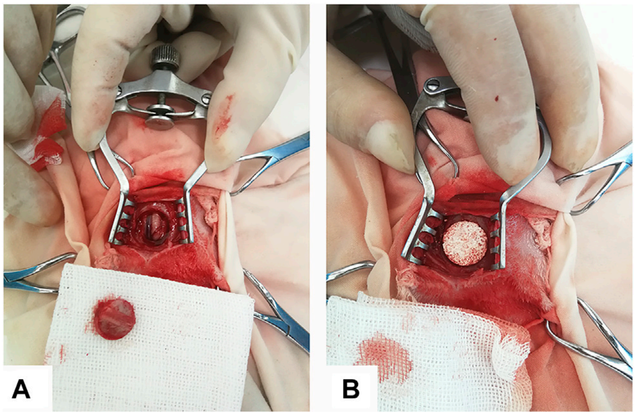

FIGURE 1 | Rabbit calvarial defect and implantation with porous scaffold. **(A)** 12.8 mm calvarial defect was created in rabbit calvarial midshaft. **(B)** CaP-based scaffold with size 12.8 mm was implanted into the defect region.

The animals were sacrificed via celiac injection of an excessive amount of pentobarbital sodium at week 8. Implants were harvested with the surrounding tissues and fixed in 4% formaldehyde at 4°C for 1 week.

Calvarial Defect Repair Surgery

Thirty-six adult male New Zealand white rabbits (body weight 2.8–3.0 kg) were used for this study. According to the results of **Section 2.4**, thirty-six rabbits were divided into two groups with M0 as the control group and M250 as the experimental group. All the animal experiments were followed the "Guidance Suggestions for the Care and Use of Laboratory Animals" by the National Science and Technology Committee of the People's Republic of China in order No. 2, 2006. The surgeries were performed under general anesthesia by abdominal injection of sodium pentobarbital (30 mg/kg body weight) under sterile conditions. After proper preparation, a midline sagittal incision in the scalp was made to expose the parietal bone and a critical-size (12.8 mm in diameter) defect was created in the middle of parietal bone using a sterile drill (**Figure 1A**). After the bone was removed, the defects were grafted with porous icaritin-CaP ceramics (**Figure 1B**) and the incision was closed in layers using 4–0 Vicryl sutures. Following the surgeries, penicillin (40 mg/kg body weight) was injected intramuscularly for three consecutive days to prevent infection. After operation, all animals were allowed to bear full weight and received a normal diet.

At week 4, week 8, and week 12, each group of experimental animals was divided into an ink injection group and a non-ink injection group, with 3 animals in each group. To observe the growth of blood vessels, the animals in the ink injection group were injected with ink diluted with physiological saline (ratio 1:4) at a dose of 40 ml/kg after semi-anaesthesia with barbiturate sodium. The non-ink injection group was killed with an excess of pentobarbital sodium. All the defects with an additional 2 mm surrounding tissue were dissected from the host bone.

The samples of the ink injection group were fixed in 4% formaldehyde for histological quantification. After each sample in the non-ink injection group was divided into two halves, half was stored in liquid nitrogen for genetic testing, the other half was fixed in 4% formalin for histological observations.

Quantitative Reverse Transcription-PCR (qRT-PCR)

VEGF and FGF are crucial factors in angiogenesis. To determine the VEGF- and FGF-promoting effects of icaritin, qRT-PCR analyses were performed. All the samples were lysed in Trizol reagent (Ambion, USA), total RNA was extracted following the manufacturer's protocol (Chengdu Lilai Technology Co. Ltd., China) and reverse transcription was performed using RevertAid First Strand cDNA Synthesis Kit (Thermo Fisher Scientific, USA). Gene expressions were quantified using SYBR Green I PCR Kit (FastStart universal SYBR Green Master (Rox); Roche, Switzerland) in Real-Time PCR System (Thermo Fisher Scientific, USA). *ß*-Actin was used as the housekeeping gene. Primers of the target genes including VEGF and FGF were listed in **Table 1**. Finally, the Real-time PCR reactin was run at 95 for 10 min, followed by 95 for 30 s, 55 for 30 s and 72 for 30 s for 45 cycles. The data were analysed using Thermo Scientific PikoReal software. The relative amounts of target genes normalized by *ß*-Actin were calculated by the $2^{-\Delta CT}$ method, where $\Delta C_T = C_{T,\ target}\text{-}C_{T,\ \beta\text{-Actin}}$.

Micro-CT

Micro-CT (medium-resolution mode, isotropic voxel size: 15 μm; mCT 80, Scanco Medical AG, Bassersdorf, Switzerland) was used to evaluate new bone formation within the implants. The horizontal plane of all samples must be oriented perpendicular to the axis of the X-ray beam. The 2D radiographic images were used to reconstruct and calculate corresponding bone volume fraction (bone volume/total volume, BV/TV) with Scanco software by thresholding ($n = 3$) (Chai et al., 2012; Ji et al., 2020).

Histological Observations

After fixation, all the harvested samples were dehydrated through a series of increasing ethanol concentrations and were subsequently embedded in methylmethacrylate. Three non-decalcified sections (10–20 μm) from mid-defect regions of each sample were made by using a diamond saw microtome (Leica SP-1600, Germany) and stained with 1% methylene blue (Sigma) and 0.3% basic fuchsin (Sigma) solutions for qualitative and quantitative histological observations.

TABLE 1 | Primer sequences for RT-PCR.

Gene	Primer sequences (5′–3′)	
	Sense	Antisense
β-Actin	GCTTCTAGGCGGACTGTTAG	CGAATAAAGCCATGCCAATCTC
VEGF	TGGCAGAAGAAGGAGACAATAAA	GAAGATGTCCACCAAGGTCTC
FGF	GCGACCCACACATCAAATTAC	GCAGTCTTCCATCTTCCTTCA

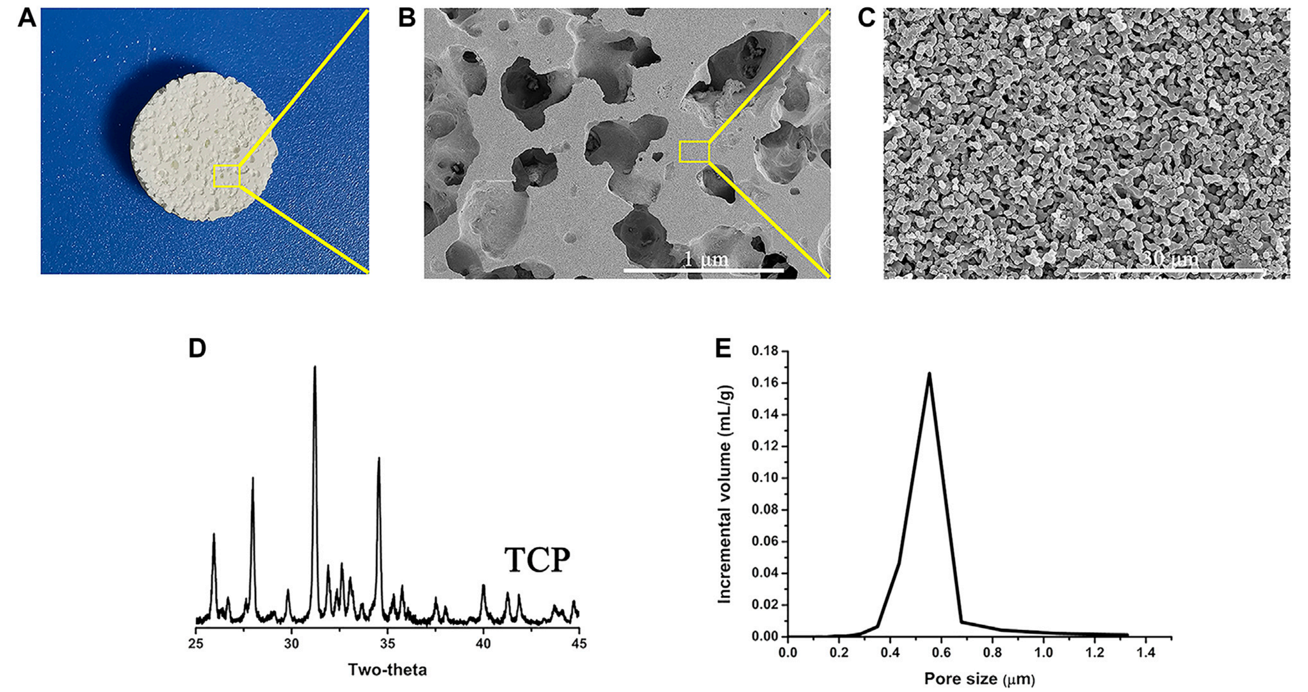

FIGURE 2 | Physical and chemical characteristics **(A)** CaP ceramic disc, **(B)** porous structure of CaP ceramic, **(C)** surface structure of CaP ceramic, **(D)** XRD pattern of the samples showing that the ceramic is *ß*-TCP, and **(E)** micropore size distribution confirmed by Mercury intrusion.

To perform histomorphometry, the histological slides were scanned (Dimage Scan Elite 5400II, Konica Minolta photo Imaging Inc., Tokyo, Japan). After that, using Adobe Photoshop CS5 software, the region of interest (ROI), the ceramic materials (M) and bone (B) were quantified as the pixel values. Bone formation in the available space was quantitatively determined as follows: B% = B*100/(ROI-M). Qualitative histology analysis of tissue formation (i.e. cell type, bone formation and presence of blood vessels) was performed by observing the slides at the light microscope (Nikon Eclipse E200, Tokyo, Japan).

STATISTICS

During the icaritin release experiment, multiple measures were performed on each sample, thus median of the measured data was used to reduce the effects of outliers. Mean was considered to represent bone formation as the sample number was limited. In the experiment of icaritin release, the data points were fitted with non-linear regression models to study the trend during time and were compared using one-way Wilcoxon signed rank-sum test. When means were considered, multiple comparisons were performed with one-way analysis of variance (ANOVA) followed by Bonferroni post-test comparisons. *p*-values lower than 0.05 were considered as statistically significant differences.

RESULTS AND DISCUSSION

The CaP Ceramic Scaffold and Release Characteristics

Figure 2B shows the porous structure of CaP ceramic, and the XRD pattern of CaP indicates that the ceramic is *ß*-TCP (**Figure 2D**). Observing the microstructure size by SEM, CaP ceramic has a grain size of 0.95 ± 0.20 µm and a micropore size of 0.65 ± 0.25 µm (**Figure 2C**). Mercury intrusion indicates that the ceramic micropores range from 0.2–1.3 µm with a peak of 0.55 µm (**Figure 2E**). It can be seen from the Mercury intrusion data that the total porosity is 62% and the microporosity is 23%.

Icaritin crystals could be observed on the surface of CaP ceramic and are rod-like with a diameter smaller than 10 µm (**Figures 3C,D**). To detect icaritin with the HPLC-MS/MS system, optimization of precursor and product ions of the icaritin for MRM analysis by a triple quadrupole mass spectrometer with electrospray ionization was performed. The m/z response observed was much better in the negative ionization mode than in the positive mode due to the phenolic hydroxyl group. The mass spectra showed deprotonated molecular ion [M-H]- peak at 385.0 m/z. On the basis of the production mass spectra, the major fragment ion was observed at 311.1 for icaritin (**Figure 3A**). A total ion chromatogram in full scan model was generated using standard icaritin solution, and icaritin could be separated and eluted at 5.50 min (**Figure 3B**). A good linearity was obtained for icaritin over the range from 2 to 500 ng/ml in culture medium (**Figure 3E**).

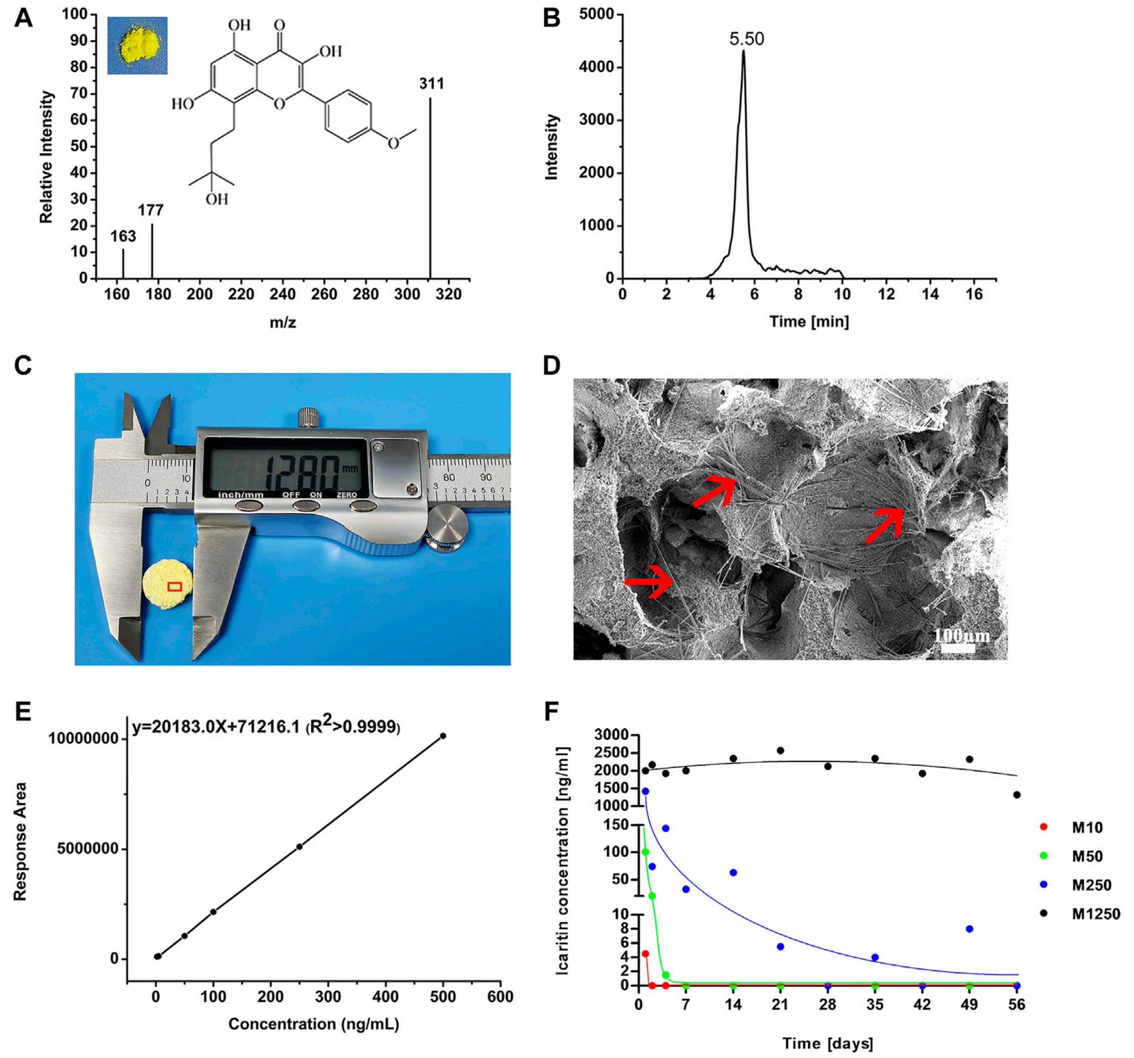

FIGURE 3 | Icaritin release and detection. **(A)** Chemical structure and full scan product ion of precursor ion of icaritin (the quantification ion at m/z 311 is generated via the loss of C_4H_9O from the precursor ion), **(B)** HPLC-MS/MS total ion chromatography of icaritin, **(C)** 12.8 mm CaP ceramic disc with icaritin, **(D)** needle-like icaritin on the surface of CaP ceramic (red arrow), **(E)** the icaritin calibration line between the concentrations from 2 to 500 ng/ml in culture medium, and **(F)** median values of the measured icaritin concentrations in the culture medium plotted against time (please note that the ordinate axis is split into three intervals for a better visualization of the results, which include all the data point measurements from all the materials).

According to the calibration line, the saturated icaritin concentrations at 37°C were 13.4 ± 2.4 μg/ml in water and 4.3 ± 0.1 μg/ml in culture medium respectively. The release of icaritin from the samples is summarized in **Table 2** and illustrated in **Figure 3F**. No icaritin was detected in any of the controls (group M0). Initial burst releases, directly correlated with the icaritin content in the discs, were observed on the first day for all those samples containing icaritin (**Figure 3F**): the lesser icaritin incorporated in the CaP ceramic, the minor the intensity of the burst. Afterwards, all materials but M1250 had exponential release decays. The samples with the smaller icaritin amount M10 ceased to release already on the second day of experiment. A similar but delayed trend was observed for those samples containing 50 μg of icaritin, which stopped releasing after one week. Discs with an initial load of 250 μg icaritin were able to have a significant longer release decay rate as compared to M10 and M50. Samples M1250, with the highest icaritin initial content, kept a steady release during the whole experiment. The four materials, until they released icaritin, had significantly different

TABLE 2 | The quantities of total (cumulative) released and remaining icaritin in the samples after 56 days soaking.

Sample	Total icaritin released after 56 days (μg)	Percentage of released icaritin
M0	0	0
M10	0.052 ± 0.065	0.52%
M50	0.37 ± 0.06	0.74%
M250	5.54 ± 0.58	2.21%
M1250	69.80 ± 11.91	5.58%

release trends ($p < 0.05$ for all data sets when compared in the periods of active release). The release measurements were corroborated by the observation that the majority of icaritin stayed in the discs after a 56-days soaking in culture medium (**Table 2**).

By its chemical nature, icaritin is theoretically not soluble in aqueous solution, and a low solubility of icaritin was seen in the study. In water, a saturated concentration of 13.4 ± 2.4 μg/ml was reached at 37°C. The saturated concentration decreased to 4.3 ± 0.1 μg/ml in the simulated body fluids (eg Dulbecco's Modified Eagle Medium plus foetal bovine serum), agreeing with the influence of proteins and ions on the solubility of chemicals (Galia et al., 1998). With a low solubility, a sustained release of icaritin was expected when it was loaded onto carriers. The sustained release was achieved in practice at the highest dose used in the study (e.g., M1250). The release profile of icaritin (**Figure 3F** and **Table 2**) indicated that icaritin was not only physically loaded into the CaP ceramic but also reacted chemically to CaP. If only physical loading was there, the constant release of icaritin from M1250 should be around 4.3 μg/ml in simulated body fluids, while it was 2.0 μg/ml in practice. Moreover, if only physical loading was there, a constant release could have happened in the case of 250 μg icaritin/disc as well, since the total theoretical release of icaritin in the tested time frame was 141.9 μg (11-time points with the theoretical constant release of 4.3 μg/ml in 3 ml), less than 250 μg icaritin loaded. As shown in **Table 2**, the majority of icaritin was retained in CaP ceramics after a 56-days soaking in simulated body fluids, further supporting the chemical reaction of icaritin to the CaP ceramic. The exact reaction of icaritin to CaP ceramic needs to be further addressed with studies, while it is likely that icaritin could react to calcium phosphate through coordination bond with Ca^{2+} ions, meaning that there might exist some dynamic equilibria involving icaritin and Ca^{2+} ions (Huskens and Sherry, 1998). As such, the saturated concentration of icaritin further decreased to 2.0 μg/ml in simulated body fluids when loaded into the CaP ceramic (**Figure 3F**, M1250).

Influence of Icaritin on hBMSCs

Bearing the possible reaction between icaritin and CaP ceramic after loading, icaritin released from CaP ceramic discs into simulated body fluids dose-dependently (**Figure 3F**). Using the saturated concentration in culture medium and dilutions of the highest icaritin release from CaP ceramic into culture medium (e. g., 2 μg/ml), the influence of icaritin on the activities of human bone marrow stromal cells was evaluated. A morphological change from spindle to polygon shape was observed by day 14 with the increasing concentration of icaritin (**Figure 4B**), regardless of the culture media used (BM vs OM). Specifically, with the increasing of icaritin up to 2,000 ng/ml, hBMSCs became more spread and larger, indicating their tailored cell fate in the presence of icaritin. In both BM and OM 2,000 ng/ml icaritin inhibited the proliferation of hBMSCs while 4,300 ng/ml icaritin showed severe cytotoxicity that it induced apoptosis, where not much cells but crystals of un-dissolved icaritin were observed under the light microscope instead of living cells (**Figure 4B**, 4,300 ng/ml).

Calcium deposition was only observed in OM group but not in BM (**Figure 4A**). By day 14 and 21 the calcium deposition was seen in 20 ng/ml and 200 ng/ml, and occasionally seen in 2,000 ng/ml and 4,300 ng/ml.

hBMSCs proliferated and peaked by day 14 in both BM and OM, except in those supplemented with 2000 ng/ml icaritin or more (**Figure 4D**). With the presence of osteogenic factor (e.g., DEX), cells, in the means of DNA content, were not much different in number among the groups of 0, 20, and 200 ng/ml, while without osteogenic factor, cells were much more in number in groups of 20 and 200 ng/ml as compared to 0 ng/ml control (**Figure 4D**).

Given the fact that a high dose of icaritin was harmful to the cells, ALP assay was not applied to the samples of 4,300 ng icaritin/ml. The ALP expression of hBMSCs is relatively low in BM as compared to OM group regardless of the concentration of icaritin (**Figure 4C**). Moreover, ALP/DNA in cells cultured with BM did not increase with time from Day 7 to Day 21, while ALP/DNA increased from Day 7 to Day 21 (**Figure 4C**) in cells cultured with OM. Furthermore, at day 21, ALP/DNA was up to the concentration of icaritin, with higher ALP/DNA at higher concentration of icaritin (at the dose range of 0–200 ng/ml) (**Figure 4C**).

So, at the saturated concentration in culture medium (4.3 μg/ml), icaritin was harmful to hBMSCs and caused cell death (**Figures 4B,D**). At the highest release from CaP ceramic (2 μg/ml from M1250), icaritin inhibited cell proliferation (**Figures 3B**, **4D**). At the concentration between 0.02–0.20 μg/ml, icaritin enhanced proliferation of hBMSCs in the absence of osteogenic factor (eg Dex), while it did not affect hBMSC proliferation when dex was used in the culture media (**Figures 4B,D**). At the concentration of 0.02–0.20 μg/ml, icaritin did not enhance osteogenic differentiation of hBMSCs when Dex was not used in the culture medium, as indicated in both mineralization assay (**Figure 4A**) and ALP/DNA assay (**Figure 4C**), with the presence of Dex in the culture media, icaritin did enhance osteogenic differentiation of hBMSCs (**Figures 4A,C**). The data agreed with the previous findings that at certain dosages icaritin did not affect bone marrow stromal cell proliferation, but enhanced ALP production and mineralization while at high doses, meaning that icaritin enhances osteogenic function of readily differentiated osteogenic cells but does not induce osteogenic differentiation of osteoprogenitors or stems cells *in vitro*.

Influence of Icaritin in Ectopic Bone Formation

When icaritin-loaded CaP ceramic discs were implanted intramuscularly in canine for 8 weeks, the dose-dependent influence of icaritin on bone formation was seen (**Figures 5**, **6**). The samples (n = 5) harvested from all animals were available for histological evaluation and histomorphometry. The least bone formation was observed in group M1250 and most bone formation occurred in groups M50 and M250 (**Figures 5**, **6**).

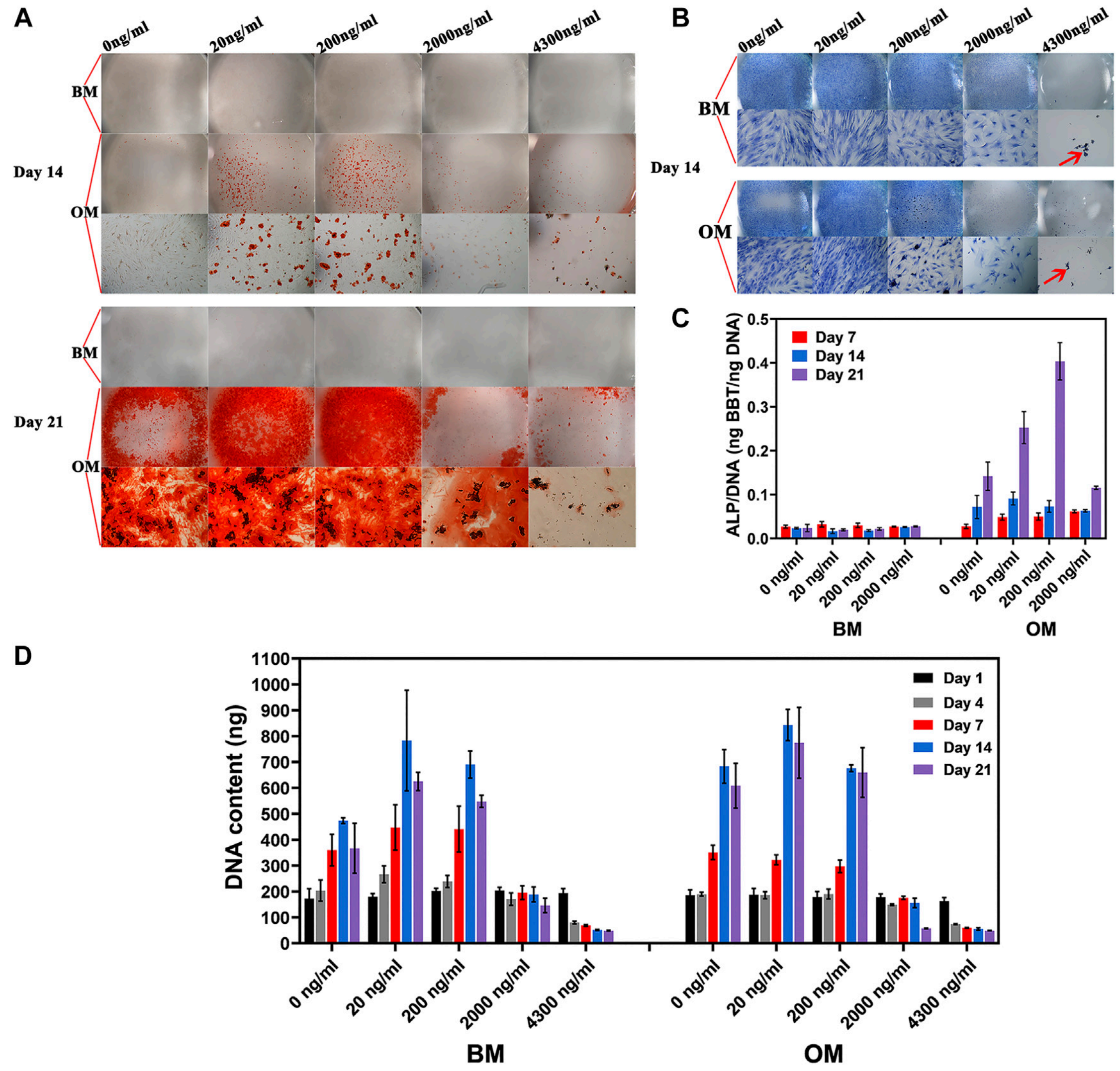

FIGURE 4 | hBMSC proliferation and osteogenic differentiation in different culture medium. **(A)** Mineralization and **(B)** cell morphology of hBMSC in basic medium and osteogenic medium as the function of icaritin dose (red arrow stands for un-dissolved icaritin crystals), **(D)** hBMSC proliferation, and **(C)** osteogenic differentiation in BM and OM as a function of icaritin dose.

The addition of 10 μg did not improve bone formation as compared to the control group. Loading 50 or 250 μg icaritin significantly increased the bone formation in the CaP ceramic. When icaritin was added in a high dose (i.e., 1,250 μg), it had an inhibitory effect on the ectopic bone formation of the ceramic.

Both the icaritin liberated from CaP ceramic and the icaritin that stayed in the CaP ceramic may have played biological roles *in vivo*. At the concentrations of 10^{-7}–10^{-5} mol/L (i.e., 0.0385–3.85 μg/ml), icaritin enhanced the differentiation and proliferation of osteoblasts *in vitro* (Huang et al., 2007). If only the icaritin liberated from CaP ceramic affected bone formation, then bone formation may not have been enhanced in the 50 μg icaritin group since the release of icaritin stopped 7 days after immersing in simulated body fluid, while it was known that inductive bone formation in canine muscle normally starts 4 weeks after implantation (Yuan et al., 2006). Similarly, if only the icaritin released from CaP ceramic had an essential contribution, then bone formation should have been enhanced in the 1,250 μg group in dogs because the 2 μg/ml concentration was still within the reported interval of efficient icaritin concentration to enhance bone formation. Instead, it was found in this study that the bone formation was inhibited in the 1,250 μg group. The inhibited bone formation in the 1,250 μg group could be attributed to the cytotoxicity of icaritin at high dosages (Chen et al., 2012; Chen et al., 2013).

Based on the *in vitro* results, it is clear that icaritin does not have osteoinductive potential as the bone morphogenetic proteins have (Chen et al., 2012), icaritin could thus only affect bone formation in an environment where bone formation was readily present. In other words, icaritin enhanced a bone formation process that was already triggered by the submicron scaled

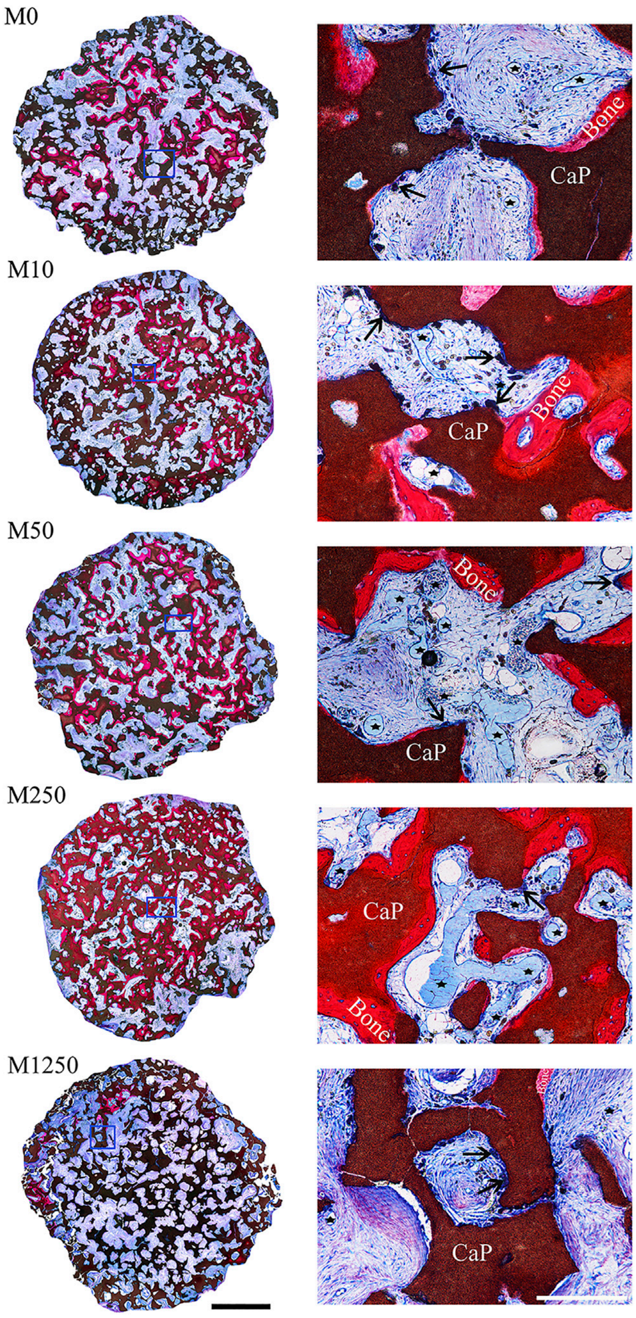

FIGURE 5 | Tissue response to icaritin-containing CaP discs implanted in muscle of dogs for 8 weeks. Left, histological overviews of M0, M10, M50, M250 and M1250 (scale = 2 mm); Right, detailed light microscopic images of the selected region in the histological overviews (scale = 250 μm) (undecalcified sections; methylene blue and basic fuchsin staining; Bone: bone tissue; CaP: CaP ceramic; star: blood vessel; arrow head: multinucleate giant cells).

surfaces of the CaP ceramic implanted in this study in dogs. Via protein adsorption (Yuan et al., 2010; Zhang et al., 2014), surface mineralization (Zhang et al., 2015; Murr, 2019), ion-release (Yuan et al., 2010; Zhang et al., 2014; Zhang et al., 2015) and surface topographic cues (Zhang et al., 2015), submicron surface structured calcium phosphate ceramic generates an osteogenic environment to which mesenchymal stem cells respond and undergo osteogenic differentiation to form bone. Together with the osteogenic environment generated by the submicron surface structured calcium phosphate ceramic, icaritin enhanced the function of mesenchymal stem cells and bone formation was eventually enhanced.

Calvarial Defect Repair Evaluation

Studies have shown that angiogenesis plays a vital role in bone tissue repair process, and enhanced neovascularization accelerates bone formation (Karageorgiou and Kaplan, 2005; Oates et al., 2007; Barralet et al., 2009). As observed in **Figure 5**, an increase in blood vessels amount was seen from M0 to M250, the pores of all implants were occupied by soft tissues including blood vessels, indicating enhanced bone formation was associated with higher density of blood vessels. It has been shown that stem cells could reach to the osteoinductive calcium phosphate ceramic via blood circulation (Song et al., 2013). It is likely that icaritin first enhanced angiogenesis from which stem cells responsible for inductive bone formation could be recruited. When the stem cells were differentiated by CaP ceramic, icaritin enhanced the function of such differentiated cells to form bone.

It is thus worthy of performing studies to test the functionality of icaritin-containing osteoinductive CaP ceramic in bone regeneration in orthopedic sites. The *in vivo* bone regeneration effect of samples was evaluated by micro-CT and histological analysis. The 3D images of Micro-CT reconstruction in **Figure 7A** demonstrate newly formed bone within implants at week 4, 8, and 12, and the quantitative data of new bone volume (BV/TV) within the implants was measured by the 2D radiographs. Compared with M0 group, there was a significant

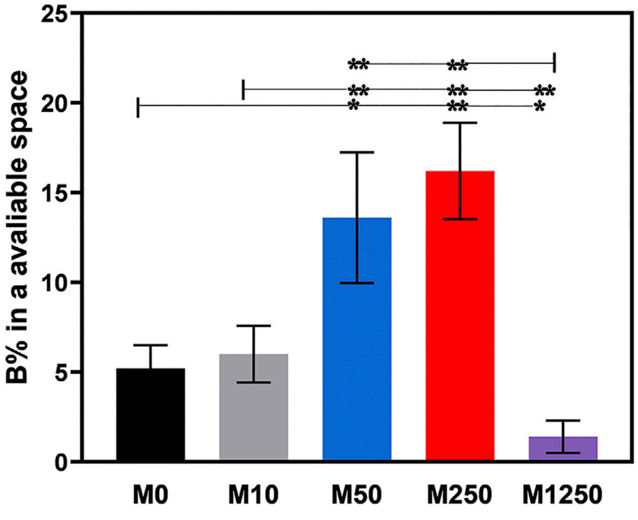

FIGURE 6 | Bone formation in the available space (%) of samples harvested from dogs (statistically significant differences are marked by $^{*}p < 0.05$, $^{**}p < 0.01$).

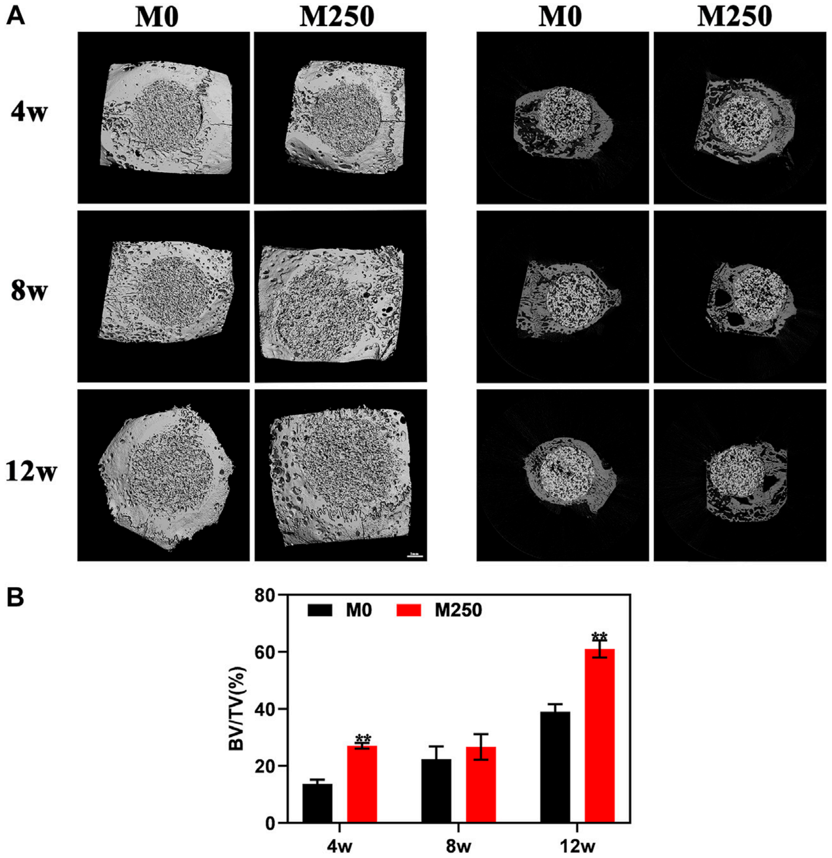

FIGURE 7 | Micro-CT analysis of M0, M1250 after calvarial implantation for 4, 8, and 12 weeks. **(A)** The corresponding three-dimensional reconstruction images of micro-CT results and representative axial sections. **(B)** Calculated bone volume/tissue volume (BV/TV) (Statistically significant differences are marked by **p*< 0.05, ***p* < 0.01).

increase in BV/TV in M250 group at week 4 (**Figure 7B**) ($p < 0.01$, n = 3). After 8 weeks post implantation, although the growth rate of the M250 group is lower than that of M0 group, the BV/TV of the M250 group is still higher than that of M0 group (**Figure 7B**). At week 12, the BV/TV in M250 group was significantly higher than that of M0 group (**Figure 7B**) ($p <$ 0.01, n = 3). And the BV/TV of all groups at week 12 was higher than that of week 8.

Figures 8 and **10** display the histological manifestations in methylene blue and basic fuchsin stains after implantation for 4, 8 and 12 weeks, respectively. Observed from the axial and sagittal direction, the newly formed bone tissue became evident at week 4 with limited bony bridging along the radial border of the bone defect (**Figure 8A**, **Figure 8a$_2$**, **Figure 8B**, **Figure 8b$_2$**, **Figure 10A**, **Figure 10a$_1$**, **Figure 10a$_2$**, **Figure 10B**, **Figure 10b$_1$**, **Figure 10b$_2$**). Compared with week 4, at week 8, more new bone tissue in both groups grew into the scaffold, along the radial direction (**Figure 8C**, **Figure 8D**, **Figure 10C**, **Figure 10D**). Obviously, at week 12, the new bone tissue of the M250 group have almost penetrated the entire material (**Figure 8F**, **Figure 10F**). Serial graphs reveal how new bone first originates at the resident bone edges from where it proceeds first along the external margins of the scaffold implant and then towards the center of the scaffold. Quantitative analysis (**Figure 9**) shows that at week 4, week 8 and week 12, the M250 group had more new bone in the defect compared to the M0 group. At week 4 and week 8, both groups had isolated new bone islands along the radial margins and within the pores of the scaffolds (**Figure 8a$_1$**, **Figure 8b$_1$**, **Figure 8c$_1$**, **Figure 8d$_1$**). The newly formed bone within the scaffold was seen to have remodelled towards mature lamellar bone with osteocytes within lacunae embedded in the bone matrix.

Newly formed vessels within the scaffold pores became visible in first 4 weeks in both groups (**Figures 11A,B**), and decreased from the next 4 weeks (**Figures 11C,D,G–I**). Quantitatively, compared with the M0 scaffold groups, the M250 scaffold group showed many more new vessels in terms of vessel volume, VEGF and FGF expression within bone defects at week 4, week 8 and week 12 ($n = 3$, **Figures 11G–I**).

Animal experiments results showed that icaritin significantly improve the ingrowth of blood vessel with a large amount of bone tissue penetrated the entire scaffold at

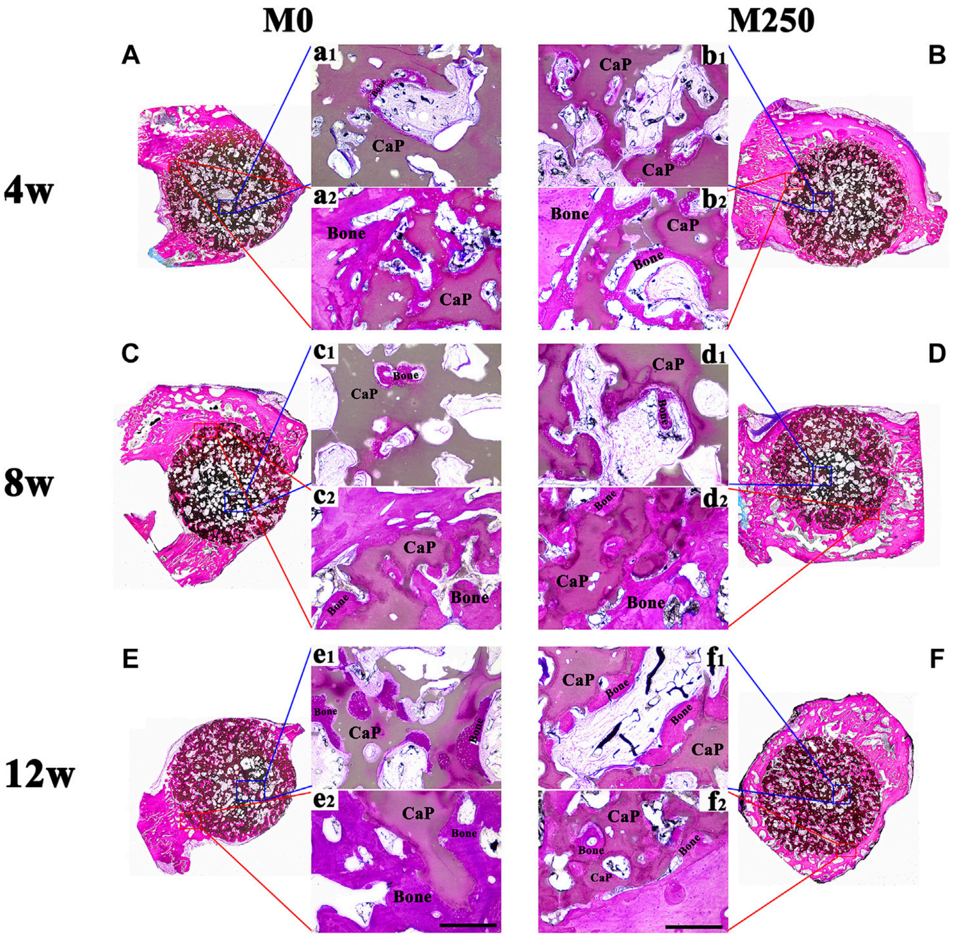

FIGURE 8 | The axial direction histological observation of M0 and M250 after calvarial implantation for 4, 8 and 12 weeks **(A), (C), (E)** The histological overviews of M0 **(B), (D), (F)** The histological overviews of M250 (a_1) (c_1) (e_1) New bone islands within the M0 scaffolds pores (b_1) (d_1) (f_1) New bone islands within the M250 scaffolds pores (a_2) (c_2) (e_2) New bone tissue crawl into the M0 scaffolds (b_2) (d_2) (f_2) New bone tissue crawl into the M250 scaffolds (scale = 500 μm), Bone: bone tissue; CaP: CaP ceramic.

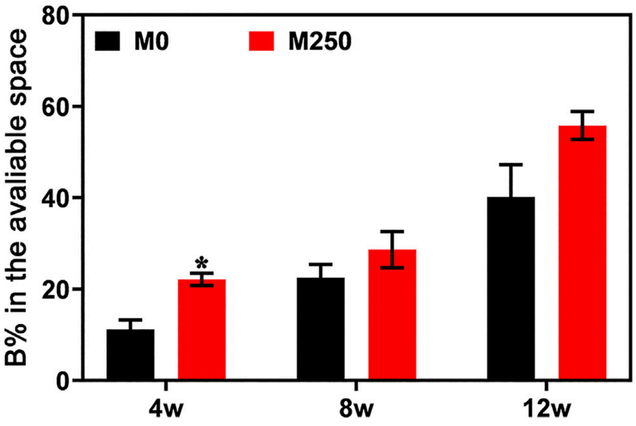

FIGURE 9 | Bone formation in the available space (%) of samples harvested from rabbits (statistically significant differences are marked by $^*p < 0.05$, $^{**}p < 0.01$).

week 12, when compared with M0 group (**Figures 7–10**). And compared with week 4, although the number of blood vessels in M250 decreased at week 8, the number of connected blood vessels increased, accompanied by more bone regeneration (**Figure 11**). At week 12, the blood vessel volume of the M250 group was still higher than that of the M0 group (**Figures 11E–I**). These results support other evidence that icaritin enhanced angiogenesis and bone formation in rabbits when icaritin was incorporated into PLGA/TCP composites (Chen et al., 2012; Chen et al., 2013), indicating a possible link between angiogenesis and bone formation which was described in the phenomenon of osteoinduction caused by icaritin-loaded CaP ceramic.

CONCLUSION

When loaded into submicron surface structured CaP ceramics, icaritin was chemically retained and released

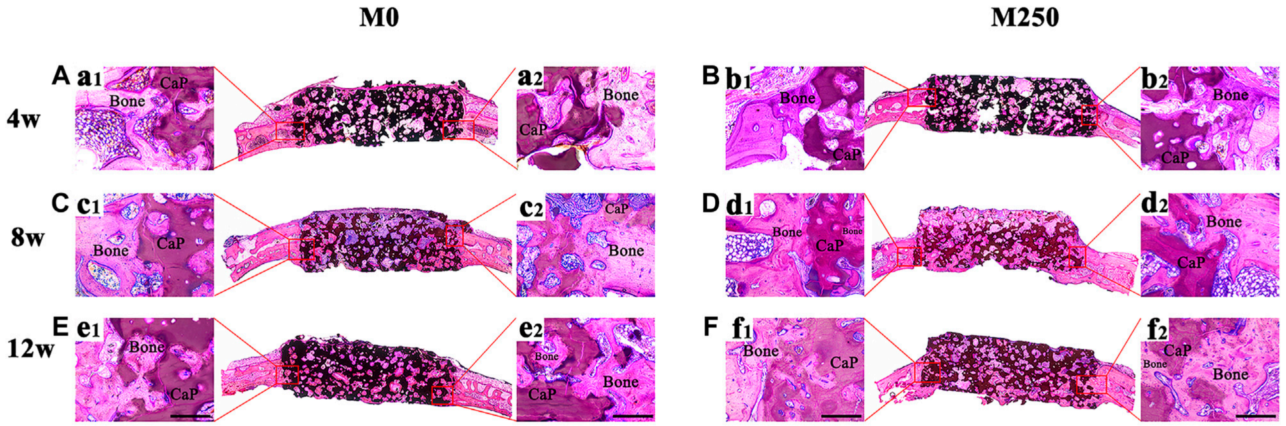

FIGURE 10 | The sagittal direction histological observation of M0 and M250 after calvarial implantation for 4, 8 and 12 weeks **(A), (C), (E)** The histological overviews of M0 **(B), (D), (F)** The histological overviews of M250 (a_1) (a_2) (c_1) (c_2) (e_1) (e_2) New bone tissue crawl into the M0 scaffolds (b_1) (b_2) (d_1) (d_2) (f_1) (f_2) New bone tissue crawl into the M250 scaffolds (scale = 500 μm), Bone: bone tissue; CaP: CaP ceramic.

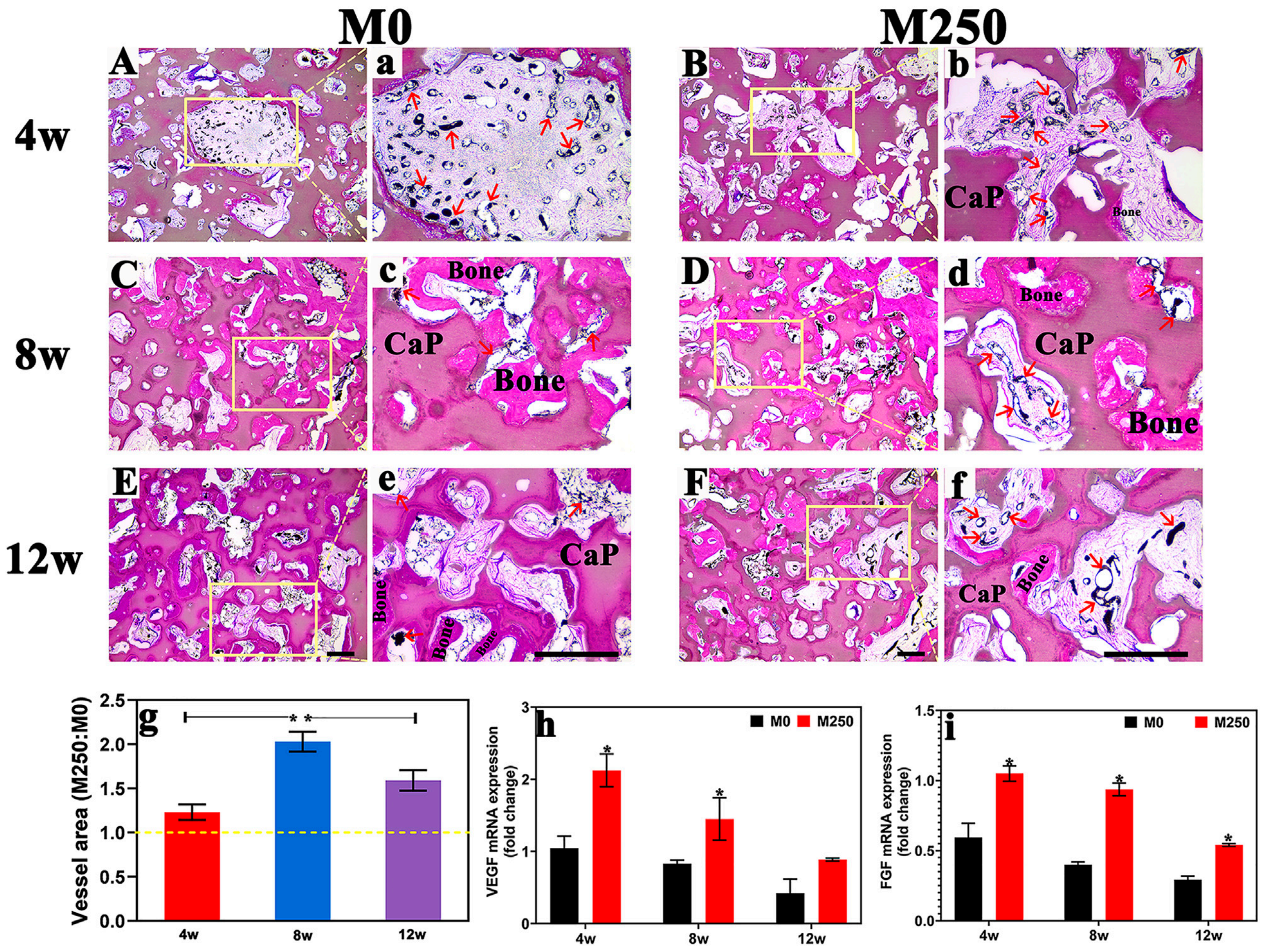

FIGURE 11 | Blood vessel formation **(A)–(F)** New blood vessel formation in M0 group and M250 group at week4 week8 and week12; **(A)–(F)** Magnified view of blood vessel within M0 and M250 scaffolds (red arrow); **(G)** The ratio of blood vessel area between group M0 and group M250; **(H)** VEGF and **(I)** FGF mRNA expression in implantations (scale = 500 μm), Bone: bone tissue; CaP: CaP ceramic (Statistically significant differences are marked by *$p < 0.05$).

dose-dependently. With its release, icaritin enhanced osteogenesis of bone marrow stromal cells *in vitro* with the presence of osteogenic factors and enhanced bone formation initiated by submicron surface structured CaP ceramic in intramuscular implantation. Due to enhanced bone formation by icaritin, icaritin-containing osteoinductive CaP ceramic scaffolds presented the desired osteogenic and angiogenic potential, as evidenced in a rabbit calvarial defect model. The combination of icaritin and submicron surface structured CaP ceramics could thus be a novel strategy for bone regeneration.

DATA AVAILABILITY STATEMENT

The raw data supporting the conclusions of this article will be made available by the authors, without undue reservation.

ETHICS STATEMENT

The animal study was reviewed and approved by The First Affiliated Hospital of Chongqing Medical University.

AUTHOR CONTRIBUTIONS

HP and JL performed the experiments, analyzed and interpreted the results. YX performed the animal experiments. GL acquired the research operating funding, advised on the conception and conduction of the experiments and data analysis.

ACKNOWLEDGMENTS

The authors thank Science and Technology Project of Sichuan Province (2018FZ0108) for providing funding for this research.

REFERENCES

Barralet, J., Gbureck, U., Habibovic, P., Vorndran, E., Gerard, C., and Doillon, C. J. (2009). Angiogenesis in calcium phosphate scaffolds by inorganic copper ion release. *Tissue Eng.* 15 (7), 1601–1609. doi:10.1089/ten.tea.2007.0370

Bohner, M., Galea, L., and Doebelin, N. (2012). Calcium phosphate bone graft substitutes: failures and hopes. *J. Eur. Ceram. Soc.* 32 (11), 2663–2671. doi:10.1016/j.jeurceramsoc.2012.02.028

Chai, Y. C., Kerckhofs, G., Roberts, S. J., Van Bael, S., Schepers, E., Vleugels, J., et al. (2012). Ectopic bone formation by 3D porous calcium phosphate-Ti6Al4V hybrids produced by perfusion electrodeposition. *Biomaterials* 33 (16), 4044–4058. doi:10.1016/j.biomaterials.2012.02.026

Chen, S. H., Wang, X. L., Xie, X. H., Zheng, L. Z., Yao, D., Wang, D. P., et al. (2012). Comparative study of osteogenic potential of a composite scaffold incorporating either endogenous bone morphogenetic protein-2 or exogenous phytomolecule icaritin: an *in vitro* efficacy study. *Acta Biomater.* 8 (8), 3128–3137. doi:10.1016/j.actbio.2012.04.030

Chen, S. H., Lei, M., Xie, X. H., Zheng, L. Z., Yao, D., and Wang, X. L. (2013). PLGA/TCP composite scaffold incorporating bioactive phytomolecule icaritin for enhancement of bone defect repair in rabbits. *Acta Biomater.* 9 (5), 6711–6722. doi:10.1016/j.actbio.2013.01.024

Damien, C. J., and Parsons, J. R. (1991). Bone graft and bone graft substitutes: a review of current technology and applications. *J. Appl. Biomater.* 2 (3), 187–208. doi:10.1002/jab.770020307

Davison, N. L., Gamblin, A. L., Layrolle, P., Yuan, H., de Bruijn, J. D., and Barrère-de Groot, F. (2014a). Liposomal clodronate inhibition of osteoclastogenesis and osteoinduction by submicrostructured beta-tricalcium phosphate. *Biomaterials* 35(19), 5088–5097. doi:10.1016/j.biomaterials.2014.03.013

Davison, N. L., Luo, X., Schoenmaker, T., Everts, V., Yuan, H., Barrère-de Groot, F., et al. (2014b). Submicron-scale surface architecture of tricalcium phosphate directs osteogenesis *in vitro* and *in vivo*. *Eur. Cell. Mater.* 27, 281–287. doi:10.22203/ecm.v027a20

Galia, E., Nicolaides, E., Hörter, D., Löbenberg, R., Reppas, C., and Dressman, J. B. (1998). Evaluation of various dissolution media for predicting *in vivo* performance of class I and II drugs. *Pharm. Res. (N. Y.)* 15 (5), 698–705. doi:10.1023/a:1011910801212

Habibovic, P., van der Valk, C. M., van Blitterswijk, C. A., De Groot, K., and Meijer, G. (2004). Influence of octacalcium phosphate coating on osteoinductive properties of biomaterials. *J. Mater. Sci. Mater. Med.* 15 (4), 373–380. doi:10.1023/b:jmsm.0000021104.42685.9f

Hench, L. L., and Wilson, J. (1984). Surface-active biomaterials. *Science* 226 (4675), 630–636. doi:10.1126/science.6093253

Huang, J., Yuan, L., Wang, X., Zhang, T. L., and Wang, K. (2007). Icaritin and its glycosides enhance osteoblastic, but suppress osteoclastic, differentiation and activity *in vitro*. *Life Sci.* 81 (10), 832–840. doi:10.1016/j.lfs.2007.07.015

Huskens, J., and Sherry, A. D. (1998). Co-ordination chemistry and molecular mechanics study of the magnesium(II) and calcium(II) complexes of trisubstituted 1,4,7-triazacyclononane derivatives. *J. Chem. Soc. Dalton Trans.* 5 (1), 177–184. doi:10.1039/a703640j

Ji, M., Chen, H., Yan, Y., Ding, Z., Ren, H., and Zhong, Y. (2020). Effects of tricalcium silicate/sodium alginate/calcium sulfate hemihydrate composite cements on osteogenic performances *in vitro* and *in vivo*. *J. Biomater. Appl.* 34 (10), 1422–1436. doi:10.1177/0885328220907784

Karageorgiou, V., and Kaplan, D. (2005). Porosity of 3D biomaterial scaffolds and osteogenesis. *Biomaterials* 26 (27), 5474–5491. doi:10.1016/j.biomaterials.2005.02.002

Lai, X., Ye, Y., Sun, C., Huang, X., Tang, X., Zeng, X., et al. (2013). Icaritin exhibits anti-inflammatory effects in the mouse peritoneal macrophages and peritonitis model. *Int. Immunopharm.* 16 (1), 41–49. doi:10.1016/j.intimp.2013.03.025

Lee, K. G., Lee, K. S., Kang, Y. J., Hwang, J. H., Lee, S. H., Park, S. H., et al. (2018). Rabbit calvarial defect model for customized 3D-printed bone grafts. *Tissue Eng. C Methods.* 24 (5), 255–262. doi:10.1089/ten.TEC.2017.0474

Luo, X., Barbieri, D., Davison, N., Yan, Y., de Bruijn, J. D., and Yuan, H. (2014). Zinc in calcium phosphate mediates bone induction: *in vitro* and *in vivo* model. *Acta Biomater.* 10(1), 477–485. doi:10.1016/j.actbio.2013.10.011

McMillan, A., Nguyen, M. K., Gonzalez-Fernandez, T., Ge, P., Yu, X., Murphy, W. L., et al.(2018). Dual non-viral gene delivery from microparticles within 3D high-density stem cell constructs for enhanced bone tissue engineering. *Biomaterials* 161, 240–255. doi:10.1016/j.biomaterials.2018.01.006

Murr, L. E. (2019). Strategies for creating living, additively manufactured, open-cellular metal and alloy implants by promoting osseointegration, osteoinduction and vascularization: an overview. *J. Mater. Sci. Technol.* 35 (2), 231–241. doi:10.1016/j.jmst.2018.09.003

Oates, M., Chen, R., Duncan, M., and Hunt, J. A. (2007). The angiogenic potential of three-dimensional open porous synthetic matrix materials. *Biomaterials* 28 (25), 3679–3686. doi:10.1016/j.biomaterials.2007.04.042

Peng, S., Zhang, G., Zhang, B. T., Guo, B., He, Y., Bakker, A. J., et al. (2013). The beneficial effect of icaritin on osteoporotic bone is dependent on the treatment initiation timing in adult ovariectomized rats. *Bone* 55 (1), 230–240. doi:10.1016/j.bone.2013.02.012

Qin, L., Zhang, G., Sheng, H., Wang, X. L., Wang, Y. X., Yeung, K. W., et al. (2008). Phytoestrogenic compounds for prevention of steroid-associated osteonecrosis. *J. Musculoskelet. Neuronal Interact.* 8 (1), 18–21. doi:10.1007/978-3-540-45456-4_38

Song, G., Habibovic, P., Bao, C., Hu, J., van Blitterswijk, C. A., Yuan, H., et al. (2013). The homing of bone marrow MSCs to non-osseous sites for ectopic bone formation induced by osteoinductive calcium phosphate. *Biomaterials* 34 (9), 2167–2176. doi:10.1016/j.biomaterials.2012.12.010

van Dijk, L. A., Duan, R., Luo, X., Barbieri, D., Pelletier, M., Christou, C., et al. (2018). Biphasic calcium phosphate with submicron surface topography in an

Ovine model of instrumented posterolateral spinal fusion. *JOR Spine.* 1 (4), e1039. doi:10.1002/jsp2.1039

Xu, S., Lin, K., Wang, Z., Chang, J., Wang, L., Lu, J., et al. (2008). Reconstruction of calvarial defect of rabbits using porous calcium silicate bioactive ceramics. *Biomaterials* 29 (17), 2588–2596. doi:10.1016/j.biomaterials.2008.03.013

Yao, D., Xie, X. H., Wang, X. L., Wan, C., Lee, Y. W., and Chen, S. H. (2012). Icaritin, an exogenous phytomolecule, enhances osteogenesis but not angiogenesis—an *in vitro* efficacy study. *PLoS One.* 7 (8), e41264. doi:10.1371/journal.pone.0041264

Yuan, H., van Blitterswijk, C. A., de Groot, K., and de Bruijn, J. D. (2006). A comparison of bone formation in biphasic calcium phosphate (BCP) and hydroxyapatite (HA) implanted in muscle and bone of dogs at different time periods. *J. Biomed. Mater. Res.* 78 (1), 139–147. doi:10.1002/jbm.a.30707

Yuan, H., Fernandes, H., Habibovic, P., de Boer, J., Barradas, A. M., and de Ruiter, A. (2010). Osteoinductive ceramics as a synthetic alternative to autologous bone grafting. *Proc. Natl. Acad. Sci. U.S.A.* 107 (31), 13614–13619. doi:10.1073/pnas.1003600107

Zhang, G., Qin, L., and Shi, Y. (2007). Epimedium-derived phytoestrogen flavonoids exert beneficial effect on preventing bone loss in late postmenopausal women: a 24-month randomized, double-blind and placebo-controlled trial. *J. Bone Miner. Res.* 22 (7), 1072–1079. doi:10.1359/jbmr.070405

Zhang, G., Pan, X. H., Xie, X. H., He, B. Y., Li, G., Leung, K. S., et al. (2008). Icaritin, a potential estrogen receptor beta antagonist molecule Icaritin, promote osteoporotic fracture repair in ovariectomized mice: preliminary finding at 3 weeks post fracture. *Bone* 43 (Suppl. S1), S76–S77. doi:10.1016/j.bone.2008.07.081

Zhang, G., Qin, L., Sheng, H., Wang, X. L., Wang, Y. X., and Yeung, D. K. (2009). A novel semisynthesized small molecule icaritin reduces incidence of steroid-associated osteonecrosis with inhibition of both thrombosis and lipid-deposition in a dose-dependent manner. *Bone* 44 (2), 345–356. doi:10.1016/j.bone.2008.10.035

Zhang, J., Luo, X., Barbieri, D., Barradas, A. M., de Bruijn, J. D., and van Blitterswijk, C. A. (2014). The size of surface microstructures as an osteogenic factor in calcium phosphate ceramics. *Acta Biomater.* 10 (7), 3254–3263. doi:10.1016/j.actbio.2014.03.021

Zhang, J., Barbieri, D., ten Hoopen, H., de Bruijn, J. D., van Blitterswijk, C. A., and Yuan, H. (2015). Microporous calcium phosphate ceramics driving osteogenesis through surface architecture. *J. Biomed. Mater. Res.* 103 (3), 1188–1199. doi:10.1002/jbm.a.35272

Conflict of Interest: The authors declare that the research was conducted in the absence of any commercial or financial relationships that could be construed as a potential conflict of interest.

frontiers
in Bioengineering and Biotechnology

REVIEW
published: 05 February 2021
doi: 10.3389/fbioe.2021.630488

Bioink Formulations for Bone Tissue Regeneration

Na Li[1], Rui Guo[2] and Zhenyu Jason Zhang[1]*

[1] School of Chemical Engineering, University of Birmingham, Birmingham, United Kingdom, [2] Key Laboratory of Biomaterials of Guangdong Higher Education Institutes, Guangdong Provincial Engineering and Technological Research Centre for Drug Carrier Development, Department of Biomedical Engineering, Jinan University, Guangzhou, China

Unlike the conventional techniques used to construct a tissue scaffolding, three-dimensional (3D) bioprinting technology enables fabrication of a porous structure with complex and diverse geometries, which facilitate evenly distributed cells and orderly release of signal factors. To date, a range of cell-laden materials, such as natural or synthetic polymers, have been deployed by the 3D bioprinting technique to construct the scaffolding systems and regenerate substitutes for the natural extracellular matrix (ECM). Four-dimensional (4D) bioprinting technology has attracted much attention lately because it aims to accommodate the dynamic structural and functional transformations of scaffolds. However, there remain challenges to meet the technical requirements in terms of suitable processability of the bioink formulations, desired mechanical properties of the hydrogel implants, and cell-guided functionality of the biomaterials. Recent bioprinting techniques are reviewed in this article, discussing strategies for hydrogel-based bioinks to mimic native bone tissue-like extracellular matrix environment, including properties of bioink formulations required for bioprinting, structure requirements, and preparation of tough hydrogel scaffolds. Stimulus mechanisms that are commonly used to trigger the dynamic structural and functional transformations of the scaffold are analyzed. At the end, we highlighted the current challenges and possible future avenues of smart hydrogel-based bioink/scaffolds for bone tissue regeneration.

Keywords: bioink, formulation, bioprinting, hydrogel reinforcement, stimuli response, bone regeneration

Edited by:
Malcolm Xing,
University of Manitoba, Canada

Reviewed by:
Jennifer Patterson,
Instituto IMDEA Materiales, Spain
Giovanni Vozzi,
University of Pisa, Italy

***Correspondence:**
Zhenyu Jason Zhang
z.j.zhang@bham.ac.uk

Specialty section:
This article was submitted to Biomaterials, a section of the journal Frontiers in Bioengineering and Biotechnology

Received: *17 November 2020*
Accepted: *13 January 2021*
Published: *05 February 2021*

Citation:
Li N, Guo R and Zhang ZJ (2021) Bioink Formulations for Bone Tissue Regeneration. Front. Bioeng. Biotechnol. 9:630488. doi: 10.3389/fbioe.2021.630488

INTRODUCTION

There are a number of challenges associated with the current restoration methods for bone defects, such as autografts and allografts (Chiarello et al., 2013; Van De Vijfeijken et al., 2018), which include a limited supply of donor tissues, risk of complications, transplant rejection, and biocontamination (Vidal et al., 2020). Bone tissue engineering, an emerging route, has demonstrated a great potential over the past decades: replacing bone tissue with a three-dimensional (3D) living scaffold implant containing cells; using bone tissue extracellular matrix (ECM) mimics and the bioactive factors to activate the growth of cells (Qu et al., 2019). In here, the ECM mimics are commonly cytocompatible polymeric matrices, such as hydrogels, polyesters, and polymer-ceramic composites (Jakus et al., 2016; Rosales and Anseth, 2016; Nicolas et al., 2020), which require extensive research input from the material research community. It has been demonstrated extensively that hydrogels are greatly suitable for the biomedical applications due to their excellent biocompatibility and biodegradability, outstanding hydrophilicity, controllable permeability, and simple manufacturing methods (Fuchs et al., 2019).

A plethora of fabrication routes for bionic 3D scaffolds have been developed (Raeisdasteh Hokmabad et al., 2017; Chocholata et al., 2019; Haider et al., 2020), which include phase separation (Bailey et al., 2012), electrospinning (Thorvaldsson et al., 2013), freeze-drying (Wu et al., 2010), and salt leaching (Chiu et al., 2009). These strategies showed an excellent capability in producing a porous matrix with controlled surface morphology and adjusted processing variables, but sometimes a less controlled structure (Zhang et al., 2013). As a contrast, 3D bioprinting technique provides a fabrication process of scaffolds with complex and diverse geometry to evenly distribute cells and orderly release signal factors when cell-laden materials, known as bioink, are deployed (Bracaglia et al., 2017; Datta et al., 2017).

To regenerate a bone tissue, constructing a complex 3D structure with customized and enriched composition of ECM is one of the most indispensable initial steps (Dutta and Dutta, 2010). It is equally vital that the dynamic changes of the scaffolding can stimulate distinctive functions of tissue (Zhang et al., 2018), which requires some intrinsic mechanism(s) that can respond to external stimuli. To meet such technical requirements for tissue regeneration (Yang G. H. et al., 2019), 3D bioprinting technology evolved into four-dimensional (4D) bioprinting, whereby time is integrated as a processing parameter. Specifically, as the fourth dimension, time, changes (Kim S. H. et al., 2020), the geometric shape and behavior of a bionic scaffold are transformed, depending on the components' response to the surrounding environmental factors (Yang G. H. et al., 2019) and/or the internal function of the scaffold that progressively matures through the interaction with the cells (Wan et al., 2019). The technological advance offers not only the ability for biomimetic scaffold to respond immediately to any internal cell force stimulation and external factors, but also a gradual maturation and functional expression of the printed scaffold implants over time (Li et al., 2016; Wan et al., 2019). As such, stimuli-responsive 4D printed scaffolds, based on hydrogel, provide an unprecedented potential for bone tissue engineering (Murphy et al., 2013).

With a focus on the strategies concerning 3D reconstruction of bone tissue, in particularly the hydrogel-based bioink for hard tissue repair, this review starts with the technical requirements for bioprinting in terms of processability, resulting scaffold structure, and the bone repair function. A number of 3D printing processes are reviewed subsequently, comparing the advantages and limitations of each technologies, followed by the stimulus-responsive mechanism commonly used in 4D printing. Finally, some of the current challenges and potential improvements of hydrogel-based bioinks for future consideration are discussed.

PROPERTY REQUIREMENTS OF BIOINKS/SCAFFOLDS

To 3D print a hard or elastic 3D hydrogel scaffold with orderly distributed components and a controlled geometry, bioink formulation with pre-defined rheological properties undergoes a complex manufacturing process. The following characteristics are therefore desirable for the bioinks:

(1) Printability: It requires an appropriate viscosity range of the formulation and fast transition kinetics from sol to gel state (Kim M. K. et al., 2020). For nozzle-based extrusion bioprinting, bioinks are expected to be shear-thinning liquids that can be extruded in a laminar flow, whilst maintaining sufficient mechanical strength to self-support over multiple layers, with controlled geometry and porosity (Jakus et al., 2016). For example, by simply processing the sodium alginate/poly(acrylamide-co-acrylic acid) bioink formulation in a solution of pH 14, the viscosity and gel rate of the hydrogel can be adjusted to an improved 3D printability (Li et al., 2018).

(2) Biocompatibility: Once it is ready, the scaffold would incorporate with the hosting biological environment, without triggering any adverse reactions, to actively promote the adhesion and proliferation of osteocytes. This would facilitate the formation of an extracellular matrix on the surface and in the pores of the scaffold, which gradually induce the development of a new bone tissue (Dong et al., 2009). In a recent report, the dental implants of minipig were grit-blasted with some ceramic particles, followed by acidic etching, to fabricate nano-structured surface. A very limited number of inflammatory cells were recorded after 4 and 12 weeks of implantation, which proves the biocompatibility of the implant (Hoornaert et al., 2020). Furthermore, the microenvironment within the scaffold is expected to encourage the formation of blood vessels in or around the implant within a few weeks after implantation, thereby providing a favorable condition for the transportation of nutrients, oxygen, and waste (Williams, 2008).

(3) Mechanical properties: An appropriate network enhancement mechanism should form between the components of the scaffold to prevent material failure and minimize fracture under large deformation (Zhang et al., 2017). The mechanical properties of the fabricated scaffold should match those of the host bone, enabling a suitable load transfer. For example, Ratheesh and co-workers tried to add 15% w/v of inorganic bone particles, whose sizes are 150–500 and 0–500 μm, to 10 and 12.5% w/v methacrylated gelatin based bioink to enhance the biomechanical properties of the scaffold (Ratheesh et al., 2020).

(4) Biodegradability: The printed scaffold is expected to degrade *in vivo* with time. Ideally, the degradation rate of scaffolds matches the production rate of ECM, whilst the degradation products have no side effects on the host (Sabir et al., 2009). For example, the mass loss of a waterborne polyurethane scaffold reached 35.62% after 90 days of degradation, while the fluorescence image showed that after 7 days of incubation, rabbit chondrocytes covered all waterborne polyurethane scaffolds (Feng et al., 2020).

(5) Surface characteristics: The interface between the scaffold and the tissue to be repaired is critical to the success of a scaffold transplantation, with numerous reactions and interactions taking place. Therefore, the surface characteristics of a scaffold, such as porosity, wettability, and morphology, require significant attention. For instance, the diameter of the initially interconnected pores should

maintain at least 100 μm, allowing nutrients and oxygen that are essential for cell survival to diffuse and the waste produced by the cells to transfer (Rouwkema et al., 2008). A pore size range of 200–350 μm was recommended for the growth of bone tissue (Murphy et al., 2010). Surface of the scaffold should be engineered to control cells spreading, proliferation, and differentiation. The morphology of the scaffold is also of great significance for anchoring cells and proteins on the surface (Haider et al., 2020).

(6) Stimulus responsiveness: When the hydrogel is subjected to an external/internal stimuli, it can respond in a timely manner by changing its physiochemical properties. A reversible process is preferred (Lui et al., 2019).

The properties of bioink and its resulting scaffolding outlined above do not exist independently at any specific stage. From the bioink in its liquid state, to the scaffold constructed, and finally to the functional implant, these characteristics are interrelated and could influence each other throughout the entire process that involves both physical and chemical transformations (**Figure 1**).

BIOPRINTING PROCESS

As an advanced approach for bone tissue engineering, 3D bioprinting was developed upon the significant advances achieved in 3D printing technology, cell biology, and materials science/engineering in recent years. **Figure 2** illustrates the overall bioprinting process, whereby bioactive scaffolds are fabricated via a layer-by-layer positioning of bioinks that commonly incorporate cells, bioactive factors, and biocompatible materials.

As the very first step, it is essential to establish the geometry and structure of the biomimic scaffold, upon examination of the impaired tissue. Computed tomography (CT) and magnetic resonance imaging (MRI) are the imaging technologies commonly used (Ozbolat and Gudapati, 2016) to establish the geometric requirements. Computer-aided design and manufacturing tools would then be deployed to construct the corresponding 3D structure. Composition of the bioinks will then be formulated, taking into account the desired characteristics specified in section Property Requirements of Bioinks/Scaffolds. Commonly used materials include biocompatible synthetic or natural polymers such as polycaprolactone and hyaluronic acid (Park et al., 2014), bioactive glass (Murphy et al., 2017), calcium phosphate (Ahlfeld et al., 2018), and natural decellularized fibers (Pati et al., 2014). It is worth noting that cells encapsulated in the bioink can be derived from autologous or allogeneic sources (Murphy and Atala, 2014).

As shown in **Figure 3**, a variety of bioprinting technologies have been developed to deposit bioink on a supporting substrate with high spatial resolution. An inkjet bioprinter can convey small droplets of formulation over predefined locations by either thermal (Cui et al., 2010, 2012) or acoustic mechanisms (Xu et al., 2008; Fang et al., 2012). The heat acts as a driving force

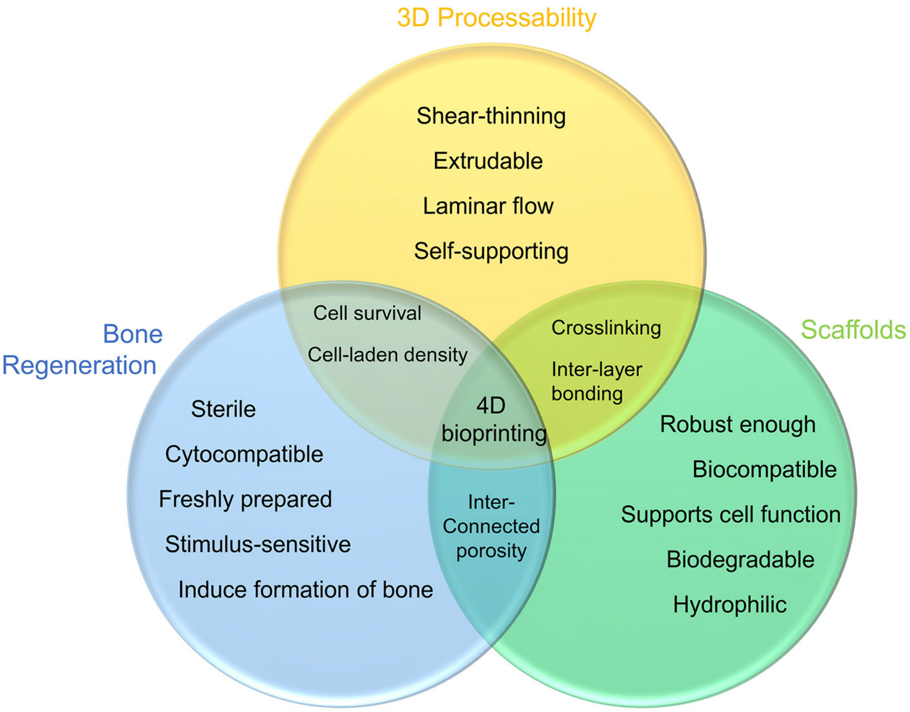

FIGURE 1 | Requirements for bioink: the shear-thinning formulation is extruded in the form of laminar flow and forms desired geometry via its self-supporting ability (yellow); bioink can be crosslinked to enhance the mechanical strength of the hydrogel scaffold, whilst the biocompatibility and biodegradability promote cell diffusion and proliferation (green); to accomplish bone tissue repair, the scaffolding will induce new tissue growth and respond to external stimuli as the new bone matures (blue).

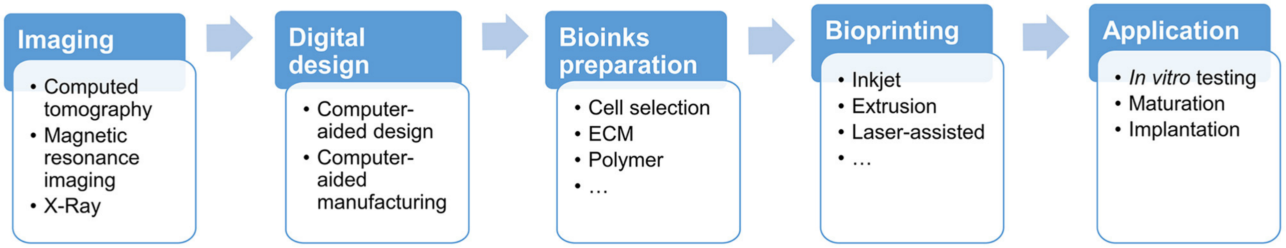

FIGURE 2 | A typical process of bioprinting 3D scaffolding: imaging and digital design; preparation of bioinks formulation and cells; bioprinting a scaffold with defined geometry and structure; *in vitro* testing and transplantation.

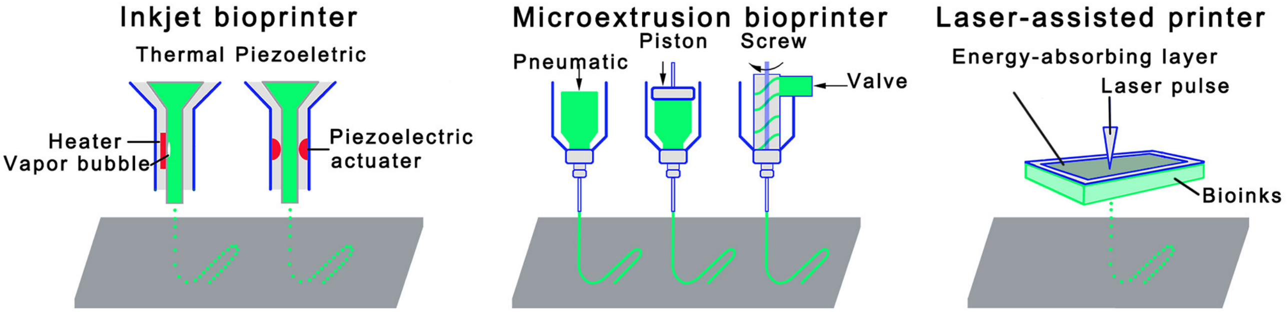

FIGURE 3 | Schematic diagrams of three primary bioprinting technologies: inkjet bioprinting, extrusion bioprinting, and laser-assisted bioprinting.

to evaporate the deposited ink into bubbles that burst and cause the ink to be ejected (Gomes et al., 2012). Piezo actuators eject ink from nozzles by offering a transient pressure (De Jong et al., 2006). Although thermal inkjet printing has several technical advantages such as high printing speed/efficiency and low operating cost, there are serious limitations, for example, the droplets cannot be completely uniformly transferred, resulting in an irregular droplet size or shape. In addition, cells and formulations that are not heat-resistant or mechanically resistant may be compromised. Piezoelectric inkjet printers have shown the capability to address the above limitations associated with the thermal one (Nakamura et al., 2005; Saunders et al., 2008), but there have been concerns with regard the potential damage to the cell membrane and lysis induced by acoustic waves at 15–25 kHz frequencies (Cui et al., 2012).

Amongst all 3D bioprinting technologies developed, extrusion bioprinting is arguably the most widely used one due to its exceptional capability of accommodating a broad spectrum of fluids whose viscosities range from 30 mPa s^{-1} to just under 6 $\times 10^7$ mPa s^{-1} (Jones, 2012). In this process, bioink formulation is dispensed to large hydrogel filaments on the substrate either pneumatically (Chang et al., 2011) or mechanically (piston- or screw-driven) (Jakab et al., 2006; Visser et al., 2013). Since the bioink is subjected to a strong shear stress when flowing through the nozzle, its rheological characteristics, in particularly the shear thinning characteristics, is critical to the processing condition (Shin et al., 2019). Compared with inkjet bioprinting, an obvious technical advantage offered by the extrusion bioprinting is a high cell deposition density, as summarized in **Table 1**. However, survival rate of cells is not as satisfying as that with inkjet bioprinting because cells may be subjected to an increased shear stress and mechanical pressure during the dispensing process. Some countermeasures, such as reducing the extruding pressure, increasing the nozzle size, are necessary to improve cell survival rate, which would compromise the printing speed and resolution.

TABLE 1 | Comparison of the advantages and disadvantages of inkjet bioprinting, extrusion bioprinting, and laser-assisted bioprinting.

Bioprinting technologies	Advantages	Disadvantages
Inkjet bioprinting	Low operating cost High efficiency	Non-uniformity of droplet size Inaccurate deposition location; Heat damage to cell behaviors Cell viability >85% Requirement for low viscosity bioinks
Extrusion bioprinting	Wide bioink printing viscosity High cell deposition densities	Low cell viability Low resolution Low printing speed
Laser-assisted bioprinting	High density of cell encapsulation Accurate and fast printing	High operating cost Complicated preparation process The trace metallic residues

The third fabrication strategy is laser-assisted bioprinting that is consisted of three primary components: a pulsed laser source; a ribbon coated with a metallic absorbing layer (e.g., gold or titanium) and a layer of bioink; and a receiving substrate such as quartz disk (Guillemot et al., 2011). During the construction of a scaffold, a pulsed laser beam scans over a ribbon, which triggers vaporization of the sacrificial absorbing layer. The resulting vapor bubbles would initially collapse on the surface of the absorbent layer, with no ejection. However, as the energy accumulates in the bubble, the pressure in the bubble increases before it bursts, expelling the bioink onto the receiving substrate (Guillemot et al., 2010). The technology could accommodate bioinks of various viscosities, and can achieve a high density of encapsulated cells and cell survival rate. There are also limitations such as the complex preparation of the ribbon, a trace amount of metallic residues in the scaffolds, and the high production cost (Murphy and Atala, 2014).

Following the 3D printing process, a bioink formulation will experience a sol-gel transformation to form a stable scaffold, no matter which printing technology is used. To ensure the survival rate of the cells, the prepared scaffold must be matured in a bioreactor for a period of time, and undergo a series of necessary *in vitro* tests before transplantation.

STRATEGIES FOR HYDROGEL BIOINK REINFORCEMENT

Once being extruded from the nozzle, bioink is expected to crosslink rapidly and solidify to maintain its geometrical integrity with an enhanced mechanical property, of which the kinetics was considered the most important processing parameter during the early stage of 3D bioprinting development. Biocompatibility, another critical factor, considers the biological activity and toxicity of each component in the bioink formulation. With the advancement of bioprinting technology, reinforcement strategies of bioink formulations received a great attention, of which the principle and mechanisms will be reviewed in this section (**Figure 4**).

Polymer Functionalization and Homogeneous Hydrogel Networks

Of the many natural polymers used in bioink formulations, some can form a physically crosslinked network through reversible conformational transitions. However, the formed network has a low bonding energy: changes in the surrounding environment can easily disrupt the conformation of the polymer chains, resulting in unsatisfactory mechanical properties (Rastogi and Kandasubramanian, 2019). To enhance the crosslinking ability of bioink formulations, a common strategy is to incorporate some new functional moieties or modify the end/side groups of the natural polymers, which could introduce additional or specific crosslinking sites and consequently promote the formation of a homogeneous network. With a uniformly distributed load, such network can minimize a localized stress concentration and, thereby improve the fracture toughness of the material (Sakai et al., 2008).

One of the common approaches used is to modify the side groups of polymers with methacrylate moieties, which has been applied to many natural polymers, including gelatin (Boere et al., 2014; Yin et al., 2018), alginate (Gao and Jin, 2019), hyaluronic acid (Skardal et al., 2010b), collagen (Chen et al., 2019), and kappa carrageenan (Mihaila et al., 2013). The modified polymers are equipped with carbon-carbon double bonds in the side chain, which can be easily crosslinked by a light source of different wavelength in the presence of photo-initiators. In a recent work, methylcellulose/gelatin-methacryloyl (MC/GelMA) bioink demonstrated an outstanding shape integrity (Rastin et al., 2020): MC provided the bioink formulation an excellent processability whilst GelMA was used not only to form a covalent crosslinked network through light radiation, but also to establish the physical interaction with the MC, improving the mechanical strength of the formed hydrogel. The addition of GelMA to pure MC can significantly improve the critical shear stress required to initiate the viscous flow of the hydrogel, with a progressive rise

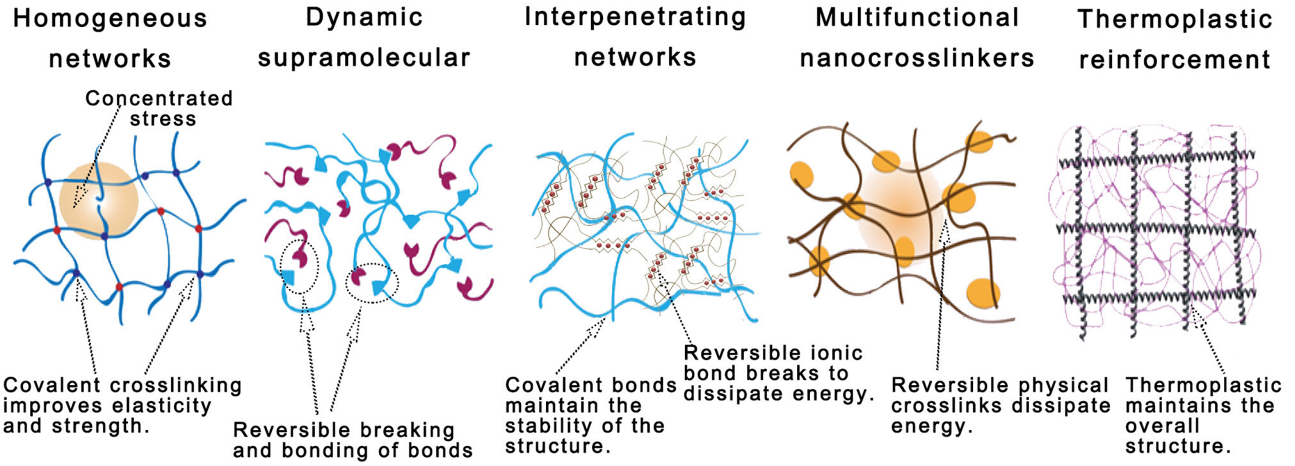

FIGURE 4 | Schematic diagrams of five established mechanical reinforcement techniques for hydrogel-based bioinks: polymer functionalization; supramolecular-reinforced hydrogels; interpenetrating networks (IPNs); nanocrosslinkers; and thermoplastic reinforcement.

in yield stress from 1356 ± 43 Pa (for pure MC) to 2354 ± 53 Pa (MC/GelMA hydrogel).

Click reactions, particularly thiol-ene click reactions (Lowe, 2010), demonstrated exceptional advantages, e.g., ease of use, high efficiency, reliability, and high selectivity (Cengiz et al., 2017), in synthesizing functional polymers or preparing polymers with topological structure for surface modification and biopharmaceutical applications (Yigit et al., 2011). For example, norbornene-modified hyaluronic acid underwent a photo-crosslinking reaction with the tetrathiol (Wang et al., 2018), and subsequently, the rheological measurements showed that the covalent networks improved the hydrogel mechanics whereby its storage modulus increased from 500 Pa to 5 kPa. Moreover, the Young's modulus of the hydrogel was enhanced from 1 to 3 kPa after photocuring.

It is feasible to develop a homogeneous network by combining two types of symmetrical multi-arm polyethylene glycols (PEG) whose end groups can react with each other. There are a number of flexibilities offered by PEG: easily changed molecular configuration, number of branches, type of end groups, and length of the arms, which offer a great platform for hydrogel reinforcement (Rutz et al., 2015) and for constructing a uniform network. Sakai and colleagues (Sakai et al., 2008) reported that the compressive strength of a gel network, once reacting two four-arm PEGs of the same size with amino and ester groups respectively, was significantly greater than that of agarose gel or acrylamide gel under the same network concentration. At a concentration of 120 mg/mL, the maximum breaking stress (9.6 MPa) of such PEG gel matched that of natural articular cartilage (∼6–10 MPa). To summarize, strategies have been developed and demonstrated to significantly improve the mechanical properties of bioprinted scaffold, in terms of ductility, malleability, and fracture toughness, by fabricating a hydrogel network that can distribute the applied stress evenly.

Dynamic Homogeneous Supramolecular Network

Enabled dynamic chemical bonds and/or physical interactions (Morgan et al., 2020), polymer can self-assemble and form a dynamic homogeneous supramolecular hydrogel.

The prominent dynamic covalent chemical reactions currently used include reversible diels-alder reactions, disulfide exchange, boronate ester formation, and aldimine formation (Morgan et al., 2020). The nature of such dynamic bonds is attributed to the combination of thermodynamically stable but kinetically unstable interactions (Jin et al., 2013). Reversible physical interactions include hydrogen bonding, ionic bonding, π-π stacking, hydrophobic interactions (Webber et al., 2016), coordination bonds (Zheng et al., 2016), and non-covalent guest–host interactions (Loebel et al., 2017). During the self-assembly process of the monomers that involve the dynamic interactions aforementioned, the inherent dynamicity does not facilitate the formation of a mechanically strong polymer structure (Mann et al., 2018), but enable the long chain polymer to entangle with each other if they are uniformly bound to a macromolecular backbone, forming macromolecular monomers initially. Such molecular configuration could reduce the free volume of chains, confine the migration ability of polymer chains, and improve the stability of the supramolecular network (Morgan et al., 2020). When being deformed, these dynamic interactions are constantly broken but reformed to mitigate a permanent disruption to the molecular network.

Figure 5 presents a number of intermolecular interactions, e.g., hydrogen bonding of petrin rings in the molecular structure, π-π stacking, and zinc ions coordination, that were used to develop an injectable fibril network based on folic acid, a natural small molecule (Liu et al., 2018). The bioink formulation exhibited a shear-thinning characteristic during the printing process, and was able to self-heal immediately after printing due to the dynamic nature of the interactions. When the molar ratio of folic acid to zinc ions and the total concentration of the coordination system were increased, it was found that the mechanical properties of the hydrogel were improved significantly whilst maintaining the excellent printability. For example, the elastic modulus of such fibril network was improved by ∼5 orders (from 10 to 10^6 Pa) when changing the molar ratio of folic acid to zinc ions from 1.7 to 2.0. The adjustable mechanical properties could be invaluable to suit the requirements for repairing various biological tissues from cartilage to cancellous bone. Moreover, the simple preparation, excellent printability, biocompatibility, and mechanical properties of supramolecular hydrogels provide an excellent platform in applications such as drug delivery.

Wang and colleagues (Wang et al., 2018) developed a bioink formulation that was enriched by dynamic covalent hydrazone bonds: hyaluronic acid was modified by hydrazide and aldehyde groups through amidation reaction and oxidation reaction, respectively (**Figure 6**). Once being exposed to an aqueous environment, the hydrazine groups can react reversibly with aldehydes to form dynamic covalent bonds. Rheological tests showed that the hydrogel exhibited the preferred shear thinning, self-healing, and injectable properties. Whilst maintaining an equal ratio between the two types of hyaluronic acid, an increased total mass fraction of the polymer (from 1.5 to 5 wt%) improved the shear modulus from c.a. 500 to 6,000 Pa, and Young's modulus to 15 kPa. However, the increased concentration of hyaluronic acid limited the self-healing efficiency of the hydrogel. It is worth noting that the viability of fibroblasts encapsulated in the hydrogel remained at a high level for each mass fraction. To further improve the mechanical properties of the hydrogel, click chemistry of norbornene-modified HA was used to generate a second network. The resulting hybrid hydrogel network was shown with an increased elastic modulus, a significantly reduced degradation rate, and a prolonged lifespan. This study demonstrates that different enhancement strategies could be deployed together to address the limitations associated with one particular crosslinking reaction, which expands the available options in developing a bioink formulation.

Interpenetrating Networks (IPNs)

IPNs consist of two polymer networks that can entangle through covalent bonds or random physical interactions. Based on the nature of the interactions, IPNs can be divided into

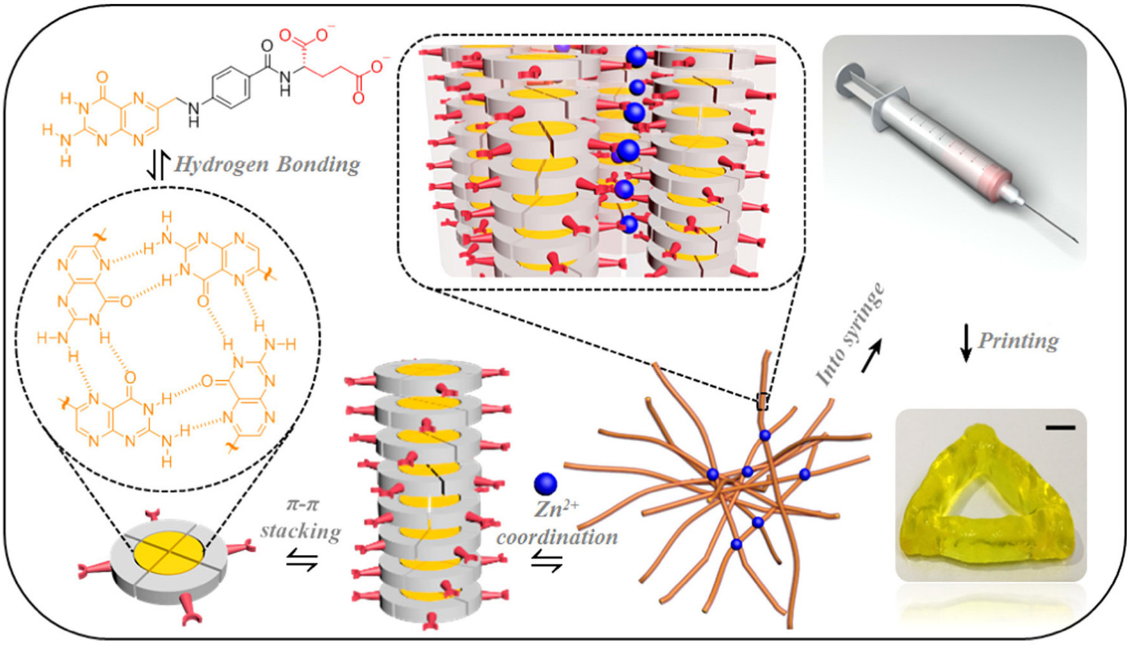

FIGURE 5 | A folic acid fibril network formed through a series of physical interactions. Reprinted with permission from Liu et al. (2018). Copyright (2018) American Chemical Society.

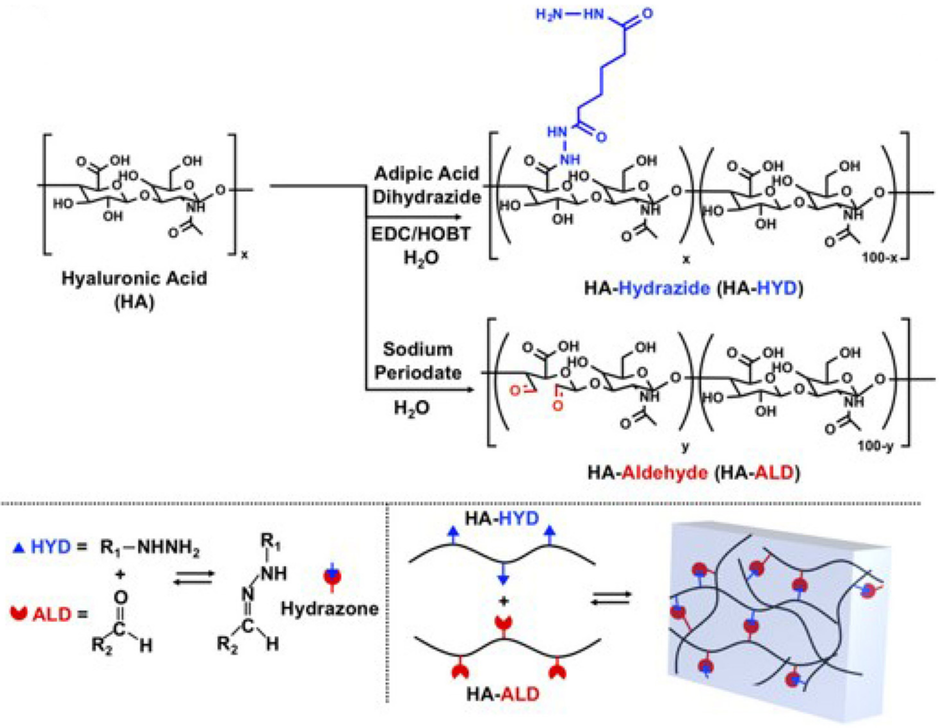

FIGURE 6 | Schematic diagram of the hydrazide and aldehyde groups modified hyaluronic acid macromonomer and dynamic covalent network. Reprinted with permission from Wang et al. (2018). Copyright (2018) John Wiley and Sons.

double networks (DNs), where each network is connected by covalent bonds, and ion-covalent entanglement networks (ICEs), where two networks rely on ionic bonds and covalent bonds, respectively (Chimene et al., 2020a).

The extensive presence of covalent bonds ensures that there is a substantial bond energy within the DNs. However, a long bonding time is required for the DNs, which might compromise their self-support ability following a bioprinting process. The interpenetrating networks of long-chain and short-chain molecules equip the DNs an excellent elasticity under deformation of up to 50%. The short chain network in the DNs would collapse first to dissipate energy, followed by the disintegration of the long chain network when the DNs undergoes a large deformation. Since the rupture of the DNs network is irreversible, their overall mechanical properties are primarily determined by the long-chain network that has a better elasticity than the short-chain network provides. For example, two networks, a hydrogel network and a hydrophobic elastomer network containing interlink initiators, were printed simultaneously (Yang H. et al., 2019): the initiators can induce covalent bonds between the two separated networks whilst each network is crosslinked during the curing process, which integrates the two networks together (**Figure 7**). It is worth noting that the interlink initiators were not deposited on the surface of the elastomer network, but evenly distributed within the elastomer network. The integrated structures provide an exceptional fracture energy (~10,000 J m^{-2} for the hydrogel and c.a. 6,000 J m^{-2} for the elastomer) as well as a high adhesion energy, above 5,000 J m^{-2}. The prepared double network structure can also withstand swelling.

In comparison with the dual networks aforementioned, ICEs systems have a greater potential in improving the mechanical properties of 3D printed hydrogel scaffolds because they are composed of two network structures with dissimilar properties (Zhao, 2014). In here,

- The ionic cross-linked network is tightly arranged, with bonds formed via physical attraction of positive and negative charges, which has a fast bonding kinetics. However, the weak bonds formed are sensitive to changes in the external environment, such as temperature and ion concentration, which underpins the instable and reversible nature of such network.
- The covalent cross-linked network is a flexible network with loose mesh and excellent ductility. It shows an excellent stability due to its high bonding energy, but cannot be recovered once broken (Gong, 2010). The advantage of ICEs over DNs is that the breakup of the sacrificial bonds is temporary. Upon external deformation, the tightly cross-linked ionic bonds break due to their brittleness, resulting in a series of microscopic segments, but the soft covalent network could use the viscous dissipation mechanism to prevent such microcracks from developing into macrocracks (Fuchs et al., 2019). If the external stress disappears at this point, ionic bonds could reform to repair the cracks. However, the cracks would likely cascade across the material if the stress gradually increases to the point where the covalent cross-linked network fails.

In a recent report, Pereira et al. (2018) used pectin, an anionic heteropolysaccharide, as a sole bioink material to prepare an ICEs hydrogel. With the ability of calcium-mediated ionic gelation, pectin was modified via methacrylation, and subsequently crosslinked chemically by UV radiation to prepare a covalent network. As illustrated in **Figure 8**, the modified pectin retained the ability to form a physically crosslinked hydrogel, allowing the design of ICEs hydrogel in which the chemical cross-linking and ionic crosslinking of the modified pectin can be performed in any order. Several processing parameters, such as the degree of methacrylation, UV exposure time, and polymer concentrations, could affect the mechanical properties of the final ICEs hydrogel. Lastly, a base-catalyzed thiol-Michael addition click reaction was carried out to attach cell adhesion moiety (RGD sequence) to the pectin backbone, which would improve the biological inertness of the pectin network. Results showed that the pectin-based hydrogel had cellular response characteristics, facilitating the printed skin fibroblasts to secrete new ECM. The 3D structured

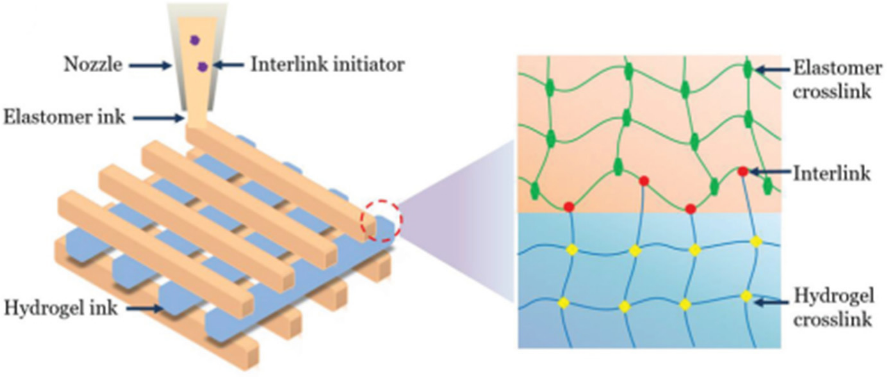

FIGURE 7 | Schematic diagrams of integrated double networks through interlink initiator. Reprinted with permission from Yang H. et al. (2019). Copyright (2019) John Wiley and Sons.

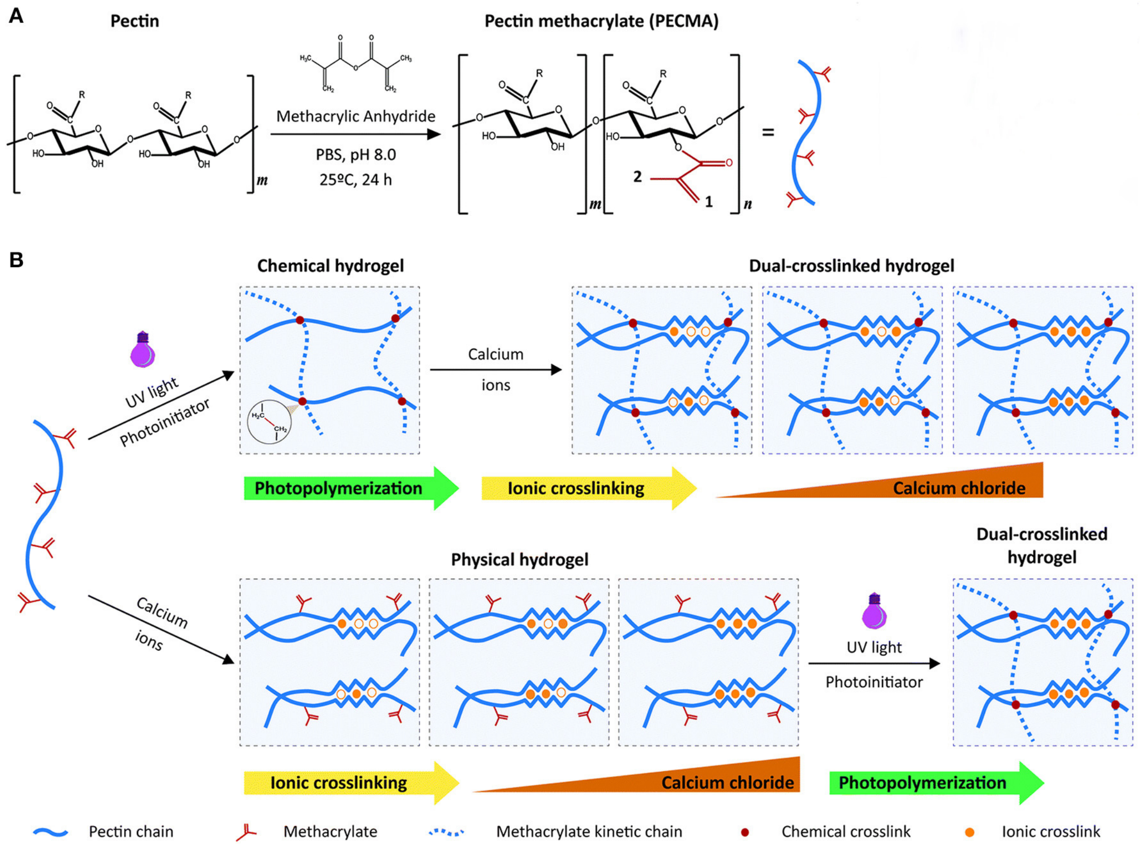

FIGURE 8 | **(A)** Modification method of single-component pectin bioink; **(B)** Strategy of preparing ICEs hydrogels. The order of implementation of ionic crosslinking and photopolymerization does not affect the formation of the ICEs hydrogels. Reprinted with permission from Pereira et al. (2018). Copyright (2018) Royal Society of Chemistry.

hydrogel, prepared with a single-component bioink formulation, has many potential applications in skin tissue engineering. It was also pointed out that the initial concentration of the bioink and the light irradiation time need to be increased if the formulation were to be used for any future bone tissue regeneration applications.

Multifunctional Nanocrosslinker

Incorporating nanocrosslinkers in the bioink formulations is a prominent method in enhancing hydrogel scaffold: with a large specific surface area, a single nanocrosslinker is able to interact with multiple polymer chains simultaneously (Fathi-Achachelouei et al., 2019). The amplified adhesion is primarily governed by physical interactions, e.g., hydrogen bonds, ionic bonds, electrostatic interactions, but can be actuated by chemical covalent cross-linking where appropriate/needed (Chimene et al., 2020a).

Once an external load is applied to a hydrogel containing nanocrosslinkers, a small fraction of polymer chains adsorbed on the nanocrosslinkers is forced to desorb and dissipate energy. However, such separation at molecular scale does not seem to have a notable impact on the overall structure of the hydrogel network. In addition, the detached polymer chains will re-adsorb onto the nanocrosslinker via physical interaction according to the principle of proximity (Zhalmuratova and Chung, 2020). The dynamic nature of the molecular interactions between nanocrosslinkers and polymers not only enhances the overall mechanical strength, but also improves the fatigue resistance of the network.

Nanocrosslinkers can also help to improve the rheological properties and processibility of the hydrogel, introduce responsiveness to stimulus such as electric or magnetic field, and promote tissue regeneration processes, such as bone formation and mineralization (Hasan et al., 2018; Tang et al., 2018). The versatility of nanocrosslinkers is primarily determined by the characteristics of the nanomaterials, such as shape, chemical nature, size, structure, and surface charge. According to the difference in their shapes, nanocrosslinkers with excellent biocompatibility can be divided into the following categories:

- dot-shaped nanoparticles (NPs), such as hydroxyapatite NPs, Fe_3O_4 magnetic NPs, gold, and silver NPs (Skardal et al., 2010a)
- nanofibers (Lu et al., 2019) and nanotubes, such as carbon nanotubes (CNTs), and nanocellulose

- layered low-dimensional nanosheets, such as nanoclay, graphene, and graphene oxide.

Example used here to demonstrate the capability of nanocrosslinkers for hydrogel reinforcement is a nanoclay, known as nanosilicate or Laponite (Chimene et al., 2018, 2020b), that is a disc-like 2D nanoplatelet with good solubility in water and satisfactory biocompatibility. Possessing negative charge on its surface but positive charge around the edge, nanosilicate could interact easily with polyelectrolyte. **Figure 9A** presents a nanosilicate (nSi) based ICEs bioink formulation (NICE) that contains gelatin methacryloyl (GelMA) and kappa-carrageenan (κCA) (Chimene et al., 2018). It appears that the addition of nanosilicates could increase the viscosities of formulations based on GelMA and κCA alone: NICE bioink formulation was used to prepare scaffolds up to 3 cm tall (150 layers), which is 10 greater than the maximum height constructed using the other single or binary bioink formulations (GelMA, GelMA/nSi, κCA, κCA/nSi, GelMA/κCA), as shown in **Figure 9B**. The substantially improved mechanical properties are likely attributed to a synergistic effect between nanoclay and ICEs, which is much greater than the effect by the individual factor. Unlike the conventional hydrogel enhancement approaches, e.g., increasing the crosslinking density and overall polymer concentration, such combined effect can construct a tough but elastic 3D scaffold without compromising the porosity of the hydrogel (**Figure 9C**). An additional benefit reported is that the nanosilicates were able to stimulate the intrachondral

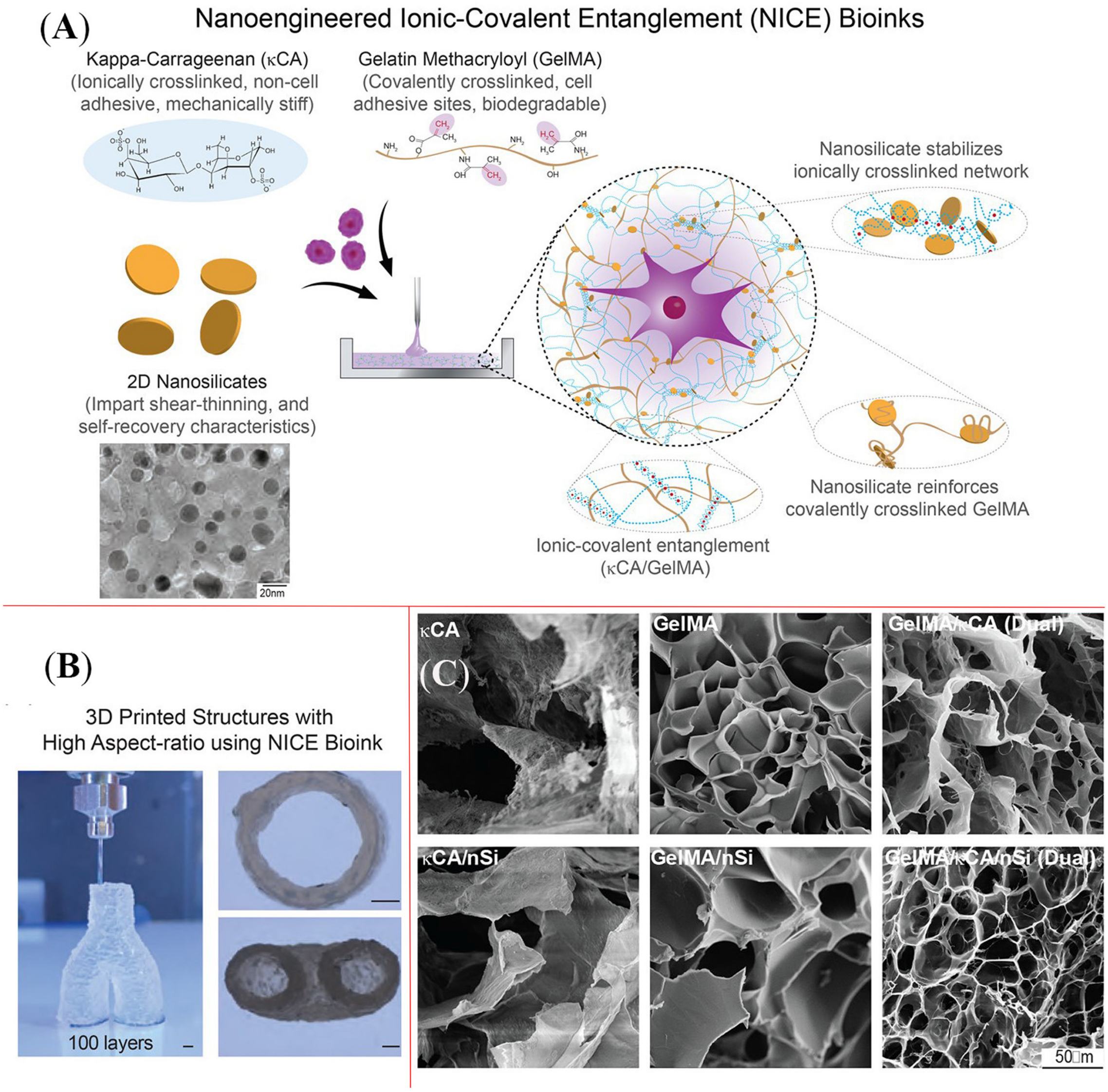

FIGURE 9 | (A) Schematic diagram shows the function of nanosilicate, gelatin methacryloyl, and kappa-carrageenan in nanoengineered ioni-covalent entanglement (NICE) bioink system; **(B)** NICE bioink was capable to print a scaffold with hing aspect-ratio, and the height of the construct reached 3 cm; **(C)** Comparison of pore structure of various bioink formulations. Reprinted with permission from Chimene et al. (2018). Copyright (2018) American Chemical Society.

differentiation of human mesenchymal stem cells and the accumulation of extracellular matrix.

Over the past few years, nanocellulose that is extracted and/or separated from plants and bacteria has received much attention due to its sustainable resource, non-toxicity, high specific surface area and aspect ratio, and excellent mechanical properties. Based on its dimensional characteristics, nanocellulose can be divided into several groups: cellulose nanocrystals (CNC), bacterial nanocellulose (BNC), cellulose nanofibers (CNF), microfibrillated cellulose (MFC), cellulose microfibrils, and nanowiskers (Curvello et al., 2019). A novel bone tissue substitute was developed by adding hydroxyapatite NPs and MFC in turn to a collagen hydrogel (He et al., 2018): the hydroxyapatite NPs could facilitate the interfacial adhesion with the tissues in contact and promote the proliferation of osteoblasts, whilst the hydrogen bonds available abundantly on the MFC promote the formation of a network, which enhances the mechanical properties and degradation properties of the scaffold. This was evidenced by an exceptional compressive strength of the prepared nanocomposite scaffold (>28.25 MPa) that is greater than what a sponge bone could offer (1–20 MPa) (Gibson, 1985) when the MFC content was over 15%. The work is one of the many recent attempts in demonstrating that the low-cost and sustainable materials such as MFC have a great potential in the bioprinting applications.

Distribution of nanocrosslinkers within a formed hydrogel scaffold is a critical factor: homogeneously distributed nanoparticles could help to minimize the formation of localized microcracks upon externally applied stress (Chimene et al., 2015). However, hydrophobic nanocrosslinkers tend to form aggregates, instead of interacting with the macromolecules involved, which might compromise the overall stability and mechanical properties of the hydrogel. One of the possible solutions to address such issue is using amphiphilic compounds. A comb-like polymer was included in a bioink formulation containing both hydrophobic CNTs and hydrophilic bacterial cellulose network (BC) to increase the binding energy and improve the overall mechanical properties of the hydrogel (CNT-BC-Syn) (Park et al., 2015). This approach not only improved the dispersibility of the CNTs in the hydrogel, enhanced the structural integrity and mechanical properties of the hydrogel, but also exhibited excellent osteoinductivity and osteoconductivity.

Thermoplastic Reinforcement

Naturally, thermoplastics possess several inherent advantages as a candidate for tissue scaffolding, such as superior mechanical strength and excellent processibility for complex-shaped objects. However, they are not suitable for bioink formulation due to their hardness and high melting temperature that is not suitable for the cell-containing hydrogel (Kim et al., 2016).

To address these technical challenges, a novel strategy was developed whereby the thermoplastic was processed in a separate chamber and printed with hydrogel bioinks in either layers or pre-defined patterns, which results in a two-phase structure where the thermoplastic component acts as the backbone. To minimize any potential damage to the cells by the thermoplastics, only the ones with low melting temperatures were considered. Of a broad range of biocompatible and biodegradable synthetic polymers, polyglycolic acid (PGA) (Day et al., 2004), polylactic acid-glycolic acid copolymer (PLGA) (Moran et al., 2003), polylactic acid (PLA) (Wang et al., 2016), polycaprolactone (PCL) with a melting temperature of about 65°C (Kang et al., 2016) have been explored in the previous studies.

Figure 10A presents a hybrid scaffold with a two-phase structure, consisting of both cell-laden alginate struts and PCL struts (Lee et al., 2013). As demonstrated by the stress-strain results of different formulations examined (**Figure 10B**), the PCL component could improve significantly the mechanical properties of the hybrid scaffolds, showing a similar characteristic to that of the pure PCL, which is significantly greater than that of the scaffold made of pure alginate. The substantial improvement (**Figure 10C**), e.g., tensile modulus from 2.5 MPa of alginate scaffolds alone to 15.4 MPa of PA-1 hybrid scaffolds, was attributed to the adhesion between PCL struts. It appeared that the large mesh space of the PCL layers was beneficial for transporting nutrients and signal factors between biologically active layers. In summary, the hybrid scaffold with thermoplastic reinforced structure met the requirements for hard tissue regeneration, with additional benefits contributed by the thermoplastic components.

The other approach of integrating thermoplastic polymer with hydrogel is to construct a defined structure in a sequence, with individual components embedded, instead of the layered printing discussed. The embedding method offers an increased degree of flexibility: build a thermoplastic scaffold (**Figure 11A**), deposit hydrogel subsequently with the planned shape and structure (**Figure 11B**), and form a hybrid scaffold with tailorable mechanical properties (Schuurman et al., 2011).

It must be noted that some porous features should be planned in advance to facilitate the diffusion of small molecules required for various behaviors of the cells when a cell-containing hydrogel fills the thermoplastic structure (Daly and Kelly, 2019). Moreover, signal factors, DNA, and hydrogels with different functions can be placed in different regions of the same scaffold to mimic the complex microenvironment of a natural tissue.

To conclude, the aforementioned enhancement methods for bioink formulation have all been demonstrated with effectiveness but also limitations. Different natural tissues would have specific and customized requirements for the matching 3D scaffolding, which is challenging to achieve with one single enhancement strategy. It is therefore critical to design a bionic entity that couples several strategies in terms of printing technology, formulation, and post-processing to meet the requirements satisfactorily.

FOUR-DIMENSIONAL BIOPRINTING

To implement one or even more "smart" features in a hydrogel scaffold, e.g., triggering mechanism upon external stimuli such as temperature, four-dimensional (4D) bioprinting method has been developed in recent years (Ashammakhi et al., 2018; Luo et al., 2019). The biomimetic scaffold contains components that are capable of responding toward either external environment

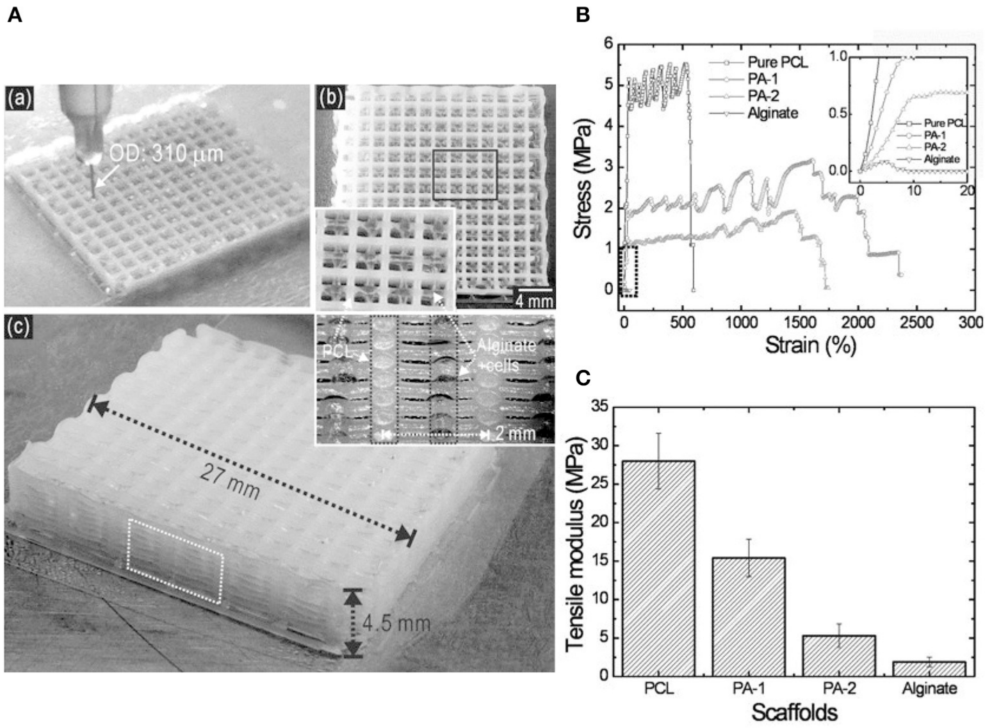

FIGURE 10 | (A) Printing process (a), a surface image (b) and geometry shape (c) of hybrid scaffold consisting of cell-laden alginate struts and PCL struts in layers; **(B)** Stress-strain curves for pure PCL, two hybrid scaffolds (PA-1 and PA-2), and alginate alone. The curves for PCL and two hybrid scaffolds experienced a similar trend, demonstrating the function of mechanical reinforcement for PCL; **(C)** Comparison of tensile modulus for PCL, PA-1, PA-2, and alginate. Reprinted with permission from Lee et al. (2013). Copyright (2013) John Wiley and Sons.

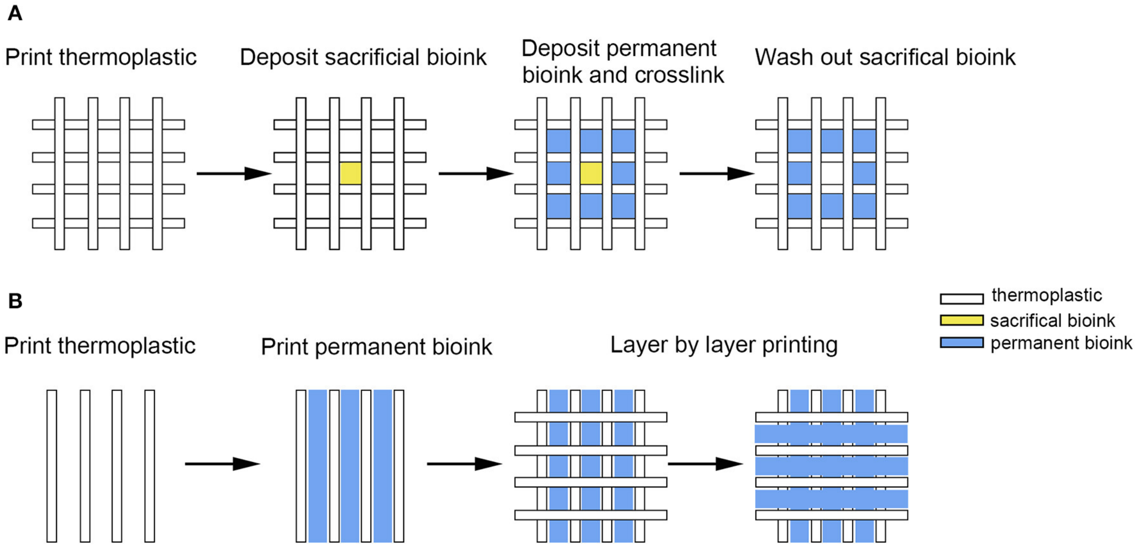

FIGURE 11 | (A) Hydrogel-based bioink was deposited into the square area formed by 2 layers of thermoplastic; **(B)** Hydrogel with cells was deposited in the middle area of 2 thermoplastic filaments or customized shape to develop constructs with tailorable mechanical properties.

or internal cells, which could either undergo immediate shape changes or may exhibit new functions over time to promote the behavioral expression of the encapsulated cells (Gao et al., 2016). The stimuli-responsive mechanism in the 4D bioprinting is not only a response function, but more importantly, a planned control of the geometrical, mechanical,

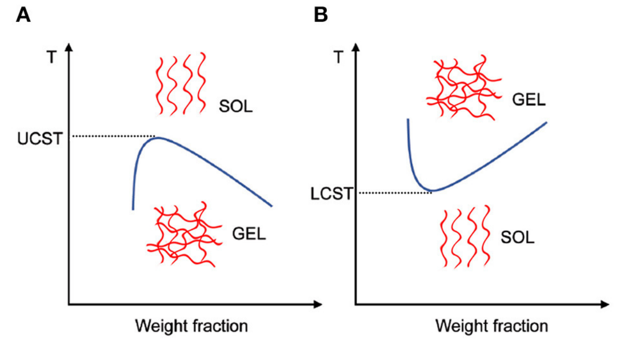

FIGURE 12 | Schematic diagrams showing **(A)** UCST hydrogels and **(B)** LCST hydrogels experience gel–sol transition or sol–gel transition, respectively with an increased temperature. The blue lines represent the phase separation boundary.

and surface/interface characteristics to be achieved through reversible response, which makes the 4D bioprinting technology more suitable for the complex dynamics of natural tissues (Li et al., 2016; Sydney Gladman et al., 2016). The specific response could be physical transformations, surface magnetism, surface hydrophilicity/hydrophobicity, modulus, antibacterial properties, cell adhesion, growth factor inducing ability, and nutrient diffusion rate (Khoo et al., 2015; Ong et al., 2018).

According to the nature of the triggering mechanisms, the stimuli used in 4D bioprinting are categorized as physical stimuli such as temperature, electric field, magnetic field, acoustic, light, shear stress; chemical stimuli including pH, ions and gases; and biological stimuli such as enzymes (Koetting et al., 2015). Of the many available options, temperature is the most commonly used to induce behavior transformation for the bioprinted object. Schematic diagrams in **Figure 12** demonstrate that the temperature-sensitive hydrogels such as poly(*N*-isopropylacrylamide), agarose and gelatin undergo a reversible volume change due to the collapse or expansion of the polymer chains in the solvent at lower critical solution temperature (LCST) or upper critical solution temperature (UCST) (Altomare et al., 2018).

Materials that are responsive to the pH of the surrounding medium have equally been widely used in tissue engineering – they are polyelectrolytes that contain functional groups such as carboxyl, sulfonic, phosphate, and pyridine (Dai et al., 2008; Wan et al., 2019). Based on the intra- and intermolecular forces that are controlled by the electrostatic interaction, polymer chains could change their configuration, e.g., from coil to globule when the charge of the functional groups is neutralized (Dai et al., 2008).

The same configurational transition mechanism can be applied for ion-responsive materials where the crosslinking and dissociation of the polymer chains are dependent on ions such as Ca^{2+} and Zn^{2+}. Changing ion types or concentrations will affect the magnitude of the electrostatic interaction and consequently control the mechanical properties of the hydrogels (Zhou et al., 2013). As such, ion-responsive hydrogels can be used to adjust the rheology of bioinks before bioprinting and/or the mechanical properties of the constructs after bioprinting to generate a hierarchically organized bone structure (Krishnakumar et al., 2019), e.g., the responsiveness of alginate to Ca^{2+} has been widely applied in bioprinting (Rastogi and Kandasubramanian, 2019).

CURRENT CHALLENGES AND FUTURE PROSPECTS

Although reconstructing the structure and function of a defective bone tissue is an extremely complex process, bioprinting technique has shown a spectrum of great advantages in fabricating biomimetic implants, with significant progress being made in the selection of bioink components, the processibility of hydrogel-based bioink formulations, and the compatibility and mechanical properties of the biomimetic scaffold. However, bionic scaffolds are not as "intelligent" as natural tissues yet. It remains a pressing and significant challenge to improve the bioink formulation to improve the dynamic relationship between natural tissues, cells, and the environment. A comprehensive understanding of the composition of the specific osteoblast extracellular matrix (Lamers et al., 2010), the internal relationships and dynamic functions of the components will certainly provide underpinning principles for the design of future bioinks (Kashte et al., 2017).

It appears that an improved biocompatibility, using smart materials, will facilitate the differentiation and proliferation characteristics of the encapsulated stem cells (Anjum et al., 2016), and the vascularization of 3D scaffolds after implantation (Santos and Reis, 2010; Lee et al., 2014; He et al., 2019; Liu et al., 2020). The responsiveness of such smart materials can be reflected by a precise regulation of the release and binding of growth factors, which promotes the production of cell instructive matrices with tissue healing and regeneration functions, and contributes to the *in situ* vascularization of tissue repair. To improve the mechanical properties of the bionic bone tissue, one could consider a combinatorial approach of the enhancement strategies reviewed here: their synergistic effects warrant some in-depth investigations.

CONCLUSION

Designing novel bioink formulations, in conjunction with using 4D bioprinting technology, to fabricate a scaffold with desired properties such as environmental sensitivity have shown significant progress and great potential. However, the complexity of the process, technique, and materials involved in reconstructing a defective bone tissue remain a challenging task. In this review, various requirements of the bioink/scaffold used for bone regeneration have been systematically discussed, and complemented with exemplar studies. The mismatched characteristics offered by the hydrogels used in the repair of hard tissues will certainly prompt the research communities to develop new solutions based on the existing reinforcement technologies. It is highly desirable to construct scaffolds replicating natural tissues in the ability of stem cell proliferation and differentiation, biomimetic material degradation, matrix remodeling, etc. Adding suitable smart materials to the bioink formulations could open up new opportunities to trigger shape transformation and adjust the aforementioned factors under specific environmental changes.

AUTHOR CONTRIBUTIONS

NL drafted the original manuscript with contributions by RG and ZZ. NL and ZZ contributed to the revision of the draft. ZZ and RG contributed to the supervision, validation, and funding acquisition. All authors contributed to the article and approved the submitted version.

FUNDING

The authors are grateful for the financial support by the Guangzhou Municipal Government. This study was supported financially by the Science and Technology Program of Guangzhou (Grant No. 201907010032), and the International Science and Technology Cooperation Project of Huangpu District/Guangzhou Development District (Grant No. 2019GH11). ZZ acknowledge the financial support by the Medical Research Council (MR/S000542/1) and Engineering & Physical Science Research Council (EP/P007864/1). NL was grateful to the China Scholarship Council for an Overseas Scholarship.

REFERENCES

Ahlfeld, T., Doberenz, F., Kilian, D., Vater, C., Korn, P., Lauer, G., et al. (2018). Bioprinting of mineralized constructs utilizing multichannel plotting of a self-setting calcium phosphate cement and a cell-laden bioink. *Biofabrication* 10:045002. doi: 10.1088/1758-5090/aad36d

Altomare, L., Bonetti, L., Campiglio, C. E., De Nardo, L., Draghi, L., Tana, F., et al. (2018). Biopolymer-based strategies in the design of smart medical devices and artificial organs. *Int. J. Artif. Organs* 41, 337–359. doi: 10.1177/0391398818765323

Anjum, F., Lienemann, P. S., Metzger, S., Biernaskie, J., Kallos, M. S., and Ehrbar, M. (2016). Enzyme responsive GAG-based natural-synthetic hybrid hydrogel for tunable growth factor delivery and stem cell differentiation. *Biomaterials* 87, 104–117. doi: 10.1016/j.biomaterials.2016.01.050

Ashammakhi, N., Ahadian, S., Zengjie, F., Suthiwanich, K., Lorestani, F., Orive, G., et al. (2018). Advances and future perspectives in 4D bioprinting. *Biotechnol. J.* 13:1800148. doi: 10.1002/biot.201800148

Bailey, B. M., Fei, R., Munoz-Pinto, D., Hahn, M. S., and Grunlan, M. A. (2012). PDMSstar–PEG hydrogels prepared via solvent-induced phase separation (SIPS) and their potential utility as tissue engineering scaffolds. *Acta Biomater.* 8, 4324–4333. doi: 10.1016/j.actbio.2012.07.034

Boere, K. W. M., Visser, J., Seyednejad, H., Rahimian, S., Gawlitta, D., van Steenbergen, M. J., et al. (2014). Covalent attachment of a three-dimensionally printed thermoplast to a gelatin hydrogel for mechanically enhanced cartilage constructs. *Acta Biomater.* 10, 2602–2611. doi: 10.1016/j.actbio.2014.02.041

Bracaglia, L. G., Smith, B. T., Watson, E., Arumugasaamy, N., Mikos, A. G., and Fisher, J. P. (2017). 3D printing for the design and fabrication of polymer-based gradient scaffolds. *Acta Biomater.* 56, 3–13. doi: 10.1016/j.actbio.2017.03.030

Cengiz, N., Gevrek, T., Sanyal, R., and Sanyal, A. (2017). Orthogonal thiol–ene 'click' reactions: a powerful combination for fabrication and functionalization of patterned hydrogels. *Chem. Commun.* 53, 8894–8897. doi: 10.1039/C7CC02298K

Chang, C. C., Boland, E. D., Williams, S. K., and Hoying, J. B. (2011). Direct-write bioprinting three-dimensional biohybrid systems for future regenerative therapies. *J. Biomed. Mater. Res. B* 98, 160–170. doi: 10.1002/jbm.b.31831

Chen, L., Yang, K., Zhao, H., Liu, A., Tu, W., Wu, C., et al. (2019). Biomineralized hydrogel with enhanced toughness by chemical bonding of alkaline phosphatase and vinylphosphonic acid in collagen framework. *ACS Biomater. Sci. Eng.* 5, 1405–1415. doi: 10.1021/acsbiomaterials.8b01197

Chiarello, E., Cadossi, M., Tedesco, G., Capra, P., Calamelli, C., Shehu, A., et al. (2013). Autograft, allograft and bone substitutes in reconstructive orthopedic surgery. *Aging Clin. Exp. Res.* 25, 101–103. doi: 10.1007/s40520-013-0088-8

Chimene, D., Alge, D. L., and Gaharwar, A. K. (2015). Two-dimensional nanomaterials for biomedical applications: emerging trends and future prospects. *Adv. Mater*. 27, 7261–7284. doi: 10.1002/adma.201502422

Chimene, D., Kaunas, R., and Gaharwar, A. K. (2020a). Hydrogel bioink reinforcement for additive manufacturing: a focused review of emerging strategies. *Adv. Mater*. 32:1902026. doi: 10.1002/adma.201902026

Chimene, D., Miller, L., Cross, L., Jaiswal, M. K., Singh, I., and Gaharwar, A. K. (2020b). Nanoengineered osteoinductive bioink for 3D bioprinting bone tissue. *ACS Appl. Mater. Interfaces* 12:14. doi: 10.1021/acsami.9b19037

Chimene, D., Peak, C. W., Gentry, J. L., Carrow, J. K., Cross, L. M., Mondragon, E., et al. (2018). Nanoengineered Ionic–Covalent Entanglement (NICE) bioinks for 3D bioprinting. *ACS Appl. Mater. Interfaces* 10, 9957–9968. doi: 10.1021/acsami.7b19808

Chiu, Y.-C., Larson, J. C., Isom, A., and Brey, E. M. (2009). Generation of porous poly(Ethylene Glycol) hydrogels by salt leaching. *Tissue Eng. C* 16, 905–912. doi: 10.1089/ten.tec.2009.0646

Chocholata, P., Kulda, V., and Babuska, V. (2019). Fabrication of scaffolds for bone-tissue regeneration. *Materials (Basel)* 12:568. doi: 10.3390/ma12040568

Cui, X., Boland, T., DD'Lima, D. K., and Lotz, M. (2012). Thermal inkjet printing in tissue engineering and regenerative medicine. *Recent Pat. Drug Delivery Formulation* 6, 149–155. doi: 10.2174/187221112800672949

Cui, X., Dean, D., Ruggeri, Z. M., and Boland, T. (2010). Cell damage evaluation of thermal inkjet printed Chinese hamster ovary cells. *Biotechnol. Bioeng.* 106, 963–969. doi: 10.1002/bit.22762

Curvello, R., Raghuwanshi, V. S., and Garnier, G. (2019). Engineering nanocellulose hydrogels for biomedical applications. *Adv. Colloid Interface Sci.* 267, 47–61. doi: 10.1016/j.cis.2019.03.002

Dai, S., Ravi, P., and Tam, K. C. (2008). pH-Responsive polymers: synthesis, properties and applications. *Soft Matter* 4, 435–449. doi: 10.1039/b714741d

Daly, A. C., and Kelly, D. J. (2019). Biofabrication of spatially organised tissues by directing the growth of cellular spheroids within 3D printed polymeric microchambers. *Biomaterials* 197, 194–206. doi: 10.1016/j.biomaterials.2018.12.028

Datta, P., Ozbolat, V., Ayan, B., Dhawan, A., and Ozbolat, I. T. (2017). Bone tissue bioprinting for craniofacial reconstruction. *Biotechnol. Bioeng.* 114, 2424–2431. doi: 10.1002/bit.26349

Day, R. M., Boccaccini, A. R., Shurey, S., Roether, J. A., Forbes, A., Hench, L. L., et al. (2004). Assessment of polyglycolic acid mesh and bioactive glass for soft-tissue engineering scaffolds. *Biomaterials* 25, 5857–5866. doi: 10.1016/j.biomaterials.2004.01.043

De Jong, J., De Bruin, G., Reinten, H., Van den Berg, M., Wijshoff, H., Versluis, M., et al. (2006). Air entrapment in piezo-driven inkjet printheads. *J. Acoust. Soc. Am.* 120, 1257–1265. doi: 10.1121/1.2216560

Dong, Z., Li, Y., and Zou, Q. (2009). Degradation and biocompatibility of porous nano-hydroxyapatite/polyurethane composite scaffold for bone tissue engineering. *Appl. Surf. Sci.* 255, 6087–6091. doi: 10.1016/j.apsusc.2009.01.083

Dutta, R. C., and Dutta, A. K. (2010). Comprehension of ECM-Cell dynamics: a prerequisite for tissue regeneration. *Biotechnol. Adv.* 28, 764–769. doi: 10.1016/j.biotechadv.2010.06.002

Fang, Y., Frampton, J. P., Raghavan, S., Sabahi-Kaviani, R., Luker, G., Deng, C. X., et al. (2012). Rapid generation of multiplexed cell cocultures using acoustic droplet ejection followed by aqueous two-phase exclusion patterning. *Tissue Eng. C* 18, 647–657. doi: 10.1089/ten.tec.2011.0709

Fathi-Achachelouei, M., Knopf-Marques, H., Ribeiro da Silva, C. E., Barthès, J., Bat, E., Tezcaner, A., et al. (2019). Use of nanoparticles in tissue engineering and regenerative medicine. *Front. Bioeng. Biotechnol.* 7:113. doi: 10.3389/fbioe.2019.00113

Feng, Z., Wang, D., Zheng, Y., Zhao, L., Xu, T., Guo, Z., et al. (2020). A novel waterborne polyurethane with biodegradability and high flexibility for 3D printing. *Biofabrication* 12:035015. doi: 10.1088/1758-5090/ab7de0

Fuchs, S., Shariati, K., and Ma, M. (2019). Specialty tough hydrogels and their biomedical applications. *Adv. Healthcare Mater.* 9:1901396. doi: 10.1002/adhm.201901396

Gao, B., Yang, Q., Zhao, X., Jin, G., Ma, Y., and Xu, F. (2016). 4D bioprinting for biomedical applications. *Trends Biotechnol.* 34, 746–756. doi: 10.1016/j.tibtech.2016.03.004

Gao, Y., and Jin, X. (2019). Dual crosslinked methacrylated alginate hydrogel micron fibers and tissue constructs for cell biology. *Mar. Drugs* 17:557. doi: 10.3390/md17100557

Gibson, L. J. (1985). The mechanical behaviour of cancellous bone. *J. Biomech.* 18, 317–328. doi: 10.1016/0021-9290(85)90287-8

Gomes, T. C., Constantino, C. J. L., Lopes, E. M., Job, A. E., and Alves, N. (2012). Thermal inkjet printing of polyaniline on paper. *Thin Solid Films* 520, 7200–7204. doi: 10.1016/j.tsf.2012.07.119

Gong, J. P. (2010). Why are double network hydrogels so tough? *Soft Matter* 6, 2583–2590. doi: 10.1039/b924290b

Guillemot, F., Guillotin, B., Fontaine, A., Ali, M., Catros, S., Kériquel, V., et al. (2011). Laser-assisted bioprinting to deal with tissue complexity in regenerative medicine. *MRS Bull.* 36, 1015–1019. doi: 10.1557/mrs.2011.272

Guillemot, F., Souquet, A., Catros, S., Guillotin, B., Lopez, J., Faucon, M., et al. (2010). High-throughput laser printing of cells and biomaterials for tissue engineering. *Acta Biomater.* 6, 2494–2500. doi: 10.1016/j.actbio.2009.09.029

Haider, A., Haider, S., Rao Kummara, M., Kamal, T., Alghyamah, A.-A. A., Jan Iftikhar, F., et al. (2020). Advances in the scaffolds fabrication techniques using biocompatible polymers and their biomedical application: a technical and statistical review. *J. Saudi Chem. Soc.* 24, 186–215. doi: 10.1016/j.jscs.2020.01.002

Hasan, A., Morshed, M., Memic, A., Hassan, S., Webster, T. J., and Marei, H. E.-S. (2018). Nanoparticles in tissue engineering: applications, challenges and prospects. *Int. J. Nanomed.* 13, 5637–5655. doi: 10.2147/IJN.S153758

He, D., Zhao, A. S., Su, H., Zhang, Y., Wang, Y. N., Luo, D., et al. (2019). An injectable scaffold based on temperature-responsive hydrogel and factor-loaded nanoparticles for application in vascularization in tissue engineering. *J. Biomed. Mater. Res. A* 107, 2123–2134. doi: 10.1002/jbm.a.36723

He, X., Fan, X., Feng, W., Chen, Y., Guo, T., Wang, F., et al. (2018). Incorporation of microfibrillated cellulose into collagen-hydroxyapatite scaffold for bone tissue engineering. *Int. J. Biol. Macromol.* 115, 385–392. doi: 10.1016/j.ijbiomac.2018.04.085

Hoornaert, A., Vidal, L., Besnier, R., Morlock, J.-F., Louarn, G., and Layrolle, P. (2020). Biocompatibility and osseointegration of nanostructured titanium dental implants in minipigs. *Clin. Oral. Impl. Res.* 31, 526–535. doi: 10.1111/clr.13589

Jakab, K., Damon, B., Neagu, A., Kachurin, A., and Forgacs, G. (2006). Three-dimensional tissue constructs built by bioprinting. *Biorheology* 43, 509–513.

Jakus, A. E., Rutz, A. L., and Shah, R. N. (2016). Advancing the field of 3D biomaterial printing. *Biomed. Mater.* 11:014102. doi: 10.1088/1748-6041/11/1/014102

Jin, Y., Yu, C., Denman, R. J., and Zhang, W. (2013). Recent advances in dynamic covalent chemistry. *Chem. Soc. Rev.* 42, 6634–6654. doi: 10.1039/c3cs60044k

Jones, N. (2012). Science in three dimensions: the print revolution. *Nature* 487, 22–23. doi: 10.1038/487022a

Kang, H.-W., Lee, S. J., Ko, I. K., Kengla, C., Yoo, J. J., and Atala, A. (2016). A 3D bioprinting system to produce human-scale tissue constructs with structural integrity. *Nat. Biotechnol.* 34, 312–319. doi: 10.1038/nbt.3413

Kashte, S., Jaiswal, A. K., and Kadam, S. (2017). Artificial bone via bone tissue engineering: current scenario and challenges. *Tissue Eng. Regener. Med.* 14, 1–14. doi: 10.1007/s13770-016-0001-6

Khoo, Z. X., Teoh, J. E. M., Liu, Y., Chua, C. K., Yang, S., An, J., et al. (2015). 3D printing of smart materials: a review on recent progresses in 4D printing. *Virtual Phys. Prototyp.* 10, 103–122. doi: 10.1080/17452759.2015.1097054

Kim, B. S., Jang, J., Chae, S., Gao, G., Kong, J.-S., Ahn, M., et al. (2016). Three-dimensional bioprinting of cell-laden constructs with polycaprolactone protective layers for using various thermoplastic polymers. *Biofabrication* 8:035013. doi: 10.1088/1758-5090/8/3/035013

Kim, M. K., Jeong, W., Lee, S. M., Kim, J. B., Jin, S., and Kang, H.-W. (2020). Decellularized extracellular matrix-based bio-ink with enhanced 3D printability and mechanical properties. *Biofabrication* 12:025003. doi: 10.1088/1758-5090/ab5d80

Kim, S. H., Seo, Y. B., Yeon, Y. K., Lee, Y. J., Park, H. S., Sultan, M. T., et al. (2020). 4D-bioprinted silk hydrogels for tissue engineering. *Biomaterials* 260:120281. doi: 10.1016/j.biomaterials.2020.120281

Koetting, M. C., Peters, J. T., Steichen, S. D., and Peppas, N. A. (2015). Stimulus-responsive hydrogels: theory, modern advances, and applications. *Mater. Sci. Eng.* 93, 1–49. doi: 10.1016/j.mser.2015.04.001

Krishnakumar, G. S., Sampath, S., Muthusamy, S., and John, M. A. (2019). Importance of crosslinking strategies in designing smart biomaterials for bone tissue engineering: a systematic review. *Mater. Sci. Eng. C* 96, 941–954. doi: 10.1016/j.msec.2018.11.081

Lamers, E., Frank Walboomers, X., Domanski, M., te Riet, J., van Delft, F. C. M. J.M., Luttge, R., et al. (2010). The influence of nanoscale grooved substrates on osteoblast behavior and extracellular matrix deposition. *Biomaterials* 31, 3307–3316. doi: 10.1016/j.biomaterials.2010.01.034

Lee, H., Ahn, S., Bonassar, L. J., and Kim, G. (2013). Cell(MC3T3-E1)-printed poly(ϵ-caprolactone)/alginate hybrid scaffolds for tissue regeneration. *Macromol. Rapid Commun.* 34, 142–149. doi: 10.1002/marc.201200524

Lee, V. K., Kim, D. Y., Ngo, H., Lee, Y., Seo, L., Yoo, S.-S., et al. (2014). Creating perfused functional vascular channels using 3D bio-printing technology. *Biomaterials* 35, 8092–8102. doi: 10.1016/j.biomaterials.2014.05.083

Li, X., Wang, H., Li, D., Long, S., Zhang, G., and Wu, Z. (2018). Dual ionically cross-linked double-network hydrogels with high strength, toughness, swelling resistance, and improved 3D printing processability. *ACS Appl. Mater. Interfaces* 10, 31198–31207. doi: 10.1021/acsami.8b13038

Li, Y.-C., Zhang, Y. S., Akpek, A., Shin, S. R., and Khademhosseini, A. (2016). 4D bioprinting: the next-generation technology for biofabrication enabled by stimuli-responsive materials. *Biofabrication* 9:012001. doi: 10.1088/1758-5090/9/1/012001

Liu, H., Du, Y., Yang, G., Hu, X., Wang, L., Liu, B., et al. (2020). Delivering proangiogenic factors from 3D-printed polycaprolactone scaffolds for vascularized bone regeneration. *Adv. Healthcare Mater.* 9:2000727. doi: 10.1002/adhm.202000727

Liu, K., Zang, S., Xue, R., Yang, J., Wang, L., Huang, J., et al. (2018). Coordination-triggered hierarchical folate/zinc supramolecular hydrogels leading to printable biomaterials. *ACS Appl. Mater. Interfaces* 10, 4530–4539. doi: 10.1021/acsami.7b18155

Loebel, C., Rodell, C. B., Chen, M. H., and Burdick, J. A. (2017). Shear-thinning and self-healing hydrogels as injectable therapeutics and for 3D-printing. *Nat. Protoc.* 12, 1521–1541. doi: 10.1038/nprot.2017.053

Lowe, A. B. (2010). Thiol-ene "click" reactions and recent applications in polymer and materials synthesis. *Polym. Chem.* 1, 17–36. doi: 10.1039/B9PY00216B

Lu, J., Zhu, W., Dai, L., Si, C., and Ni, Y. (2019). Fabrication of thermo-and pH-sensitive cellulose nanofibrils-reinforced hydrogel with biomass nanoparticles. *Carbohydr. Polym.* 215, 289–295. doi: 10.1016/j.carbpol.2019.03.100

Lui, Y. S., Sow, W. T., Tan, L. P., Wu, Y., Lai, Y., and Li, H. (2019). 4D printing and stimuli-responsive materials in biomedical aspects. *Acta Biomater.* 92, 19–36. doi: 10.1016/j.actbio.2019.05.005

Luo, Y., Lin, X., Chen, B., and Wei, X. (2019). Cell-laden four-dimensional bioprinting using near-infrared-triggered shape-morphing alginate/polydopamine bioinks. *Biofabrication* 11:045019. doi: 10.1088/1758-5090/ab39c5

Mann, J. L., Anthony, C. Y., Agmon, G., and Appel, E. A. (2018). Supramolecular polymeric biomaterials. *Biomater. Sci.* 6, 10–37. doi: 10.1039/C7BM00780A

Mihaila, S. M., Gaharwar, A. K., Reis, R. L., Marques, A. P., Gomes, M. E., and Khademhosseini, A. (2013). Photocrosslinkable kappa-carrageenan hydrogels for tissue engineering applications. *Adv. Healthcare Mater.* 2, 895–907. doi: 10.1002/adhm.201200317

Moran, J. M., Pazzano, D., and Bonassar, L. J. (2003). Characterization of polylactic acid–polyglycolic acid composites for cartilage tissue engineering. *Tissue Eng.* 9, 63–70. doi: 10.1089/107632703762687546

Morgan, F. L. C., Moroni, L., and Baker, M. B. (2020). Dynamic bioinks to advance bioprinting. *Adv. Healthcare Mater.* 9:1901798. doi: 10.1002/adhm.201901798

Murphy, C., Kolan, K., Li, W., Semon, J., Day, D., and Leu, M. (2017). 3D bioprinting of stem cells and polymer/bioactive glass composite scaffolds for bone tissue engineering. *Int. J. Bioprint* 3, 54–64. doi: 10.18063/IJB.2017.01.005

Murphy, C. M., Haugh, M. G., and O'brien, F. J. (2010). The effect of mean pore size on cell attachment, proliferation and migration in collagen–glycosaminoglycan scaffolds for bone tissue engineering. *Biomaterials* 31, 461–466. doi: 10.1016/j.biomaterials.2009.09.063

Murphy, S. V., and Atala, A. (2014). 3D bioprinting of tissues and organs. *Nat. Biotechnol.* 32, 773–785. doi: 10.1038/nbt.2958

Murphy, S. V., Skardal, A., and Atala, A. (2013). Evaluation of hydrogels for bio-printing applications. *J. Biomed. Mater. Res. A* 101, 272–284. doi: 10.1002/jbm.a.34326

Nakamura, M., Kobayashi, A., Takagi, F., Watanabe, A., Hiruma, Y., Ohuchi, K., et al. (2005). Biocompatible inkjet printing technique for designed seeding of individual living cells. *Tissue Eng.* 11, 1658–1666. doi: 10.1089/ten.2005.11.1658

Nicolas, J., Magli, S., Rabbachin, L., Sampaolesi, S., Nicotra, F., and Russo, L. (2020). 3D extracellular matrix mimics: fundamental concepts and role of materials chemistry to influence stem cell fate. *Biomacromolecules* 6, 1968–1994. doi: 10.1021/acs.biomac.0c00045

Ong, C. S., Nam, L., Ong, K., Krishnan, A., Huang, C. Y., Fukunishi, T., et al. (2018). 3D and 4D bioprinting of the myocardium: current approaches, challenges, and future prospects. *Biomed Res. Int.* 2018:6497242. doi: 10.1155/2018/6497242

Ozbolat, I., and Gudapati, H. (2016). A review on design for bioprinting. *Bioprinting* 3, 1–14. doi: 10.1016/j.bprint.2016.11.001

Park, J. Y., Choi, J.-C., Shim, J.-H., Lee, J.-S., Park, H., Kim, S. W., et al. (2014). A comparative study on collagen type I and hyaluronic acid dependent cell behavior for osteochondral tissue bioprinting. *Biofabrication* 6:035004. doi: 10.1088/1758-5082/6/3/035004

Park, S., Park, J., Jo, I., Cho, S. P., Sung, D., Ryu, S., et al. (2015). In situ hybridization of carbon nanotubes with bacterial cellulose for three-dimensional hybrid bioscaffolds. *Biomaterials* 58, 93–102. doi: 10.1016/j.biomaterials.2015.04.027

Pati, F., Jang, J., Ha, D.-H., Kim, S. W., Rhie, J.-W., Shim, J.-H., et al. (2014). Printing three-dimensional tissue analogues with decellularized extracellular matrix bioink. *Nat. Commun.* 5, 1–11. doi: 10.1038/ncomms4935

Pereira, R. F., Sousa, A., Barrias, C. C., Bártolo, P. J., and Granja, P. L. (2018). A single-component hydrogel bioink for bioprinting of bioengineered 3D constructs for dermal tissue engineering. *Mater. Horiz.* 5, 1100–1111. doi: 10.1039/C8MH00525G

Qu, H., Fu, H., Han, Z., and Sun, Y. (2019). Biomaterials for bone tissue engineering scaffolds: a review. *RSC Adv.* 9, 26252–26262. doi: 10.1039/C9RA05214C

Raeisdasteh Hokmabad, V., Davaran, S., Ramazani, A., and Salehi, R. (2017). Design and fabrication of porous biodegradable scaffolds: a strategy for tissue engineering. *J. Biomater. Sci.* 28, 1797–1825. doi: 10.1080/09205063.2017.1354674

Rastin, H., Ormsby, R. T., Atkins, G. J., and Losic, D. (2020). 3D bioprinting of Methylcellulose/Gelatin-Methacryloyl (MC/GelMA) bioink with high shape integrity. *ACS Appl. Bio Mater.* 3, 1815–1826. doi: 10.1021/acsabm.0c00169

Rastogi, P., and Kandasubramanian, B. (2019). Review of alginate-based hydrogel bioprinting for application in tissue engineering. *Biofabrication* 11:042001. doi: 10.1088/1758-5090/ab331e

Ratheesh, G., Vaquette, C., and Xiao, Y. (2020). Patient-specific bone particles bioprinting for bone tissue engineering. *Adv. Healthcare Mater.* 9:2001323. doi: 10.1002/adhm.202001323

Rosales, A. M., and Anseth, K. S. (2016). The design of reversible hydrogels to capture extracellular matrix dynamics. *Nat. Rev. Mater.* 1, 1–15. doi: 10.1038/natrevmats.2015.12

Rouwkema, J., Rivron, N. C., and van Blitterswijk, C. A. (2008). Vascularization in tissue engineering. *Trends Biotechnol.* 26, 434–441. doi: 10.1016/j.tibtech.2008.04.009

Rutz, A. L., Hyland, K. E., Jakus, A. E., Burghardt, W. R., and Shah, R. N. (2015). A multimaterial bioink method for 3D printing tunable, cell-compatible hydrogels. *Adv. Mater. Weinheim.* 27, 1607–1614. doi: 10.1002/adma.201405076

Sabir, M. I., Xu, X., and Li, L. (2009). A review on biodegradable polymeric materials for bone tissue engineering applications. *J. Mater. Sci.* 44, 5713–5724. doi: 10.1007/s10853-009-3770-7

Sakai, T., Matsunaga, T., Yamamoto, Y., Ito, C., Yoshida, R., Suzuki, S., et al. (2008). Design and fabrication of a high-strength hydrogel with ideally homogeneous network structure from tetrahedron-like macromonomers. *Macromolecules* 41, 5379–5384. doi: 10.1021/ma800476x

Santos, M. I., and Reis, R. L. (2010). Vascularization in bone tissue engineering: physiology, current strategies, major hurdles and future challenges. *Macromol. Biosci.* 10, 12–27. doi: 10.1002/mabi.200900107

Saunders, R. E., Gough, J. E., and Derby, B. (2008). Delivery of human fibroblast cells by piezoelectric drop-on-demand inkjet printing. *Biomaterials* 29, 193–203. doi: 10.1016/j.biomaterials.2007.09.032

Schuurman, W., Khristov, V., Pot, M. W., van Weeren, P. R., Dhert, W. J., and Malda, J. (2011). Bioprinting of hybrid tissue constructs with tailorable mechanical properties. *Biofabrication* 3:021001. doi: 10.1088/1758-5082/3/2/021001

Shin, M., Galarraga, J. H., Kwon, M. Y., Lee, H., and Burdick, J. A. (2019). Gallol-derived ECM-mimetic adhesive bioinks exhibiting temporal shear-thinning and stabilization behavior. *Acta Biomater.* 95, 165–175. doi: 10.1016/j.actbio.2018.10.028

Skardal, A., Zhang, J., McCoard, L., Oottamasathien, S., and Prestwich, G. D. (2010a). Dynamically crosslinked gold nanoparticle–hyaluronan hydrogels. *Adv. Mater. Weinheim.* 22, 4736–4740. doi: 10.1002/adma.201001436

Skardal, A., Zhang, J., McCoard, L., Xu, X., Oottamasathien, S., and Prestwich, G. D. (2010b). Photocrosslinkable hyaluronan-gelatin hydrogels for two-step bioprinting. *Tissue Eng. A* 16, 2675–2685. doi: 10.1089/ten.tea.2009.0798

Sydney Gladman, A., Matsumoto, E. A., Nuzzo, R. G., Mahadevan, L., and Lewis, J. A. (2016). Biomimetic 4D printing. *Nature Mater.* 15, 413–418. doi: 10.1038/nmat4544

Tang, J., Tong, Z., Xia, Y., Liu, M., Lv, Z., Gao, Y., et al. (2018). Super tough magnetic hydrogels for remotely triggered shape morphing. *J. Mater. Chem. B* 6, 2713–2722. doi: 10.1039/C8TB00568K

Thorvaldsson, A., Silva-Correia, J., Oliveira, J. M., Reis, R. L., Gatenholm, P., and Walkenström, P. (2013). Development of nanofiber-reinforced hydrogel scaffolds for nucleus pulposus regeneration by a combination of electrospinning and spraying technique. *J. Appl. Polym. Sci.* 128, 1158–1163. doi: 10.1002/app.38316

Van De Vijfeijken, S. E., Münker, T. J., Spijker, R., Karssemakers, L. H., Vandertop, W. P., Becking, A. G., et al. (2018). Autologous bone is inferior to alloplastic cranioplasties: safety of autograft and allograft materials for cranioplasties, a systematic review. *World Neurosurg.* 117, 443–452. doi: 10.1016/j.wneu.2018.05.193

Vidal, L., Kampleitner, C., Brennan, M. Á., Hoornaert, A., and Layrolle, P. (2020). Reconstruction of large skeletal defects: current clinical therapeutic strategies and future directions using 3D printing. *Front. Bioeng. Biotech.* 8:61. doi: 10.3389/fbioe.2020.00061

Visser, J., Peters, B., Burger, T. J., Boomstra, J., Dhert, W. J., Melchels, F. P., et al. (2013). Biofabrication of multi-material anatomically shaped tissue constructs. *Biofabrication* 5:035007. doi: 10.1088/1758-5082/5/3/035007

Wan, Z., Zhang, P., Liu, Y., Lv, L., and Zhou, Y. (2019). Four-dimensional bioprinting: current developments and applications in bone tissue engineering. *Acta Biomater.* 101, 26–42. doi: 10.2139/ssrn.3423498

Wang, L. L., Highley, C. B., Yeh, Y.-C., Galarraga, J. H., Uman, S., and Burdick, J. A. (2018). Three-dimensional extrusion bioprinting of single- and double-network hydrogels containing dynamic covalent crosslinks. *J. Biomed. Mater. Res. A* 106, 865–875. doi: 10.1002/jbm.a.36323

Wang, M., Favi, P., Cheng, X., Golshan, N. H., Ziemer, K. S., Keidar, M., et al. (2016). Cold atmospheric plasma (CAP) surface nanomodified 3D printed polylactic acid (PLA) scaffolds for bone regeneration. *Acta Biomater.* 46, 256–265. doi: 10.1016/j.actbio.2016.09.030

Webber, M. J., Appel, E. A., Meijer, E. W., and Langer, R. (2016). Supramolecular biomaterials. *Nat. Mater.* 15, 13–26. doi: 10.1038/nmat4474

Williams, D. F. (2008). On the mechanisms of biocompatibility. *Biomaterials* 29, 2941–2953. doi: 10.1016/j.biomaterials.2008.04.023

Wu, X., Liu, Y., Li, X., Wen, P., Zhang, Y., Long, Y., et al. (2010). Preparation of aligned porous gelatin scaffolds by unidirectional freeze-drying method. *Acta Biomater.* 6, 1167–1177. doi: 10.1016/j.actbio.2009.08.041

Xu, T., Kincaid, H., Atala, A., and Yoo, J. J. (2008). High-throughput production of single-cell microparticles using an inkjet printing technology. *J. Manufact. Sci. Eng.* 130:021017. doi: 10.1115/1.2903064

Yang, G. H., Yeo, M., Koo, Y. W., and Kim, G. H. (2019). 4D bioprinting: technological advances in biofabrication. *Macromol. Biosci.* 19:1800441. doi: 10.1002/mabi.201800441

Yang, H., Li, C., Yang, M., Pan, Y., Yin, Q., Tang, J., et al. (2019). Printing hydrogels and elastomers in arbitrary sequence with strong adhesion. *Adv. Funct. Mater.* 29:1901721. doi: 10.1002/adfm.201901721

Yigit, S., Sanyal, R., and Sanyal, A. (2011). Fabrication and functionalization of hydrogels through "click" chemistry. *Chem. Asian J.* 6, 2648–2659. doi: 10.1002/asia.201100440

Yin, J., Yan, M., Wang, Y., Fu, J., and Suo, H. (2018). 3D Bioprinting of low-concentration cell-laden gelatin methacrylate (GelMA) bioinks with a two-step cross-linking strategy. *ACS Appl. Mater. Interfaces* 10, 6849–6857. doi: 10.1021/acsami.7b16059

Zhalmuratova, D., and Chung, H.-J. (2020). Reinforced gels and elastomers for biomedical and soft robotics applications. *ACS Appl. Polym. Mater.* 2, 1073–1091. doi: 10.1021/acsapm.9b01078

Zhang, K., Wang, S., Zhou, C., Cheng, L., Gao, X., Xie, X., et al. (2018). Advanced smart biomaterials and constructs for hard tissue engineering and regeneration. *Bone Res.* 6, 1–15. doi: 10.1038/s41413-018-0032-9

Zhang, L., Morsi, Y., Wang, Y., Li, Y., and Ramakrishna, S. (2013). Review scaffold design and stem cells for tooth regeneration. *Jpn. Dent. Sci. Rev.* 49, 14–26. doi: 10.1016/j.jdsr.2012.09.001

Zhang, X.-Y., Fang, G., and Zhou, J. (2017). Additively manufactured scaffolds for bone tissue engineering and the prediction of their mechanical behavior: a review. *Materials* 10:50. doi: 10.3390/ma10010050

Zhao, X. (2014). Multi-scale multi-mechanism design of tough hydrogels: building dissipation into stretchy networks. *Soft Matter* 10, 672–687. doi: 10.1039/C3SM52272E

Zheng, S. Y., Ding, H., Qian, J., Yin, J., Wu, Z. L., Song, Y., et al. (2016). Metal-coordination complexes mediated physical hydrogels with high toughness, stick–slip tearing behavior, and good processability. *Macromolecules* 49, 9637–9646. doi: 10.1021/acs.macromol.6b02150

Zhou, S., Bismarck, A., and Steinke, J. H. (2013). Ion-responsive alginate based macroporous injectable hydrogel scaffolds prepared by emulsion templating. *J. Mater. Chem. B* 1, 4736–4745. doi: 10.1039/c3tb20888e

Conflict of Interest: The authors declare that the research was conducted in the absence of any commercial or financial relationships that could be construed as a potential conflict of interest.

frontiers
in Bioengineering and Biotechnology

MINI REVIEW
published: 09 February 2021
doi: 10.3389/fbioe.2021.591796

Dental Implants Loaded With Bioactive Agents Promote Osseointegration in Osteoporosis: A Review

Cheng Zhang[1]†, Tianjia Zhang[3]†, Tengyu Geng[2], Xudong Wang[3], Kaili Lin[3]* and Penglai Wang[1,2]*

[1] School of Stomatology, Xuzhou Medical University, Xuzhou, China, [2] Affiliated Stomatological Hospital of Xuzhou Medical University, Xuzhou, China, [3] Department of Oral & Cranio-Maxillofacial Surgery, Shanghai Ninth People's Hospital, Shanghai Jiao Tong University School of Medicine, Shanghai Key Laboratory of Stomatology, Shanghai Research Institute of Stomatology, Shanghai, China

Implant-supported dentures are widely used in patients with defect or loss of dentition because these have higher chewing efficiency and do not damage the adjacent teeth compared with fixed or removable denture. An implant-supported denture carries the risk of failure in some systemic diseases, including osteoporosis, because of a non-ideal local microenvironment. Clinically common physical and chemical modifications are used to change the roughness of the implant surface to promote osseointegration, but they have limitations in promoting osteoinduction and inhibiting bone resorption. Recently, many researchers have focused on the study of bioactive modification of implants and have achieved promising results. Herein we have summarized the progress in bioactive modification strategy to promote osseointegration by regulating the local osteoporotic microenvironment.

Keywords: dental implants, bioactive agents, osseointegration, osteoporosis, controlled release

INTRODUCTION

With innovations in implant design and surgery technology, the applicable conditions of implant surgery have become more extensive, and the 10-year survival rate of an implant-supported denture has exceeded 95% (Buser et al., 2017). There is a risk of failure in a number of systemic diseases (Liu et al., 2020), including osteoporosis, because the severe decrease in bone mass and alteration of trabecular bone microstructure affect the initial stability and osseointegration of the implants.

Currently, the common sand blasting and acid etching strategy is used to increase the surface roughness of implants, which enhances adhesion, proliferation, and differentiation of mesenchymal stem cells (Zhang et al., 2020; Zhao et al., 2020). In addition to the implant design, it is necessary to promote osteoinduction and inhibit bone resorption locally in osteoporotic patients (Lin et al., 2013). Systemic administration orally or intravenously provides low bioavailability, which makes it difficult to maintain an effective concentration around the implants and might cause severe side effects, such as necrosis of the jaw bone (Eguia et al., 2020). Local administration ensures adequate drug concentration in the target tissue and reduces toxicity in the non-target areas. Hence, it is necessary to biologically modify the implants for loading bioactive agents, such as anti-osteoporosis drugs, bioactive molecules, or bioactive inorganic elements, onto the implant surface. In addition, to avoid burst release in a short time, it is critical to take optimal approaches to optimize the locally

Edited by:
Gang Wu,
Vrije Universiteit Amsterdam,
Netherlands

Reviewed by:
Monica Mattioli-Belmonte,
Marche Polytechnic University, Italy
Zhongru Gou,
Zhejiang University, China
Jianmin Yang,
Fuzhou University, China
Changchun Zhou,
Sichuan University, China

***Correspondence:**
Kaili Lin
lklecnu@aliyun.com;
linkaili@tongji.edu.cn
Penglai Wang
wpl0771@qq.com

†These authors have contributed equally to this work

Specialty section:
This article was submitted to Biomaterials,
a section of the journal Frontiers in Bioengineering and Biotechnology

Received: 05 August 2020
Accepted: 04 January 2021
Published: 09 February 2021

Citation:
Zhang C, Zhang T, Geng T, Wang X, Lin K and Wang P (2021) Dental Implants Loaded With Bioactive Agents Promote Osseointegration in Osteoporosis: A Review.
Front. Bioeng. Biotechnol. 9:591796.
doi: 10.3389/fbioe.2021.591796

controlled release of bioactive agents and maintain an effective concentration. Herein we briefly summarize the main progress in this field.

LOADING BIOACTIVE AGENTS TO PROMOTE OSSEOINTEGRATION

Loading Anti-osteoporosis Drugs

Anti-osteoporosis drugs are categorized according to their functions and effects and include anti-catabolic drugs, anabolic drugs, and dual-acting drugs (**Figure 1**). The commonly used anti-catabolic agents for loading on the implant surfaces for local treatment include bisphosphonates, receptor activator of nuclear factor kB ligand (RANKL) antibodies, and selective estrogen receptor modulators (SERMs), which inhibit the activity and recruitment of osteoclasts or promote the apoptosis of osteoclasts. Bisphosphonates reduce osteoclast activity by inhibiting farnesyl pyrophosphate synthase and protein prenylation in the mevalonate pathway, and SERMs have an agonist effect on the estrogen receptor in osteoclasts, thereby inducing apoptosis (Apostu et al., 2017). Beck et al. (2019) immobilized the RANKL antibody denosumab on the implant surface to inhibit osteoclast differentiation, which could competitively block the interaction between receptor activator of nuclear factor kB and RANKL.

Being an anabolic drug, the parathyroid hormone (PTH) activates the cyclic adenosine monophosphate/protein kinase A (cAMP/PKA) signaling pathway by acting on the PTH receptors in osteoblasts to promote osteointegration (Tang et al., 2020). PTH 1–34 or teriparatide, a fragment of endogenous PTH, was the main regulator of calcium and phosphate metabolism in bone and the first anabolic drug proven to increase the osseointegration of implants. Other anabolic drugs targeting the Wnt/β-catenin signaling pathway have also been studied, such as romosozumab and DKK1 antagonists (Gennari et al., 2020).

Strontium ranelate and simvastatin play dual effects of promoting bone formation and inhibiting bone absorption through various signaling pathways (Apostu et al., 2017). Loading simvastatin and strontium ranelate on the implant surface effectively improves the local bone microenvironment, which is a promising method to enhance the osseointegration of implants in osteoporotic patients (Lai et al., 2018).

Loading Bioactive Molecules

The term "bioactive agents" is not limited only to therapeutic agents used in the clinic. The scope of this term has been broadened to bioactive molecules, including growth factors, proteins, and genes (Meng et al., 2016; Souza et al., 2019). Although the clinical application of these bioactive molecules is limited because of high production costs and concerns about biosafety, researchers have conducted a lot of research in this area. Loading various growth factors and proteins on the implant surfaces can promote osteogenic differentiation and the mineralization of bone marrow stem cells. Platelet-derived growth factor, insulin-like growth factor, fibroblast growth factor, vascular endothelial growth factor (VEGF), and bone morphogenetic protein (BMP) have been widely used in this field (Chen and Zou, 2019; Jurczak et al., 2020). VEGF can promote angiogenesis and regulate bone regeneration; Zavan et al. (2017) loaded VEGF on the surface of the implant *in vitro*, which effectively enhanced the osteogenic differentiation of stem cells. The release of BMP from the implant surface facilitated the proliferation, differentiation, and mineralization of bone cells *in vitro* and enhanced bone healing *in vivo* (Teng et al., 2019).

In addition, the extracellular matrix, such as type I collagen, showed good biological activity and osteoinductivity, which could improve adhesion and differentiation and promote bone-to-implant integration (Wang et al., 2019). Similarly, genes can be incorporated into the implant surface to transfect local osteoblasts or osteoclasts around the implants to promote osteoblastogenesis and inhibit osteoclastogenesis. Takanche et al. (2018) performed an experiment in which c-myb, a transcription factor, was delivered from chitosan-gold nanoparticle-coated titanium surface to the target tissue, where it promoted bone formation under osteoporotic conditions.

Modification by Bioactive Inorganic Elements

Some essential elements, including calcium (Ca), strontium (Sr), magnesium (Mg), zinc (Zn), and silicon (Si), can be also loaded on implants to stimulate osteogenesis (Lin et al., 2013; Liu et al., 2020, 2021). Compared with anti-osteoporosis drugs and bioactive molecules, more efficient strategies can be applied to construct inorganic element coating on the implant surface, which costs less (Asri et al., 2017). Ca is one of the essential micronutrients in bone, and bone structure abnormalities in osteoporotic patients occur as a result of the loss of Ca. At present, Ca-phosphate biomimetic coating on the implant surface is widely used to promote adhesion and differentiation of osteoblasts because of the chemical similarity between the synthetic materials and the bone mineral components (Xia et al., 2018). Sr is often used in the treatment of osteoporosis because of its dual role in bone regulation. An Sr-incorporated implant surface obtained by hydrothermal reaction could promote early osseointegration in osteoporotic rabbits (Lin et al., 2019). Moreover, Mg-immersed titanium-dioxide (TiO_2) coatings on the implant surface had both osteogenic and antibacterial effects (Zhao et al., 2019). Zn-modified coating on the implant surface facilitated the osteogenic differentiation of bone marrow-derived pericytes through the transforming growth factor-beta/Smad signaling pathway (Yu et al., 2017).

CONTROLLING THE RELEASE BEHAVIORS OF BIOACTIVE AGENTS

There are many ways to build bioactive organic or inorganic coatings on the implant surface, including physical methods (such as plasma spraying, ion implantation, and physical vapor deposition), chemical methods (such as acid etching and alkali-heat treatment), and electrochemical strategies (such as anodization, micro-arc oxidation, electropolymerization, and electrophoretic deposition) (Asri et al., 2017; Xue et al., 2020).

Covalent grafting and layer-by-layer self-assembly technology have been used to load bioactive proteins and growth factors. The release of bioactive agents from the implant surface is different because of the different construction methods of the coatings. In practical applications, however, we expect that the drugs loaded on the implants should maintain an effective concentration locally for a long time because burst release not only fails to maintain long-term efficacy but also might cause side effects due to toxicity in local tissues. The controlled release behaviors of the loaded bioactive agents can be achieved mainly by the following means: (1) constructing micro-/nano-structures on the implant surface, (2) introducing a stable immobilization strategy, and (3) encapsulating the bioactive agents.

Constructing Micro-/Nano-structures on the Implant Surface

Nano- and micro-topography construction on the implant surface not only can provide better biological responses but also may benefit drug adhesion and controlled release (Wang et al., 2018, 2020; Long et al., 2019). The modification of titanium dioxide nanotubes (TNTs) on implant surfaces can significantly increase the surface-to-volume ratio, and this porous surface provides more substantial space for drug loading with better biocompatibility (**Figure 2A**). More importantly, bioactive agents incorporated on the surface and inside TNTs achieve sustained steady release (Ion et al., 2020). A study conducted by Liu et al. (2018) showed that zoledronate adsorbed on the surface of TNTs can be released steadily for a long time to enhance implant osseointegration. Moreover, the drug release behaviors can be regulated by the diameter and length of TNTs by varying the process conditions of anodic oxidation. Hamlekhan et al. (2015) found that the diameter, length, aspect ratio, and volume were related to the prolonged release process. Moreover, the aspect ratio had the highest correlation with the release rate, and the release process of TNTs with high aspect ratio was significantly slow.

Introducing a Stable Immobilization Strategy

Bioactive agents can be attached to the implant surface by means of physical adsorption, such as dipping, spray coating, or drop casting, to promote local osseointegration (Alenezi et al., 2019). Physical adsorption characterized by Van der Waals forces or hydrogen bonds, however, leads to burst release at an early stage. Hence, bioactive agents can be covalently immobilized on the surface of titanium indirectly through a separate linker molecule that mediates the binding between titanium substrates and bioactive agents (**Figure 2B**), which can greatly improve the stability of coatings compared with physical adsorption (Jin et al., 2020). Linker molecules are generally synthetic linkers, such as silane and polyethylene glycol, or biologically derived molecules, such as heparin, dopamine, and chitosan. Linker molecules attach to hydroxyl-functionalized titanium substrates through condensation reactions, and then the bioactive agents are covalently immobilized on the functional group of the linker molecules (Stewart et al., 2019). Covalent bonding is more complex and time consuming than the other techniques, however, and the bioactive agents are not easily released because of the tight covalent bonding (Ma et al., 2020). The layer-by-layer self-assembly technique is being increasingly used for drug loading and controlled release, which can formulate polyelectrolyte multilayers by electrostatic attractions between components with different electric charges (**Figure 2C**). The self-assembly process is simple and mild, which does not affect the

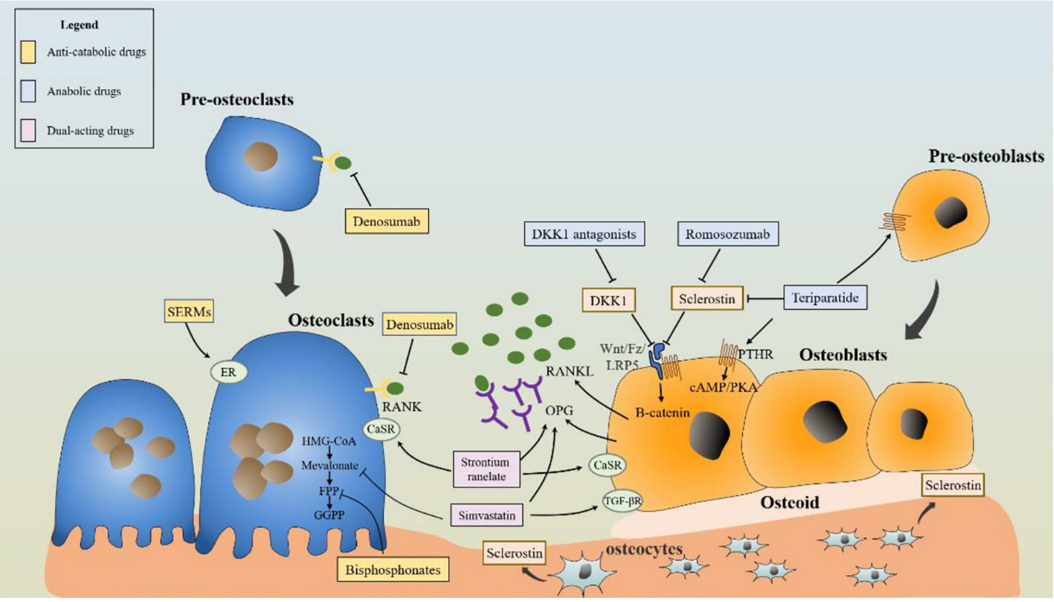

FIGURE 1 | Schematic diagram of anti-osteoporosis drugs acting on osteoblasts and osteoclasts.

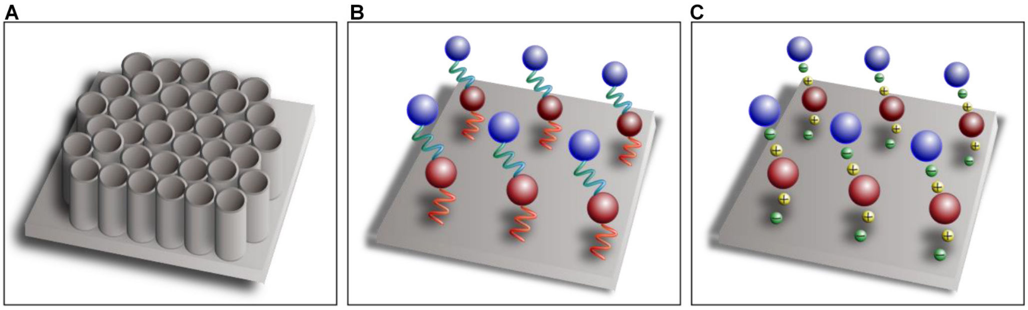

FIGURE 2 | Schematic diagram of titanium dioxide nanotubes **(A)**, covalent immobilization **(B)**, and layer-by-layer self-assembly technique **(C)**.

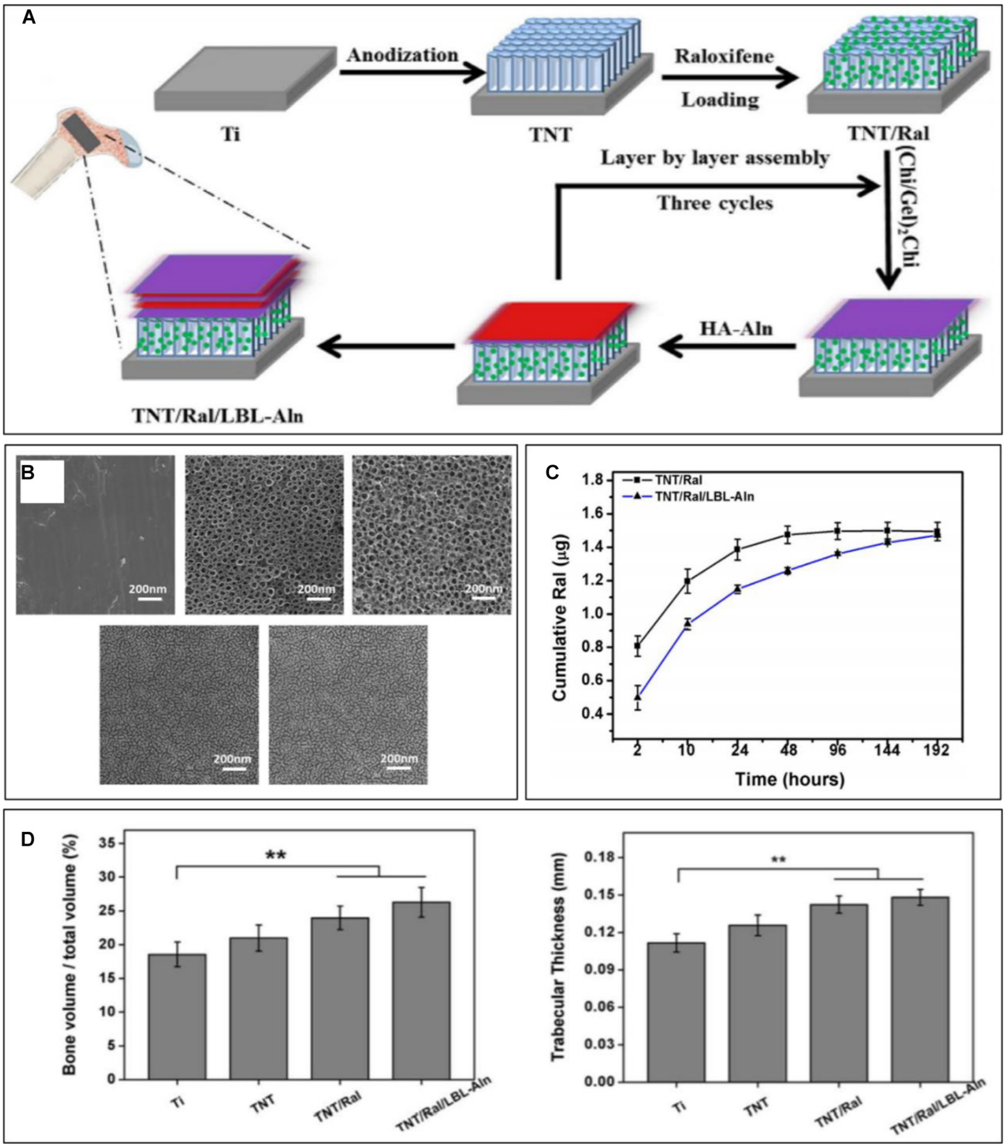

FIGURE 3 | Sustained raloxifene release from TiO_2 nanotubes to enhance osteointegration. **(A)** Schematic illustration of the fabrication of multilayered coating. **(B)** SEM images of each group. **(C)** Cumulative release curve of each sample. **(D)** Quantitative analysis of new bone volume and trabecular thickness [reprinted with permission from Mu et al. (2018); copyright (2018) Elsevier]. "**" Means Statistically significant differences are denoted by symbols, $^{**}p < 0.01$.

activity of the components, and sustained-release administration can be achieved by adjusting the physical and chemical properties of the materials (Shi et al., 2017).

Encapsulating the Bioactive Agents

Bioactive agents can be encapsulated by biocompatible materials with appropriate biodegradability, including natural organic polymers [such as chitosan (CS) and gelatin], synthetic organic polymers [such as hyaluronic acid (HA) and polycaprolactone (PCL)], and inorganic materials (such as calcium phosphate). With continuous degradation of the encapsulation materials, the bioactive agents are gradually released into the target area to achieve sustained release (**Figure 3**). To locally release microRNA-21, Wang et al. (2015) used CS and HA to encapsulate miRNA-21 to fabricate the CS/HA/miRNA-21 nanoparticles, which were then crosslinked with gelatin and loaded onto the implant surface, ultimately promoting the expression of the osteogenic gene. PCL and poly(lactic-co-glycolic) acid can also be used as encapsulation materials of bioactive agents to achieve local controlled release (Littuma et al., 2020). Biomimetic coprecipitation is a method of encapsulating bioactive agents with inorganic materials. With absorption of the hard coating, the bioactive agents are released gradually.

CONCLUSION AND PERSPECTIVE

Herein we have summarized the bioactive agents available to improve osseointegration in osteoporotic patients and the methods of controlled release of bioactive agents. High bioavailability and low toxicity in tissues outside the target make biomodification of implants suitable for achieving local osseointegration. Concerns about biosafety, however, limit the popularization of bioactive modification of implants, which is the direction of follow-up research. Implant osseointegration also must be accompanied by angiogenesis and ingrowth, and it is an inflammatory regulatory process, which is initially mediated by M1 phenotype macrophages and subsequently by M2. In addition, bacterial colonization and formation of plaque biofilms on the surface of implants may cause peri-implantitis, ultimately leading to failure of the implant. Therefore, angiogenesis and ingrowth, regulation of the inflammatory response, and inhibition of biofilm formation also should be considered in future studies.

AUTHOR CONTRIBUTIONS

CZ and TZ wrote the original draft equally. TG helped to prepare the manuscript. XW gave conceptualization on this manuscript. KL and PW led the conceptualization and project administration, and supervised the writing and editing of the manuscript. All authors contributed to the article and approved the submitted version.

FUNDING

The National Natural Science Foundation of China (81871490 and 81700954), Program of Shanghai Academic/Technology Research Leader (19XD1434500), and Two-Hundred Talent (20191819) supported this study.

ACKNOWLEDGMENTS

We thank LetPub (www.letpub.com) for its linguistic assistance during the preparation of this manuscript. We also thank Xudong Wang of Shanghai Ninth People's Hospital, China, for feedback on drafts of this article.

REFERENCES

Alenezi, A., Galli, S., Atefyekta, S., Andersson, M., and Wennerberg, A. (2019). Osseointegration effects of local release of strontium ranelate from implant surfaces in rats. *J. Mater. Sci. Mater. Med.* 30:116. doi: 10.1007/s10856-019-6314-y

Apostu, D., Lucaciu, O., Lucaciu, G. D., Crisan, B., Crisan, L., Baciut, M., et al. (2017). Systemic drugs that influence titanium implant osseointegration. *Drug Metab. Rev.* 49, 92–104. doi: 10.1080/03602532.2016.1277737

Asri, R. I. M., Harun, W. S. W., Samykano, M., Lah, N. A. C., Ghani, S. A. C., Tarlochan, F., et al. (2017). Corrosion and surface modification on biocompatible metals: a review. *Mater. Sci. Eng. C Mater. Biol. Appl.* 77, 1261–1274. doi: 10.1016/j.msec.2017.04.102

Beck, F., Hartmann, E. S., Koehler, M. I., Redeker, J. I., Schluessel, S., Schmitt, B., et al. (2019). Immobilization of denosumab on titanium affects osteoclastogenesis of human peripheral blood monocytes. *Int. J. Mol. Sci.* 20:1002. doi: 10.3390/ijms20051002

Buser, D., Sennerby, L., and De Bruyn, H. (2017). Modern implant dentistry based on osseointegration: 50 years of progress, current trends and open questions. *Periodontol 2000* 73, 7–21. doi: 10.1111/prd.12185

Chen, J., and Zou, X. (2019). Self-assemble peptide biomaterials and their biomedical applications. *Bioact. Mater.* 4, 120–131. doi: 10.1016/j.bioactmat.2019.01.002

Eguia, A., Bagan-Debon, L., and Cardona, F. (2020). Review and update on drugs related to the development of osteonecrosis of the jaw. *Med. Oral. Patol. Oral. Cir. Bucal.* 25, e71–e83. doi: 10.4317/medoral.23191

Gennari, L., Merlotti, D., Falchetti, A., Eller Vainicher, C., Cosso, R., and Chiodini, I. (2020). Emerging therapeutic targets for osteoporosis. *Expert. Opin. Ther. Targets* 24, 115–130. doi: 10.1080/14728222.2020.1726889

Hamlekhan, A., Sinha-Ray, S., Takoudis, C., Mathew, M. T., Sukotjo, C., Yarin, A. L., et al. (2015). Fabrication of drug eluting implants: study of drug release mechanism from titanium dioxide nanotubes. *J. Phys. D Appl. Phys.* 48, 275401. doi: 10.1088/0022-3727/48/27/275401

Ion, R., Necula, M. G., Mazare, A., Mitran, V., Neacsu, P., Schmuki, P., et al. (2020). Drug delivery systems based on titania nanotubes and active agents for enhanced osseointegration of bone implants. *Curr. Med. Chem.* 27, 854–902. doi: 10.2174/0929867326666190726123229

Jin, A., Wang, Y., Lin, K., and Jiang, L. (2020). Nanoparticles modified by polydopamine: working as "drug" carriers. *Bioact Mater.* 5, 522–541. doi: 10.1016/j.bioactmat.2020.04.003

Jurczak, P., Witkowska, J., Rodziewicz-Motowidło, S., and Lach, S. (2020). Proteins, peptides and peptidomimetics as active agents in implant surface functionalization. *Adv. Colloid. Interface Sci.* 276:102083. doi: 10.1016/j.cis.2019.102083

Lai, M., Yan, X., and Jin, Z. (2018). The response of bone cells to titanium surfaces modified by simvastatin-loaded multilayered films. *J. Biomater. Sci. Polym. Ed.* 29, 1895–1908. doi: 10.1080/09205063.2018.1517483

Lin, G., Zhou, C., Lin, M., Xu, A., and He, F. (2019). Strontium-incorporated titanium implant surface treated by hydrothermal reactions promotes early bone osseointegration in osteoporotic rabbits. *Clin. Oral. Implants Res.* 30, 777–790. doi: 10.1111/clr.13460

Lin, K., Xia, L., Li, H., Jiang, X., Pan, H., Xu, Y., et al. (2013). Enhanced osteoporotic bone regeneration by strontium-substituted calcium silicate bioactive ceramics. *Biomaterials* 34, 10028–10042. doi: 10.1016/j.biomaterials.2013.09.056

Littuma, G. J. S., Sordi, M. B., Borges Curtarelli, R., Aragonês, Á, da Cruz, A. C. C., and Magini, R. S. (2020). Titanium coated with poly(lactic-co-glycolic) acid incorporating simvastatin: biofunctionalization of dental prosthetic abutments. *J. Periodontal. Res.* 55, 116–124. doi: 10.1111/jre.12695

Liu, J., Pathak, J. L., Hu, X., Jin, Y., Wu, Z., Al-Baadani, M. A., et al. (2018). Sustained release of zoledronic acid from mesoporous TiO2-Layered implant enhances implant osseointegration in osteoporotic condition. *J. Biomed. Nanotechnol.* 14, 1965–1978. doi: 10.1166/jbn.2018.2635

Liu, L., Wang, X., Zhou, Y., Cai, M., Lin, K., Fang, B., et al. (2020). The synergistic promotion of osseointegration by nanostructure design and silicon substitution of hydroxyapatite coatings in a diabetic model. *J. Mater. Chem. B* 8, 2754–2767. doi: 10.1039/c9tb02882j

Liu, L., Yu, F., Li, L., Zhou, L., Zhou, T., Xu, Y., et al. (2021). Bone marrow stromal cells stimulated by strontium-substituted calcium silicate ceramics: release of exosomal miR-146a regulates osteogenesis and angiogenesis. *Acta Biomater.* 119, 444–457. doi: 10.1016/j.actbio.2020.10.038

Long, E. G., Buluk, M., Gallagher, M. B., Schneider, J. M., and Brown, J. L. (2019). Human mesenchymal stem cell morphology, migration, and differentiation on micro and nano-textured titanium. *Bioact. Mater.* 4, 249–255. doi: 10.1016/j.bioactmat.2019.08.001

Ma, Q., Jiang, N., Liang, S., Chen, F., Fang, L., Wang, X., et al. (2020). Functionalization of a clustered TiO(2) nanotubular surface with platelet derived growth factor-BB covalent modification enhances osteogenic differentiation of bone marrow mesenchymal stem cells. *Biomaterials* 230:119650. doi: 10.1016/j.biomaterials.2019.119650

Meng, H. W., Chien, E. Y., and Chien, H. H. (2016). Dental implant bioactive surface modifications and their effects on osseointegration: a review. *Biomark Res.* 4:24. doi: 10.1186/s40364-016-0078-z

Mu, C., Hu, Y., Huang, L., Shen, X., Li, M., Li, L., et al. (2018). Sustained raloxifene release from hyaluronan-alendronate-functionalized titanium nanotube arrays capable of enhancing osseointegration in osteoporotic rabbits. *Mater. Sci. Eng. C Mater. Biol. Appl.* 82, 345–353. doi: 10.1016/j.msec.2017.08.056

Shi, Q., Qian, Z., Liu, D., and Liu, H. (2017). Surface modification of dental titanium implant by layer-by-layer electrostatic self-assembly. *Front. Physiol.* 8:574. doi: 10.3389/fphys.2017.00574

Souza, J. C. M., Sordi, M. B., Kanazawa, M., Ravindran, S., Henriques, B., Silva, F. S., et al. (2019). Nano-scale modification of titanium implant surfaces to enhance osseointegration. *Acta Biomater.* 94, 112–131. doi: 10.1016/j.actbio.2019.05.045

Stewart, C., Akhavan, B., Wise, S. G., and Bilek, M. M. M. (2019). A review of biomimetic surface functionalization for bone-integrating orthopedic implants: mechanisms, current approaches, and future directions. *Prog. Mater. Sci.* 106:100588. doi: 10.1016/j.pmatsci.2019.100588

Takanche, J. S., Kim, J. E., Kim, J. S., Lee, M. H., Jeon, J. G., Park, I. S., et al. (2018). Chitosan-gold nanoparticles mediated gene delivery of c-myb facilitates osseointegration of dental implants in ovariectomized rat. *Artif Cells Nanomed. Biotechnol.* 46, S807–S817. doi: 10.1080/21691401.2018.1513940

Tang, J., Yan, D., Chen, L., Shen, Z., Wang, B., Weng, S., et al. (2020). Enhancement of local bone formation on titanium implants in osteoporotic rats by biomimetic multilayered structures containing parathyroid hormone (PTH)-related protein. *Biomed. Mater.* 15:045011. doi: 10.1088/1748-605X/ab7b3d

Teng, F. Y., Tai, I. C., Ho, M. L., Wang, J. W., Weng, L. W., Wang, Y. J., et al. (2019). Controlled release of BMP-2 from titanium with electrodeposition modification enhancing critical size bone formation. *Mater. Sci. Eng. C Mater. Biol. Appl.* 105:109879. doi: 10.1016/j.msec.2019.109879

Wang, H., Zhang, X., Wang, H., Zhang, J., Li, J., Ruan, C., et al. (2018). Enhancing the osteogenic differentiation and rapid osseointegration of 3d printed ti6al4v implants via nano-topographic modification. *J. Biomed. Nanotechnol.* 14, 707–715. doi: 10.1166/jbn.2018.2551

Wang, H., Liu, J., Wang, C., Shen, S. G., Wang, X., and Lin, K. (2020). The synergistic effect of 3D-printed microscale roughness surface and nanoscale feature on enhancing osteogenic differentiation and rapid osseointegration. *J. Mater. Sci. Technol.* (in press). doi: 10.1016/j.jmst.2019.12.030

Wang, J., He, X. T., Xu, X. Y., Yin, Y., Li, X., Bi, C. S., et al. (2019). Surface modification via plasmid-mediated pLAMA3-CM gene transfection promotes the attachment of gingival epithelial cells to titanium sheets in vitro and improves biological sealing at the transmucosal sites of titanium implants in vivo. *J. Mater. Chem. B* 7, 7415–7427. doi: 10.1039/c9tb01715a

Wang, Z., Wu, G., Feng, Z., Bai, S., Dong, Y., Wu, G., et al. (2015). Microarc-oxidized titanium surfaces functionalized with microRNA-21-loaded chitosan/hyaluronic acid nanoparticles promote the osteogenic differentiation of human bone marrow mesenchymal stem cells. *Int. J. Nanomed.* 10, 6675–6687. doi: 10.2147/IJN.S94689

Xia, L., Xie, Y., Fang, B., Wang, X., and Lin, K. (2018). In situ modulation of crystallinity and nano-structures to enhance the stability and osseointegration of hydroxyapatite coatings on Ti-6Al-4V implants. *Chem. Eng. J.* 347, 711–720. doi: 10.1016/j.cej.2018.04.045

Xue, T., Attarilar, S., Liu, S., Liu, J., Song, X., Li, L., et al. (2020). Surface modification techniques of titanium and its alloys to functionally optimize their biomedical properties: thematic review. *Front. Bioeng. Biotechnol.* 8:603072. doi: 10.3389/fbioe.2020.603072

Yu, J., Xu, L., Li, K., Xie, N., Xi, Y., Wang, Y., et al. (2017). Zinc-modified calcium silicate coatings promote osteogenic differentiation through TGF-beta/Smad pathway and osseointegration in osteopenic rabbits. *Sci. Rep.* 7:3440. doi: 10.1038/s41598-017-03661-3665

Zavan, B., Ferroni, L., Gardin, C., Sivolella, S., Piattelli, A., and Mijiritsky, E. (2017). Release of VEGF from dental implant improves osteogenetic process: preliminary in vitro tests. *Materials (Basel)* 10:1052. doi: 10.3390/ma10091052

Zhang, J., Liu, J., Wang, C., Chen, F., Wang, X., and Lin, K. (2020). A comparative study of the osteogenic performance between the hierarchical micro/submicro-textured 3D-printed Ti6Al4V surface and the SLA surface. *Bioact. Mater.* 5, 9–16. doi: 10.1016/j.bioactmat.2019.12.008

Zhao, C., Lin, K., and Wang, X. (2020). Maintenance and modulation of stem cells stemness based on biomaterial designing via chemical and physical signals. *Appl. Mater. Today* 19:100614.

Zhao, Q., Yi, L., Jiang, L., Ma, Y., Lin, H., and Dong, J. (2019). Osteogenic activity and antibacterial ability on titanium surfaces modified with magnesium-doped titanium dioxide coating. *Nanomedicine (Lond)* 14, 1109–1133. doi: 10.2217/nnm-2018-2413

Conflict of Interest: The authors declare that the research was conducted in the absence of any commercial or financial relationships that could be construed as a potential conflict of interest.

Advantages of publishing in Frontiers

OPEN ACCESS
Articles are free to read
for greatest visibility
and readership

FAST PUBLICATION
Around 90 days
from submission
to decision

HIGH QUALITY PEER-REVIEW
Rigorous, collaborative,
and constructive
peer-review

TRANSPARENT PEER-REVIEW
Editors and reviewers
acknowledged by name
on published articles

Frontiers
Avenue du Tribunal-Fédéral 34
1005 Lausanne | Switzerland

Visit us: www.frontiersin.org
Contact us: frontiersin.org/about/contact

REPRODUCIBILITY OF RESEARCH
Support open data
and methods to enhance
research reproducibility

DIGITAL PUBLISHING
Articles designed
for optimal readership
across devices

FOLLOW US
@frontiersin

IMPACT METRICS
Advanced article metrics
track visibility across
digital media

EXTENSIVE PROMOTION
Marketing
and promotion
of impactful research

LOOP RESEARCH NETWORK
Our network
increases your
article's readership